

VOLUME 76

AUGUST 31, 1972

NUMBER 18

JPCHAX

THE JOURNAL OF

PHYSICAL

CHEMISTRY

ห้องสมุด กรมวิทยาศาสตร์

PUBLISHED BIWEEKLY BY THE AMERICAN CHEMICAL SOCIETY

THE JOURNAL OF PHYSICAL CHEMISTRY

BRYCE CRAWFORD, Jr., *Editor*

STEPHEN PRAGER, *Associate Editor*

ROBERT W. CARR, Jr., FREDERIC A. VAN-CATLEDGE, *Assistant Editors*

EDITORIAL BOARD: A. O. ALLEN (1970-1974), J. R. BOLTON (1971-1975),
F. S. DAINTON (1972-1976), M. FIXMAN (1970-1974),
H. S. FRANK (1970-1974), R. R. HENTZ (1972-1976), J. R. HUIZENGA (1969-1973),
W. J. KAUZMANN (1969-1973), R. L. KAY (1972-1976), W. R. KRIGBAUM (1969-1973),
R. A. MARCUS (1968-1972), W. J. MOORE (1969-1973), J. A. POPLE (1971-1975),
B. S. RABINOVITCH (1971-1975), H. REISS (1970-1974), S. A. RICE (1969-1975),
F. S. ROWLAND (1968-1972), R. L. SCOTT (1968-1972),
R. SEIFERT (1968-1972), W. A. ZISMAN (1972-1976)

CHARLES R. BERTSCH, *Manager, Editorial Production*

AMERICAN CHEMICAL SOCIETY, 1155 Sixteenth St., N.W., Washington, D. C. 20036

Books and Journals Division

JOHN K. CRUM, *Director*

JOSEPH H. KUNEY, *Head, Business Operations Department*

RUTH REYNARD, *Assistant to the Director*

©Copyright, 1972, by the American Chemical Society. Published biweekly by the American Chemical Society at 20th and Northampton Sts., Easton, Pa. 18042. Second-class postage paid at Washington, D. C., and at additional mailing offices.

All manuscripts should be sent to *The Journal of Physical Chemistry*, Department of Chemistry, University of Minnesota, Minneapolis, Minn. 55455.

Additions and Corrections are published once yearly in the final issue. See Volume 75, Number 26 for the proper form.

Extensive or unusual alterations in an article after it has been set in type are made at the author's expense, and it is understood that by requesting such alterations the author agrees to defray the cost thereof.

The American Chemical Society and the Editor of *The Journal of Physical Chemistry* assume no responsibility for the statements and opinions advanced by contributors.

Correspondence regarding accepted copy, proofs, and reprints should be directed to Editorial Production Office, American Chemical Society, 20th and Northampton Sts., Easton, Pa. 18042. Manager: CHARLES R. BERTSCH. Assistant Editor: EDWARD A. BORGER. Editorial Assistant: JOSEPH E. YURVATI.

Advertising Office: Centcom, Ltd. (formerly Century Communications Corporation), 142 East Avenue, Norwalk, Conn. 06851.

Business and Subscription Information

Remittances and orders for subscriptions and for single copies,

notices of changes of address and new professional connections, and claims for missing numbers should be sent to the Subscription Service Department, American Chemical Society, 1155 Sixteenth St., N.W., Washington, D. C. 20036. Allow 4 weeks for changes of address. Please include an old address label with the notification.

Claims for missing numbers will not be allowed (1) if received more than sixty days from date of issue, (2) if loss was due to failure of notice of change of address to be received before the date specified in the preceding paragraph, or (3) if the reason for the claim is "missing from files."

Subscription rates (1972): members of the American Chemical Society, \$20.00 for 1 year; to nonmembers, \$60.00 for 1 year. Those interested in becoming members should write to the Admissions Department, American Chemical Society, 1155 Sixteenth St., N.W., Washington, D. C. 20036. Postage to Canada and countries in the Pan-American Union, \$5.00; all other countries, \$6.00. Single copies for current year: \$3.00. Rates for back issues from Volume 56 to date are available from the Special Issues Sales Department, 1155 Sixteenth St., N.W., Washington, D. C. 20036.

This publication and the other ACS periodical publications are now available on microfilm. For information write to: MICROFILM, Special Issues Sales Department, 1155 Sixteenth St., N.W., Washington, D. C. 20036.

THE JOURNAL OF PHYSICAL CHEMISTRY

Volume 76, Number 18 August 31, 1972

JPCHAx 76(18) 2485-2642 (1972)

Yields and Reactions of Lowest Excited Singlet and Triplet States in the Radiolysis of Naphthalene and 1-Methylnaphthalene	R. A. Holroyd* and C. Capellos	2485
Ultraviolet Photochemistry of Formatepentaamminecobalt(III) Ion in Aqueous Solution. Hydrogen Atom Formation and Oxygen \rightarrow Carbon Linkage Isomerization	Evan R. Kantrowitz, Morton Z. Hoffman,* and Kenneth M. Schilling	2492
Kinetic Analysis and Mechanism of Chlorine-38 and Bromine-82 Recoil Reactions in $K_2[ReBr_6]/K_2[ReCl_6]$ Mixed Crystals	K. Rössler, J. Otterbach, and G. Stöcklin*	2499
Identity Scrambling and Isomerization Networks in Systems of Excited Alkyl Radicals	C. W. Larson,* Peter T. Chua, and B. S. Rabinovitch	2507
On the Lifetime of Trifluoromethyl Radical in Aqueous Solution	Jochen Lilie, D. Behar, Richard J. Sujdak, and Robert H. Schuler*	2517
Hot-Atom Chemistry of Carbon-14 in Solid Benzene at Kinetic Energies at or below 5 Electron Volts	Jacques Lintermans, Wallace Erwin, and Richard M. Lemmon*	2521
Electron Spectroscopy for Chemical Analysis (ESCA) Studies on Catalysts. Rhodium on Charcoal	J. S. Brinen* and A. Melera	2525
Temperature Dependence of the Electron Spin Resonance Spectra of Zinc Oxide Powder	K. M. Sancier	2527
Oxidation of Metal Films by Nitrous Oxide.	S. A. Isa and J. M. Saleh*	2530
Dielectric Evidence of Two-Dimensional Condensation of Halides Adsorbed on Nonporous Sodium Chloride	G. K. Kouvarellis, R. McIntosh,* and N. S. Snider	2535
Diffusion-Controlled Condensation and Evaporation in Wedge-Shaped Pores	Jean-Yves Parlange	2543
Surface Charge Development on Porous Silica in Aqueous Solution.	R. P. Abendroth	2547
Resistive Effects in Thin Electrochemical Cells: Digital Simulations of Electrochemistry in Electron Spin Resonance Cells	Ira B. Goldberg, Allen J. Bard,* and Stephen W. Feldberg	2550
Irreversible Potentiometric Behavior of Isotactic Poly(methacrylic acid)	J. C. Leyte,* H. M. R. Arbouw-van der Veen, and L. H. Zuiderweg	2559
Molecular Structure of Ethanol- d_1 Solutions. A Near-Infrared Study of Hydrogen Bonding	Aaron N. Fletcher	2562
Tracer Diffusion and Viscosity Study at 25° in Binary and Ternary Liquid Systems	Keichi Aoyagi and John G. Albright*	2572
Excess Partial Molal Heat Capacities of <i>n</i> -Tetraamylammonium Bromide in Water from 10 to 80° and in Aqueous <i>tert</i> -Butyl Alcohol Solvent System at 30° and the Effects on the Water Structure	R. K. Mohanty, S. Sunder, and J. C. Ahluwalia*	2577
Thermodynamics of Tetrabutylammonium Bromide in Aqueous Sodium Chloride and the Effects on the Water Structure	B. Chawla and J. C. Ahluwalia*	2582
Adsorption Isotherm and Surface Area Determination below the Triple Point.	G. G. Litvan	2584
Chromatographic Peak Shapes. Their Origin and Dependence on the Experimental Parameters	Eli Grushka	2586
The Crystal Structures of Hydrated and Dehydrated Thallium-Exchanged Zeolite A	Paul E. Riley, Karl Seff,* and David P. Shoemaker	2593
The Crystal Structure of an Ammonia Sorption Complex of Zeolite 4A	Russell Y. Yanagida and Karl Seff*	2597

The Crystal Structure of a Sulfur Sorption Complex of Zeolite 4A	Karl Seff	2601
Transitions in Mesophase Forming Systems. IV. Transformation Behavior and Pretransition Effects in <i>p</i> -Azoxyanisole	Fraser P. Price* and Joachim H. Wendorff	2605
Formation of Vapor Nuclei in High Temperature Melts	Herman S. Levine	2609
Two Familiar Gas Reactions at Suprahigh Pressure	Melvyn L. Dutton, Don L. Bunker,* and Harold H. Harris	2614
The Photochemistry of the Monoxalatoiron(III) Ion	G. D. Cooper and B. A. DeGraff*	2618
Effects of Neutron Radiation on the Catalytic Activities of Lithium-Doped Copper, Nickel, and Copper-Nickel	Toyosaburo Takeuchi,* Daisaku Miyatani, Yutaka Takada, and Kinji Okamoto	2625
Photochemical Reactions of Borazine with Ammonia and Methyl Bromide	Melvin A. Neiss and Richard F. Porter*	2630

COMMUNICATIONS TO THE EDITOR

On the Existence of a Spin-Forbidden Predissociation in the Mass Spectrum of Isocyanic Acid	C. G. Rowland, J. H. D. Eland, and C. J. Danby*	2636
Electron Spin Resonance Evidence for the Photosensitized Dissociation of Hydrogen Molecules on Vanadium Oxide	Takashi Katsu, Mitsuo Sato, and Yuzaburo Fujita*	2637
Hot-Atom Reactions of Iodine in the Liquid Phase Induced by X-Ray Resonance Absorption	Bodo Diehn* and V. George Thomas	2639
Time-Dependent Scavenging of Trapped Electrons in 2-Methyltetrahydrofuran Glass at 77°K	J. R. Miller and John E. Willard*	2641

AUTHOR INDEX

Abendroth, R. P., 2547	DeGraff, B. A., 2618	Kantrowitz, E. R., 2492	Okamoto, K., 2625	Seff, K., 2593, 2597
Ahluwalia, J. C., 2577, 2582	Diehn, B., 2639	Katsu, T., 2637	Otterbach, J., 2499	2601
Albright, J. G., 2572	Dutton, M. L., 2614	Kouvarellis, G. K., 2535		Shoemaker, D. P., 2593
Aoyagi, K., 2572	Eland, J. H. D., 2636	Larson, C. W., 2507	Parlange, J.-Y., 2543	Snider, N. S., 2535
Arbouw-van der Veen, H. M. R., 2559	Erwin, W., 2521	Lemmon, R. M., 2521	Porter, R. F., 2630	Stöcklin, G., 2499
	Feldberg, S. W., 2550	Levine, H. S., 2609	Price, F. P., 2605	Sujdak, R. J., 2517
Bard, A. J., 2550	Fletcher, A. N., 2562	Leyte, J. C., 2559		Sunder, S., 2577
Behar, D., 2517	Fujita, Y., 2637	Lilie, J., 2517	Rabinovitch, B. S., 2507	Takada, Y., 2625
Brinen, J. S., 2525	Goldberg, I. B., 2550	Lintermans, J., 2521	Riley, P. E., 2593	Takeuchi, T., 2625
Bunker, D. L., 2614	Grushka, E., 2586	Litvan, G. G., 2584	Rössler, K., 2499	Thomas, V. G., 2639
	Harris, H. H., 2614	McIntosh, R., 2535	Rowland, C. G., 2636	
Capellos, C., 2485	Hoffman, M. Z., 2492	Melera, A., 2525		Wendorff, J. H., 2605
Chawla, B., 2582	Holroyd, R. A., 2485	Miller, J. R., 2641	Saleh, J. M., 2530	Willard, J. E., 2641
Chua, P. T., 2507	Isa, S. A., 2530	Miyatani, D., 2625	Sancier, K. M., 2527	
Cooper, G. D., 2618		Mohanty, R. K., 2577	Sato, M., 2637	Yanagida, R. Y., 2597
		Neiss, M. A., 2630	Schilling, K. M., 2492	
Danby, C. J., 2636			Schuler, R. H., 2517	Zuiderweg, L. H., 2559

In papers with more than one author the name of the author to whom inquiries about the paper should be addressed is marked with an asterisk in the by-line.

Yields and Reactions of Lowest Excited Singlet and Triplet States in the Radiolysis of Naphthalene and 1-Methylnaphthalene¹

by R. A. Holroyd*

Chemistry Department, Brookhaven National Laboratory, Upton, New York 11973

and C. Capellos

Feltman Research Laboratory, Picatinny Arsenal, Dover, New Jersey 07801 (Received March 10, 1972)

Publication costs assisted by Brookhaven National Laboratory

The yields of the lowest excited singlet and triplet states in the pulse radiolysis of liquid naphthalene and 1-methylnaphthalene were determined by measuring the triplet state absorption under various conditions. The yield of the triplet is enhanced by the addition of benzophenone and reduced by carbon tetrachloride. Both of these solutes quench the fluorescence by approximately 50% at 2 mM. The results are interpreted in terms of excitation transfer. The yields of the lowest states formed by ion recombination and by direct excitation in naphthalene are $G(^3N^*) = 3.8$, $G(^1N^*) = 2.4$; and in 1-methylnaphthalene $G(^3M^*) = 3.3$, $G(^1M^*) = 2.7$. The results provide a measure of the relative importance of various modes of excitation in radiolysis. Intersystem crossing from the excimer in 1-methylnaphthalene occurs with comparable efficiency as a dilute solution at 25°. However at 85° the intersystem crossing efficiency is reduced to 6% in molten naphthalene and 17% in methylnaphthalene. The decrease in lifetime of fluorescence at higher temperatures is shown not to be due to enhanced intersystem crossing but to a faster rate of internal conversion.

Introduction

It is well known that excited states are formed in the radiolysis of aromatic compounds, and recent studies have been concerned with establishing the yields of such states.^{2a} The yields of the lowest excited singlet and triplet states of benzene were measured in a pulse radiolysis study to be $G = 1.6$ and 1.8 molecules/100 eV, respectively;^{2b} in addition, evidence for the formation of a higher singlet state (¹E_{1u}) was obtained.² However, methods based on cis-trans isomerization of solutes during steady-state γ irradiation have indicated the triplet yield to be higher, 4.1-4.7.^{3a} A study^{3b} based on the decomposition of 3,5-cycloheptadienone in benzene showed that the yield of triplets is 4.0 and of singlets is 1.4. A recent reinvestigation^{3c} of benzene by pulse radiolysis utilizing several solutes as triplet acceptors has shown that $G(\text{triplets})$ is 4.2 in agreement with the chemical methods.

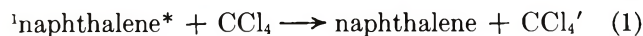
In this work the initial yield of the lowest excited singlet state, $G(^1N^*)^\circ$, and triplet state, $G(^3N^*)^\circ$, and the yield of triplets formed by intersystem crossing in naphthalene and 1-methylnaphthalene are measured.^{3d} The triplet yield is determined spectroscopically; its absorption band peaks at 420 μ in naphthalene.⁴ The singlet yield is deduced from the change in triplet yield on addition of solutes.

(1) Work performed under the auspices of the U. S. Atomic Energy Commission.

(2) (a) J. K. Thomas, *Ann. Rev. Phys. Chem.*, **21**, 17 (1970); (b) R. Cooper and J. K. Thomas, *J. Chem. Phys.*, **48**, 5097 (1968).

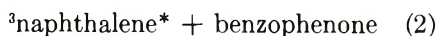
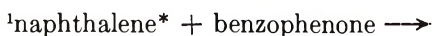
(3) (a) R. B. Cundall and W. Tippett, *Advan. Chem. Ser.*, **No. 82**, 387 (1968); R. R. Hentz and H. G. Altmiller, *J. Phys. Chem.*, **74**, 2646 (1970); (b) R. R. Hentz and L. M. Perkey, *ibid.*, **74**, 3047 (1970); (c) J. H. Baxendale and M. Fiti, *Trans. Faraday Soc.*, **68**, 218 (1972). (d) The symbol ¹N* is used to denote the lowest excited singlet state, which includes both the monomeric and excimer states. The symbol ³N* is used to denote the lowest excited triplet state.

To measure the *initial* yield of triplet excited states requires the use of a solute which quenches the singlet state (to remove the contribution of intersystem crossing) but leaves the triplet unaffected. Aromatic compounds are unsuitable for this since if their triplet energy is lower than that of naphthalene, they will also quench the triplet, and if higher, they may enhance the triplet yield. Carbon tetrachloride is a suitable quencher as it quenches the singlet of naphthalene to form a vibrationally excited CCl_4 molecule which dissociates; the quenching rate constant k_1 is reported



to be approximately $2 \times 10^8 \text{ M}^{-1} \text{ sec}^{-1}$ in cyclohexane.⁵ This reaction does not produce naphthalene triplet states;⁶ thus the yield of triplet naphthalene in the presence of CCl_4 provides a measure of $G(^3\text{N}^*)^\circ$. Fortunately the naphthalene triplet is not readily quenched by CCl_4 . The difference in the yield of triplets formed in the presence and absence of CCl_4 provides a measure of the yield of triplets formed by intersystem crossing. Since the rate of excitation transfer is enhanced by excitation migration in naphthalene,⁷ the concentration of solute necessary to quench singlets can be kept low and ionic reactions are minimized. The previous suggestion⁴ that intersystem crossing is of minor importance in molten naphthalene is confirmed by this study.

The yield of singlet excited states is obtained from the triplet yield in the presence of benzophenone. Benzophenone quenches the singlet state forming singlet benzophenone which intersystem crosses in solution with 99% efficiency^{8a} in 5 psec⁹ to the triplet state. The benzophenone triplet transfers its energy to naphthalene since the triplet energy of benzophenone is greater than that of naphthalene.^{8b} The net effect of benzophenone is that of a catalyst enhancing intersystem



crossing in naphthalene, reaction 2. Thus the yield of triplet naphthalene in the presence of sufficient benzophenone can be used to measure the total yield of excited states, $G(^1\text{N}^*)^\circ + G(^3\text{N}^*)^\circ$.

Experimental Section

Naphthalene (Matheson) was purified by several recrystallizations from ethyl alcohol. 1-Methylnaphthalene (Eastman Kodak) was passed through activated silica gel; this completely removed an impurity absorbing at 410 $\text{m}\mu$, and the product showed no spectroscopically detectable impurities.

The pulse radiolysis cells were made of rectangular quartz tubing ($0.5 \times 2 \text{ cm}$) equipped with Suprasil windows. To each cell was attached a 25-cm³ reservoir in which the samples of naphthalene were placed and degassed by repeated cycles of freeze-pump-melt. Samples were irradiated *in vacuo*.

For pulse radiolysis the naphthalene samples were placed in a thermostat made of styrofoam which also contained the cell holder and was equipped with double quartz windows to pass the analyzing light beam. The temperature was maintained at approximately 85° by a thermistor-type temperature regulator (Yellow Springs Inst. Co.) which controlled current to a heat gun mounted in the thermostat wall. The analyzing light from a 450-W Xe lamp was filtered to remove light of short wavelengths which would be absorbed by the naphthalene. The filtered beam crossed the reaction cell three times (total optical path = 6.1 cm) before emerging and was brought out of the Van de Graaff vault by mirrors and focused on the front slit of a Bausch & Lomb monochromator. Light from the monochromator fell on an Amperex XP1003 P M tube, and the signal was fed to a dual-beam oscilloscope.

Samples received 2- μsec pulses of 1.85-MeV electrons ($\sim 800 \text{ rads}$) from a Van de Graaff accelerator. The dose was monitored by integrating the charge collected on the cell and holder. The ferrous sulfate dosimeter was used for absolute dosimetry; the dose was calculated from the change in OD at 305 $\text{m}\mu$, 5 sec after a 3-msec pulse.¹⁰ The dose in the naphthalene was calculated from the dose in the ferrous sulfate solution by correcting for differences in electron density.

Data analysis was complicated by the fluorescence and by the short life of the naphthalene triplet relative to the pulse length. The former was accounted for by measuring the fluorescence with the analyzing light off and adding it to the signal. Because of the short lifetime of the triplet, the OD data was first extrapolated back to the end of the pulse and then corrected for decay in the pulse by relation I, where k is the first-order rate constant for decay of the triplet and Δt is

$$\text{OD}_{\text{cor}} = \text{OD}_{t=\Delta t} \times k\Delta t / (1 - e^{-k\Delta t}) \quad (I)$$

the length of the pulse.

Some of the 1-methylnaphthalene experiments were done using a 705 system Febetron as the electron source. In this case the analyzing light was flashed which minimized the fluorescence correction; also since the pulse length was less than 0.1 μsec , correction for decay in the pulse was unnecessary.

Measurements of the absolute yield of excited states required determination of the extinction coefficients

(4) L. M. Thread, F. C. Peterson, and R. A. Holroyd, *J. Chem. Phys.*, **51**, 4126 (1969).

(5) G. Kallmann-Oster, *Acta Phys. Pol.*, **26**, 435 (1964).

(6) D. Schulte-Frohlinde and R. Pfefferkorn, *Ber. Bunsenges. Phys. Chem.*, **72**, 330 (1968).

(7) R. A. Holroyd, L. M. Theard, and F. C. Peterson, *J. Phys. Chem.*, **74**, 1895 (1970).

(8) J. G. Calvert and J. N. Pitts, Jr., "Photochemistry," Wiley, New York, N. Y., 1967, (a) p 309; (b) p 298.

(9) P. M. Rentzepis, *Science*, **169**, 239 (1970).

(10) R. J. Hagemann and H. A. Schwarz, *J. Phys. Chem.*, **71**, 2694 (1967).

of the triplets in the neat liquids. For naphthalene this was accomplished by integrating the triplet absorption spectrum plotted as relative OD *vs.* wave number. Since the f value of the naphthalene triplet is 0.12 in several solvents,¹¹ it was assumed to be the same in naphthalene. The extinction coefficient at the maximum (420 m μ) necessary to make the f value = 0.12 in eq II is $\epsilon_{420} = 7100$.

$$f = 4.33 \times 10^{-9} \int \epsilon(\nu) d\nu \quad (\text{II})$$

For methylnaphthalene the f value of the triplet is not known; however, it was assumed to be constant independent of solvent. The extinction coefficient of the methylnaphthalene triplet was first determined to be $\epsilon_{420} = 14,200$ in cyclohexane by the benzophenone method.¹² In this method reduction in yield of ketyl radicals in a 0.1 M benzophenone solution on addition of small amounts of methylnaphthalene (5–20 mM) is measured along with the corresponding increase in yield of methylnaphthalene triplet. The value of ϵ_{420} in methylnaphthalene was then determined to be 6350, from the ratio of the integrated triplet spectra in cyclohexane to that in methylnaphthalene.

Results and Discussion

Naphthalene. In the pulse radiolysis of naphthalene both the lowest excited singlet and triplet states have been detected.⁴ The triplet absorption is broad with a maximum at 420 m μ ; its lifetime is 1.2 μsec at 100°. The singlet, which was also detected in absorption, was shown to be partially in the form of the excimer by the fluorescence. The excimer emits at wavelengths around 400 m μ .

When either benzophenone or carbon tetrachloride is added to naphthalene an intermediate is observed which has the same absorption spectrum as the triplet. The half-life of the triplet is $\sim 2 \mu\text{sec}$ at 85° with or without these solutes present. The solutions of benzophenone as well as pure naphthalene are relatively radiation stable, and samples repetitively pulsed give reproducible results. However solutions of CCl_4 are unstable, as a product is formed by radiolysis which quenches the triplet state. Also it is necessary to filter the analyzing light to prevent photolysis, which has the same effect as radiolysis for these solutions. A long-lived free radical is formed with CCl_4 present which absorbs weakly from 370 to 420 m μ . There is no absorption at 540 m μ which can be associated with the charge-transfer complex of chlorine with naphthalene, detected in dilute solutions of naphthalene in CCl_4 .¹³

In pure naphthalene the yield of triplet excited states is 4.0 molecules/100 eV. The addition of small amounts of benzophenone causes a dramatic increase in this yield (Figure 1). The effect saturates at higher concentrations where $G = 6.2$. The net increase of 2.2 is a lower limit for the yield of singlets; the yield

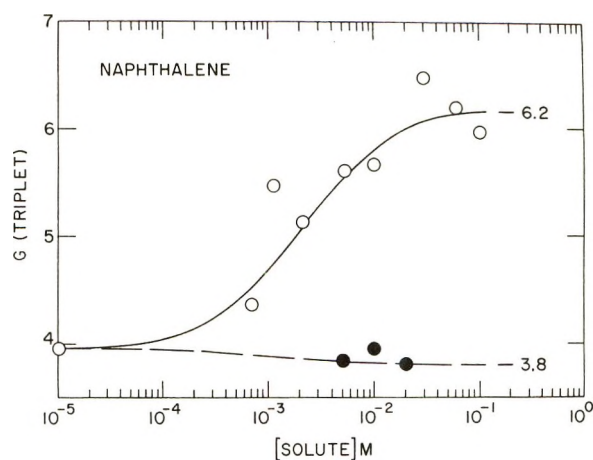


Figure 1. The yield of triplet excited states of naphthalene as a function of solute concentration: \circ , benzophenone; \bullet , CCl_4 . Solid line calculated assuming $k_2 = 10^{10} M^{-1} \text{sec}^{-1}$; dotted line calculated assuming $k_1 = 1.5 \times 10^{10} M^{-1} \text{sec}^{-1}$.

must be at least 2.2 but may be larger if there is significant intersystem crossing. Figure 1 indicates that one-half of this increase is obtained at approximately 2 mM benzophenone. Measurements of the fluorescence (monitored at 420 m μ) during the pulse show that at 10 mM benzophenone 85% of the singlets are quenched.

For solutions of CCl_4 in naphthalene, fluorescence measurements indicate that at 5 mM CCl_4 82% of the singlets are quenched and at 20 mM 92% are quenched. At these concentrations CCl_4 has hardly any effect on the triplet yield (see Figure 1), indicating that the yield of triplets from intersystem crossing is small.

1-Methylnaphthalene. The singlet excited state of 1-methylnaphthalene is detected by fluorescence emission during the pulse. The spectrum of the emission at 25° is shown in Figure 2 and compared to the emission observed by photoexcitation¹⁴ of the neat liquid (solid line). The maximum in the emission occurs at 400 m μ , and since the excited monomer fluorescence peaks at 340,¹⁴ the singlet excited state is present exclusively as the excimer in the radiolysis at 25°. At 88° the fluorescence emission (dotted line, Figure 2) is reduced in intensity, and the spectrum shows another peak at shorter wavelengths. This is attributed to monomer emission although the spectrum is distorted due to self-absorption at wavelengths $< 360 \text{ m}\mu$. The observation of monomer emission shows that the rate

(11) D. Lavalette, R. Bensasson, B. Amand, and E. J. Land, *Chem. Phys. Lett.*, **10**, 331 (1971).

(12) E. J. Land, *Proc. Roy. Soc., Ser. A*, **305**, 457 (1968).

(13) R. E. Bühler and M. Ebert, *Nature (London)*, **214**, 1220 (1967).

(14) (a) N. Mataga, M. Tomura, and H. Nishimura, *Mol. Phys.*, **9**, 367 (1965); (b) W. T. Ware, in "Creation and Detection of the Excited State," Vol. IA, Marcel Dekker, New York, N. Y., 1971, Chapter 5.

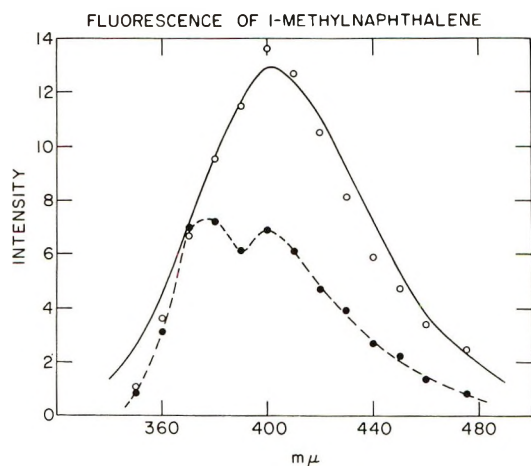


Figure 2. Fluorescence for pure 1-methylnaphthalene during radiolysis; dose/pulse = 290 rads: \circ at 25° ; \bullet at 88° ; solid line is fluorescence during photoexcitation at 25° (ref 14).

of excimer dissociation is enhanced at higher temperatures. The fluorescence lifetime at $400\text{ m}\mu$ was measured following a pulse from the Febetron source and found to be 64 nsec at 25° and 42 nsec at 87° . The lifetime was also measured by the single photon technique;^{14b} for excitation at $337\text{ m}\mu$ the lifetime was found to be 67 nsec at 24° , and 43 nsec at 83° . The room temperature results are in reasonable agreement with a previous report of 60 nsec.¹⁴

A longer-lived transient, the absorption spectrum of which is shown in Figure 3, was detected in 1-methylnaphthalene. The yield of this species is enhanced by benzophenone and depressed by CCl_4 . The spectrum is the same with either benzophenone or CCl_4 present as it is in the neat liquid. This species is the triplet

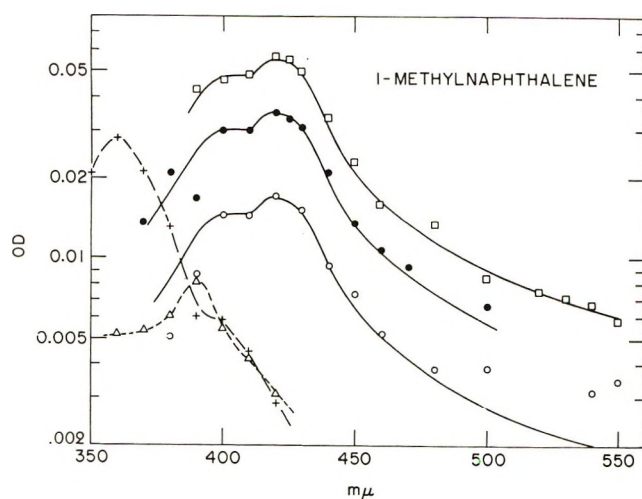


Figure 3. Absorption spectra of transients in radiolysis of 1-methylnaphthalene: \bullet , short-lived species in pure liquid; \square , short-lived species with benzophenone added; \circ , short-lived species with CCl_4 added; Δ , long-lived species in pure 1-methylnaphthalene; $-+-$, long-lived species in CCl_4 solutions.

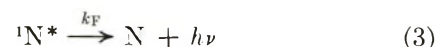
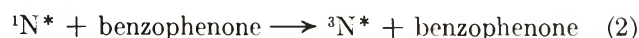
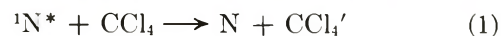
excited state, which was first detected by flash photolysis.¹⁵ The half-life of the triplet is $3.5\text{ }\mu\text{sec}$ in the presence and absence of benzophenone and at concentrations of $\text{CCl}_4 < 10\text{ mM}$. The half-life drops to $3\text{ }\mu\text{sec}$ at 50 mM CCl_4 . Thus the rate constant for quenching of the triplet by CCl_4 is $< 10^6\text{ M}^{-1}\text{ sec}^{-1}$. In this work no significant absorption is found at $550\text{ m}\mu$, where Bühler observed an intermediate for solutions of 1-methylnaphthalene in CCl_4 .¹³

In pure methylnaphthalene there is another absorption around $390\text{ m}\mu$ (see Figure 3) due to an even longer-lived species. This is most likely a radical, possibly the benzyl-like species $\text{C}_{10}\text{H}_7\text{CH}_2\cdot$; it decays by a second-order process and at $390\text{ m}\mu$ $k/\epsilon = 2.3 \times 10^6\text{ cm}^2/\text{sec}$. A transient absorption in this spectral region is also formed in CCl_4 solutions (Figure 3). This intermediate is partially present at the end of the pulse and grows during the first $60\text{ }\mu\text{sec}$. The decay is second order: $k/\epsilon = 1.4 \times 10^5\text{ cm}^2/\text{sec}$ at $370\text{ m}\mu$. This species is identified as a radical which must result from the reaction of either Cl or CCl_3 or both (which are formed by singlet quenching), with methylnaphthalene.

In pure 1-methylnaphthalene at 25° the yield of triplet excited states is $G = 4.6$. Benzophenone increases the yield to a value near $G = 6.0$ and CCl_4 depresses the yield (Table I). The percentage of singlet quenched is determined at each concentration by monitoring the fluorescence during the pulse. Note that at 1 mM of either solute the singlet is quenched by about 45%. At 86° CCl_4 depresses the triplet yield much less than at 25° .

Calculation of Initial Yields. The effect of benzophenone and CCl_4 on the yields of triplet excited states is interpreted on the basis of excitation transfer. Reactions with geminate ions are considered negligible in importance at solute concentrations less than 0.05 M in these solvents. CCl_4 does react with free ions to reduce the triplet yield, but the magnitude of this effect is limited to $G(\text{free ions}) < 0.1$. This assertion is supported by the 85° results where CCl_4 has little effect on $G(\text{triplet})$ but quenches the singlet. The opposite effect, reducing the triplet more than the singlet yield, would be expected if CCl_4 reacted with electrons since ion neutralization preferentially leads to triplet states.¹⁶

The results are interpreted in terms of the following reactions: energy transfer, solvent fluorescence, intersystem crossing, and internal conversion, reactions 1-5. The fluorescence yield ϕ should vary with solute



(15) G. Porter and M. W. Windsor, *Proc. Roy. Soc., Ser. A*, **245**, 238 (1958).

(16) S. Siegal and J. Stewart, *J. Chem. Phys.*, **55**, 1775 (1971).

Table I: Yields of Excited States in 1-Methylnaphthalene^a

Temp. °C	Sample	% of fluorescence quenched	$G(^3N^*)_{\text{obsd}}$	Eff _{ISC}	$G(^1N^*)^\circ$	$G(^3N^*)^\circ$
25	Pure	0	4.55			
	0.2 mM benzophenone	12	4.75			
	1.2 mM benzophenone	46	5.59			
	3 mM benzophenone	74	5.28			
	11 mM benzophenone	86	5.38			
	20 mM benzophenone	88	6.04			
	30 mM benzophenone	96	5.85			
	1 mM CCl ₄	43	4.30	0.29	2.04	3.96
	5 mM CCl ₄	72	3.45	0.52	3.02	2.98
	10 mM CCl ₄	85	3.53	0.45	2.64	3.36
	20 mM CCl ₄	92	3.40	0.46	2.69	3.31
	31 mM CCl ₄	87	4.14	0.25	1.93	4.07
	52 mM CCl ₄	86	2.68	0.60	3.63	2.37
	0.1 mM CCl ₄	83	3.14	0.54	3.15	2.85
86	Pure	0	3.78			
	50 mM benzophenone	98	6.0 ^a			
	20 mM CCl ₄	94	3.33	0.17	2.70	3.30

^a The value of ϵ was not determined at 86°; the yields are normalized to a total yield of $G(^3N^*) + G(^1N^*) = 6.0$.



concentration according to eq III, where ϕ is the yield in the absence of solutes. Figure 4 shows a plot of the

$$\phi^\circ/\phi = 1 + (k_1[CCl_4] + k_2[BP]) / (k_F + k_{ISC} + k_{IC}) \quad (III)$$

data for 1-methylnaphthalene containing benzophenone and CCl₄. From the slope of these lines and the lifetime of fluorescence, τ_f , in the absence of quencher the rate constants for quenching were determined to be $k_2 = 1.2 \times 10^{10}$ and $k_1 = 1.1 \times 10^{10}$. These values are very close to those determined for these solutes in 1-ethylnaphthalene.¹⁷ The large values of the rate constants are associated with efficient energy migration in this solvent and the high electron affinity of the solutes.¹⁷

The yields of singlet and triplet excited states produced by all processes involving direct interaction of secondary electrons with molecules and by ion recombination are denoted $G(^1N^*)^\circ$ and $G(^3N^*)^\circ$, respectively. The latter yield does not include those triplets formed by intersystem crossing. These initial yields were derived from the triplet yield data in the following way. In the presence of benzophenone the singlets react with the solute and eventually form solvent triplets; a one-to-one conversion is assumed. The yield is given by eq IV according to the above mechanism.

$$G(\text{triplets}) = G(^3N^*)^\circ + G(^1N^*)^\circ \times \frac{k_{ISC} + k_2[BP]}{k_F + k_{IC} + k_{ISC} + k_2[BP] + k_1[CCl_4]} \quad (IV)$$

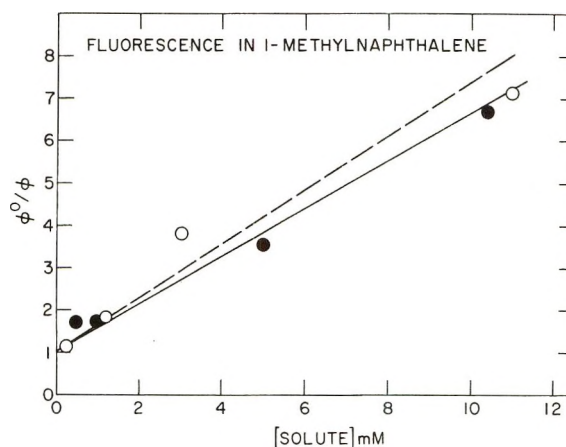


Figure 4. Ratio of fluorescence yield in pure 1-methylnaphthalene to that in solution as a function of solute concentration: O, benzophenone as solute; ●, CCl₄ as solute.

At high concentrations of benzophenone, intersystem crossing is quenched along with fluorescence, thus the yield of triplets can be equated to the total yield of excited states, eq V.

$$G(\text{triplets})_{BP} = G(^3N^*)^\circ + G(^1N^*)^\circ \quad (V)$$

In the pure liquid additional triplets are formed only by intersystem crossing and the total yield of triplets will be given by eq VI

$$G(\text{triplets})_{\text{pure}} = G(^3N^*)^\circ + G(^1N^*)^\circ \times \text{Eff}_{ISC} \quad (VI)$$

where $\text{Eff}_{ISC} = k_{ISC} / (k_F + k_{IC} + k_{ISC})$. Equations V and VI cannot be solved simultaneously without in-

(17) J. W. Eastman, E. J. Smutny, and G. M. Coppinger, *J. Chem. Phys.*, **53**, 4346 (1970).

formation about the value of the intersystem crossing ratio.

This information is provided by the CCl_4 data. In the presence of CCl_4 , the triplet yield is given by eq VII.

$$G(\text{triplets})_{\text{CCl}_4} = G(^3\text{N}^*)^\circ + G(^1\text{N}^*)^\circ \times \text{Eff}_{\text{ISC}} / \left(1 + \frac{k_1[\text{CCl}_4]}{k_F + k_{\text{ISC}} + k_{\text{IC}}} \right) \quad (\text{VII})$$

The term

$$1 / \left(1 + \frac{k_1[\text{CCl}_4]}{k_F + k_{\text{ISC}} + k_{\text{IC}}} \right)$$

is just the fraction of singlets not quenched by CCl_4 , and this is known from the fluorescence data (Table I). Thus the yield of triplets along with the fraction of singlets not quenched, as determined from the fluorescence, were combined in eq VII and this was solved at each concentration of CCl_4 by combining with eq V and VI to evaluate initial yields as well as the intersystem crossing ratio. The results for 1-methylnaphthalene as given in Table I show $G(^3\text{N}^*)^\circ = 3.3 \pm 0.5$ and $G(^1\text{N}^*)^\circ = 2.7 \pm 0.5$.

The results, for naphthalene evaluated from the data in Figure 1, are $G(^3\text{N}^*)^\circ = 3.8$, $G(^1\text{N}^*)^\circ = 2.4$, and the efficiency of intersystem crossing ~ 0.06 . The curves drawn through the data in Figure 1 were calculated from these yields and the values of the rate constants, $k_2 = 10^{10} \text{ M}^{-1} \text{ sec}^{-1}$ and $k_1 = 1.5 \times 10^{10} \text{ M}^{-1} \text{ sec}^{-1}$, derived from fluorescence data and the known lifetime of fluorescence at 85° .⁴ The dotted line is a plot of eq VII; the solid line is a plot of eq IV for $[\text{CCl}_4] = 0$. The fit is reasonable and further confirms the interpretation. The rate constant for quenching by CCl_4 exceeds the diffusion-controlled rate which is consistent with the earlier suggestion of excitation migration in molten naphthalene.⁷

Intersystem Crossing and Internal Conversion. The results show that the efficiency of intersystem crossing in neat 1-methylnaphthalene is 0.44 ± 0.12 at 25° . This is in reasonable agreement with the value of 0.48 reported for a dilute solution in benzene,¹⁸ indicating the excimer undergoes intersystem crossing with an efficiency comparable to that of the monomer. However at 85° the intersystem crossing efficiency is less (0.17) in pure methylnaphthalene.

The effect of temperature is similar in naphthalene where the intersystem crossing efficiency is only 0.06 at 85° ; whereas it is variously reported to be 0.34 at 77°K ,¹⁹ 0.8²⁰ in solution at 25° , and 0.44 in a solid matrix, independent of temperature.²¹ For molten naphthalene the lifetime of the singlet is only 50 nsec at 85° ,⁴ compared to 100 nsec at 25° . Since k_F is $\sim 0.2 \times 10^7$ and independent of temperature,²² and since k_{ISC} , equal to $\text{Eff}_{\text{ISC}} \times 1/\tau_F$, is only 0.1×10^7 at 85° , there must be some other process depopulating the singlet

at 85° (see eq VIII). This process is "presumed"

$$1/\tau_F = k_F + k_{\text{IC}} + k_{\text{ISC}} \quad (\text{VIII})$$

to be internal conversion. If this is correct, then $k_{\text{IC}} \cong 1.7 \times 10^7 \text{ sec}^{-1}$ which corresponds to 82% deactivation by internal conversion.

The 1-methylnaphthalene results afford a more quantitative treatment since data are available at two temperatures in the same solvent. At 25° $1/\tau_F = 1.5 \times 10^7$ thus $k_{\text{ISC}} = 0.66 \times 10^7$, and we can estimate that $k_F \sim 0.3 \times 10^7$.²² Therefore from eq VIII, $k_{\text{IC}} \cong 0.5 \times 10^7$. At 85° $1/\tau_F = 2.2 \times 10^7 \text{ sec}^{-1}$, $\text{Eff}_{\text{ISC}} = 0.17$ thus $k_{\text{ISC}} = 0.37 \times 10^7$; therefore $k_{\text{IC}} \cong 1.6 \times 10^7 \text{ sec}^{-1}$, and the singlet is 73% deactivated by internal conversion at this temperature.

These rates of internal conversion are much higher than usually reported. That is, the values of k_{IC} are expected to be 1.2×10^5 and $3 \times 10^5 \text{ sec}^{-1}$ for naphthalene and 1-methylnaphthalene, respectively.^{22,23} These numbers apply to the excited monomer. For the excimer the rate constants are expected to be larger for the following reason. The formation of the excimer lowers the singlet energy by 6500 cm^{-1} .²² The rates of internal conversion increase as the S_1-S_0 energy gap decreases because of an increase in the Frank-Condon factor.²³ On the basis of this correlation²⁴ for aromatic compounds one can estimate that k_{IC} should be approximately 10^7 sec^{-1} for the 1-methylnaphthalene excimer. Thus the rates observed here are not unreasonable.

The increase in rate of internal conversion and accompanying decrease in intersystem crossing at the higher temperature are unexpected. However, a similar behavior has recently been reported for the excimer in pyrene²⁵ where the decrease in lifetime of the singlet with increasing temperature has been ascribed to a temperature-dependent internal conversion. Molecular motion distorts the excimer structure and leads to a better overlap of the vibrational wave function of the two electronic states. This may be a general phenomena since the naphthalenes appear to behave like pyrene.

Mechanisms of Excitation. In aromatic liquids several mechanisms can lead to the formation of excited states: direct excitation of singlet states; ion recom-

(18) A. A. Lamola and G. S. Hammond, *J. Chem. Phys.*, **43**, 2129 (1965).

(19) S. G. Hadley, *Chem. Phys. Lett.*, **6**, 549 (1970); ϕ_{ISC} was adjusted to correct value of ϵ given in ref 11.

(20) (a) C. A. Parker and T. A. Joyce, *Trans. Faraday Soc.*, **62**, 2785 (1966); (b) A. R. Horrocks and F. Wilkenson, *Proc. Roy. Soc., Ser. A*, **306**, 257 (1968).

(21) P. F. Jones and A. R. Calloway, *J. Chim. Phys. Suppl.*, **67**, 110 (1970).

(22) J. B. Birks, "Photophysics of Aromatic Molecules," Wiley, New York, N. Y., 1970.

(23) W. Siebrand and D. F. Williams, *J. Chem. Phys.*, **49**, 1860 (1968).

(24) Reference 22, Figure 5.2 and discussion on p 160.

(25) J. B. Birks, A. J. H. Alwattar, and M. D. Lumb, *Chem. Phys. Lett.*, **11**, 89 (1971).

bination, excitation by slow electrons, and intersystem crossing. The results presented here, viewed in light of current theory, provide some insight into the relative importance of these various processes. The role of intersystem crossing has already been discussed.

The most important mechanism is probably ion recombination. The total yield of ion pairs in naphthalene should be very similar to that for benzene which is 4.3 based on gas phase W values.²⁶ This value is reasonable in light of actual measurements of ion yields in hydrocarbon liquids.²⁷ Thus about 70% of the total yield of excited states can be accounted for if each ion pair yields one excited state on neutralization. The negative ions are probably naphthalene anions, N^- , formed by electron attachment; the positive ions may be molecular ions, N^+ , or dimer cations, N_2^+ . On neutralization both triplet and singlet states will be formed.^{16,28} The ratio of singlets to triplets is the same for neutralization of N^+ with N^- as for N_2^+ with N^- ,²⁸ but the magnitude of this ratio is not known precisely. Presumably most of the observed yield of triplets ($G \simeq 3.5$) is formed this way. The only other mechanism which leads to triplet states is excitation by low energy electrons, and this has been shown to be relatively unimportant for naphthalene.¹⁶

That singlet states are formed in ion neutralization is known from fluorescence studies,²⁸ but the entire observed yields ($G \simeq 2.5$) cannot be accounted for in this way. Direct excitation of singlet states must be a significant mode of excitation. (All singlet states above

the first excited state are expected to immediately internally convert into S_1 in the liquid phase; rate constants for such processes are $\sim 10^{12} \text{ sec}^{-1}$.)²² The yield of singlet states can be estimated from the optical approximation^{26,29} which relates G to the oscillator strength. From the sum of the oscillator strengths of all transitions up to the ionization potential, the total yield of excited singlet states is estimated to be $G = 0.6$. Although this is only an estimate, the observed yield is much larger, and we cannot exclude a significant fraction of the singlets being formed from "super-excited states" which fail to ionize. The formation of such states is quite probable according to the optical approximation since the greater part of the oscillator strength of a molecule lies above the ionization potential.

Acknowledgments. We would like to thank H. Schwarz and A. O. Allen for their advice and encouragement. We also wish to thank R. Weston and T. Barker for making lifetime measurements on 1-methylnaphthalene, and K. Walther, F. Kummer, and P. Roman for construction of the irradiation cells.

(26) C. E. Klots in "Fundamental Processes in Radiation Chemistry," P. Ausloos, Ed., Interscience, New York, N. Y., 1968, Chapter 1.

(27) W. F. Schmidt, *Radiat. Res.*, **42**, 73 (1970).

(28) B. Brocklehurst and R. D. Russell, *Trans. Faraday Soc.*, **65**, 2159 (1969).

(29) R. L. Platzman, *Vortex*, **23**, No. 8 (1962).

Ultraviolet Photochemistry of Formatopentaamminecobalt(III) Ion in Aqueous Solution. Hydrogen Atom Formation and Oxygen→Carbon Linkage Isomerization¹

by Evan R. Kantrowitz, Morton Z. Hoffman,* and Kenneth M. Schilling

Department of Chemistry, Boston University, Boston, Massachusetts 02215 (Received March 20, 1972)

The 254-nm photolysis of $\text{Co}(\text{NH}_3)_5\text{O}_2\text{CH}^{2+}$ in deoxygenated acidic aqueous solution generates Co^{2+} , CO_2 , and H_2 with quantum yields of 0.55, 0.43, and 0.15, respectively. Scavenging studies with O_2 , 2-propanol, and allyl alcohol show that Co^{2+} and CO_2 arise from both scavengable and non-scavengable sources, while H_2 is completely scavengable. Flash photolysis generates an intermediate which decays *via* first-order kinetics with a rate constant that is dependent upon pH with an activation energy of 23 kcal mol⁻¹. This intermediate is identified as the C-bonded formate linkage isomer, $\text{Co}(\text{NH}_3)_5\text{CO}_2\text{H}^{2+}$, generated as a result of intraligand proton transfer and rotation of the ligand; the $\text{p}K_a$ of the ligand is 2.6. This non-scavengable species decays *via* ligand-to-metal intramolecular electron transfer releasing Co^{2+} and the $\cdot\text{CO}_2\text{H}$ radical which disproportionates to CO_2 . Irradiation of $\text{Co}(\text{NH}_3)_5\text{O}_2\text{CH}^{2+}$ in its ligand-to-metal charge-transfer band generates an excited state which, by radiationless transition, degrades to a dissociative state yielding Co^{2+} , H atoms, and CO_2 and to an excited state which is largely ligand localized, yielding the C-bonded isomer.

Introduction

The most predominant process resulting from the irradiation of pentaammine complexes of Co(III) (of the general form $\text{Co}(\text{NH}_3)_5\text{X}^{2+}$) in their intense ligand-to-metal charge transfer band is the formation of Co^{2+} and a free radical derived from the one-electron oxidation of the X ligand. In our recent report² of the ultraviolet photochemistry of $\text{Co}(\text{NH}_3)_5\text{O}_2\text{CCH}_3^{2+}$, we showed that charge-transfer irradiation at 254 nm generated stoichiometric quantities of Co^{2+} , CO_2 , and CH_3 radicals. These CH_3 radicals, arising from the decarboxylation of the CH_3CO_2 radicals formed by intramolecular electron transfer, disappeared mainly by combination reactions producing C_2H_6 . Methyl radical attack on the complex, occurring with a rate constant of $4 \times 10^3 \text{ M}^{-1} \text{ sec}^{-1}$, produced a small quantity of CH_4 . The use of H-atom transfer scavengers such as methanol and 2-propanol increased the CH_4 yield at the expense of the C_2H_6 while at the same time generating alcohol radicals which themselves could reduce the complex to Co^{2+} . The $\text{Co}(\text{NH}_3)_5\text{O}_2\text{CCH}_3^{2+}$ system was characterized by its relative simplicity compared with the complicated behavior exhibited by $\text{Co}(\text{NH}_3)_5\text{-Cl}^{2+}$,³ $\text{Co}(\text{NH}_3)_5\text{N}_3^{2+}$,⁴ $\text{Co}(\text{NH}_3)_5\text{O}_2\text{CCO}_2\text{H}^{2+}$,⁵ and some other "simple" amine complexes.⁶

By analogy to $\text{Co}(\text{NH}_3)_5\text{O}_2\text{CCH}_3^{2+}$, one would expect formatopentaamminecobalt(III) ion, $\text{Co}(\text{NH}_3)_5\text{O}_2\text{-CH}^{2+}$, upon charge-transfer irradiation, to generate Co^{2+} and the HCO_2 radical, which in turn would produce H atoms and CO_2 in stoichiometric quantities by decarboxylation. The generation of H atoms in aqueous solution by photochemical means has received

considerable attention⁷ as an alternative to radiolytic⁸ and microwave⁹ techniques. Just as the acetato complex serves as a convenient photochemical source of CH_3 radicals in aqueous solution,² the formate complex could do the same for H atoms. However, as we described in a recent communication,¹⁰ $\text{Co}(\text{NH}_3)_5\text{-O}_2\text{CH}^{2+}$ also undergoes photochemically induced oxygen→carbon linkage isomerization to generate $\text{Co}(\text{NH}_3)_5\text{CO}_2\text{H}^{2+}$ which is thermodynamically and kinetically unstable with respect to Co^{2+} . The first-order decay of the C-bonded formate linkage isomer is dependent upon pH in a way that indicates that the $\text{p}K_a$ of the formate ligand is 2.6; the higher rate of decay under deprotonated conditions reflects the greater re-

(1) This work was supported by Grant No. GP 11213 from the National Science Foundation and was presented, in part, at the 162nd National Meeting of the American Chemical Society, Washington, D. C., Sept 1971.

(2) E. R. Kantrowitz, M. Z. Hoffman, and J. F. Endicott, *J. Phys. Chem.*, **75**, 1914 (1971).

(3) G. Caspari, R. G. Hughes, J. F. Endicott, and M. Z. Hoffman, *J. Amer. Chem. Soc.*, **92**, 6801 (1970).

(4) J. F. Endicott, M. Z. Hoffman, and L. S. Beres, *J. Phys. Chem.*, **1021** (1970).

(5) A. F. Vaudo, E. R. Kantrowitz, M. Z. Hoffman, E. Papaconstantinou, and J. F. Endicott, *J. Amer. Chem. Soc.*, in press.

(6) V. Balzani and V. Carassiti, "Photochemistry of Coordination Compounds," Academic Press, New York, N. Y., 1970.

(7) W. A. Pryor and R. W. Henderson, *J. Amer. Chem. Soc.*, **92**, 7234 (1970); W. A. Pryor and J. P. Stanley, *ibid.*, **93**, 1412 (1971), and references quoted therein.

(8) See, for example, M. Simic and M. Z. Hoffman, *ibid.*, **92**, 6096 (1970).

(9) G. Navon and G. Stein, *J. Phys. Chem.*, **69**, 1384 (1965).

(10) A. F. Vaudo, E. R. Kantrowitz, and M. Z. Hoffman, *J. Amer. Chem. Soc.*, **93**, 6698 (1971).

ducing ability of the formate ion as compared to formic acid.¹¹ The activation energy for the decay and the spectrum of this intermediate are the same whether the species is generated from $\text{Co}(\text{NH}_3)_5\text{O}_2\text{CH}^{2+}$, $\text{Co}(\text{NH}_3)_4\text{C}_2\text{O}_4^+$, or $\text{Co}(\text{NH}_3)_5\text{C}_2\text{O}_4^+$. This paper will present the data about the C-bonded formate linkage isomer referred to in the communication¹⁰ as well as the details of the continuous photolysis of $\text{Co}(\text{NH}_3)_5\text{O}_2\text{CH}^{2+}$ in the presence and absence of scavengers.

Experimental Section

$[\text{Co}(\text{NH}_3)_5\text{O}_2\text{CH}](\text{ClO}_4)_2$ was prepared by the general method of Sebera and Taube¹² in which a solution of $\text{Co}(\text{NH}_3)_5\text{OH}_2^{3+}$ was heated at 70–80° for 2 hr in the presence of excess formic acid and sodium formate. The desired complex was precipitated upon the addition of 60% HClO_4 ; the crystals were filtered and washed successively with 60% perchloric acid, ethanol, and ether. The salt was recrystallized twice before use from acidified water. The absorption spectrum of the complex (λ_{max} 500 nm, ϵ_{500} 69.6 $M^{-1} \text{cm}^{-1}$) agreed very well with the literature.¹³

$\text{Co}(\text{en})_2(\text{OH}_2)\text{O}_2\text{CH}^{2+}$ was prepared in solution by two methods. In the first, 0.2 g of *trans*- $[\text{Co}(\text{en})_2\text{Cl}_2]\text{Cl}$ was dissolved in a minimum amount of water at 40°, to which was added 0.2 g of sodium formate and 1 ml of formic acid. The mixture was heated at 50° for 1 hr. After about 10 min, the solution turned dark brown. Upon cooling, 0.2 g of AgNO_3 was added; AgCl precipitated immediately. After a wait of about 1 hr, the filtered solution was placed on anion-exchange column (Dowex 50W-X4, 200–400 mesh, H^+ form) and eluted with increasingly more concentrated solutions of HClO_4 (0.1–1.5 M). The first fraction eluted was green and was identified as the 1+ starting material. The next fraction, corresponding to a 2+ cation, was red-orange and had spectral characteristics common to $\text{Co}(\text{III})$ -ammine complexes with O-bonded carboxylato ligands (λ_{max} 360, 500 nm). In the second method, 0.25 g of $[\text{Co}(\text{en})_2\text{CO}_3]\text{ClO}_4$ and 0.05 g of sodium formate were dissolved at 70° in a minimum amount of water. The solution was adjusted to pH 3.75 (the $\text{p}K_a$ of formic acid) and heated for 4–5 hr, during which time the reaction was followed by ion-exchange chromatography. The pH was readjusted every 2 hr to 3.75. After 5 hr of reaction, the solution was cooled and ion exchanged as before. The 2+ fraction was collected and used directly. The spectrum of this fraction was the same as in the first method. Although the isomeric structure of $\text{Co}(\text{en})_2(\text{OH}_2)\text{O}_2\text{CH}^{2+}$ could be questioned in the first method, the second method should give the *cis* isomer.

The continuous and flash photolysis units and techniques and the analytical procedures have all been described in detail before.^{2–4} Solutions were prepared from the solid $\text{Co}(\text{NH}_3)_5\text{O}_2\text{CH}^{2+}$ complex immediately before use and were deoxygenated (if desired) by

purging with Cr^{2+} -scrubbed N_2 for 20–30 min before irradiation. During continuous photolysis, N_2 bubbling and magnetic stirring ensured the homogeneity of the solution. A continuous purge of O_2 could also be applied. Temperature was controlled by air or water thermostating. For gaseous products, the photolyses were conducted *in vacuo* and the analyses performed by gas chromatography.

In the flash photolysis experiments, the solution was forced into the N_2 -flushed optical cell ($l = 22$ cm) from a storage flask by a positive pressure of N_2 . All solutions were discarded after one flash. Experiments were normally conducted at room temperature; however, for the determination of activation energies, a jacketed cell was used through which thermostated water was circulated. The temperature of the solution in the optical cell could be maintained within $\pm 0.3^\circ$.

For the determination of the quantum yield of Co^{2+} production, $\phi_{\text{Co}^{2+}}$, samples were removed from the photolysis cell periodically by means of a syringe fitted with a Teflon needle passing through a rubber serum cap. Co^{2+} determinations² were performed as soon after photolysis as possible. The yield of Co^{2+} as a function of exposure time generally gave linear plots; the extent of reaction was limited to <25% and the concentration of complex was chosen such that all the 254-nm radiation was absorbed during exposure (ϵ_{254} 2650 $M^{-1} \text{cm}^{-1}$). The rate of Co^{2+} formation was determined from the slope of such zero-order plots. Although primary actinometry had been performed on each photolysis unit, secondary actinometry was performed at the time of each photolysis in order to account for any variation in the output of the lamps. Specifically, each photolysis run or series of runs was bracketed by an irradiation of $\text{Co}(\text{NH}_3)_5\text{O}_2\text{CCH}_3^{2+}$ under identical conditions of solution absorbance. The value of $\phi_{\text{Co}^{2+}}$ for the 254-nm photolysis of that complex at pH 1 and 25° in deoxygenated solution has been very well established to be 0.19.² The values of $\phi_{\text{Co}^{2+}}$ determined in this way are known to within $\pm 10\%$ with excellent reproducibility.

Results

Quantum Yields. The major stable products from the 254-nm irradiation of $\text{Co}(\text{NH}_3)_5\text{O}_2\text{CH}^{2+}$ are Co^{2+} , CO_2 , H_2 , and a trace of CO . Table I summarizes our determinations of the quantum yields of product formation in the presence of N_2 , O_2 , 2-propanol, and allyl alcohol at pH 1. $\phi_{\text{Co}^{2+}}$ under N_2 purge was not noticeably dependent on $[\text{complex}]$ (2.5×10^{-3} – 5.0×10^{-2} M). Because of the generation of large quantities of

(11) W. M. Latimer, "Oxidation Potentials," Prentice-Hall, Englewood Cliffs, N. J., 1952, p 130.

(12) D. K. Sebera and H. Taube, *J. Amer. Chem. Soc.*, **83**, 1785 (1961).

(13) C. Andrade, R. B. Jordan, H. Taube, *Inorg. Chem.*, **9**, 711 (1970).

Table I: Quantum Yields of Products from the 254-nm Photolysis of $\text{Co}(\text{NH}_3)_5\text{O}_2\text{CH}^{2+}$ ^{a, b}

Added solute	Gas purge	$\phi_{\text{Co}^{2+}}$ ^c	ϕ_{H_2} ^d	ϕ_{CO_2} ^d
	N ₂	0.55 ± 0.04^e	0.15 ± 0.01^f	0.43 ± 0.03^f
	O ₂	0.42	<i>g</i>	<i>g</i>
5 M 2-propanol	N ₂	0.54	0.14	0.27
1 M allyl alcohol	N ₂	0.40	0.0	0.28

^a $[\text{Co}(\text{NH}_3)_5\text{O}_2\text{CH}^{2+}] = 1.0 \times 10^{-2} \text{ M}$; $[\text{HClO}_4] = 0.1 \text{ M}$; 25° . ^b All N₂ detected could be accounted for as leakage. Trace quantities of CO were detected. ^c $I_a \simeq 6.0 \times 10^{-4} \text{ einstein l.}^{-1} \text{ min.}^{-1}$. ^d $I_a \simeq 4.9 \times 10^{-3} \text{ einstein l.}^{-1} \text{ min.}^{-1}$. ^e Average of eight determinations. ^f Average of four determinations. ^g Under our experimental conditions it was not possible to analyze for gaseous products when the solution was kept saturated with O₂ during the period of photolysis.

base in the photolysis, experiments at pH >4 produced insoluble $\text{Co}(\text{OH})_2$ when the solution became basic rendering the results under those conditions of doubtful validity. It appears that the quantum yields are not significantly dependent on $[\text{H}^+]$ from pH 0 to 4. Furthermore, $\phi_{\text{Co}^{2+}}$ is independent of I_a over almost three orders of magnitude of light intensity. The dependence of the quantum yields of the various products on [2-propanol] and [allyl alcohol] in N₂-purged solutions at pH 1 are shown in Figures 1 and 2, respectively.

A sample of $1.0 \times 10^{-2} \text{ M}$ $\text{Co}(\text{NH}_3)_5\text{O}_2\text{CH}^{2+}$ was photolyzed at 254 nm for 10 min ($I_a \simeq 6.0 \times 10^{-4} \text{ einstein l.}^{-1} \text{ min.}^{-1}$) and ion exchanged on Dowex 50W-4X resin (200-400 mesh, H⁺ form) using 0.6 M $\text{Mg}(\text{ClO}_4)_2$ as the eluent. The 2+ charged substrate was eluted under these conditions; no noticeable material was left on the column.

A $1.0 \times 10^{-2} \text{ M}$ sample of complex was photolyzed at 366 nm for 17 hr using a Bausch and Lomb high-intensity monochromator with a super-pressure mercury lamp ($I_a \sim 1 \times 10^{-4} \text{ einstein l.}^{-1} \text{ min.}^{-1}$). The photolyte was ion exchanged using 0.35 M $\text{Mg}(\text{ClO}_4)_2$ as the eluent. Three fractions were observed: a purple 2+ fraction which moves just ahead of the main substrate fraction and a 3+ fraction. The quantities of the 2+ purple and 3+ fractions were too small to be taken off the column for spectral analysis. Note that similar behavior was observed for the photolysis of $\text{Co}(\text{NH}_3)_5\text{O}_2\text{CCH}_3^{2+}$ at 366 nm.²

Flash Photolysis. Two distinguishable intermediate species were observed from the flash photolysis (500 J) of deoxygenated solutions of $\text{Co}(\text{NH}_3)_5\text{O}_2\text{CH}^{2+}$. Intermediate SL had a very short lifetime (<100 μsec) and was weakly superimposed upon the longer lived intermediate LL. It was not possible to evaluate the kinetics of the decay of SL nor the details of its spectrum; its absorbance appeared to increase with decreasing wavelength in the region 260-300 nm. The absorption of SL was not affected by the presence of O₂ or the other scavenger solutes. Because of the superimposition of the spectra of SL and LL, it is not possible to establish if SL decays to form LL or if both species are independent of each other.

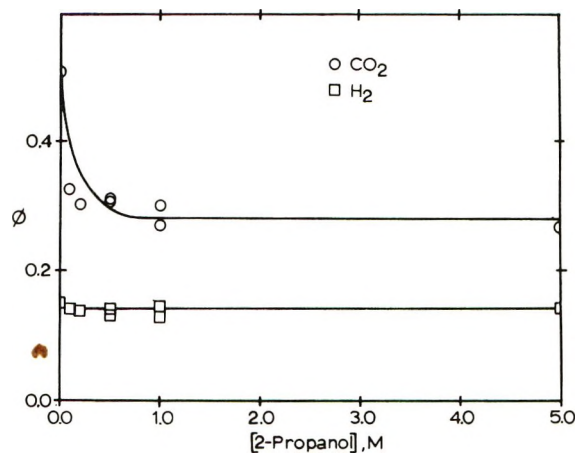


Figure 1. Dependence of quantum yields of CO₂ and H₂ upon [2-propanol] in the 254-nm photolysis of $\text{Co}(\text{NH}_3)_5\text{O}_2\text{CH}^{2+}$. [Complex] = $1.0 \times 10^{-2} \text{ M}$, pH 1, 25° .

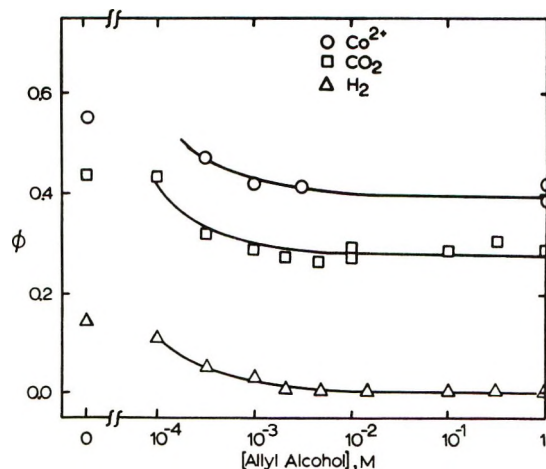


Figure 2. Dependence of quantum yields of Co²⁺, CO₂, and H₂ upon [allyl alcohol] in the 254-nm photolysis of $\text{Co}(\text{NH}_3)_5\text{O}_2\text{CH}^{2+}$. [Complex] = $1.0 \times 10^{-2} \text{ M}$, pH 1, 25° .

The spectrum of LL was obtained by a point-by-point evaluation of the absorbance of LL read after the flash as a function of λ and is shown in Figure 3. Because of the absorption by the substrate, the recording of points at $\lambda < 260 \text{ nm}$ was not possible. The λ_{max} for LL is in the region of $\sim 268 \text{ nm}$, although the exact

wavelength is obscured by the substrate absorption, which required a large monochromator slit opening with a concomitant loss in resolution.

Intermediate LL decays *via* first-order kinetics, a fact that was established by computer fit of the decay to the usual equations (standard deviation <5%) and by the independence of $t_{1/2}$ to the change of flash intensity and thus concentration of the transient. The first-order rate constant was dependent upon pH over the range pH 0–6 in the manner shown in Figure 4. The amount of LL and its decay kinetics are independent of the presence of O_2 , allyl alcohol, 2-propanol, and (except for the decay rate) H^+ . The activation energy for the decay of LL was determined at pH 1.5 and 4.4. The plots of $\log k$ vs. $1/T$ are shown in Figure 5 and result in a value of $E_a = 23.2 \pm 0.5$ kcal mol $^{-1}$ at both acidities.

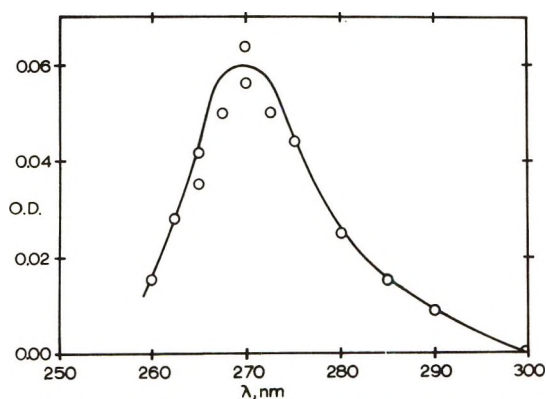


Figure 3. Absorption spectrum of the long-lived intermediate from the flash photolysis of $Co(NH_3)_5O_2CH^{2+}$. [Complex] = 5×10^{-5} M. Spectrum is independent of pH.

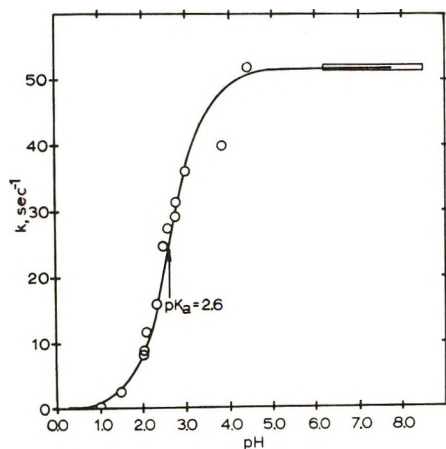


Figure 4. Rate constants for the decay of the long-lived intermediate as a function of pH. $[Co(NH_3)_5O_2CH^{2+}] = 5 \times 10^{-5}$ M; monitoring wavelength = 280 nm. The bar represents the increase in pH through the course of the experiment.

Experiments with $Co(en)_2(OH_2)O_2CH^{2+}$. The purpose of these experiments was to determine if the pres-

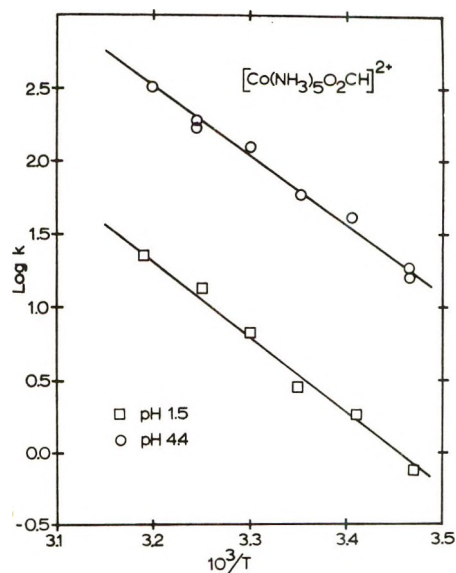


Figure 5. Dependence of the rate constant for the decay of the long-lived intermediate upon temperature. $[Co(NH_3)_5O_2CH^{2+}] = 5 \times 10^{-5}$ M.

ence of the chelating en groups retarded the rate of decay of the long-lived intermediate. In fact, LL formed here should be identical with that produced from the photolysis of $Co(en)_2(C_2O_4)^+$ if our hypothesis^{5,10} about the mechanism of the reaction is correct. Solutions of $Co(en)_2(OH_2)O_2CH^{2+}$ were subjected to flash photolysis which generated a long-lived intermediate. The decay of the intermediate was monitored either at 280 nm using the flash photolysis monitoring system or at 262 nm using double-beam spectrophotometry (Cary 16). The results are given in Table II together with data from the flash photolysis of $Co(en)_2(C_2O_4)^+$ for comparison. The decay rate for the LL intermediate was faster at higher temperature; $E_a \sim 20$ kcal mol $^{-1}$. Because of the low quantum yield for the photolysis of this complex, as evidenced by the small amount of LL intermediate detected and the almost negligible decomposition upon continuous 254-nm irradiation, the values quoted here carry uncertainties greater than those indicated for the $Co(NH_3)_5O_2CH^{2+}$ results.

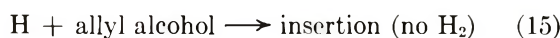
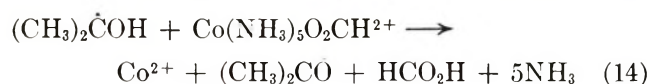
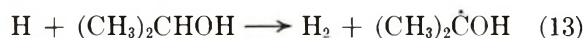
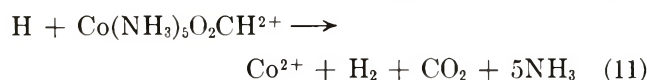
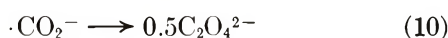
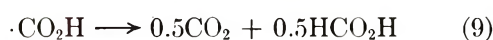
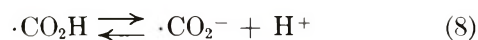
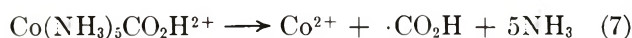
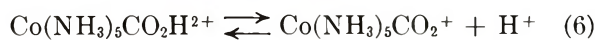
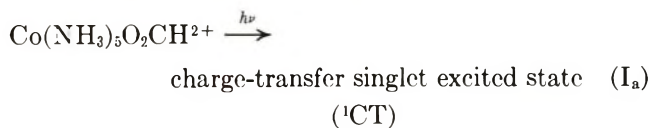
Discussion

Examination of the quantum yield data shows that the simple stoichiometry of the $Co(NH_3)_5O_2CCH_3^{2+}$

Table II: Decay of the Long-Lived Intermediate

Complex	pH	k , sec $^{-1}$
$Co(en)_2(OH_2)O_2CH^{2+}$	1.75	3.6×10^{-4}
	1.95	7.5×10^{-4}
		8.8×10^{-4}
$Co(en)_2(C_2O_4)^+$	1.75	4.7×10^{-4}
	2.1	9.5×10^{-4}
		8.6×10^{-4}

system² ($\phi_{\text{Co}^{2+}} \simeq \phi_{\text{CO}_2} \simeq \phi_{\text{CH}_3}$) is not repeated here for $\text{Co}(\text{NH}_3)_5\text{O}_2\text{CH}^{2+}$. Furthermore, the scavenging data show that while H_2 arises from a scavengable source, Co^{2+} and CO_2 arise from both scavengable and non-scavengable sources. On the basis of this information and the identification of the LL intermediate as the C-bonded formate linkage isomer which is unstable with respect to Co^{2+} , we propose the following mechanism which accounts for all the observations.



Absorption of radiation in the intense ligand-to-metal charge-transfer band of the complex causes a spin-allowed transition to produce a charge-transfer excited state of singlet multiplicity ${}^1\text{CT}$.⁶ Although a detailed description of this excited state is almost completely lacking, the range of processes resulting from the excitation in $\text{Co}(\text{III})$ -ammine complexes requires that the ${}^1\text{CT}$ state undergo a number of transitions to electronic states that eventually lead to X-ligand oxidation (all complexes),⁶ NH_3 oxidation ($\text{Co}(\text{NH}_3)_5\text{Cl}^{2+}$),¹⁴ X-ligand aquation ($\text{Co}(\text{NH}_3)_4\text{CO}_3^+$),¹⁵ NH_3 aquation ($\text{Co}(\text{NH}_3)_5\text{Cl}^{2+}$ and $\text{Co}(\text{NH}_3)_5\text{N}_3^{2+}$),^{16,17} X-ligand decomposition ($\text{Co}(\text{NH}_3)_4\text{C}_2\text{O}_4^+$, $\text{Co}(\text{en})_2\text{C}_2\text{O}_4^+$, and $\text{Co}(\text{NH}_3)_5\text{C}_2\text{O}_4^+$),⁵ and linkage isomerization ($\text{Co}(\text{NH}_3)_5\text{NO}_2^{2+}$ and $\text{Co}(\text{NH}_3)_5\text{O}_2\text{CH}^{2+}$).^{10,13} Reactions 1 and 2 describe the radiationless transitions to a charge-transfer state of triplet multiplicity, ${}^3\text{CT}$,

which leads to Co^{2+} and the oxidized ligand (reaction 3), and a ligand-localized excited state, L^* , which leads to the isomerization process (reaction 5). The scheme presented here does not include the deactivation of the excited states back to the ground state, which must be an important process as demonstrated by the less-than-unity values of the overall quantum yields.

We have no evidence that the $\text{HCO}_2\cdot$ radical from reaction 3 is actually released into solution to undergo rapid decarboxylation reaction 4 or, alternatively, that H and CO_2 are produced directly from the excited state. In any event, there appears to be no question that H atoms are generated in the photolysis and can be scavenged by the substrate or by added solutes. A flash photolysis experiment involving $\text{Co}(\text{NH}_3)_5\text{O}_2\text{CH}^{2+}$ ($5 \times 10^{-4} M$) and benzoic acid ($5 \times 10^{-5} M$) at pH 1 demonstrated the existence of H atoms free in solution. Under these conditions, the absorbance of the complex was ~ 18 times that of the benzoic acid at 230 nm where benzoic acid shows an absorption maximum. At all other wavelengths the complex absorption was even greater than that of the benzoic acid, assuring that at least 95% of the light was absorbed by the complex. The transient absorption read 100 μsec after the start of the flash showed λ_{max} 346 nm and is identified as the H adduct to benzoic acid.¹⁹ The H + benzoic acid reaction, with $k = 1 \times 10^9 M^{-1} \text{sec}^{-1}$, would be competitive under these conditions with H + complex ($k \sim 10^7 M^{-1} \text{sec}^{-1}$) and H + H ($k = 2 \times 10^{10} M^{-1} \text{sec}^{-1}$).²⁰ The transient absorption decayed *via* second-order kinetics with $2k/\epsilon = 3.0 \times 10^5$. Taking $\epsilon_{\text{max}} = 4.0 \times 10^3 M^{-1} \text{cm}^{-1}$ for the H adduct to benzoic acid,¹⁹ we obtain $2k = 1.2 \times 10^9 M^{-1} \text{sec}^{-1}$ compared with $2k = 1 \times 10^9 M^{-1} \text{sec}^{-1}$ for the decay of $\cdot\text{C}_6\text{H}_5\text{CO}_2\text{H}$ from the direct pulse radiolysis study.²¹ The flash photolysis of benzoic acid solution in the absence of the complex does not give a transient absorption spectrum with these characteristics.

Although k_{11} is not known, we estimate it to be on the order of $10^7 M^{-1} \text{sec}^{-1}$ by analogy to the H + $\text{Co}(\text{NH}_3)_5\text{O}_2\text{CCH}_3^{2+}$ reaction ($k \leq 1.3 \times 10^6 M^{-1} \text{sec}^{-1}$)²² and the fact that formate is more reactive to H abstraction by H atoms ($k = 2.2 \times 10^8 M^{-1} \text{sec}^{-1}$) than is

(14) R. G. Hughes, J. F. Endicott, and M. Z. Hoffman, *J. Chem. Soc. D*, 195 (1969).

(15) V. W. Cope and M. Z. Hoffman, *ibid.*, 227 (1972).

(16) L. Moggi, N. Sabbatini, and V. Balzani, *Gazz. Chim. Ital.*, **97**, 980 (1967).

(17) J. F. Endicott and M. Z. Hoffman, *J. Amer. Chem. Soc.*, **90**, 4740 (1968).

(18) V. Balzani, R. Ballardini, N. Sabbatini, and L. Moggi, *Inorg. Chem.*, **7**, 1398 (1968).

(19) R. Wander, P. Neta, and L. M. Dorfman, *J. Phys. Chem.*, **72**, 2946 (1968).

(20) M. Anbar and P. Neta, *Int. J. Appl. Radiat. Isotopes*, **18**, 493 (1967).

(21) M. Simic and M. Z. Hoffman, *J. Phys. Chem.*, **76**, 1398 (1972).

(22) J. Halpern and J. Rabani, *J. Amer. Chem. Soc.*, **88**, 699 (1966).

acetate ($2.7 \times 10^5 M^{-1} \text{sec}^{-1}$).^{20,23} Under the condition of [substrate] $\simeq 10^{-3} M$, the disappearance of H atoms *via* combination can be ignored. Reaction 11 would generate, as an intermediate, $\text{Co}(\text{NH}_3)_5\text{O}_2\text{C}\cdot^{2+}$. Such a Co(III) complex, in which the strongly reducing radical $\cdot\text{CO}_2^-$ is coordinated to the metal center, is probably very short-lived, undergoing facile intramolecular electron transfer to form Co^{2+} and release of CO_2 .²⁴ The rate constants for reactions 12, 13, and 15 are well known²⁰ to be 2×10^{10} , 5×10^7 , and $2 \times 10^9 M^{-1} \text{sec}^{-1}$, respectively. The HO_2 radical formed in reaction 12 does not reduce $\text{Co}(\text{NH}_3)_6^{3+}$ and appears to be inert to other Co(III) complexes such as the easily reducible $\text{Co}(\text{C}_2\text{O}_4)_3^{3-}$.²⁶ Its conjugate base, O_2^- , is a stronger reducing agent but would not be involved in this study inasmuch as the $\text{p}K_a$ for HO_2 is 4.8.²⁷ The reduction of Co(III) complexes by electron transfer from the $(\text{CH}_3)_2\dot{\text{C}}\text{OH}$ radical appears to be firmly established for a variety of systems ($\text{Co}(\text{NH}_3)_6^{3+}$, $\text{Co}(\text{NH}_3)_5\text{O}_2\text{CCH}_3^{2+}$, and $\text{Co}(\text{NH}_3)_5\text{O}_2\text{CC}_6\text{H}_4\text{NO}_2^{2+}$)^{2, 28, 29} with rate constants in the range of 10^7 – $10^9 M^{-1} \text{sec}^{-1}$ depending upon the structure of the X ligand.³⁰ Thus, reaction 14 must be included here when 2-propanol is used as a H-atom scavenger.

The rate of decay of the C-formato linkage isomer *via* reaction 7 is dependent upon pH, indicating that the $\text{p}K$ for reaction 6 is 2.6. However, the result of reaction 7 is the formation of Co^{2+} and the $\cdot\text{CO}_2\text{H}$ radical. It should be noted that the $\text{p}K$ of reaction 8 is 3.9³¹ and that the bimolecular nature of the decay of those radicals ($2k_9 \simeq 2k_{10} \simeq 1.5 \times 10^9 M^{-1} \text{sec}^{-1}$)³² into products is known.³³ Although the $\cdot\text{CO}_2^-$ radical is effective in reducing Co(III) complexes,^{5, 28–30} our results here imply that the more weakly reducing $\cdot\text{CO}_2\text{H}$ radical does not attack $\text{Co}(\text{NH}_3)_5\text{O}_2\text{CH}^{2+}$; we have already shown that $\cdot\text{CO}_2\text{H}$ is effective in the reduction of $\text{Co}(\text{NH}_3)_4\text{C}_2\text{O}_4^+$ and $\text{Co}(\text{NH}_3)_5\text{C}_2\text{O}_4^+$ but does not reduce $\text{Co}(\text{en})_2\text{C}_2\text{O}_4^+$.⁵ Differences in the redox potential of the complexes in question may be sufficient to render the $\cdot\text{CO}_2\text{H} + \text{Co}(\text{NH}_3)_5\text{O}_2\text{CH}^{2+}$ reaction endoergic.

In the absence of added scavengers, the reactions to consider in acidic medium are I_a , 1–5, 7, 9, and 11. Writing the quantum yields of the various products in terms of these mechanistic steps, $\phi_{\text{Co}^{2+}} = \phi_3 + \phi_7 + \phi_{11} = 0.55$, $\phi_{\text{H}_2} = \phi_{11} = 0.15$, and $\phi_{\text{CO}_2} = \phi_4 + \phi_{11} + 0.5\phi_9 = 0.43$. Furthermore, $\phi_3 = \phi_4 = \phi_{11}$ and $\phi_5 = \phi_7 = \phi_9$. Therefore, $\phi_5 = 0.24$ and $\phi_3 = 0.15$.

The scavenging data can be reconciled in the same way. In the presence of O_2 , where reaction 11 is eliminated in favor of (12), $\phi_{\text{Co}^{2+}} = \phi_3 + \phi_7 = 0.39$ (calcd) $\simeq 0.42$ (obsd). In the presence of 2-propanol, reaction 11 is replaced by reactions 13 and 14 and $\phi_{\text{Co}^{2+}} = \phi_3 + \phi_7 + \phi_{14} = 0.54$. $\phi_{\text{H}_2} = \phi_{13} = 0.14$ inasmuch as $\phi_{13} = \phi_4 = \phi_3$; $\phi_{\text{CO}_2} = \phi_4 + 0.5\phi_9 = 0.27$. In the presence of allyl alcohol, where reaction 15 replaces (11), $\phi_{\text{Co}^{2+}} = \phi_3 + \phi_7 = 0.40$, $\phi_{\text{H}_2} = 0.0$, and $\phi_{\text{CO}_2} = \phi_4 + 0.5\phi_9 =$

0.28. The agreement between the experimental results and the proposed mechanism is excellent. The 254-nm photolysis of this complex could serve as a convenient photochemical source of H atoms except for the rather fast rate of reaction 11 and the formation and decay of the C-bonded formato isomer.

There is one other documented case of photolytically induced linkage isomerization in a Co(III)-ammine complex, the nitro \rightarrow nitrito intramolecular conversion in $\text{Co}(\text{NH}_3)_5\text{NO}_2^{2+}$.¹⁸ (It is to be noted that nitrite and formate ions are isoelectronic.) At 254 nm, the quantum yields for Co^{2+} production and linkage isomerization are 0.51 and 0.13, respectively. In this case, the isomerization product, $\text{Co}(\text{NH}_3)_5\text{ONO}^{2+}$, is a stable species. We also subjected $\text{Co}(\text{NH}_3)_5\text{NO}_2^{2+}$ to flash photolysis and monitored the absorbance of the solution at 320 nm, where the nitrito complex shows an absorption maximum.¹⁸ The absorbance of the solution increased "instantaneously" during the lifetime of the flash ($1/e$ time = 30 μsec), indicating that the intramolecular isomerization process has a first-order rate constant $\geq 10^5 \text{sec}^{-1}$. The concurrent formation of Co^{2+} and NO_2 and the nitrito isomer was explained¹⁸ on the basis of the "radical-pair" model then in vogue. The two processes were seen to arise from the same photoreactive excited state which produced a Co(II) $\cdot\cdot\text{NO}_2$ species. During the lifetime of this pair, the NO_2 group could either rotate in the solvent cage and isomerize or escape the cage, leading to the redox products. Because the sum of the quantum yields is less than unity, attachment of the NO_2 group (N bonded) coupled with electron transfer from the Co(II) center would reform the original substrate.

It is easy to see that this mechanistic approach cannot be applied to the formato system. Rotation of a $\text{HCO}_2\cdot$ radical within the solvent cage does not expose any other coordination site to the Co(II) center unless isomerization of the radical to $\cdot\text{CO}_2\text{H}$ also takes place within the solvent cage. There is no evidence that this

(23) However, note that $k(\text{H} + \text{formic acid}) \sim 10k(\text{H} + \text{acetic acid})$,²⁰ which is probably more analogous to the Co(III) complexes. The dependence of the quantum yields of products on [scavenger] as shown in Figures 1 and 2 is consistent with $k(\text{H} + \text{complex}) \sim 10^7 M^{-1} \text{sec}^{-1}$.

(24) J. P. Candlin and J. Halpern, *J. Amer. Chem. Soc.*, **85**, 2518 (1963).

(25) N. Zevos, *J. Phys. Chem.*, **72**, 1506 (1968).

(26) N. S. Rowan, R. M. Milburn, and M. Z. Hoffman, *Inorg. Chem.*, in press.

(27) B. H. J. Bielski and J. M. Gebicki, *Advan. Radiat. Chem.*, **2**, 177 (1970).

(28) E. P. Vanek and M. Z. Hoffman, manuscript in preparation.

(29) M. Z. Hoffman and M. Simic, *J. Amer. Chem. Soc.*, **94**, 1757 (1972).

(30) M. Simic and M. Z. Hoffman, manuscript in preparation.

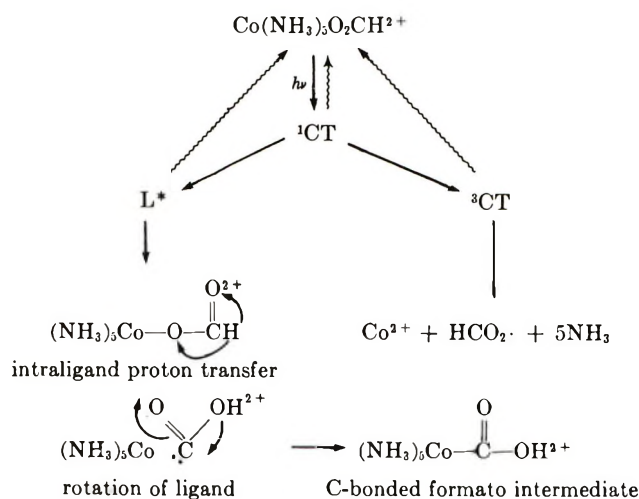
(31) A. Fojtik, G. Czapski, and A. Henglein, *J. Phys. Chem.*, **74**, 3204 (1970).

(32) P. Neta, M. Simic, and E. Hayon, *ibid.*, **73**, 4207 (1969).

(33) H. Fricke, E. J. Hart, and H. P. Smith, *J. Chem. Phys.*, **6**, 229 (1938); E. J. Hart, *J. Amer. Chem. Soc.*, **83**, 567 (1961).

process occurs to the radicals free in solution. Furthermore, escape of $\cdot\text{CO}_2\text{H}$ and $\text{HCO}_2\cdot$ radicals from the solvent cage would not lead to equivalent products inasmuch as $\text{HCO}_2\cdot$ most likely undergoes decarboxylation and $\cdot\text{CO}_2\text{H}$ is known to disproportionate.³³ In addition, in order to explain the less-than-unity value of the sum of the quantum yields, isomerization would have to occur to the $\cdot\text{CO}_2\text{H}$ radical in order to regenerate the original substrate.

Instead, we suggest that a radiationless transition from the original singlet charge-transfer excited state (^1CT) to an excited state of the ligand (L^*) causes carbon \rightarrow oxygen proton transfer. Although the carbon hydrogen is normally *extremely* weakly acidic ($\text{p}K_a \sim 20?$), its lability could be markedly increased in the excited state such that intraligand proton transfer takes place. The resulting "carbene" will be an extremely good Lewis base and could displace the carboxylate oxygen from its coordination site. Such rotation of the ligand must take place within the coordination sphere of the complex in a time period short compared to entrance of the solvent into the inner sphere and the protonation of the "carbene." Pro-



tonation of carboxylato ligands has been demonstrated in highly acidic solution, although it is not clear whether the site of protonation is the carbonyl or the coordinated oxygen.³⁴ Likewise, it is not possible here to identify the site of protonation in the intraligand proton transfer, although loosening of the ligand can easily be seen to result from attack at either oxygen atoms. While it is tempting to assign the short-lived intermediate (SL) observed in the flash to one of the precursors of the C-formato linkage isomer, there is no evidence to support this view; the short lifetime of SL and its dull absorption spectrum are also characteristic of free radicals and other transient species.

From the ratio of $\phi_5/\phi_3 = 1.6$, we see that the formation of the C-bonded formate species from the ligand excited state is a more probable process than formation of Co^{2+} and the oxidized ligand. We have shown⁵ in

the case of $\text{Co}(\text{en})_2\text{C}_2\text{O}_4^+$ that ligand excitation causing heterolytic C-C bond scission and the ultimate formation of the C-bonded formato isomer is about four times more probable than the redox processes. Thus, "intramolecular sensitized" ligand excitation by charge-transfer absorption may be a more dominant process in the photochemistry of $\text{Co}(\text{III})$ complexes than even the ubiquitous formation of Co^{2+} . The extent to which this intramolecular sensitized ligand excitation is dependent upon the electronic structure of the ligand and its overlap with the orbitals of the central metal will be the subject of future investigations. Note, however, that ϕ_3 , the quantum yield for direct primary formation of Co^{2+} via the ^3CT state, has the same value (0.1-0.2) for the corresponding process in $\text{Co}(\text{III})$ -ammine complexes containing saturated, simple, aliphatic carboxylic acids (including oxalate). Thus, in the cases of $\text{Co}(\text{NH}_3)_5\text{O}_2\text{CCH}_3^{2+}$ and $\text{Co}(\text{NH}_3)_5\text{O}_2\text{CCH}_2\text{CO}_2\text{H}^{2+}$, for example, $\phi_{\text{Co}^{2+}} = 0.19$ and 0.15, respectively, with no evidence apparent for other significant sources of Co^{2+} , linkage isomerization, or ligand excitation.^{2,35} This is not to say that ligand excitation is absent, merely that there is no evidence one way or the other. The similarity of these quantum yield results for direct primary Co^{2+} formation argues strongly that there is a common electronic process occurring that is largely independent of the nature of the carboxylic acid serving as the sixth ligand.

The results of the experiments with $\text{Co}(\text{en})_2(\text{OH}_2)\text{O}_2\text{CH}_2^+$ reemphasize the fact that the chelating en groups diminish the photosensitivity of the complex, perhaps by introducing additional pathways for energy degradation to the ligands. In addition, it is clear that this complex and $\text{Co}(\text{en})_2\text{C}_2\text{O}_4^+$ generate identically behaving long-lived intermediates, which supports the mechanistic hypothesis presented in our communication¹⁰ concerning the decomposition of the oxalate ligand.

Finally, the results of the long irradiation at 366 nm in the ligand-field absorption band of $\text{Co}(\text{NH}_3)_5\text{O}_2\text{CH}_2^+$ indicate that the behavior of this complex parallels that of $\text{Co}(\text{NH}_3)_5\text{O}_2\text{CCH}_3^{2+}$, where we showed² that NH_3 aquation was an important process and acetate aquation was of secondary importance. Although the absorptivity of the complex at 366 nm and the quantum yields are low, which prevent an appreciable buildup of product, it appears that NH_3 aquation to form $\text{Co}(\text{NH}_3)_4(\text{OH}_2)\text{O}_2\text{CH}_2^{2+}$ is an important process here as well. Presumably, a small amount of Co^{2+} is also formed at 366 nm from the slight overlap of the tail of the charge-transfer band with the ligand-field absorption band. Radiationless transition to a ligand-field

(34) M. B. Barrett, J. H. Swinehart, and H. Taube, *Inorg. Chem.*, **10**, 1983 (1971).

(35) D. D. Campano, E. R. Kantrowitz, and M. Z. Hoffman, manuscript in preparation.

state from the charge-transfer excited state populated by 254-nm radiation resulting in NH_3 aquation is a

possible process also. However, no evidence could be found for the process from the 254-nm photolyses.

Kinetic Analysis and Mechanism of Chlorine-38 and Bromine-82 Recoil

Reactions in $\text{K}_2[\text{ReBr}_6]/\text{K}_2[\text{ReCl}_6]$ Mixed Crystals^{1a}

by K. Rössler, J. Otterbach,^{1b} and G. Stöcklin*

Institut für Radiochemie der Kernforschungsanlage Jülich GmbH, D-517 Jülich, Germany (Received March 23, 1972)

Publication costs assisted by Kernforschungsanlage Jülich GmbH

The solid state reactions occurring during energy loss of (n,γ) -produced ^{38}Cl and ^{82}Br recoils have been studied in $\text{K}_2[\text{ReBr}_6]/\text{K}_2[\text{ReCl}_6]$ mixed crystals. The product yields (free radiohalide and monosubstituted complexes) have been determined as a function of the mixed crystal composition. The yield curves obtained can be described by zero-, first-, and second-order terms, corresponding to three basic mechanisms: (1) correlated recombination (primary retention), (2) direct substitution, and (3) multistep process involving ligand vacancy exchange followed by combination. From the kinetic analysis the number of ligand vacancies required for product formation has been calculated to be 2.37γ and $0.66\gamma'$ per recoil event for ^{38}Cl and ^{82}Br , respectively ($\gamma, \gamma' =$ mole fraction of parent complex). Recoil ranges of ≥ 15 and about 10 \AA have been estimated for the primary atoms ^{38}Cl and ^{82}Br , respectively. Thermal annealing, which has also been studied as a function of the mixed crystal composition, exclusively leads to reformation of the labeled parent complex by correlated ($^{82}\text{Br}^-$) and noncorrelated ($^{37}\text{Cl}^-$) combination with a ligand vacancy.

Introduction

The *in situ* production of radioactive recoil atoms *via* nuclear processes provides a possibility of examining solid state reactions of individual atoms during and after their energy loss in ionic crystals [for a review *cf.* ref 2-4]. Hexahalocomplexes of transition metals are particularly well suited for the study of halogen recoils since their ligand sphere is a sensitive matrix for the detection of such reactions.⁵ The choice of the monovalent halogen makes these systems the most simple ones next to alkali halides. In contrast to the latter, the reactions of the recoil halogens can easily be traced since the radiohalogen appears in two different stable chemical forms, namely, as free halide and as ligand (labeled complex), which can be easily distinguished. Most important, the species found after dissolution of the crystal seem to be identical with those present in the solid matrix. In contrast to many other systems, metastable precursors do not give rise to an additional product formation upon dissolution. Unlike the complex recoil behavior of central atoms, the halogen ligand recoils, as shown in our previous studies on hexahalorhenates,⁵ come to rest in a rather undisturbed zone, predominantly involving complexes with only one missing ligand. The small number of ligand vacancies, together with the simple halogen interstitials, presents

a system close to the solid state physical model for single isolated point defects. A further unique advantage of the hexabromo and -chloro complexes of Re(IV) is the lack of dose effects;^{6,7} obviously redox or similar electronic processes complicating most of the hitherto known recoil experiments do not play any significant role.

Valuable kinetic and mechanistic information can be obtained from mixed crystals, which allow the performance of intermolecular competition experiments under identical conditions. In the case of the $\text{K}_2[\text{ReBr}_6]/\text{K}_2[\text{ReCl}_6]$ system the Br ligand recoil has already been

(1) (a) Presented in part at the Sixth International Hot Atom Chemistry Symposium at Brookhaven National Laboratory, Upton, N. Y., Sept 7-10, 1971. (b) In partial fulfillment of the requirements for a Ph.D. degree.

(2) (a) G. Harbottle, *Ann. Rev. Nucl. Sci.*, **15**, 89 (1965); (b) A. G. Maddock and R. Wolfgang in "Nuclear Chemistry," Vol. II, L. Yaffe, Ed., Academic Press, New York, N. Y., 1968, pp 186-248.

(3) G. Stöcklin, "Chemie heisser Atome, Chemische Taschenbücher," Bd. 6, Verlag Chemie, Weinheim/Bergstr., Germany, 1969; "Chimie des atomes chauds," Masson et Cie, Paris, 1972.

(4) H. Müller, *Atomkernenergie*, **16**, 237, 323 (1970).

(5) R. Bell, K. Rössler, G. Stöcklin, and S. R. Upadhyay, *J. Inorg. Nucl. Chem.*, **34**, 461 (1972).

(6) R. Bell, K. Rössler, G. Stöcklin, and S. R. Upadhyay, Report JÜL-625-RC (1969).

(7) R. Bell and G. Stöcklin, *Radiochim. Acta*, **13**, 57 (1970).

studied.^{5,6,8} The drastic differences observed between the recoil behavior of bromine and chlorine⁹ prompted us to investigate the kinetics of product formation by both ³⁸Cl and ⁸²Br in the same sample as a function of the mixed crystal composition. A detailed kinetic analysis was expected to provide a key to the mechanisms of the solid state reactions and the types of defects involved.

Experimental Section

Materials and Irradiation. Among the hexahalo-rhenates(IV) only the hexabromo and the hexachloro complex crystallize in a similar face-centered cubic lattice of K₂[PtCl₆] type, with lattice constants $a_0 = 9.843 \text{ \AA}$ for K₂[ReCl₆] and $a_0 = 10.387 \text{ \AA}$ for K₂[ReBr₆]. Thus, only mixed crystals of hexabromo- and hexachlororhenate can be found. K₂[ReCl₆] was obtained from Heracus GmbH, and K₂[ReBr₆] was prepared according to the method of Krauss, *et al.*¹⁰ The products were recrystallized from 0.5 N CH₃COOH solutions by adding isopropyl alcohol for the elimination of free halide traces. Mixed crystals were prepared from the acetic acid solutions as described by Müller.¹¹ Homogeneity was checked by X-ray diffraction, only minor deviation of the lattice constants from the Vegard rule could be observed.¹² The thermodynamic instability of mixed crystals with small concentrations of one component¹¹ does not lead to gross demixing. This also becomes obvious from the totally changed solid state chemical behavior in the mixed systems as compared to the pure components.

Each mixed crystal composition was checked by activation analysis of the [ReBr₆]²⁻ and [ReCl₆]²⁻ spots obtained after electrophoretic (Cellogel) separation (see below), using semiconductor spectroscopic measurement of the 0.137 and 0.155 MeV γ radiation of ^{186,188}Re (*cf.* ref 12).

For the *in situ* production of the recoil halogens we used the thermal neutron induced nuclear reactions ³⁷Cl(n, γ)³⁸Cl ($T = 37.3 \text{ min}$) and ⁸¹Br(n, γ)^{82m}Br-(I.T.)⁸²Br ($T = 35.4 \text{ hr}$). The isomeric transition of bromine, which in 92% follows the preceding (n, γ) event, should not affect the ⁸²Br product distribution, as has been shown before.^{5,13}

Neutron activation was carried out in a Merlin type swimming pool reactor (FRJ-1) in the pneumatic tube irradiation facility BE 25 (thermal neutron flux density, $3 \times 10^{13} \text{ cm}^{-2} \text{ sec}^{-1}$; fast neutron flux density, $3 \times 10^{12} \text{ cm}^{-2} \text{ sec}^{-1}$; γ -dose rate, $2 \times 10^8 \text{ R/hr}$). Irradiation times ranged from 5 to 10 min, corresponding to thermal neutron doses of 1 to $2 \times 10^{16} \text{ cm}^{-2}$. Samples of about 1 mg were sealed in quartz ampoules, cooled to -70° during activation, and stored at this temperature until separation. Further reduction of the temperature to -170° did not affect the results.

Product Separation and Radiometric Analysis. For

the analysis of the halogen recoil products the irradiated samples were dissolved in 0.4 M H₂SO₄. Previous studies^{5,6} had shown that hydrolysis and/or isotopic exchange do not take place during the dissolution and separation procedure applied. Owing to the short half-life of ³⁸Cl the exact but slow high voltage paper electrophoresis (4 hr per run), used in the previous experiments, could not be applied. A rapid separation, however, of the ligand and central atom recoil products (ReO₂, ReO₄⁻, [ReBr_nCl_{6-n}]²⁻, Cl⁻, Br⁻) could be achieved in less than 20 min by electrophoresis on cellulose acetate strips (Cellogel, Chemetron, Milano). Ten micrograms of the complexes were dissolved in 20 μ l of the electrolyte, which consisted of 0.4 M H₂SO₄ with 0.004 M lactic acid. When applying a voltage of 600 V (current about 1 mA) for 20 min, the [ReCl₆]²⁻ had migrated about 10 cm from the starting point, the [ReBr₆]²⁻ about 5 cm. The carrier-free mixed ligand complexes could be detected between these two visible spots by means of autoradiography. The free halides (³⁸Cl⁻, ⁸²Br⁻) were both found at about 20 cm from the starting point (for further details *cf.* also ref 12). Since it had already been known from paper electrophoretic studies^{5,6} that the radiohalogen activity almost exclusively appears in the monosubstituted complexes and the free halide, it was not necessary to separate all the individual mixed ligand complexes. Thus, the Cellogel strip was only cut into four segments, corresponding to (1) [ReBr₅⁸²Br]²⁻ + [ReBr₅³⁸Cl]²⁻, (2) higher substituted: [ReBr_{1<n<5}Cl_{6-n}]²⁻, (3) [ReCl₅⁸²Br]²⁻ + [ReCl₅³⁸Cl]²⁻, and (4) free halides ⁸²Br⁻, ³⁸Cl⁻. The individual spots now contained a mixture of ³⁸Cl and ⁸²Br together with a large amount of ^{186,188}Re activity. Thus, γ -ray spectrometric techniques had to be applied for the determination of the radiohalogen distribution. Four electrophoretic runs were carried out from one sample, and the corresponding segments were combined and subjected to activity measurement, applying a semiconductor detector (Canberra) and a multichannel analyzer (DIDAC 4000, Intertechnique). The 1.64- and 2.17-MeV γ lines were used for ³⁸Cl and the 0.78- and 0.55-MeV γ rays for ⁸²Br. In some cases, where the activity level of the ^{186,188}Re background was too high, a special dead-time correction procedure had to be used (*cf.* ref 12).

(8) H. Müller and S. Martin, *Inorg. Nucl. Chem. Lett.*, **5**, 761 (1969).

(9) K. Rössler and J. Otterbach, Sixth International Hot Atom Chemistry Symposium, Brookhaven National Laboratories, Upton, N. Y., Sept 1971.

(10) K. Krauss and H. Steinfeld, *Ber. Deut. Chem. Ges.*, **64**, 2554 (1931).

(11) H. Müller, Habilitationsschrift, University of Freiburg/Breisgau (1964).

(12) J. Otterbach, Thesis, University of Köln (1972); Report JÜL-832-RC (1972).

(13) G. B. Schmidt and W. Herr in "Chemical Effects of Nuclear Transformations," Vol. I, IAEA, Vienna, 1961, p 525.

Results and Discussion

The radiochemical yields of the individual ³⁸Cl- and ⁸²Br-labeled products have been determined as a function of the mixed crystal composition. Yields are expressed in per cent of the total induced ³⁸Cl and ⁸²Br activity, neglecting the higher substituted complexes. The total yields of the latter products ([ReBr₂Cl₄]²⁻, [ReBr₃Cl₃]²⁻, [ReBr₄Cl₂]²⁻) generally range only between 1 and 3%; considering the experimental error involved it cannot be definitely decided whether these complexes are formed at all. The radiohalogen almost exclusively appears in three major products: the free halide, the labeled parent, and the monosubstituted complex of the other mixed crystal component. In Figure 1 the radiochemical yields *Y* of these products are plotted *vs.* the mole fractions γ and γ' , respectively, of the corresponding parent complex. For the ⁸²Br-labeled products only straight lines are observed. The individual values generally agree within the experimental error with those obtained by Müller and Martin.⁸ Small differences can be attributed to the fact that these authors carried out the irradiations without cooling, thus allowing a partial annealing due to nuclear heating (see below). When compared with ⁸²Br a completely different picture is obtained for the ³⁸Cl distribution, which has now also been studied. These yield curves show a complex parabolic shape. It is noteworthy that for both recoil chlorine and bromine the yield curves do not show an additive linear behavior resulting from the two individual systems involved. This in turn provides independent evidence that we indeed deal with true homogeneous mixed crystals, which are not subjected to demixing.

Kinetic Analysis. The dependence of the radiochemical yields *Y* of the individual products on the mole fraction of the hexachloro and hexabromo component γ and γ' , respectively, can be expressed by simple functions corresponding to kinetics of zero, first, and second order or their combinations.

In the case of the ⁸²Br yields, the constants of these linear relations can be immediately obtained graphically from the slopes and the intercepts with the ordinate, respectively. If this is carried out for the products [ReBr₅⁸²Br]²⁻ and [ReCl₅⁸²Br]²⁻, the remaining constants for the ⁸²Br⁻ yield function result from the activity balance to 100%. With the numerical values thus obtained, the following kinetic relations are found for the ⁸²Br product yields, depending on the mole fraction γ' of the [ReBr₅]²⁻ component

$$Y_{[\text{ReBr}_5^{82}\text{Br}]^{2-}} = 14 + 66\gamma' \quad (1)$$

$$Y_{[\text{ReCl}_5^{82}\text{Br}]^{2-}} = 61(1 - \gamma') \quad (2)$$

$$Y_{^{82}\text{Br}^-} = 25 - 5\gamma' \quad (3)$$

In the case of ³⁸Cl the [ReBr₅³⁸Cl]²⁻ yields show a maximum at about $\gamma = 0.5$, thus indicating that the formation of this product predominantly follows a second-

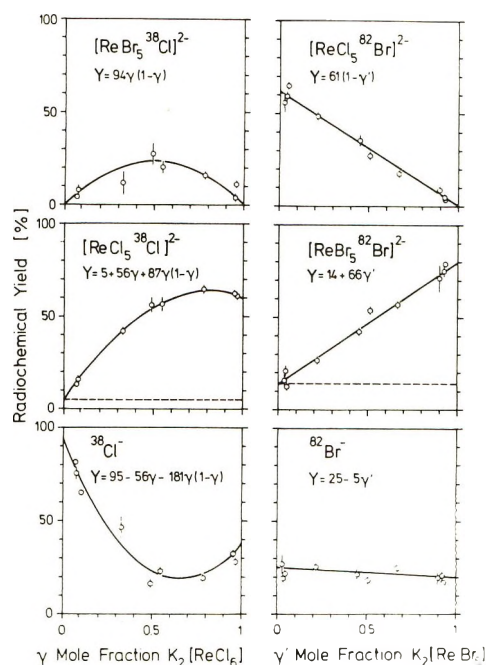


Figure 1. Effect of mixed crystal composition on the ³⁸Cl and ⁸²Br product distribution in the K₂[ReBr₆]/K₂[ReCl₆] system. (The drawn curves represent the theoretical functions, *cf.* text.)

order kinetics. In any case, the yield must be zero for $\gamma = 1$, while the relatively large experimental errors leave some doubt whether the yield can also be extrapolated to zero at $\gamma = 0$. However, it seems reasonable to assume a symmetrical curve which can be represented by a second-order parabola function. Thus, with $Y = 0$ at $\gamma = 0$ and at $\gamma = 1$ we obtain

$$Y_{[\text{ReBr}_5^{38}\text{Cl}]^{2-}} = s\gamma(1 - \gamma) \quad (4)$$

where *s* is a constant.

For the more complex picture of the [ReCl₅³⁸Cl]²⁻ yield curve we assume zero-, first-, and second-order terms, obtaining a more general form of the parabola

$$Y_{[\text{ReCl}_5^{38}\text{Cl}]^{2-}} = p + q\gamma + r\gamma(1 - \gamma) \quad (5)$$

For the evaluation of the best constants for eq 4 and 5 we used a graphic error and trial procedure¹² leading to the following numerical values

$$Y_{[\text{ReBr}_5^{38}\text{Cl}]^{2-}} = 94\gamma(1 - \gamma) \quad (6)$$

and

$$Y_{[\text{ReCl}_5^{38}\text{Cl}]^{2-}} = 5 + 56\gamma + 87\gamma(1 - \gamma) \quad (7)$$

From the difference of eq 6 and 7 to 100% we obtain for the ³⁸Cl⁻ yield

$$Y_{^{38}\text{Cl}^-} = 95 - 237\gamma + 181\gamma^2 \quad (8)$$

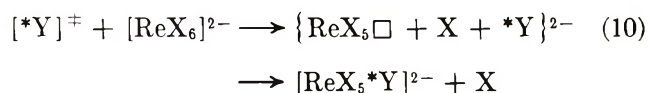
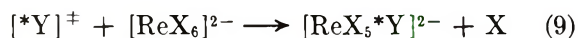
In Figure 1 these functions are represented by the solid lines. It can be seen that the fitting of the experimental points is good.

Mechanism. The zero-, first-, and second-order terms of the yield functions can be attributed to three different types of reactions.

1. *Primary Retention (Zero Order)*. For the labeled parent complexes $[\text{ReBr}_5^{82}\text{Br}]^{2-}$ and $[\text{ReCl}_5^{38}\text{Cl}]^{2-}$ the intercept with the ordinate represents the primary retention.⁸ This is defined as the fraction of labeled parent complex formed either by a direct correlated recombination or, more unlikely, by a lack of bond rupture. The value for the primary retention appears in eq 1 and 7 as a constant. From the symmetrical shape of the $[\text{ReBr}_5^{38}\text{Cl}]^{2-}$ yield curve it can be shown that the primary retention of ^{38}Cl is practically independent of the mixed crystal composition within the experimental error.¹² In the case of ^{82}Br , however, this is an open question.

As expected from the larger recoil energy and range (see below) the primary retention of ^{38}Cl is smaller (5%) as compared to that of ^{82}Br (14%).

2. *Substitution Reactions (First Order)*. The first-order terms can be understood, when postulating substitution reactions to occur either as a direct replacement (eq 9) or as a rapid combination following a preceding displacement within a reaction cage (eq 10). These processes can be formally described as

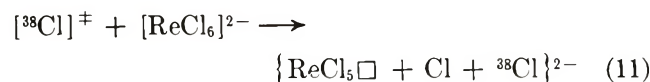


where $[*\text{Y}]^\ddagger$ represents the radioactive recoil halogen with excess kinetic energy and \Box a ligand vacancy.

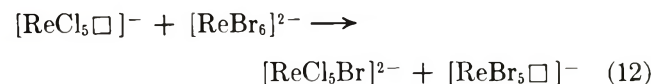
This substitution mechanism would imply a direct proportionality of the yield to the substrate concentration, corresponding to the above kinetics with first-order terms. The formation of $[\text{ReBr}_5^{82}\text{Br}]^{2-}$ and $[\text{ReCl}_5^{82}\text{Br}]^{2-}$ should therefore exclusively proceed *via* these substitution reactions (*cf.* eq 1 and 2). On the other hand, it becomes obvious that the ^{38}Cl recoil atoms cannot replace bromine ligands *via* such substitution processes, because the yield function for $[\text{ReBr}_5^{38}\text{Cl}]^{2-}$ does not contain a first-order term (*cf.* eq 6). This is also reflected by the extremely high free ^{38}Cl -yield at $\gamma = 0$ (*cf.* Figure 1), a fact which may be simply due to the inefficient energy transfer in collisions of chlorine with the heavier bromine ligands. A chlorine for chlorine substitution, on the other hand, should be possible as indicated by the first-order term in eq 7, even though the other terms of this equation indicate a contribution from different mechanisms to the formation of the labeled parent complex (see below).

3. *Multistep Process via Exchange of Ligand Vacancies (Second Order)*. The formation of $[\text{ReBr}_5^{38}\text{Cl}]^{2-}$ obviously requires the participation of both the hexabromo and the hexachloro components. As a working hypothesis we postulate a ligand vacancy exchange preceding the combination with the ^{38}Cl recoil atom. The product formation could then be explained by the following reaction scheme.

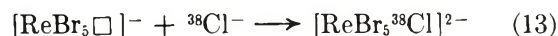
Formation of a secondary ligand vacancy



Formation of a tertiary ligand vacancy *via* ligand exchange



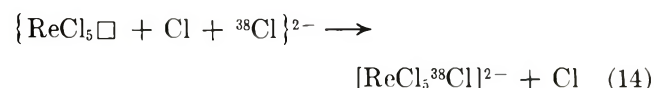
Product formation *via* combination



As postulated in eq 11, the formation of secondary ligand vacancies (the primary vacancy is that remaining in the parent complex after the nuclear process) by ^{38}Cl recoils should be much more likely for a Cl/Cl than for a Cl/Br collision. Evidence for the migration of ligand vacancies as formulated in eq 12 can be drawn from previous experiments of solid state ligand exchange in radiohalide doped hexahalorhenates.^{5,6} From the same work it can be deduced that the recoil halogen comes to rest as a halide ion and thus, the final substitution process in eq 13 is likely to proceed similar to a $\text{S}_{\text{N}}1$ substitution. In addition, it can be expected that any loss of a ligand caused by energetic collisions leaves a quasi positive hole in the ligand sphere. Furthermore, the effects of electrical fields on the annealing phenomena, recently observed in these systems,⁹ indicate the participation of charged entities. In any case, preceding electronic processes, leading to a stabilization of the recoil halogen as halide, should be fast and are not expected to interfere with the postulated kinetics. This is also demonstrated by the lack of dose effects in these systems.^{6,7}

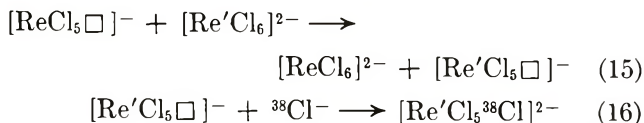
Since the formation of the secondary ligand vacancies $[\text{ReCl}_5\Box]^-$ is proportional to the mole fraction γ of $\text{K}_2[\text{ReCl}_6]$, the number of tertiary ligand vacancies $[\text{ReBr}_5\Box]^-$ should be proportional to $\gamma(1 - \gamma)$ as postulated in eq 4. If the proportionality factor is c , it follows $c \geq s$ (*cf.* eq 4), since not every tertiary vacancy leads to product formation.

The asymmetrical $[\text{ReCl}_5^{38}\text{Cl}]^{2-}$ yield curve cannot exclusively be explained *via* the above mechanism (eq 11–13). A reaction scheme, however, can be found which fits eq 7. In this case, the secondary chlorine ligand vacancies formed according to eq 11 should undergo one of the following reactions. Product formation *via* first-order reactions, *cf.* eq 10¹⁴



(14) For simplification we do not distinguish between the direct substitution and the cage combination immediately after displacement. This means that even for a direct substitution we now formally assume the preceding formation of secondary vacancies

or *via* second-order reactions including the formation of a tertiary chlorine ligand vacancy (eq 15), followed by a combination process (eq 16)



From an originally formed number $B\gamma$ of secondary ligand vacancies (*cf.* eq 11), $b\gamma$ undergo reactions according to eq 12, 14, and 15. Only the reaction of eq 14 directly leads to the product. The formation of tertiary vacancies diminishes the number $b\gamma$ of reactive secondary vacancies and with it the product yield by $c\gamma(1 - \gamma)$ (formation of $[\text{ReBr}_5\Box]^-$) and by $d\gamma^2$ (formation of $[\text{Re}'\text{Cl}_5\Box]^-$). Since only $e\gamma^2$ of the latter lead to the formation of $[\text{Re}'\text{Cl}_5{}^{38}\text{Cl}]^{2-}$, we obtain the following general expression

$$Y_{[\text{ReCl}_5{}^{38}\text{Cl}]^{2-}} = a + b\gamma - c\gamma(1 - \gamma) - d\gamma^2 + e\gamma^2 \quad (17)$$

With $f = d - e$, eq 17 can be converted into

$$Y_{[\text{ReCl}_5{}^{38}\text{Cl}]^{2-}} = a + b\gamma - c\gamma(1 - \gamma) - f\gamma^2 \quad (18)$$

Further transformation with $b_1 = b - f$ leads to

$$Y_{[\text{ReCl}_5{}^{38}\text{Cl}]^{2-}} = a + b_1\gamma - (f - c)\gamma^2 - (c - f)\gamma \quad (19)$$

or

$$Y_{[\text{ReCl}_5{}^{38}\text{Cl}]^{2-}} = a + b_1\gamma + (f - c)\gamma(1 - \gamma) \quad (20)$$

Equation 20 is formally identical with the experimentally derived kinetic expression eq 7. (The term $b_1\gamma$ also contains a contribution from the postulated ligand exchange mechanism, therefore the first-order term of eq 7 cannot exclusively be attributed to direct substitution processes.) By comparing eq 7 with eq 19 and 20 we obtain $f - c = 87$ or $b_1 + (f - c) = b - c = 143$.

With eq 6 and 18 it follows that $c \geq 94$. For the constants in eq 18 we obtain $b \geq 237$; $f \geq 181$; $a = 5$; and hence

$$A_{[\text{ReCl}_5{}^{38}\text{Cl}]^{2-}} = 5 + 237\gamma - 94\gamma(1 - \gamma) - 181\gamma^2 \quad (21)$$

Equation 21 is in agreement with eq 6 and 7, thus providing evidence for the postulated mechanism. Furthermore, each equation of the general form of eq 18 is allowed, if $b = 237 + x$, $c = 94 + x$, and $f = 181 + x$, where x is a positive number.

In the above discussion we have neglected a possible formation of higher order vacancies, but it could be shown that for the explanation of our experimental results it was not necessary to postulate vacancies higher than third order.¹²

Number of Ligand Vacancies and Recoil Range. Even though the fitting of the experimental results of the $[\text{ReCl}_5{}^{38}\text{Cl}]^{2-}$ yield curve can be achieved with

different sets of constants, it is still possible to make at least semiquantitative statements about the number of ligand vacancies involved for product formation and the range of the recoil atom.

When applying eq 21 to the microscopic recoil zone, it follows, that at least 2.37γ secondary ligand vacancies are formed per recoil event within the ³⁸Cl reaction volume, *i.e.*, for $\gamma = 1$ at least 2.37. Hence, for the formation of 0.61 product molecules of $[\text{ReCl}_5{}^{38}\text{Cl}]^{2-}$ at least 2.37 secondary ligand vacancies are required. The total number produced is probably greater ($B > b$, *cf.* eq 11, 17), since a certain fraction of vacancies cannot be reached by the recoil atom, except by migration, *e.g.*, during postirradiation annealing.

In the case of recoil bromine the corresponding number of secondary ligand vacancies is obtained from eq 1 and 2, namely $61 + 5\gamma'$, *i.e.*, 0.66 ligand vacancies per recoil event for $\gamma' = 1$. Comparison with ³⁸Cl shows for the pure systems a ratio of $2.37:0.66 = 3.6$, indicating that retention forming processes involve 3.6 times more ligand vacancies for ³⁸Cl recoils in $\text{K}_2[\text{ReCl}_6]$ than for ⁸²Br in $\text{K}_2[\text{ReBr}_6]$. The greater number of participating ligand vacancies in the case of recoil chlorine is in agreement with our mechanistic assumption that here product formation occurs *via* tertiary ligand vacancies, while recoil bromine undergoes substitution reactions.

As far as the reaction volume is concerned, a similar pattern can be expected. In the case of recoil chlorine the primary vacancy is only pertinent with respect to the formation of the primary retention. The nearly symmetrical $[\text{ReBr}_5{}^{38}\text{Cl}]^-$ yield curve, which can be extrapolated to zero at $\gamma = 0$, indicates that a bromine ligand vacancy formed by exchange with a primary chlorine ligand vacancy in one of the nearest complexes does not come within reach of the ³⁸Cl recoil atom.

Since for $\gamma = 1$, on the other hand, 2.37 ligand vacancies are involved in retention formation, it follows that these vacancies can hardly be found in complexes next to the primary vacancy. This means that the range exceeds at least 1.5 lattice distances; in other words, the average recoil range of ³⁸Cl in $\text{K}_2[\text{ReCl}_6]$ cannot be smaller than 15 Å.

In the case of recoil bromine such information is not immediately available since bromine undergoes substitution without tertiary vacancy formation. The range will certainly be smaller and can roughly be estimated to be 10 Å, when compared with the ¹⁸⁶Re recoil range of about 5 Å in $\text{K}_2[\text{ReBr}_6]/\text{K}_2[\text{SnCl}_6]$ mixed crystals.¹¹

The range of the primary atom and the number of defects produced are directly proportional to the recoil energy. Since these numbers can, in principle, be calculated, a comparison with our results should be possible. Unfortunately, relevant data of neutron capture γ -ray spectra are not available for the two nuclear processes under investigation.

The observed ratio of ligand vacancies participating in product formation by ^{38}Cl and ^{82}Br , respectively (in pure systems $2.37:0.66 = 3.6$), might reflect the recoil energy ratio. For the $^{35}\text{Cl}(n,\gamma)^{36}\text{Cl}$ spectrum^{15a} with $E_{\gamma_{\text{max}}} = 6.13$ MeV Hsiung and Gordus^{15b} have calculated a mean recoil energy of about 300 eV. In the case of the natural bromine the capture γ -ray spectrum is completely different, showing a much larger contribution of low energy transitions.¹⁶ A rough estimation indicates that the mean recoil energy will be about 80–100 eV.^{17,18} Even though these numbers can only provide the right order of magnitude for the nuclear processes $^{37}\text{Cl}(n,\gamma)^{38}\text{Cl}$ and $^{81}\text{Br}(n,\gamma)^{82\text{m}}\text{Br}$ (I.T.) ^{82}Br involved in our experiments, it is interesting that a similar ratio is obtained. This may indicate that mean recoil energies of about 300 and 100 eV for ^{38}Cl and ^{82}Br , respectively, are a reasonable assumption. It remains questionable whether the isomeric transition, which in 92% follows the preceding (n, γ) activation of ^{81}Br , will significantly contribute to the recoil energy and range. At least this additional process should not influence the product formation. It has been shown, that the free recoil halide yield in $\text{K}_2[\text{ReBr}_6]$ is identical with the $^{79}\text{Br}(n,\gamma)^{80\text{m}}\text{Br}$ and the $^{81}\text{Br}(n,\gamma)^{82\text{m}}\text{Br}$ (I.T.) ^{82}Br process.⁵ Also, Schmidt and Herr¹³ did not observe any free halide after the isomeric transition in $^{80\text{m}}\text{Br}$ -labeled $\text{K}_2[\text{ReBr}_6]$. Similar results have been obtained by Müller and Cramer¹⁹ for the isomeric transition in $\text{K}_2[\text{ReBr}_6]/\text{K}_2[\text{SnCl}_6]$ mixed crystals. If bond rupture occurs at all, the $^{80\text{g}}\text{Br}$ formed by isomeric transition obviously remains in the immediate vicinity of its primary ligand vacancy having a good chance for fast recombination. The same should be true for the isomeric transition of $^{82\text{m}}\text{Br}$.

The absolute number of vacancies formed can now be calculated from the theory of Kinchin and Pease.²⁰ For a 100-eV event one obtains one to two and for a 300-eV event three to five vacancies, assuming a displacement threshold of $E_d \approx 25$ eV, and taking into account the energy loss by potassium displacements. It remains questionable, however, whether this classical displacement threshold for the formation of a stable interstitial vacancy pair is meaningful in a complicated crystal with the possibility of an easy recombination.

Although the calculated numbers represent the maximum values of permanent vacancies, while those obtained by our kinetic approach are the minimal number of permanent and intermediate vacancies, the agreement is relatively good. It is interesting to note that these values are similar to those obtained by Erginsoy, *et al.*,²¹ in such a different material as α -iron (one and three displacements for 100 and 250 eV, respectively). Also, the mean vector ranges obtained from recoil experiments in ionic mixed crystals ($0.5a_0$ for central atom recoils of some 30–50 eV;^{22,23} $\approx 1.0a_0$ and $\leq 1.5a_0$ for ^{82}Br and ^{38}Cl recoils of some 80–100 and 300 eV, respectively) are in reasonable agreement with

those computed for 40- to 130-eV events in Cu, α -Fe, and KCl ($\approx 1a_0$)^{21,24,25}.

Thermal Postrecoil Annealing. Further information on the specific location of the recoil atoms after thermalization and their correlation to nearby vacancies can be obtained by investigating the annealing behavior. In a previous study of the kinetics of such processes in the individual systems we have shown that heating of the complexes after neutron activation causes a decrease of the free halide yield and a concomitant increase of the labeled parent.^{5,6} It could also be demonstrated that this thermal annealing reactions can mainly be attributed to two processes: a solid state exchange *via* ligand vacancies in the bulk of the crystal and a combination of recoil defects (primary atoms and vacancies) in the specific disorder zone formed by the recoil atom.⁹ The basic differences between the recoil phenomena in the individual systems and the mixed crystal and the completely different behavior of recoil chlorine and bromine prompted us to study also the annealing of both radiohalides in the mixed crystal systems.

For this purpose, the product yields have again been determined as a function of the mole fraction of the components after annealing the irradiated sample for 30 min at 200°. Under these conditions the plateau values of annealing are reached.⁵ Figure 2 shows the graphical representation of the annealed product yields as a function of the mixed crystal composition (solid lines). The curves for the unannealed values as taken from Figure 1 are also given (dashed lines without experimental points).

For recoil bromine it can be seen that the free $^{82}\text{Br}^-$ exclusively enters the parent complex $[\text{ReBr}_6]^{2-}$, even when highly diluted with the chloro complex. The $[\text{ReBr}_5^{82}\text{Br}]^{2-}$ yield curves with and without annealing are represented by two almost parallel straight lines, *i.e.*, the extent of annealing is independent from the composition of the mixed crystal. From this it follows

(15) (a) L. V. Groshev, B. P. Adyasevich, and A. M. Demidov, Proceedings of the International Conference on Peaceful Uses of Atomic Energy, Geneva, 1955, United Nations, New York, N. Y., 1956; (b) C. Hsiung, H. Hsiung, and A. A. Gordus, *J. Chem. Phys.*, **34**, 535 (1961).

(16) N. C. Rasmussen, Y. Hukai, T. Inoye, and V. J. Orphan, AFCRL-69-0071 (1969).

(17) J. W. Cobble and G. B. Boyd, *J. Amer. Chem. Soc.*, **74**, 1282 (1952).

(18) M. T. Robinson, K. Rössler, and I. M. Torrens, KFA-Jülich and ORNL, to be published.

(19) H. Müller and D. Cramer, *Radiochim. Acta*, **14**, 78 (1970).

(20) G. H. Kinchin and R. S. Pease, *Rept. Progr. Phys.*, **18**, 1 (1955).

(21) C. Erginsoy, G. H. Vineyard, and A. Englert, *Phys. Rev. A*, **133**, 595 (1964).

(22) H. Müller in "Chemical Effects of Nuclear Transformations," Vol. II, IAEA, Vienna, 1965, p 359.

(23) W. J. van Ooij, Thesis, Technische Hogeschool Delft (1971).

(24) G. H. Vineyard, J. B. Gibson, A. N. Goland, and M. Milgram, *Phys. Rev.*, **120**, 1229 (1960).

(25) I. M. Torrens and L. T. Chadderton, *ibid.*, **159**, 671 (1967).

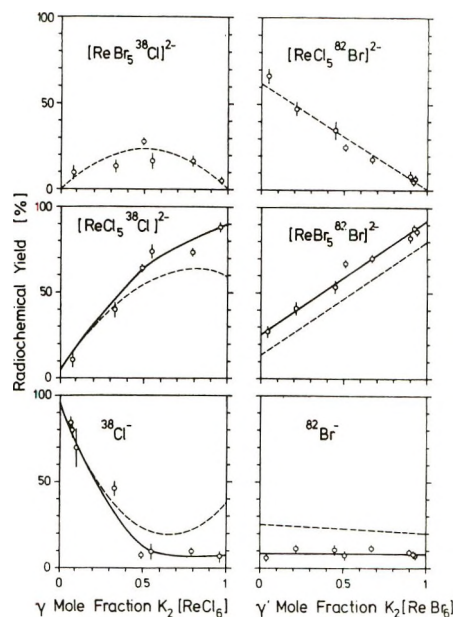


Figure 2. Effect of mixed crystal composition on the ^{38}Cl and ^{82}Br product distribution in the $\text{K}_2[\text{ReBr}_6]/\text{K}_2[\text{ReCl}_6]$ system after thermal annealing (solid lines and experimental values, radiochemical yields after 30-min annealing at 200° ; dotted lines, radiochemical yields without annealing *cf.* Figure 1).

that the $^{82}\text{Br}^-$ only undergoes recombination with the primary ligand vacancy.

The exclusively correlated annealing of the recoil bromine provides further evidence that the ^{82}Br only finds a very small number of secondary ligand vacancies in its immediate vicinity (0.66 per recoil event, *cf.* last paragraph) and remains within easy reach of its primary vacancy.

The annealing of ^{38}Cl is more difficult to understand. Again, the free $^{38}\text{Cl}^-$ exclusively enters the parent complex $[\text{ReCl}_6]^{2-}$. Since, however, the recoil chlorine at least produces 2.37γ secondary vacancies in its immediate vicinity (see above), it has other reaction possibilities than correlated recombination. Also, the greater recoil range makes the latter process rather unlikely. The most striking evidence against a correlated recombination in the case of ^{38}Cl is obtained from the fact that at high dilution with $\text{K}_2[\text{ReBr}_6]$ practically no annealing occurs (*cf.* Figure 2).

Since the primary vacancy is not available for the annealing of $^{38}\text{Cl}^-$, it only has the possibility of undergoing thermal product formation with secondary and tertiary vacancies or to a lesser extent by solid state exchange *via* thermally produced ligand vacancies.^{5,12} The number of secondary vacancies (at least 2.37γ per recoil event) decreases with increasing concentration of the hexabromo component, thus preventing an annealing at the $\text{K}_2[\text{ReCl}_6]$ -rich side of the mixed crystals (*cf.* Figure 2).

In agreement with the above-postulated radiation damage picture, the annealing reactions of both radiohalide ions proceed almost exclusively *via* ligand vacan-

cies in the immediate vicinity of the thermalized recoil halogen, either correlated ($^{82}\text{Br}^-$) or with secondary and tertiary vacancies ($^{38}\text{Cl}^-$).

Conclusion

The kinetic analysis of product formation in the mixed crystal system has shown to provide new detailed information on the radiation damage caused by (n,γ) recoils and their solid state reactions in complex ionic crystals. The almost exclusive formation of the monosubstituted complexes clearly indicates that the damage in the vicinity of the thermalized recoil atom is small, involving mainly complexes with only one or, to a lesser extent, two missing ligands. The different modes of solid state reactions leading to the formation of these products by both the hot processes during irradiation and the post recoil thermal annealing of the remaining lattice defects are summarized in Table I.

The hot processes involve correlated recombination (primary retention), direct substitution, or rapid cage combination and combination following ligand vacancy exchange. Thermal annealing exclusively leads to the reformation of the labeled parent by correlated ($^{82}\text{Br}^-$) and noncorrelated ($^{38}\text{Cl}^-$) combination.

The question remains, whether the drastic differences between the reactions of recoil chlorine and those of recoil bromine are mainly due to chemical parameters or the different primary recoil energy or collision dynamical factors such as mass disparity. In a previous paper we have pointed out the influence of bond energies and steric parameters, particularly on thermal reactions occurring during annealing and solid state exchange.⁵ These effects, however, should play a minor role as far as hot reactions are concerned. Also, the different recoil energies of ^{82}Br and ^{38}Cl , which are much greater than bond energies and displacement thresholds, cannot explain the fundamental mechanistic differences observed. This is also demonstrated by the fact, that (n,γ) and $(n,2n)$ activation of halogen ligands does not lead to different free halide yields.⁵

In view of the fact that defect densities as well as the ranges are quite similar for different types of solids one is tempted to place more importance to the influence of general collision dynamics than to the individual chemical factors. Mass disparity certainly is one reason for the lack of direct chlorine for bromine replacement, which should be possible on energetic and steric grounds. If a displacement occurs at all when a chlorine atom collides with a bromine ligand, it can recoil away from the site. The heavier bromine comes to rest close to the vacancy, having a much better chance for recombining with it than the more distant ^{38}Cl ; thus, $[\text{ReBr}_5^{38}\text{Cl}]^{2-}$ is not likely to be formed. While the mass disparity factor is also operative for the opposite process, namely, the collision of a recoil bromine with a chlorine ligand, the better combination chance for bromine here leads to the formation of $[\text{ReCl}_5-$

Table I: Types of Processes for Hot and Thermal Product Formation after Ligand Recoil in $K_2[ReBr_6]/K_2[ReCl_6]$ Mixed Crystals

Recoil atom	Products ^a			
	Hot processes		Thermal annealing	
	$[ReX_5 \cdot X]^{2-}$	$[ReX_5 \cdot Y]^{2-}$	$[ReX_5 \cdot X]^{2-}$	$[ReX_5 \cdot Y]^{2-}$
³⁶ Cl	(a) Primary retention <i>via</i> correlated recombination (zero order) (b) Substitution (first order) (c) Combination after ligand vacancy exchange (second order)	Combination after ligand vacancy exchange (second order)	Yes (for > 0.25), noncorrelated combination	No
⁸² Br	(a) Primary retention <i>via</i> correlated recombination (zero order) (b) Substitution (first order)	Substitution (first order)	Yes, correlated recombination	No

^a X = parent halogen; Y = halogen from other mixed crystal component.

$^{82}Br]^{2-}$. This case can be considered as a substitution proceeding *via* a rapid cage combination following a displacement.

It is remarkable that those products which—on the basis of collision dynamics—are expected to be formed by these substitution processes (namely Cl for Cl, Br for Br, and Br for Cl) are indeed governed by first-order kinetics either exclusively or partly. Their maximum yields, obtained by extrapolation to the corresponding pure systems, range from 56 to 66%, reflecting the 50% chance for a replacement after a proper collision.

In any case, the relative simplicity of halogen-halogen interactions mainly involved in the ligand recoil reaction in hexahalorhenates lends itself for computer simulation studies. For the pure systems, preliminary results of binary collision cascade calculations,²⁶ which are presently being carried out in this laboratory,¹⁸ show an excellent agreement with the experimental results obtained.

(26) I. M. Torrens and M. T. Robinson, Proceedings of the International Conference on Radiation Induced Voids in Metals, Albany, N. Y., June 1971.

Identity Scrambling and Isomerization Networks in Systems of Excited Alkyl Radicals¹

by C. W. Larson,* Peter T. Chua, and B. S. Rabinovitch

Departments of Chemical Engineering and Chemistry, University of Washington, Seattle, Washington 98196
(Received March 30, 1972)

Publication costs assisted by the Petroleum Research Fund

The gas phase isomerization by H-atom transfer of vibrationally excited alkyl radicals of general structure GCC(C)CC has been studied; G was an H, methyl, ethyl, isopropyl, or *tert*-butyl group. The radicals were produced by chemical activation by the addition of an H atom to an appropriate α -olefin, GCC(C)C=C. This study expands on earlier findings and shows that alkyl radicals, vibrationally excited above 40 kcal mol⁻¹, are involved in a characteristic process of rapid competitive, consecutive isomerization. If the radical skeleton is large enough, all possible radical sites on the skeletal framework are occupied in the process of identity scrambling. The steady-state proportions of isomeric radical species depend both on thermodynamic properties of the radicals and kinetic parameters associated with their decompositions and stabilizations. Details of Rice-Ramsperger-Kassel-Marcus (RRKM) rate calculations for the more important isomerization processes, including a general formulation for alkyl radical and activated complex frequency assignments, are described.

I. Introduction

Isomerization of vibrationally excited alkyl radicals by intramolecular hydrogen atom abstraction forms an important class of alkyl radical reactions.² However, until recently these reactions had received little study.³⁻⁶ Previously,⁶ we reported on the isomerization of some ten large (C₆ to C₉) chemically activated alkyl radicals. Exothermic and thermoneutral 1,4-, 1,5-, and 1,6-hydrogen atom shifts were the most important processes in all systems where such reaction paths existed. Related conclusions derived from the mechanistic study of the pyrolysis of C₆ to C₉ paraffins have been reported recently by Doue and Guiochon.⁷

Measurements of Arrhenius parameters for alkyl radical isomerization have been limited. To date, only two exothermic radical isomerizations, pentyl-1· → pentyl-2^{3c} and hexyl-1· → hexyl-2·,⁵ have been studied; abnormally low *A* factors ($\sim 10^7$ sec⁻¹) and activation energies (8-10 kcal mol⁻¹) were reported in both cases. These values have been questioned and higher values supported.⁴⁻⁶

Chemically activated alkyl radicals of any desired structure may be directly produced by the exothermic chemical reaction between a hydrogen atom and an olefin. Radicals produced in this way are characterized by a well-defined and relatively narrow energy distribution above 40 kcal mol⁻¹. This energy range is of considerable interest in chemical kinetics: alkyl radicals containing ~ 45 kcal mol⁻¹ internal excitation may undergo several competitive primary processes including β -carbon-carbon bond rupture, internal hydrogen atom abstraction, and collisional stabilization. The H + olefin chemical activation technique provides

an extremely powerful tool for the quantitative investigation of alkyl radical reactions in general.

1,4-, 1,5-, and 1,6-hydrogen (and higher) shifts are believed to occur²⁻⁷ primarily by cyclic mechanisms involving five-, six-, or seven-membered ring transition states, respectively. In this paper we describe systems in which *net* 1,2-H-atom shifts occur. Both endothermic and exothermic processes are reported.

II. Present Investigation: Isomerization Networks

A series of five vibrationally excited 3-methylalkyl-2-radicals, GCC(C)CC*, were produced by addition of H atoms to terminal 3-methylalkenes. The series included radicals where G was hydrogen (H), methyl (Me), ethyl (Et), isopropyl (iPr), and *tert*-butyl (tBu).

Isomerization networks, schematic diagrams which represent all paths of communication between the several radicals of a given carbon skeleton, may be constructed for each of these systems. Communication

(1) This work was supported by the Office of Naval Research.

(2) (a) A. Kossiakoff and F. O. Rice, *J. Amer. Chem. Soc.*, **65**, 590 (1943); (b) H. M. Frey and R. Walsh, *Chem. Rev.*, **69**, 103 (1969); (c) P. G. Ashmore, F. S. Dainton, and T. M. Sugden, "Photochemistry and Reaction Kinetics," Cambridge University Press, New York, N. Y., 1967, Chapter 12.

(3) (a) V. B. Stefton and D. J. LeRoy, *Can. J. Chem.*, **34**, 41 (1956); (b) A. S. Gordon and J. R. McNesby, *J. Chem. Phys.*, **31**, 853 (1959); (c) L. Endrenyi and D. J. LeRoy, *J. Phys. Chem.*, **70**, 4081 (1966).

(4) C. W. Larson, D. C. Tardy, and B. S. Rabinovitch, *J. Chem. Phys.*, **49**, 299 (1968); (b) C. W. Larson and B. S. Rabinovitch, *ibid.*, **51**, 2293 (1969).

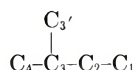
(5) K. W. Watkins and L. A. Ostreko, *J. Phys. Chem.*, **73**, 2080 (1969).

(6) (a) E. A. Hardwidge, C. W. Larson, and B. S. Rabinovitch, *J. Amer. Chem. Soc.*, **92**, 3278 (1970); (b) K. W. Watkins and D. R. Lawson, *J. Phys. Chem.*, **75**, 1632 (1971).

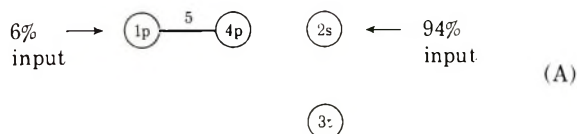
(7) F. Doue and G. Guiochon, *ibid.*, **73**, 2804 (1969).

between two radical species is greatly favored when they are linked by a five-, seven-, or especially, six-membered ring H-atom transfer transition state; pathways with smaller transition states have not been observed to be in competition with stabilization, decomposition, or other isomerization processes;^{3b,8} in any case, they would be negligible for the present systems and pressures.

A. *3-Methylbutene-1 + H System; G ≡ H.* H-Atom addition to 3-methylbutene-1 produces a mixture of approximately 94% secondary (R_2 , parent) radical and 6% primary (R_1 , anti-Markovnikov) radical. The carbon skeleton is numbered as shown, where

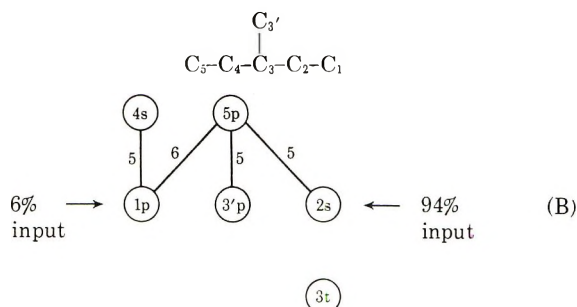


R_4 and $R_{3'}$ (*i.e.*, radicals where the odd electron is located on carbon number 4 or 3, respectively) are distinguishable only under isotopic labeling. The isomerization network is represented by



The circled symbols represent vibrationally excited radicals and denote the free electron position (1, 2, etc., as indicated in the labeled carbon skeleton) and the radical type (p, s, or t for primary, secondary, or tertiary, respectively). A thermoneutral isomerization pathway *via* a five-membered ring transition state exists between the primary R_1 and $R_{3'}$ radicals; no other H-atom transfer reactions occur appreciably in this system and R_3 is not formed.

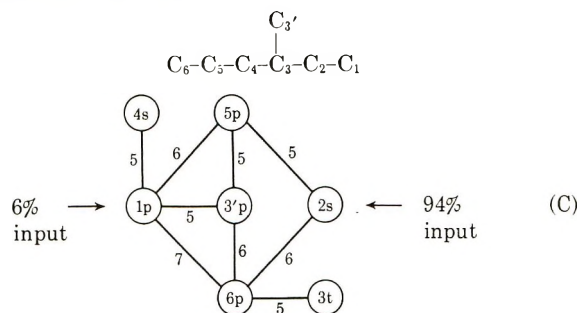
B. *H + 3-Methylpentene-1 System; G ≡ Me.* As before, two reaction paths for H atom addition to the α -olefin provide entrance into the isomerization network from two directions. The carbon skeleton and isomerization network are



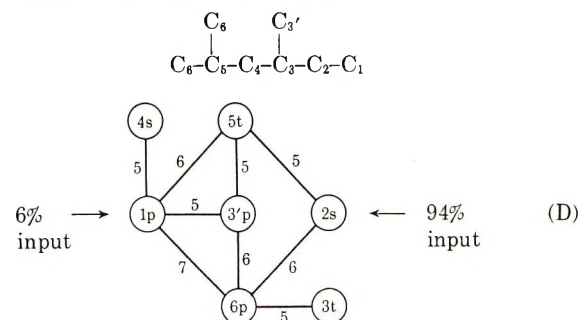
The tertiary R_3 radical is again inaccessible as in the $G = H$ system. Also, since the carbon skeleton is symmetric, the R_1 and R_2 radicals are indistinguishable from the R_5 and R_4 radicals, respectively, in the absence of isotopic labeling.

C. *H + 3-Methylhexene-1 System; G ≡ Et.* Communication between all the possible radical species

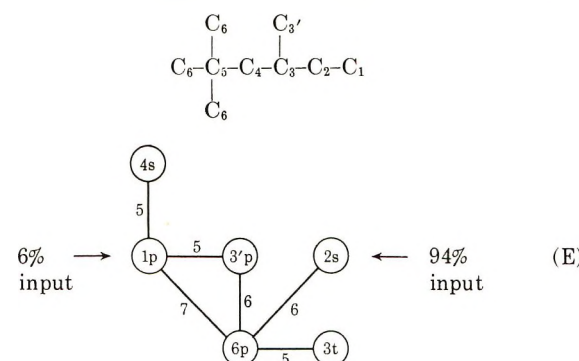
occurs in the $G \equiv Et$ system; the carbon skeleton and isomerization network are



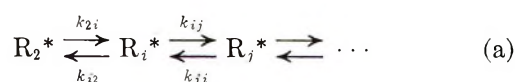
D. *H + 3,5-Dimethylhexene-1 System; G ≡ iPr.* Additional methyl substitution at the no. 5 carbon introduces no new complexities into the isomerization network. However relationships between the several isomerization paths are altered inasmuch as the R_5 radical is a tertiary species; the reaction path degeneracies to form the R_6 radical are doubled. The carbon skeleton and isomerization network are



E. *H + 3,5,5-Trimethylhexene-3 System; G ≡ tBu.* In this system, methyl substitution at C_5 is complete and the isomerization network is simpler than the previous two examples because the R_5 radical is eliminated. The carbon skeleton and isomerization network are



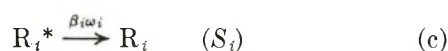
F. *General Reaction Scheme.* A scheme of reactions following the $H + \alpha$ -olefin (O_p) reaction which produces a mixture of parent secondary radical (R_2^*) and anti-Markovnikov primary radical (R_1^*) includes a series of competitive and consecutive H-atom transfer isomerizations



The extent of the exploration by an initial radical of a given isomerization network depends on the nature of the carbon skeleton and on the relative magnitudes of the various isomerization, collisional stabilization, and decomposition rates of the several radical species of the network. Collisional stabilization may be controlled by variation of the total pressure and the nature of the heat bath. In this work, the energy of the radical species ranged from ~ 10 to 25 kcal mol^{-1} in excess of the various β -C-C rupture reaction thresholds; decomposition was frequently an important competing process. Decomposition by β -C-H rupture was negligible. Decomposition products of R_i^* are olefins designated as O_i , O_i' , etc., and a smaller, essentially thermal radical, r_i , r_i' , etc.



The O_i and r_i product species are diagnostic of the structure and concentration of the R_i^* present in the network at steady state. Collisionally stabilized R_i is incapable of decomposition



ω_i is the specific collision rate and β_i is the collisional stabilization efficiency (with respect to the lowest decomposition threshold). Previously,⁶ we studied chemically activated alkyl radical isomerization by measuring the relative yields of the R_i species (S_i) with use of radical trapping techniques. Some of the usual complexities of radical chemistry are avoided at low temperature (25°). Thermalized radicals (R_i and r_i) mainly undergo simple radical-radical termination by various disproportionation and combination reactions. Also, abstraction of hydrogen from parent α -olefin by H atoms is minor relative to H-atom addition.^{9,10}

III. Experimental Section

A. Materials. α -Olefins from the following sources were used: Phillips Petroleum research grade butene-1 (B1) and 3-methylbutene-1 (3MB1); Columbia Chemicals 3-methylpentene-1 (3MP1); American Petroleum Institute 3-methylhexene-1 (3MH1); Chemical Samples Co. 3,5-dimethylhexene-1 (35DMH1) and 3,5,5-trimethylhexene-1 (355TMH1). All olefins were purified by glpc on a 12-ft squalane column (0.25-in. diam.) at temperatures between 70 and 100° . In some instances, a 3-ft length of AgNO_3 -ethylene glycol (0.25-in. diam.) column at room temperature preceded the squalane. Commercial tank hydrogen was purified by passage through BTS (Badische Anilin und Soda Fabrik AG) catalyst and silica gel at -196° . The CF_4 obtained from Matheson and was purified by BTS treatment followed by passage through a packed trap at -182° .

B. Apparatus and Procedure. A conventional Pyrex vacuum system fitted with Teflon-viton O-ring

stopcocks was used. A standard mixture of olefin-hydrogen (1:200) was stored in a blackened 5-l. vessel. Aliquots of this mixture were expanded into 20- or 200-l. reaction vessels; pressures were measured with a McLeod gauge and conventional manometer.

The reactors were fitted with quartz lamp wells and contained mercury vapor at room temperature. Hydrogen atoms were generated *in situ* by $\text{Hg}(^3\text{P}_1)$ photosensitized decomposition of hydrogen; the source of 2537-\AA radiation was an 8-W GE germicidal lamp. Reaction times varied from 10 to 60 min; approximately 10% of parent olefin reacted. The reaction mixture was pumped through a glass wool packed trap at -196° ; inert gas and noncondensable products were pumped away. Transfer to a gas chromatography injection trap, also packed with glass wool, was facilitated with use of a noncondensable carrier (H_2 or He) gas.

C. Analysis. Gas chromatographic analyses were made with use of several columns of varying selectivity including AgNO_3 -glycol, hexamethylphosphoramide, and squalane. Both packed and support coated open tubular (scot) columns were used. Multiple analysis of a single product mixture was made by splitting the helium input and recollecting and reanalyzing the split-off fraction; the splitting procedure did not fractionate the product mixture.

Calibration of the flame ionization detector was made with standard mixtures; product amounts were proportional to the peak areas, corrected for carbon number.

IV. Results and Discussion

A. Decomposition Product Array. Each radical isomer may decompose into a variety of olefin and smaller radical fragments. The possible decomposition products for each system are summarized in Table I.

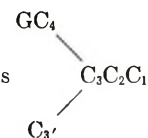
Six radicals are possible in the $\text{G} \equiv \text{tBu}$ system; these decompose to produce 16 different olefins and 6 different radicals. The radical fragments themselves may disproportionate and produce 21 heavier alkane dimers. The olefin products of disproportionation are identical with some of those produced by decomposition; generally, however, this contribution to a specific olefin yield is small and may be estimated from the observed congruent alkane yield.

Table I indicates a number of symmetric relationships and analogies, between different systems and within the same system. A single olefin, 2MB1, is indicative of the presence of the R_3 radical in all systems; relatively large amounts were observed in the

(8) D. C. Tardy, private communication, has described evidence for a 1,3 shift in a system where only C-H rupture was possible.

(9) R. J. Cvetanović and L. C. Doyle, *J. Chem. Phys.*, **50**, 4705 (1969).

(10) G. R. Woolley and R. J. Cvetanović, *ibid.*, **50**, 4697 (1969).

Table I: Olefin and Radical Products^a from β -Carbon-Carbon Bond Rupture of Chemically Activated Radicals

R _i	Carbon skeleton of chemically activated radical									
	G = tBu		G = iPr		G = Et		G = Me		G = H	
	C ₆	C _{3'}	C ₆	C _{3'}	C _{3'}	C _{3'}	C _{3'}	C _{3'}	C _{3'}	C _{3'}
	C ₆ C ₄ C ₄ C ₂ C ₂ C ₁	C ₆ C ₄ C ₄ C ₂ C ₂ C ₁	C ₆ C ₄ C ₄ C ₂ C ₂ C ₁	C ₆ C ₄ C ₄ C ₂ C ₂ C ₁	C ₆ C ₄ C ₄ C ₂ C ₂ C ₁	C ₆ C ₄ C ₄ C ₂ C ₂ C ₁	C ₆ C ₄ C ₄ C ₂ C ₂ C ₁	C ₆ C ₄ C ₄ C ₂ C ₂ C ₁	C ₆ C ₄ C ₄ C ₂ C ₂ C ₁	C ₆ C ₄ C ₄ C ₂ C ₂ C ₁
	O _i	r _i	O _i	r _i	O _i	r _i	O _i	r _i	O _i	r _i
R ₁	E	44DMP2·	E	4MP2·	E	P2·	E	sBu	E	iPr
R ₂	c,tB2 c,t55DMH2	neoP Me	c,tB2 c,t5MH2	iBu Me	c,tB2 c,tH2	nPr Me	c,tB2 c,tP2	Et Me	c,tB2 c,tB2	Me Me
R ₃	2MB1 244TMP1	tBu Me	2MB1 24DMP1	iPr Me	2MB1 2MP1	Et Me	2MB1 2MB1	Me Me	2MB1 iBe	H Me
R ₄	c,t44DMP2 c,t24DMH2 c,t22DMH3	Et Me Me	c,t4MP2 c,t4MH2 c,t2MH3	Et Me Me	c,tP2 3MP1 c,tH3	Et Me Me	c,tB2	Et		
R ₅			iBe	sBu	P	sBu	E	sBu		
R ₆	iBe	2MB1·	P	2MB1·	E	2MB1·				
R _{3'}	B1 44DMP1	neoP Et	B1 4MP1	iBu Et	B1 P1	nPr Et	B1 B1	Et Et	B1 P	Me Et

^a Abbreviations for olefins are (E) ethylene, (P) propylene, (iBe) isobutene, (B1) butene-1, (c,tB2) *cis*-, *trans*-butene-2, (P1) pentene-1, (c,tP2) *cis*-, *trans*-pentene-2, (2MB1) 2-methylbutene-1, (3MB1) 3-methylbutene-1, (c,tH2) *cis*-, *trans*-hexene-2, (c,tH3) *cis*-, *trans*-hexene-3, (2MP1) 2-methylpentene-1, (244TMP1) 2,4,4-trimethylpentene-1, (c,t24DMH2) *cis*-, *trans*-2,4-dimethylhexene-2, etc. Abbreviations for radicals are (Me) methyl, (Et) ethyl, (nPr) *n*-propyl, (iPr) isopropyl, (nBu) *n*-butyl, (sBu) *sec*-butyl, (iBu) isobutyl, (neoP) neopentyl, (2MB1·) 2-methylbutyl-1·, (44DMP2·) 4,4-dimethylpentyl-2·, etc.

G \equiv tBu, iPr, and Et systems but none was detected in the G \equiv Me and H systems. The 2-methylbutyl-1· radical (2MB1·), which is uniquely evidenced by its alkane disproportionation product, isopentane, is produced by decomposition of R₆. Isopentane from this source can arise and was observed in three of the five systems, G \equiv tBu, iPr, Et. In the G \equiv tBu system, the neopentyl radical is a product of both R₂ and R_{3'} decomposition; mass balance considerations suggest that a significant portion is produced by R_{3'} decomposition.

trans-Butene-2 (tB2) is common to all systems as the predominant decomposition product of the parent radical, R₂. The tB2 yield provides a convenient internal standard to which the yields of other products may be referred. However, in the G \equiv iPr and G \equiv Et systems, *sec*-butyl radical (sBu), produced from R₅ decomposition, may disproportionate to produce tB2, cB2, B1, and *n*-butane (nBa). In these systems the amount of tB2 from disproportionation, $Y[\text{tB2}]_{\text{disp}}$, was independently estimated from the observed nBa yield, *viz.*, $Y[\text{tB2}]_{\text{disp}} = (2/3)(2/5)(Y[\text{nBa}])$.

Virtually all of the possible products listed in Table I have been positively identified in the present work. Also, previous work has exhaustively demonstrated the importance of the R₅* species.⁴ A particularly com-

prehensive study was made by us of the G \equiv iPr system; olefin decomposition products (Table I) from each of the seven possible radicals were observed, and they show quite complex pressure dependence.¹¹ In the sections below we consider those aspects of the product spectra which indicate that certain isomer species are important. Products heavier than the parent olefin will not be discussed. Methyl rupture decompositions are of lesser importance whenever they compete with rupture of larger fragments. Methane was not measured; ethane and ethylene were only qualitatively measured. Isobutene and butene-1 were usually left unseparated and measured together.

B. *Net 1,2-Hydrogen Atom Shifts: Formation of R₃**. Relative decomposition product yields, D_i/D_2 , may be obtained from

$$D_i/D_2 = \frac{f_m \int_{E_i}^{\infty} k_i(E) R_i^*(E) dE + f_a \int_{E_i}^{\infty} k_i(E) R_i^*(E) dE}{f_m \int_{E_2}^{\infty} k_2(E) R_2^*(E) dE + f_a \int_{E_2}^{\infty} k_2(E) R_2^*(E) dE} \quad (1)$$

where f_m and f_a are relative amounts of Markovnikov

(11) P. T. Chua, M.S. Thesis, Department of Chemical Engineering, University of Washington (1971).

(M) and anti-Markovnikov (AM) H-addition to parent olefin, normalized to $f_m + f_a = 1$. The RRKM energy dependent rate constant for decomposition of R_i^* via its principal β -C-C rupture reaction channel is denoted $k_i(E)$ and is integrated over the (unnormalized) steady-state population distribution $R_i^*(E)$ from E_i , the decomposition threshold energy of the principal β -C-C rupture of R_i , to infinity. $R_i(E)$ refers to those radical population distributions which originate from AM addition. AM addition amounts to $\sim 6\%$ and produces radicals whose minimum energy is below M input radicals by 1.7 kcal mol $^{-1}$.

The distribution of $R_i^*(E)$ depends on the competition between isomerization, β -C-C rupture, and collisional stabilization. In previous work,^{4b,12} the nature of the collisional transition probability distributions and the magnitude of the net collisional stabilization efficiencies have been determined for collisional processes between large alkyl radicals and weak colliders, notably H_2 and CF_4 . In that work the isomerization and β -C-C rupture rates were negligible or known. In this work, we may assume that the collisional processes for the weak collider heat bath are well understood.

Figure 1 shows the pressure dependence of the yield of 2-methylbutene-1 (2MB1) from R_3^* decomposition relative to the yield of *trans*-butene-2 (D_2) from R_2^* decomposition for the three systems where G was tBu, iPr, and Et. 2MB1 was not observed in the $G \equiv H$ ($D_3/D_2 < 0.001$) and $G \equiv Me$ ($D_3/D_2 < 0.03$) systems because R_3 is isolated and inaccessible in the networks of these systems. However, the formation of R_3^* in the remaining systems is strikingly evidenced by large yields of 2MB1, especially at low pressure where collisional stabilization is unimportant and the ultimate fate of all R_i^* is decomposition by β -C-C rupture.

A simple yet rigorous algebraic equation illustrating the pressure dependence of the D_3/D_2 ratio cannot be written down. However, an approximate form of eq 1 which includes the interesting properties of the isomerization network may be derived¹¹

$$D_3/D_2 = A/(\beta^2\omega^2 + \beta\omega B + C) \quad (2)$$

where the "constants," A , B , and C , are only weak functions of ω

$$A = (k_{63})(k_3/k_2)[k_{26} + k_{3'6}(R_3^*/R_2^*) + k_{16}(R_1^*/R_2^*)] \quad (3)$$

$$B = (k_3 + k_{36}) + (k_6 + k_{61} + k_{63'}) + (k_{63}) \quad (4)$$

$$C = (k_3 + k_{36})(k_6 + k_{61} + k_{63'}) + k_3(k_{63}) \quad (5)$$

Equation 2 ignores the contribution to D_3 and D_2 by decomposition of radicals originating from AM network input. Not only is the AM radical source negligible but also any contribution of decomposition products from this source would produce a D_3/D_2 ratio only negligibly lower than the D_3/D_2 ratio of the Markovnikov input. The composite collisional efficiency for

stabilization with respect to decomposition (β) introduced in eq 2 is the geometric average of β_2 and β_3 : $\beta = (\beta_2\beta_3)^{1/2}$. In the range of collision rates where collisional efficiencies decrease drastically with decreasing pressure (*i.e.*, the "turn-up" region)¹³ the terms $\beta^2\omega^2$ and $\beta\omega B$ are negligible so that β may, in this treatment, be considered independent of pressure. Also, radical cross sections are assumed identical: $\omega_2 = \omega_3 = \omega$. The most severe approximation in eq 2, namely the premature averaging of the rate constants over the $R_i^*(E)$ population distributions,^{12a} the average energies of which increase with increasing ω , causes a weak ω dependence of A , B , and C . Thus, over the collision number range where S_i/D_i increases from 1 to ~ 10 (*i.e.*, $5 \times 10^{-3} < \omega \lesssim 5 \times 10^{-2}$ sec $^{-1}$), decomposition rate constants double and isomerization rate constants increase by factors of less than ~ 1.5 . Here S_i refers to the amount of R_i^* which is stabilized with respect to decomposition (but not isomerization).

Minimum permissible values of A , B , and C , deduced by fitting eq 2 to the experimental points of Figure 1, are summarized for each system in Table II. Larger values of A , B , and C produce flatter curves with less severe fall-off; values greater than those tabulated do not change curve shapes significantly if the $A:B:C$ ratio is maintained. Curves derived by decreasing the A , B , and C values by a factor of 4 provide noticeably poorer fits. The ratios of A to C and A to B are approximately independent of the absolute values of the constants. A minimum value of the collisional efficiency ($\beta = 0.1$) has been used in these calculations.

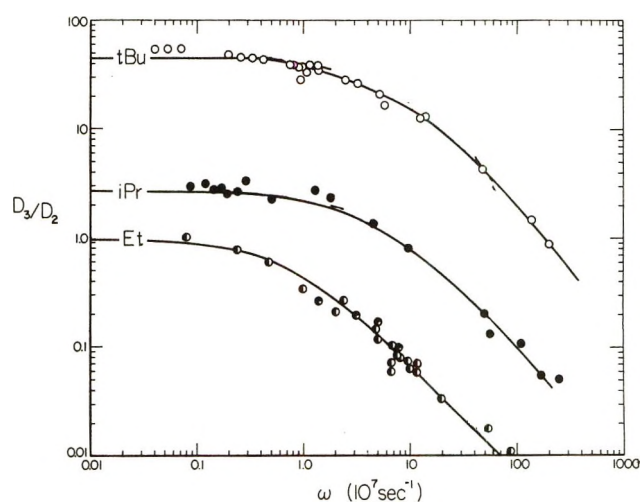


Figure 1. Fall-off curves for the $G = \text{tBu}$, iPr , and Et systems. $R\text{-H}_2$ collision rates were calculated on a hard-sphere model with use of $\sigma(\text{H}_2) = 2.9$ and $\sigma(\text{radical}) = 7.0$ (Et), 7.5 (iPr), and 8.0 (tBu).

(12) (a) D. C. Tardy, C. W. Larson, and B. S. Rabinovitch, *Can. J. Chem.*, **46**, 341 (1968); (b) D. C. Tardy and B. S. Rabinovitch, *J. Chem. Phys.*, **48**, 5194 (1968).

(13) J. G. Georgakakos, B. S. Rabinovitch, and E. A. McAluff, *J. Phys. Chem.*, **52**, 2143 (1970).

Use of the upper limit appropriate to alkyl radical-hydrogen-heat bath system ($\beta = 0.2$) would require still greater values of A , B , and C to provide the same fit. Thus, the tabulated values are our best estimates of lower limits of these constants.

Table II: Minimum Values of Constants^a for Eq 2

Constant (eq 2)	System		
	G = Et	G = iPr	G = tBu
A (10^{14} sec ⁻²)	10	110	1800
B (10^6 sec ⁻¹)	140	100	80
C (10^{14} sec ⁻²)	10	40	40

^a Tabulated values obtained with $\beta = 0.1$. An identical fit of eq 2 to the data may be obtained with $\beta = 0.2$ if the values of A and C are quadrupled and the values of B are doubled.

Order of magnitude estimates of the largest rate constants may be obtained by ignoring those rates which contribute negligibly to the values of A , B , and C . Thus

$$A \simeq k_{26}k_{63}(k_3/k_2)$$

$$B \simeq k_{63}$$

and

$$C \simeq k_3k_{63}$$

The most striking result is the extremely large minimum value found for the rate of the 8 kcal mol⁻¹ exothermic isomerization of a *primary* to *tertiary* radical via a five-membered ring (5tp): $k_{63} \gtrsim 10^8$ sec⁻¹. Over the series G \equiv Et, iPr, tBu, k_{63} should decrease by a factor of about 20 due to quantum statistical effects. Table III lists estimated values of all the rate constants, based on the minimum value k_{63} for the G \equiv Et system of 10^8 sec⁻¹.

Table III: Rate Constants^a (10^6 sec⁻¹) for Isomerization and Decomposition

Rate constant	System		
	G = Et	G = iPr	G = tBu
k_3/k_2	1	20	900
k_2^b	0.5	0.1	0.02
k_3^c	0.5	2.0	18.0
k_{26} (6ps)	>1.0 (3) ^e	>3.0 (6)	>4.0 (9)
k_{63} (5tp)	100 (1)	18 (1)	5 (1)
k_{62} (6sp) ^d	>10 (2)	>10 (2)	>10 (2)
k_{36} (5pt) ^d	2 (3)	1 (6)	0.4 (9)

^a Accuracy is at least one order of magnitude. ^b Measured values from ref 4a, 11, and 14. ^c Calculated values; see ref 15 and 16. ^d Calculated values. ^e Reaction path degeneracy in parentheses.

The rate constants k_2 for R_2^* decomposition to GC + tB2 over the series G = Et,^{4a} iPr,¹¹ tBu¹⁴ (*i.e.*, nPr,

iBu, neoP rupture) have been measured previously and found to decrease by a factor of 25. Statistical effects account for about one-half and an increasing threshold energy accounts for the remainder of the total decrease in k_2 observed over the series.

The statistical effects tending to cause the rate of R_3^* decomposition to G + 2MB1 to decrease over the series are counteracted by increasingly lower decomposition threshold energies over the series. Thus, k_3 increases^{15,16} by a factor of 35 over the series from G \equiv Et to G \equiv tBu.

The rate of the $R_2^* \rightarrow R_6^*$ isomerization (6ps) is relatively constant over the series because statistical effects tending to lower k_{26} are opposed by an increase in the reaction path degeneracy (*viz.*, 3 for G \equiv Et, 6 for G \equiv iPr, 9 for G \equiv tBu). The *minimum* value of k_{26} , based on a fixed k_{63} value, is 10^6 sec⁻¹.

The rates of the reverse isomerization reactions k_{36} , k_{62} for these high energy systems may be obtained from simple eigenstate density calculations. Thus, $k_{36} = k_{63}(\sigma_{36}/\sigma_{63})[N_6(E - \Delta E)/N_2(E)]$, where σ_{36} and σ_{63} are reverse and forward reaction path degeneracies for $R_6^* \rightarrow R_3^*$ and N_6 and N_3 are eigenstate densities of R_6^* and R_3^* at energy E above the zero point energy of R_3 ; ΔE is the zero-point energy difference between R_6 and R_3 . A simple, but sufficient calculation, based on identical frequency assignments for R_2^* , R_6^* , and R_3^* , shows that in the range $E = 44$ to 50 kcal mol⁻¹, $k_{63} \approx 50k_{36}$ and $k_{62} \approx 10k_{26}$.

V. Conclusions

The following picture of alkyl radical behavior emerges from this work. Alkyl radicals which are vibrationally excited by chemical activation to high levels of excitation, around 40 to 50 kcal mol⁻¹ in the present work, undergo many rapid consecutive and competitive changes of identity before they finally decompose or are stabilized. In anthropomorphic terms, these species are multiply schizophrenic. In the absence of collisional perturbations, a state of quasiequilibrium exists for the faster (five-, six-, and seven-membered ring) isomerization processes which is nearly unaffected by the radical decomposition processes.

It is of some interest to extract threshold energies for these isomerization processes by fitting RRKM calculated rate constants to the observed values. Detailed prescriptions for synthesis of the activated complex and radical frequency assignments required for

(14) C. W. Larson, E. A. Hardwidge, and B. S. Rabinovitch, *J. Chem. Phys.*, **50**, 2769 (1969).

(15) The RRKM rate constant calculations for these molecules have been made but need not be elaborated upon here since calculational details for similar group ruptures in a closely related series, G'C(C)CC \rightarrow G' + tB2, G' \equiv tBu, iPr, Et, have been reported previously (ref 16).

(16) (a) C. W. Larson, B. S. Rabinovitch, and D. C. Tardy, *J. Chem. Phys.*, **47**, 4570 (1967); (b) C. W. Larson and B. S. Rabinovitch, *ibid.*, **50**, 871 (1969); (c) C. W. Larson and B. S. Rabinovitch, *ibid.*, **52**, 5181 (1970).

Table IV: Measured and Calculated^a Absolute Rates of Isomerization Processes

Radical size	Reactant and formation mode ^b	Process	k_{ij} , 10 ⁶ sec ⁻¹	Meas ^c method	E_{ij}° , kcal mol ⁻¹	$E_{\min.}^d$ kcal mol ⁻¹	Product	σ_{ij}^e
C ₆	I 3MP1·	5pp	<1.0	1		38.3	2EtB1·	3
C ₇	III Hp3·	5ss	9.0	1	20.0	37.5	Hp2·	2
C ₇	II 3MH2·	5ss	9.0	1, 2	17.0	40.0	4MH2·	2
C ₈	III Oc4·	5ss	0.29	1	22.0	37.5	Oc2·	2
C ₈	II Oc2·	5ss	8.0	1	20.0	40.0	Oc4·	2
C ₈	II 33DMH2·	5ss	16.0	1, 2	17.0	40.0	44DMH2·	2
C ₈	II 44DMH2·	5ss	16.0	1, 2	17.0	40.0	33DMH2·	2
C ₉	II N2·	5ss	1.8	1	18.0	40.0	N5·	2
C ₆	I 3MP1·	5sp	<10	1		38.3	3MP2·	2
C ₇	IV 4MH1·	5tp	1000 ^f	2	12.0	36.0	3MH3·	1
C ₈	IV 24DMH1·	5tp	180 ^f	2	12.0	36.0	35DMH3·	1
C ₉	IV 224TMH1·	5tp	50 ^f	2	12.0	36.0	355TMH3·	1
C ₇	III Hp3·	6ps	<9	1		37.5	Hp1·	3
C ₇	II 3MH2·	6ps	>10 ^f	2	≤20.8	40.0	4MH1·	3
C ₈	II 35DMH2·	6ps	>10 ^f	2	≤15.8	40.0	24DMH1·	6
C ₉	II 355TMH2·	6ps	>10 ^f	2	≤14.3	40.0	224TMH1·	9
C ₈	II Oc2·	6ss	600	1	11.0	40.0	Oc3·	2
C ₉	II N2·	6ss	180	1	10.0	40.0	N4·	2
C ₇	I 3MH1·	6sp	>1000	1	≤13.0	38.3	4MH2·	2
C ₈	I Oc1·	6sp	>300	1	≤11.0	38.3	Oc4·	2
C ₈	I 33DMH1·	6sp	>800	1	≤10.0	38.3	44DMH2·	2
C ₉	II N2·	7ss	9.0	1	16.0	40.0	N3·	2

^a Calculated RRKM rates agree with the measured rates with specified value of E_{ij}° chosen to give agreement; frequency models and other energetics are described in the Appendix. ^b The four formation modes are I, AM addition to α -olefin; II, M addition to α -olefin; III, M addition to interior olefin; IV, radical formation by consecutive isomerization process, $R_2 \rightarrow R_6$. ^c Rate constants calculated from measured relative yields of stabilized isomers (method 1) or measured relative yields of decomposition products (method 2). ^d The approximate average energy of the isomerizing species studied by method 2 may be obtained by adding 4.0 (C₆), 5.0 (C₇), 6.0 (C₈), 7.0 (C₉) kcal mol⁻¹ to these minimum energies; in general, the average values are less than E_{\min} when studied by method 1. ^e Reaction path degeneracy. ^f Present work; all others from ref 6.

these calculations have been given previously¹⁷ and are summarized in the Appendix. Threshold energies for thermoneutral five-membered ring isomerization have been shown in earlier chemical activation work^{4b, 6a} to lie between 15 and 20 kcal mol⁻¹; correction of thermal studies corroborates⁵ these values. Theoretical rate calculations for the present systems indicate that the threshold energies for the 5tp process $R_6 \rightarrow R_3$ (8 kcal mol⁻¹ exothermic) and the 6ps process $R_2 \rightarrow R_6$ (4 kcal endothermic) are substantially lower, $E_0 \simeq 15$ kcal mol⁻¹ for the latter. Thus, threshold energies for isomerization reactions appear to be representable as a sum of two terms—one which varies with transition state ring size and a second which varies with enthalpy of isomerization.

A compilation of absolute isomerization rates including results from previous⁶ work is presented in Table IV. The tabulation includes only the measured rates; reverse isomerization rates may be calculated as described above. In general, the exothermic sp, ts, and tp processes are approximately 10, 10, and 50

times faster, respectively, than the reverse endothermic ps, st, and pt processes in these H-atom chemically activated alkyl radical systems.

Acknowledgment. Two of us, C. W. L. and P. T. C., wish to express our appreciation to the Research Corporation and the Donors of the Petroleum Research Fund, administered by the American Chemical Society, for partial support of this research.

Appendix

A. Vibrational Frequency Assignments. The vibrational frequency assignments of the alkyl radical and H-atom transfer activated complex are required in the calculation of the RRKM specific reaction rate, $k_{ij}(E)$. In the past¹⁷ we have used the congruent alkane frequency assignment as the basis for prescribing these assignments. For this work a general formulation for synthesis of alkane assignments was developed

(17) C. W. Larson, Ph.D. Dissertation, University of Washington (1969).

Table V: Fixed Frequencies for Approximation of Alkane Assignment^a

	Major internal coordinate	Frequency, cm ⁻¹	Degeneracy	Degeneracy assignment for sample alkanes		
				3MHa	35DMHa	355TMHa
CH ₃ str	C _p -H	2964	2n _p	6	8	10
CH ₃ str	C _p -H	2882	n _p	3	4	5
CH ₂ str	C _s -H	2928	n _s	3	2	2
CH ₂ str	C _s -H	2854	n _s	3	2	2
CH str	C _t -H	2904	n _t	1	2	1
CC str	C-C	950	n - 1	6	7	8
CH ₃ def	H-C _p -H	1462	2n _p	6	8	10
CH ₃ def	H-C _p -H	1374	n _p	3	4	5
CH ₂ def	H-C _s -H	1450	n _s	3	2	2
CH ₃ rock	H-C _p -C	1168	n _p	3	4	5
CH ₃ rock	H-C _p -C	950	n _p	3	4	5
CH ₂ wag	H-C _s -C	1310	n _s	3	2	2
CH ₂ twist	H-C _s -C	1260	n _s	3	2	2
CH ₂ rock	H-C _s -C	768	n _s	3	2	2
CH rock	H-C _t -C	1346	2n _t	2	4	2
skel def	C-C _t -C	352	3n _t	3	6	3
skel def	C-C _q -C	496	n _q	0	0	1
skel def	C-C _q -C	358	3n _q	0	0	3
skel def	C-C _q -C	226	n _q	0	0	1
CH ₃ tors	C _p -C _s	212	n _p	2	1	1
CH ₃ tors	C _p -C _t , C _q	200	n _p	1	3	4

^a Adapted from Schachtschneider and Snyder.¹⁸

so that the assignment for any alkane could be obtained with greater ease and consistency than in the past. The formulation is based on a correlation between about 20 standard alkane frequency assignments given by Schachtschneider and Snyder.¹⁸

The prescription assigns a particular frequency and degeneracy to the normal modes according to the type of carbon atom (primary C_p, secondary C_s, tertiary C_t, or quaternary C_q) and the number of each type of carbon atom in the alkane (n_p, n_s, n_t, n_q, respectively). Table V summarizes assignments of frequencies and degeneracies of those modes with unique frequencies. To illustrate the use of the prescription the assignments for 355TMHa, 35DMHa, and 3MHa are included in the table.

Torsional modes (except CH₃-R torsions) and skeletal bending frequencies about secondary carbon atoms (*i.e.*, C-C_s-C angle deformation) do not have a unique frequency. Rather, the torsion frequency C_n-C_m (n and m represent the total number of carbon atoms on the left and right side of the bond) decreases as n and m increase but increases as only one or the other of n or m increases. Table VIA, a double entry table, gives the C_n-C_m torsion frequencies as a function of the values of m and n. Also, C_n-C_s-C_m skeletal bending modes vary with the magnitude of n and m according to the pattern shown in Table VIB. The internal torsions and skeletal bendings assigned to 355TMHa, 35DMHa, and 3MHa are included for illustrative purposes in the table.

Table VI: Skeletal Bend and Internal Torsion Frequencies for Approximation of Alkane Assignment (cm⁻¹)^a

A. C _n -C _m Torsion Frequencies							
m	n					Assignments for sample alkanes	
	1	2	3	4	5		
1	279					3MHa	61 (1)
2	210	102					122 (2)
3	209	95	61				
4	212	109	61	37		35DMHa	37 (1)
5	212	122	78	40	25		78 (1)
6	212	130	92	58			130 (1)
7	212	134	104				
8	212	139				355TMHa	40 (2)
9	213						134 (1)
B. C _n -C _s -C _m Skeletal Bending Frequencies							
m	n				Assignments for sample alkanes		
	1	2	3	4			
1	382				3MHa	455 (2)	
2	346	188				276 (1)	
3	403	216	105				
4	420	276	140	67	35DMHa	477 (1)	
5	455	280	204	101		140 (1)	
6	477	359	235		355DMHa	483 (1)	
7	483	384				61 (1)	
8	490						

^a Adapted from Schachtschneider and Snyder.¹⁸

(18) J. H. Schachtschneider and R. G. Snyder, *Spectrochim. Acta, Part A*, **19**, 117 (1963); R. G. Snyder and J. H. Schachtschneider, *ibid.*, **21**, 169 (1965).

Table VII: Frequency Changes for $I^{+}_{i,j}$ Assignments

Mode	355TMH2·		35DMH2·		3MH2·	
	$I^{+}_{2,6}$	$I^{+}_{3,6}$	$I^{+}_{2,6}$	$I^{+}_{3,6}$	$I^{+}_{2,6}$	$I^{+}_{3,6}$
C-C tors	40	40	37	37	61	61
	40	40	78	78	122	122
	134	200	130	200	122	212
	200		200		212	
C-C-C bend	67	67	140	140	276	276
	352	358	352	352	352	455
	358		352		455	
	950 (4)	950 (3)	950 (4)	950 (3)	950 (4)	950 (3)
C-H str	2854	2854	2854	2854	2854	2854
C-C-H bend	768	768	768	768	768	768
Log A (300°K) ^a	10.39	10.63	10.80	11.05	11.39	11.66

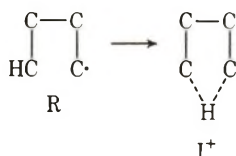
B. Ring Modes of I^{+} Replacing Deleted Modes
 $I^{+}_{2,6}$ (six-membered ring): 850 (5), 370 (4), 1100 (3)
 $I^{+}_{3,6}$ (five-membered ring): 850 (4), 370 (2), 1100 (3)

$$^a A = (kT/h)(Q^{\ddagger}/Q^*_{v}).$$

Frequency assignments for the three radicals, 355TMH2·, 35DMH2·, and 3MH2· were obtained by eliminating one C_s-H str (2928 cm⁻¹) and two H-C_s-C bending modes (1310, 1260 cm⁻¹) from the corresponding alkane assignments.

Frequency assignments for the H + parent olefin association complexes are required to compute the distribution function for the formed vibrationally excited radicals, $f(E)$. They were derived from the terminal olefin assignments by reducing the -C=C torsion and stretch by 20% and by adding two 150 cm⁻¹ partial C=C...H bending motions.¹⁹ The terminal olefin assignments, 3MH1, 35DMH1, and 355TMH1, were obtained as in the past by altering 16 frequencies in the corresponding radical to frequencies characteristic of the -CH=CH₂ group.²⁰

The isomerization activated complexes, I^{+} , are five-, six-, or seven-membered ring structures containing four, five, or six carbon atoms and one hydrogen atom; I^{+} frequency assignments were derived from those of their radical precursors as follows. Consider the formation of a five-membered I^{+} ring skeleton from the radical skeleton, R



Structure R has ten identifiable internal coordinates: three C-C str, three C-C tors, two C-C-C bends, one C-C-H bend, and one C-H str; and structure I^{+} has nine vibration modes (five bond stretching modes and four bond angle bending modes) and the reaction coordinate translation. Thus ten radical frequencies

can be identified, removed, and replaced by nine ring frequencies to obtain the activated complex assignment. An estimate of some of the values of the nine I^{+} ring frequencies can be obtained by examining cyclic alkane frequency assignments.²¹ The C_nH_{2n} ($n = 3$ to 6) cyclic alkanes have $3n - 6$ ring deformation modes which may be grouped into n 850 cm⁻¹ (C-C str) and $2n - 6$ 370 cm⁻¹ (C-C-C bend) modes. Since the I^{+} ring contains four carbon atoms, six of the nine ring modes were assigned: 850 (4), 370 (2). The remaining three modes involve motion of H and were therefore assigned the somewhat high frequency of the C-C-H bending, *i.e.*, 1100 (3). Assignments for the five- and six-membered ring I^{+} structures are summarized in Table VII. The Arrhenius A factors, $A = (kT/h)(Q^{\ddagger}/Q)$, obtained from these frequency assignments are of the correct order of magnitude for unimolecular reactions involving cyclic transition states, *i.e.*, 10¹⁰ to 10¹¹ sec⁻¹.²²

B. *Energetics and Rate Calculations.* Eigenstate sums, calculated by a harmonic oscillator model with the frequency assignments described in part A, are listed in Table VIII as of function of energy for the six I^{+} and three radical species. Specific $R_i \rightarrow R_j$ isomerization rates at energy E_i , $k_{ij}(E_i)$, were calcu-

(19) J. H. Current and B. S. Rabinovitch, *J. Chem. Phys.*, **38**, 783 (1963); B. S. Rabinovitch, R. F. Kubin, and R. E. Harrington, *ibid.*, **38**, 405 (1963).

(20) L. M. Sverdlov, M. G. Borisov, and N. V. Tarasova, *Opt. Spektrosk.*, **5**, 354 (1958).

(21) (a) Cyclohexane: R. G. Snyder and J. H. Schachtschneider, *Spectrochim. Acta, Part A*, **21**, 169 (1965); cyclopentane: J. E. Kilpatrick, K. S. Pitzer, and R. Spitzer, *J. Amer. Chem. Soc.*, **69**, 2483 (1947); (c) cyclobutane: G. W. Rathjens, Jr., N. K. Freeman, W. D. Gwinn, and K. S. Pitzer, *ibid.*, **75**, 5634 (1953); (d) cyclopropane: S. J. Cyvin, *Spectrochim. Acta, Part A*, **16**, 1022 (1960).

(22) H. E. O'Neal and S. W. Benson, *J. Phys. Chem.*, **71**, 2903 (1967).

lated from the RRKM expression

$$k_{ij}(E_i) = \frac{\sigma_{ij}}{h} \frac{\sum_{E^+=0}^{E^+=E_i-E_{ij}^{\circ}} P(E^+)}{N_i^*(E_i)}$$

The eigenstate density of R_i at energy E_i above its zero-point energy is denoted $N_i^*(E_i)$. Vibrational eigenstate sums extend from energy $E^+ = 0$ to $E^+ = E_i - E_{ij}^{\circ}$ where E_{ij}° is the threshold energy for the $R_i \rightarrow R_j$ process. The reaction path degeneracy, σ_{ij} ,

Table VIII: Eigenstate Sums of Radicals and Isomerization Complexes

A. Eigenstate Sums of $I_{2,6}^+$ and $I_{3,6}^-$ Species

E^+ , 10^3 cm^{-1}	—355TMH2—		—35DMH2—		—3MH2—	
	$I_{6,3}^+$	$I_{6,2}^+$	$I_{6,3}^+$	$I_{6,2}^+$	$I_{6,3}^+$	$I_{6,2}^+$
7.2	285-10 ^a	813-9	155-9	690-8	144-8	604-7
9.2	311-12	801-11	129-11	479-10	724-9	297-9
11.2	210-14	499-13	676-12	218-12	244-11	991-10
13.2	996-15	219-15	255-14	718-13	611-12	245-12
14.8	176-17	258-16	380-15	971-14	671-13	266-13

B. Eigenstate Sums of Radicals

E , 10^3 cm^{-1}	355TMH2· (10^{22}) ^b	35DMH2· (10^{20})	3MH2· (10^{18})
14.8	1.56	1.40	0.87
15.2	3.17	2.70	1.59
15.6	6.39	5.17	2.87
16.0	12.7	9.77	5.14
16.4	25.1	1.83	9.13
16.8	49.3	3.40	1.60

^a 285-10 means 285×10^{10} eigenstates, etc. ^b Units of eigenstate sum.

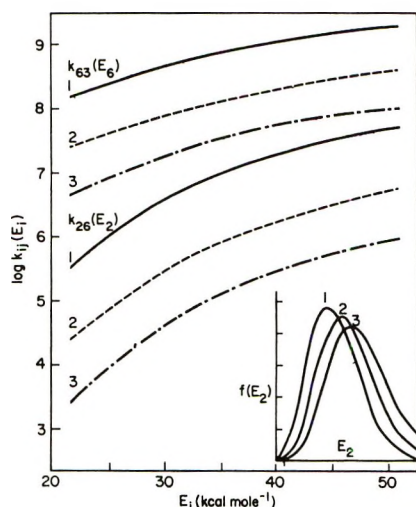


Figure 2. Calculated energy dependence of specific rate of five-membered, 8-kcal mol⁻¹ exothermic isomerization (k_{63}) and six-membered, 4-kcal mol⁻¹ endothermic isomerization (k_{26}) for the three systems: 1, $G \equiv \text{Et}$; 2, $G \equiv \text{iPr}$; 3, $G \equiv \text{tBu}$.

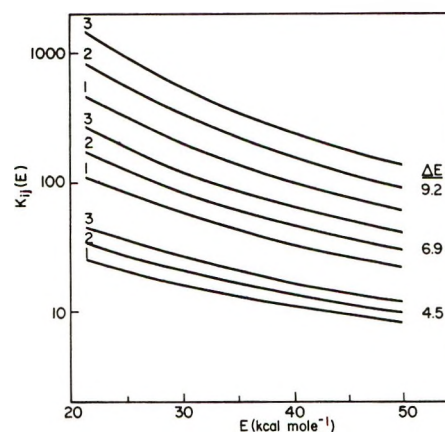


Figure 3. Calculated energy dependence of $K_{ij}(E_i)$ equilibrium constants for $R_i \rightleftharpoons R_j$. Curve 1, $G = \text{Et}$; 2, $G \equiv \text{iPr}$; 3, $G \equiv \text{tBu}$.

is the number of H atoms located on the j th carbon atom. The adiabatic partition function ratio for overall rotations is close to unity. Torsional modes have been treated as librations rather than as rotors.

Table IX summarizes calculated isomerization rates as a function of E_{ij}° and E_i . The average energy of

Table IX: Calculated Isomerization Rates^a as a Function of Energetics for $G = \text{tBu}$, iPr , Et

A. $R_2 \rightarrow R_6$ Process; Six-Membered Ring

E_{26}° , kcal mol ⁻¹	E_2 , kcal mol ⁻¹	$k_{26}(E_2)$, ^a sec ⁻¹		
		$G = \text{tBu}$	$G = \text{iPr}$	$G = \text{Et}$
8.6	46.3	21.3-6	102.0-6	738-6
14.3	46.3	4.74-5	30.8-5	298-5
20.0	46.3	7.76-3	67.7-3	894-3
8.6	44.0	18.6-6	89.0-6	656-6
14.3	44.0	3.73-5	24.1-5	237-5
20.0	44.0	5.07-3	45.2-3	619-3
Measured k_{26} value ^a		>4.5-5	>5.0-5	>3.3-5
Maximum E_{26}° , kcal mol ⁻¹		14.3	15.8	20.8

B. $R_6 \rightarrow R_3$ Process; Five-Membered Ring

E_{63}° , kcal mol ⁻¹	E_6 , kcal mol ⁻¹	$k_{63}(E_6)$, sec ⁻¹		
		$G = \text{tBu}$	$G = \text{iPr}$	$G = \text{Et}$
8.6	44.0	82.3-6	302.0-6	1630-6
14.3	44.0	15.2-5	70.5-5	584-5
20.0	44.0	18.9-3	114.0-3	1490-3
4.0	41.7	1.50-9	4.53-9	18.4-9
8.6	41.7	63.0-6	230.0-6	1300-6
14.3	41.7	11.0-5	49.0-5	460-5
Measured k_{63} value		5-6	18-6	100-6
Estimated E_{63}° , kcal mol ⁻¹		12.0	12.0	12.0

^a Tabulated rates are for one reaction path. Actual reaction path degeneracies in the $R_2 \rightarrow R_6$ process (σ_{26}) are 9, 6, and 3 in $G = \text{tBu}$, iPr , and Et , respectively. $\sigma_{6,3}$ values are unity for each system

the isomerizing R₂* radicals, $\langle E_2 \rangle^I$, is only slightly less than the average energy of the formed R₂* species, $\langle E_2 \rangle^f$; the latter quantities are¹⁷ 45.1, 46.3, and 47.4 kcal mol⁻¹ for the G = tBu, iPr, and Et system, respectively. Neglecting energy state fractionation by reaction and collisional perturbations, the average energies of the reacting (isomerizing) R₆* species, $\langle E_6 \rangle^I$, are approximately 4 kcal mol⁻¹ less than $\langle E_2 \rangle^I$. From Table IX it may be seen that the calculated rates are relatively insensitive to $\langle E_2 \rangle^I$ and $\langle E_6 \rangle^I$. However, an uncertainty of a factor of 3 in the experimental isomerization rate introduces a 1.5-kcal mol⁻¹ uncertainty in the deduced E_{ij}° value. On this basis, plausible

lower estimates of thresholds in the 6ps and 5tp processes are 14 and 12 kcal mol⁻¹, respectively.

Figure 2 shows the energy dependence of the six specific isomerization rate constants obtained with $E_{26}^\circ = 14$ and $E_{63}^\circ = 9$ kcal mol⁻¹. The energy distribution of the formed R₂* species are also included.

Figure 3 reveals the energy dependence of the equilibrium constants for C₇, C₈, and C₉ radical isomers, R_i ⇌ R_j, having 4 (*i.e.*, for a ps or st process) or 8 (*i.e.*, for a pt process) kcal mol⁻¹ differences in zero-point energy, ΔE . $K_{ij}(E_i)$ is equal to $N_i^*(E_i + \Delta E) / N_j^*(E_j)$, for $\sigma_{ij} = \sigma_{ji}$, and for a model of identical frequency assignments for R_i and R_j.

On the Lifetime of Trifluoromethyl Radical in Aqueous Solution¹

by Jochen Lilie, D. Behar, Richard J. Sujdak, and Robert H. Schuler*

Radiation Research Laboratories, Center for Special Studies and Department of Chemistry, Mellon Institute of Science, Carnegie-Mellon University, Pittsburgh, Pennsylvania 15213 (Received April 10, 1972)

Publication costs assisted by Carnegie-Mellon University and the U. S. Atomic Energy Commission

Radiolysis of aqueous solutions of CF₃Cl produces CF₃ radicals which can readily be trapped as the addition product to nitromethane anion. Intercomparison of the effects of scavengers on the esr signals of this adduct radical and on the production of fluoride ion indicates that CF₃ reacts with water with a period of ~30 msec. Conductometric pulse radiolysis studies in the presence of 1 mM methanol, where OH radicals are rapidly removed from the system, show that no significant hydrolysis of CF₃ occurs on the millisecond time scale. In the absence of methanol, however, secondary reactions which produce a large yield of HF occur at shorter times. This HF can be accounted for by reactions involving combination of CF₃ radicals with OH. It is expected that the CF₃OH produced from such a combination will eliminate HF rapidly. However, it also appears from the magnitude of the increase in conductivity that CF₂O must hydrolyze completely within the period of these conductivity experiments. From the limiting growth period at high doses the period of the initial hydrolysis of CF₂O is estimated to be ~10 μsec.

Balkas, Fendler, and Schuler have examined the radiolysis of aqueous solutions of CF₃Cl by steady-state and conductometric pulse radiolysis methods and have concluded that decomposition of the CF₃Cl occurs entirely as a result of initial attack of e_{aq}⁻ on the solute to produce chloride ion.² At low dose rates,



however, a yield of fluoride ion which corresponds to the complete hydrolysis of the CF₃ is also produced,² and a major question exists as to the reactions responsible for the appearance of this fluoride and the time scale over which they occur. In their conductometric studies, Balkas, *et al.*, found, as expected, that for each hydrated electron produced the conductivity increment corresponded to the production of 1 equiv of HCl within the several microsecond resolving time of the

apparatus. They also found an additional growth of conductivity on the 10-μsec time scale which corresponded to the production of ~1 additional equiv of HX and suggested that this growth was the result of the initial stage of hydrolysis of the CF₃. If so, this pseudo-first-order reaction would provide a convenient reference against which one could make absolute determinations of the rate of reaction of CF₃ with added solutes. It was estimated, for example, that the reaction of CF₃ with ethylene had a rate constant of ~7 × 10⁸ M⁻¹ sec⁻¹.² Bullock and Cooper³ have made an absolute pulse radiolytic determination of the rate of attack of CF₃ radicals on the formate ion and have

(1) Supported in part by the U. S. Atomic Energy Commission.

(2) T. I. Balkas, J. H. Fendler, and R. H. Schuler, *J. Phys. Chem.*, **75**, 455 (1971).

(3) G. Bullock and R. Cooper, *Trans. Faraday Soc.*, **66**, 2055 (1970).

used the rate constant measured ($3.4 \times 10^6 M^{-1} \text{sec}^{-1}$) together with the results from competitive experiments to determine the rate constants for reaction with other solutes. They estimated that the rate constant for addition of CF_3 to ethylene had a value of only 4×10^7 . Such a low rate constant makes the pronounced effect of ethylene on the fluoride yield incompatible with a 10- μsec hydrolysis period, and it was suggested² that further studies were in order. In the present work we have examined the effects of methyl, ethyl, and isopropyl alcohols on fluoride production in the radiolysis of aqueous solutions of CF_3Cl . Low concentrations of these solutes are effective in reducing the fluoride yield so that either attack of $\text{CF}_3\cdot$ on the alcohols, which stabilizes the fluorine as CF_3H ,³ proceeds very rapidly or hydrolysis is relatively slow. ESR experiments in which CF_3 radicals are trapped as the adduct of $\text{CH}_2=\text{NO}_2^-$ show that the rate of attack on the alcohols must be low. We must conclude from an intercomparison of the results of the ESR and steady-state scavenging experiments that hydrolysis of CF_3 occurs on a time scale longer than milliseconds and that, therefore, the conductivity increase observed on the 10- μsec time scale must result from complicating secondary reactions other than the direct hydrolysis of CF_3 . The previous discussion² of the reactions responsible for fluoride production drew heavily on the assignment of this short-term increase to the hydrolysis of CF_3 and must be reconsidered in view of the fact that this assignment now appears to be incorrect. Unfortunately the hydrolysis period is sufficiently long that it cannot easily be used as the reference reaction in competitive pulse experiments.

Experimental Section

Fluoride ion production in the radiolysis of solutions containing $\sim 10^{-3} M$ CF_3Cl was determined with a fluoride ion selective electrode in much the same way as in the previous study.² The required amount of CF_3Cl was added to an outgassed sample containing $2 \times 10^{-3} M$ phosphate buffer (at pH 6.3) and also the desired concentration of alcohol. Irradiations were carried out in a ^{60}Co source at an absorbed dose rate of $1.6 \times 10^{16} \text{eV g}^{-1} \text{sec}^{-1}$. Irradiations were from 100 to 300 sec so that product concentrations were $\sim 10^{-4} M$. Because of this, experiments with added scavenger were limited to concentrations $> 5 \times 10^{-4} M$.

ESR absorption of the CF_3 adduct of nitromethane was examined in *in situ* radiolysis experiments of the type described by Eiben and Fessenden⁴ and Behar and Fessenden.⁵ Saturated solutions of CF_3Cl containing CH_3NO_2 at pH 12 were irradiated and the reduction in intensity of the signals of the $\text{CF}_3\text{CH}_2\dot{\text{N}}\text{O}_2^-$ radical anion at constant beam current was examined as a function of added solute.

Conductometric pulse radiolysis studies were carried out with the 10-MHz ac conductivity bridge described

by Lilie and Fessenden.⁶ Sampling methods were employed with pulse operation and data accumulation being under control of a PDP-8 computer as described in this previous work.⁶ Data were stored on magnetic tape for subsequent computerized data analysis. Solutions were outgassed, saturated with CF_3Cl (0.0009 M), and continuously flowed through the conductivity cell. Pulses were of $\sim 0.5\text{-}\mu\text{sec}$ duration at current densities of 1–100 mA/cm². Doses deposited were 10^{16} to 10^{18} eV/g.

In certain preliminary experiments anomalous conductivity results were obtained which were traced to the presence of significant concentrations of CCl_4 in the CF_3Cl samples. The CF_3Cl used for the results reported here was examined mass spectrometrically and shown to be free of multiply chlorinated impurities.

Results and Discussion

The fluoride yield determined in the absence of added scavenger was ~ 3.7 . This value is considerably lower than the previous value of 5.4 determined at the same dose rate.² It is obvious from the present experiments that the fate of the CF_3 radical can sensitively depend on the experimental conditions (*e.g.*, pH, irradiation period, trace impurities). In spite of this difficulty it is evident that unless the CF_3 radicals are removed they will ultimately react with the water to give F^- . It is known, for example, that at very low dose rates, where the radical lifetimes are seconds or greater, the fluoride yield approaches a limit of three times that of the chloride (which is equal to G_{aq}^-) so that complete hydrolysis occurs. We will be concerned here with the way in which the observed yield is reduced upon the addition of a CF_3 scavenger. Results with added isopropyl, ethyl, and methyl alcohols are presented in Figure 1. It is seen that the addition of $10^{-3} M$ ethanol or isopropyl alcohol reduces $G(\text{F}^-)$ to ~ 1 whereas the same concentration of methanol has essentially no effect. The competition kinetics involved are, of course, quite complex since the secondary reactions involve a number of sequential steps. Curves calculated assuming simple competition between scavenging and the reaction producing fluoride ion are given by the solid curves. Even though the kinetic treatment may not be completely accurate in detail, the relative reactivities of the different solutes should be given reasonably well by the displacement of these latter curves along the concentration coordinate. We estimate the relative scavenging rate constants as 1:0.5:0.014 for isopropyl, ethyl, and methyl alcohols. Bullock and Cooper measured relative rate constants of 1:0.5:0.09, but the fact that the fluoride yield is not affected by relatively high concentrations of methanol

(4) K. Eiben and R. W. Fessenden, *J. Phys. Chem.*, **75**, 1186 (1971).

(5) D. Behar and R. W. Fessenden, *ibid.*, **76**, 1710 (1972).

(6) J. Lilie and R. W. Fessenden, *ibid.*, in press.

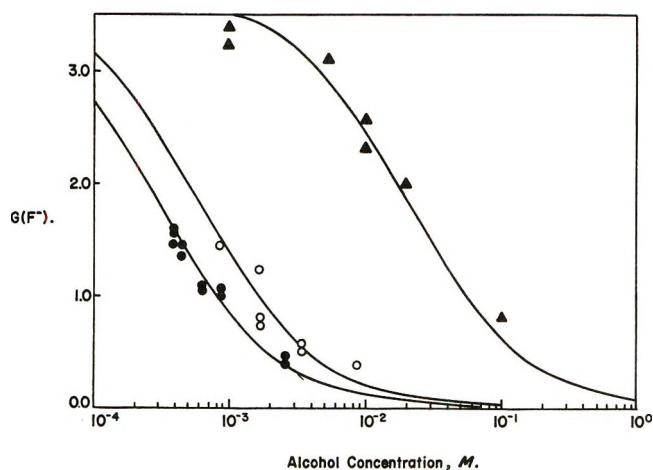


Figure 1. Fluoride yield as a function of added alcohol: ●, isopropyl alcohol; ○, ethyl alcohol; ▲, methyl alcohol. Curves correspond to a competitive elimination of the fluoride yield of 3.7 observed in the absence of added alcohol.

indicates that the abstraction rate from methanol must be somewhat less than indicated by them.

In esr experiments, the CF_3 adduct to nitromethane anion ($\text{CF}_3\text{CH}_2\text{NO}_2^-$) is clearly identifiable from its 2.06-G CF_3 quartet substructure.⁷ The observed signal-to-noise ratio for this spectrum is $\sim 50:1$ so that the intensity can readily be followed upon adding scavengers. In the initial experiments with 10^{-3} M nitromethane it was found that 1 M methanol had no effect on the intensity of the CF_3 adduct signals. Experiments with 2×10^{-4} M nitromethane were then carried out, and it was found that 1 M isopropyl alcohol was required to reduce the signal intensity by $\sim 50\%$. Assuming that the rate of disappearance of the total adduct radical population is not significantly affected by the change in the identity of the radicals, we find that

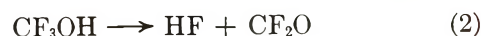
$$\frac{k_{\text{CF}_3 + \text{CH}_2\text{NO}_2^-}}{k_{\text{CF}_3 + i\text{-PrOH}}} \sim \frac{1}{2 \times 10^{-4}} = 5 \times 10^3$$

Using Bullock and Cooper's rate constant of 9×10^4 $M^{-1} \text{sec}^{-1}$ for the denominator of the above, we estimate a rate constant of 5×10^8 $M^{-1} \text{sec}^{-1}$ for the rate of addition of CF_3 to nitromethane anion. This rate constant is of the magnitude quoted for addition of CF_3 to 1,3-butadiene³ but an order of magnitude faster than that for addition to more simple unsaturated compounds. Experiments with 4 M methanol showed a $\sim 25\%$ reduction in signal intensity which implies that the rate constant for reaction of CF_3 with CH_3OH is approximately ten times less than that for reaction with isopropyl alcohol. This ratio should, however, only be regarded as approximate because of the high concentration of methanol required by the low rate for the scavenging reaction which makes competitive esr experiments very difficult. Potentially it is possible to use this competitive approach to measure rate

constants for reactions of CF_3 with solutes provided the rate constant is greater than $\sim 10^4$ $M^{-1} \text{sec}^{-1}$. Since a second-order termination reaction is involved here, accurate quantitative application will require a lengthy examination of a number of experimental parameters. Further work along these lines is planned.

These esr experiments show that reaction of CF_3 with isopropyl alcohol is a factor of at least 5000 slower than for reaction with nitromethane anion. The rate constant for the latter reaction cannot be greater than that for a diffusion-controlled reaction, *i.e.*, $\sim 5 \times 10^9$ $M^{-1} \text{sec}^{-1}$, so that this result demonstrates quite conclusively that the rate constant for the reaction with the alcohol cannot be greater than $\sim 10^6$ $M^{-1} \text{sec}^{-1}$. The fact that millimolar concentrations of isopropyl alcohol are efficient in eliminating F^- formation in the steady-state experiments requires that any hydrolysis which occurs must take place on a time scale greater than milliseconds. If, in fact, we accept the value of 9×10^4 $M^{-1} \text{sec}^{-1}$ for the rate constant of the abstraction reaction³ then the competitive experiments of Figure 1 show that the period of the hydrolysis must be ~ 30 msec.

At this point we must ask what is the significance of the rise in conductivity observed on the 10–100 μsec time scale. Since CF_3 does not react directly with H_2O in these short times, some other complicating secondary process must be involved. In the absence of OH scavenger, radical combination reactions between CF_3 and OH will result in the formation of CF_3OH which is expected, in turn, to rapidly eliminate HF. This difficulty was previously recognized as a complication at high doses but not thought able to explain either the period or the magnitude of the decrease at low doses.² The present results indicate that at initial CF_3 concentrations $> 10^{-6}$ M radical combination will occur to a significant extent at times > 10 μsec . Work at lower radical concentrations is difficult because of the reaction of CF_3 radicals with traces of residual oxygen. Assuming that the mutual and intercombination reactions of CF_3 and OH are statistical one expects that only 50% of the CF_3 will react to produce CF_3OH . The conductivity change observed on the millisecond time scale is illustrated in Figure 2a. The observed step height corresponds to the production of 1.0 equiv of HF per electron in addition to the initial yield of 1 equiv of HCl. Since elimination of HF from the CF_3OH can only account for $\sim 50\%$ of this increase,

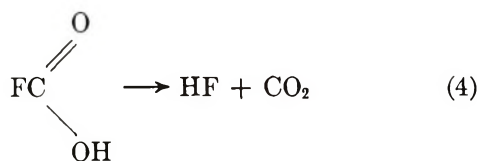
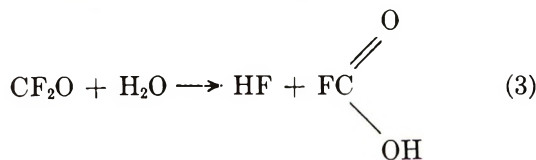


subsequent hydrolysis of the CF_2O formed must take place on a time scale < 100 μsec . Examination of this system out to 10 sec showed that no additional increase in conductivity occurred. The increase noted in Figure 2a is only two-thirds that expected from random com-

(7) D. Behar and R. W. Fessenden, to be published.

combination of CF_3 and OH so that there seems to be some selectivity in the radical termination step. Fluoride production in pulse experiments at high dose rates indicates a similarly low yield ($G(\text{F}^-)/G(\text{Cl}^-) = 1.02$ at a dose rate of $2 \times 10^{23} \text{ eV g}^{-1} \text{ sec}^{-1}$).²

From the above the second-order radical combination reaction appears to be followed rapidly by a first-order elimination reaction (reaction 2) and two further steps (reactions 3 and 4). A complete kinetic descrip-



tion is obviously quite complicated. Conductivity experiments were carried out over the dose region where the concentrations of CF_3 radicals initially produced were from 5×10^{-7} to $5 \times 10^{-5} \text{ M}$. In this region the growth period increased somewhat with decreased dose. At low doses where the CF_3 concentration was initially from 5×10^{-7} to $3 \times 10^{-6} \text{ M}$ the buildup followed second-order kinetics (Figure 2c) and gave, as an average, a second-order rate constant for disappearance of radicals of $4 \times 10^9 \text{ M}^{-1} \text{ sec}^{-1}$. In this concentration range, the recombination of (primary) radicals is evidently the rate-determining process. At higher doses ($[\text{CF}_3]_0 > 10^{-5} \text{ M}$) the buildup was exponential (Figure 2d) with a half-period of $\sim 12 \mu\text{sec}$. At the concentration of radicals present here the median radical lifetime is less than $5 \mu\text{sec}$ so that the combination step is not rate determining. The initial conductivity change observed at very short times (Figure 2d) is $\sim 20\%$ greater than expected for the formation of HCl . This difference indicates that reaction 2 takes place very rapidly ($< 5 \mu\text{sec}$). It seems very likely that the 12- μsec growth period of Figure 2d corresponds approximately to the period of the first step in the hydrolysis of CF_2O (reaction 3) with the final step (reaction 4) being very rapid.

Finally we can consider the dependence of the F^- yield with dose rate previously noted in the steady-state experiments. A drop of 50% at a dose rate of approximately $10^{16} \text{ eV g}^{-1} \text{ sec}^{-1}$ was observed. If we assume that this drop results from competition between a pseudo-first-order hydrolysis reaction and CF_3 combination (so that a fraction of the CF_3 radicals are stabilized as C_2F_6), then we estimate the hydrolysis reaction occurs with a period of $\sim 35 \text{ msec}$ in agree-

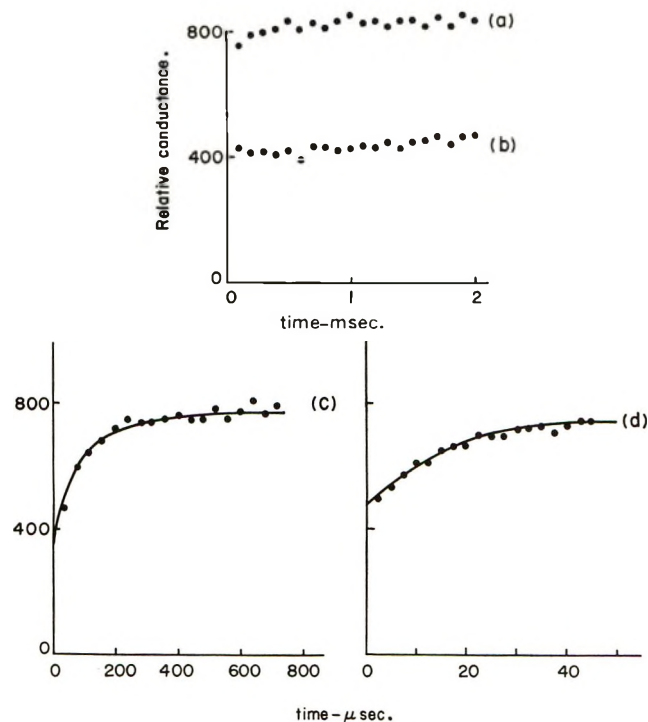


Figure 2. Relative conductance at a pH ~ 6 as a function of time (a) on the millisecond time scale for solutions saturated with CF_3Cl at a dose of $3 \times 10^{16} \text{ eV/g}$; (b) under identical conditions but after the addition of 1 mM methanol. Buildup at shorter times is illustrated for doses of (c) 5×10^{16} and (d) $9 \times 10^{17} \text{ eV/g}$ where the initial radical concentrations are 5×10^{-6} and $8 \times 10^{-5} \text{ M}$, respectively. The curve of c is a computerized least-means-squares second-order fit which gives a radical combination rate constant of $5 \times 10^9 \text{ M}^{-1} \text{ sec}^{-1}$. The data of d has been fitted with a simple exponential growth with a period of $12 \mu\text{sec}$. The response time of the apparatus is $\sim 1 \mu\text{sec}$ (see ref 6) so that the growths exhibited in c and d unquestionably result from secondary postirradiation reactions.

ment with the estimate made above from the isopropyl alcohol scavenging experiments. Such a period would not be observable in pulse experiments since appropriate experiments would require radical concentrations $< 10^{-8} \text{ M}$. We have pulse irradiated a CF_3Cl solution containing 10^{-3} M CH_3OH . In this case all of the OH radicals will react with the methanol in a period of $\sim 10^{-6} \text{ sec}$ and the only radical combination reactions which will take place will involve CF_3 and CH_2OH radicals. It is seen in Figure 2b that in the presence of the methanol no significant growth in conductivity is observed on the millisecond time scale confirming that hydrolysis of CF_3 is unimportant at these times. However, it is seen in Figure 1 that at low dose rates a large F^- yield is observed even in the presence of methanol. Presumably the only possible reaction which can account for this fluoride is direct hydrolysis of the CF_3 . This hydrolysis appears to occur, as is indicated above, with a period of the order of 30 msec.

Hot-Atom Chemistry of Carbon-14 in Solid Benzene at Kinetic Energies at or below 5 Electron Volts

by Jacques Lintermans, Wallace Erwin, and Richard M. Lemmon*

Laboratory of Chemical Biodynamics, Lawrence Berkeley Laboratory, University of California, Berkeley, California 94720 (Received April 12, 1972)

Publication costs assisted by the U. S. Atomic Energy Commission

The yields of seven major hydrocarbon products from the irradiation of solid benzene with accelerated carbon-14 ions were determined at very low kinetic energies, namely, down to 2 eV. The ultimate fate of the irradiating carbon ions was determined by chemical degradation of the products to reveal the per cent of ^{14}C activity at a given position in the molecule. This work has shown (a) throughout the 5000–2-eV energy range, an essentially constant yield of benzene (about 3–4% of the irradiating $^{14}\text{C}^+$ ions), (b) a decrease in the yields of toluene, cycloheptatriene, and phenylacetylene as one goes from 100 down to 2 eV, (c) an increase in the yields of phenylcycloheptatriene and biphenyl when the 5–2 eV-energy range is reached, and (d) the appearance of maximum activity in the phenyl groups of toluene and diphenylmethane at about 5 eV. These results suggest the mechanisms involved in the formations of these products.

Introduction

Previous papers from this laboratory^{1–5} have reported the principal chemical results obtained when a beam of accelerated $^{14}\text{C}^+$ ions is impinged upon a target of solid benzene at -196° . As a function of the kinetic energy of the impinging ions, we determined the yields and (with the exception of benzene- ^{14}C) the activity distributions of the major, labeled hydrocarbon products (toluene, cycloheptatriene, diphenylmethane, phenylacetylene, biphenyl, and phenylcycloheptatriene). The kinetic energy range studied was from 5000 to 5 eV. These studies provided insight into the energetic states (both kinetic and internal) and into the extent of hydrogen-to-carbon attachment (C, CH, CH_2 , or CH_3) before the bond-forming event with the benzene molecule takes place.

Recent improvements in our carbon-ion accelerator have made it possible for us to reduce the kinetic energy of our impinging $^{14}\text{C}^+$ ions down to about 2 eV. The lower energy region is important to minimize the hydrogen attachments mentioned above, the internal energy of the initially formed C_7 species, and radiation damage effects. This energy region also enables us to correlate better our energetic system with the known photochemistry and thermal chemistry of carbon and methylene with benzene. The present paper reports the observations that we have made in the 5–2-eV region and summarizes the added information gained concerning the energetic reactions of carbon and its hydrogen-containing adducts with benzene. We also report some toluene and xylene irradiations that have provided further information on the mechanism of the benzene- ^{14}C formation.

Experimental Section

Ion Accelerator. The instrument used in these

studies has been described in a recent publication.⁶ Since that paper appeared we have added probes for monitoring the ion beam position and shape and have adjusted the position and angle of our decelerator lens system. These improvements have enabled us to reduce the $^{14}\text{C}^+$ beam's kinetic energy down to 2 eV; at this energy we still have an approximately 0.25 μA current striking the target.

Irradiation Conditions and Analytical Techniques. A 1-hr operation of the 0.25- μA beam embeds about 0.6 μCi of ^{14}C in the benzene (which is added steadily to the target during the irradiation; a total of about 100 λ is used). A product formed in 1% yield of the incoming carbon ions would, therefore, contain about 6 nCi, or about 13,200 dpm. The ratio of incoming ions to benzene molecules in the target is about 10^{-4} . At the conclusion of an irradiation the solid benzene target is scraped into a rubber-capped vial, to which hydrocarbon carriers are added, and from which aliquot portions are removed *via* syringe needles for subsequent radiogas chromatography. Details of the chromatographic techniques were given in an earlier publication.¹

Degradations. The chemical degradations were performed by procedures whose main details have been reported earlier.^{2,4,5} However, several significant im-

(1) H. M. Pohlit, T.-H. Lin, W. Erwin, and R. M. Lemmon, *J. Amer. Chem. Soc.*, **91**, 5421 (1969).

(2) H. M. Pohlit, T.-H. Lin, and R. M. Lemmon, *ibid.*, **91**, 5425 (1969).

(3) H. M. Pohlit, W. Erwin, T.-H. Lin, and R. M. Lemmon, *J. Phys. Chem.*, **75**, 2555 (1971).

(4) H. M. Pohlit and R. M. Lemmon, *ibid.*, **75**, 2558 (1971).

(5) T.-H. Lin and R. M. Lemmon, *ibid.*, **75**, 3524 (1971).

(6) H. M. Pohlit, W. Erwin, F. R. Reynolds, R. M. Lemmon, and M. Calvin, *Rev. Sci. Instrum.*, **41**, 1012 (1970).

improvements were made in these procedures. (1) In the oxidation of labeled products (toluene, diphenylmethane, phenylacetylene, and phenylcycloheptatriene) to benzoic acid, the excess chromic acid was destroyed with aqueous Na_2SO_3 instead of with methanol. Subsequently, the reaction mixture was not taken to dryness, but instead was extracted by ether for 5 hr in a liquid-liquid extractor. This change reduced losses of the volatile benzoic acid and increased its yield from about 55 to 75%, an improvement especially valuable for toluene and phenylacetylene, whose yields from the $^{14}\text{C}^+$ beam are only about 0.2%.

(2) The crude benzoic acid was purified by silylation with bis(trimethylsilyl)trifluoroacetamide, followed by glpc (SE-30, 5% on DMCS Chromosorb W, 70/80 mesh, 0.25 in. \times 10 ft, He flow 100 cm^3/min). The silyl benzoate peak was trapped in a mixture of water-acetone-NaOH (slight excess of the hydroxide). The ester hydrolysis was fast, and evaporation of the solvent gave dry sodium benzoate suitable for the subsequent Schmidt reaction. The recovery of the benzoate (as the Na salt from the glpc operation) was 99%. This almost quantitative purification is especially good for eliminating traces of acetic acid (the solvent for the CrO_3 oxidation). Any such traces would decrease the specific activity of the $^{14}\text{CO}_2$ coming from the Schmidt reaction on the benzoic acid.

(3) The phenyl-ring activity was determined by bubbling gaseous HCl through the aniline-in-ether solution coming from the Schmidt reaction, and the ether was then evaporated to dryness in a stream of dry N_2 . An excess of dry diethylamine (60 λ to 1 λ of aniline) was added, with good stirring, to the dry aniline hydrochloride. The aniline-in-diethylamine solution was injected into the glpc column with a Flath-Lundin filter syringe (Hamilton Co.) that retains the solid particles of $\text{Et}_2\text{NH} \cdot \text{HCl}$.

(4) In our previous work, in which benzophenone was an intermediate in the degradation of diphenylmethane,² we used benzene as the solvent in the reaction between benzophenone and hydrazoic acid. However, since small amounts of aniline may be formed by reaction with benzene,⁷ we abandoned that solvent and, in its place, used trichloroacetic acid; we followed the reaction conditions of Smith⁸ and achieved a benzanilide yield of 92%. The benzanilide was hydrolyzed by an overnight refluxing with KOH in an alcohol-water solution, from which, after dilution with water, the aniline (85% yield) was extracted with ether.

(5) The values of the mass peaks on the glpc columns were determined by a digital integrator (Hewlett-Packard Model 3370A). Relationships between mass and peak areas were determined by previous injections into the glpc columns of known amounts of a particular compound.

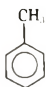

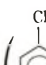
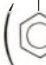




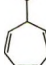
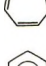

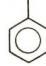

Toluene and Xylene Irradiations. In an attempt to learn more about the interesting processes that lead to

labeled benzene, we also irradiated (separately) solid toluene, *o*-xylene, and *p*-xylene at -196° , with a 10-eV $^{14}\text{C}^+$ beam; we then determined the yields of labeled benzene, toluene, ethylbenzene, styrene, methylstyrenes, and the xylenes.

Results

Activity Distributions. The degradation results are recorded in Table I. For comparison, we have included some previous results that were obtained at 5 eV, and at higher kinetic energies. Because of small analytical and counting errors the results do not necessarily add up to 100%.

Table I: Product Activity Distributions (%) as a Function of $^{14}\text{C}^+$ Energy

Product	Energy					
	5 keV	6 eV	5 eV	4.5 eV	3 eV	2 eV
	85	86	45 ^a	76	92	94
	13	15	54 ^a		10	6
	91		76		87	
	9		18		11	
	30		33			30
	66		62			63
	4		7			6
	16		22		9	
	52		57		85	
	30		19		6	
	9	8				
	81	84			100	100
	9	8				

^a These figures are averages for three independent 5-eV irradiations and degradations; the individual CH_3/ring results were 29/66, 62/41, and 44/56. Since there is an obvious sharp rise in ring activity at or about 5 eV (*cf.* the 6-, 4.5-, and 3-eV data), the discrepancies probably result from slight (within ± 0.5 eV) energy differences in the three nominal 5-eV irradiations.

Yields. The product yields as a function of energy are recorded in Table II. Yield is defined as the percent of the activity, in an aliquot portion of the target, that appears in the glpc peak of the product. We believe that these yield determinations are valid to within $\pm 25\%$.

(7) H. Wolff in "Organic Reactions," Vol. III, Wiley, New York, N. Y., 1946, p 308.

(8) P. A. S. Smith, *J. Amer. Chem. Soc.*, **70**, 320 (1948).

Table II: Product Yields as a Function of Energy

Product	% yield at indicated energy			
	5 keV	100 eV	5 eV	2 eV
Benzene	3.4	5.7	3.9	3.5
Toluene	1.0	1.1	0.2	0.2
Cycloheptatriene	2.5	2.2	0.5	0.9
$\text{C}_6\text{H}_5\text{C}\equiv\text{CH}$	1.6	3.1	0.3	0.2
Biphenyl	1.3	2.9	1.7	5.5
$\text{C}_6\text{H}_5\text{CH}_2\text{C}_6\text{H}_5$	1.5	3.8	2.6	2.9
Phenylcycloheptatriene	5.3	6.6	10.8	13.0

Irradiation of Toluene, o-Xylene, and p-Xylene. The products and their yields, obtained on the separate irradiations of these solid targets (at -196°) with 10-eV $^{14}\text{C}^+$ ions, are given in Table III.

Table III: Labeled Product Yields (%) from ^{14}C -Irradiated Toluene, o-Xylene, and p-Xylene

Product	Toluene	o-Xylene	p-Xylene
Benzene	0.3	<0.03	<0.01
Toluene	1.0	0.4	0.8
Ethylbenzene	0.8
Styrene	17
Methylstyrene	...	11	14
o-Xylene	0.3	0.8	...
m- + p-Xylene	1.1
p-Xylene	2.2

Discussion

As we have discussed previously,³ we interpret the decreases in yields of toluene and cycloheptatriene below 100 eV as reflecting a diminished opportunity for the incoming carbon-14 atom⁹ to pick up hydrogens to form CH or CH_2 ¹⁰ before the bond-forming interaction with a benzene molecule. The toluene yields, apparently, reflect the involvement of CH_2 , CH, and C in the reactions leading to toluene at energies above 5 eV, but only C for reactions at or below that energy. We cannot, however, assume that ring-labeled toluene is formed only by C atom interactions, a result that would be implied if the toluene-ring absolute yield (toluene yield \times fraction of the ^{14}C that is in the ring) was constant down to 5 eV. The absolute yield is indeed constant (with a value of about 0.16) from 5 keV to 100 eV, but drops to 0.06 at 31 eV and 0.03 at 10 eV. An additional insecurity in our interpretations regarding toluene is the formation of an oxygenated product, benzaldehyde (from the residual, 10^{-6} Torr, O_2 in our instrument). At 10 eV or lower energy, the benzaldehyde yields appear to be inversely related to those of toluene. The implications of scavenging-by-oxygen processes and of changes in the target's temperature will be the subject of a forthcoming paper.

The cycloheptatriene yield appears to rise as one goes from 5 to 2 eV; however, we are less than certain

that this is indeed true. As we surmised previously,³ the diminished yield of phenylacetylene at 5 eV must reflect a diminished opportunity for a C-stripping reaction leading to a reactive C_2H_2 fragment; our 2-eV result recorded here adds strength to that suggestion.

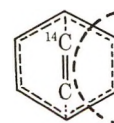
We interpret the increased yields of phenylcycloheptatriene and biphenyl, as one goes from 5- to 2-eV irradiations, as being due to the lessened internal energy that a reactive intermediate must dispose of to avoid decomposition before the product-forming reaction with a benzene molecule.

The yield of labeled benzene has stayed remarkably constant throughout the entire 5000-2-eV energy range. It continues to intrigue us how such a low kinetic energy (2 eV) ^{14}C can replace a ^{12}C to form a new, labeled benzene molecule. Our present hypothesis is that there must be an excited C_7 intermediate such as



Similar intermediates have been proposed by Rose, *et al.*,¹¹ who studied the interactions of energetic ^{11}C with benzene and observed many of the products discussed here. Without, for the moment, specifying anything about hydrogen-atom and electronic redistributions, we can visualize such an excited intermediate splitting out C-2 to produce the new, labeled product. A partial test of this notion has been carried out in our irradiations (results reported in Table III) of toluene and xylenes. Benzene- ^{14}C is formed from toluene but is a negligible, if not nonexistent, product from the xylenes. This is in accord with the above formulation and also in accord with the results obtained in carbon-recoil studies.¹² Also in accord is the higher yield of toluene (0.8%) from xylene, compared to that of benzene (0.3%) from toluene.

These results also appear to rule out any significant "C-2 adduct" mechanism as a route to labeled benzene from the irradiation of benzene—as might be suggested by the phenylacetylene product. In other words, benzene- ^{14}C might come from an excited adduct such as



that would then split out the indicated two-carbon species to give labeled benzene. Such a mechanism

(9) We believe that the ion is very rapidly neutralized on reaching the target. This question was discussed in ref 1.

(10) The low yields of methane from carbon-recoil studies on benzene (see ref 12) indicate that little CH_3 is formed.

(11) T. Rose, C. MacKay, and R. Wolfgang, *J. Amer. Chem. Soc.*, **89**, 1529 (1967).

(12) R. L. Williams and A. F. Voigt, *J. Phys. Chem.*, **73**, 2538 (1969).

could also give benzene- ^{14}C from *o*-xylene, but not from *p*-xylene. In fact, both xylenes give no detectable benzene (the difference between the <0.03 and $<0.01\%$ yields in Table III may be ignored—it has only to do with the background activity contaminations in our radiogas chromatographic equipment).

If labeled benzene is formed *via* the C_7 intermediate above, and if the postulated C-1 "bridge" attachments are unaffected by the presence of a methyl group, then we should expect that the irradiated toluene would give a toluene- ^{14}C /benzene- ^{14}C product ratio of 5.0. We found $1.0/0.3 = 3.3$. The same reasoning for the irradiated xylenes would give a xylene- ^{14}C /toluene- ^{14}C product ratio of 2.0. We found for the two xylenes, respectively, $0.8/0.4 = 2.0$, and $2.2/0.8 = 2.8$. Our agreement with the expected results of "random C-1 bridge" attachments is, therefore, not as good as Williams and Voigt reported in their products from ^{11}C recoils striking aromatic targets.¹² However, their targets were liquids, not solids, and it may be that our much lower energy (10 eV) carbons are showing some selectivities in their interactions with aromatic molecules.

The data of Table I show that the phenyl group activities for toluene, diphenylmethane, and phenylcycloheptatriene reach a maximum at about 5 eV. In the case of toluene, for which we have carried out three irradiations of the benzene target at 5 eV (and others at 6, 4.5, 3, and 2 eV), there is no doubt whatever of the reality of this maximum. Our interpretation is that at 5 eV the predominant process leading to labeled toluene

is the reaction with benzene of a bare (unhydrogenated) C atom, and that 5 eV gives the maximum internal energy that the intermediate, excited, C_7 species can accommodate without disintegration. The maximum internal energy would give a maximum of "activity scrambling," by processes such as those suggested earlier,^{2,5} giving maximum labeling in the phenyl group. In contrast, an ion striking the benzene surface at 6-eV energy might not be able to interact to form a product intermediate until it had experienced an energy-degrading collision; thus a 6-eV ion beam can be looked upon as one that interacts at all energies between 6 and 0 eV. Corresponding arguments also apply to the phenyl activities in diphenylmethane and phenylcycloheptatriene.

The 100% labeling in the C-1 position(s) of biphenyl is an interesting result and directly attributable to the low kinetic energies (2–3 eV) of our irradiating ions. To our knowledge, this is the first example of specific labeling in any product obtained in carbon-recoil or accelerated-carbon experiments. This result indicates that the new, labeled C_6 ring reacts with another molecule of benzene (to form biphenyl), making use of the excess vibrational or electronic energy in the ^{14}C atom, but without transferring that energy to another carbon atom of the C_6 ring.

Acknowledgments. This work was supported by the U. S. Atomic Energy Commission. We also express thanks for the technical assistance of Mr. Glenn A. Fisher.

Electron Spectroscopy for Chemical Analysis

(ESCA) Studies on Catalysts. Rhodium on Charcoal

by J. S. Brinen*

Central Research Division, American Cyanamid Company, Stamford, Connecticut 06904

and A. Melera

Scientific Instrument Division, Hewlett Packard, Palo Alto, California (Received April 10, 1972)

Publication costs assisted by American Cyanamid Company

ESCA (electron spectroscopy for chemical analysis) spectra have been obtained for rhodium foil, rhodium sesquioxide, and several rhodium catalysts. The spectra reveal the presence of both metal and oxide on the catalyst surface. Catalysts with high activity are characterized by a metal:oxide ratio of less than unity while for poor catalysts the metal:oxide ratio is greater than unity.

Introduction

In a recent review article,¹ the potential application of ESCA (electron spectroscopy for chemical analysis) or photoelectron spectroscopy to catalyst studies was discussed. Since ESCA measurements reveal the chemical composition and chemical states of the atoms on the surface of solids it provides a new probe for catalytic research. Important questions dealing with chemical composition of the catalyst surface and chemical differences, if any, between catalysts of high and low activity may be directly investigated. In this communication some preliminary results of such a study on hydrogenation catalysts composed of rhodium on charcoal² are presented. Examination of the rhodium 3d electron lines of some standard rhodium materials as well as several catalysts provides a clue to the chemistry of the catalyst surface. The spectra clearly differentiate between catalysts established to have high and low activity.

Experimental Section

The catalysts, rhodium on charcoal, as well as the rhodium foil were obtained from Englehard Industries. Rhodium sesquioxide was obtained from Pfaltz and Bauer, Inc.

ESCA measurements were performed on a Hewlett Packard 5950A spectrometer using monochromatic Al K α radiation. The binding energies reported here are not absolute in the sense that we have not corrected for shifts which may be attributable to charging effects. Such measurements using the gold deposition technique described by Perlman, *et al.*,³ will be performed in the near future. However, a knowledge of the absolute binding energies does not alter the results regarding the relative efficiencies of the catalysts under investigation.

Results and Discussion

Figure 1 shows the 3d_{5/2} and 3d_{3/2} photoelectron lines observed from rhodium foil. In addition to the lines from the metal (307.1 and 311.9 eV), lines from a surface oxide are also observed. By graphical curve resolution⁴ the surface rhodium oxide 3d_{5/2} electron line is at \sim 308.4 eV as indicated in the figure. A weak oxygen 1s photoelectron line is also observed in support of the assignment of a surface oxide coating.

The spectra in Figure 2 show the 3d electron lines from rhodium foil and from rhodium sesquioxide, Rh₂O₃. A chemical shift of 1.6 eV is observed between rhodium metal and Rh₂O₃. A significant difference in line width is observed between the oxide and the metal. By graphical analysis the line width of the 3d_{5/2} electron line for metallic rhodium and for Rh₂O₃ is 0.7 and 1.6 eV, respectively, while for the surface oxide a line width of \sim 1.8 eV is estimated.

Spectra of three catalyst samples examined by ESCA are shown in Figure 3. The catalytic activity with respect to the efficiency of selective hydrogenation by each catalyst was independently determined. The spectra of catalysts A and B are quite similar. Two lines were observed indicating the presence of at least two distinct rhodium species on the catalytic surface. The lowest binding energy peak, \sim 307.1 eV, corresponds to the presence of metallic rhodium. The

(1) W. N. Delgass, T. R. Hughes, and C. S. Fadley, *Catal. Rev.*, **4**, 179 (1970).

(2) R. L. Augustine, "Catalytic Hydrogenation," Marcel Dekker, New York, N. Y., 1965, p 39.

(3) D. J. Hnatowich, J. Hudis, M. L. Perlman, and R. C. Ragaini, *J. Appl. Phys.*, **42**, 4883 (1971).

(4) The low binding energy edge of the Rh 3d_{5/2} line was folded about the peak maximum and was then subtracted from the observed spectrum to obtain the line positions and line widths for the metal and surface oxide.

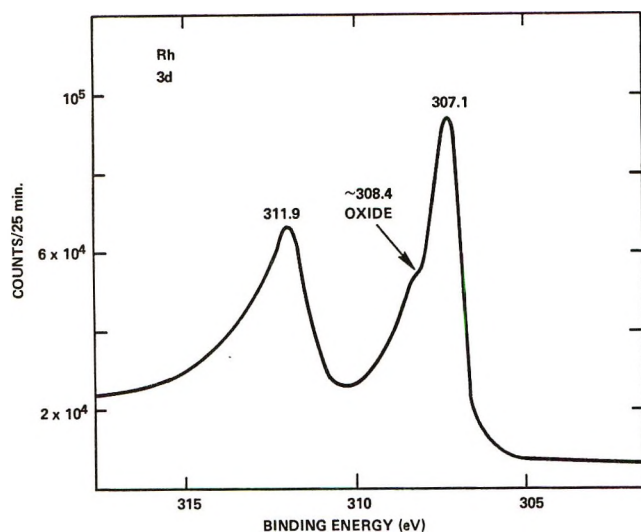


Figure 1. ESCA spectrum of rhodium 3d electrons obtained from rhodium foil.

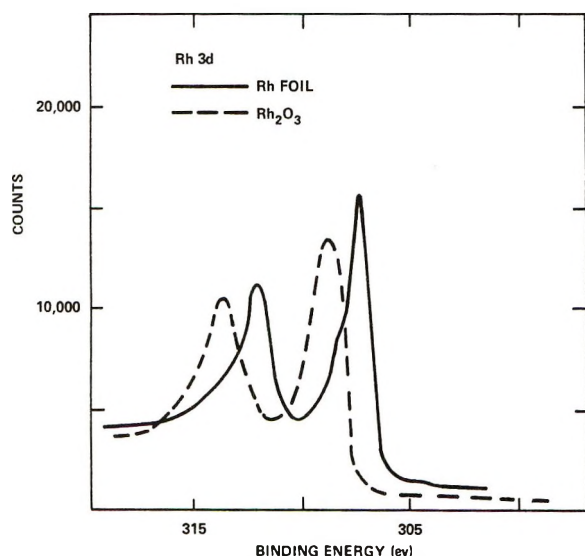


Figure 2. ESCA spectra of rhodium 3d electrons obtained from foil (—) and Rh_2O_3 (---).

second $3d_{5/2}$ electron line, at ~ 308.4 eV, corresponds to either the surface oxide observed on the metal foil or to Rh_2O_3 . Absolute binding energy measurements, as discussed above, are required to make a more definitive statement regarding the nature of this species. The photoelectron spectrum obtained from Catalyst C is different from that of Catalysts A and B. The same lines are observed with different relative inten-

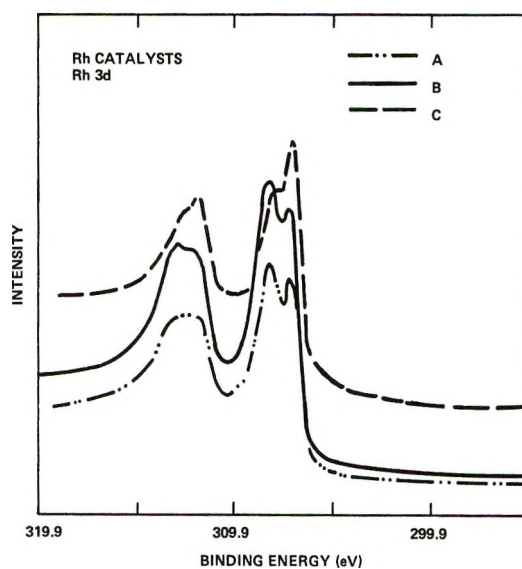


Figure 3. ESCA spectra of rhodium 3d electrons obtained from three different catalyst samples. Spectra A and B are from catalysts of high activity while C is from a catalyst with low activity.

sities. For C, the intensity of the line corresponding to metallic rhodium is greater than the intensity of the oxide line, which is the reverse of situation existing in Catalysts A and B. Catalysts A and B are high-performance catalysts while C exhibits low performance. The bulk chemical analysis of all these catalysts is the same.⁵ The desirable catalytic properties may then be attributable to the higher concentration of surface oxide(s) of rhodium in catalysts A and B.⁶

Summary

ESCA measurements have been performed on three rhodium catalyst systems. The spectra reveal the presence of multiple rhodium species on the catalyst surface. A direct correlation exists between the catalytic activity and the oxide to metal ratio. This investigation demonstrates the potential power of ESCA in relating performance and surface composition of catalyst systems.

(5) The surface areas of the carbon substrate for these catalysts are similar. The dispersion of rhodium on the carbon surface is not known. X-Ray measurements show broad lines indicating the presence of small rhodium particles.

(6) It should be kept in mind, however, that these differences are observed in the precursors to actual catalysts in their working states. Direct ESCA measurements of catalysts in the course of a reaction may never be realizable. Nonetheless, the correlation which exists between catalytic activity and oxide to metal ratio still retains its importance.

Temperature Dependence of the Electron Spin Resonance

Spectra of Zinc Oxide Powder

by K. M. Sancier

Stanford Research Institute, Menlo Park, California 94026 (Received April 10, 1972)

Publication costs assisted by Stanford Research Institute

The temperature dependence of the esr signal at $g \sim 1.96$ of vacuum-heated ZnO was examined in the temperature range of 97–470°K. The results of the first moment $M^*_{1.96}$ of the resonance normalized for changes in cavity Q indicate that the relative population of the paramagnetic center $M^*_{1.96}T$ increases with temperature. This result along with considerations of oxygen chemisorption on ZnO provides a basis for proposing that the paramagnetic centers for the temperature range studied are mainly conduction band electrons and to a lesser extent ionized donors due to excess zinc precipitated at defects.

Introduction

Various interpretations of the paramagnetic center in ZnO that gives rise to the esr signal at a g value of about 1.96 have recently been summarized.¹ Among these interpretations, several have been developed partly from data on the temperature dependence of the resonance intensity. However, the experimental data are sometimes incomplete and the interpretations need reexamination. For example, in an esr study of ZnO single crystals, the data of Schneider and Rauber² on the temperature dependence of the peak intensity of the resonance were corrected by Müller and Schneider³ by applying approximations based on estimates of the temperature dependences of magnetic susceptibility, microwave skin depth, and resonance line width. The spin density of the resonance was found to be temperature independent, and therefore it was proposed that the paramagnetic electron was simultaneously in the conduction band and in a shallow donor band.

In another study of ZnO single crystals, hyperfine structure of the $g \sim 1.96$ line due to ⁶⁷Zn was observed at temperatures less than 20°K. The paramagnetic center was ascribed to an F-center defect, *e.g.*, to an electron that is in the vicinity of zinc ions and that is trapped on oxygen ion vacancies.⁴ This assignment probably applies primarily at very low temperatures, as we shall discuss later.

In two studies^{5,6} of ZnO powder, the peak intensity of the $g \sim 1.96$ line was reported to decrease with an increase in temperature. However, consideration was not taken of two factors that are necessary for proper interpretation of the effect of temperature on the population of the paramagnetic center: the effects of temperature on the resonance line width and on the electrical conductivity of ZnO that alters the cavity Q.

Different temperature dependences have been reported for the two components of the $g \sim 1.96$ line that occurs in ZnO powder which has been heated under

vacuum, then in oxygen.⁷ As the temperature was increased, the peak intensity of the $g = 1.957$ component decreased faster than that of the $g = 1.963$ component; from these and other considerations it was suggested that the former component is due to conduction band electrons and the latter to an electron trapped at interstitial zinc ions.^{1,7}

In view of the interest in the fundamental properties of ZnO, it appeared warranted to obtain more complete information on the temperature dependence of the population of the paramagnetic center that gives rise to the $g \sim 1.96$ line and to discuss the implications of these results on the probable nature of the paramagnetic center.

Experimental Details

Powdered ZnO (New Jersey Zinc Co., S.P. 500) was introduced as a 1.5-cm column in a quartz tube of 3 mm i.d. The sample was evacuated (oil diffusion pump and traps in liquid nitrogen) and heated to 575°K for 30 min until the pressure was about 10^{-5} Torr. The tube was then sealed off under vacuum, and the sample was cooled by lowering the furnace. This pretreatment resulted in a symmetrical resonance with no structure.

The esr measurements were made with an X-band spectrometer (Varian V-4502) equipped with a 12-in. magnet, a Fieldial, and a dual cavity (TE₀₁₄) operated from the microwave bridge in the low-power mode.

- (1) K. M. Sancier, *Surface Sci.*, **21**, 1 (1970).
- (2) J. Schneider and A. Rauber, *Z. Naturforsch. A*, **16**, 713 (1961).
- (3) K. A. Müller and J. Schneider, *Phys. Lett.*, **4**, 288 (1963).
- (4) A. Hausmann, *Z. Phys.*, **237**, 86 (1970).
- (5) R. J. Kokes, *J. Phys. Chem.*, **66**, 99 (1962).
- (6) R. L. Kroes, A. P. Kulshreshtha, T. Mookherji, and J. D. Hayes, Paper No. 69-639, American Institute of Aeronautics and Astronautics, San Francisco, Calif., June 1969.
- (7) M. Setaka, S. Fujieda, and T. Kwan, *Bull. Chem. Soc. Jap.*, **43**, 2377 (1970).

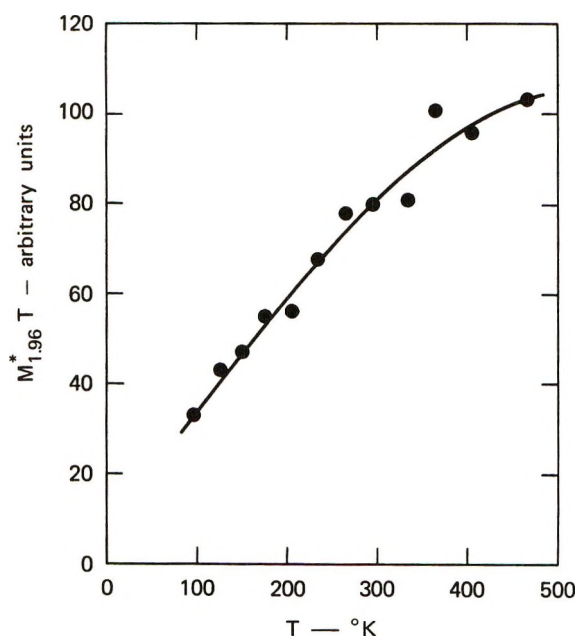


Figure 1. Temperature dependence of the parameter $M^*_{1.96}T$ for vacuum heated ZnO powder.

The ZnO sample was inserted in one cavity employing 10^5 -Hz modulation at 2.5 Oe and containing a temperature-controlled dewar (Varian). A sample of 0.1% pitch in KCl was inserted in the other cavity (at room temperature) employing 400-Hz modulation, and the peak intensity of the carbon signal I_p was used to monitor changes in cavity Q caused by the temperature effect on the electrical conductance of ZnO.

Results and Discussion

In the analysis of the temperature dependence of the $g \sim 1.96$ we evaluated the parameter $M^*_{1.96}T$ which is proportional to the number of paramagnetic centers and which assumes a Curie law dependence of magnetic susceptibility with temperature.⁸ $M^*_{1.96}$ is the first moment of the first derivative of the $g \sim 1.96$ line that has been normalized for changes in cavity Q according to $M^*_{1.96} = M_{1.96}/I_p$, where $M_{1.96}$ is the measured first moment. The experimental results are tabulated in Table I, and the temperature dependence of $M^*_{1.96}T$ is shown in Figure 1. The measurements were made starting at low temperatures and the results were reproducible within $\pm 5\%$.

The temperature dependence of $M^*_{1.96}T$ shows that the number of paramagnetic centers increased as the temperature was increased. This result contradicts the conclusions made directly and implied in earlier work.^{2,3,5-7} Part of the problem in earlier work is that compensation was not made for changes in the cavity sensitivity due to the temperature effect on the electrical conductance of ZnO. The extent of this effect can be pronounced, as indicated by the considerable change of I_p (Table I) over the temperature range studied.

Table I: Temperature Dependence of I_p , $M_{1.96}$, and $M^*_{1.96}T^a$ for Vacuum-Heated ZnO Powder

T , °K	I_p , mm	$M_{1.96}$	$M^*_{1.96}T$
97	176	59	33
127	182	62	43
149	173	55	47
176	161	50	55
206	145	39	56
233	137	40	68
263	128	38	78
296	118	32	80
332	111	27	81
363	108	30	101
403	105	25	96
470	109	24	103

$$^a M^*_{1.96} = M_{1.96}/I_p.$$

Some information on the nature of the paramagnetic center may be inferred from the results. The fact that the number of resonance centers increases with temperature indicates that the center is an ionized donor and/or the electron is the conduction band. The tendency of $M^*_{1.96}T$ to approach a limiting value at high temperatures (Figure 1) suggests that donor ionization is approaching completion, as may be expected.⁹ The two most likely ionized donors that are paramagnetic are interstitial zinc ions Zn_i^+ , and singly ionized oxygen ion vacancies. However, from the results on the temperature dependence alone, it is not possible to determine whether one of these two ionized donors or the conduction band electron gives rise to the $g \sim 1.96$ line.

Further clues about the nature of the paramagnetic center are provided by oxygen chemisorption experiments carried out by exposing vacuum-heated ZnO powder at room temperature to gaseous oxygen: (1) the electrical conductance decreases rapidly as sorbed oxygen captures conduction band electrons that are swept from the space charge region; (2) concurrently and about as rapidly, the $g \sim 1.96$ spin density decreases to about 10% of its original value;^{7,10-12} and (3) the g value of the resonance shifts from 1.957 to 1.960.¹²

To account for this rapid and large decrease of the $g \sim 1.96$ line, the paramagnetic centers can either be highly mobile species such as conduction band electrons that are swept out of the space charge region during oxygen chemisorption or donors localized at the ZnO surface where they can react directly with adsorbed oxygen. Bulk donors such as interstitial zinc or oxygen ion vacancies are ruled out because, at the temper-

(8) M. Setaka, K. M. Sancier, and T. Kwan, *J. Catal.*, **16**, 44 (1970).

(9) A. R. Hutson, *Phys. Rev.*, **108**, 222 (1957).

(10) K. M. Sancier, *J. Catal.*, **5**, 314 (1966).

(11) K. M. Sancier, *ibid.*, **9**, 331 (1967).

(12) K. M. Sancier, unpublished work.

ature of oxygen chemisorption, bulk diffusion rates of these solid state defects are too small.^{13,14} However, excess zinc may precipitate at dislocations and surface defects¹⁵ when the solubility of excess zinc in the lattice is exceeded, for example upon slow cooling after vacuum heating. For the ZnO used here (vacuum heated at 575°K), the total donor density obtained from an absolute spin intensity determination was $8 \pm 4 \times 10^{15} \text{ cm}^{-3}$. This value is not significantly different from the solubility of excess zinc at 575°K estimated to be 10^{15} cm^{-3} by extrapolation of the data of Thomas.¹³ Even if the amount of excess zinc does not exceed its solubility at 575°K, the solubility could be exceeded when the sample is cooled slowly. From Thomas' data¹³ it is estimated that the time for diffusion over a distance of 0.1μ (average ZnO particle diameter) is about 0.05 sec at 500°K and 0.5 sec at 400°K. Bulk diffusion of oxygen ion vacancies would be much too slow even at 575°K.¹⁴

The above data are consistent with the concept of two types of paramagnetic centers. One is probably due to conduction band electrons, perhaps localized as polarons. The other may be electrons in a region of highly concentrated (precipitated) zinc which is less sensitive to oxygen adsorption perhaps because of the high density of the zinc and because the activation of the electrons could be different. The shift of g value upon oxygen adsorption probably results from the substantial decrease in the intensity of the component of the resonance ($g = 1.957$) ascribed to conduction electrons while the relatively weak component ($g = 1.960$,¹ 1.963 ³) of the resonance ascribed to excess zinc becomes observable because less overlap by the $g = 1.957$ component occurs.

It is of interest to examine Hausmann's⁴ assignment of the resonance with hyperfine splitting to an F center,

i.e., oxygen ion vacancy. Such vacancies will be paramagnetic only when singly ionized. However, at sufficiently low temperatures, the vacancies will be largely un-ionized and not paramagnetic because the spins of the two electrons will be paired. His data show that the electrical conductivity of the ZnO and the anisotropic g value and line width of the resonance all exhibit unusual behavior at temperatures below 75°K. For example, the fact that the electrical conductivity was constant at temperatures below 20°K led Hausmann to conclude that a donor conduction band existed. In the case of his esr data, raising the temperature from 5 to 75°K caused the average g value to increase from 1.9552 to 1.9568 and the line width to decrease from 15 to 1.5 Oe, but from 75 to 120°K (the upper limit of his measurements) the values of these three parameters remained constant.⁴ By comparison, for our ZnO powder at 95°K the g value was 1.9578, in satisfactory agreement with Hausmann's value, and it increased linearly with temperature to 1.9600 at 550°K; in this temperature interval the line width decreased from 5.6 to 4.5 Oe. From these considerations it appears that the F-center assignment suggested by Hausmann probably applies primarily at the lowest temperatures (<75°K). At temperatures where donor ionization becomes significant, the resonance is due mainly to conduction band electrons and to excess zinc precipitated at defects.

Acknowledgment. Valuable discussions with Dr. S. Roy Morrison are gratefully acknowledged.

(13) D. G. Thomas, *J. Phys. Chem. Solids*, **9**, 31 (1958).

(14) J. W. Hoffman and I. Lauder, *Trans. Faraday Soc.*, **66**, 2346 (1970).

(15) S. R. Morrison, *J. Vac. Sci. Technol.*, **7**, 84 (1970).

Oxidation of Metal Films by Nitrous Oxide

by S. A. Isa and J. M. Saleh*

*Department of Chemistry, College of Science, University of Baghdad, Baghdad, Republic of Iraq
(Received November 5, 1971)*

Publication costs assisted by the University of Baghdad

The oxidation, by N_2O , of evaporated films of Fe, Ni, W, Pd, and Pb has been investigated in the temperature range -78 to 250° . Rapid dissociative chemisorption, which was accompanied by N_2 evolution, occurred on the first four metals at -78° . The completion of the surface layer on Fe film at -78° was followed by the formation of bulk oxide. The oxidation of Fe and Ni films by N_2O gas became extensive above 30° , but the oxidation of W film was slow and far less extensive than of the former two metals. The oxidation of Pd film was confined exclusively to the surface phase and the incorporation reaction became extremely slow even at temperatures as high as 200° . Pb film, on the other hand, did not take up N_2O irreversibly at any temperature in the range -78 to 250° . Both the activation energy (E_X) and the preexponential factor (A_X) increased as the extent of the oxidation (X) of each of the Fe, Ni, W, and Pd films increased, so that the experimental rate remained constant; a marked compensation effect existed for the oxidation processes. The effect was likely to arise from energetically heterogeneous reacting sites. The slow step of the oxidation process was assumed to be the dissociative chemisorption of N_2O . The deposition of a Pb film on a film of Fe caused a substantial decrease in the surface area of the latter film. The behavior of the resulting Pb-Fe film toward N_2O in the temperature range -78 to 100° was very similar to that of the Pb film; reaction occurred only at $T \geq 100^\circ$ and was associated with high values of both the energy of activation and the preexponential factor compared with those for the Fe film.

Introduction

There have been no previous investigations on the interaction of N_2O , at low pressures (10^{-2} – 8 nm $^{-2}$) and over the temperature range -78 to 250° , with evaporated metal films, compared with numerous investigations on bulk metals, oxides, reduced powders, and metal filaments.¹⁻⁴ The published information refers mostly to adsorption studies which were carried out at high N_2O pressures (>10 nm $^{-2}$) and elevated temperatures ($>200^\circ$). We have selected Fe, Ni, W, Pd, and Pb as typical metals upon which to investigate the initial chemisorption of N_2O and the subsequent incorporation of oxygen.

A Pb film did not react with N_2O , but a thick film of Pb deposited on a sintered Fe film was active in the temperature range -78 to $+80^\circ$.

Experimental Section

The apparatus, the preparation of metal films, and the general procedure have been described.⁵ The films were always sintered at 70° for 20 min. After degassing of the glass and the metal filaments, the rate of degassing with the reaction vessel at 400° was $<10^{-2}$ nm $^{-2}$ hr $^{-1}$. During the deposition of each film the reaction vessel was maintained open to the pumps and the pressure was always $<10^{-4}$ nm $^{-2}$. Mixtures of $N_2O + N_2$ were analyzed by condensing the former gas in a glass coldfinger which was kept at -195° .

Nitrous oxide was prepared from the reaction of hydroxylamine hydrochloride and sodium nitrite (both pure) at room temperature. The gas was passed through a trap which was maintained at -78° and

finally freed from permanent gases by condensing at -195° and pumping. New supplies of the gas were prepared frequently, and its vapor pressure at -195° , as measured by a McLeod gauge, was $\sim 10^{-2}$ nm $^{-2}$, uncorrected for thermomolecular flow. The gas was condensed at -195° and pumped before use and the doses were admitted to the reaction system through a trap which was kept at -78° . Calibration experiments showed that the gas was sufficiently stable, in the absence of the metal films, at temperatures below 250° . The surface area of each film was determined by krypton adsorption at -195° as before,⁵⁻⁷ and the monolayer adsorption was represented as V_{Kr} . The krypton was thoroughly pumped away before admission of N_2O .

Lead films were prepared by the evaporation of Pb wire (1.0 mm in diameter) from an electrically heated W coil as described before.⁶ A "two-metal" film of Pb on Fe (Pb-Fe) was prepared by the evaporation of Pb on top of a thin Fe film.⁸ This was done by using a

(1) N. N. Kavtaradze and E. A. Zelyaeva, *Dokl. Akad. Nauk SSSR*, **172**, 1133 (1967).

(2) R. M. Dell, F. S. Stone, and P. F. Tiley, *Trans. Faraday Soc.*, **49**, 201 (1953).

(3) R. P. H. Gasser and C. J. Marsay, *Surface Sci.*, **20**, 116 (1970).

(4) E. R. S. Winter, *J. Catal.*, **19**, 32 (1970).

(5) J. M. Saleh, C. Kembal, and M. W. Roberts, *Trans. Faraday Soc.*, **57**, 1771 (1961).

(6) J. M. Saleh, B. R. Wells, and M. W. Roberts, *ibid.*, **60**, 1865 (1964).

(7) J. M. Saleh, *ibid.*, **64**, 796 (1968).

(8) Y. M. Dadiza, M.Sc. Thesis, Department of Chemistry, Baghdad University, Iraq, 1971.

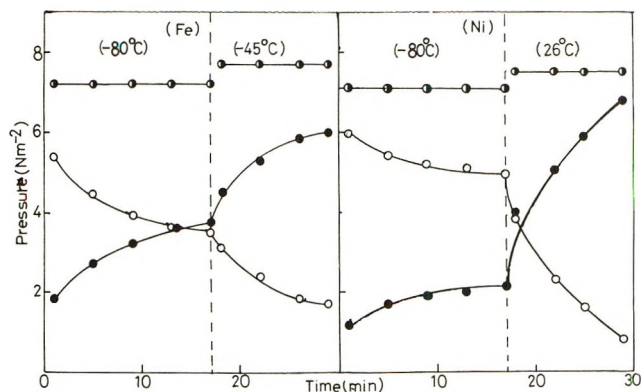


Figure 1. Interaction of N_2O with evaporated Fe and Ni films at different temperatures: (●) total pressure, (○) pressure of N_2O , (●) N_2 pressure.

special reaction vessel which carried two glass-metal seals; the Fe filament was spot-welded to one seal and the W coil, carrying the Pb wire, to the other. The area of the Fe film was measured, after sintering at 70° for 20 min, before the deposition of the Pb film. The resulting two-metal film of Pb on Fe was resintered as before prior to area measurement and the subsequent adsorption studies.

Results

The extent of N_2O chemisorption and the subsequent metal oxidation are expressed as $X = V_{N_2O}/V_{Kr}$, where V_{N_2O} is the volume of N_2O uptake and V_{Kr} is the volume of krypton required to form a monolayer on the film.

Uptake at -78° . Fast dissociative chemisorption of N_2O occurred at -78° and a gas pressure of ~ 6 nm^{-2} on films of Fe, Ni, Pd, and W until X was ~ 0.2 . This was followed by a rate process in which N_2 was evolved. On Fe and Ni films, the total pressure in each dose above $X = 0.2$ remained almost constant as the volume of N_2O adsorbed (V_{N_2O}) in a given time was equivalent to the volume of N_2 desorbed (\bar{V}_{N_2}), as indicated in Figure 1; the reaction may be represented as



where (s) and (g) refer to the solid and the gaseous states, respectively. The overall values of \bar{V}_{N_2}/V_{N_2O} on both Fe and Ni films at -78° were < 1.0 , as given in Table I, because at $X \leq 0.2$ less N_2 was desorbed than N_2O adsorbed ($\bar{V}_{N_2} < V_{N_2O}$). The rate of N_2O uptake at -78° and $P_{N_2O} = 6$ nm^{-2} became < 2.0 μl hr^{-1} cm^{-2} at $X = 2.9$ on Fe and $X = 1.4$ on Ni; the extent of N_2O adsorption at this temperature was thus more extensive on Fe than on Ni.

With the Pd film, the final value of X at -78° was only 0.75 when the rate of N_2 uptake became negligibly small (< 2.0 μl hr^{-1} cm^{-2}). The evolution of N_2 (\bar{V}_{N_2})

Table I. Adsorption of N_2O on Films of Fe, Ni, Pd, W, and Pb at -78° and a Gas Pressure of 6.0 nm^{-2} ^a

Film	V_{Kr}	V_{N_2O}	X	\bar{V}_{N_2}	\bar{V}_{N_2}/V_{N_2O}	\bar{V}_{N_2O}
Fe	41.7	120.2	2.88	113.4	0.94	
Ni	39.3	53.9	1.40	50.3	0.93	
Pd	63.6	48.0	0.75	35.0	0.72	6.3
W	58.6	65.4	1.20	37.4	0.57	6.9
Pb	3.4	2.8	0.82			2.8

^a All volumes are expressed in μl at STP. \bar{V}_{N_2O} is the volume of N_2O desorbed on warming the film to 30° .

was also less than N_2O adsorption (V_{N_2O}), as shown in Table I. Moreover, a small fraction ($\sim 10\%$) of N_2O adsorption on Pd at -78° was reversible; the same amount of N_2O was desorbed rapidly on warming the film to 30° and a similar amount of gas could be re-adsorbed on cooling back to -78° .

The maximum value of X on W film at -78° was 1.2 (Table I), but a fraction of the adsorption was molecular and reversible as with Pd film. Furthermore, the evolution of N_2 (\bar{V}_{N_2}) on W film at -78° was less extensive as compared with corresponding results on Fe, Ni, and Pd; this is shown by a comparatively low value of the ratio \bar{V}_{N_2}/V_{N_2O} in Table I for W. The adsorption of N_2O on Pb was completely reversible and the maximum value of X at -78° was only 0.82 (Table I).

Adsorption of N_2O on Oxidized Films at -78° . Molecular adsorption of N_2O took place at -78° on films of Fe, Ni, W, and Pd which had been oxidized with oxygen at 30° and $P_{O_2} = 7$ nm^{-2} . The adsorbed amount on each film could be completely removed either by pumping the reaction vessel for a few minutes at -78° or by warming the film to 30° . Table II shows the relationship of the adsorbed oxygen (V_{O_2}) to both the initial area of the film (V_{Kr}) and the volume of N_2O uptake on the oxidized film (V_{N_2O}); the last column gives the volume of N_2O which was desorbed (\bar{V}_{N_2O}) when the film was warmed to 30° . The results of Table II indicate also that the extent of N_2O adsorption on oxidized Fe and Ni films was appreciably greater than on oxidized W and Pd films. Oxygen adsorption on clean films caused a substantial decrease in the area of the films; the area after oxidation (\bar{V}_{Kr}) was considerably less than the area before oxidation (V_{Kr}), especially in the case of Fe and Ni films where the oxidation was more extensive.

Incorporation. The uptake of N_2O continued on Fe, Ni, W, and Pd films at and above 30° with complete N_2 evolution; the oxidation rate increased with temperature. The reaction became immeasurably fast on Fe and Ni films at 200° ; the total pressure was always constant owing to the desorption of one N_2 molecule for each adsorbed N_2O molecule. Under identical conditions of temperature, N_2O pressure, and value of X , the rate of oxidation by N_2O was consid-

Table II: Adsorption of N₂O on Oxidized Films of Fe, Ni, Pd, and W at -78° and P_{N₂O} = 6.0 nm⁻² ^c

Film	V _{Kr}	V _{O₂}	V _{O₂} /V _{Kr}	\bar{V}_{Kr}	V _{N₂O}	X	\bar{V}_{N_2O}
Fe	36.8	276	7.51	8.1	6.0	0.75	5.8
Ni	13.4	82	6.10	7.8	7.0	0.90	6.7
Pd	25.2	18	0.70	20.1	6.0	0.30	5.8
W	58.6	64.1	1.10	36.1	6.4	0.18	6.0

^c Volumes are expressed in μl at STP.

erably slower on the W film than on either the Fe or the Ni film. The total gas pressure increased on raising the temperature of the W film due to more N₂ evolution than N₂O adsorption, but at a constant temperature the total pressure remained constant because $V_{N_2O} = \bar{V}_{N_2}$.

The oxidation of Pd film by N₂O became extremely slow as X approached 0.75 and, thereafter, the rate increased only slightly with temperature. More N₂ desorbed than N₂O adsorbed on heating a Pd film to higher than 30°, as described for W. No reaction was possible between N₂O and Pb film at any temperature up to 250°. On the other hand, there was a slow N₂O desorption from a Pb film which had adsorbed the gas at -78° on warming to 30 and 60°.

Further slow N₂O uptake which was accompanied by N₂ evolution was observed above 30° on films of Fe, Ni, and W which had been saturated with oxygen at 30°. The constancy of the total pressure and the gradual N₂ evolution were again the characteristic of the slow oxidation. Oxidized Pd and Pb films did not tend to take up further N₂O in the temperature range 30-250°.

Kinetics of Oxidation by N₂O. By comparing the rates of N₂O uptake at two different temperatures, but essentially the same surface coverage X, activation energies E_X were determined. Figure 2 shows that E_X values increased as X increased on Fe, Ni, and W films. The relationship of E_X with X was less pronounced on Pd film because the oxidation of the metal proceeded only to a limited extent; E_X increased from 10 to 32 kJ mol⁻¹ when X increased from 0.7 to 0.82. The plot of E_X values against the reciprocal of X was always in the form of a smooth curve as indicated in Figure 2 for Fe film.

The rate of oxidation by N₂O gas depended directly on P_{N₂O} as the value of the exponent n in the expression

$$\text{rate} \propto (P_{N_2O})^n \quad (1)$$

was found from a great number of experiments to be close to unity. Furthermore, the kinetics of oxidation by N₂O was found to obey adequately a first-order equation; the plot of log P_{N₂O} vs. the time (t) was quite linear (Figure 3) over the period of decay of each of the N₂O doses at the same temperature.

From the experimental rate of N₂O dissociation at temperature T, coverage X, and the appropriate value

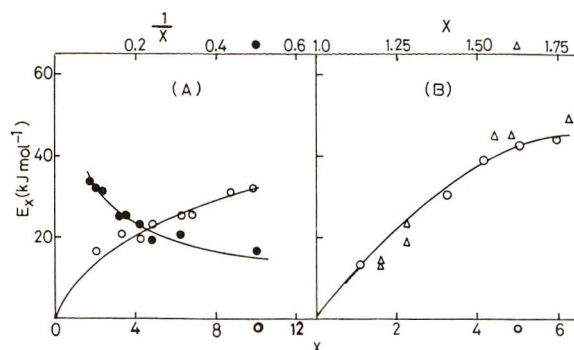


Figure 2. Activation energies (E_X) plotted against the extent of oxidation X (for Fe, Ni, and W films) and 1/X (for Fe film): (A) for Fe, (B) for Ni (O) and W (Δ) films.

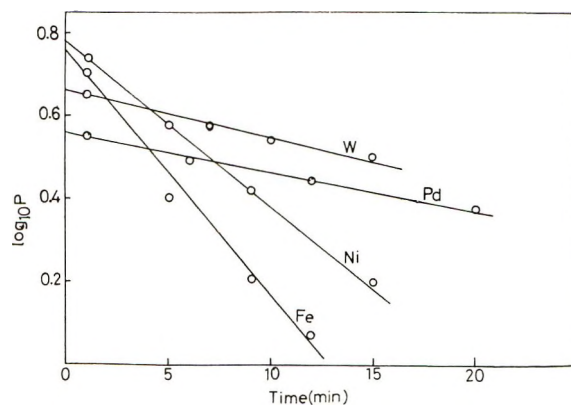


Figure 3. First-order plots for N₂O uptake on Fe (80°), Ni (26°), Pd (20°), and W (22°) films at various temperatures. P is expressed in nm⁻².

of the activation energy E_X, the value of the preexponential factor A_X in an Arrhenius-type rate equation

$$(\text{rate})_{X,T} = A_X \exp(-E_X/RT) \quad (2)$$

was determined. Table III shows that for approximately the same N₂O pressure (4-7 nm⁻²) the value of A_X increased as E_X and X increased on Fe, Ni, and W films, so that the experimental rate remained almost constant. Figure 4 indicates that a plot of log A_X against E_X was linear for Fe, Ni, and W films.

At a given value of X (X = 1.5), the corresponding values of E_X and log A_X were determined for N₂O uptake on clean films of Fe, Ni, W, and Pd and oxidized films of the former three metals, and the results are plotted as log A_X vs. E_X in Figure 5. The values of A_X and E_X for clean Pd and oxidized W films corresponded to X = 0.82 and 0.7, respectively, as higher values of X were not attainable at temperature <250°.

Uptake of N₂O on a Pb Film Which Had Been Deposited on a Film of Fe. The deposition of a Pb film on a film of Fe caused a substantial decrease in the accessible area of the latter film. In a typical experiment, a film of Fe was first deposited on the glass walls of the reaction vessel and after normal sintering process its area was estimated to be V_{Kr} = 76 μl of Kr. On subse-

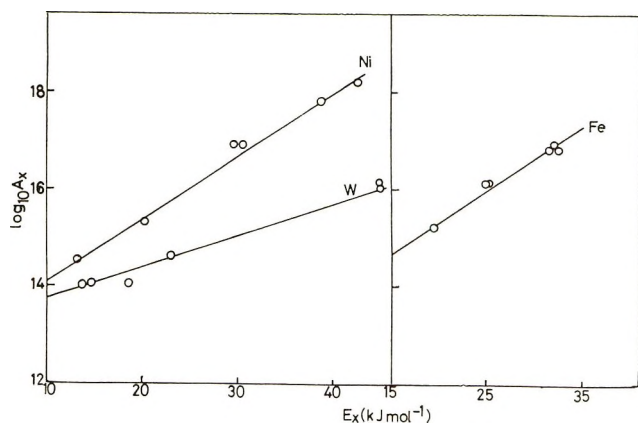


Figure 4. Compensation effect in oxidation of Fe, Ni, and W films over a range of X values corresponding to E_X values of Figure 2. A is given in molecules $\text{cm}^{-2} \text{sec}^{-1}$.

Table III: Experimental Values of Activation Energy (E_X) and Frequency Factor (A_X) at Various Values of X at $P_{\text{N}_2\text{O}} = 4\text{--}7 \text{ nm}^{-2}$ on Films of Fe, Ni, and W

Film	X	Temp, °K	Rate, molecules $\text{cm}^{-2} \text{sec}^{-1}$	E_X , J mol^{-1}	A_X , molecules $\text{cm}^{-2} \text{sec}^{-1}$
Fe	2.0	193	1.73×10^{14}	16,530	4.88×10^{14}
	4.2	273	2.90×10^{14}	19,656	1.59×10^{16}
	5.8	296	4.30×10^{14}	25,260	1.17×10^{16}
	9.8	345	9.20×10^{14}	31,940	8.27×10^{16}
Ni	1.07	193	1.0×10^{14}	13,200	2.89×10^{14}
	3.27	299	3.8×10^{14}	30,510	7.62×10^{16}
	4.17	317	2.8×10^{14}	38,700	6.16×10^{17}
	5.94	347	3.05×10^{14}	43,790	1.10×10^{18}
W	1.20	193	1.77×10^{13}	13,800	9.24×10^{13}
	1.30	295	1.56×10^{13}	23,000	5.75×10^{14}
	1.55	393	1.00×10^{13}	44,940	8.70×10^{16}

quent deposition of a thick Pb film on top of the Fe film and after resintering of the Pb-Fe film, the area \bar{V}_{Kr} decreased to only $11.2 \mu\text{l}$ of Kr. The latter area is still greater by a factor of 4 than the area of a Pb film which had been deposited on a glass substrate and subjected to the same pretreatment before area measurement. On a Pb-Fe film ($\bar{V}_{\text{Kr}} = 11.2 \mu\text{l}$), there was a rapid reversible adsorption of N_2O to the extent $X = 0.22$ at -78° and $P_{\text{N}_2\text{O}} = 6 \text{ nm}^{-2}$; the gas was completely desorbed on warming the film to 30° .

Chemisorption of N_2O on a film of Pb-Fe began clearly only at 100° . Over several hours of N_2O reaction with a Pb-Fe film at 100° , the value of X increased only to 1.3, and the only value of E_X that could be determined in the temperature range $100\text{--}200^\circ$ was 91 kJ mol^{-1} . Using the latter value of E_X and the experimental rates of N_2O uptake in the range $100\text{--}200^\circ$, values of A_X were obtained; the values were almost constant at 10^{21} molecules $\text{cm}^{-2} \text{sec}^{-1}$. The latter value is compared with $A_X = 10^{16}$ for Fe reaction with N_2O at identical values of X but at lower temperature

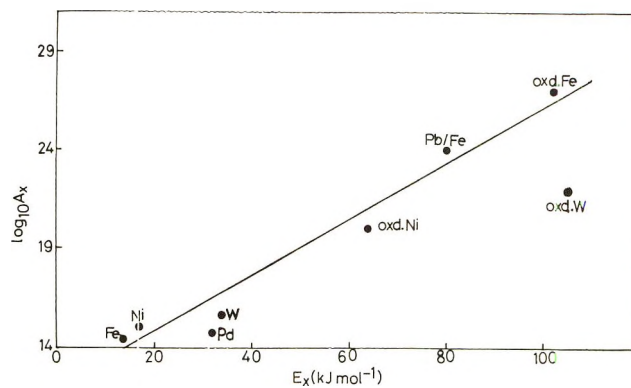


Figure 5. Compensation effect in oxidation by N_2O of various clean and oxidized metal films at constant value of X . The units of A are as in Figure 4.

(-78°). The corresponding value of A_X on oxidized Fe film (at $X = 1.3$ and $T = 116^\circ$) was 10^{24} molecules $\text{cm}^{-2} \text{sec}^{-1}$. The experimental point which represented the relationship between $\log A_X$ and E_X (at $X = 1.3$) is shown in Figure 5. No nitrogen of the adsorbed N_2O was retained by the film at any temperature.

Discussion

The evolution of N_2 as a consequence of N_2O adsorption on the four transition metals Fe, Ni, Pd, and W at -78° provides clear evidence for a dissociative chemisorption. The maximum value of $X = 2.9$ on Fe at -78° was comparatively higher than the corresponding values on Ni, Pd, and W, and this might be due to some oxygen penetration in the Fe lattice at this temperature. These results agree with the general tendency of the four metals for oxidation by gaseous oxygen at temperatures between -195 and 30° . It has been reported⁹ that at -195° around six oxide layers were formed, by gaseous oxygen, on the Fe film at a very fast rate at an oxygen pressure of $\sim 10^{-3} \text{ nm}^{-2}$. The oxidation of Ni and W films by oxygen is known to be generally less extensive than of the Fe film.¹⁰⁻¹² On the other hand, the maximum value of X on Pd at -78° was the smallest ($X = 0.75$) compared with the values for the other three metals (Table I). The low amount adsorbed on Pd indicates that the heat of adsorption must fall fairly sharply as the surface is covered, and also the activation energy for adsorption must rise with coverage. Pd film is less active than Ni and W films for oxygen adsorption; the total amount adsorbed is insufficient to saturate the surface layer of the Pd film even when the temperature is raised to 30° .⁸ The heat of adsorption of N_2O on Pb film was likely to be sufficiently low so that only physical adsorption of

(9) M. W. Roberts, *Trans. Faraday Soc.*, **56**, 128 (1960).

(10) D. Brennan, D. O. Hayward, and B. M. W. Trapnell, *Proc. Roy. Soc., Ser. A*, **256**, 81 (1960).

(11) M. W. Roberts and B. R. Wells, *Discuss. Faraday Soc.*, **No. 41**, 162 (1966).

(12) M. W. Roberts, *Quart. Rev., Chem. Soc.*, **16**, 71 (1962).

the gas was possible on the metal at -78° . This might be attributed to both the smaller work function and the lower heat of sublimation of Pb as compared with corresponding values for Fe, Ni, and W; both factors are known to contribute to the calculated heat of adsorption of a gas on a metal.^{13,14}

According to the Cabrera and Mott theory,¹⁵ the slow step in the formation of a thin oxide layer on a metal is considered to be the cation diffusion under the influence of the superimposed electric field arising from chemisorbed oxygen. The experimental evidence for the applicability of the Cabrera-Mott equation¹⁵ stems from a linear relationship between the observed activation energy (E_X) and the reciprocal of X . Now the experimental E_X in the present work was not a linear function of $1/X$, which suggests the inapplicability of the above mechanism and, hence, that the cation diffusion cannot be the slow step in N_2O dissociation and associated oxide growth. Furthermore, the pre-exponential factor (A_X) in the Cabrera-Mott equation¹⁵ is constant during oxide growth so that the theory cannot account for the observed continuous increase in A_X during oxidation by N_2O . The observed pressure dependence of close to unity together with the applicability of a first-order kinetic equation are also against the applicability of the Cabrera-Mott equation to the present systems.

The relationship observed between E_X and A_X for N_2O dissociation and subsequent metal oxidation on each of the four transition metals (Figure 4) conforms to the following equation

$$\log A_X = mE_X + C \quad (3)$$

which is referred usually to as a compensation effect. Such a relationship between E_X and A_X was frequently observed for a given reaction over a series of related metals and catalysts.¹⁶ The above equation indicates that simultaneous increases or decreases in E_X and $\log A_X$ for each system tend to compensate from the standpoint of the reaction rate. Various interpretations of the compensation effect have been offered.¹⁷⁻¹⁹ The effect may be attributed to the presence of energetically heterogeneous reacting sites;¹⁷ these probably involved the surface sites as well as those sites that were created throughout the incorporation process by the outward diffusion of the bulk atoms through the oxide layer. The dependence of A_X values on E_X conforms to a rate equation which may be represented as

$$\text{rate} = K' \exp(E_X/b) \exp(-E_X/RT) \quad (4)$$

where both K' and b are constants¹⁶ and have different values for each metal. The activation energy E_X in eq 4 appears in an exponential term in the preexponential factor $A_X = K' \exp(E_X/b)$ with opposite sign, and, accordingly, A_X increases as E_X increases. Equation 4 is based on an assumption that the oxidation takes

place first on metal sites where E_X is minimum and the reaction gradually spreads to those sites on which E_X values are higher.

The results of Figure 5 reflect a more general picture for the operation of the compensation effect in the oxidation, by N_2O , of a series of clean and oxidized metal films; the experimental points relating $\log A_X$ to E_X values at a given value of X ($X = 1.5$) lie properly on a straight line. The points corresponding to Pd and oxidized W films seem to deviate from the linear relationship in Figure 5 because of the low X values ($X < 1.0$) at which $\log A_X$ and E_X , for both metals, were determined. The fact that values of E_X and $\log A_X$ for N_2O reaction with an oxidized film (at the same N_2O uptake) are considerably higher than the corresponding values on clean film of the same metal may support the above interpretation; the reacting sites on an oxidized film of a metal should require a higher energy of activation than on the clean film. The results of Figure 5 also indicate that the nature of the oxidation process by either N_2O or O_2 should be very much the same because the results (E_X and $\log A_X$) for the N_2O reaction with both clean and oxidized films of each metal lie on the same straight line.

Uptake of N_2O by Pb-Fe Film. The surface "coating" of the Pb-Fe film in the temperature range -78 to 100° may be composed mainly of Pb atoms. In this way, the inactive behavior of the Pb-Fe film toward N_2O gas below 100° can then be ascribed to the direct exposure of the "inactive" Pb atoms to N_2O gas. Since Pb is a low-melting metal (mp 327°), there is a possibility for Pb atoms to migrate on the surface and acquire considerable mobility as the temperature of the film is raised above 100° . Such mobility probably facilitates the exposure of the underlying Fe atoms to the gas molecules. Once a thin oxide layer is formed on the surface an electric field is developed, due to the surface potential of the chemisorbed oxygen atoms,¹⁵ under the influence of which the diffusion of Fe atoms through the Pb lattice may become significant. Thus, the slow chemisorption of N_2O on the Pb-Fe film above 100° , followed by N_2 evolution, can be accounted for.

Figure 5 shows that the relationship between $\log A_X$ and E_X at $X = 1.5$ for N_2O uptake on Pb-Fe film lies far away from the corresponding point for the Fe film. This suggests that the reaction of N_2O with a Pb-Fe film is associated with a high energy of activa-

(13) B. M. W. Trapnell, "Chemisorption," Butterworths, London, 1955, p 148.

(14) D. P. Stevenson, *J. Chem. Phys.*, **23**, 203 (1955).

(15) N. Cabrera and N. F. Mott, *Rep. Progr. Phys.*, **12**, 163 (1948).

(16) G. C. Bond, "Catalysis by Metals," Academic Press, New York, N. Y., 1962, p 140.

(17) F. H. Constable, *Proc. Roy. Soc., Ser. A*, **108**, 355 (1925).

(18) E. Cremer and G. M. Schwab, *Z. Phys. Chem., Abt. A*, **144**, 243 (1929).

(19) C. Kemball, *Proc. Roy. Soc., Ser. A*, **217**, 376 (1953).

tion, in contrast to the behavior of the Fe film. This may arise from a high energy barrier that has to be surmounted by Fe atoms in diffusing from normal Fe sites, *via* interstitial positions in Fe and Pb lattices, to the surface to contact N_2O molecules. Some of Fe

atoms, probably those with low values of E_x , may be involved in the formation of a solid solution with Pb and, therefore, the sites available for reaction with N_2O are likely those which are associated with high values of E_x .

Dielectric Evidence of Two-Dimensional Condensation of Halides

Adsorbed on Nonporous Sodium Chloride¹

by G. K. Kouvarellis, R. McIntosh,* and N. S. Snider

Department of Chemistry, Queen's University, Kingston, Ontario, Canada (Received March 14, 1972)

Publication costs assisted by the National Research Council of Canada

The dielectric constant and dielectric loss of methyl, ethyl, and propyl chlorides adsorbed on finely divided sodium chloride have been determined over the frequency range 3 kHz–8 MHz and temperature range -20 to -110° . The results for the three halides are qualitatively similar. Adsorption studies suggest that two-dimensional condensation may be occurring. Dielectric dispersion and absorption have been observed and these have been found to be markedly dependent on the temperature and the volume of gas adsorbed. At constant frequency the dielectric parameters pass through large maxima with increasing surface coverage in the submonolayer region. These maxima are sensitive functions of temperature. The dielectric results for these systems appear to be analogous to those for partially miscible liquid systems near the consolute point. They are thus believed to be related to the two-dimensional condensation suggested by the form of the adsorption isotherms. An attempt has been made to explain the results qualitatively in terms of critical fluctuation theory.

Introduction

Recently, the dielectric behavior was investigated for hydrogen and ethyl chlorides adsorbed separately on a finely divided nonporous sample of sodium chloride.² The dielectric constant of adsorbed hydrogen chloride was found to pass through a sharp maximum at the monolayer surface coverage. No loss was observed. In the ethyl chloride system both the dielectric constant and the dielectric loss revealed maxima at about one-fourth monolayer coverage. It was concluded² that for certain conditions in the adsorbed state the hydrogen and ethyl chlorides behave as rotational oscillators, but that it can also be argued that strong dipole-dipole correlations give rise to the pronounced maxima. A more extensive investigation of the dielectric behavior at low surface coverage has now been carried out in an attempt to decide between these two explanations. In addition, the behavior of the adsorbates methyl and propyl chloride has been studied.

Experimental Section

A detailed description of the experimental procedure

has already been given.² The dielectric cell (volume 113.0 cm^3 and capacitance 125.0 pF) was filled with 24.72 g of the sodium chloride powder using a drybox to maintain anhydrous conditions. The volume fraction of solid was 0.1014 .

The methyl chloride (minimum purity 99.5%) and the ethyl chloride (minimum purity 99.7%) were supplied by Matheson of Canada, Ltd. The propyl chloride (minimum purity 99.5%) was supplied by the Eastman Organic Chemicals Co. Each gas was further treated by passing it twice at low pressure through a column packed with Union Carbide Type 3A molecular sieve. Thereafter, the gas was fractionally distilled several times.

Results

1. *General.* The overall dielectric constant ϵ' and dielectric loss ϵ'' of methyl, ethyl, and propyl chlorides adsorbed on finely divided sodium chloride

(1) Based on a thesis by G. K. Kouvarellis, presented in partial fulfillment of the requirements of the Ph.D. degree.

(2) T. McMullen, E. D. Crozier, and R. McIntosh, *Can. J. Chem.*, **46**, 2945 (1968).

were determined in the frequency range 3 k Hz–8 MHz and temperature range -20 to -110° . A dielectric constant ϵ_2' and a dielectric loss $-\epsilon_2''$ were assigned to the adsorbed matter by a modification^{3a} of a method^{3b,4} which has been found to yield reasonable values when applied to other adsorbate–adsorbent systems. This modified procedure assumes that spherical particles are inserts in a medium to form a composite of dielectric constant ϵ . The particles, the adsorbate, and the interstices are treated as three phases. It is further assumed that the average field within the largest phase (interstitial space) does not alter with adsorbate concentration in the composite system. The treatment yields the equation

$$\frac{3(\epsilon_2 - 1)}{4\pi(\epsilon_2 + 2)} = \frac{\frac{\epsilon - 1}{4\pi} - \frac{3\delta_1\epsilon(\epsilon_1 - 1)}{4\pi(2\epsilon + \epsilon_1)}}{\frac{\epsilon + 2}{3} - \frac{\delta_1\epsilon(\epsilon_1 + 2)}{(2\epsilon + \epsilon_1)} - \frac{\delta_3}{(1 - \delta_1)}} \times \left[\frac{\epsilon_0 + 2}{3} - \frac{(\epsilon_0 - 1)(\epsilon_1 + 2)}{3(\epsilon_1 - 1)} \right]$$

Subscripts 1, 2, and 3 refer to the solid, adsorbed, and gaseous phases, respectively. Subscript 0 refers to the sodium chloride powder without adsorbate. δ is the volume fraction of the appropriate phase. It should be pointed out that all the “ ϵ ” quantities are complex in the general case.

2. *The Adsorption Isotherms.* The adsorption isotherms for the systems, methyl chloride (at -40 , -60 , and -80°), ethyl chloride (at -50°), and propyl chloride (at -20 and -40°), are shown in Figures 1a, 1b, and 1c, respectively. The dotted lines represent the saturation vapor pressures of the bulk adsorbates. Duplicate runs were carried out (approximately 1 year apart) for the propyl chloride system at -40° (see Figure 1c) and the reproducibility of the adsorption and dielectric results was found to be good. Good agreement was also found for the adsorption and dielectric results of the present study and those determined by McMullen² for the ethyl chloride system. These facts support the view that the surface of the sodium chloride remained unchanged.

The BET multilayer plots were not linear. This is not unexpected since the BET theory considers lateral interactions between adsorbed molecules to be negligible, which is not the case when two-dimensional condensation occurs. The monolayer volumes of methyl, ethyl, and propyl chlorides were estimated directly from the adsorption isotherms by the point B method and found to be 120, 105, and 90 cc at STP, respectively. The co-areas of the methyl, ethyl, and propyl chloride molecules were evaluated by a standard procedure⁵ and were found to be 20.1, 24.8, and 29.1 \AA^2 , respectively. It was assumed that the adsorbed molecules have the same packing as the molecules of the condensed phase possess in their plane of closest packing. The

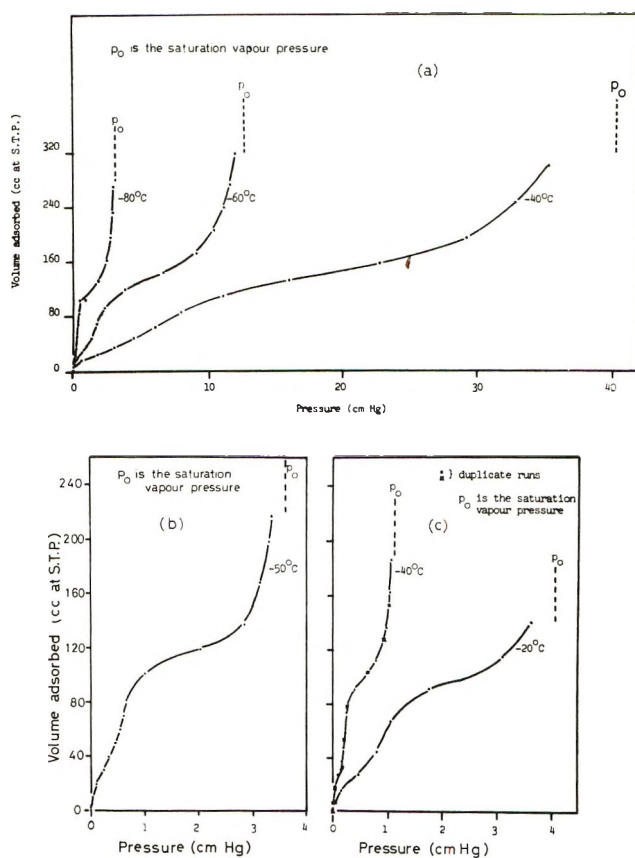


Figure 1. Adsorption isotherms: a, methyl chloride; b, ethyl chloride; c, propyl chloride.

specific surface areas of the sodium chloride powder, calculated from the above monolayer volumes and co-areas, are 26.2, 28.4, and 28.5 m^2/g , respectively. These values of the specific surface area are consistent with that of 24 m^2/g reported^{3a} using both hydrogen and ethyl chlorides.

The isosteric heats of adsorption q_{st} for methyl and propyl chlorides, shown in Figure 2 as a function of volume of gas adsorbed, were calculated from the adsorption isotherms at two temperatures using the analog of the Clausius–Clapeyron equation. The values of q_{st} are thus average values over the temperature range indicated on the graphs. The dotted lines represent the latent heats of condensation for the bulk adsorbates.

3. *The Dielectric Behavior of the Adsorbate–Adsorbent Systems.* The results obtained for the methyl, ethyl, and propyl chloride systems are qualitatively similar. Consequently, for the purpose of this discussion, graphs of the methyl chloride system are shown in the majority of cases.

(3) (a) T. McMullen and R. McIntosh, *Can. J. Chem.*, **47**, 1001 (1969); (b) E. W. Channen and R. McIntosh, *ibid.*, **33**, 172 (1955).

(4) R. McIntosh, E. K. Rideal, and J. A. Snelgrove, *Proc. Roy. Soc., Ser. A*, **208**, 292 (1951).

(5) D. M. Young and A. D. Crowell, "Physical Adsorption of Gases," Butterworths, London, 1962.

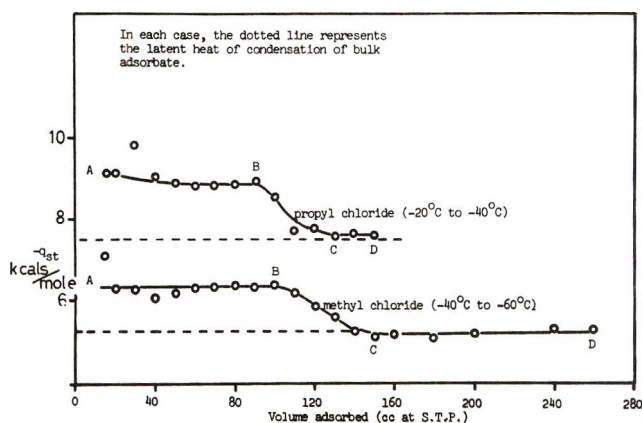


Figure 2. Isosteric heats of adsorption as a function of quantity adsorbed.

The variations of the overall dielectric constant ϵ' and dielectric loss $-\epsilon''$ of the methyl chloride system with the logarithm of frequency are shown in Figure 3 as typical primary data. The amount of gas adsorbed and the temperature are recorded on the graph. The changes of the dielectric constant ϵ_2' and dielectric loss $-\epsilon_2''$ of the adsorbed methyl chloride with the logarithm of frequency are shown in Figures 4a-e. In order to ascertain if the Debye or Maxwell-Wagner equations⁶ obtain, the $-\epsilon_2''$ values are plotted against the ϵ_2' values as in a Cole-Cole semicircular plot.⁷ It was found that the dispersion and absorption yielded approximate semicircular plots except at the lowest temperatures. An example of such a plot, using data from Figure 4b, is shown in Figure 5. A measure of the distribution of relaxation times is given by β , which may have a value between 0 and 1 and is obtained from the angle $\beta\pi/2$ formed by the base of the semicircle and the ϵ_2' axis. The semicircle which best fitted the experimental points was obtained by inspection. Because of the small changes of the dielectric parameters in the primary data, in many cases there is a large error in the value of β making it difficult to observe its variation with the volume of gas adsorbed, temperature, or adsorbate. However, it does appear that β has a value in the range 0.1-0.3.

The effect of temperature on the dispersion and absorption is illustrated in Figures 4a-c, in which the volumes of gas adsorbed are approximately constant. As the temperature is decreased, the dispersion and absorption increase markedly and also shift to lower frequency. Fröhlich⁸ has utilized a model of the dipole turning from one equilibrium position over a potential energy barrier to a second position under the influence of the field to deduce the activation energy barrier for the motion. Values of 11.0 ± 0.2 , 12.75 ± 0.2 , and 8.5 ± 0.6 kcal/mol were calculated from the slopes of the linear plots, shown in Figure 6, for the most probable potential energy barrier height H of methyl, ethyl, and propyl chlorides, respectively.

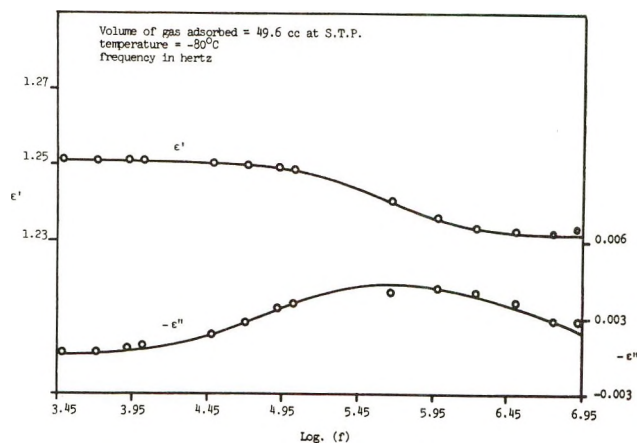


Figure 3. The overall dielectric parameters ϵ' and $-\epsilon''$ as a function of frequency for methyl chloride. Typical primary dielectric data.

The dispersion and absorption were also affected by the amount of gas adsorbed. This is illustrated in Figures 4d, b, and e for the methyl chloride system at a fixed temperature. The dispersion and absorption initially increase and shift to lower frequency with volume of gas adsorbed until some critical volume of gas has been taken up. Thereafter, the dispersion and absorption decrease and return to higher frequency with increasing volume of gas adsorbed (see Table II). The overall effect of temperature and volume of gas adsorbed is reflected in Figures 7a and 7b, which show the variation at a fixed frequency of ϵ_2' and $-\epsilon_2''$, respectively, with volume of gas adsorbed at a number of temperatures. Plots such as these which show positive temperature coefficients occur despite the fact that dispersion and absorption increase with decreasing temperature. The reason is that the maxima of these parameters shift to lower frequencies with diminished temperature. Also included for reference and shown in Figure 8 is a plot of the overall dielectric parameters ϵ' and $-\epsilon''$ at a fixed frequency and temperature against volume of gas adsorbed.

Discussion

1. *The Adsorption Isotherms.* The general shape of the adsorption isotherms, shown in Figure 1, and their variation with temperature suggest that a process akin to a gas-liquid transition is taking place on the surface. Cassel⁹ and Hill¹⁰ have compared the two-dimensional analog of the van der Waals equation with the three-dimensional expression and have shown that $T_{2c}/T_{3c} = 0.50$, where T_{2c} and T_{3c} are the two-dimen-

(6) C. P. Smyth, "Dielectric Behaviour and Structure," McGraw-Hill, New York, N. Y., 1955.

(7) K. S. Cole and R. H. Cole, *J. Chem. Phys.*, **9**, 341 (1941).

(8) H. Fröhlich, "Theory of Dielectrics: Dielectric Constant and Dielectric Loss," Clarendon Press, Oxford, 1949.

(9) H. M. Cassel, *J. Phys. Chem.*, **48**, 195 (1944).

(10) T. L. Hill, *J. Chem. Phys.*, **14**, 441 (1946).

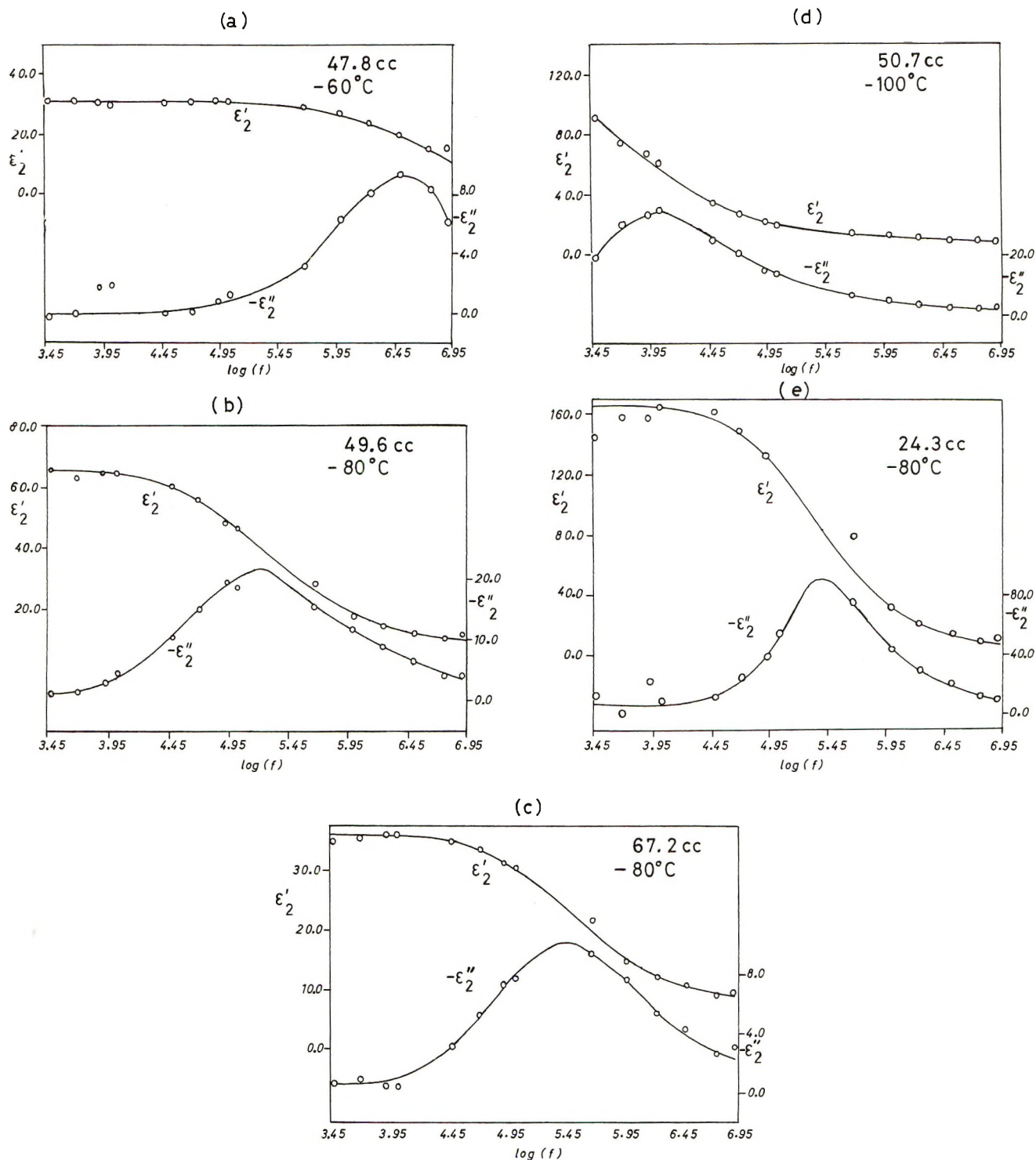


Figure 4. The effect of temperature on the dispersion and absorption of the adsorbate at approximately constant amount adsorbed (a, b, and c). Adsorbate methyl chloride. The effect of quantity adsorbed on the dispersion and absorption at fixed temperature; (b, c, e) adsorbate, methyl chloride.

sional and three-dimensional critical temperatures, respectively. Values of T_{30} for methyl, ethyl, and propyl chlorides were obtained from tables,¹¹ and the corresponding values of T_{2c} calculated by using the above expression of Cassel and Hill are -64.5 , -43.0 , and -21.5° . The experimental determination of an accurate value of T_{2c} in the present work is difficult

because of the small number of isotherms determined for each system and because of the large difference of the temperatures between isotherms. However, the fact that the adsorption isotherms were measured at

(11) "Handbook of Chemistry and Physics," 49th ed, The Chemical Rubber Co., Cleveland, Ohio, 1969.

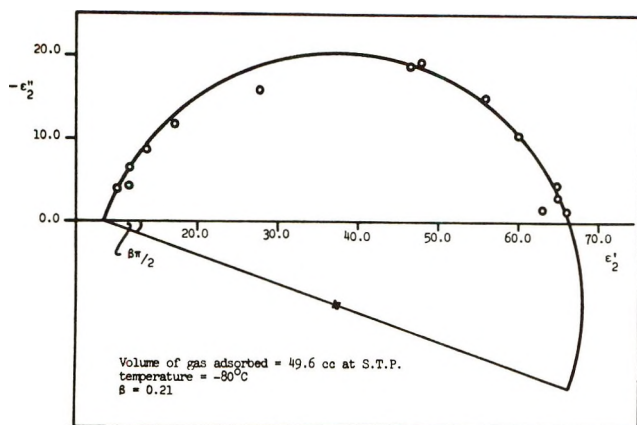
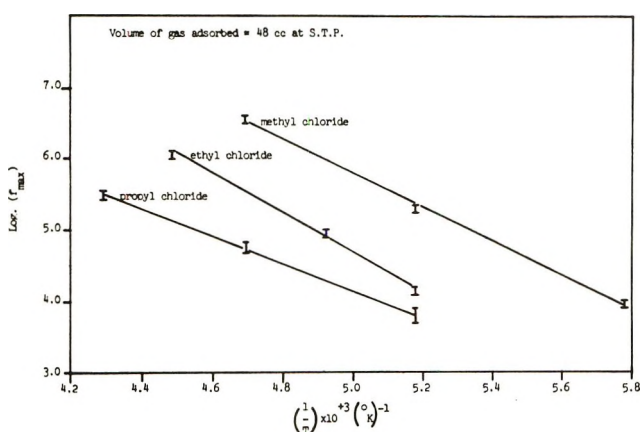


Figure 5. A Cole-Cole type of plot for methyl chloride.

Figure 6. The evaluation of the Fröhlich potential energy barrier H for the adsorbate.

temperatures in the neighborhood of the predicted values of T_{2c} supports the conclusion that two-dimensional condensation may be occurring.

It is believed that the surface of the sodium chloride powder is fairly uniform. Evidence of this is provided by the constant value of q_{st} (see Figure 2, region AB) in the submonolayer region. Also, Davis and Pierce¹² have reported that a highly uniform surface is a necessary but not a sufficient condition for the occurrence of two-dimensional condensation.

2. *The Dielectric Parameters.* Since a plot of $-\epsilon_2''$ against ϵ_2' yielded approximate semicircles (see Figure 5), it might be reasoned that the adsorbed molecules are showing Debye behavior or Maxwell-Wagner behavior, although this statement would require modification for low temperatures and high frequencies. It has been found (see Figures 4a-c) that the absorption maximum increases markedly with decreasing temperature in accordance with the Debye behavior. Furthermore, Maxwell-Wagner polarization arises only when the two phases differ from each other in dielectric constant and conductivity.⁶ The dielectric constant of the adsorbent and that of the adsorbate are of the same order of magnitude. In ref 2 there are reported

values of order $10^{-10} \text{ ohm}^{-1} \text{ cm}^{-1}$ for the conductivities of methyl and ethyl chlorides. Also, sodium chloride is considered to be loss-less. Hence, Maxwell-Wagner behavior is not expected to occur. It thus appears that the dielectric behavior observed is of the Debye type with a spectrum of relaxation times. However, it was found that for methyl and propyl chlorides the values of H were appreciably higher than that of q_{st} . An approximate value of q_{st} of 7 to 8 kcal/mol may be assigned for ethyl chloride in the submonolayer region, since its latent heat of condensation in this temperature range is about 6 kcal/mol, and on this basis H for ethyl chloride also exceeds q_{st} for that adsorbate. Therefore, the Fröhlich theory apparently does not apply to these systems. This is not surprising, since the Fröhlich treatment considers the adsorbed molecules to be independent, whereas in a system undergoing two-dimensional condensation there exist strong intermolecular interactions. Thus the dielectric behavior observed in the present study is not true Debye behavior with a spectrum of relaxation times, but resembles it. Also, the unusually large values of ϵ_2' and $-\epsilon_2''$ observed for all adsorbates under certain conditions tend to support this conclusion. To emphasize the generality of the phenomena and to demonstrate the magnitude of the maxima, representative data for four adsorbates are collected in Table I.

Table I: Approximate Values of ϵ_2' and $-\epsilon_2''$ Near the Critical Conditions for Condensation

	ϵ_2'	$-\epsilon_2''$	Frequency, kHz	Temp, °C	Amount adsorbed, cm ³ (STP)	ϵ for liquid ^a
HCl	43	3	50	-110	160	14
MeCl	165	70	50	-80	25	18
EtCl	150	89	8	-90	15	18
	55	7	30	-70	21	16
PrCl	55	3	3	-80	16	...

^a Reference 2.

Dielectric values of adsorbates of this magnitude do not appear to have been reported previously. Anomalous high values are known, however, for partially miscible binary liquid systems near the consolute temperature and composition in the single phase region. Arkhangelskii and Semchenko¹³ have reviewed much of the work done in this field since 1932. It appears that in a binary liquid system close to the critical concentration the dielectric constant and dielectric loss pass through sharp maxima at the phase separation temperature and that the heights of the maxima are greatest for systems nearest to the critical concentra-

(12) B. W. Davis and C. Pierce, *J. Phys. Chem.*, **70**, 1051 (1966).

(13) K. V. Arkhangelskii and V. K. Semchenko, *Russ. J. Phys. Chem.*, **41**, 692 (1967).

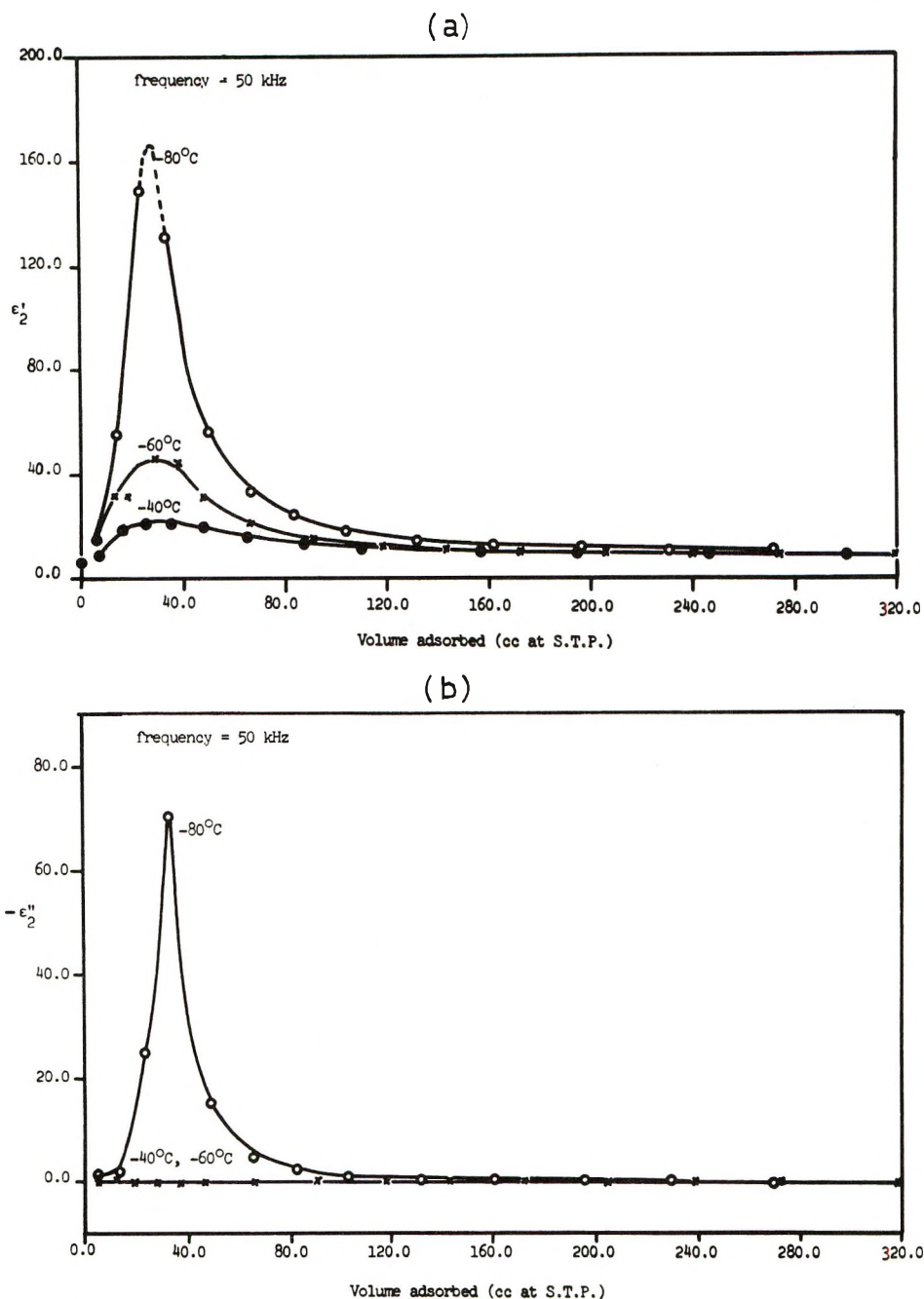


Figure 7. The effects of temperature and amount adsorbed on the dielectric parameters ϵ_2' and $-\epsilon_2''$ for methyl chloride.

tion. A similar behavior is observed for the three adsorbates since the dielectric constant and dielectric loss exhibit maxima at a specific volume of gas adsorbed as shown in Figures 7a and b, using the data for methyl chloride for illustrative purposes. The heights of these maxima increase as the temperature of the system decreases into the range where two-dimensional condensation appears to occur. As mentioned previously, this is only true if the frequency of observation lies below the frequency of maximum absorption in the temperature range considered.

Quinn and Smyth^{14,15} have studied the binary liquid system nitrobenzene-trimethylpentane over a wide

range of temperature and frequency. They observed a dielectric dispersion and absorption for the system close to the phase separation temperature, which yielded good Cole-Cole semicircular plots. It was found that the system could be characterized by a single relaxation time over most of the temperature range. At temperatures close to the phase separation temperature some broadening of the spectrum of relaxation times was observed, and the most probable relaxation time decreased slightly. In addition, the low-frequency value of ϵ'

(14) R. G. Quinn and C. P. Smyth, *J. Chem. Phys.*, **39**, 3285 (1963).

(15) R. G. Quinn and C. P. Smyth, *ibid.*, **41**, 2037 (1964).

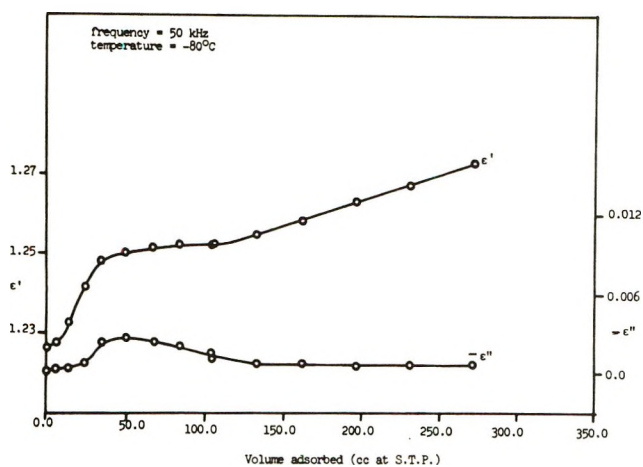


Figure 8. The overall dielectric parameters ϵ' and $-\epsilon''$ for methyl chloride as a function of amount adsorbed.

increased slightly. Whereas these effects are qualitatively similar to those we have observed for the adsorbed molecules, they are quantitatively much smaller. Nevertheless, the theory we shall propose may explain both sets of results. This theory predicts contributions to ϵ' and $-\epsilon''$ which become progressively larger (in the appropriate frequency range) as the critical point is approached. In the work of Quinn and Smyth these critical contributions probably constitute only a small part of the overall ϵ' and $-\epsilon''$ since the composition at which their measurements were made was far from the critical composition.

It should be pointed out that the two-dimensional critical temperatures T_{2c} indicated by the dielectric data appear to be lower than predicted in the early part of this discussion. This may be illustrated by referring to Figure 7a and recalling that for methyl chloride the predicted value of T_{2c} is -64.5° . However, it was not possible to determine accurate values of T_{2c} from the dielectric data. In order to do this one must observe the behavior with temperature of the low-frequency or static value of ϵ_2' at constant volume of gas adsorbed. These values may be obtained from the Cole-Cole semicircular plots. However, in the present investigation this method is unreliable at the lower temperatures since the dispersion and absorption now occur at frequencies which lie below the range of frequencies employed. It appears, however, that in all three systems the respective two-dimensional critical temperatures were reached and that the values of T_{2c}/T_{3c} lie in the range 0.40–0.46. Another factor which complicates the determination of an accurate value of T_{2c} is the large degree of scatter in the values of ϵ_2' and $-\epsilon_2''$ which exists at low temperatures in the neighborhood of T_{2c} . The values of T_{2c}/T_{3c} reported above are lower than the theoretical value of 0.50 discussed earlier, but are consistent with the experimental findings for similar systems.⁵ For example, values of 0.43, 0.47, 0.46, and 0.36 have been reported

for the adsorption of ethane, methane, diborane, and xenon, respectively, on sodium chloride.

3. *Interpretation in Terms of Critical Fluctuation Theory.* From a study of the viscosity,¹⁶ the specific heat,¹⁷ and the static dielectric constant¹⁸ of binary liquid mixtures near the critical temperature, Semenchko and his associates have concluded that the primary process of formation of a dispersed system is of the growth of microheterogeneous regions. Under any conditions there is microheterogeneity on a sufficiently small scale. As the critical point is approached the size of regions of microheterogeneity increases. Critical microheterogeneity can be thought of in terms of fluctuations of quantities associated with semimicroscopic volume elements of the system. Because refractive index may be a fluctuating quantity, a system near its liquid-liquid critical point usually scatters light strongly (critical opalescence). Semenchko^{19,20} has explained the occurrence of the maximum in the value of the dielectric constant on the basis of the Gibbs criteria²¹ for the existence of critical phases. The treatment has been extended²² to include the general case of a time-dependent electrical field. It is worth mentioning that the treatment of ref 22 predicts the occurrence of a maximum in the value of ϵ'_∞ at the critical temperature for a binary liquid system near the critical concentration. This phenomenon has not been observed. In the present study it has been found that, at frequencies much greater than the frequency of maximum absorption, ϵ_2' and $-\epsilon_2''$ do not pass through maxima with volume of gas adsorbed.

Recently,²³ the theory of critical fluctuations has been employed in an attempt to elucidate the singular behavior of the static dielectric constant described above for partially miscible liquids. The treatment is similar to existing theoretical treatments²⁴ of the specific heat singularity. A critical contribution to the static dielectric constant arises from the response to an electric field of composition fluctuations in semimicroscopic volume elements of the liquid. This contribution was found to depend on the correlation length and on the second derivative of the logarithm of the osmotic compressibility with respect to the

(16) V. K. Semenchko and E. L. Zorina, *Dokl. Akad. Nauk SSSR*, **80**, 903 (1951); National Research Council Technical Translation TT298.

(17) V. K. Semenchko and V. P. Skripov, *Zh. Fiz. Khim.*, **25**, 362 (1951); National Research Council Technical Translation TT243.

(18) V. K. Semenchko and M. Azimov, *Zh. Fiz. Khim.*, **30**, 2228 (1956).

(19) V. K. Semenchko, *ibid.*, **25**, 121 (1951).

(20) V. K. Semenchko, *Dokl. Akad. Nauk SSSR*, **99**, 1045 (1954).

(21) J. A. V. Butler, "In Commentary of the Scientific Writings of J. Willard Gibbs," Vol. I, Yale University Press, 1936.

(22) B. D. Ripley and R. L. McIntosh, *Can. J. Chem.*, **39**, 526 (1961).

(23) N. S. Snider, *J. Chem. Phys.*, **55**, 3994 (1971).

(24) L. Mistura and D. Sette, *ibid.*, **49**, 1419 (1968).

electric field. The theory has been extended²⁵ to the case of nonzero frequency in a similar fashion to the way in which the specific heat theory was extended to treat the anomalous absorption and dispersion of sound near a critical point.²⁶⁻²⁹ The extended theory predicts critical dielectric absorption and dispersion arising from a coupling of molecular rotation to diffusion. The critical composition fluctuations produce semimicroscopic dipole moments which respond to the periodic electric field. This response manifests itself as diffusion, and the characteristic time of the response is ω_D^{-1} where ω_D is defined below. The critical contributions ϵ'_D and $-\epsilon''_D$ to the real and imaginary parts of the complex dielectric constant $\epsilon^*(\omega)$, arising from the critical composition fluctuations, were found to be functions of a reduced angular frequency ω^* given by

$$\omega^* = \omega/\omega_D$$

$$\omega_D = D/L^2$$

where D is the mass diffusion coefficient and L is the correlation length.

The phase transition apparently undergone by the adsorbates studied is a two-dimensional liquid-vapor transition. The theory of ref 23 and 25 is therefore not immediately applicable, but it can be adapted to apply to the liquid-vapor critical region. One proceeds as in ref 28 and 29. The resulting theory of dielectric behavior near a liquid-vapor critical point differs from the corresponding theory for the liquid-liquid critical region in two important ways: the osmotic compressibility is replaced by the bulk compressibility and $\omega_D L^2$ is no longer D but rather $\lambda/\rho C_p$ where λ is the thermal conductivity, ρ is the mass density, and C_p is the heat capacity per unit mass at constant pressure. The dielectric loss is now assumed to be due to heat flow arising from perturbation of critical density fluctuations by the field. In that part of the critical region which is easily accessible experimentally, $\omega_D/2\pi$ is approximately 0.1 MHz. By analogy with critical ultrasonic absorption and dispersion, the dielectric dispersion and absorption curves are expected to resemble the Debye curves for a system having a spectrum of relaxation times. This appears to be borne out by experiment.^{14,25} The distribution of relaxation times is expected to be asymmetric. The theory predicts that the dispersion and absorption shift to zero frequency as the critical point is approached.²⁵

The theory of critical fluctuations has not yet been applied to an adsorbate-adsorbent system exhibiting two-dimensional condensation. We shall proceed on the assumption that this theory, as summarized above, is applicable to the adsorbate system. The observed maxima in ϵ'_2 and $-\epsilon''_2$ would then be explained as arising from large critical contributions, and the maxima would be expected to occur roughly at the critical volume adsorbed. The theoretical prediction of this

critical volume of gas adsorbed for a mobile monolayer is approximately $1/3$ of the monolayer volume.⁵ Thus for the methyl, ethyl, and propyl chloride systems the respective critical volumes of gas at STP adsorbed are 40, 35, and 30 cm³, and the corresponding volumes at which the maxima in ϵ'_2 and $-\epsilon''_2$ occur are approximately 38, 31, and 25 cm³. The agreement is considered satisfactory.

Furthermore we expect that the adsorbate will exhibit dispersion and absorption in the critical region and at a relatively low frequency. Hence at frequencies much greater than this characteristic frequency the critical contributions to ϵ'_2 and $-\epsilon''_2$ are no longer present. This accounts for the absence of maxima in ϵ'_2 and $-\epsilon''_2$ with volume of gas adsorbed in certain instances at high frequencies and low temperatures. However, in such a case the normal orientational polarization of the adsorbate is still present. It has been found that the value of ϵ'_2 and its temperature coefficient are considerably less than those for bulk matter. For example, for the methyl chloride system, the observed value of ϵ'_2 is approximately 10, which changes very little with temperature. On the other hand, the dielectric constant of liquid methyl chloride increases from a value of 14 to a value of 18 for a change in temperature -40 to -80° .³⁰ A low value of the orientational polarization and a negligible temperature coefficient are two of the main characteristics of the rotational oscillator model proposed by Kurbatov and others^{31,32} for an adsorbate molecule. Such a system is expected to exhibit resonance absorption at frequencies much greater than those employed here. Consequently, the expected resonance absorption could not be observed. Nevertheless, it is believed that the adsorbed molecules are behaving as rotational oscillators at all volumes of gas adsorbed. This conclusion is consistent with that stated in ref 2 for the hydrogen and ethyl chloride systems. McMullen, *et al.*,² and the present study support the theoretical prediction³² that polar molecules resembling hydrogen chloride adsorbed on a sodium chloride {100} surface would perform rotational oscillations.

In the present system the observed dispersion and absorption curves resemble the Debye curves for a system having a spectrum of relaxation times. This result is predicted by the theory. The theory also predicts the distribution of relaxation times to be asymmetric, the predicted asymmetry being such as to

(25) N. S. Snider, *J. Chem. Phys.*, **56**, 233 (1972).

(26) M. Fixman, *ibid.*, **36**, 1957 (1962).

(27) M. Fixman, *ibid.*, **36**, 1961 (1962).

(28) W. Botch and M. Fixman, *ibid.*, **42**, 196 (1965).

(29) W. Botch and M. Fixman, *ibid.*, **42**, 199 (1965).

(30) E. D. Crozier, Ph.D. Thesis, Queen's University, 1965.

(31) L. N. Kurbatov, *Russ. J. Phys. Chem.*, **24**, 899 (1950).

(32) G. C. Benson, E. W. Channen, and R. L. McIntosh, *J. Colloid Sci.*, **11**, 593 (1956).

Table II: Frequency of Maximum Absorption Methyl Chloride at -100°

Vol of gas ads, cm ³ (STP)	Frequency, kHz	Max value of $-\epsilon_D''$
13.6	178	77
24.3	25	127
35.2	<3	340 (approx)
50.7	10	34
68.7	30	13
86.3	35	8

produce a relatively slow decrease in ϵ_D' and $-\epsilon_D''$ at high frequencies. Some indication of this effect is provided by the data (see Figures 4b, d, e). This is

reflected in the Cole-Cole plots at low temperatures where good fits to semicircles are not obtained in the region of low ϵ_2' . Finally the theory predicts that the dispersion and absorption found for the adsorbate will shift to zero frequency as the two-dimensional critical point is approached. The observed effect of temperature and volume of gas adsorbed on the dispersion and absorption in the region of the two-dimensional critical point (see Table II) is at least qualitatively in accord with this prediction. We conclude that the critical fluctuation theory provides a satisfactory explanation of the results obtained in the present study.

Acknowledgment. Grateful acknowledgment is made to the National Research Council of Canada for financial support of this investigation.

Diffusion-Controlled Condensation and Evaporation in Wedge-Shaped Pores

by Jean-Yves Parlange¹

CSIRO Division of Environmental Mechanics, Canberra, Australia (Received February 4, 1972)

Publication costs assisted by CSIRO, Australia

A theoretical study of condensation and evaporation of a liquid in a wedge is presented. The theory applies for any initial condition and wedge angle as long as molecular diffusion in the vapor phase is the controlling physical process. The results depend primarily on one physical parameter only, when the variables are expressed in a properly reduced form. The theory should be useful whenever moisture movement in a porous medium occurs in the vapor phase.

At very low water content, moisture movement in a porous medium occurs in the vapor phase. This phenomenon has received increasing attention in the past 20 years as it is of considerable importance in a variety of fields, ranging from soil physics^{2a} to the drying of food.^{2b} Even when moisture moves in vapor form, virtually all water present in the porous medium is in the liquid form. A basic process entering the phenomenon is then the phase change of water and the diffusion of water vapor to and from the interface. Often this diffusion process takes place very rapidly, compared with some characteristic macroscopic time, and it is appropriate to assume that there is thermodynamic equilibrium between the liquid and vapor phase.^{2,3} However, even when equilibrium is indeed a correct assumption it is important to estimate the relaxation time necessary to bring equilibrium and justify *a priori* the validity of the assumption.

When very little water is present between the grains of the porous medium, one principal radius of curvature (x) of the interface is very small compared with

the grain size and the other principal radius of curvature. It is then possible to reduce the problem to a two-dimensional one and replace two adjacent grains by a wedge with apical angle 2α ($0 < \alpha < \pi/2$). If x is in turn large compared with the mean free path in the vapor phase, macroscopic equations can be used to describe the physical process. In general both molecular diffusion of water vapor and heat conduction have to be considered. For simplicity, it is assumed in the following that the process is isothermal and that diffusion alone is important. This is the case when conduction in the walls of the wedge or in the vapor phase is sufficiently rapid compared with the diffusion process. The present problem was considered earlier by Philip⁴ for

(1) On leave from Yale University and the Connecticut Agricultural Experiment Station, New Haven, Conn.

(2) (a) J. R. Philip and D. A. de Vries, *Trans. Amer. Geophys. Un.*, **38**, 222 (1957); (b) B. Makower, *Advan. Chem. Ser.*, No. 3, 37 (1950).

(3) C. W. Rose, *Aust. J. Soil Res.*, **6**, 31, 45 (1958).

(4) J. R. Philip, *J. Chem. Phys.*, **41**, 911 (1964).

the case of condensation in an initially dry wedge, using an approximate method. The problem is now solved using a more rigorous approach and the solution extended to include drying (evaporation) as well as condensation in a wedge, not necessarily dry initially. The governing equations were given by Philip⁴ and, following his notations

$$\partial h / \partial t = D \nabla^2 h \quad (1)$$

$$t = 0; \quad h = h_0 \quad (2)$$

$$t > 0; \quad h = h^*(t) \text{ at the interface} \quad (3)$$

$$t > 0, \text{ zero flux at the walls of the wedge} \quad (4)$$

In these equations h is the relative humidity in the gas phase, D is the molecular diffusivity of water vapor in air, t is the time, h_0 is a given constant less than or equal to 1, and h^* satisfies⁴

$$h^* = \exp(-\sigma / \rho^* R T x) \quad (5)$$

We call x_0 the value of x for $h^* = h_0$, R is the gas constant per gram of vapor, T is the absolute temperature, σ is the surface tension, and ρ^* is the density of the condensate. The interface is a circular cylinder of radius x which varies with time, assuming, for instance, that the condensate wets the wedge. Assume also that the change in the amount of liquid is only caused by the flux of water Q , across the interface, Q being given per unit wedge angle and unit wedge length. Then⁴

$$Q = \beta^2 \rho^* x dx / dt \quad (6)$$

with

$$\beta^2 = [(\alpha + \cot \alpha - \pi/2) / \alpha] \quad (7)$$

The time scale τ which characterizes the change in the amount of liquid is

$$\tau \approx \rho^* x^2 / \rho_1 D \quad (8)$$

where ρ_1 is the gas density and by definition

$$\rho^* \gg \rho_1 \quad (9)$$

On that time scale $\partial h / \partial t$ in eq 1 is negligible at distances from the interface of order $x(t)$. This simplification is well known in three-dimensional problems as the quasi-steady approximation^{5,6} and it has been fully justified elsewhere.^{7,8} For two-dimensional problems and at distances larger than $x(t)$ the time derivative cannot be neglected in the equation, but the diffusion problem is radial in that region. Philip⁴ simplified the problem further by replacing the interface by a circular arc centered at the apex of the wedge. The radius of the arc, r^* , is chosen so that the amount of liquid remains unchanged, or

$$r^* = \beta x \quad (10)$$

This transformation permits the treatment of cases for which inequality 9 does not hold. It is quite intuitive

that Philip's transformation is correct when $\alpha \approx 0$ but becomes less precise as α increases. For instance as $\alpha \rightarrow \pi/2$, the transformation replaces an interface of finite area by one that has a zero area. Clearly Philip's method must yield a flux Q smaller than the actual flux, as α increases.

In the neighborhood of the interface, the problem is quasisteady and the solution satisfies

$$\nabla^2 h = 0 \quad (11)$$

It is possible to solve the problem by conformal mapping. Call z the complex variable of the original physical plane and Z the transformed variable. Consider the transformation

$$Z = z^{\pi/2\alpha} \quad (12)$$

which replaces the wedge by a straight line, $A'A$ (see Figure 1). The interface is replaced by the curved line ACA' . We solve Laplace's equation replacing the true interface ACA' by the segment AOA' . The substitution is, of course, exact when $\alpha \approx \pi/2$ and approximate for smaller α . The error can be easily estimated by comparing the lengths of AOA' and ACA' . In the case $\alpha \approx 0$, when the approximation is less precise, the

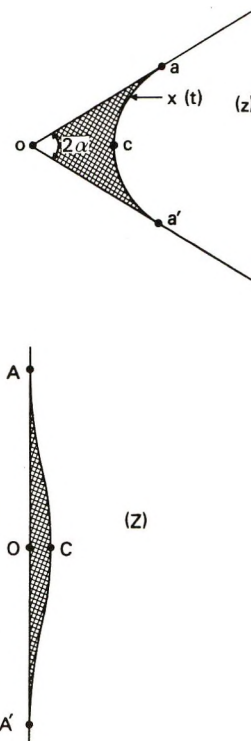


Figure 1. Transformation of the wedge aOa' , from the original space (z) to a segment AOA' in the space (Z), by conformal mapping.

(5) N. A. Fuchs, "Evaporation and Droplet Growth in Gaseous Media," Pergamon Press, New York N. Y., 1959.

(6) D. E. Rosner, *J. Phys. Chem.*, **73**, 382 (1969).

(7) J. R. Philip, *J. Atm. Sci.*, **22**, 196 (1965).

(8) J.-Y. Parlange, submitted to *J. Atm. Sci.*

error is about 3%. Hence it is expected that the present method will yield rates that are only very slightly below the actual rates. The small error decreases further as α increases and it will be checked later that the present method and Philip's method yield identical results as $\alpha \approx 0$. The solution of Laplace's equation with $h = h^*$ on AOA' is trivial and

$$h - h^* = [2\alpha Q / \rho_1 D \pi] \times [\ln |2\zeta| - (\pi/2\alpha) \ln (x/tg\alpha)] \quad (13)$$

with

$$\zeta + (x/tg\alpha)^{\pi/\alpha} / (4\zeta) = iz^{\pi/2\alpha} \quad (14)$$

This form of the solution applies near the interface; far from the interface the problem is radial and the solution is of the form⁴

$$(h - h^*) / (h_0 - h^*) = 1 + \lambda E_i(-\eta^2) \quad (15)$$

where E_i is the exponential integral and the similarity variable is given by

$$\eta = r / (4Dt)^{1/2} \quad (16)$$

The value of λ has to be found by equating the limits of the expression in eq 13 as $|\zeta| \rightarrow \infty$ and of the expression in eq 15 as $\eta \rightarrow 0$. We find at once

$$\lambda = Q / [2\rho_1 D (h_0 - h^*)] \quad (17)$$

and

$$2\rho_1 D Q^{-1} (h_0 - h^*) - (4\alpha/\pi) \ln 2 + \gamma - \ln 4Dt + 2 \ln (x/tg\alpha) = 0 \quad (18)$$

where γ is Euler's constant. In order to get $x(t)$ and solve the problem entirely, Q must be replaced in this equation in terms of dx/dt from eq 6 and h^* in terms of x from eq 5. The resulting differential equation has to be solved with a boundary condition, for instance the value of $x(t) = x(0)$ at $t = 0$. Of some interest is the value of $Q(t)$; when $x(0) = t = 0$, we obtain

$$Q(0) = 2h_0\rho_1 D / \{ (4\alpha/\pi) \ln 2 - \gamma + 2 \ln (\beta tg\alpha) - \ln [Q(0)/2D\rho^*] \} \quad (19)$$

It can be checked at once that, as expected, $Q(0)$ reduces to Philip's result⁴ when $\alpha \approx 0$ and is larger as α increases. The interest of eq 19 is more theoretical than practical since it applies when $h^* \approx 0$ or from eq 5

$$x \ll \sigma / \rho^* RT \quad (20)$$

Inequality 20 holds when x is less than 1 Å, but for those values of x the present macroscopic approach has little meaning. In fact the theory is appropriate when

$$x \gg \sigma / \rho^* RT \quad (21)$$

When this inequality applies, the problem is greatly simplified and $x(t)$ can be found analytically. Equation 18 becomes

$$\frac{dx}{dt} \approx \frac{2\sigma\rho_1 D (1/x - 1/x_0)}{\rho^* RT \beta^2 \ln ((4Dt)tg^2\alpha/x^2)} \quad (22)$$

Remembering that by definition of the quasisteady approximation $4Dt \gg x^2$, the integration of eq 22 yields

$$\frac{2\sigma\rho_1 Dt}{\rho^* RT \beta^2 X_0^3 \ln ((4Dt)tg^2\alpha/x^2)} = \frac{x(0) - x}{x_0} + \frac{1}{2} \left\{ \left[\frac{x(0)}{x_0} \right]^2 - \left[\frac{x}{x_0} \right]^2 \right\} - \ln \left[\frac{x_0 - x}{x_0 - x(0)} \right] \quad (23)$$

Equation 23 agrees very well with results of numerical integration obtained by Philip⁴ for $\alpha = \pi/12$ and $x(0) = 0$. The curve $x(t)$ given by eq 23 is asymptotic to $x = x_0$ as $t \rightarrow \infty$ and to the curve representing the growth law for $h_0 = 1$

$$\frac{6\sigma\rho_1 Dt}{\rho^* RT \beta^2} = [x^3 - x(0)^3] \ln ((4Dt)tg^2\alpha/x^2) \quad (24)$$

when $x \ll x_0$ (for the case of condensation). For the case of evaporation the second asymptote is obtained for $x \gg x_0$ or

$$\frac{4\sigma\rho_1 Dt}{\rho^* RT x_0 \beta^2} = -[x^2 - x(0)^2] \ln ((4Dt)tg^2\alpha/x^2) \quad (25)$$

Actually it is sufficient for all practical purposes to replace eq 23 by either eq 24 or 25 until equilibrium is reached. In particular those two equations give an estimate of the time necessary to reach equilibrium simply replacing x by x_0 in eq 24 for condensation and in eq 25 for evaporation. For instance, if $\alpha \approx \pi/12$ and $x_0 \approx 10 \mu$ or more, the relaxation time given by eq 24 is of the order of 1 hr or more. If the characteristic macroscopic time of interest is much longer, then thermodynamic equilibrium can be assumed; otherwise the nonequilibrium physical process studied here has to be taken into account. Equation 24 indicates that the time necessary to fill the wedge with water is essentially proportional to x_0^3 as soon as $x(0)$ is not too close to x_0 . The drying time given by eq 25 shows a different behavior. As soon as x_0 is slightly less than $x(0)$, the relaxation time given by eq 25 is proportional to $x_0 \cdot x^2(0)$; *i.e.*, it increases with the volume of water to be removed and decreases with x_0 , when the outside air is dryer. These results are qualitatively obvious but it would be incorrect to conclude that $t \rightarrow 0$ as $x_0 \rightarrow 0$ in the case of drying. Equation 25 was derived assuming that $x_0 \gg \sigma / \rho^* RT$. In fact, it is elementary to show from eq 18 that the shortest drying time is obtained for $h_0 = 0$. This limiting drying time is still given qualitatively by eq 25, where x_0 is replaced by $\sigma / \rho^* RT$.

Equation 23 indicates the dependence of growth and evaporation on the physical parameters entering the problem. By a proper choice of variables it is possible to obtain a very simple representation of condensation and evaporation which depends practically on the value

of $x(0)/x_0$ alone. In the case of growth, x/x_0 is an appropriate independent variable, since most of the growth occurs when x is of the order of x_0 . For instance, 75% of the growth takes place for $x/x_0 > 0.5$. We choose for dependent variable the quantity

$$z = 2\sigma\rho_1Dt / [\rho^{*2}RT\beta^2x_0x^2(\gamma + \ln \gamma)] \quad (26)$$

where γ is the parameter

$$\gamma = \ln [2\rho^{*2}RT\beta^2t^2\alpha x_0/\sigma\rho_1] \quad (27)$$

Equation 23 yields

$$z / \{ 1 + (\gamma + \ln \gamma)^{-1} \ln [z(1 + \gamma^{-1} \ln \gamma)] \} = \left(\frac{x_0}{x} \right)^2 \left\{ \frac{x(0) - x}{x_0} + \frac{1}{2} \left[\frac{x(0)}{x_0} \right]^2 - \frac{1}{2} \left[\frac{x}{x_0} \right]^2 - \ln \left[\frac{x_0 - x}{x_0 - x(0)} \right] \right\} \quad (28)$$

The reason for the choice of the dependent variable is that in practice γ is of order 10 or more and z is of order 1. Hence the left-hand side of eq 28 is almost equal to z . In that case the asymptotic equation for $\gamma \rightarrow \infty$

$$z = \left(\frac{x_0}{x} \right)^2 \left\{ \frac{x(0) - x}{x_0} + \frac{1}{2} \left[\frac{x(0)}{x_0} \right]^2 - \frac{1}{2} \left[\frac{x}{x_0} \right]^2 - \ln \left[\frac{x_0 - x}{x_0 - x(0)} \right] \right\} \quad (29)$$

is a good approximation of eq 28 for finite but large γ 's. We note that in eq 28, z as a function of x/x_0 depends only on the two parameters γ and $x(0)/x_0$, and in eq 29 $x(0)/x_0$ is the only parameter left. Figure 2 gives z as a function of x/x_0 for various $x(0)/x_0 < 1$, i.e., in the case of growth. The solid lines correspond to $\gamma \gg 1$, i.e., eq 29. The dotted lines correspond to $\gamma = 13$ in eq 28. As expected the dotted and solid lines are so close that in practice the solid lines could be used, as long as γ is not much smaller than 13. This particular value of γ is obtained for water at 20°, $\alpha \simeq \pi/12$, and a relative humidity h_0 of 1%. In practice h_0 might be very close to 1, particularly for growth.⁴ In that case γ could be much larger than 13 and the solid lines be even more appropriate. Once $x(0)/x_0$ is given, the proper trajectory for growth is chosen among the curves in Figure 2, taking into account the value of γ if necessary. Then at any x/x_0 the corresponding z is read. From the knowledge of all the physical parameters entering eq 26 the time is then easily deduced.

Figure 3 gives a similar plot in the case of evaporation, and similar remarks can be made. The only difference is that we chose $x/x(0)$ as the independent variable rather than x/x_0 . This choice is physically more appropriate here since most of the evaporation takes place when $x/x(0)$ is of the order of 1, whatever the value of x_0 is.

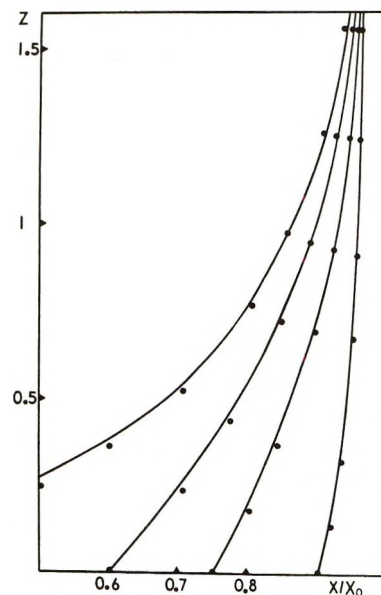


Figure 2. Case of condensation. Representation of z as a function of x/x_0 for four different values of $x(0)/x_0$ (0, 0.6, 0.75, 0.9). The solid lines correspond to eq 29 and the dotted lines to eq 28 with $\gamma = 13$.

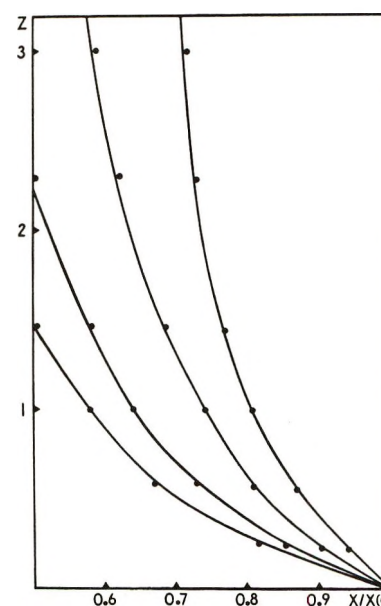


Figure 3. Case of evaporation. Representation of z as a function of $x/x(0)$ for four different values of $x_0/x(0)$ (0, 0.25, 0.5, $2/3$). The solid lines correspond to eq 29 and the dotted lines to eq 28 with $\gamma = 13$.

In order to apply the previous results, the value of α must be given. The value of α was assumed to be constant for convenience. Clearly there is no special difficulty in integrating eq 22 for varying α as long as it is a known function of x . For instance if the grains of the porous medium are roughly spheres of radius R , then for small α

$$2x\beta^2 \approx R \quad (30)$$

Integration of eq 22 can now be carried out for that particular case with no difficulty, and results similar to the previous ones are obtained. For instance, the drying time is still given qualitatively by eq 25, replacing $x_0\beta^2$ by $R/2$. This again shows that the drying time for $x(0)$ greater than $10\ \mu$ is of the order of a few hours. The drying of lyophilized food products^{2b,9} also takes place in a few hours and may well correspond to the case discussed here. On the contrary, the drying of nonlyophilized products is much slower^{2b,9} and the controlling factor is clearly the very slow transport of liquid water from the core to the surface of the sample.

In conclusion, the present study justifies Philip's theory of condensation in sharp wedges initially dry. The theory is then generalized to condensation and evaporation in any wedge under arbitrary initial conditions. The results are of importance whenever moisture movement in a porous medium occurs in the vapor phase.

Acknowledgment. The author is grateful to Dr. J. R. Philip for many helpful discussions.

(9) B. Makower and E. Nielsen, *Anal. Chem.*, **20**, 856 (1948).

Surface Charge Development on Porous Silica in Aqueous Solution

by R. P. Abendroth

Corporate Research Laboratories, Owens-Illinois Technical Center, Toledo, Ohio 43661 (Received March 22, 1972)

Publication costs assisted by Owens-Illinois, Incorporated

Charge densities on three porous silicas of varying pore parameters suspended in aqueous solution were determined by potentiometric titration. Comparison with results obtained on nonporous silica showed that the porous silica charge densities were less, and the deviations were a function of pore size, electrolyte ionic strength, and pH. The extent of diminution of the porous silica charge densities could be qualitatively accounted for by consideration of diffuse layer interactions in the pores.

In this study, surface charge density determinations were made on porous silicas of varying pore sizes to determine whether the presence of porosity significantly alters the behavior of these silicas in aqueous solutions.

Comparison with results obtained in a previous study¹ on nonporous silica (Cab-O-Sil) showed the porous silica surface charge densities to be less. The extent of the deviations appeared to be a function of pore size, electrolyte ionic strength, and pH. Lyklema² has described a porous surface that can account for charge development far in excess³ of that to be expected strictly from the density of surface groups. Owing to porosity, potential determining ions and counterions are allowed to penetrate past the surface into the solid, excluding the solution phase. Ions associated with the diffuse double layer play little part in compensating for the total charge, their effects being limited to the fraction of charge located on the surface. The results of this study show that these porous silica charge densities are less than those for nonporous silica, and Lyklema's model apparently is not applicable here. Instead, the porosity of the silicas studied here is considered to be an extension of the external surface into

the interior of the solid. Charged groups are located only on these surfaces and are compensated by ions in the solution phase that enters the pore structure.

The experimental results will be interpreted in terms of diffuse double layer interactions in the pore structure. Nonporous silica surface charge densities will be used as a reference level to correlate the relative diminution of observed porous charge densities. It has been shown¹ that widely different methods of preparation do not lead to significantly large differences in nonporous charge densities; precipitated and pyrogenic silicas have similar charge densities in simple electrolytes. It is assumed then that the method of silica preparation will not significantly affect the conclusions reached in this work. It will be shown that the experimentally observed reductions in charge density can be qualitatively accounted for by using theory developed for interactions of diffuse double layers originating at plane surfaces.

(1) R. P. Abendroth, *J. Colloid Interface Sci.*, **34**, 591 (1970).

(2) J. Lyklema, *J. Electroanal. Chem.*, **18**, 341 (1968).

(3) Th. F. Tadros and J. Lyklema, *ibid.*, **17**, 267 (1968).

Experimental Section

The porous silicas studied were formed⁴ by addition of a solution of sulfuric acid and isopropyl alcohol to an aqueous solution of sodium silicate. Addition of sodium chloride causes liquid phase separation, and the precipitated porous silica particles are removed, washed, and dried at about 300°. The three porous silicas used were washed in distilled, deionized water until the effluent pH became constant and then were dried at 120°. The properties, reported in Table I, did not change as a result of this treatment. The pore parameters were estimated from the hysteresis portion of a gas adsorption-desorption plot using Ar. Potentiometric titration was used to determine charge densities, and the experimental details are as previously reported.¹ The usual silica concentration was 2.0 g/400 ml of electrolyte. Results were found to be independent of the amount of silica present. The silica was introduced approximately 18 hr before titration commenced. Equilibrium, as evidenced by constant pH readings in a 30-min period, was established in 2 hr or less when approached *via* base additions, but required at least 24 hr from the acid side. No hysteresis in the equilibrium quantities adsorbed was observed. The electrolytes used were 10⁻², 10⁻¹, and 10⁰ M KCl for silicas A, B, and C, and additionally, 10⁻¹ M LiCl and CsCl for silica A. The sequence of counterion adsorbability on silica A was established as Cs⁺ > K⁺ > Li⁺.

Table I

	A	B	C
Surface area, m ² /g	400	450	861
Pore volume, ml/g	0.55	0.55	0.55
Pore radii, Å			
Largest	>50	>50	27
Smallest	10	12	9
Average	21	36	11
Particle size, μm	75-150	75-150	<50

Discussion

Titration results in 10⁻¹ M KCl for silicas A, B, and C and for nonporous silica¹ are shown in Figure 1. The charge densities are based on the Ar BET surface areas. In the following discussion, comparison is made between these results and those for nonporous silica, assuming the deviations are due to porosity. The porous silica results are plotted in Figure 2 as a fraction of the nonporous silica charge densities for the same pH range and electrolyte ionic strength. The ratios for the wider pore silicas (A and B) are very similar, ranging from 0.50 to 0.95 depending on ionic

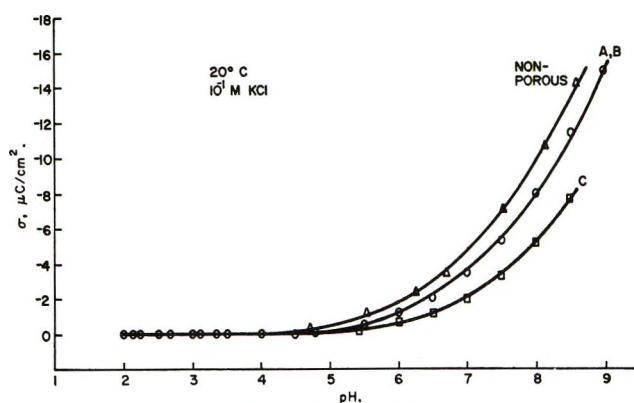


Figure 1. Charge densities on porous and nonporous silicas.

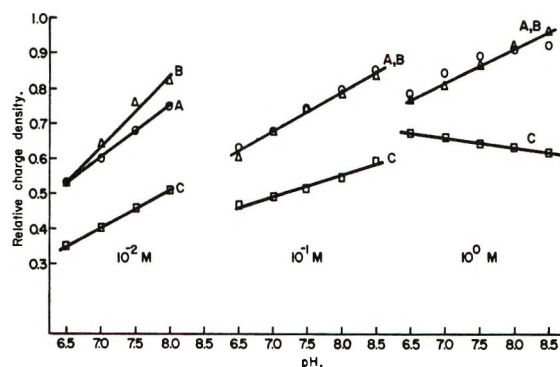


Figure 2. Charge densities on porous silicas relative to nonporous silicas as a function of pH and ionic strength.

strength and pH; the narrow pore silica (C) ranges from 0.35 to 0.65. The ratios for both types of silica increase with surface potential (pH) and ionic strength.

The diameters of the pores (Table I) for silicas A, B, and C are such that the diffuse double layers originating on opposite sides of the pore can interact more or less extensively in the center of the pore. The charge density on the pore walls cannot achieve its maximum value since it cannot be fully compensated for by an unhindered diffuse double layer. For interacting diffuse double layers originating from plane surfaces, the charge density is found to be a function of surface separation distance, surface potential, and potential midway between the surfaces.⁵ Application of this relation is made to double layers interacting within a closed system such as a pore, although originally derived for double layers originating at plane surfaces

$$\sigma = \left(\frac{nekT}{2\pi} \right)^{1/2} (2 \cosh Z - 2 \cosh U)^{1/2}$$

where

$$U = \frac{ze\psi_d}{kT} = 8 \left(\frac{e^{Z/2} - 1}{e^{Z/2} + 1} \right) e^{-\kappa_d}$$

(4) H. F. Kummerle, U. S. Patent No. 3,489,516 (Jan 13, 1970).

(5) J. Th. G. Overbeek, "Colloid Science," Vol. 1, H. R. Kruyt, Ed., Elsevier, Amsterdam, 1952, p 252.

and

$$Z = \frac{ze\psi_0}{kT}$$

ψ_0 and ψ_d are the potentials on the wall and midway between the surfaces, respectively, and κ_d is the ratio of half the distance between the plates to the thickness of the diffuse double layer. The relative diminution of charge density is obtained by taking the ratio of charge density due to interaction, σ , to that for no interaction, σ_m

$$\frac{\sigma}{\sigma_m} = \left(\frac{\cosh Z - \cosh U}{\cosh Z - 1} \right)^{1/2}$$

Calculation of σ/σ_m is accomplished through a tabulation of values of κ_d as a function of Z and U .⁶ Values of κ_d for silicas A, B, and C, assuming cylindrical pores, are 0.70, 1.20, and 0.37, respectively. Values of Z chosen correspond approximately to 1-3 pH units above that for a neutral surface. The results of this calculation are given in Table II. The dependencies shown in Figure 2 for relative surface charge as a function of potential and pore size at ionic strength 10^{-2} and $10^{-1} M$ are qualitatively accounted for, for roughly similar values of κ_d and Z . At $10^0 M$, the wider pore

silicas (A, B) show the same kind of behavior as at lower ionic strengths, but silica C exhibits an apparent reversal in behavior, relative surface charge decreasing slightly with an increase in potential. This behavior cannot presently be accounted for.

Table II: Values of σ/σ_m

Z	κ_d				
	0.2	0.3	0.4	0.5	0.6
6	0.87	0.92	0.95	0.97	0.98
4	0.63	0.72	0.80	0.85	0.89
3	0.42	0.55	0.66	0.77	0.80

The increase in relative surface charge with ionic strength is ascribed to the well-known⁷ compression of the diffuse double layer with increasing ionic strength. This results in decreasing interaction in the center of the pores, equivalent to a decrease in ψ_d , consequently allowing greater charge densities on the pore walls.

(6) Reference 5, p 251.

(7) K. J. Mysels, "Introduction to Colloid Chemistry," Interscience, New York, N. Y., 1959, p 315.

Resistive Effects in Thin Electrochemical Cells: Digital Simulations of Electrochemistry in Electron Spin Resonance Cells

by Ira B. Goldberg, Allen J. Bard,*

Department of Chemistry, University of Texas, Austin, Texas 78712

and Stephen W. Feldberg

Brookhaven National Laboratory, Upton, New York 11973 (Received December 6, 1971)

Publication costs assisted by Robert A. Welch Foundation and National Science Foundation

A digital simulation technique has been used to treat electrochemical reactions in a thin cell in which non-uniform current densities result from high electrolyte resistance. These calculations have been applied to conventional *in situ* electron spin resonance electrolytic cells. It has been shown that the time dependence of the esr signal is strongly dependent upon the precise electrode placement. The conventional cell is found to be unsuitable for use in pulse electrochemical-esr experiments for the measurement of kinetic parameters because secondary electrode processes can occur during a pulse and rearrangement of electrogenerated products at the electrode following the pulse must be considered. These results are also applicable to thin layer electrochemical cells, spectroelectrochemical cells, electroplating baths, and large-scale electrosynthetic cells.

Introduction

Electrochemical cells which exhibit high resistances and nonuniform current distributions include thin-layer electrochemical cells,¹ thin-layer spectroelectrochemical cells,² cells with porous electrodes,³ and *in situ* electrochemical electron spin resonance (esr) cells.^{4,5} Two kinds of resistive effects are observed with these cells. The resistance between the working electrode and the reference electrode, or the uncompensated resistance, R_u , causes the actual potential at the working electrode to be different than the measured potential by an amount iR_u where i is the current. The second resistive effect is caused by the differences in solution resistance between different points of the solution near the working electrode and the auxiliary electrode which causes different iR drops at different points parallel to the working electrode, and therefore, a nonuniform current distribution across the surface of the working electrode.

Generally, the theoretical treatments of electrochemical techniques do not consider nonuniform current densities because, in most cases, it is difficult to calculate these in closed form. Newman^{6a} and Harrar and Shain,^{6b} however, have carried out several calculations which represent situations where resistive effects cause significant nonuniform current densities and cause deviations from the usual theoretical treatments. We report here digital simulations⁷⁻⁹ of electrochemical problems involving these effects. Although the results here deal mainly with electron spin resonance cells, the techniques described should also be applicable to other electrochemical problems involving non-uniform current distributions, such as thin layer electrochemical cells, large-scale electrosynthetic cells, various electroanalytical cells, etc.

The inherent problem of high resistance in esr-electrochemical cells arises from the necessity of using only a thin layer of solution in the cavity of the esr spectrometer to avoid dielectric losses from the interaction of the microwave field with the solvent.⁴ For aqueous media, only a 0.5-mm layer of solution can be tolerated. A diagram of the conventional esr cell is shown in Figure 1a. The reference electrode cannot usually be placed near the working electrode, and thus there is considerable uncompensated iR drop between the reference electrode and the portion of the working electrode in the esr cavity. At best, the reference probe is extended to the top of the working electrode, but even here there are still significant iR drops between the segment of the working electrode closest to the reference electrode and the solution adjacent to any other segment of the working electrode.

Since cells of this design are frequently used in esr spectroscopy, it is important that the behavior of these

(1) (a) A. T. Hubbard and F. C. Anson, *Electroanal. Chem.*, **4**, 129 (1970); (b) C. N. Reilly, *Rev. Pure Appl. Chem.*, **18**, 1221 (1967), and references therein.

(2) R. W. Murray, W. R. Heineman, and G. W. O'Dom, *Anal. Chem.*, **39**, 1666 (1967).

(3) R. deLevie, *Advan. Electrochem. Electrochem. Eng.*, **6**, 329 (1967).

(4) L. H. Piette, P. Ludwig, and R. N. Adams, *Anal. Chem.*, **34**, 916 (1962).

(5) I. B. Goldberg and A. J. Bard, *J. Phys. Chem.*, **75**, 3281 (1971).

(6) (a) J. Newman, *Electroanal. Chem.*, **6**, in press; (b) J. E. Harrar and I. Shain, *Anal. Chem.*, **38**, 1148 (1966).

(7) S. W. Feldberg, *Electroanal. Chem.*, **3**, 199 (1969), and references therein.

(8) K. B. Prater and A. J. Bard, *J. Electrochem. Soc.*, **117**, 209, 335, 1517 (1970).

(9) S. W. Feldberg in "Applications of Computers to Chemical Instrumentation," J. S. Mattson, H. P. Mark, Jr., H. C. MacDonald, Jr., Ed., Marcel Dekker, New York, N. Y., and references therein.

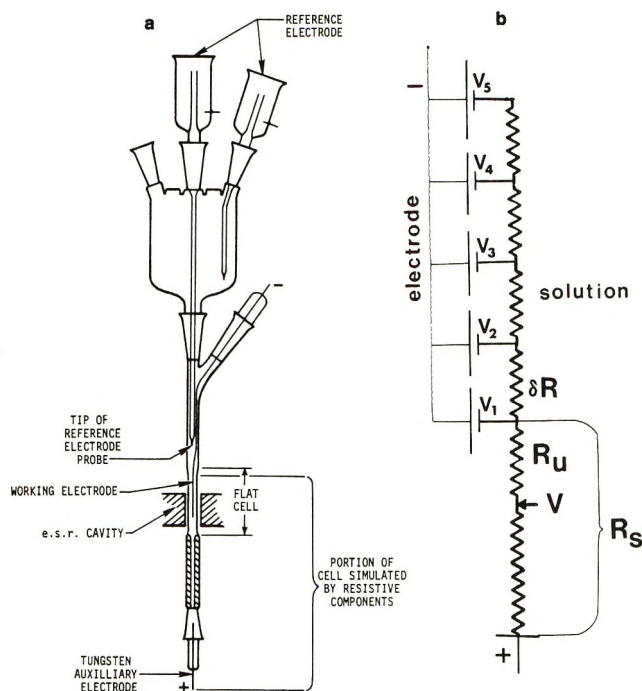


Figure 1. (a) Diagram of conventional esr-electrochemical cell. (b) Schematic representation of a thin-layer electrochemical cell. V_i represents the potential at the center of electrode segment i .

cells is understood. To this date, very little work concerning this aspect of the electrogeneration of radicals has been presented. We present here a semi-quantitative study of this type of cell using the simplest model possible. The conditions which are selected for this calculation are: (1) each of the charge-transfer steps is nernstian; (2) the double-layer capacitance is negligible; (3) there are no adsorbed species; (4) there is no deposition of material at the electrode and the diffusion coefficients of all species are nearly equal; (5) at the beginning of the simulated experiment the entire solution consists of the neutral species of the electroactive material; (6) the cell can be represented as shown in Figure 1b and (7) convection is negligible. These conditions appear to describe the electrochemical behavior of the majority of systems of organic compounds in nonaqueous solvents studied by esr. Modifications to include slow electron-transfer steps, coupled homogeneous chemical reactions, double-layer charging, etc., can be included in the simulation using procedures previously described;⁷⁻⁹ however, since our aim is to demonstrate difficulties in behavior even under the simplest conditions, we do not deal with these additional complications here.

Digital Simulation

Simulations of electrochemical processes are discussed in detail by Feldberg.⁷ To incorporate the differing resistances to different parts of the working electrode, as well as the finite cell thickness, some modifications must be made in the procedures of the pre-

vious simulations involving uniform current densities and semiinfinite linear diffusion. Details of the method employed are given in the Appendix and only an outline of the procedure is given here. The model chosen to represent the electrochemical cell is shown in Figure 1b.

Rather than considering a cell in which the reference electrode is above the working electrode, as shown in Figure 1a, we chose to consider the reference electrode adjacent to the lower edge of the working electrode. This system is more amenable to the method of digital simulation and provides a suitable reference point for later discussion. The total resistance between the counter electrode and the end of the working electrode is R_s . The total electrolysis current, I , flows through R_s . The resistances between different higher segments along the working electrode and the counter electrode are given by $R_s + \delta R$, $R_s + 2\delta R$, etc. The fraction of the total current flowing into each segment of the working electrode is given by δi_1 , δi_2 , etc., so that

$$I = \sum_{k=1}^{N_{\max}} \delta i_k \quad (1)$$

where N_{\max} is the number of segments of the working electrode. It is further assumed that the resistance across the double layer is negligible. The cell thickness is simulated by a finite number of solution layers, 1, 2, ..., N_{lim} , where N_{lim} is the number of increments of thickness. The model is used for the case of a single working electrode with the nonconducting cell wall terminating diffusion, such as the usual esr cell (Figure 2).

If the length of each electrode segment is much larger than the increment of cell thickness, then the cell may be treated as a series of smaller, independent cells, and diffusion between the vertical solution elements can be neglected. This lateral diffusion can be included in the calculation if necessary.

The current of the k th element, δi_k , depends upon

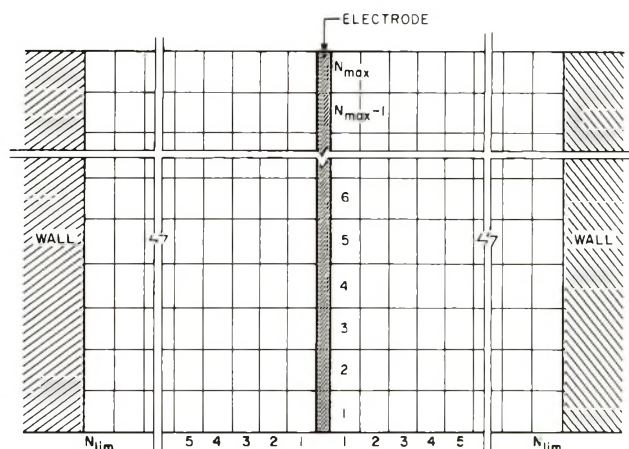


Figure 2. Digital representation of thin electrochemical cell.

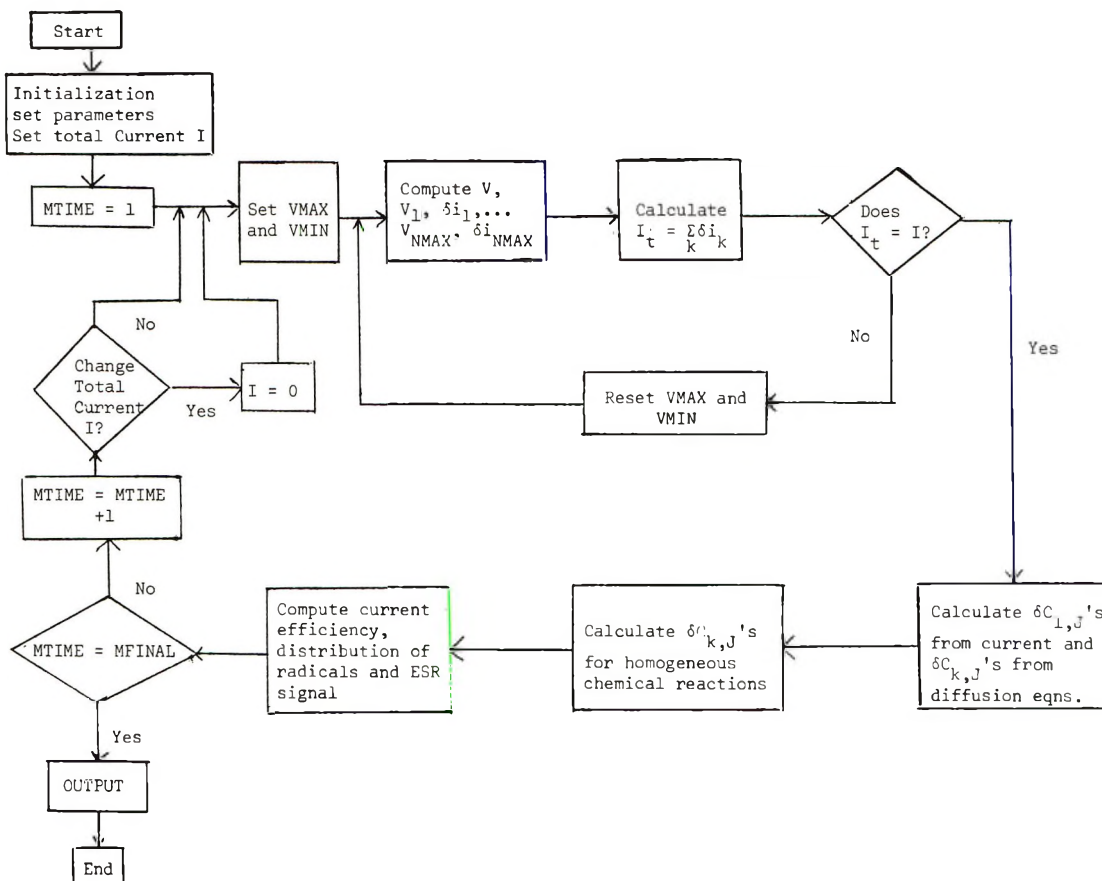


Figure 3. Flow chart of digital simulation program.

the potential of that element, V_k . To determine the potential V_k , it is necessary to determine the potential of the first element of the electrode, V_1 , and then determine the other potentials by computing the voltage drops between the elements. Since these voltage drops depend upon δi_k , an iterative procedure is used to find the V_k 's and the δi_k 's which satisfy the resistive drops along the electrode and also satisfy eq 1. Note also that V_1 differs from V by the amount iR_u . The iterative method employed to calculate V was the bisection method.¹⁰ In this method, reasonable positive and negative limits of V , denoted V_{max} and V_{min} , are guessed. The first trial value of V is taken as $1/2(V_{max} + V_{min})$, and values of δi_k and V_k are calculated for all segments of the electrode. The total current, *via* eq 1, is then determined. If this current is too large, V_{min} is replaced by V , or if the current is too small, V_{max} is replaced by V , and the calculations are repeated until the desired degree of convergence is obtained. A flow chart of the program is shown in Figure 3.

Either parallel plate or single electrode systems with potential or current step processes can be treated by this method. The only difference among them is that the boundary conditions are slightly different. Details of these simulations are given in the Appendix.

Experimental Section

Simulations of In Situ Electrolysis in ESR. Two aspects of electrochemical generation of radical ions in esr were investigated with these calculations. The first problem was to examine the effects of solution resistance and electrode placement in the microwave cavity during continuous electrolysis, and the second was to investigate the feasibility of pulse experiments in conventional esr electrolysis cells, such as the Varian V-4556 or E246 (cell dimensions $4 \times 0.9 \times 0.05$ cm), Bruker BER-400 2E or the Jeolco JES-ELIO cell.

In continuous generation of radical ions in esr, several effects have been noted: (1) the rate of increase of the initial esr signal varies considerably between experiments; (2) during electrolysis, the esr signal reaches a peak after a certain time and then diminishes; (3) there may be a sudden increase of the esr signal when the current is stopped; and (4) the esr signal due to even stable radicals often decreases shortly after the current is stopped.

A characteristic system which may be used as an

(10) H. M. Lieberstein, "A Course in Numerical Analysis," Harper and Row, New York, N. Y., 1968, pp 3, 6; A. Ralston, "A First Course in Numerical Analysis," McGraw-Hill, New York, N. Y., 1965, p 495; R. W. Hamming, "Numerical Methods for Scientists and Engineers," McGraw-Hill, New York, N. Y., 1962, p 352.

illustration of the behavior of electrogeneration in esr is that of anthraquinone. The half-wave potentials of anthraquinone in dimethylformamide (DMF) are -0.83 and -1.40 V vs. sce¹¹ for the first and second waves, respectively. In aprotic media both the anion and dianion are stable. Typical of the solvents used in esr studies are dimethylformamide (DMF) and 1,2-dimethoxyethane (DME) with 0.1 M supporting electrolyte. The specific resistances of these solvent systems are about 250 ¹² and 4000 ohm-cm,¹³ respectively.

The sensitivity in the microwave cavity of the spectrometer is not uniform. In an unloaded cavity of the TE 102 and TE 104 modes, the signal S resulting from a paramagnetic sample distributed inside the cavity will follow an expression of the form^{14,15}

$$S = A \int_0^z \cos^2 \left(\frac{\pi}{2} \left(\frac{y}{z} - 1 \right) \right) N(y) dy \quad (2)$$

where z is the height of the cavity (for x band, $z = 2.290$ cm), y is the distance from the bottom of the cavity, $N(y)$ is the number of radicals at y , and A is the proportionality constant which depends upon the instrumental conditions and upon the degeneracy and line width of the paramagnetic material. Although the presence of the cell, the solution, and the electrode and the use of field modulation will cause some deviation of the signal from that predicted by eq 2, it is still accurate enough for our purposes. It is also useful to treat the proportionality constant as unity. In this way, when all of the radicals are located at the center of the cavity, the signal will equal the number of radicals. After the calculation of the concentrations in each of the volume elements (see Appendix), $N(y)$ is determined by adding the number of radicals in all of the volume elements in each vertical level. A digital form of eq 2 is used in the calculation.

In most electrolytic cells which have been used for *in situ* generation, the reference electrode is not near the working electrode and as a result, the uncompensated resistance is extremely high. Even though the electrolysis is carried out under controlled potential conditions, the high uncompensated voltage drop effects an essentially constant current generation.⁵

Consider the simulation of the generation of the anthraquinone anion radical for 100 sec at $100 \mu\text{A}$ in a 2.5 mM anthraquinone solution in DMF where the electrode dimensions are 0.5×3 cm and the cell thickness is 0.05 cm. The length of the electrode was divided into 25 sections and the experiment duration into 200 time units. The counter electrode is located below the esr cell and outside the cavity. Figure 4 shows the relative current distribution at several times during the electrolysis. Initially ($t = 0$) all of the current is used to produce the radical at segments of the electrode closest to the counter electrode. Shortly afterward ($t = 25$ sec), the dianion is formed near the lower edge of the working electrode, while the anion

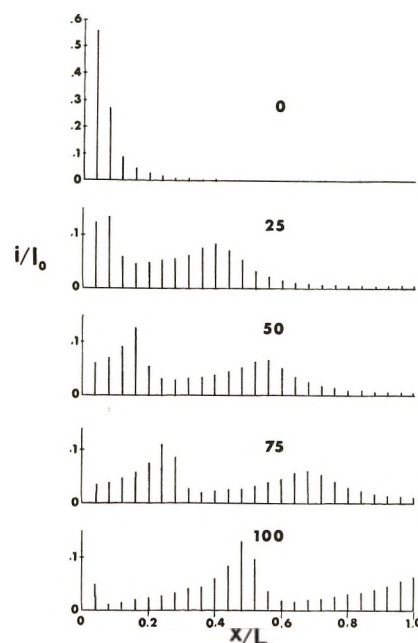


Figure 4. Simulation results showing fraction to total current at different segments of the working electrode at various times during the constant current electrolysis of 2.5 mM anthraquinone in 0.1 M tetrabutylammonium iodide-dimethylformamide solution: total current $100 \mu\text{A}$; electrode width, 0.5 cm; length, 3.00 cm. Time of electrolysis (sec) given above distribution diagram. Bars represent current at the center of each segment.

is generated further up. Two current peaks are evident from the diagram. At longer times, the peaks move further along the electrode as the electroreducible material is depleted ($t = 50$ to 75 sec, respectively). During the last time unit shown, solvent decomposition begins as the potential of the first element of the electrode becomes sufficiently negative.

Curve R of Figure 5a shows the relative quantity of radicals during the generation, where the maximum amount of radicals is normalized to 1. In addition, the esr signal is shown for several different electrode placements. Curve A shows the esr signal when the edge closest to the counter electrode is located at the point of maximum sensitivity in the cavity, that is at the center of the cavity [$(z - y_0)/z = 1/2$ where z is the height of the cavity and y_0 is the lower edge of the electrode]. Curve B represents the esr signal when the lower edge is placed $z/4$ above the bottom of the cavity, and curve C represents the esr signal when the bottom of the electrode is at the bottom of the

(11) P. H. Given, M. E. Peover, and J. M. Schoen, *J. Chem. Soc.*, 2764 (1958).

(12) F. K. Andryushchenko, K. G. Parfenova, and O. A. Slotin, *Sov. Electrochem.*, 2, 689 (1966); D. S. Reid and C. A. Vincent, *J. Electroanal. Chem.*, 18, 427 (1968), and references therein.

(13) Estimated from the measurements of C. Carvajal, K. J. Tolle, J. Smid, and M. Szwarc, *J. Amer. Chem. Soc.*, 87, 5548 (1965).

(14) B. Kastening, *Ber. Bunsenges. Phys. Chem.*, 72, 20 (1968).

(15) C. P. Poole, Jr., "Electron Spin Resonance," Interscience, New York, N. Y., pp 263-270.

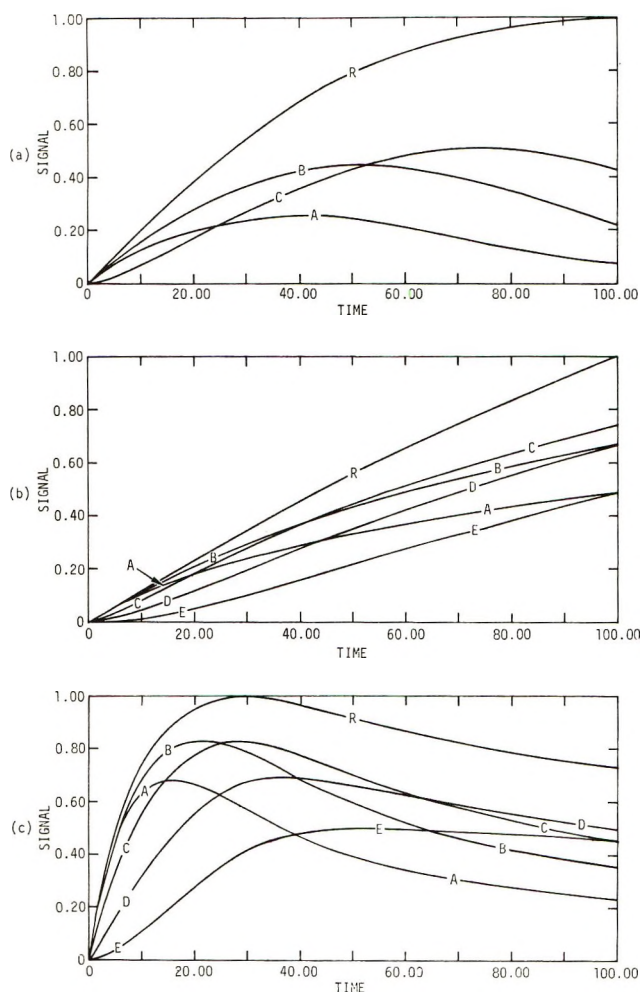


Figure 5. Simulation results showing the quantity of radical (R) and the esr signal vs. time for various placements of the working electrode. See text for description of electrode placements. Concentration of electroactive material is 2.5 mM: a, specific resistance of solution 250 ohm-cm; stable anion and dianion, cf. Figure 4, current 100 μ A; b, specific resistance of solution = 4000 ohm-cm; stable anion and dianion, $E_{1/2} = -0.83$ V, -1.40 V, current 50 μ A; cathodic limit 50 μ A at -3 V; c, specific resistance of solution is 4000 ohm-cm; no dianion is generated. $E_{1/2}$ of reduction to anion = -0.83 V, rate of decomposition of anion is 0.125 sec^{-1} , cathodic limit 50 μ A at -3 V.

cavity. Several differences between these curves are immediately apparent. Initially, the most rapid rise of the esr signal will be when the edge of the electrode is at the center of the cavity, but during a long electrolysis, this positioning gives rise to the smallest signal. When the electrode is placed $z/4$ of the distance above the bottom cavity (curve B), the rise of the esr signal is nearly as rapid, but after 4 sec the signal is more intense than in the position corresponding to curve A. Under the conditions represented by curve C, at the start of the electrolysis, the radicals are generated at the bottom of the electrode. This produces a very small esr signal, and consequently the rise of the signal is very slow. At longer times the

radicals at the edge of the electrode are depleted due to further reduction to the dianion. When the electrode is at the center of the cavity (curve A), the esr signal will decrease, but this will have a smaller effect upon the signal when the bottom of the electrode is below the center (curves B or C). When the electrode is at these positions, represented by B and C, the material near more of the electrode is detected by the spectrometer, and as a result of the movement of the current waves up the electrode, the signal represented by B reaches a maximum before that represented by C.

Figure 5b shows a similar constant current generation for a solution of 2.5 mM anthraquinone in the higher resistance solvent DME. The only differences are that the cell thickness was 0.1 cm, and that the current was 50 μ A. Because of the higher resistance, the electrochemical reactions are confined to the lower portions of the electrode. Curves A, B, C, D, and E show the signals obtained when the bottom edge of the electrode is placed at $z/2$, $3z/8$, $z/4$, $z/8$, and 0 cm above the bottom of the cavity. The total amount of radicals is shown by curve R. As before, the initial rise of the esr signal is greatest when the lower edge of the electrode is placed at $z/2$. Here, however, the greatest signal will occur when the edge of the electrode is placed $z/4$ above the cavity floor because the total electrolytic reaction occurs over a smaller portion of the electrode than that shown in Figure 5a.

Figure 5c shows the same conditions of electrogeneration as Figure 5b, except that there it is assumed the dianion is not formed, and the radical is assumed to decompose in a first-order process when the rate constant is about 0.125 sec^{-1} . The apparent signal-time curves are significantly dependent upon the precise electrode position, and the rate of decomposition. A similar problem was found by Kastening¹⁴ when using electrochemical flow systems in esr for the measurement of kinetic parameters.

Simulations of In Situ Current Pulse Experiments. In order to carry out pulse electrolytic experiments to measure the stability of radicals, it is necessary to use moderately high currents, depending upon the lifetime of the radical. The anthraquinone-DMF system was again chosen as an ideal system to represent this process. The conditions simulated were the same as for the previous constant current generations in DMF, except that the length of the electrode in this case was 1.15 cm (equal to $z/2$) and the current pulse was 1 mA for 0.5 sec. The concentration of anthraquinone was 5 mM. Under these conditions, and if semiinfinite linear diffusion were possible, then the transition time for a 1 e process would be 0.43 sec. Using a 2.3-cm electrode so that the transition time is longer does not significantly alter the shape of the curve because the reaction is still localized mostly at the bottom of the electrode.

Figure 6 shows the current distributions at several

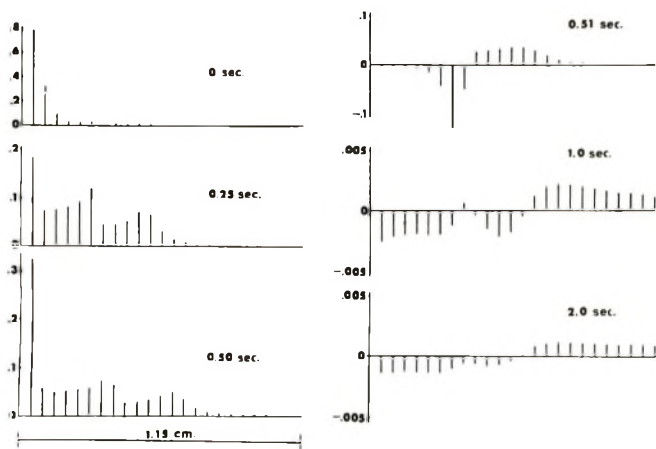


Figure 6. Simulation results showing fraction of current at different segments of the working electrode during and following a short current pulse. Bars represent current at the center of each segment of the electrode. Solution 5.0 mM; current 1.0 mA; pulse duration = 0.50 sec; specific resistance 250 ohm-cm; $D = 10^{-5}$ cm²/sec; half-wave potentials -0.83 V and -1.40 V; background current = 1 mA at -3.00 V; electrode size 0.5 cm \times 1.15 cm.

times during and following the current pulse. At the instant of application of current the entire current is used in the production of the anion. After about 0.02 sec some dianion is produced. By $t = 0.25$ sec a large portion of the current goes toward the generation of the dianion and about 11% goes toward solvent decomposition. Thus, 100% current efficiency for the generation of anion cannot be maintained for an appreciable fraction of the transition time. At $t = 0.50$ sec a much larger portion of current goes toward production of the dianion and solvent decomposition. At the end of the 0.5-sec pulse, the *net* current efficiency for generation of the anion is about 65%. It should also be mentioned here that the anthraquinone-DMF system is close to ideal for definition of the electrochemical waves, because there is 0.57 V difference between the first and second waves, and about 1.3 V between the second wave and the cathodic limit for solvent decomposition. If the first and second waves were closer together and the cathodic limit was not so far removed, then the current efficiency would be much less than obtained here.

After the current is stopped, the iR drops between elements which have been changing throughout the pulse are sharply reduced. Still, however, the potential established by the R^{2-} - R^- and R^- - R couples would be different along the electrode unless current is allowed to flow within the electrode, enabling redistribution of R^{2-} , R^- and R at the electrode surface. The current distribution immediately following the pulse is shown in Figure 6, where $t = 0.51$ sec. Observe that at the bottom of the electrode there is an anodic current, indicating that R^{2-} is oxidized to R^- , while at the end of the electrode R is reduced to R^- .

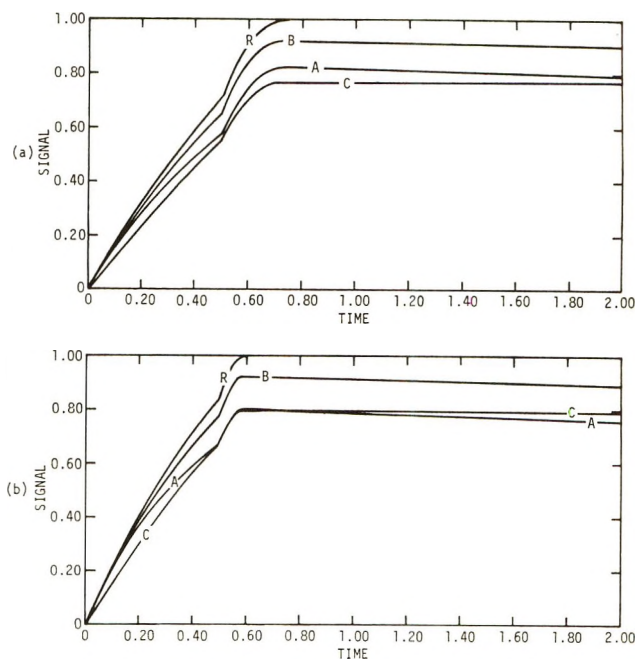


Figure 7. Quantity of radicals (R) and esr signal for different electrode placement vs. time during and following a 0.50-sec pulse. See text for description of electrode placements. Same parameters simulated as in Figure 6: a, stable anion and dianion; b, stable anion; dianion decomposes in a first order process $k = 5$ sec⁻¹.

This internal current is quite large until the dianion is nearly exhausted from the solution either by current flow or by reacting with neutral R to form $2R^-$. After this, however, there are still gradients of R and R^- adjacent to the electrode. This causes a smaller current which tends to equalize the relative amounts of these species. Thus, R^- is oxidized to R at the first elements of the electrode and R is reduced to R^- at the last elements [Figure 6 ($t = 1.0, 2.0$)]. The esr signal which results from this system is shown in Figure 7a. As before, the curve marked R represents the amount of radicals in the cell. Curves A, B, and C represent electrode placements where the edge of the electrode is $Z/2$, $3Z/8$, and $Z/4$ above the bottom of the cavity. As before, the most rapid increase of the signal occurs when the edge of the electrode is in the most sensitive region of the cavity. However, because dianion is produced first at the edge of the electrode, this position does not give the maximum signal. When the current is stopped, the amount of radical in solution increases rapidly as does the esr signal because of the internal current. However, even after the amount of radicals present reaches a steady state (curve R approaches 1), the esr signal still changes. In curves A and B there is a noticeable decrease in the esr signal as radicals are removed from a more sensitive region and generated in a less sensitive region. Curve C, on the other hand, exhibits a small increase of signal (about 0.3% from $t = 0.8$ sec to $t = 2$ sec) because in this case, radicals are removed from a position which

gives rise to a smaller signal and are regenerated at a position which gives rise to a larger one (cf. Figure 6). When the conventional electrode is used, such as the longer 3-cm gauze electrode supplied with commercial cells,¹¹ the decrease of the esr signal after the current pulse is considerably greater than shown here, especially when the edge of the electrode is placed at the center of the cavity. In cases where the dianion is not stable, the rise of the signal after the pulse is stopped is considerably less pronounced, as shown in Figure 7b. In this simulation the dianion was assumed to have a first-order decomposition rate of $k = 5 \text{ sec}^{-1}$.

Effects similar to those discussed here have been observed experimentally for both constant current and current pulse experiments (Figure 8a and b). Figure 8a shows a solution of anthracene electrolyzed at 0.5 mA for 100 sec in DMF. Since the dianion is unstable, only a small rise is seen when the current is stopped. Also, because the radical may be slightly unstable in DMF, the decrease of the esr signal is more rapid than expected. Figure 8b shows a solution of anthraquinone generated for 120 sec. A very rapid rise of the esr signal and then a slow decay is observed. These experiments were carried out in the conventional cell.

The results of these calculations show that due to the high resistance in the cell, secondary electrode processes may occur even before the transition time of the first electrode process. Since in long term generation there is probably a significant amount of convection with the cell, the actual experimental system will exhibit a greater current efficiency for production of a radical than that calculated here. The results of these calculations also indicate that even if it were possible to place a reference electrode adjacent to the lower edge of the working electrode and the potential here maintained on the plateau of the reduction to the radical, the potential on the upper portions of the electrode would still be much more positive, and although R^{2-} should not be formed, there would still be a galvanic effect between R and R^- at different areas of the electrode surface when the circuit was opened. Thus, the conventional esr cell would not be suitable for pulse experiments.

Conclusions

These calculations have indicated several problems which are inherent in electrogeneration of radicals for esr. First of all, pulse experiments are not easily carried out in conventional esr cells because of the change of the iR drop during and following the applied pulse, so that the amount of radicals adjacent to different parts of the electrode are redistributed after the pulse. Conceivably, an electrode could be constructed of a material which would produce an electrode resistance such that the resistance of the solution between the bottom of the electrode and a point adjacent to the

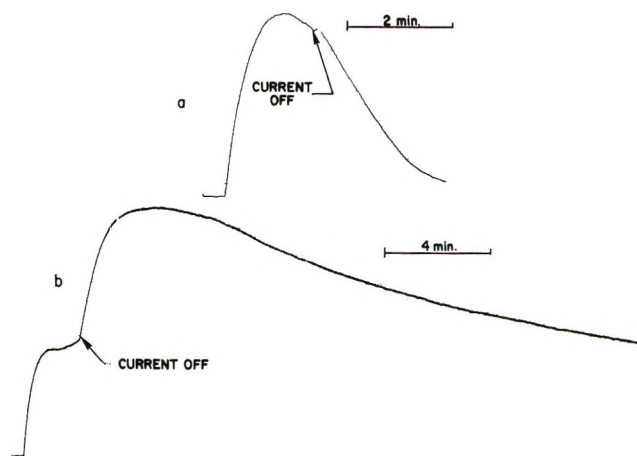


Figure 8. Experimental signal-time curves: a, 5 mM anthracene in 0.1 M tetrabutylammonium iodide-dimethylformamide solution for 100 sec generation at 100 μA ; results typical of unstable dianion; b, 5 mM anthraquinone generated under same conditions for 120 sec; results typical of stable anion radical and dianion.

electrode would be the same as the resistance of the electrode between the top of the electrode and that point on the electrode. Although this would permit a uniform current density over the electrode surface, this design would have poor qualities as an electrochemical cell. On the other hand, the counter electrode and reference electrode may also be placed in the flat portion of the electrochemical cell so that both uniform current densities and good cell characteristics would be attainable.⁵ The electrode size and placement in the esr experiment is critical to the intensity and time dependence of the esr signal. The optimum parameters for a given solvent system must be chosen experimentally. In the highest resistive media, the edge of the electrode is best placed in the region just below the center of the cavity where the sensitivity is greatest because the electrolysis occurs over a fairly small region of the electrode. On the other hand, if an extremely high current is used when the edge of a long electrode is placed at the bottom of the cavity, and assuming that no secondary radicals are produced, then the desired radical may be generated at more sensitive regions of the spectrometer so that an esr signal can be observed.

With solutions of lower resistance, the current becomes more uniform, and the optimum signal is obtained when the electrode is placed deeper into the cavity. Similarly, as the current becomes greater, the zone where radicals are produced moves farther up the electrode.

An interesting effect was observed in these simulations. If only one electrochemical process was assumed to occur and allowing semiinfinite diffusion, then regardless of the electrical resistance of the medium, the chronopotentiometric transition time was constant. Here the transition time must be defined as the time

when the surface concentration of R, in the reaction $R + e \rightarrow R^-$, becomes zero over all regions of the electrode.

Acknowledgment. The support of the National Science Foundation (GP6688X) and the Robert A. Welch Foundation is gratefully acknowledged. The electron paramagnetic resonance spectrometer was purchased under a grant from the National Science Foundation (GP2090). Part of this work was performed under the auspices of the U. S. Atomic Energy Commission.

Appendix

Digital Simulation. The models for digital simulation of electron transfer, homogeneous kinetics, and semiinfinite diffusion have been discussed in detail.⁷ Because in many cases the cells described here are thinner than the effective diffusion layer in semiinfinite linear diffusion, the treatment of diffusion must be slightly modified. In order to simulate diffusion to a planar electrode, the solution is divided into layers parallel to the electrode surface. In thin cells, the solution must be divided into an integral number of equal volume elements between the electrode and the wall as shown in Figure 2.

For semiinfinite diffusion the number of volume elements that must be considered in the simulation is⁷

$$M_{lim} = 6\sqrt{D_m M_t} \quad (A1)$$

where M_{lim} is the number of segments of length perpendicular to the electrode, D_m is the diffusion parameter used in the simulation (0.40 has been chosen here) where we have assumed that the diffusion coefficients of all species are equal, and M_t is the number of time units desired in the simulation. Equation A1 corresponds to

$$\delta = 6\sqrt{Dt} \quad (A2)$$

where δ is the diffusion layer thickness, D is the diffusion coefficient, and t is the total time of the experiment. From (A1) and (A2)

$$\delta = M_{lim} \sqrt{\frac{DT}{D_m M_t}} \quad (A3)$$

In thin cells, diffusion must be constrained within the cell walls. Using a relationship similar to (A3), the number of volume elements, N_{lim} in a thin layer cell of thickness l is given by

$$N_{lim} = l \sqrt{\frac{D_m M_t}{Dt}} \quad (A4)$$

The number of volume elements which must be used in the simulation is, therefore, the minimum value of N_{lim} and M_{lim} . In the program D_m is adjusted to make the right side of (A4) an integer.

To account for the different current densities at dif-

ferent portions of the electrode, the electrode is divided into N_{max} segments (indexed by I) as shown in Figure 2. The length of the electrode segment is not related to the length of the volume element normal to the electrode. The number of segments selected depends upon the degree of precision desired and the resistance of the solution. Diffusion perpendicular to the electrode (between layers of $k = 1$ and $k = N_{lim}$) is treated by finite difference forms of Fick's equations.⁷ The relative concentration of the j th species in box $I, k, F_j(I, k)$ because of diffusion occurring during one time increment, for $k = 2$ to $N_{lim} - 1$ is⁷

$$F_j'(I, k) = F_j(I, k)(t) + D_m [F_j(I, k - 1) - 2F_j(I, k) + F_j(I, k+1)] \quad (A5)$$

where $F_j(I, k)$ is the relative concentrations of species j at the end of the preceding time increment. In the cell such as diagrammed in Figure 2 for box $k = N_{lim}$ the relative concentration is

$$F_j'(I, N_{lim}) = F_j(I, N_{lim}) + D_m [F_j(I, N_{lim} - 1) - F_j(I, N_{lim})] \quad (A6)$$

For box $k = 1$, any amount of substance j generated at the electrode surface must be added to the concentration of box 1. Assume $J_j(I)$ is the flux of species j electrogenerated at element I of the electrode. The concentration in boxes $k = 1$ is then given by

$$F_j'(I, 1) = F_j(I, 1) + D_m [F_j(I, 2) - F_j(I, 1)] - J_j(I) \quad (A7)$$

where we neglect lateral diffusion.

If the electron-transfer reactions are assumed to be nernstian and the diffusion coefficients of all of the species are equal, then the flux of each species may be calculated in the following way. The electrode is assumed to be at the edge of the first box. Since the flux is proportional to the concentration gradient, and the concentration in the simulation represents the concentration at the center of that box, then the flux is given by

$$J_j(I) = D_m [F_j'(I, 1) - F_j^0(I)] / 0.5 \quad (A8)$$

where $F_j^0(I)$ is the relative concentration of species j at the electrode surface. The factor 0.5 enters (A8) because the distance between the electrode surface and the center of box $k = 1$ is $1/2$ of the unit length of each box. The relative surface concentrations of each species are given by the Nernst equation

$$\frac{F_1^0(I)}{F_2^0(I)} = \exp\left\{\frac{F}{RT}[E(I) - E^0]\right\} \quad (A9)$$

where the potential $E(I)$ is the potential of segment I and E^0 is the standard potential. Since the total flux at the electrode surface must be zero, if there is no accumulation of material at the surface, then

$$\sum_{j=1}^{N_s} J_j(I) = 0 \quad (A10)$$

where N_s is the number of species in the solution. Equations A8 through A10 can be solved simultaneously with the elimination of the parameters $F_j(I)$ and from this the flux of each species and the current at each electrode segment can be calculated as a function of potential. Diffusion between horizontal layers can be neglected because the length of each segment of the electrode given by h/N_{\max} , where h is the overall length of the electrode, is smaller than $6\sqrt{Di}$.

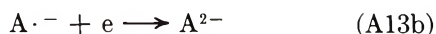
Constant Current Steps: ESR and Thin-Layer Cells. We assume that a current of magnitude i is passed through the cell. This may be converted to a dimensionless parameter Z_t which corresponds to the flux, given by

$$Z_t = \frac{iN_{\max}}{FCwh} \frac{tD_m}{DM_t} \quad (\text{A11})$$

where F is the Faraday, C is the experimental concentration, and w and h are the width and length of the electrode. If the current parameter at each element I of the electrode is given by $Z(I)$ then during a constant current experiment

$$Z_t = \sum_{I=1}^{N_{\max}} Z(I) \quad (\text{A12})$$

For a reduction, the following electrode reactions contribute to $Z(I)$



where A is electroactive substance and S is solvent or supporting electrolyte. For simplicity, we have assumed that the reactions in (A13a) and (A13b) are Nernstian and (A13c) is irreversible. Species A is denoted as $j = 1$, $A \cdot^-$ as $j = 2$, and A^{2-} as $j = 3$. The current due to the reduction of species A is given by $J_1(I) - J_3(I)$.⁷ The current due to the decomposition of solvent is denoted by $Z_b(I)$. Therefore, the current at element I of the electrode becomes

$$Z(I) = J_1(I) - J_3(I) + Z_b(I) \quad (\text{A14})$$

To include the resistance between segments of the electrode, the parameter used to represent the resistance must be made compatible to the dimensionless parameters representing the potential and the current. Thus, the resistance R_m between each segment of solution at the electrode surface, as shown in Figure 1, is given by

$$R_m = \left[\frac{\sigma h i F}{l w N_{\max} Z R T} \right] \quad (\text{A15})$$

where σ is the specific resistance and RT is 2.4777×10^3 J at 298°K. The first term in (A15) is the resistance between electrode segments. The uncompensated resistance is represented in a similar way except

that the value of R_u is substituted for the bracketed term of (A15).

In order to determine the measured potential, V , the bisection method¹⁰ was used. The most positive possible value of the potential, V_{\max} , and the most negative possible value, V_{\min} , are selected. The first guess for the measured potential is

$$V = 0.5(V_{\max} + V_{\min}) \quad (\text{A16})$$

From the value of V , the potential of the first segment of the electrode $E(1)$ is calculated

$$E(1) = V + Z_t R_u \quad (\text{A17})$$

and from this value, $Z(I)$ is calculated. Since the current flowing beyond the first electrode segment, Z_r is $Z_t - Z(1)$, the potential at the second electrode segment is given by

$$E(2) = E(1) + Z_r R_m = V + Z_t R_u + Z_r R_m \quad (\text{A18})$$

From this, the current in segment 2, $Z(2)$, is calculated. The procedure is repeated for all N_{\max} segments. The currents of all electrode segments are then totalled and compared to Z_t . If the total current is too large, then V_{\min} is replaced by V , and if the current is too small, V_{\max} is replaced by V . The procedure from (A16) is repeated until the total current is within a certain error of Z_t . A flow chart of the computer program is given in Figure 3.

A word of caution is necessary in using this method of calculation. Convergence of the calculated value of the total current to Z_t is very rapid when high currents are simulated. In the case of low currents, however, such as in thin layer electrochemical cells or zero current following a current pulse as in the esr cells, it is often necessary to use double precision to calculate $Z(I)$ from V , V_{\max} , V_{\min} , and the half-wave potentials. The 14 decimal digits carried by the CDC 6600 and CDC 6400 computers are often not sufficient to obtain a convergent value. This effect becomes most pronounced at zero current when many electrode elements are used in the calculation.

Nomenclature

1. Dimensional Variables.

- δ = distance perpendicular to the electrode, cm
- C = concentration, mol/cm³
- D = diffusion coefficient, cm²/sec
- i = current, A
- t = time, sec
- h = length of working electrode, cm
- w = width of working electrode, cm
- l = cell thickness, cm
- F = Faraday's constant, 96,500 Coul/equiv
- σ = specific resistance, ohm-cm

2. Indices

- I = index of segment of working electrode
- j = index of species: $j = 1$, A; $J = 2$, A⁻; $j = 3$, A²⁻
- k = index of length segment perpendicular to working electrode

3. Variables

N_s	= number of electroactive species	$J_j(I)$	= fractional flux of species j at the surface of segment I of the working electrode current due to background reactions
N_{\max}	= number of segments of working electrode	$Z_b(I)$	= current due to background reactions at segment I of the working electrode
M_{lim}	= number of segments of length required to represent semiinfinite linear diffusion	Z_t	= total current
N_{lim}	= number of segments of length required to represent cell thickness	$E(I)$	= potential measured between segment I of the working electrode and the reference electrode
M_t	= number of time increments of the calculation	$E^{\circ'}$	= standard formal potential
D_m	= diffusion parameter used in finite difference equations	R_m	= resistance (dimensionless) between solution segments at the surface of the electrode
$F_j'(I,k)$	= fractional concentration of j in the center of the segments of coordinates (I,k) after applying finite difference equations	R_u	= uncompensated resistance
$F_j(I,k)$	= same as $F_j'(I,k)$ but before application of finite difference equation	V	= trial potential
$F_j^{\circ}(I)$	= fractional concentration of j at the surface of segment I of the working electrode	V_{\max}	= positive and negative limits of potential
		V_{\min}	

Irreversible Potentiometric Behavior of Isotactic Poly(methacrylic Acid)¹

by J. C. Leyte,* H. M. R. Arbouw-van der Veen, and L. H. Zuiderweg

Gorlaeus Laboratories, Department of Physical Chemistry, University of Leyden, Leyden, The Netherlands (Received February 7, 1972)

Experimental evidence is presented for the irreversibility of the potentiometric titration curve of isotactic poly(methacrylic acid). A description in terms of thermodynamically irreversible conformation changes is given and it is shown that the dissipation due to the transition of a monomeric unit is independent of its state of dissociation.

In recent literature,² some attention has been given to irreversible behavior of macromolecular systems because of the implicit importance of these phenomena in the quest for molecular mechanisms for information storage. It has been pointed out³ that hysteresis loops in physical-chemical properties of macromolecules offer, at least in principle, the possibility of storing, on a molecular level, information about the history of the system.

The investigated macromolecular systems are, however, rather complicated from a physical-chemical point of view: RNA from several sources, mixtures of poly A and poly U, etc. In all these systems complicated chemical equilibria as well as polymer conformational equilibria shift simultaneously as a function of the driving physical variable (usually pH). We wish to report the occurrence of hysteresis in a relatively simple polyelectrolyte molecule, poly(methacrylic acid) (PMA).

Experimental Section

Isotactic poly(methyl methacrylate) (PMMA) was synthesized according to the standard procedure.⁴ Molecular weights were estimated from intrinsic viscos-

ities of the CHCl_3 solutions using the relation $[\eta] = 4.8 \times 10^{-5} (\bar{M}_v)^{0.80}$ given by Goode.⁵ For the polymer used in this investigation we found $\bar{M}_v = 3.9 \times 10^5$.

The tacticity of the PMMA was determined from nmr spectra (100 MHz) of CHCl_3 solutions, run at 60°. The signals from the α -methyl group showed an isotactic triad content of 95–98%.

Hydrolysis of the ester was achieved by dissolving 6 g of the dry ester in 300 ml of oxygen-free 96% H_2SO_4 solution. After maintaining the system for 10 hr at room temperature the ester was dissolved. The temperature was raised to 60°; after 2 hr the solution was cooled to 0° and 1.2 l. of distilled water was added to the yellow solution. After filtering and washing, the

(1) Dedicated to Professor Dr. H. Veldstra on the occasion of his retirement from the chair of Biochemistry of the University of Leyden.

(2) A. Katchalsky, "International Symposium on Macromolecules: Leiden, 1970," Butterworths, London, 1971, p 368.

(3) A. Katchalsky, A. Oplatka, and A. Litan in "Molecular Architecture in Cell Physiology," T. Hayashi and A. G. Szent. Györgyi, Ed., Prentice-Hall, New York, N. Y., 1966, p 3.

(4) G. C. Overberger, *Macromol. Syn.*, 1, 29 (1963).

(5) W. E. Goode, F. H. Owens, R. P. Fellemann, W. H. Snijder, and J. E. Moore, *J. Polym. Sci.*, 46, 321 (1960).

polymer was dissolved in dimethylformamide and dialyzed for 3 weeks against the daily refreshed solvent in an effort to remove the yellow color of the polymer. The solution remained slightly yellow.

From the ir spectra of the sodium salt it was concluded that hydrolysis was complete. A portion of the obtained isotactic PMA was reesterified;⁶ the nmr spectrum of the resulting product was exactly the same as the spectrum of the PMMA used for the hydrolysis.

The nmr spectra of D₂O solutions of the Na salt of isotactic PMA yielded an estimated spin-coupling constant $J = 15$ Hz and an estimated shift of 0.1 Hz for the methylene protons in agreement with the results of Muroga, *et al.*⁷

Potentiometric titrations were performed using a Radiometer titrator (TTTI) and titrigraph (SBR 2) with a TTA 3 titration set allowing titration under N₂. The temperature was maintained at 20°. A calomel electrode K401 and a Type A glass electrode were used, both from Radiometer. In view of the length of the titration time (7 hr for a single titration curve) the calomel electrode was checked for KCl leakage which was found to be negligible for the PMA solutions used (these contained at least 0.02 equiv l.⁻¹ of KCl).

Results and Discussion

As shown in Figure 1 the potentiometric titration curve of isotactic PMA is irreversible. The vertical bandwidths of the acid and alkaline titration curves demonstrate a relatively serious irreproducibility for both pathways. However, the hysteresis loop is clearly present, there being a range of degrees of neutralization in which acid and alkaline titration curves never overlap even on repeated cycling. From Figure 2 it may be seen that after an initial time dependence the pH of solutions with equal degrees of neutralization prepared in the A and the B regions become stable with an appreciable pH difference.

It is therefore safe to conclude that either or both of the titration paths are along a series of metastable states.

Titration curves of isotactic PMA have of course been published before⁸ in connection with model calculations but only the alkaline titration curve (B) was given and the irreversibility of the potentiometric titration was not reported.

It has been demonstrated previously⁹⁻¹¹ that the potentiometric titration curve of atactic PMA can be consistently interpreted by assuming the existence of a compact conformation at low degrees of neutralization (the a form) and an extended conformation (b form) at high charge densities. In the region from 10 to 30% neutralization a conformational transition takes place. In the same region both the acid and the alkaline titration curves of isotactic PMA show the peculiar weak dependence of pH on the degree of neutralization that is characteristic for the conformational transition

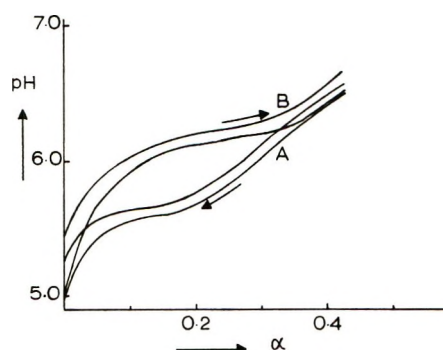


Figure 1. Boundaries for titration cycles of isotactic PMA: A, titration by addition of HCl; B, titration by addition of NaOH. The figure summarizes the results of six titration cycles on three different PMA solutions, each containing 0.002 equiv l.⁻¹ of PMA and 0.02 M KCl. The degree of neutralization of the polyacid is indicated by α .

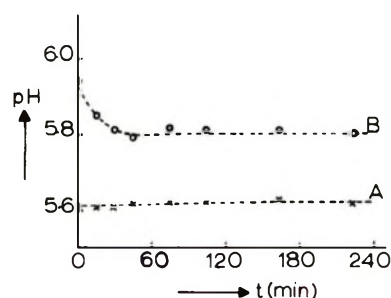


Figure 2. Time dependence of pH of solutions of isotactic PMA. The degree of neutralization (α) of both solutions is 0.22. B was prepared by addition of NaOH to a solution in which $\alpha \approx 0$ while A was obtained by addition of HCl to a PMA solution in which $\alpha = 0.44$. The solutions contained 4.4×10^{-3} equiv l.⁻¹ of PMA and 5×10^{-2} M KCl.

in atactic PMA. A similar transition therefore appears to occur in the isotactic polyacid. In this case, however, one or several irreversible processes take place during the titration cycle. Now, reversion of the titration direction after titrating along A to $\alpha \approx 0.2$ did not produce a significant hysteresis loop. The irreversible processes responsible for the hysteresis are therefore confined to the alkaline titration curve B and possibly a portion of the acid titration curve at very low degrees of neutralization.

It has been shown³ that the area enclosed by a hysteresis loop in a titration curve is, apart from a numerical factor, equal to the sum of the irreversible changes in the Gibbs free energy during the cycle which equals

(6) W. L. Miller, W. S. Brey, Jr., and G. B. Butler, *ibid.*, **54**, 329 (1961).

(7) Y. Muroga, I. Noda, and M. Nagasawa, *J. Phys. Chem.*, **73**, 667 (1969).

(8) M. Nagasawa, T. Murase, and K. Kondo, *ibid.*, **69**, 4005 (1965).

(9) J. C. Leyte and M. Mandel, *J. Polym. Sci., Part A-2*, **1879** (1964).

(10) J. C. Leyte, *Polym. Lett.*, **4**, 245 (1966).

(11) M. Mandel, J. C. Leyte, and M. G. Stadhouder, *J. Phys. Chem.*, **71**, 603 (1967).

the energy dissipation ΔQ . The relation with thermodynamically irreversible conformation changes in PMA (assuming all other processes to be fast on the time scale relevant for pH measurements) may be derived as follows.

The thermodynamic potential associated with the monomeric units⁹ will be indicated with $\mu(A)$ and $\mu(HA)$ for the units bearing dissociated and undissociated carboxylic acid groups, respectively. The different polymer conformations (random coil, ordered conformations, partially ordered conformations with a variable ordering range) in which the monomeric units may occur will be denoted with subscripts: $\mu(A)_i, \mu(A)_j, \dots$

For an isothermal and isobaric change in the Gibbs free energy G per mole of polyelectrolyte molecules we may then write

$$dG = \sum_i \{ \mu(A)_i dn_i^A + \mu(HA)_i dn_i^{HA} \} \quad (1)$$

Acid dissociation equilibrium will be assumed to be established within every class i of monomeric units.

$$\begin{aligned} \mu(H^+) &= \mu(HA)_i - \mu(A)_i = \\ &= \mu(HA)_j - \mu(A)_j = \dots \quad (2) \end{aligned}$$

The thermodynamic potential of the hydrogen ions $\mu(H^+)$ acts as a kind of common reservoir for the classes i, j, \dots , which equalizes the differences $\mu(HA)_i - \mu(A)_i$. Consequently, if at constant pH part of a polymer chain transforms irreversible (*e.g.*, $i \rightarrow j$) the change in chemical potential is the same for ionized and un-ionized groups

$$\mu(HA)_j - \mu(HA)_i = \delta\mu(HA)_{ji} = \delta\mu(A)_{ji} \quad (3)$$

Conservation of the number of monomeric units (Z) per macromolecule is expressed by

$$\sum_i (dn_i^A + dn_i^{HA}) = 0 \quad (4)$$

Elimination of all $\mu(A)_i$ from (1) yields (5) which is essentially the titration equation

$$\begin{aligned} -\mu(H^+) \sum_i dn_i^A = \\ dG - \sum_i \mu(HA)_i (dn_i^A + dn_i^{HA}) \quad (5) \end{aligned}$$

For a titration cycle returning the polymer molecules to their original states the integral of G along the cycle is zero

$$\oint \text{pH} d\alpha = -\frac{1}{2.303ZRT} \times \oint \sum_i \mu(HA)_i (dn_i^A + dn_i^{HA}) \quad (6)$$

Here $\alpha = \sum_i n_i^A / (\sum_i n_i^A + n_i^{HA})^{-1}$ is the degree of dissociation.

If conformational equilibrium is realized along the titration curve $\mu(HA)_i$ is independent of the index and, using eq 4, the right-hand side of eq 6 is zero. Any cyclic integral of pH corresponding to a titration cycle disappears of course in this case.

In the absence of conformational equilibrium every irreversible $i \rightarrow j$ transition contributes and an integral of pH along a closed loop will not equal zero. Designating the change in n_i^A due to a transformation $l \rightarrow i$ with dn_{il}^A and noting that the $(HA)_i \rightleftharpoons H^+ + (A)_i$ equilibrium does not contribute to $d(n_i^A + n_i^{HA})$ we have

$$dn_i^A + dn_i^{HA} = \sum_l (dn_{il}^A + dn_{il}^{HA}) = \sum_l dn_{il} \quad (7)$$

The dn_{il} are, of course, antisymmetric in the indices and using (7) and (3) we may therefore rewrite the summation in (6)

$$\begin{aligned} \sum_{i,l} \mu(HA)_i dn_{il} &= \frac{1}{2} \sum_{i,l} [\mu(HA)_i - \\ &= \mu(HA)_l] dn_{il} = \sum_{i<l} \delta\mu(HA)_{il} dn_{il} = \\ &= \sum_{i<l} \{ \delta\mu(HA)_{il} dn_{il}^{HA} + \delta\mu(A)_{il} dn_{il}^A \} \quad (8) \end{aligned}$$

Thus the cyclic pH integral may be related to the sum of the Gibbs free energy changes due to irreversible conformation changes involving the ionized and un-ionized monomeric units, respectively

$$\oint \text{pH} d\alpha = -\frac{1}{2.303ZRT} \oint \sum_{i<l} \{ \delta\mu(HA)_{il} dn_{il}^{HA} + \delta\mu(A)_{il} dn_{il}^A \} = -\frac{\Delta Q}{2.303ZRT} \quad (9)$$

The potentiometric results summarized in Figure 1 yielded $\Delta Q = -0.3RT/\text{mol}$ of monomeric units. Thus in one titration cycle of these solutions about 1.3×10^{-3} cal/ml is dissipated. At higher ionic strengths the absolute value of ΔQ tends to decrease. The determination of ΔQ is, however, as yet too inaccurate to admit a detailed discussion of small changes in its magnitude. The reversibility of potentiometric titration curves of atactic PMA has been checked before.⁹

We have found no evidence for appreciable hysteresis in syndiotactic PMA.¹² The irreversible behavior of the isotactic molecule is therefore not due to stereoregularity *per se* but depends on the exact structure of the polymer. At this moment a microscopic interpretation cannot be deduced from our results. From the partial reversibility of the acid titration curve (A) it seems that at low pH structures are formed which on recharging are metastable. This suggests that a large number of monomeric units are involved cooperatively in the breakdown of these structures.

(12) Unpublished results of this laboratory.

Molecular Structure of Ethanol-*d*₁ Solutions. A Near-Infrared

Study of Hydrogen Bonding

by Aaron N. Fletcher

Chemistry Division, Research Department (Code 6052), Naval Weapons Center,
China Lake, California 93555 (Received October 18, 1971)

Publication costs assisted by Naval Weapons Center, China Lake

By making use of the absorptivity of monomer and polymer bands, a near-infrared study of CH₃CH₂OD solutions has been made. Using *n*-decane as a solvent, formal concentrations of ethanol-*d*₁ were varied from between 0.01 and 17 *M* at -10, 25, and 60°. The hydrogen-bonded molecular structure of pure CH₃CH₂OD at 25° was found to consist primarily of monomer, acyclic tetramer, and cyclic tetramer in ratios of 1:3.4:10.9, respectively. The concentration of the (acyclic) dimer was estimated as being less than 0.01% of the formal concentration of CH₃CH₂OD. The average energy of the ²H hydrogen bonds was found to be 5.37 ± 0.03 and 4.83 ± 0.03 kcal for the acyclic and cyclic tetramer, respectively. The difference in these values suggests that ring strain exists in the cyclic tetramer, *i.e.*, that its O—H···O grouping is not linear. Concentration equilibrium quotients and most O—H absorption band wavelengths were found to be independent of the proportions of the solvent. More than one band was observed for the cyclic tetramer and the wavelengths of its bands were essentially constant over the 70° temperature range. Comparison with results of other studies showed that the extent of self-association in saturated hydrocarbon solvents for 1-alcohols was in the order 1-octanol > 1-butanol > ethanol-*d*₁ > methanol. Dimer and tetramers appear to be the major self-association species that can be detected in both the gas phase and in saturated hydrocarbon solvents for a wide range of nonhindered alcohols. It is proposed that cyclization of the acyclic tetramer, along with a symmetrical splitting of the cyclic tetramer when two hydrogen bonds are broken, is a major cause of the preponderance of the observed species.

Introduction

Background. The hydrogen-bonded molecular structure¹ of alcohols has not received the same attention as has that of water. This is somewhat surprising, since the alcohols, in contrast to water, are soluble over a wide range of concentrations in solvents that have a low degree of specific interaction with O—H groups. It should be possible to determine the hydrogen-bonded molecular structure of an alcohol by following experimental parameters that are sensitive to different self-association species from low concentrations, where only the monomer is found, up to the concentration of the neat alcohol. Unfortunately, however, most workers have so limited their range of concentrations in solution that a variety of self-association models could be fit equally well to their data.² Furthermore, most solution quantitative studies have used carbon tetrachloride or even more reactive solvents so that a wider range of concentrations would have invalidated the already questionable results.³

Self-association studies in the gas phase, where there are no limitations due to solvent interaction, have led to the monomer-dimer-tetramer as the model used to explain the experimental data for a number of monohydric alcohols.^{4,5} The major exception has been the work on methanol where Christian and coworkers,^{6,7} using vapor density and vapor pressure methods, proposed a monomer-trimer-octamer model. Fletcher,⁴

however, pointed out that the limited-range data at 25° of Cheam, Farnham, and Christian⁷ could have been fit equally well by the monomer-dimer-tetramer model and that their vapor density results showed no evidence for the octamer. Furthermore, the dimer and tetramer were necessary to account for the polymer absorption bands of methanol vapor in the fundamental O—H stretch region observed over the much wider range of concentrations available at 40, 80, and 120°.⁴ Eliminating the limited-range results of Tucker, Farnham, and Christian⁶ on methanol because of the questionability of their octamer, most quantitative experimental results limited to saturated hydrocarbon solvents favor a monomer-tetramer model for the self-association of monohydric nonhindered alcohols when the authors tested for specific *n*-mers.

(1) The hydrogen-bonded structure is considered here as being represented by the proportions of the major self-association species rather than by an averaging of distance between the molecules. These species are, of course, very short-lived. In this study "poly" will indicate any number greater than one. Polymer, thus, will be equivalent to oligomer, multimer, or *n*-mer.

(2) A. N. Fletcher and C. A. Heller, *J. Phys. Chem.*, **71**, 3742 (1967).

(3) A. N. Fletcher, *ibid.*, **73**, 2217 (1969).

(4) A. N. Fletcher, *ibid.*, **75**, 1808 (1971).

(5) N. S. Berman, *AIChE J.*, **14**, 497 (1968).

(6) E. E. Tucker, S. B. Farnham, and S. D. Christian, *J. Phys. Chem.*, **73**, 3820 (1969).

(7) V. Cheam, S. B. Farnham, and S. D. Christian, *ibid.*, **74**, 4157 (1970).

Fletcher and Heller⁸ found that the rate constant for the autoxidation of tetrakis(dimethylamino)ethylene was dependent over a range of 10^5 upon the first and fourth power of the concentration of the monomer of 1-octanol. More recently, Fletcher⁹ showed that this dependence could be explained in terms of a reactive monomer and acyclic tetramer and an inactive cyclic tetramer. Fletcher and Heller,² working in the near infrared, showed that their data for 1-butanol and 1-octanol could be explained by monomer and tetramers as the only species affecting material-balance equations at concentration up to that of the neat alcohol. Aveyard and Mitchell¹⁰ have successfully fit the tetramer equilibrium quotients and enthalpy data for 1-octanol in *n*-decane to heats of solution data at 20, 25, and 30°. Using nmr, Dixon¹¹ has found that the monomer-tetramer model was needed to account for the self-association of methanol in solutions of cyclohexane or cyclopentane. His data also indicated a significant interaction of methanol with carbon tetrachloride, benzene, and acetonitrile. Fletcher³ has found that the same self-association equilibrium quotients found for 1-octanol in *n*-decane² could be used for carbon tetrachloride solutions if a portion of the alcohol monomer molecules bonded to the carbon tetrachloride. It was found possible to account for the experimental data at concentrations up to 100% 1-octanol as long as a specific interaction between carbon tetrachloride and the alcohol monomer was taken into consideration.

Of the alcohols, only 1-octanol has had a quantitative determination made on both forms of the tetramer. The 1-octanol study was questioned by Murty¹² because of the absence of dimers in the mass balance equations and by Christian and coworkers^{6,13} because it used high-concentration data.

Objectives. The primary objective of the present work is not only to determine the hydrogen-bonded molecular structure of ethanol- d_1 but also to examine the constancy of self-association equilibrium quotients of a short-chain alcohol up to the concentrations of the neat alcohol. The short-chain alcohol will allow higher concentrations and dielectric constants than were possible for 1-octanol and will thus give a second and more stringent test of the validity of the use of concentration equilibrium quotients for the self-association of alcohols in a saturated hydrocarbon solvent. Ethanol- d_1 was chosen as it is the shortest chain monohydric alcohol that is completely miscible with *n*-decane at room temperature and allows examination in a different wavelength region than that used for 1-octanol.

On the basis of the previous gas-phase and saturated hydrocarbon studies, the tetramer will be considered as the major *probable* self-association polymer. It is recognized that other self-association species will be present in *small* amounts and that other self-association models could be fit to the data.¹⁴ However, since computer examination of a wide range of other possible self-

association models in studies on methanol, 1-butanol, and 1-octanol have already been performed, there appeared little to be gained by repeating such an analysis *if* evidence for the tetramer was again found over an extended range of concentrations.

Secondary objectives will be to obtain thermodynamic data for comparison with the results of other alcohols, to check whether acyclic and cyclic tetramers again can be observed, to look at the question of the dimer raised by Murty,¹² and to propose a new explanation for the preponderance of the observed species. An overall objective is to demonstrate that a self-consistent general picture for the self-association of monohydric alcohols can be seen *if evidence is limited to that from gas-phase and saturated hydrocarbon solvent studies.*

Experimental Section

Reagents. The $\text{CH}_3\text{CH}_2\text{OD}$ (99% D isotopic purity) was purchased from Stohler Isotope Chemicals (Montreal, Canada) and was used without further purification. The *n*-decane was obtained from Phillips Petroleum Co. and purified as described earlier.²

Equipment. A Cary Model 14RI spectrophotometer with the grating blazed for maximum energy at 1.6 μm was used to obtain the spectra. The widest spectral band width was calculated to be 0.7 nm. The instrument was equipped with a Cary Universal Slidewire. All calculations were determined with the full scale of the chart paper set equal to 20% transmittance. The absorption found for *n*-decane in the sample beam was used to determine 100% transmittance. A Cary Model 1444100 thermostatable cell jacket was used to hold the sample to within $\pm 0.2^\circ$ of the required temperature. Dispersed radiation was necessary (using the unfiltered lead sulfide detector) because undispersed radiation would heat the sample $5\text{--}6^\circ$ even when thermostated. Changing sample concentrations would have required changing the cell jacket temperatures for each sample using undispersed radiation owing to differences in heat absorption. A glove bag was used for all solution transfers. Both the glove bag and the Cary 14RI were continuously flushed with dry air. The reference beam always passed through a 1-cm cell filled with *n*-decane that was at "instrument" temper-

(8) A. N. Fletcher and C. A. Heller, *J. Catal.*, **6**, 263 (1966).

(9) A. N. Fletcher, *J. Phys. Chem.*, **73**, 3686 (1969).

(10) R. Aveyard and R. W. Mitchell, *Trans. Faraday Soc.*, **65**, 2645 (1969).

(11) W. B. Dixon, *J. Phys. Chem.*, **74**, 1396 (1970).

(12) T. S. S. R. Murty, *Can. J. Chem.*, **48**, 184 (1970).

(13) S. D. Christian and E. E. Tucker, *J. Phys. Chem.*, **74**, 214 (1970).

(14) A logical rationale is presented in the present study to account for deviations from the tetramer relationships based upon the effects of overlap from neighboring absorption bands. The evidence for this interference is most easily seen through an examination of spectra obtained over a range of temperatures. Without the restraint of an *a priori* selection of the tetramer as a probable major species, each temperature would likely yield a different "best" self-association model owing to the effects of band overlap.

ature. A single 1-cm Infracell (with a tight-fitting Teflon stopper) was used for the sample. The cell was always almost completely filled so as to minimize any of the head-space loss problems reported by Swenson.¹⁵

Procedure. Samples were prepared by weight. Volumes were calculated assuming zero volume change upon mixing. Densities used for -10 , 25 , and 60° were 0.7528 , 0.7270 , and 0.7004 for *n*-decane and 0.8308 , 0.8010 , and 0.7710 for ethanol- d_1 , respectively.¹⁶ Measurements were made at the exact wavelengths indicated independent of peak location. As exact peak location was not the intent of the present study, wavelengths given only "name" the bands, *i.e.*, the listed wavelengths may or may not correspond to the exact wavelength of the peak. Band integration was not performed for two reasons: (a) the breadths of the absorption bands are quite wide compared to the resolution of the spectrophotometer making integration unnecessary and (b) there is a considerable amount of band overlap in some regions, making normal band separation techniques uncertain. The effects of band overlap were tested by means of an intercomparison of absorbance values at different wavelengths, concentrations, and temperatures making use of the premise that the tetramer is a probable major self-association species.

Results

Preliminary Wavelength Assignments. The spectra of ethanol- d_1 at a variety of formal¹⁷ concentrations in *n*-decane are shown in Figure 1. The monomer band peak at low concentrations is at $1.89 \mu\text{m}$ as is evident by the slow decrease in the intensity of this peak compared to those of the polymer bands seen at longer wavelengths. Bonner¹⁸ finds this band at $1.891 \mu\text{m}$ for CH_3OD . The uniform shape of the polymer bands at different concentrations is of particular note. A plot of the monomer absorbance measured at $1.89 \mu\text{m}$ vs. the formal ethanol- d_1 concentration in Figure 2 shows from the equivalence of the 60 and 25° results at low concentrations that the molar absorptivity of the monomer is 0.808 , independent of temperature. The value of the molar absorptivity at -10° also appears to approach 0.808 . The molar absorptivity of the O-D monomer of ethanol- d_1 is half the 1.65 found for the O-H of 1-octanol.² Swenson¹⁹ found this 1:2 relationship for the integrated absorptivities of the hydrogen-bonded O-D and O-H bands of water, and Bonner¹⁸ also reported it for the nonintegrated monomer bands of methanol.

Two phases formed for high concentrations of ethanol- d_1 , limiting the amount of data at -10° . Figure 3 shows that the peak found at $1.86 \mu\text{m}$ is linearly dependent upon the formal alcohol concentration, but that its molar absorptivity increases with decreasing temperature. This increase proved to be an annoying problem, as the $1.86\text{-}\mu\text{m}$ peak completely obscures the monomer band in neat ethanol- d_1 at -10° (Figure 4).

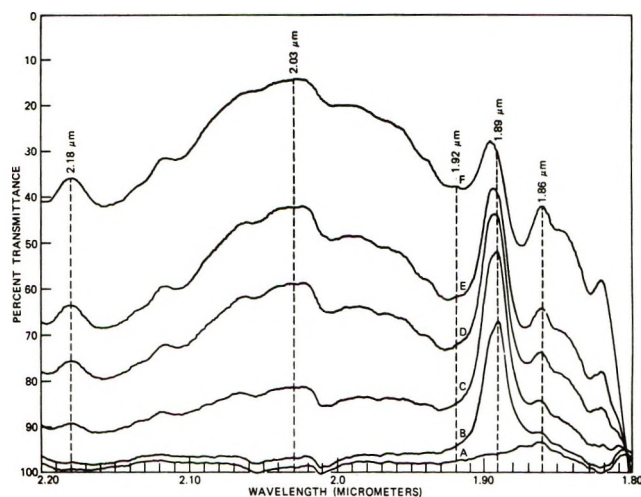


Figure 1. Spectra of ethanol- d_1 in *n*-decane at varying concentrations at 60° in a 1-cm cell; *n*-decane in a 1-cm cell in the reference beam; formal (added) ethanol- d_1 concentration in moles liter $^{-1}$: (A) 0.0, (B) 0.28, (C) 1.43, (D) 3.29, (E) 5.11, (F) 10.98.

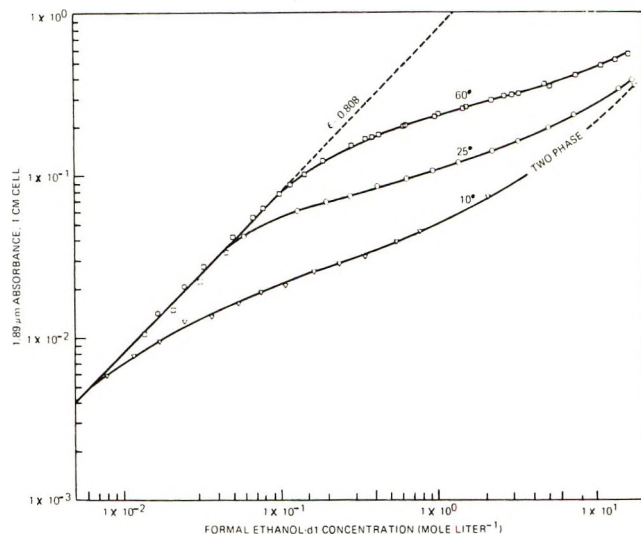


Figure 2. Effect of concentration upon absorbance at the wavelength of the first overtone of the monomer; *n*-decane in a 1-cm cell in the reference beam.

Since the $1.86\text{-}\mu\text{m}$ peak is a linear function of the formal alcohol concentration, it must be a (combination) band that does not involve the O-H stretch vibration.

(15) C. A. Swenson, *J. Phys. Chem.*, **71**, 3108 (1967).

(16) The density of ethanol- d_1 was estimated using the temperature coefficient for $\text{C}_2\text{H}_5\text{OH}$ and the 25° density of $\text{C}_2\text{H}_5\text{OD}$ listed in the "Handbook of Chemistry and Physics," 47th ed, Chemical Rubber Publishing Co., Cleveland, Ohio. The density of *n*-decane was that reported in the "International Critical Tables," Vol. III, McGraw-Hill, New York, N. Y., 1928, p 30. The zero volume change approximation usually results in an error not greater than 1%.³

(17) The term formal (*F*) is used to express the mathematical concentration of the added material without consideration of any chemical reaction within the solution. Molar (*M*) is used to express known (tentative or real) concentrations.

(18) O. D. Bonner, *J. Chem. Thermodyn.*, **2**, 577 (1970).

(19) C. A. Swenson, *Spectrochim. Acta*, **21**, 987 (1965).

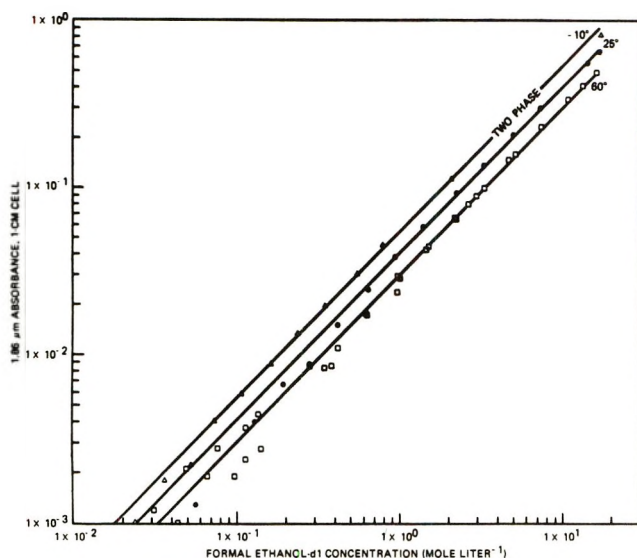


Figure 3. Absorbance at $1.86 \mu\text{m}$ as a function of the concentration of ethanol- d_1 ; n -decane in a 1-cm cell in the reference beam.

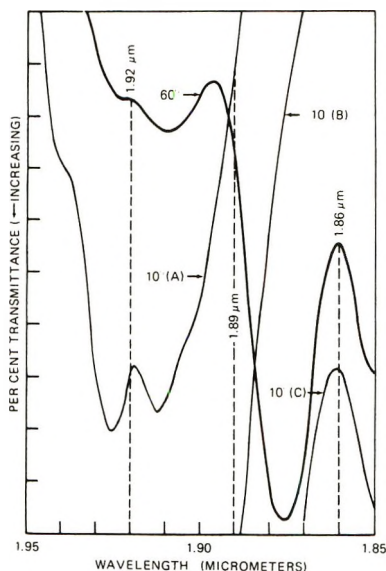


Figure 4. A comparison of absorption at -10 and 60° for neat ethanol- d_1 in a 1-cm cell, ordinate range: 60° , 20–40%; -10° (A), 40–60%; -10° (B), 20–40%; -10° (C), 0–20%. n -Decane in a 1-cm cell in the reference beam.

The uniform band shape with changing concentrations of the polymer observed in Figure 1 is tested further in Figure 5. The uniform ratio of the absorbance at $2.03 \mu\text{m}$, $a_{2.03}$, to that found at $2.18 \mu\text{m}$, $a_{2.18}$, indicates that there is no change in the proportions of the molecular species causing these peaks with a change in concentration. The change in the ratio $a_{2.03}/a_{2.18}$ with temperature, however, shows that at least one of the peaks represents more than one self-association species (assuming that the absence of a temperature dependence in the molar absorptivity of the monomer also occurs for the polymer bands). As the monohydric alcohols only have two bonding sites, they can only form two

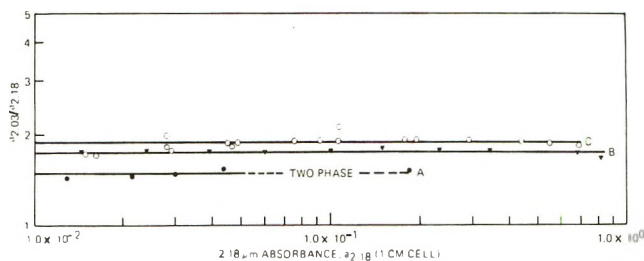
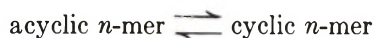


Figure 5. Comparison of absorbance ratios as a function of absorbance at $2.18 \mu\text{m}$. Line A represents -10° data, B represents 25° data, and C represents 60° data. n -Decane in a 1-cm cell in the reference beam.

species, acyclic or cyclic, having the same number, n , of monomer units. Thus the variation of $a_{2.03}/a_{2.18}$ with temperature reflects the equilibrium



$$K_{n_a, n_c} = A_{n_c}/A_{n_a} \quad (1)$$

where A_{n_a} represents the molar concentration of the acyclic n -mer, A_{n_c} represents the concentration of the cyclic n -mer, and K_{n_a, n_c} is the corresponding equilibrium quotient. Since the $2.18\text{-}\mu\text{m}$ band retains its maximum at the same wavelength at all three temperatures (Figure 6), it will be considered as representing a single self-association polymer. As the cyclic tetramer was found to absorb at the longest wavelengths for 1-octanol, the $2.18\text{-}\mu\text{m}$ band will tentatively be assigned to the cyclic tetramer. The shift in the location (Figure 6), of the major polymer band peaks at about 2.03, 2.04, and $2.06 \mu\text{m}$ at 60 , 25 , and -10° , respectively, is additional evidence that $a_{2.03}$ represents absorption from more than one species.

The "free" end of acyclic species, $\cdots\text{O}-\text{H}$, is the only $\text{O}-\text{H}$ group of a monohydric alcohol self-association polymer not having the proton involved in a hydrogen bond. Its absorption band is expected at wavelengths close to that of the monomer. The closest polymer peak can be seen to absorb at about $1.92 \mu\text{m}$ for the -10° results in Figure 4, and it will be tentatively assigned to the free end of the acyclic tetramer. The $1.92\text{-}\mu\text{m}$ absorption band partially overlaps the monomer band and causes the apparent shift of the monomer peak to longer wavelengths with increasing concentration (Figure 1). Since the frequencies of the $\text{O}-\text{H}$ peaks are further apart by a factor of about $\sqrt{2}$ compared to $\text{O}-\text{D}$, this degree of overlap was not observed in the 1-octanol studies. The absorbance at $1.92 \mu\text{m}$ is tested further in Figure 7, where it is shown to vary in the same manner as the $2.18\text{-}\mu\text{m}$ absorption peak over a range of concentrations. The ratio of $a_{1.92}/a_{2.18}$ increases at lower concentrations due to the overlap of the $1.92\text{-}\mu\text{m}$ band by the monomer band at $1.89 \mu\text{m}$ (and perhaps by the $1.86\text{-}\mu\text{m}$ band). This is evident by the curvature of the ratio $a_{1.92}/a_{2.18}$ throughout all of the 60° results, where the monomer values

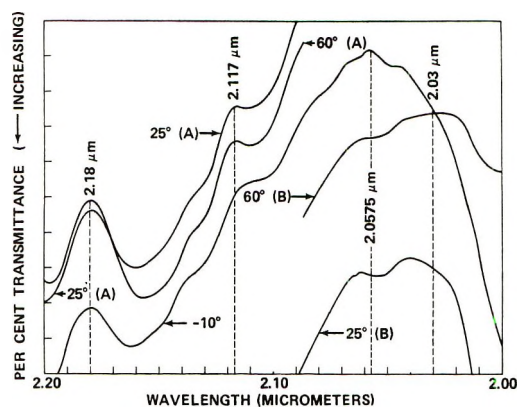


Figure 6. Effect of temperature on peak wavelengths of ethanol- d_1 . Formal concentrations in moles liter $^{-1}$: 60°, 16.37 (neat); 25°, 3.30; -10°, 2.07. Per cent transmittance ranges: 60° (A), 10-30; 60° (B), 0-20; 25° (A), 60-80; 25° (B), 40-60; -10°, 60-80. n -Decane is used as the solvent for the 25 and -10° solutions and is in a 1-cm cell in the reference beam.

are larger (Figure 2) for a given formal concentration of ethanol- d_1 than at lower temperatures, *i.e.*, the lower the temperature, the larger the range of constant $a_{1.92}/a_{2.18}$ values.

Although the 1.86- and the 1.92 μm -bands interfere with the monomer absorption at 1.89 μm , it is still possible to determine regions at low concentrations where the interference is minimal. Thus the ratio of $a_{2.18}/(a_{1.89})^4$ is constant (Figure 7) over more than a tenfold formal concentration range at 25 and 60°. The data are consistent with the tetramer as a major self-association species, assuming that Beer's law holds for the polymer (it was shown to hold for the monomer and the 1.86- μm peak) and that the mass action law is valid

$$A_n/(A_1)^n = K_{1,n} \quad (2)$$

$$a_n/(a_1)^n = K_{1,n}(\epsilon_n)/(\epsilon_1)^n = \text{constant} \quad (3)$$

where $K_{1,n}$ is a mass action law equilibrium quotient between the monomer having absorbance a_1 and the n -mer having absorbance a_n , while ϵ_1 and ϵ_n are the molar absorptivities of the monomer and the n -mer, respectively.

A fundamental question remains as to whether n -mers other than the tetramer are also present in significant amounts. The variation of the concentrations in Figure 1 does not show the development of any obvious new polymer bands. If we write a material balance equation for the formal concentration of ethanol- d_1 , A_0

$$A_0 = A_1 + 2A_2 + 3A_3 + 4A_4 + \dots + nA_n = A_1 + \bar{A}_p \quad (4)$$

$$A_0 - A_1 = \bar{A}_p \quad (5)$$

where \bar{A}_p is the formal total polymer concentration, then the ratio $\bar{A}_p/(A_1)^4$ will be a constant only if all self-association polymers other than the tetramers have

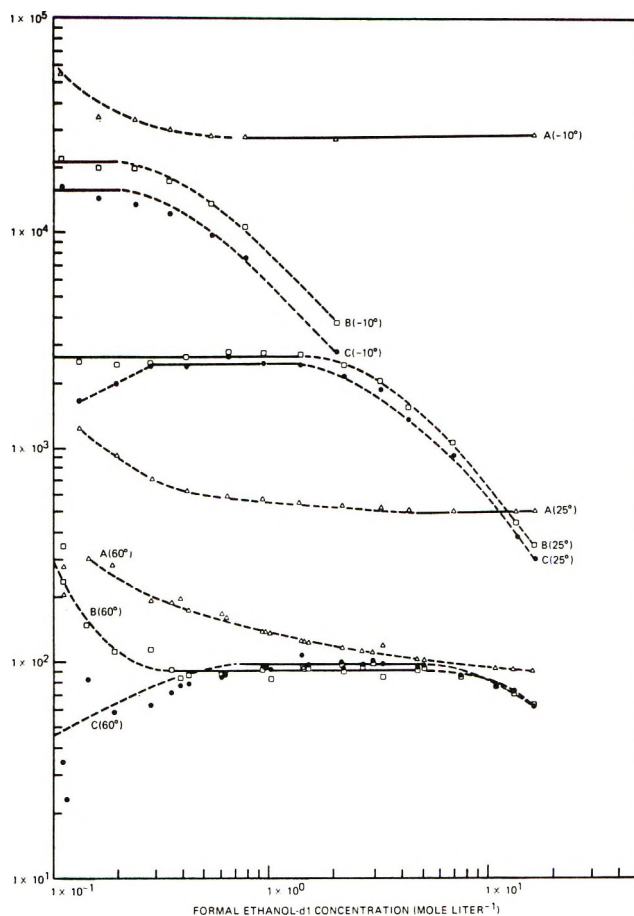


Figure 7. Evidence of band overlap at different concentrations. Curves A: absorbance at 1.92 μm divided by absorbance at 2.18 μm : A (60°) $10^{-2} \times$ ordinate scale shown, A (25°) $10^{-3} \times$ ordinate, A (-10°) $10^{-5} \times$ ordinate. Curves B: absorbance at 2.18 μm divided by the fourth power of the absorbance at 1.89 μm : B (60°) to scale, B (25°) $10^{-1} \times$ ordinate, B (-10°) to scale. Curves C: $\bar{A}_p/(A_1)^4$, where A_1 is calculated assuming that the absorbance at 1.89 μm is entirely due to the monomer. Solid lines represent regions relatively free from significant amounts of overlap. Dashed lines show regions of overlap or bias due to effect of low absorbance values.

insignificant concentrations. Curves C in Figure 7 show that the function $\bar{A}_p/(A_1)^4$ is a constant over a range of concentrations and that it deviates from a constant value in the same manner as does $a_{2.18}/(a_{1.89})^4$ shown by curves B; *i.e.*, the deviation of $\bar{A}_p/(A_1)^4$ appears only to be due to the interference in the measurement of the monomer peak rather than being due to additional polymer species.

Determination of the Molar Absorptivities of the Acyclic and Cyclic Tetramers. Considering that the formal polymer concentration is primarily tetramer and applying Beer's law to solutions in a 1-cm cell

$$\bar{A}_p = \bar{A}_{4a} + \bar{A}_{4c} = a_{4a}/\bar{\epsilon}_{4a} + a_{4c}/\bar{\epsilon}_{4c} = a_{1.92}/\bar{\epsilon}_{1.92} + a_{2.18}/\bar{\epsilon}_{2.18} \quad (6)$$

or

$$a_{2.18}/\bar{A}_p = \bar{\epsilon}_{2.18} - (\bar{\epsilon}_{2.18}/\bar{\epsilon}_{1.92})(a_{1.92}/\bar{A}_p) \quad (7)$$

Table I: Formal Equilibrium Constants of Ethanol-*d*₁

Temp, °C	$\bar{K}_{1,4c}, F^{-1}$	$\bar{K}_{1,4a}, F^{-1}$	$\bar{K}_{1,4}, F^{-1}$	
			Using polymer bands ($\bar{K}_{1,4c} + \bar{K}_{1,4a}$)	Using ($A_0 - A_1$)/(A_1) ^a
60	$6.02 \pm 0.07 \times 10^1$	$0.363 \pm 0.004 \times 10^2$	$9.65 \pm 0.11 \times 10^1$ [18] ^a	$9.50 \pm 0.13 \times 10^1$ [15]
25	$1.73 \pm 0.03 \times 10^3$	$0.536 \pm 0.009 \times 10^3$	$2.27 \pm 0.04 \times 10^3$ [7]	$2.42 \pm 0.05 \times 10^3$ [5]
-10	$1.40 \pm 0.07 \times 10^5$	$0.239 \pm 0.012 \times 10^5$	$1.64 \pm 0.08 \times 10^5$ [5]	$1.56 \pm 0.05 \times 10^5$ [5]

^a Values in brackets are the number of replications used to determine the mean values. The \pm values are estimated standard deviations of the mean value.

where the bar over a symbol indicates a formal¹⁷ quantity. The best values (Figure 7) of $a_{1,92}$ occur for the neat ethanol-*d*₁ at 25 and -10°, but this is the concentration region where there is the greatest amount of overlap occurring at 1.89 μm caused by the 1.92- and the 1.86- μm bands. However, by using the known ratio of $a_{2,18}/(a_{1,89})^4$ determined at low concentrations (21,140 and 260 for -10 and 25°, respectively), it is possible to calculate what the monomer portion of $a_{1,89}$ should be knowing $a_{2,18}$. Using the corrected values, A_1' was calculated (using $\epsilon_{1,89} = 0.808$) and \bar{A}_p' determined by means of eq 5 for the neat solutions at 25 and -10°. The corrections in \bar{A}_p' only changed \bar{A}_p values in the third place. Using eq 7, $\bar{\epsilon}_{2,18}$ was found to be $0.0642 \text{ cm}^{-1} F^{-1}$ and $\bar{\epsilon}_{1,92}$ equaled $0.102 \text{ cm}^{-1} F^{-1}$.

Determination of Thermodynamic Values. Knowing the formal (or molar) absorptivities of the cyclic and acyclic tetramer, it is a simple matter to calculate the equilibrium constants

$$\bar{K}_{1,4c} = a_{2,18}(\epsilon_{1,89})^4 / (a_{1,89})^4 \bar{\epsilon}_{2,18} = 6.64 a_{2,18} / (a_{1,89})^4 \quad (8)$$

and

$$K_{1,4a} = K_{1,4c}(\bar{\epsilon}_{2,18} / \bar{\epsilon}_{1,92})(a_{1,92} / a_{2,18}) = 0.63 \bar{K}_{1,4c}(a_{1,92} / a_{2,18}) \quad (9)$$

The ratio $a_{1,92}/a_{2,18}$ for the neat alcohol was used in eq 9, since ratios at this concentration should have the smallest error due to overlap from the monomer band at 1.92 μm (Figure 7). Table I compares the $\bar{K}_{1,4}$ values calculated from eq 8 and 9 with $\bar{K}_{1,4}$ determined using only A_0 and A_1 values. There is only an average relative error of 4.3% between these two types of determination of $\bar{K}_{1,4}$. Table II presents the thermodynamic relationships calculated from least-squares plots using molar quantities.

Since the cyclic tetramer has one more hydrogen bond than the acyclic, its ΔH° of formation should also be larger. As this is the order observed in Table II, the tentative wavelength assignments at 1.92 and 2.18 μm to the acyclic and cyclic species are considered as being correct. The question as to whether the acyclic band is due to the free end still remains to be decided.

Discussion

Effect of Saturated Hydrocarbon Solvent Concentration

Table II: Thermodynamic Relationships^a for the Self-Association of Ethanol-*d*₁ at 25°

Tetramer formed	$-\Delta G^\circ$, kcal/mol	$-\Delta H^\circ$, kcal/mol	$-\Delta S^\circ$, eu
Cyclic	3.60 ± 0.01	19.3 ± 0.1	52.4 ± 0.3
Acyclic	2.90 ± 0.01	16.1 ± 0.1	44.0 ± 0.4

^a $-\Delta G^\circ$ values were calculated from the molar equivalents of $\bar{K}_{1,4c}$ and $\bar{K}_{1,4a}$ of Table I. $-\Delta H^\circ$ and $-\Delta S^\circ$ values were determined from least-squares plots using the molar form of the 30 equilibrium quotients used to determine the average polymer band \bar{K} values in Table I.

upon the Self-Association Equilibrium Quotients. It has been argued by Christian and Tucker¹³ that evidence for the tetramer of 1-octanol was not valid, since Beer's law and the mass action equilibrium quotients should be limited to dilute solutions. The linear plots of the absorbance at 1.86 μm extending up to the neat alcohol concentration at three different temperatures (Figure 3) clearly demonstrate that Beer's law is not necessarily restricted to dilute solutions. Since the tetramer has been shown to be a major self-association species in the gas-phase studies of methanol, where special care to reduce absorption band overlap of the monomer by acyclic polymers was possible,⁴ it would appear that measurements made at high concentrations of 1-octanol were not just "by chance" when they also gave evidence of tetramers. Thus, there is prior evidence of alcohol self-association quotients being constant up to the concentration of the neat alcohol. With ethanol-*d*₁, however, the neat alcohol is about 17 *M* and has a dielectric constant of about 24. Furthermore, band overlap prevents the determination of the monomer concentration at the higher concentrations of alcohol. Thus the conditions are more stringent and the evidence is more difficult to acquire than for 1-octanol. The fourth-order relationship can be shown to hold for formal ethanol-*d*₁ concentrations of 0.05 at -10° up to only around 5.0 *M* at 60°. But although the monomer-tetramer equilibrium is limited in range to the lower concentrations because of band overlap, the acyclic-cyclic tetramer equilibrium is not. Thus we can see in Figures 5 and 7 that the relative proportions of the acyclic to cyclic tetramer are not changed at con-

centrations greater than 5 *F* in ethanol-*d*₁. Equally important, the use of the molar absorptivities determined at 1.92 and 2.18 μm using the data from the neat alcohol leads to the same total tetramer equilibrium quotients, $\bar{K}_{1,4}$, as those determined at the low concentrations using only the formal alcohol and monomer concentrations (Table I). This agreement also confirms that the molar absorptivities of the polymers, like the monomer, were independent of temperature. That the band positions of the peaks, other than that of the overlapped monomer and acyclic tetramer at 1.92 μm , do not change wavelengths with different concentrations (Figures 1 and 6) is additional evidence of a negligible "solvation." More evidence of the effect of "inert" solvents upon hydrogen-bond equilibrium can be seen in studies on mixed dimers. Fletcher²⁰ has pointed out that equilibrium quotients of studies by Buchowski, *et al.*,²¹ and Huong, *et al.*,²² showed little variation using the solvents that did not have any atoms with nonbonding electrons in spite of a range of solubility parameters for these solvents.

As to why the saturated hydrocarbon solvent concentration has such a small effect upon the concentration equilibrium quotients for self-association, it should be noted that the major change in environment upon increasing the concentrations of alcohol is caused by the species whose equilibrium is under study. This is in contrast to the usual situation in water solutions, where the equilibrium of charged species is markedly affected by the variation in the unknown structure of the polar (and polarizable) solvent. But, even in water, it is possible to have a minimal "solvation" effect with uncharged species. Both sucrose and hydrogen peroxide show a constant freezing point depression per mole up to very high concentrations—10 *M* in the case of hydrogen peroxide.²³

Use of the equilibrium quotients of Table I allows a determination of the major self-association species at the concentration of the neat alcohol. For example, the molar ratio of monomer:acyclic tetramer:cyclic tetramer is found to be 1:3.4:10.9 at 25°.

Comparison of Equilibrium Quotients and Bond Energies of Different Alcohols. There is now sufficient evidence to compare the $K_{1,4}$ equilibrium constants for a range of alcohols in saturated hydrocarbon solvents using the data from other studies.^{2,11,24} Table III shows that the extent of self-association is in the order 1-octanol > 1-butanol > ethanol-*d*₁ > methanol. Straight-chain alcohols have a higher degree of self-association than a branched-chain alcohol. Steric hindrance no doubt plays a major role in this difference, but electron inductomeric effects should oppose the steric hindrance, as suggested by the above series. Table IV shows the values from other studies^{6,7,25-28} of the equilibrium quotients for 1-alcohols that have been determined in the gas phase. The order of the

Table III: Comparison of Monomer-Tetramer Equilibrium Constants, $K_{1,4}$, for Different Alcohols in Saturated Hydrocarbon Solvents

Alcohol	$K_{1,4}, M^{-3}$	Method	Ref
25°			
Methanol	$4.0 \pm 0.3 \times 10^2$	Nmr	11
Ethanol- <i>d</i> ₁	$5.7 \pm 0.1 \times 10^2$	Ir	This study
1-Octanol	$7.8 \pm 0.4 \times 10^2$	Ir	2
27°			
<i>tert</i> -Butyl alcohol	3.2×10^2	Ultra-sonic	24
30°			
Ethanol- <i>d</i> ₁	$3.4 \pm 0.1 \times 10^2$	Ir	This study
1-Butanol	$4.3 \pm 0.5 \times 10^2$	Ir	2
1-Octanol	$5.2 \pm 0.3 \times 10^2$	Ir	2

Table IV: Gas-Phase Equilibrium Constants of 1-Alcohols at 25°

Alcohol	$K_{1,2}, M^{-1}$	$K_{1,4}, M^{-3}$	Ref
Methanol	0.65	1.29×10^4	4
	1.8	7.58×10^3	25
	1.4	1.4×10^4	26
	Av 1.3	1.1×10^4	
Ethanol	1.8	3.5×10^4	27
	2.3	1.5×10^4	25
	Av 2.1	2.5×10^4	
Propanol	3.3	1.39×10^6	28

equilibrium quotients is the same as was found in the saturated hydrocarbon solvents.

The average ²H bond energy of the cyclic tetramer for ethanol-*d*₁ was found to be 4.83 ± 0.03 kcal compared to the value of 5.1 kcal found for the ¹H bond of 1-octanol. The values for the acyclic tetramer were 5.37 ± 0.03 and 5.5 kcal, respectively.

Wavelength Assignments. If the 1.92- μm band is due to the "free" $\cdots\text{O}-\text{D}$ group of the acyclic tetramer, then the 1.89- μm absorption of the monomer will be relatively free from interference by polymer end-group absorption. On the other hand, if the 1.92- μm band is due to the $\text{O}-\text{D}\cdots$ group of the acyclic tet-

(20) A. N. Fletcher, *J. Phys. Chem.*, **74**, 216 (1970).

(21) H. Buchowski, J. Devaure, P. V. Huong, and J. Lascombe, *Bull. Soc. Chim. Fr.*, 2532 (1966).

(22) P. V. Huong, N. Platzter, and M. L. Josien, *J. Amer. Chem. Soc.*, **91**, 3669 (1969).

(23) J. H. Hildebrand, *J. Chem. Educ.*, **48**, 224 (1971).

(24) R. S. Musa and M. Eisner, *J. Chem. Phys.*, **30**, 227 (1959).

(25) C. N. Kretschmer and R. Wiebe, *J. Amer. Chem. Soc.*, **76**, 2579 (1954).

(26) W. Weltner and K. S. Pitzer, *ibid.*, **73**, 2606 (1951).

(27) G. M. Barrow, *J. Chem. Phys.*, **20**, 1739 (1952).

(28) J. F. Mathews and J. J. McKetta, *J. Phys. Chem.*, **65**, 758 (1961).

ramer, then the whole approach of this study fails, as the shorter wavelength $\cdots\text{O}-\text{D}$ group would overlap the $1.89\text{-}\mu\text{m}$ band of the monomer. In the liquid-phase study of 1-butanol and 1-octanol, it was argued that the regular fourth-order relationships could not have occurred if there had been overlap of the $\cdots\text{O}-\text{H}$ group with that of the monomer. This argument also applies for ethanol- d_1 solutions.

The observation of Bellamy and Pace²⁹ that the $\cdots\text{O}-\text{H}$ of the acyclic dimer of methanol in CCl_4 occurs only 5 cm^{-1} from the wavelength of the monomer in the $\text{O}-\text{H}$ stretch fundamental region, on the other hand, could be considered to be in conflict with the above "monomer only" argument. It should be noted, however, that both the $\text{O}-\text{H}\cdots$ and the $\cdots\text{O}-\text{H}$ end groups absorb at shorter wavelengths than do the $\cdots\text{O}-\text{H}\cdots$ groups.³⁰ Consequently, the $1.92\text{-}\mu\text{m}$ band for ethanol- d_1 (and the $1.43\text{-}\mu\text{m}$ band for 1-octanol) should be due to one of these two end groups but $1.92\text{ }\mu\text{m}$ is too close to the monomer wavelength for it to be assigned to the $\text{O}-\text{D}\cdots$ end group based upon the data of Bellamy and Pace. The 83-cm^{-1} separation from the monomer is not only less than the 152-cm^{-1} shift that can be estimated³¹ if the solvent had been CCl_4 , but is markedly less than the 320-cm^{-1} shift if we use Glew and Rath's data³² for the monomer in an inert solvent and the $\text{O}-\text{H}\cdots$ in methanol.

Further evidence for a minimal amount of end-group absorption at the wavelength of the monomer in the overtone region can be seen at low temperatures, where the total absorption at the wavelength of the monomer becomes less than any of the self-association polymer absorption bands, e.g., -5° results of Figure 2 in ref 2. Thus the $1.92\text{-}\mu\text{m}$ absorption band is assigned to the free $\cdots\text{O}-\text{D}$ end of the acyclic tetramer, and it is concluded that the additional hydrogen-bonded groups of the acyclic tetramer shift the absorption of one, and likely both, of the $\text{O}-\text{H}$ end groups to longer wavelengths than those found for the acyclic dimer. Because of its low concentrations, dimer absorption has never been reported in the overtone region.

The shift of the $\text{O}-\text{H}$ σ bonds to longer wavelengths, the Badger-Bauer relationship, has been taken to indicate the weakening of the σ bond due to the formation of a hydrogen bond.³⁰ Hydrogen bonds involving both the hydrogen and the oxygen of an $\text{O}-\text{H}$, forming a doubly bonded $\text{O}-\text{H}$, are expected to lead to even stronger hydrogen and weaker σ bonds.^{29,30} $\text{O}-\text{D}$ absorption of the cyclic tetramer being observed at a longer wavelength than that of the acyclic would consequently appear to be in conflict with the present $-\Delta H^\circ$ results, showing an average bond energy for the cyclic tetramer that is less than that of the acyclic tetramer. This same conflict was observed for the tetramer of 1-octanol, but it was concluded that band overlap had caused errors in the enthalpy data. The more distinct peaks for ethanol- d_1 and the same order of

the enthalpy data suggest that the energy of a hydrogen bond for a doubly bonded $\text{O}-\text{H}$ for the cyclic species may indeed be less than that of the acyclic. As only two of the $\text{O}-\text{H}$ groups of the acyclic tetramer are doubly hydrogen bonded, $\cdots\text{O}-\text{H}\cdots$, the energy for these specific bonds should be even higher than the average 5.37 kcal . The ring formed by the cyclic tetramer would not be planar if it has linear $\text{O}-\text{H}\cdots\text{O}$ angles. It is quite possible that steric and electronic repulsion would force the ring toward a planer configuration, bending the $\text{O}-\text{H}\cdots\text{O}$ angle and thus weakening the hydrogen bond. The absorption of the cyclic tetramer at longer wavelengths than the acyclic could consequently reflect the effect upon the $\text{O}-\text{H}$ σ bond by the ring strain rather than because its $\cdots\text{O}-\text{H}\cdots$ hydrogen bonds were stronger than that of the acyclic tetramer. Moreover, since the Badger-Bauer relationship is known to fail for many systems,³⁰ the relative frequencies of the $\cdots\text{O}-\text{H}\cdots$ bands of the acyclic and cyclic tetramer should not be given too much consideration. This is particularly so because although the σ $\text{O}-\text{H}$ bonds of the cyclic tetramer can be considered equivalent, in contrast to the four² (or at least three) different σ $\text{O}-\text{H}$ bonds of the acyclic tetramer, this does not mean that the cyclic σ bonds should necessarily have only a single absorption band. The band at $2.18\text{ }\mu\text{m}$ was selected to measure the cyclic tetramer because of its isolation from the other bands (Figures 1 and 6). In a study on 1-octanol, a wavelength ($1.61\text{ }\mu\text{m}$) on the low-energy side of the broad polymer band was selected as a region where a high proportion of cyclic species might have been expected.² A corresponding region for ethanol- d_1 would be about $2.065\text{ }\mu\text{m}$ (Figure 1). Dividing $a_{2.18}$ by the absorption at $2.065\text{ }\mu\text{m}$, $a_{2.065}$, results in average ratios of 0.589 ± 0.003 [14], 0.574 ± 0.003 [10], and 0.603 ± 0.006 [5] at 60 , 25 , and -10° , respectively. The integers in brackets represent the number of ratios examined. Thus $a_{2.065}$ could have been used rather than $a_{2.18}$ to measure the cyclic tetramer, and it can be seen that widely separated absorption bands can be attributed to the cyclic tetramer. Thus the major $\cdots\text{O}-\text{H}\cdots$ bands of the acyclic and cyclic tetramer are fairly close to each other (Figure 6). The specific vibrational modes causing the observed frequencies is outside the scope of the present study.

The Monomer-Acyclic Dimer-Acyclic Tetramer-Cyclic Tetramer General Self-Association Model for Non-hindered Alcohols. Peak location and mass action equilibria have been used to show evidence for the dimer of 1-alcohols in the gas phase^{4,33} and in solu-

(29) L. J. Bellamy and R. J. Pace, *Spectrochim. Acta*, **22**, 525 (1966).

(30) S. N. Vinogradov and R. H. Linnell, "Hydrogen Bonding," Van Nostrand Reinhold, New York, N. Y., 1971, Chapters 3 and 5.

(31) Estimated by doubling the frequency shift in the fundamental region and dividing by $\sqrt{2}$ to take in the effect of ^2H in place of ^1H .³⁰

(32) D. N. Glew and N. S. Rath, *Can. J. Chem.*, **49**, 837 (1971).

tion.³⁴⁻³⁶ Bond energies,³⁵ band frequencies,²⁹ and relative peak intensities^{37,38} have been used as evidence that the dimer is acyclic; the cyclic dimer has been opposed by theoretical arguments.³⁹

Fletcher and Heller² have been critical of studies that have made *a priori* decisions as to the presence of measurable quantities of self-association dimer. Murty,¹² in turn, has questioned the monomer-acyclic tetramer-cyclic tetramer equilibrium proposed by the above authors because it did not account for the qualitative evidence for dimers. Fletcher and Heller, on the other hand, were not opposed to the qualitative evidence for the dimer (having shown it themselves),³⁵ but had only proposed that there was not enough dimer "to effect material-balance equations."^{2,35}

If the equilibrium constant for the dimer, $K_{1,2}$, has the same proportion to $K_{1,4}$ in the liquid phase as it does in the gas phase, we can calculate the amount of dimer in solution using the data from Tables III and IV. Thus, the dimer constant for either methanol or ethanol- d_1 (assuming ethanol and ethanol- d_1 have about the same self-association constants) in solution at 25° is calculated as being about 0.05. The maximum amount of methanol in the form of dimer ($1 \times 10^{-3} F$) at the maximum concentration (0.29 F) employed by Dixon¹¹ in cyclohexane would consequently have amounted to only 0.3% of the total methanol present. Figure 8 shows estimations of the relative molar proportions of dimer of ethanol- d_1 over a wide range of concentrations. It is obvious that although the dimer may reach concentrations where it can qualitatively be detected by infrared polymer band absorption in the fundamental O-H stretch region, it never reaches a concentration where it represents even 1% of the formal concentration of the total alcohol species in solution. In the neat ethanol- d_1 it amounts to only 0.005% of the total alcohol present. These amounts of dimer are obviously too low to be detected by material balance equations that depend upon knowledge of the total amount of added alcohol.

Arguments have previously been presented to explain how the formation of the cyclic tetramer could stabilize a monohydric alcohol at discrete species rather than form a wide range of polymer types.^{2,3} A point to consider in addition to the previous arguments is that bond breakage of a polymer species may not be random. Breakage of a single bond of the cyclic tetramer leads, of course, to the other major polymer, the acyclic tetramer. But if sufficient energy is supplied to break two bonds in the cyclic tetramer (such as caused by molecular collision), the applied leverage would preferentially break the bond diametrically opposite to the first broken bond, since the lever arm is twice as long as that applied to the other two remaining hydrogen bonds. This symmetrical splitting would form two acyclic dimers in preference to a monomer and an acyclic trimer.

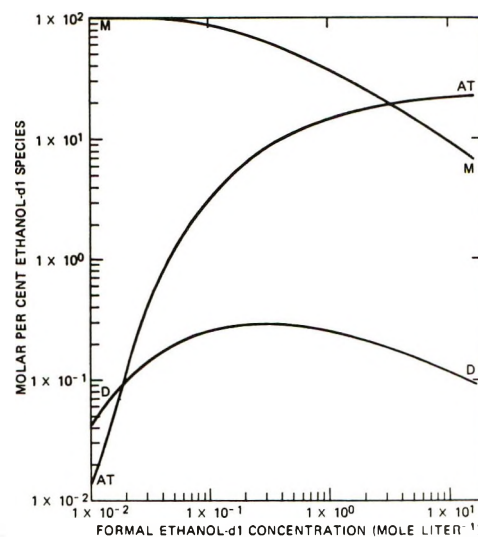


Figure 8. Relative molar proportions of major self-association species of ethanol- d_1 in *n*-decane at 25°: (curve M) monomer, (curve D) dimer, (curve AT) acyclic tetramer; cyclic tetramer (not shown) is 3.23 times the molar per cent of the value for the acyclic tetramer at any given concentration.

The Long-Chain Concept. The results of the near-infrared studies on ethanol- d_1 and 1-octanol^{2,3} indicate that a decrease in temperature increases the proportion of cyclic tetramer to acyclic tetramer rather than increasing the chain lengths of acyclic polymers. To quote Murty,¹² "This is in dramatic contrast with the extensive literature available on the self-association of alcohols and phenols." Space will not permit counter arguments against all of the "extensive literature" other than to note that most of the studies were performed in other than the more inert saturated hydrocarbon solvents and that the presence of long chains was an *a priori* decision. One example will be chosen to show the effects of making the *a priori* decision that a range of long-chain multimers is present in significant amounts in alcohol solutions at the higher concentrations. Finch and Lippincott⁴⁰ examined the O-H fundamental stretch vibration region of methanol, ethanol, 2-propanol, 1-butanol, 2-pentanol, 1-hexanol, phenol, *o*-chlorophenol, and 2-methyl-4-methoxy-2-pentanol in carbon tetrachloride from 30 to -80°. They noted that the peak positions of the polymers re-

(33) I. H. Reece and R. L. Werner, *Spectrochim. Acta, Part A*, **24**, 1271 (1968).

(34) R. M. Hammaker, R. M. Clegg, L. K. Patterson, P. E. Rider, and S. L. Rock, *J. Phys. Chem.*, **72**, 1837 (1968).

(35) A. N. Fletcher and C. A. Heller, *ibid.*, **72**, 1839 (1968).

(36) F. A. Smith and E. C. Creitz, *J. Res. Nat. Bur. Stand.*, **46**, 145 (1951).

(37) A. J. Barnes and H. E. Hallam, *Trans. Faraday Soc.*, **66**, 1920 (1970).

(38) A. J. Barnes and H. E. Hallam, *ibid.*, **66**, 1932 (1970).

(39) A. S. N. Murty, R. E. Davis, and C. N. R. Rao, *Theor. Chim. Acta*, **13**, 81 (1969).

(40) J. N. Finch and E. R. Lippincott, *J. Phys. Chem.*, **61**, 894 (1957).

mained at constant wavelengths when the concentrations were changed at a fixed temperature (which is in agreement with the present study). From this fixed frequency and the *a priori* wide-range multimer concept, they were forced to conclude that the hydrogen bond of the (supposedly present) long acyclic polymers must all absorb at the same wavelength. This long polymer wavelength (3333 cm^{-1} at room temperature), on the other hand, shifts to lower frequencies with a reduction in temperature (and also has an increase in formal absorptivity). From this information, Finch and Lippincott developed theoretical arguments to explain an apparent temperature sensitivity of the hydrogen bond. These same experimental observations, however, can be explained by the equilibrium between the monomer, the acyclic tetramer, and the cyclic tetramer: the increased formal absorptivity is due to the increased molar absorptivity of the $\cdots\text{O}-\text{H}\cdots$ groups compared to the free $\cdots\text{O}-\text{H}$ of the acyclic tetramer; the apparent frequency shift is due to the increased proportions of the cyclic tetramer at lower temperatures over that of the acyclic, noting that the cyclic absorbs at the lower frequencies (Figure 6). Since the polymer σ O-H groups absorb more than the monomer in the fundamental region but less than the monomer in the overtone region,³⁰ Finch and Lippincott did not have the information that can be seen in Figure 6; namely, there is no doubt but that the O-H peak at $2.18\ \mu\text{m}$ is free from significant temperature shifts and peaks at 2.117 and $2.0575\ \mu\text{m}$, although slightly overlapped, also appear to be little changed in location by a 70° temperature change. Thus it is evident that the

band frequency and hence the hydrogen bond are not as temperature dependent as reported by Finch and Lippincott.

If there were an increase in the proportions of long acyclic species with increasing concentrations of alcohol, with the $\cdots\text{O}-\text{H}\cdots$ groups being observed at a fixed frequency, then the two high-frequency "ends" of the acyclic species should show a decreased absorption compared to that of the low-frequency $\cdots\text{O}-\text{H}\cdots$ groups. But the data of the two studies on 1-octanol and the present study⁴¹ on ethanol- d_1 (Figures 1 and 7) show no evidence for such a decrease.⁴² It is important to note, however, that the increase in the ratio of cyclic tetramer:acyclic tetramer with a decrease in temperature (Figures 5 and 7) indicates that the proportions of polymers having more than four hydrogen bonds should increase, and may become significant, at temperatures below -10° .

(41) Absorbance values will appear immediately following this article in the microfilm edition of this volume of the journal. Single copies may be obtained from the Business Operations Office, Books and Journals Division, American Chemical Society, 1155 Sixteenth Street, N.W., Washington, D. C. 20036, by referring to code number JPC-72-2562. Remit check or money order for \$3.00 for photo copy or \$2.00 for microfiche.

(42) The ratio $a_{1.92}/a_{2.18}$ in Figure 7 is not the best to show a negligible change in the high- to low-frequency ratios due to overlap at $1.92\ \mu\text{m}$ by the monomer band, particularly at 60° . Taking the ratio of the 16 highest concentrations of the 60° data for $a_{2.18}/a_{1.965}$ resulted in an estimated standard deviation for a single value of ± 0.018 for a mean ratio of 0.695—a relative deviation of only 2.6%. Formal concentrations varied from 0.60 to 16.38 M . At 25° , the mean value of $a_{2.18}/a_{1.965}$ was 1.095 for ten samples, with an estimated standard deviation of single value of 0.035. The formal concentrations varied from 0.041 up to 17.01 M .

Tracer Diffusion and Viscosity Study at 25° in Binary and Ternary Liquid Systems¹

by Keichi Aoyagi and John G. Albright*

Department of Chemistry, Texas Christian University, Fort Worth, Texas 76129 (Received December 9, 1971)

Publication costs assisted by the Robert A. Welch Foundation

The intradiffusion coefficients of benzene-*l*-¹⁴C, *n*-hexane-*l*-¹⁴C, and cyclohexane-*l*-¹⁴C and viscosities were measured over the whole concentration range in the binary systems benzene-cyclohexane, benzene-*n*-hexane, and cyclohexane-*n*-hexane, and at four concentrations in the ternary system benzene-cyclohexane-*n*-hexane. The semiempirical equations proposed by one of the authors were tested with these data and with data reported for additional binary systems by other authors. Agreement between measured and calculated viscosities was excellent for nonpolar systems, but rather poorer results were observed for polar systems. A comparison of intradiffusion and mutual diffusion coefficients supports the existence of an effect of mass on rate of diffusion.

Introduction

Onsager² pointed out that "Viscous flow is a relative motion of its different constituents. Diffusion is a relative motion of its different constituents. Strictly speaking, the two are inseparable, . . ." The attempt to correlate diffusion coefficients and viscosities in liquid systems has been the subject of many theoretical and experimental studies. Perhaps the most successful equations put forth over the years have been the Stokes-Einstein equation, the modification of that equation for zero surface friction by Sutherland,³ and the similar equation based on a lattice model due to Eyring.⁴ These equations have an accuracy of the order of ±20%.

From an argument based on the thermodynamics of irreversible processes, where it has been assumed that the frictional coefficients in the linear law description of isothermal diffusion processes may be applied to friction in isotropic viscous flow, Albright⁵ proposed the equation which relates the intradiffusion coefficients, D_i^+ , of components i in a solution to the viscosity, η , of a solution as

$$\eta \simeq RT \sum_{i=0}^n (\xi_i C_i \bar{V}_i^{2/3} / D_i^+) \quad (1)$$

Here, R is the gas constant, T is the absolute temperature, and C_i and \bar{V}_i are respectively the concentration in moles per cubic centimeter and the partial molar volume of each component in solution. The constants ξ_i for each component, which have the units mole^{2/3} when cgs units are used throughout, are chosen to make the equation exact for pure solvent, for pure solutes if totally miscible, and otherwise for saturated solutions of solutes in pure solvent. From a hydrodynamic argument, a value of ξ_i was predicted as 2.398×10^{-17} when spherical monomer molecules diffuse in a continuous medium.

For the cases of spherical dimers and trimers in a continuous medium, ξ_i 's were predicted to be 1.903×10^{-17} and 1.663×10^{-17} , respectively. The actual ξ_i values for many compounds agree within ±4% of the value expected for a dilute solution of spherical monomers in a continuous medium. By assuming that the partial molar volume, \bar{V}_i , stays constant and equal to the value for the pure component, \bar{V}_i^0 , eq 1 was written as

$$\eta \simeq \frac{RT}{\bar{V}_m} \sum_{i=0}^n (\beta_i X_i / D_i^+) \quad (2)$$

where $\beta_i = \xi_i \bar{V}_i^{2/3}$. Each coefficient β_i is a constant which is evaluated in the same limit as the coefficient ξ_i , \bar{V}_m is the molar volume, and X_i is the mole fraction of each component. Both eq 1 and 2 had been applied to the systems benzene-cyclohexane⁶ and benzene-biphenyl⁷ at 25°. The values of viscosities calculated from eq 1 and 2 agreed with experimental values with an average deviation of less than 1%. Thus, it was of interest to apply these equations to other binary systems and as an important test extend the application to a ternary system. Since the significance of intermolecular forces was neglected in the development of these equations, it was considered to be reasonable to choose systems composed of completely miscible non-electrolytic, nonpolar liquids. The system benzene-

(1) Part of this work was presented before the Division of Physical Chemistry at the 162nd National Meeting of the American Chemical Society, Washington, D. C., Sept 12-17, 1971.

(2) L. Onsager, *Ann. N. Y. Acad. Sci.*, **46**, 241 (1945).

(3) W. Sutherland, *Phil. Mag.*, **9**, 871 (1905).

(4) (a) A. E. Stern, E. M. Irish, and H. Eyring, *J. Phys. Chem.*, **44**, 981 (1940); (b) T. Ree and H. Eyring, *Proc. Nat. Acad. Sci. U. S.*, **47**, 526 (1961).

(5) J. G. Albright, *J. Phys. Chem.*, **73**, 1280 (1969).

(6) R. Mills, *ibid.*, **69**, 3116 (1965).

(7) R. Mills, *ibid.*, **67**, 600 (1963).

n-hexane–cyclohexane was chosen to meet these conditions. A further consideration was to give a partial intercomparison of the data from this laboratory with data obtained by Mills.

It also is of interest to apply both equations to data previously reported by others for the binary intradiffusion in nonpolar as well as polar and hydrogen bonding systems.

Experimental Section

Materials. Matheson Coleman and Bell Chromatography benzene (99.9 + mol %), *n*-hexane (99.6 mol %), and cyclohexane (99.8 mol %) were used without further purification. The purity of these chemicals was confirmed by means of gas chromatography in our laboratory. Benzene-*1-¹⁴C*, *n*-hexane-*1-¹⁴C*, and cyclohexane-*1-¹⁴C* were obtained from Mallinckrodt Nuclear. Each sample had been taken from a preparative chromatograph and a chromatogram was supplied. The purities appeared to be better than 99.8%. BBOT (2,5-bis[2-(5-*tert*-butylbenzoxazolyl)]thiophene), Packard Instrument Co., and toluene, Matheson Coleman and Bell reagent grade, were used in the scintillation stock solutions. A portion of benzene-*1-¹⁴C* was fractionally recrystallized and distilled. The radioactive sample from recrystallization and the original sample were used to measure the intradiffusion coefficient of benzene in benzene. The results from both samples were in agreement within experimental error.

Tracer Diffusion Measurements. Three conventional Stokes type diaphragm cells⁸ with a bottom plug similar to the design of Albright and Mills⁹ were used. The total volumes of the cell were about 50, 40, and 30 ml, respectively, and the ratio of the volume of top and bottom compartment in each cell was within 0.1% of unity. The cell was attached to brass mounting plate which positioned the cell kinematically in the constant-temperature bath with the diaphragm always within 1° of horizontal. The bath temperature was maintained at 24.98 ± 0.01° by means of a vacuum-seal mercury regulator. Two Brooklyn calorimeter thermometers with a 2° range were calibrated with a triple-point apparatus and used for temperature measurement.

Correction of intradiffusion coefficients to 25° based on experimental activation energies for benzene¹⁰ and *n*-hexane¹¹ is less than 0.03%. Thus, within experimental error, data presented here for 24.98° are equally valid for 25.00°.

Prediffusion times were estimated from the Gordon inequality,¹² $D\tau/l^2 > 1.2$, where D is the diffusion coefficient and l is the apparent thickness of the frit. The duration of each experiment closely followed Robinson's¹³ rule for minimum experimental error. At first, the diaphragm cells were calibrated by allowing aqueous 0.8 *M* urea to diffuse into pure water. A Brice-Phoenix differential refractometer was used to

determine final concentrations of the urea solutions. The calibrations were based on the precise data of Gosting and Akeley¹⁴ for the urea–water system at 25°. Later calibrations were performed periodically by allowing benzene-*1-¹⁴C* to diffuse into pure benzene. For these calibrations the intradiffusion coefficient of benzene-*1-¹⁴C* was assumed to be $2.197 \times 10^{-5} \text{ cm}^2 \text{ sec}^{-1}$. This value for benzene was obtained from initial experiments and is thus based on calibration with urea. This value was also obtained in an extensive series of experiments performed at this laboratory by Eppstein.¹⁵

All solutions were prepared gravimetrically. Room temperature was maintained close to that of the water bath in order to minimize error due to thermal expansion when the solutions in the top and bottom compartment were sampled at the end of the diffusion experiment. The top compartment was always sampled before removal of the cell from the bath, and diffusion into the bottom compartment was then quenched within 30 sec by removing the cell, inverting it, and forcing the bottom solution through the frit. This was important because of the high thermal expansion coefficients of the organic liquids. Scintillation stock solutions were prepared by dissolving 4 g of BBOT in 1 l. of toluene. Counting procedures were similar to those in ref 15.

Viscosity Measurements. Viscosities were measured with an Ubbelohde type viscometer with an automatic viscometer reader (Rehovoth Instruments, Ltd.). The viscometer was calibrated with pure water, benzene, *n*-hexane, cyclohexane, carbon tetrachloride, toluene, methanol, and absolute ethanol. Observed values of efflux time, density, and viscosity from the literature^{16,17} were fit to the equation

$$\eta/\rho = at - (b/t) \quad (3)$$

by the method of least squares to calculate calibration constants a and b , which were found to be 9.641×10^{-3} and -0.3937 , respectively. Here η , ρ , and t are the viscosity in poise, the density, and the efflux time in seconds, respectively. With these values of a and b , the average deviation between calculated viscosity

- (8) R. H. Stokes, *J. Amer. Chem. Soc.*, **72**, 763 (1950).
- (9) J. G. Albright and R. Mills, *J. Phys. Chem.*, **69**, 3120 (1965).
- (10) A. F. Collings and R. Mills, *Trans. Faraday Soc.*, **66**, 2761 (1970).
- (11) J. C. Shieh and P. A. Lyons, *J. Phys. Chem.*, **73**, 3258 (1969).
- (12) A. R. Gordon, *Ann. N. Y. Acad. Sci.*, **46**, 285 (1945).
- (13) R. Mills and L. A. Woolf, "The Diaphragm Cell," Australian National University Press, Canberra, Australia, 1968, ref 24.
- (14) L. J. Gosting and D. F. Akeley, *J. Amer. Chem. Soc.*, **74**, 2058 (1952).
- (15) L. B. Eppstein and J. G. Albright, *J. Phys. Chem.*, **75**, 1315 (1971).
- (16) A. Weissberger and E. S. Proskauer, "Technique of Organic Chemistry," Vol. VII, Interscience, New York, N. Y., 1955.
- (17) R. A. Robinson and R. H. Stokes, "Electrolyte Solutions," Butterworths, London, 1955.

Table I: Constants for Polynomial Representations^a

System		a_0	a_1	a_2	a_3	a_4
Benzene-cyclohexane ^b	$D_0^+{}^e$	2.1942	0.4944	0.0527	-1.8200	0.9429
	D_1^+	2.0700	0.2736	-0.6837	-0.6075	0.3830
	ρ^f	0.8733	-0.1431	0.0483	-0.0033	-0.0020
	η^g	0.6016	-0.1848	0.5305	-0.3898	0.3272
Benzene- <i>n</i> -hexane ^c	D_0^+	2.1970	3.5700	-0.7454	-1.0809	0.7733
	D_2^+	2.2772	3.0743	-1.5464	0.5020	-0.2116
	ρ	0.8734	-0.3223	0.1172	0.6851	-0.0202
	η	0.6010	-0.9403	1.4179	-1.1638	0.3890
Cyclohexane- <i>n</i> -hexane ^d	D_1^+	3.8833	-2.5897	0.8754	-1.2339	0.4999
	D_2^+	4.1054	-2.1487	-1.1027	1.9294	-1.0909
	ρ	0.6552	0.0966	0.0159	0.0006	0.0050
	η	0.3043	0.1884	0.3132	-0.5569	0.6346

^a Data Y were represented by equations of the form $Y = \sum_{j=0}^4 a_j X_j^j$. ^b With respect to the mole fraction of cyclohexane. ^c With respect to the mole fraction of *n*-hexane. ^d With respect to the mole fraction of cyclohexane. ^e The D_1^+ 's have units of $10^{-5} \text{cm}^2 \text{sec}^{-1}$. ^f The units of ρ are g cm^{-3} . ^g The units of η are cP.

and literature value of viscosity was only 0.1% for the eight solvents.¹⁸ The densities used in these calculations were measured with a graduated pycnometer.

Results

A number of duplicate experiments were performed. Analysis of these experiments indicated that the experimental precision was $\pm 0.2\%$.

Experimental values of intradiffusion coefficients, densities, and viscosities were equated to polynomials in mole fractions by the method of least squares with a Wang 700 programable calculator. The recalculated value from polynomial expansion at any mole fraction agreed with the experimental value with an average deviation less than $\pm 0.1\%$. The coefficients of polynomial representation of diffusion coefficients, viscosities, and densities are listed in Table I, where X_i is mole fraction of the i th component in the solution. Subscripts 0, 1, and 2 denote benzene, cyclohexane, and *n*-hexane, respectively. These results and the viscosities calculated from eq 2 are plotted in Figures 1, 2, and 3, where for better comparison the viscosities were converted to fluidities. Results for the ternary system are given in Table II.

Data obtained from the literature for other binary systems were also put into polynomial representations in order to test eq 1 and 2. These data thus analyzed were for the systems *n*-hexane-*n*-dodecane at 25 and 35°,¹¹ *n*-octane-*n*-dodecane at 25°,¹⁹ $\text{CCl}_4\text{-CHCl}_3$ at 25°,²⁰ acetone-water at 25°,²¹ methanol-benzene at 25°,²² ethanol-benzene at 25°,²³ and ethanol-methanol at 25°. Data for the latter system are plotted vs. mole fraction in Figure 4.²⁴

Discussion

In a recent article,²⁵ Mills presented a corrected value for the self-diffusion coefficient of benzene which had been previously reported with experimental data for the system benzene-cyclohexane.⁶ The intra-

Table II: Intradiffusion Coefficients^a and Calculated Values of Viscosity^b at 25° for Solutions Containing Benzene, Cyclohexane, and *n*-Hexane as Components 0, 1, and 2, Respectively

	I	II	III	IV
X_0	0.3490	0.2689	0.2518	0.5000
X_1	0.3277	0.4884	0.2500	0.2507
X_2	0.3234	0.2427	0.4982	0.2493
D_0^+	3.114	2.847	3.533	2.990
D_1^+	2.707	2.450	3.032	2.638
D_2^+	2.926	2.667	3.230	2.859
$\eta(\text{exptl})$	0.440	0.493	0.390	0.452
$\eta(\text{calcd})$	0.437	0.489	0.390	0.448

^a The units of D_i^+ are $10^{-5} \text{cm}^2 \text{sec}^{-1}$. ^b The units of η are cP.

diffusion coefficient of benzene- 1^{14}C in benzene obtained in our study is 0.4% lower than his recent value of $2.205 \times 10^{-5} \text{cm}^2 \text{sec}^{-1}$.

(18) Dr. R. E. Manning suggested in a private communication that even the better data available in the literature may only be reliable from 1 to 3% and also pointed out that a kinetic correction of the form $\eta/\rho = at - (b/t^2)$ may be more appropriate (see R. E. Manning, M. R. Cannon, and J. D. Bell, *Anal. Chem.*, **32**, 355 (1960)). From the point of view of this experimental work, it is the change of viscosity in going from pure solvents to mixed solutions that is important. The results of the calibration experiments suggest that these relative changes are accurate within a few tenths of a per cent.

(19) A. L. Van Geet and A. W. Anderson, *J. Phys. Chem.*, **68**, 238 (1964).

(20) C. M. Kelly, G. B. Wirth, and D. K. Anderson, *ibid.*, **75**, 3293 (1971).

(21) Y. Kamei and Y. Oishi, *Nippon Kagaku Zasshi*, **91**, 403 (1970).

(22) (a) S. A. Genchur and J. G. Albright, unpublished data; (b) P. A. Johnson and A. L. Babb, *J. Phys. Chem.*, **60**, 14 (1956).

(23) P. A. Johnson and A. L. Babb, *Chem. Rev.*, **56**, 387 (1956).

(24) Data from this laboratory for intradiffusion coefficients and viscosity of the system methanol-benzene and figures for the systems listed above will appear following these pages in the microfilm edition of this volume of the journal. Single copies may be obtained from the Business Operations Office, Books and Journals Division, American Chemical Society, 1155 Sixteenth St., N.W., Washington, D. C. 20036, by referring to code number JPC-72-2572. Remit check or money order for \$4.00 for the photocopy or \$2.00 for microfiche.

(25) R. Mills, *Ber. Bunsenges. Phys. Chem.*, **75**, 195 (1971).

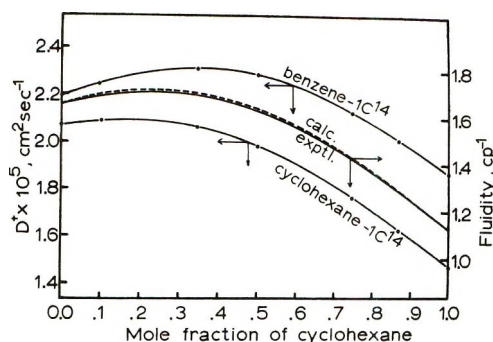


Figure 1. Binary intradiffusion coefficients and values of fluidity of the system benzene and cyclohexane at 25°.

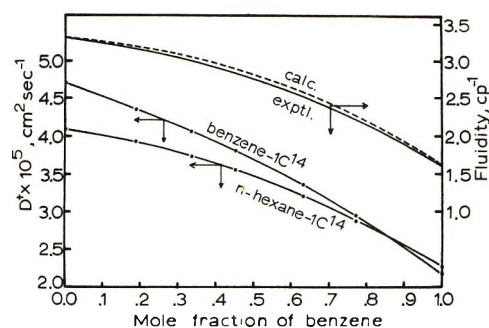


Figure 2. Binary intradiffusion coefficients and values of fluidity of the system *n*-hexane and benzene at 25°.

Our values of benzene- $1-^{14}\text{C}$ and cyclohexane- $1-^{14}\text{C}$ fall approximately 3% below Mills' earlier values. Dunlop and coworkers²⁶ reported the same deviation from Mills' data, although the numerical values for entire range of concentration were not reported. Values for limiting intradiffusion coefficient of cyclohexane in benzene in this work are found to be 0.6% lower than their values. The intradiffusion coefficients of benzene- $1-^{14}\text{C}$ in the system benzene-*n*-hexane observed in this work are also consistently 0.6% smaller than their values. They also reported diffusion coefficients of labeled *n*-hexane at three concentrations in the same system, and the results presented here differ by 0.7–4% from their values. Except in case of labeled hexane, the consistent deviation in diffusion coefficients observed in this work from the data of ref 26, is suggestive of systematic error, or errors, where the possibilities include error in the calibration of the diaphragm cells, an isotope effect due to differences in the extent of ^{14}C content of labeled molecules, and an error in the sampling technique of the organic solvents.

The question of the effect of mass on rates of diffusion is still unresolved. Different theoretical arguments tend to lead to different expectations for this result. For example, simple hydrodynamic arguments used in the development of the Stokes-Einstein equation do not directly involve the mass of the solute components.

The significant structure theory developed by Eyring,⁴ *et al.*, suggests that the diffusion coefficient of

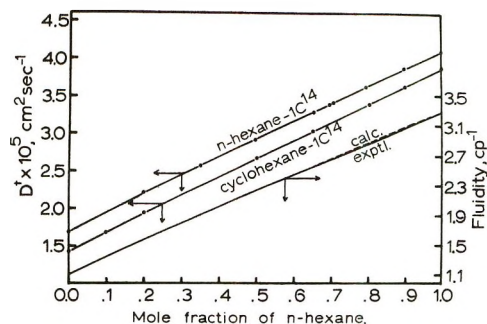


Figure 3. Binary intradiffusion coefficients and values of fluidity of the system cyclohexane and *n*-hexane at 25°.

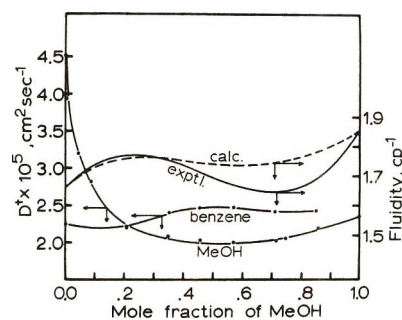


Figure 4. Binary intradiffusion coefficients and values of fluidity of the system benzene and methanol at 25°.

a solute component should be proportional to the inverse square root of mass.²⁷ Dunlop, *et al.*, investigated²⁶ the question by measuring the tracer diffusion coefficients in benzene of three samples of labeled benzene which were reported to have respectively 1.5, 3, and 5 labels per labeled molecule. They did not find a measurable mass effect. However, experimental work at this laboratory has supported the existence of a mass effect. Thus, it has been proposed¹⁵ that limiting intradiffusion coefficient, D^+ , be related to the limiting mutual diffusion coefficient, D^0 , by the equation

$$D^0/D^+ = (M^+/M^0)^{1/2} \quad (4)$$

where M^+ is the molecular weight of the isotopically substituted species and M^0 is the molecular weight of the unsubstituted species. As it is seen in Table III, the limiting intradiffusion coefficients are consistently lower than reported limiting mutual diffusion coefficients.²⁸ The ratio of the limiting mutual and intradiffusion coefficients observed in this work, however, deviate –0.3–0.6% from the ratio of inverse square

(26) K. R. Harris, C. K. N. Pua, and P. J. Dunlop, *J. Phys. Chem.*, **74**, 3518 (1970).

(27) E. McLaughlin, *Trans. Faraday Soc.*, **55**, 28 (1959).

(28) It has been pointed out by Bearman (R. J. Bearman, *J. Phys. Chem.*, **65**, 1961 (1961)) that mutual diffusion and tracer diffusion (intradiffusion) become identical for nonelectrolyte solute components at infinite dilution. Actual differences in rate of diffusion are thus the result of change in physicochemical properties due to isotopic labeling.

Table III: Comparison of Limiting Intradiffusion Coefficients^a with Limiting Mutual Diffusion Coefficients^a

Tracer component	Solvent component	D_i^{+b}	D_i^{+c}	D_i^{+d}	D_i^e
Benzene- $I-^{14}C$	<i>n</i> -Hexane	4.714	4.740	4.747	4.758 ^f
Benzene- $I-^{14}C$	Cyclohexane	1.863	1.873	1.835	1.880 ^g
					1.876 ^h
Cyclohexane- $I-^{14}C$	Benzene	2.071	2.082	2.084	2.090 ^g
					2.101 ^h
<i>n</i> -Hexane- $I-^{14}C$	Benzene	2.278	2.290	2.294	2.312 ^f

^a The diffusion coefficients have the units $10^{-5} \text{ cm}^2 \text{ sec}^{-1}$. ^b Values obtained in this work. ^c Values based on an 0.4% decrease ("correction") in the calibration constant. ^d Values from ref 26. ^e The limiting mutual diffusion coefficients from the literature. ^f Reference 26. ^g L. Rodwin, J. A. Harpst, and P. A. Lyons, *J. Phys. Chem.*, **69**, 2783 (1965). ^h H. S. Harned, *Discuss. Faraday Soc.*, No. 24, 7 (1947).

roots of mass. Values in ref 26 were examined in the same manner assuming singly labeled tracer compounds were used. Deviation observed are -1.2 – 1.0% .

It should be noted that a systematic error of 0.4% in the calibration would bring the measured value of the intradiffusion coefficient of benzene reported here to the value reported in ref 25. If such a systematic error is assumed, the ratio of the mutual diffusion coefficients to the intradiffusion coefficients in Table III would differ from the ratio of the inverse square roots of the mass by 0.2 – 1.0% , but in all cases the intradiffusion coefficients would still be less than the mutual diffusion coefficients.

Although these data do not directly support the effect of mass on rate of diffusion in a definite expression such as eq 4, they indicate that the tracer molecules which are heavier due to isotopic substitution diffuse at slower rate.²⁹

As noted, a small problem in the calibration would significantly alter the interpretation of the mass effect, and at this time there are controversies in the literature over calibration. It should be pointed out that other workers^{10,24,30} in the field have extensively used the system KCl– H_2O for calibration of the diaphragm cell. The use of the system urea– H_2O has been preferred at this laboratory because of concern over known difficulties in the measurement of diffusion coefficients of electrolytes in dilute solutions by the diaphragm cell method. Also, the concentration dependence of the diffusion coefficients of urea is much less than for the electrolyte case, leading to less error in interpretation of the data. However, Dunlop, *et al.*,²⁶ have compared the urea calibration to the KCl calibration and found that the two methods gave the same results.

Conclusions

Equations 1 and 2 are found to give approximations of viscosity for nonpolar systems considered in this article at a level of experimental error. Equations 1 and 2 may be considered equally valid based on a comparison of measured and calculated viscosities. Maximum deviations of 2, 0.9, and 0.7% are found for the

binary systems *n*-hexane–benzene, benzene–cyclohexane, and cyclohexane–*n*-hexane, respectively. The values of viscosity calculated from eq 2 for the ternary systems show excellent agreement with those from experiments. The average deviation from all ternary measurements was found to be 0.6% . This excellent agreement is particularly significant because the concentration of each component in the solutions was less than 50 mol fraction, whereas the values of ξ_i were calculated from the pure components.

Maximum deviations and average deviations of the mean in calculated viscosities from experimental values are found as follows: *n*-octane–*n*-dodecane at 25° , 4.0 and 1.2% ; $CHCl_3$ – CCl_4 at 25° , 1.7 and 1.0% ; *n*-hexane–*n*-dodecane at 25° , 3.2 and 1.3% ; *n*-hexane–*n*-dodecane at 35° , 4.9 and 2.9% ; ethanol–benzene at 25° ,³¹ 5.0 and 2.4% ; and methanol–ethanol at 25° ,³¹ 8.0 and 3.4% , respectively.

For all hydrocarbons listed in the Table IV, the higher values of ξ_i in most cases are consistent with the prediction from hydrodynamic arguments that the deviation from a sphere model should increase the value of ξ_i .

Table IV: Values of ξ_i^a for Various Hydrocarbons

Benzene	2.382 ^b	<i>n</i> -Heptane	2.509 ^d
Cyclohexane	2.444 ^b	<i>n</i> -Octane	2.664 ^e
<i>n</i> -Hexane	2.558 ^b	<i>n</i> -Dodecane	2.841 ^c
	2.544 ^c		2.763 ^e
	2.557 ^d		

^a The constants ξ_i have the units $10^{-17} \text{ mol}^{-2/3}$. ^b D_i^{+} in this work. ^c Reference 11. ^d Reference 26. ^e Reference 19.

(29) Recently Mills²⁵ made an extensive review of the literature on self-diffusion in each of systems benzene, water, and liquid argon and found strong evidence to support a mass effect, with the rates of diffusion decreasing with increased mass.

(30) R. Mills, *Trans. Faraday Soc.*, **67**, 1654 (1971).

(31) The values of viscosity and density are from J. Timmermans, "The Physico-Chemical Constants of Binary Systems in Concentrated Solutions," Interscience, New York, N. Y., 1959.

Rather large deviations, 13.7% maximum deviation and 6.9% average deviation of the mean, are observed for the water–acetone system. However, there is a wide variation in the values reported in the literature for the tracer diffusion coefficient of water.²⁵ Thus, the observed deviation could be partially due to experimental difficulties of obtaining intradiffusion coefficients of water. Similar results were observed for the methanol–benzene system, as seen in Figure 4. From hydrodynamic arguments, it was shown⁵ that the ξ_t value for methanol was consistent with the formation of trimers in its liquid phase. Since the calculated viscosities of solutions at any concentration depend on the values of ξ_t of methanol as well as on that of ben-

zene, the disagreement may be explained if for methanol the extent of association due to hydrogen bonding changes with concentration. Since significant interaction between molecules was neglected in the proposed equations, disagreements are not surprising and further extensive study of polar systems and refinement of these equations must be necessary.

Acknowledgment. The authors would like to express their appreciation to the Robert A. Welch Foundation (Grant No. P-225) and the T. C. U. Research Foundation for their financial support of this research. The authors wish to thank Miss Sue Genchur for the use of unpublished data for the system methanol–benzene.

Excess Partial Molal Heat Capacities of *n*-Tetraamylammonium Bromide in Water from 10 to 80° and in Aqueous *tert*-Butyl Alcohol Solvent System at 30° and the Effects on the Water Structure

by R. K. Mohanty, S. Sunder, and J. C. Ahluwalia*

Department of Chemistry, Indian Institute of Technology, Kanpur-16, India (Received December 28, 1971)

The integral heats of solution, ΔH_s , of *n*-Am₄NBr in water from 5 to 85° and in aqueous *tert*-butyl alcohol solvent system containing 0.0–0.30 mol fraction of *tert*-butyl alcohol at 25 and 35° have been determined at very low concentrations. The limiting excess partial molal heat capacities, ΔC_p° , of *n*-Am₄NBr in water from 10 to 80° and in aqueous *tert*-butyl alcohol solutions at 30° have been derived by the integral heat method. The results for *n*-Am₄NBr are compared with those of Bu₄NBr and NaBPh₄ and are discussed in terms of the influence of such hydrophobic solutes on the structure of water in pure water as a function of temperature and in the water rich region of aqueous *tert*-butyl alcohol solvent system as a function of mole fraction of *tert*-butyl alcohol.

Introduction

In continuation of our previous studies on the excess partial molal heat capacities ΔC_p° of electrolytes containing hydrophobic nonpolar moieties, in water^{1–5} and in water plus nonaqueous solvent systems,^{6,7} we report in this paper the limiting excess partial molal heat capacities ΔC_p° of *n*-Am₄NBr in water from 10 to 80° and in water + *tert*-butyl alcohol solvent system at 30° with a view to obtaining further information about the structural changes occurring in aqueous solutions of such hydrophobic solutes.

In our previous studies^{1,2} we had observed that both NaBPh₄ and *n*-Bu₄NBr give rise to large positive values of ΔC_p° in water, indicating their strong water-structure-promoting characteristics; however, the tempera-

ture dependence behavior of their ΔC_p° values differed very much from each other. This difference was explained on the basis of the different mode of interaction

- (1) S. Subramanian and J. C. Ahluwalia, *J. Phys. Chem.*, **72**, 2525 (1968).
- (2) T. S. Sarma and J. C. Ahluwalia, *Trans. Faraday Soc.*, **67**, 2528 (1971).
- (3) T. S. Sarma, R. K. Mohanty, and J. C. Ahluwalia, *ibid.*, **65**, 2333 (1969).
- (4) T. S. Sarma and J. C. Ahluwalia, *J. Phys. Chem.*, **74**, 3547 (1970).
- (5) R. K. Mohanty and J. C. Ahluwalia, *J. Chem. Thermodyn.*, **4**, 53 (1972).
- (6) R. K. Mohanty, T. S. Sarma, S. Subramanian, and J. C. Ahluwalia, *Trans. Faraday Soc.*, **67**, 305 (1971).
- (7) R. K. Mohanty and J. C. Ahluwalia, *J. Solution Chem.*, in press.

of alkyl and aryl nonpolar groups with water.² A number of reports support the above contention.^{6,8-11} It was also observed by us recently that increasing the alkyl chain length from *n*-Bu₄NBr to *n*-Am₄NBr did not result in any saturation effect on ΔC_p° ; on the contrary, the increment in ΔC_p° per CH₂ group was found to be unusually large.⁵ We thought it interesting to study the temperature dependence of ΔC_p° of *n*-Am₄NBr in water to shed further light on the effect of the nature and size of hydrophobic group on the structure of water as a function of temperature.

The occurrence of the phenomena of extrema¹²⁻¹⁵ for various properties in the water-rich region of water + alcohol and water + other nonaqueous cosolvent systems has resulted in a new impetus in the studies⁶ of highly aqueous binary solvent mixtures with a view to understanding the perturbation of water structure induced by the addition of relatively small amounts of nonaqueous cosolvent. In continuation of our previous studies^{6,7} on such systems, we report in this paper the partial molal enthalpies $\Delta \bar{H}_s^\circ$ and excess partial molal heat capacities $\Delta \bar{C}_p^\circ$ of *n*-Am₄NBr in the water-rich region of aqueous-*tert*-butyl alcohol (*tert*-butyl alcohol to be hereafter referred as TBA) solvent system, which shows more dramatic structural changes than any other aqueous-nonaqueous cosolvent system studied so far.^{6,12-15}

Values of $\Delta \bar{C}_p^\circ$ have been derived from heat of solution measurements at very low concentrations by the integral heat method.^{16,17}

Experimental Section

The precision calorimeter and the procedure for measurements of integral heats of solution have been described earlier.^{1,3} The submarine calorimeter (550-ml glass dewar flask) was immersed in a thermostat whose temperature was kept constant to $\pm 0.002^\circ$ by a Sargent Thermonitor. A 10-kohm thermistor formed one arm of the Wheatstone bridge which was constructed from precision decade resistors. The signal was fed into an amplifier which in turn drove a Sargent recorder. The minimum temperature change that could be detected was of the order of $2 \times 10^{-5}^\circ$. The calorimeter was calibrated by measuring heats of solution of KCl in water and that of THAM (tris(hydroxy methyl)aminomethane) in 0.1 *N* HCl. The values obtained were within 0.2% of those reported by Gunn.¹⁸ *n*-Am₄NBr was obtained from Eastman Organic Chemical Distillation Products Industries and recrystallized from acetone-ether mixture and dried *in vacuo* at 65°. The sample bulbs filled with samples were further dried at 80° for about 12 hr, cooled, weighed to constant mass, and sealed. Deionized distilled water was used in the calorimeter. *tert*-Butyl alcohol was obtained from BDH Ltd. and was purified by the standard method.¹⁹ The weights of the samples of *n*-Am₄NBr were chosen so as to result in a calorimetric

solution of 10^{-4} – 10^{-3} *m*. The measurements on conductivity of aqueous solutions of *n*-Am₄NBr at room temperature and of the same solutions heated to 85° and cooled to room temperature give no evidence of their decomposition up to 85° even when the concentrations are about four times as large as the maximum concentration used in the calorimetric measurements and the time factor is as large as about ten times the time involved in the actual measurements after dissolution of the sample.

Results and Discussion

(A) ΔC_p° of *n*-Am₄NBr in Water from 10 to 80°. The values of the integral heats of solution ΔH_s of *n*-Am₄NBr in water at concentrations ranging from 1×10^{-4} to 1×10^{-3} *m* and from 5 to 85° (except the values at 25 and 35°, which were reported earlier⁵) are given as supplementary material.²⁰ The values of the heats of solution at infinite dilution, ΔH_s° , were obtained by averaging the values of ΔH_s , since the determined values were measured in very dilute solutions wherein any effect of molality is masked by the experimental error. The average values of ΔH_s° computed with 95% confidence limits at these temperatures, along with the values at 25 and 35° reported by us earlier,⁵ are given in Table I. The values of excess partial molal heat capacities ΔC_p° of *n*-Am₄NBr in water from 10 to 80° derived from the ΔH_s° values by the integral heat method^{16,17} are listed in Table I and plotted as a function of temperature in Figure 1. For comparison, ΔC_p° values for Bu₄NBr,² NaBPh₄,¹ and Me₄NBr²¹ as a function of temperature are also plotted in Figure 1.

(8) G. C. Krescheck and L. Benjamin, *J. Phys. Chem.*, **68**, 2476 (1964).

(9) W. A. Hargraves and G. C. Krescheck, *ibid.*, **73**, 3249 (1969).

(10) F. J. Millero, *J. Chem. Eng. Data*, **15**, 562 (1970).

(11) G. Kalfoglou and L. H. Bowen, *J. Phys. Chem.*, **73**, 2728 (1969).

(12) F. Franks in "Hydrogen-Bonded Solvent Systems," A. K. Covington and P. Jones, Ed., Taylor and Francis, London, 1968, p 31.

(13) F. Franks in "Physico-chemical Processes in Mixed Aqueous Solvents," F. Franks, Ed., Heinemann, London, 1967.

(14) F. Franks and D. J. G. Ives, *Quart. Rev., Chem. Soc.*, **20**, 1 (1966).

(15) E. M. Arnett in ref 13, p 105.

(16) C. M. Criss and J. W. Cobble, *J. Amer. Chem. Soc.*, **83**, 3223 (1961).

(17) J. C. Ahluwalia and J. W. Cobble, *ibid.*, **86**, 5317 (1964).

(18) S. Gunn, *J. Phys. Chem.*, **69**, 2902 (1965).

(19) A. I. Vogel, "Textbook of Practical Organic Chemistry," Longmans, Green and Co., London, 1959.

(20) The detailed listing of ΔH_s values will appear following these pages in the microfilm edition of this volume of the Journal. Single copies may be obtained from the Business Operations Office, Books and Journals Division, American Chemical Society, 1155 Sixteenth St., N.W., Washington, D. C. 20036, by referring to code number JPC-72-2577. Remit check or money order for \$3.00 for photocopy or \$2.00 for microfiche.

(21) C. M. Criss, personal communication; see also M. J. Mastrotianni and C. M. Criss, *J. Chem. Thermodyn.*, **4**, 321 (1972).

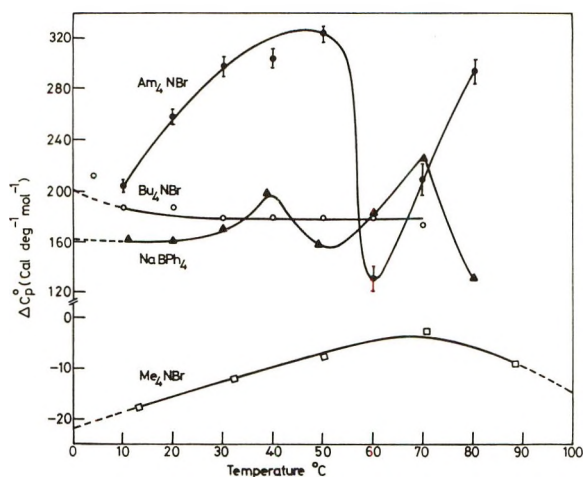


Figure 1. Excess partial molal heat capacities of n -Am₄NBr (this work), Bu₄NBr (ref 2), NaBPh₄ (ref 1), and Me₃NBr (ref 21) in water as a function of temperature.

Table I: Excess Partial Molal Heat Capacities, ΔC_p° , of n -Am₄NBr from 10 to 80°

Temp., °C	ΔH_s° , cal mol ⁻¹	Temp., °C	ΔC_p° , cal °K ⁻¹ mol ⁻¹
5	-4,018 ± 36	10	224 ± 4
15	-1,782 ± 26	20	258 ± 5
25	796 ± 29	30	300 ± 6
35	3,791 ± 39	40	304 ± 6
45	6,827 ± 40	50	325 ± 6
55	10,076 ± 35	60	131 ± 9
65	11,386 ± 84	70	210 ± 13
75	13,482 ± 102	80	292 ± 12
85	16,400 ± 60		

^a The ΔH_s° values are the computed average values with 95% confidence limits. ^b The uncertainty in the ΔC_p° value at temperature T ($e\Delta C_p^\circ T$) is calculated as follows: $e\Delta C_p^\circ T = [1/(T_2 - T_1)] [(e\Delta H_s^\circ T_1)^2 + (e\Delta H_s^\circ T_2)^2]^{1/2}$, where $T = (T_1 + T_2)/2$.

It may be seen from Table I that ΔH_s° values increase enormously with increasing temperature. The increase from 5 to 85° is as much as 20.4 kcal mol⁻¹. Table I and Figure 1 show that ΔC_p° of n -Am₄NBr in water is very large and positive over the entire range of temperature, indicating that n -Am₄NBr is a very strong structure-making solute. ΔC_p° of n -Am₄NBr at 30° is 300 cal deg⁻¹ mol⁻¹, which is larger by 120 cal deg⁻¹ mol⁻¹ than that of n -Bu₄NBr. This is much more than one would expect from the increase of the alkyl chain by four -CH₂ groups.^{5,22}

However, even more interesting and puzzling is the variation of ΔC_p° of n -Am₄NBr with temperature: ΔC_p° goes on increasing appreciably with temperature until it gives rise to a maximum ($\Delta C_p^\circ = 325$ cal deg⁻¹ mol⁻¹) around 50°, followed by a sharp decrease of about 200 cal deg⁻¹ mol⁻¹, giving rise to a minimum around 60°. Thereafter, ΔC_p° is again found to increase enormously from 131 cal deg⁻¹ mol⁻¹ at 60° to

292 cal deg⁻¹ mol⁻¹ at 80°. It would be interesting to see how ΔC_p° varies after 80°, but unfortunately, owing to practical difficulties, we could not carry out accurate measurements on heats of solution above 85°.

We have no doubt that the gyrations in the ΔC_p° -temperature profile of aqueous solution of n -Am₄NBr above 50° are real and must represent the true state of affairs, as these gyrations are many times the uncertainty limits and also since no evidence of decomposition of aqueous solutions of n -Am₄NBr (see Experimental Section) was found up to 85°.

The temperature dependence of ΔC_p° of n -Am₄NBr, which appears to be quite complex at this stage, for a suitable interpretation could possibly be explained tentatively in terms of the combined effect of increasing melting of icebergs with increasing temperature (causing an increase in ΔC_p°); increasing hydrophobic bond strength with temperature, the temperature of maximum hydrophobic bond strength being about 58° for the aliphatic hydrophobic solute²³ (which may possibly be responsible for the minimum in the ΔC_p° - T curve); and the possible existence of a third state of nontetrahedral hydrogen-bonded^{4,24} species in water which disintegrates more and more to monomers at higher temperatures. Rather than hastily speculate in an attempt to explain the results reported in this paper, we would wait for more information on the temperature dependence of ΔC_p° and other properties of aqueous solutions of such hydrophobic solutes before offering a suitable explanation for the above behavior.

It would be interesting to compare the temperature dependence of ΔC_p° of n -Am₄NBr with those of Bu₄NBr, NaBPh₄, and Me₃NBr to see the effect of size as well as the nature of the hydrophobic solute on the structure of water. The ΔC_p° of Bu₄NBr in water (Figure 1) decreases appreciably with increasing temperature at lower temperatures, followed by little change at high temperatures up to 70°. Considering that the temperature dependence of ΔC_p° of Bu₄NBr is just opposite to those of Me₃NBr²¹ and common electrolytes, it is rather surprising and unexpected that n -Am₄NBr, which is more hydrophobic in character than Bu₄NBr, should behave in a reverse and more complex manner than Bu₄NBr in affecting water structure. On the other hand, n -Am₄NBr appears to resemble NaBPh₄ in its temperature dependence of ΔC_p° in water.

(B) ΔC_p° of n -Am₄NBr in Water + *tert*-Butyl Alcohol Solvent at 30°. Since the measurements of partial molal enthalpies $\Delta \bar{H}_s$ of n -Am₄NBr in water + TBA system were carried out in very dilute solutions of n -Am₄NBr, wherein any concentration effect is masked by the experimental error, the value of limiting partial

(22) H. Ruterjans, F. Schreiner, U. Sage, and Th. Ackermann, *J. Phys. Chem.*, **73**, 986 (1969).

(23) G. Nemethy and H. A. Scheraga, *ibid.*, **66**, 1773 (1962).

(24) E. Wicke, *Angew. Chem., Int. Ed. Engl.*, **5**, 106 (1966).

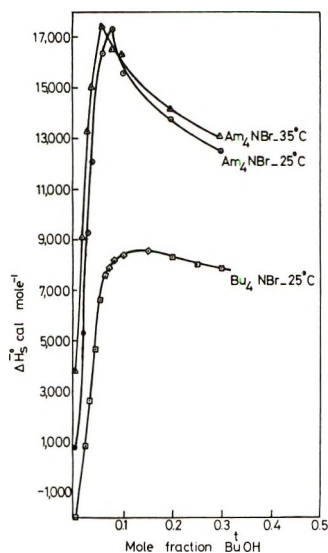


Figure 2. Partial molal enthalpies of n -Am₄NBr and Bu₄NBr (ref 5) in aqueous *tert*-butyl alcohol solvent system as a function of mole fraction of *tert*-butyl alcohol.

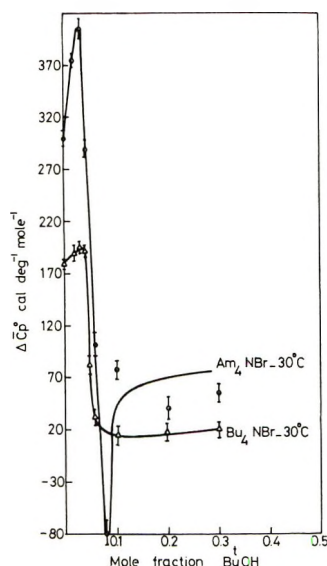


Figure 3. Excess partial molal enthalpies of n -Am₄NBr and Bu₄NBr (ref 5) in aqueous *tert*-butyl alcohol solvent system at 30° as a function of mole fraction of *tert*-butyl alcohol.

molal enthalpy $\Delta\bar{H}_s^\circ$ was taken as the average of $\Delta\bar{H}_s^\circ$ values. The average values of $\Delta\bar{H}_s^\circ$ of n -Am₄NBr in water + TBA solvent system containing 0–0.3 mol fraction of TBA, computed with 95% confidence limits, at 25 and 35°, are listed in Table II and plotted as a function of mole fraction of TBA in Figure 2. The derived values of $\Delta\bar{C}_p^\circ$ at 30° are listed in Table II and plotted as a function of mole fraction of TBA in Figure 3. For comparison, $\Delta\bar{H}_s^\circ$ and $\Delta\bar{C}_p^\circ$ of Bu₄NBr in water + TBA system reported earlier from this laboratory⁶ are also plotted in Figures 2 and 3, respectively.

The $\Delta\bar{H}_s^\circ$ –mole fraction of TBA profile of n -Am₄NBr in water + TBA system at 25 and 35° (Figure 2) shows

Table II: Partial Molal Enthalpies and Excess Partial Molal Heat Capacities of n -Am₄NBr in Aqueous *tert*-Butyl Alcohol Solvent System

TBA mole fraction	$\Delta\bar{H}_s^\circ, ^\circ \text{ cal mol}^{-1}$		$\Delta\bar{C}_p^\circ, ^b \text{ cal } ^\circ \text{K}^{-1} \text{ mol}^{-1}$ 30.0°
	25.0°	35.0°	
0.0°	796 ± 29	3,791 ± 39	300 ± 6
0.02	5,320 ± 48	9,076 ± 60	376 ± 8
0.03	9,283 ± 50	13,340 ± 60	406 ± 8
0.04	12,123 ± 60	15,015 ± 45	289 ± 8
0.06	16,400 ± 50	17,420 ± 65	102 ± 8
0.08	17,295 ± 65	16,500 ± 50	-80 ± 8
0.10	15,590 ± 40	16,356 ± 70	77 ± 8
0.20	13,170 ± 65	14,105 ± 55	40 ± 9
0.30	12,540 ± 70	13,095 ± 55	56 ± 9

^a The $\Delta\bar{H}_s^\circ$ values are the computed average values with 95% confidence limits. ^b The uncertainty in the $\Delta\bar{C}_p^\circ$ value at 30° has been calculated as follows: $e\Delta\bar{C}_p^\circ(30^\circ) = [1(35^\circ - 25^\circ)] \cdot \{[e\Delta\bar{H}_s^\circ(35^\circ)]^2 + [e\Delta\bar{H}_s^\circ(25^\circ)]^2\}^{1/2}$. ^c The values in pure water are taken from ref 5.

that the value of $\Delta\bar{H}_s^\circ$ increases enormously with increasing mole fraction of TBA, giving rise to a maximum around 0.08 mol fraction of TBA, followed by an appreciable decrease from 0.08 to 0.30 mol fraction of TBA. The maximum values of enthalpy of transfer, ΔH_{tr}^{\max} ($\Delta H_{tr}^{\max} = \Delta\bar{H}_s^{\circ\max} - \Delta H_s^\circ$), from water to water + TBA system are 16.5 and 13.6 kcal mol⁻¹ at 25 and 35°, respectively.

It may be interesting to compare the behavior of n -Am₄NBr with those of Bu₄NBr and NaBPh₄, for which similar data have been reported.^{6,25} The $\Delta\bar{H}_s^\circ$ –mole fraction of TBA profiles of both NaBPh₄ and Bu₄NBr appear to be similar to that of n -Am₄NBr from 0.0 to 0.06 mol fraction of TBA, except that the value of ΔH_{tr}^{\max} (endothermic maxima) is large and comparable for n -Am₄NBr and NaBPh₄ (~17 kcal mol⁻¹) but is less for Bu₄NBr (10.6 kcal mol⁻¹). However, at mole fractions of TBA higher than 0.08, $\Delta\bar{H}_s^\circ$ decreases sharply and enormously with increasing mole fraction of TBA for NaBPh₄, while for Bu₄NBr it increases slowly to 0.15 mol fraction of TBA, followed by a small decrease at higher mole fractions of TBA. These observations indicate that structural effects of n -Am₄NBr on water + TBA system possibly are closer to NaBPh₄ than to Bu₄NBr.

The $\Delta\bar{C}_p^\circ$ –mole fraction of TBA profile of n -Am₄NBr at 30° (Figure 3) shows that the $\Delta\bar{C}_p^\circ$ value in water at 30°, which is probably the largest of all the hydrophobic solutes studied so far ($\Delta\bar{C}_p^\circ = 300 \text{ cal deg}^{-1} \text{ mol}^{-1}$), increases appreciably with the addition of TBA to water, giving rise to a maximum at 0.3 mol fraction of TBA ($\Delta\bar{C}_p^\circ = 406 \pm 7 \text{ cal deg}^{-1} \text{ mol}^{-1}$, which represents an increase of about 106 cal deg⁻¹ mol⁻¹ over

(25) E. M. Arnett and D. R. McKelvey, *J. Amer. Chem. Soc.*, **88**, 5031 (1966); **87**, 1393 (1965).

the value in pure water). Further addition of TBA from 0.03 to 0.08 mol fraction results in a dramatic decrease of about 486 cal deg⁻¹ mol⁻¹ in $\Delta \bar{C}_p^\circ$, the minimum in $\Delta \bar{C}_p^\circ$ occurring at 0.08 mol fraction of TBA. Thereafter, $\Delta \bar{C}_p^\circ$ increases from 0.08 to 0.30 mol fraction of TBA.

The increase in $\Delta \bar{C}_p^\circ$ of Am₄NBr in water + TBA up to 0.03 mol fraction of TBA indicates an appreciable enhancement of water structure by *n*-Am₄NBr in water + TBA system relative to that in pure water. The dramatic decrease of 486 cal deg⁻¹ mol⁻¹ with increasing mole fraction of TBA from 0.03 to 0.08 indicates the dramatic collapse of the three-dimensional water structure. The increase in $\Delta \bar{C}_p^\circ$ thereafter probably reflects the increase in the structure by dissolution of TBA in water by substitution. The $\Delta \bar{C}_p^\circ$ -mole fraction of TBA profile for NaBPh₄ appears to be very similar to that for *n*-Am₄NBr in that the maximum and minimum in $\Delta \bar{C}_p^\circ$ occur around the same mole fraction of TBA and the increase and decrease in $\Delta \bar{C}_p^\circ$ also seems to be of the same order of magnitude. On the other hand, although a maximum in $\Delta \bar{C}_p^\circ$ is also observed for Bu₄NBr at about the same mole fraction but the increase in $\Delta \bar{C}_p^\circ$ is relatively much smaller in magnitude, similarly the decrease in $\Delta \bar{C}_p^\circ$ of Bu₄NBr, which occurs after 0.04 mol fraction of TBA, although sharp, seems to be about half as much as that of *n*-Am₄NBr and NaBPh₄.

The above observations on $\Delta \bar{C}_p^\circ$ point out the similarities as well as the differences in the influence of hydrophobic solutes on the structure of water existing in the water-rich region of water + TBA solvent mixtures. For instance, all the three highly structure-making hydrophobic solutes *n*-Am₄NBr, Bu₄NBr, and

NaBPh₄ enhance their structure-making propensity in the presence of small amounts of TBA, maximum enhancement occurring around 0.03–0.04 mol fraction of TBA. This must be by a mechanism of mutual enhancement of water structure by TBA and the hydrophobic solute, rather than by a competition process. The above results support the contention^{6,12–15} that TBA possibly forms a liquid clathrate of the specific composition corresponding to 0.03–0.04 mol fraction of TBA and that TBA which enters into interstices can only be accommodated up to this extent, further addition of TBA resulting in a complete collapse of the structure. This is justified by the dramatic decrease of $\Delta \bar{C}_p^\circ$ in all cases. The exact shape of the $\Delta \bar{C}_p^\circ$ -mole fraction of TBA profile also seems to depend on the size and nature of the solute.⁶ In this connection, it is interesting to note that the effect of *n*-Am₄NBr is more similar to that of NaBPh₄ than to that of Bu₄NBr, as was also observed in the temperature dependence behavior of $\Delta \bar{C}_p^\circ$ in water, in spite of the fact that *n*-Am₄NBr is larger in size compared to both Bu₄NBr and NaBPh₄, which suggests that the size as well as the aliphaticity and aromaticity of the hydrophobic solute play an important role in determining the mode of interaction of a hydrophobic solute with water in pure water as well as in water-rich aqueous binary solvent systems.

Acknowledgment. We are thankful to the Council of Scientific and Industrial Research, India, for the award of Junior Research Fellowships to R. K. Mohanty and Shyam Sunder. We are also grateful to the Department of Atomic Energy, India, for part of the financial support.

Thermodynamics of Tetrabutylammonium Bromide in Aqueous Sodium Chloride and the Effects on the Water Structure

by B. Chawla and J. C. Ahluwalia*

Department of Chemistry, Indian Institute of Technology, Kanpur-16, India (Received December 28, 1971)

The partial molal enthalpies $\Delta\bar{H}_s^\circ$ of Bu_4NBr in aqueous sodium chloride solutions (containing 2, 3, 4, and 5 *M* sodium chloride) have been determined calorimetrically at 25, 35, and 45° and have been used to derive excess partial molal heat capacities $\Delta\bar{C}_p^\circ$ at 30 and 40°. These values have been further combined with the integral heats of solution ΔH_s° (at 25, 35, and 45°), as well as with the excess partial molal heat capacities ΔC_p° (at 30 and 40°) of Bu_4NBr in water reported earlier, to derive thermodynamic transfer functions ΔH_{tr} and $\Delta C_{p, tr}$ for the transfer of Bu_4NBr from water to aqueous sodium chloride solutions. The results show that transfer of Bu_4NBr from water to aqueous sodium chloride is accompanied by a positive enthalpy change and an increase in partial molal heat capacity. Comparison with similar results on thermodynamics of transfer of Bu_4NBr from water to aqueous urea indicates that the structure-breaking effect of urea is different from that of sodium chloride.

Introduction

In continuation of our studies in the binary urea-water^{1,2} and ternary urea-water-hydrophobic solute systems,^{3,4} we report in this paper the thermodynamic study of the Bu_4NBr - NaCl -water ternary system with a view to understanding the influence of urea on the effect of hydrophobic solute on the structure of water. Our previous thermodynamic studies in the ternary systems of Bu_4NBr -urea-water³ and NaBPh_4 -urea-water⁴ indicated that hydrophobic and highly structure-making solutes find aqueous urea less structured than pure water (as evidenced by the decrease in their excess partial molal heat capacities $\Delta\bar{C}_p^\circ$ in aqueous urea relative to that in pure water), an effect which increased with increasing urea concentration. These observations were found to be consistent with the model of Frank and Franks,⁵ which depicts urea acting as a statistical water structure breaker. This model also suggests that the structure-breaking mechanism of urea on water would be different from that of common electrolytes. With a view to further verifying this model, we undertook the thermodynamic investigation of the Bu_4NBr - NaCl -water ternary system. The comparison of the thermodynamics of this system with those of the Bu_4NBr -urea-water system indeed shows a difference in the structure-breaking action of sodium chloride and that of urea on the water structure.

Experimental Section

The submarine calorimeter and the operational procedure for measurements of the integral heats of solution have been described previously.^{3,6,7}

Bu_4NBr was obtained from Eastman Organic Chemicals Distillation Products Industries and was recrystallized by the method reported in the literature.⁸ The recrystallized salt was dried *in vacuo* at 60–80°. The

sample bulbs were filled with the salt, dried to constant mass at 80°, and then sealed. Analytical reagent grade sodium chloride (assay >99.9%) was obtained from BDH Ltd. and was used as such. Deionized distilled water was used for making aqueous sodium chloride solutions.

Results

The values of partial molal heats of solution $\Delta\bar{H}_s^\circ$ of Bu_4NBr in 2, 3, 4, and 5 *M* aqueous sodium chloride solutions at 25, 35, and 45° are given as supplementary material.⁹ Since the measurements of $\Delta\bar{H}_s^\circ$ of Bu_4NBr were carried out in very dilute solutions of Bu_4NBr (0.2×10^{-3} – 0.8×10^{-3} *M*) wherein any concentration effect is masked by the experimental error, the value of the limiting partial molal enthalpy $\Delta\bar{H}_s^\circ$ was taken as the average of $\Delta\bar{H}_s^\circ$ values. The uncertainties in the $\Delta\bar{H}_s^\circ$ values are computed as 95% confidence limits. The values of $\Delta\bar{H}_s^\circ$ of Bu_4NBr in 2, 3, 4, and

(1) S. Subramanian, D. Balasubramanian, and J. C. Ahluwalia, *J. Phys. Chem.*, **73**, 266 (1969).

(2) S. Subramanian, T. S. Sarma, D. Balasubramanian, and J. C. Ahluwalia, *ibid.*, **75**, 815 (1971).

(3) T. S. Sarma and J. C. Ahluwalia, *ibid.*, **76**, 1366 (1972).

(4) B. Chawla, S. Subramanian, and J. C. Ahluwalia, *J. Chem. Thermodyn.*, in press.

(5) H. S. Frank and F. Franks, *J. Chem. Phys.*, **48**, 4746 (1968).

(6) S. Subramanian and J. C. Ahluwalia, *J. Phys. Chem.*, **72**, 2525 (1968).

(7) T. S. Sarma, R. K. Mohanty, and J. C. Ahluwalia, *Trans. Faraday Soc.*, **65**, 2333 (1969).

(8) A. K. R. Unni, L. Elias, and H. I. Schiff, *J. Phys. Chem.*, **67**, 1216 (1963).

(9) The detailed listing of $\Delta\bar{H}_s^\circ$ values will appear following these pages in the microfilm edition of this volume of the journal. Single copies may be obtained from the Business Operations Office, Books and Journals Division, American Chemical Society, 1155 Sixteenth St., N.W., Washington, D. C. 20036, by referring to code number JPC-72-2582. Remit check of money order for \$3.00 for photocopy or \$2.00 for microfiche.

Table I: Enthalpies^a of Transfer of Tetrabutylammonium Bromide from Water to Aqueous Sodium Chloride at 25, 35, and 45°

Concn of NaCl , M	25.0°		35.0°		45.0°	
	$\Delta\bar{H}_s^\circ$ ^b	ΔH_{tr}	$\Delta\bar{H}_s^\circ$ ^b	ΔH_{tr}	$\Delta\bar{H}_s^\circ$ ^b	ΔH_{tr}
0 ^c	-2050 ± 15		-260 ± 15		1525 ± 33	
2	-1857 ± 25	193 ± 29	61 ± 11	321 ± 19	2215 ± 15	690 ± 36
3	-1360 ± 53	690 ± 55	460 ± 24	720 ± 28	2676 ± 32	1151 ± 46
4	-873 ± 25	1177 ± 29	928 ± 18	1188 ± 24	2973 ± 41	1448 ± 53
5	514 ± 11	2564 ± 19	2302 ± 51	2562 ± 53	4232 ± 39	2707 ± 51

^a ΔH values are in calories per mole. ^b $\Delta\bar{H}_s^\circ$ values are computed average values with 95% confidence limits. ^c The values of $\Delta\bar{H}_s^\circ$ in pure water are taken from ref 7 and 10.

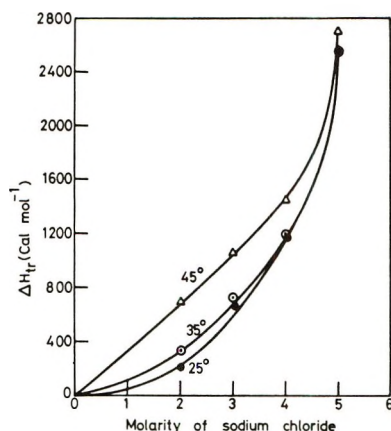


Figure 1. The enthalpy of transfer of Bu_4NBr from water to aqueous NaCl solutions as a function of molarity of NaCl : (●) ΔH_{tr} at 25°, (○) ΔH_{tr} at 35°, and (△) ΔH_{tr} at 45°.

5 M aqueous sodium chloride solutions at 25, 35, and 45° are given in Table I, along with the $\Delta\bar{H}_s^\circ$ values in pure water at the same temperatures reported earlier from this laboratory.^{7,10} The enthalpies of transfer ΔH_{tr} ($\Delta H_{tr} = \Delta\bar{H}_s^\circ - \Delta H_s^\circ$) of Bu_4NBr from water to aqueous sodium chloride solutions at 25, 35, and 45° are also listed in Table I and plotted as a function of molarity of sodium chloride in Figure 1. The excess partial molal heat capacities $\Delta\bar{C}_p^\circ$ of Bu_4NBr in aqueous sodium chloride solutions at 30 and 40° derived from the $\Delta\bar{H}_s^\circ$ values by the integral heat method^{6,7} are given in Table II. The partial molal heat capacities of transfer ΔC_{ptr} of Bu_4NBr from water to aqueous sodium chloride solutions are listed in Table II and plotted as a function of molarity of sodium chloride in Figure 2. For comparison, the ΔC_{ptr} of Bu_4NBr ³ from water to aqueous urea is also plotted as a function of molarity of urea in Figure 2.

Discussion

The results given in Table I and Figure 1 show that the transfer of highly structure-making hydrophobic solute Bu_4NBr from water to aqueous sodium chloride solutions is accompanied by a positive enthalpy change at 25, 35, and 45°. This effect increases with increase in sodium chloride concentration. The effect of in-

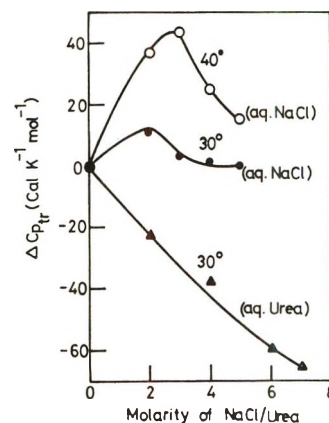


Figure 2. The partial molal heat capacity of transfer of Bu_4NBr from water to aqueous NaCl and aqueous urea solutions: (●) ΔC_{ptr} of Bu_4NBr from water to aqueous NaCl at 30°, (○) ΔC_{ptr} of Bu_4NBr from water to aqueous NaCl at 40°, (▲) ΔC_{ptr} of Bu_4NBr from water to aqueous urea at 30° (ref 3).

Table II: Heat Capacities^a of Transfer of Tetrabutylammonium Bromide from Water to Aqueous Sodium Chloride at 30 and 40°

Concn of NaCl , M	30.0°		40.0°	
	$\Delta\bar{C}_p^\circ$	ΔC_{ptr}	$\Delta\bar{C}_p^\circ$	ΔC_{ptr}
0	179 ± 2	0	179 ± 4	0
2	192 ± 3	13 ± 4	215 ± 2	36 ± 4
3	182 ± 6	3 ± 6	222 ± 4	43 ± 6
4	180 ± 3	1 ± 4	205 ± 5	26 ± 6
5	179 ± 5	0 ± 5	193 ± 6	14 ± 7

^a Heat capacities are in calories per degree Kelvin per mole.

creasing temperature is to increase slightly the value of ΔH_{tr} . The ΔH_{tr} values of Bu_4NBr from water to 5 M aqueous sodium chloride solutions at 25, 35, and 45° are found to be 2564, 2562, and 2707 cal mol⁻¹, respectively.

The results given in Table II and Figure 2 show that the transfer of Bu_4NBr from water to aqueous sodium chloride solutions at 30 and 40° is accompanied by an

(10) T. S. Sarma and J. C. Ahluwalia, *Trans. Faraday Soc.*, **67**, 2528 (1971).

increase in excess partial molal heat capacity, indicating an increase in the structure-making propensity of Bu_4NBr . This effect increases with increasing sodium chloride concentration, up to around 2 M at 30° and around 3 M at 40°, followed by a decrease with further increase in sodium chloride concentration. On the other hand, the transfer of Bu_4NBr from water to aqueous urea³ solutions (see Figure 2) is accompanied by a decrease in its excess partial molal heat capacity, an effect which goes on increasing with urea concentration and reaches about saturation limit at 7 M urea. Since the structure-making propensity of Bu_4NBr decreases in aqueous urea and increases in aqueous NaCl relative to that in pure water, it appears, therefore, that the structure-breaking mechanism of urea is different from that of sodium chloride. This observation supports the model of Frank and Franks,⁵ according to which

water is pictured as containing two distinct species, dense monomers and bulky clusters containing the tetrahedrally hydrogen-bonded water molecules, and urea, being debarred from entering into clusters for geometrical reasons, dissolves in the denser species and acts as a diluent of the same. This process, which causes a shift of some of the clusters into the denser species in order to keep the equilibrium constant of dense-bulky water equilibrium unchanged, results in a decrease in the structure of water; the net statistical structure-breaking action of urea is in result, rather than in mechanism, unlike the structure-breaking action of common electrolytes.⁵

Acknowledgment. We are thankful to the Council of Scientific and Industrial Research, India, for the award of a Junior Research Fellowship to B. Chawla.

Adsorption Isotherm and Surface Area Determination below the Triple Point

by G. G. Litvan

Building Materials Section, Division of Building Research, National Research Council of Canada, Ottawa, Canada (Received March 13, 1972)

Publication costs assisted by National Research Council of Canada

Attention is drawn to the consequences of the finding that adsorbates are in a liquidlike state at temperatures below their bulk freezing point. If the relative pressure is based on the saturation vapor pressure of the undercooled liquid, differences between the N_2 and Kr surface areas and those between the BET and Dubinin-Raduskevich areas become minimal. On application of inappropriate relative pressure values in constructing isotherms, apparent supersaturation may be indicated.

Adsorptive properties of systems are commonly characterized by isotherms where the experimentally determined amount of adsorbed vapor is plotted against the relative pressure, p/p° (p is the vapor pressure (vp) of the adsorbate and p° , the vp of the substance in the bulk state at the temperature of the experiment). At temperatures, T , above the triple point, T_{tr} , p° is taken as that of the bulk liquid, p°_{l} , and at $T < T_{\text{tr}}$ that of the solid p°_{s} .

In calorimetric¹⁻⁵ and dilatometric^{5,6} experiments no evidence can be found for "freezing" in the first two adsorbed layers at any T , and recently it has been shown⁷ that even at higher coverages the adsorbate is in a liquidlike state.

The direct consequence of this finding is that in estimating the surface area by the BET method the value of p°_{l} has to be substituted in the equation even if $T < T_{\text{tr}}$. The failure to follow this practice, sug-

gested by the first proponents of the Kr method,⁸ is the reason for the discrepancies observed between the N_2 and Kr surface areas, when the experimental temperature is 77°K, 39° below the T_{tr} of krypton. This is proved by the discovery that the surface area values obtained by the two methods can be brought into alignment when p°_{s} is substituted with adjustable

- (1) H. P. R. Frederikse, *Physica*, **15**, 860 (1949).
- (2) J. A. Morrison and L. E. Drain, *J. Chem. Phys.*, **19**, 1063 (1951).
- (3) J. A. Morrison, L. E. Drain, and J. S. Dugdale, *Can. J. Chem.*, **30**, 890 (1952).
- (4) K. S. Dennis, E. L. Pace, and Ch. S. Baughman, *J. Amer. Chem. Soc.*, **75**, 3267 (1953).
- (5) G. G. Litvan, *Can. J. Chem.*, **44**, 2617 (1966).
- (6) G. G. Litvan and R. McIntosh, *ibid.*, **41**, 3095 (1963).
- (7) E. W. Sidebottom and G. G. Litvan, *Trans. Faraday Soc.*, **67**, 2726 (1971).
- (8) R. A. Beebe, J. B. Beckwith, and J. M. Honig, *J. Amer. Chem. Soc.*, **67**, 1554 (1945).

parameters $p^{\circ 9}$ and Q^{10} the value of which was identical with $p^{\circ 1}$ calculated by extrapolation. The authors of ref 9 and 10 take the view, however, that the close agreement between Q and $p^{\circ 1}$ is fortuitous.

The purpose of this note is to show that recognizing the liquidlike state of the adsorbate at $T < T_{tr}$ provides theoretical support for the practice of applying $p^{\circ 1}$ in the krypton surface area calculation and implies that similar practice has to be followed in the case of other adsorbates, *e.g.*, argon, xenon, and methane at liquid nitrogen temperature.

Furthermore, if experimentally determined adsorption data are plotted in terms of inappropriate p° value, (such as $p^{\circ s}$) distortion of the curve results.⁷ For example, in the case of krypton at 77°K, $p^{\circ s} = 1.75$ Torr while $p^{\circ 1} = 2.63$ Torr, thus when $p/p^{\circ s} = 1$ the value of $p/p^{\circ 1}$ is only 0.66. When the pressure in the cell exceeds this value, condensation on the walls of the cell restores it to $p^{\circ s}$. The obtained isotherm, if plotted as a function of $p/p^{\circ s}$, crosses the ordinate at unity relative pressures instead of approaching it asymptotically. This was reported¹⁰ in 1965 and more recently in a study of the adsorption on nonpolar gases on oxide, metal, and salt surfaces.¹¹ It should be emphasized that the phenomenon considered here occurs below T_{tr} and is distinct from that discussed by Brunauer and coworkers.¹²

If nucleation on the walls is delayed, p may exceed $p^{\circ s}$ temporarily, but this phenomenon is not related in

any way to the adsorbent since it is not yet saturated. In the study of xenon adsorption on porous silver at 77.4°K,¹³ $p/p^{\circ s}$ rose temporarily to a value of approximately 1.08 but, if the values are recalculated the true relative pressure was apparently only ~ 0.02 (applying $p^{\circ} = 2.06 \times 10^{-2}$ Torr, obtained by extrapolation¹⁴). Supersaturation is clearly an artefact as shown not only by the above consideration but also by the reasonably good superimposition of the Ar, Kr, and Xe isotherms when they were plotted in terms of $p/p^{\circ 1}$. It is very probable that the differences between the BET and Dubinin-Raduskevich areas will become minimal when the proper $p^{\circ 1}$ values are used. Difficulties are encountered, however, in determining accurate $p^{\circ 1}$ values which, in some cases, are 80° below T_{tr} (xenon at 77°K).

Acknowledgment. This paper is a contribution from the Division of Building Research, National Research Council of Canada, and is published with the approval of the Director of the Division.

(9) J. M. Haynes, *J. Phys. Chem.*, **66**, 182 (1962).

(10) P. Chenebault and A. Schurenkamper, *ibid.*, **69**, 2300 (1965).

(11) R. H. van Dongen, J. H. Kaspersma, and J. H. DeBoer, *Surface Sci.*, **28**, 237 (1971).

(12) S. Brunauer, J. Skalny, and E. E. Bodor, *J. Colloid Interface Sci.*, **30**, 546 (1969).

(13) J. P. Hobson, *J. Phys. Chem.*, **73**, 2720 (1969).

(14) "Landolt-Börnstein Zahlenwerte und Funktionen," part 2a, Springer-Verlag, Berlin, 1960, p 4.

Chromatographic Peak Shapes. Their Origin and Dependence on the Experimental Parameters

by Eli Grushka

Department of Chemistry, State University of New York at Buffalo, Buffalo, New York 14214
(Received February 14, 1972)

Central moments and quantities related to them, such as skew and excess, can be used as chromatographic peak shape indicators. Theoretically, this paper demonstrates that the moments of a chromatographic peak are given in terms of the parameters that determine the shape, *i.e.*, partition coefficients, column length, etc. Consequently, the effect of the experimental condition on the peak shape can be studied by observing the moments. Examples as to how the moments vary with the experimental system are given. Possible utilization of the information thus obtained is indicated.

Introduction

The peak shape is one of the most important parameters in chromatography, since it is a reflection of the processes occurring in (as well as outside) the column and thus contains all the information which one might wish to obtain. Chromatography nowadays is used to determine thermodynamics, kinetics, and molecular kinetics quantities over and above its conventional use as a separating tool. In order to correctly interpret the chromatographic data, the peak shape, its origin, and its dependence on the experimental parameters must be clearly understood. Once these things are known, a critical assessment of the routinely made chromatographic assumptions can be carried out. Regarding these assumptions, the following questions arise. (1) Under what conditions is the chromatographic peak a gaussian one? (2) When is the usually made assumption of infinitely fast transfer of the solute molecules through the stationary–mobile phases interface a valid one? (3) Under what conditions can one assume the apparent partition coefficient to be truly independent of the carrier velocity? Knowledge of the peak shape and the factors influencing it can answer these questions.

The majority of the published work dealing with chromatographic theories was concerned mainly with the broadening of a zone undergoing the chromatographic process. Relatively few workers concerned themselves with the overall shape of the peak. Although the bandwidth is an important quantity in determining the column efficiency, resolution,¹ and peak capacity,^{2,3} the peak shape is, inherently, the more fundamental parameter.

Much of the earlier work, which is adequately reviewed elsewhere,⁴ concentrated on demonstrating that the peak shape can be reduced to a gaussian form. In addition, the role of molecular diffusion in the mobile phase was frequently neglected. In 1952, Lapidus and

Amundson⁵ treated the problem of adsorption chromatography. They solved a system of differential equations describing the mass balance in the column. They obtained an expression for the concentration profile of the solute as it emerges from the system. That expression, however, is too complex for practical use, unless the diffusion in the mobile phase is neglected. van Deemter, *et al.*, in their classic paper,⁶ utilized Amundson's work in their derivation of the often used "van Deemter" equation. Giddings and his coworkers,⁷ as well as McQuarrie,⁸ approached the problem of the peak shape in adsorption chromatography from a stochastic point of view. They showed that the concentration profile of the solute is given in terms of a product of an exponential and a Bessel function. With some simplification they show that in the "long-time" limit the resultant shape is, again, gaussian. Provided that one knows the adsorption and desorption rate constants, the peak shape can be easily predicted, even in the case where the long-time limit does not hold.

In 1962, Bocke and Parke,⁹ instead of solving the set of differential equations suggested by Lapidus and Amundson,⁵ found the statistical moments of the concentration profile of a solute zone obeying the mass balance relations suggested by the latter authors. As

- (1) J. C. Giddings, "Dynamics of Chromatography, Part I: Principles and Theory," Marcel Dekker, New York, N. Y., 1965.
- (2) J. C. Giddings, *Anal. Chem.*, **39**, 1027 (1967).
- (3) E. Grushka, *ibid.*, **42**, 1142 (1970).
- (4) See ref 1, Chapter 2.
- (5) L. Lapidus and N. R. Amundson, *J. Phys. Chem.*, **56**, 984 (1952).
- (6) J. J. van Deemter, F. J. Zuiderweg, and A. Klinkenberg, *Chem. Eng. Sci.*, **5**, 271 (1956).
- (7) See ref 1, Chapter 2, Section 13, and references therein.
- (8) D. A. McQuarrie, *J. Chem. Phys.*, **38**, 437 (1963).
- (9) J. Bocke and N. G. Parke, III, "Gas Chromatography," N. Brenner, Ed., Academic Press, New York, N. Y., 1962, p 391.

we shall soon indicate, the statistical moments are important in characterizing the shape of the chromatographic peak. In 1965, the usage of moments in chromatography gained in popularity when Kubin¹⁰ and Kucera¹¹ independently calculated them, again using the mass balance equations. A similar method of approach has since been carried out by Vink,¹² Kaminskii, *et al.*,¹³ Grubner, *et al.*,¹⁴⁻¹⁷ Yamazaki,¹⁸ and Kocirik.¹⁹

The usage of the statistical moments is attractive because they completely characterize the chromatographic peak. Their importance in terms of peak areas, retention times, peak widths, and asymmetry was already discussed by us²⁰ as well as by Grubner.¹⁷ In addition, the moments can be used as the coefficients in a series approximation of the peak shape when its exact mathematical description is not known. One such series is the Gram-Charlier

$$f(t) = \frac{1}{\sigma\sqrt{2\pi}} \exp\left[-\frac{(t - m_1)^2}{2\sigma^2}\right] \times \left[1 + \sum_{i=3}^{\infty} \frac{C_i}{i!} H_i\left(\frac{t - m_1}{\sigma}\right)\right] \quad (1)$$

Here t is time, m_1 is the first moment (center of gravity of the peak), σ^2 is the variance of the peak, and $H_i(x)$ is the i th Hermite polynomial. The coefficients C_i are in terms of the moments, *i.e.*

$$C_3 = m_3/m_2^{3/2} \quad (2)$$

$$C_4 = (m_4/m_2^2) - 3 \quad (3)$$

$$C_5 = (m_5/m_2^{5/2}) - 10(m_3/m_2^{3/2}) \quad (4)$$

etc. Here m_i is the i th central moment. Grubner¹⁷ and McQuarrie⁸ have compared the actual chromatogram to its approximation given by eq 1. The coefficients C_3 and C_4 are called the skew and excess, respectively. A complete discussion on the Gram-Charlier series, as well as on the skew and excess, is given by Cramer.²¹ Hence, the moments of a chromatographic peak, or more specifically the skew and excess, can be utilized in studying its shape and its dependence on the experimental parameters.

The peak shape depends, among other things, on the partition coefficient, the diffusion coefficients, the carrier velocity, the amount of stationary phase in the column, the column length, and, if such exists, on extra-column effects. All these parameters are obviously affected by the experimental conditions. If the skew and excess (the first two coefficients in the Gram-Charlier series) are to be used as shape indicators, their dependence on the above parameters must be demonstrated. For that purpose, we shall describe a theoretical framework of a simplified, but none the less real, model which relates the skew and excess (or the moments) to the aforementioned quantities.

The Moments and Column Processes

The mass balance equations can, in principle, yield all the information needed to describe the system. A rigorous solution of the mass balance equations is difficult even for dispersion in empty tubes, without inter-phase mass transport (*viz.*, ref 22 and 23). However, since our primary aim is to demonstrate the relation between the skew and excess (or the moments) and the various parameters in chromatography, we shall make some simplifying assumptions which reduce the mathematical treatment but not the method of approach or the physical concepts of chromatography. The chromatographic column is assumed to be made of two infinitely long and wide slabs which are parallel to each other. The "infinitely wide slab" condition is fulfilled when the width of the channel is much greater than the gap between the two slabs. Equally as well, we could have chosen an infinitely long cylindrical column (either empty or packed with spherical solid support particles). As will be indicated later, the results for the model chosen here can, with slight numerical modification, describe cylindrical columns. The inner walls of the slabs are uniformly coated with a stationary phase with d_f cm as its depth. The velocity profile of the mobile phase was assumed to have a plug shape. This assumption for a packed chromatographic column is frequently not a bad one. Similarly, for the model described here, when d_f is large the error introduced by taking the velocity profile to be a plug shape is not serious, since the peak dispersion and shape depend largely on the mass transfer in the stationary phase. We also assumed that no mixed chromatographic mechanisms, *e.g.*, adsorption and partitioning, exist. Recent works by Lorenz and Rogers²⁴ and by Karger, *et al.*,²⁵ show that, at times, this assumption can be a serious one, since frequently mixed mechanisms do exist. Since the immediate purpose of the paper is to

(10) M. Kubin, *Collect. Czech. Chem. Commun.*, **30**, 1104 (1965).

(11) E. Kucera, *J. Chromatogr.*, **19**, 237 (1965).

(12) H. Vink, *ibid.*, **20**, 305 (1965).

(13) V. A. Kaminskii, S. F. Timashev, and N. N. Tunitskii, *Russ. J. Phys. Chem.*, **39**, 1354 (1965).

(14) O. Grubner, M. Ralek, and A. Zikanova, *Collect. Czech. Chem. Commun.*, **31**, 852 (1966).

(15) O. Grubner, M. Ralek, and E. Kucera, *ibid.*, **31**, 2629 (1966).

(16) O. Grubner, A. Zikanova, and M. Ralek, *J. Chromatogr.*, **28**, 209 (1967).

(17) O. Grubner, *Advan. Chromatogr.*, **6**, 173 (1968).

(18) H. Yamazaki, *J. Chromatogr.*, **27**, 14 (1967).

(19) M. Kocirik, *ibid.*, **30**, 459 (1967).

(20) E. Grushka, M. N. Myers, P. D. Schettler, and J. C. Giddings, *Anal. Chem.*, **41**, 889 (1969).

(21) H. Cramer, "Mathematical Methods of Statistics," Princeton University Press, Princeton, N. J., 1946.

(22) W. N. Gill and R. Sankarasubramanian, *Proc. Roy. Soc., Ser. A*, **316**, 341 (1970).

(23) W. N. Gill and R. Sankarasubramanian, *ibid.*, **322**, 101 (1971).

(24) L. J. Lorenz and L. B. Rogers, *Anal. Chem.*, **43**, 1593 (1971).

(25) B. L. Karger, R. C. Castells, P. A. Sewell, and A. Hartkof, *J. Phys. Chem.*, **75**, 3870 (1971).

verify the validity of the moment approach to peak-shape analysis, we have assumed only partitioning effects. In general, mixed mechanisms can be taken into account by including them in the mathematical model.

The system described above is characterized by the following mass balance equations

$$\frac{\partial C_m}{\partial t} - D \frac{\partial^2 C_m}{\partial z^2} + U \frac{\partial C_m}{\partial z} + k_t(KC_m - C_s|_{z=d_t}) = 0 \quad (5)$$

for the mobile phase, and

$$\frac{\partial C_s}{\partial t} = D_s \frac{\partial^2 C_s}{\partial x^2} \quad (6)$$

for the stationary phase. C indicates concentration, subscripts m and s denote mobile and stationary phase, respectively, D_s is the diffusion coefficient of the solute in the stationary phase, D is the dispersion coefficient in the mobile phase, U is the average carrier velocity, t is time, k_t is the mass transfer coefficient across the mobile-stationary interface, K is the partition coefficient of the solute, z is the column length coordinate and x is the lateral coordinate. The symbol $|_{z=d_t}$ indicates values at the stationary-mobile phases interface. d_t is the thickness of the stationary phase film. The initial and boundary conditions are

$$C_m(z, 0) = C_i; \quad C_m(\pm \infty, t) = 0 \quad (7)$$

$$C_s(z, 0) = 0 \quad (8)$$

$$\left. \frac{dC_s}{dx} \right|_{x=0} = 0 \quad (9)$$

$$A_s D_s \left. \frac{dC_s}{dx} \right|_{x=d_t} = V_m k_t (KC_m - C_s|_{z=d_t}) \quad (10)$$

A_s is the stationary phase area per unit column volume, and it can be written as V_s/d_t . V_s is the volume of the stationary phase per unit column volume. This area is small compared with the chromatographic zone so that the concentration of the solute in the mobile phase above it is uniform. V_m is the volume of the mobile phase per unit column volume. A somewhat similar set of differential equations was described by Kucera¹¹ and more recently by Horn.²⁶ The system described here is especially designed to describe a partitioning system.

Ideally, one would like to obtain an exact solution of $C_m(z, t)$. The set of differential equations, on the other hand, is difficult to solve analytically. The moments of $C_m(z, t)$, however, can be found by using either the Laplace or the Fourier transformation. In the Laplace domain the equations describing the mass balance are given as

$$S\bar{C}_m - C_i - D \frac{d^2 \bar{C}_m}{dz^2} + U \frac{d\bar{C}_m}{dz} + k_t(K\bar{C}_m - \bar{C}_s|_{z=d_t}) = 0 \quad (11)$$

and

$$S\bar{C}_s = D_s \frac{d^2 \bar{C}_s}{dx^2} \quad (12)$$

In eq 11 use was made of the initial condition $C_m(z, 0) = C_i$. The bars above the various \bar{C} 's indicate Laplace transforms. S is the Laplace variable. The boundary and initial conditions, in the Laplace domain, are

$$\bar{C}_m(\pm \infty, S) = 0 \quad (13)$$

$$\bar{C}_s(z, 0) = 0 \quad (14)$$

$$\left. \frac{d\bar{C}_s}{dx} \right|_{x=0} = 0 \quad (15)$$

$$\left. \frac{V_s}{d_t} D_s \frac{d\bar{C}_s}{dx} \right|_{x=d_t} = V_m k_t (K\bar{C}_m - \bar{C}_s|_{z=d_t}) \quad (16)$$

A solution of eq 12 is

$$\bar{C}_s(x, S) = C_1 \exp(x\sqrt{S/D_s}) + C_2 \exp(-x\sqrt{S/D_s}) \quad (17)$$

where C_1 and C_2 are constants of integration. From the boundary conditions, one gets

$$\bar{C}_s(x, S) = \frac{\bar{C}_m k_t K \cosh(x\sqrt{S/D_s})}{\frac{V_s}{d_t V_m} \sqrt{SD_s} \sinh(d_t \sqrt{S/D_s}) + k_t \cosh(d_t \sqrt{S/D_s})} \quad (18)$$

This expression can be utilized in eq 11, which upon rearrangement becomes

$$\frac{d^2 \bar{C}_m}{dz^2} - \frac{U}{D} \frac{d\bar{C}_m}{dz} - \frac{\bar{C}_m}{D} \left\{ S + \frac{V_s K k_t}{d_t V_m} \times \left[\frac{\sqrt{SD_s} \sinh(d_t \sqrt{S/D_s})}{\frac{V_s}{d_t V_m} \sqrt{SD_s} \sinh(d_t \sqrt{S/D_s}) + k_t \cosh(d_t \sqrt{S/D_s})} \right] \right\} = -C_i/D \quad (19)$$

In the above equation $V_s K/V_m$ is equal to the capacity factor k . A solution of eq 19 is

$$\bar{C}_m(z, S) = \frac{1}{2D \left[\left(\frac{U}{2D} \right)^2 + \frac{A}{D} \right]^{1/2}} \int_{-\infty}^{\infty} C_i \times \exp \left[\frac{U}{2D} - \sqrt{\left(\frac{U}{2D} \right)^2 + A/D} \right] (z - z') dz' \quad (20)$$

(26) F. J. M. Horn, *AIChE J.*, **17**, 613 (1971).

where A is

$$A = S + \frac{kk_f}{d_f} \times \left[\frac{\sqrt{SD_s} \sinh(d_f \sqrt{S/D_s})}{\frac{V_s}{V_m d_f} \sqrt{SD_s} \sinh(d_f \sqrt{S/D_s}) + k_f \cosh(d_f \sqrt{S/D_s})} \right] \quad (21)$$

As is customary, we assume that the injection of the solute is a δ function

$$C_i = B\delta(z) \quad (22)$$

where B is related to the mass of the solute. Since we are interested in $\bar{C}_m(z, S)$ at a particular point, L , in the column, *i.e.*, the detector, eq 20, upon integration, yields

$$\bar{C}(z, S) = \frac{B \exp\left[\frac{UL}{2D} - L\sqrt{\left(\frac{U}{2D}\right)^2 + A/D}\right]}{2D \left[\left(\frac{U}{2D}\right)^2 + A/D\right]^{1/2}} \quad (23)$$

This equation is difficult, if at all possible, to invert back to the time domain. However, by using the following property of the Laplace transform the moments of $C(z, t)$ can be obtained.

$$\int_0^\infty t^n f(t) dt = (-1)^n \lim_{s \rightarrow 0} \frac{\partial^n f(S)}{\partial S^n} \quad (24)$$

The first five moments, including the zeroth one, are (moments higher than the first are central moments)

$$m_0(\text{unnormalized}) = B/U \quad (25)$$

$$m_1 = \left(\frac{L}{U} + \frac{2D}{U^2}\right)(1+k) \quad (26)$$

$$m_2 = \left(\frac{2DL}{U^3} + \frac{8D^2}{U^4}\right)(1+k)^2 + \left(\frac{L}{U} + \frac{2D}{U^2}\right)k \left(\frac{2d_f^2}{3D_s} + \frac{V_s}{V_m k_f}\right) \quad (27)$$

$$m_3 = \left(\frac{12D^2L}{U^5} + \frac{64D^3}{U^6}\right)(1+k)^3 + \left(\frac{DL}{U^3} + \frac{4D^2}{U^4}\right)k(1+k) \left(\frac{4d_f^2}{D_s} + \frac{V_s}{V_m k_f}\right) + \left(\frac{L}{U} + \frac{2D}{U^2}\right)k \left[\frac{12d_f^4}{15D_s^2} + \frac{4d_f^2 V_s}{D_s V_m k_f} + 6\left(\frac{V_s}{V_m k_f}\right)^2\right] \quad (28)$$

$$m_4 = \left(\frac{12D^2L^2}{U^6} + \frac{216D^3L}{U^7} + \frac{960D^4}{U^8}\right)(1+k)^4 + \left(\frac{DL^2}{U^4} + \frac{12D^2L}{U^5} + \frac{D^3}{U^6}\right)(1+k)^2 \left(\frac{8d_f^2}{D_s} + \frac{24V_s}{V_m k_f}\right) + \left(\frac{L^2}{U^2} + \frac{6DL}{U^3} + \frac{12D^2}{U^4}\right)k^2 \left(\frac{4d_f^2}{D_s} + \frac{12V_s}{V_m k_f}\right) +$$

$$\left(\frac{DL}{U^3} + \frac{4D^2}{U^4}\right)k(1+k) \left[\frac{32d_f^4}{5D_s^2} + \frac{32d_f^2 V_s}{D_s V_m k_f} + 48\left(\frac{V_s}{V_m k_f}\right)^2\right] + \left(\frac{L}{U} + \frac{2D}{U^2}\right)k \left[\frac{136d_f^6}{105D_s^3} + \frac{136d_f^4 V_s}{15D_s^2 V_m k_f} + \frac{16d_f^2}{D_s} \left(\frac{3V_s^2}{V_m^2 k_f^2} + \frac{V_s^3}{V_m^3 k_f^3}\right)\right] \quad (29)$$

Although higher central moments can theoretically be obtained, one is limited in practice, owing to experimental difficulties, to the first five. A more complicated moment expression, for adsorption chromatography, was derived by Kucera.¹¹

The first moment, as was indicated by us previously,²⁰ is the retention time, t_R , of the solute. Under normal conditions the term $2D/U^2$ is much smaller than L/U and the first moment is reduced to the well-known relation

$$t_R = m_1 \approx \frac{L}{U}(1+k) \quad (30)$$

The second moment, being the peak variance, leads to a direct derivation of the plate height

$$H = \frac{\sigma^2}{L} = \frac{Lm_2}{m_1^2} \quad (31)$$

σ^2 is the length-based variance. It should be noted that the moments found by us are time based, since they were obtained for a particular position in the column (the detector) as a function of time. Under normal condition $2DL/U^3 \gg 8D^2/U^4$ and

$$H = \frac{2D}{U} + \frac{2kd_f^2 U}{3(1+k)^2 D_s} + \frac{kV_s U}{(1+k)^2 V_m k_f} \quad (32)$$

The first two terms on the right-hand side of eq 32 are the usual molecular diffusion and resistance to mass transfer in the stationary phase terms in capillary columns. They are identical with the equivalent terms in the Golay equation.²⁷ The last term in eq 32 is due to the finite rate of mass transfer across the mobile-stationary phases interface and is similar to the expression obtained by Giddings, *et al.*²⁸ In chromatography, it is normally assumed that $k_f = \infty$. In reality, this assumption can be a serious one, especially in high-speed chromatography, and only a detailed analysis of the peak shape can indicate the condition under which it can be made.

With slight modification, the original set of differential equations can describe a column packed with spherical beads on which the stationary phase is coated. In this case, the moments of eq 25–29, with some numerical constant adjustments, still hold. The dis-

(27) M. J. E. Golay, "Gas Chromatography—1955," R. P. W. Scott, Ed., Butterworths, Washington, D. C., 1960, p 139.

(28) M. R. James, J. C. Giddings, and H. Hying, *J. Phys. Chem.*, **68**, 725 (1964).

persion coefficient, D , in packed columns can be written as¹¹

$$D = D_m + AU + BU^2 + \dots \quad (33)$$

where D_m is the diffusion coefficient of the solute in the mobile phase and A and B are constants. The plate expression for packed columns can be shown to be (assuming k_t to be infinity)

$$H = A + \frac{2D_m}{U} + BU + \frac{2kd_t^2U}{15(1+k)^2D_s} \quad (34)$$

If B is proportional to the diameter of the solid support particle divided by D_m , then eq 34 is the familiar plate expression.¹

The behavior of the moments, and hence of the skew and excess and the peak shape, depends upon the column length, the carrier velocity, the amount and nature (*via* k) of the stationary phase, the solute's diffusion coefficients, and the nature of the transfer across the two-phase interface. The moments depend implicitly on the temperature and the pressure of the system. Since all these parameters are influenced and affected by the experimental techniques, the moments indeed provide the theoretical connection between the peak shape and the laboratory conditions.

Grubner¹⁷ was among the first to investigate the influence of some experimental conditions on the moments. He described the behavior of $(m_3/m_1^3)L^2$ and $(m_4/m_1^4)L^3$ as a function of the carrier velocity only. Although important, these quantities do not have the same basic significance that the skew and excess possess. More recently, Grubner and Underhill,²³ in discussing the bed capacity in gas-solid chromatography, described the effect of some operating conditions on the breakthrough curves as obtained from a much simplified Gram-Charlier series. They did not, however, investigate the dependence of the skew and excess, nor of the actual peak shape, on these conditions.

To further demonstrate the usefulness of the moments and the information that can be obtained from them, few illustrative examples will be briefly discussed. Although the moment equations are perfectly correct for liquid-liquid chromatography, we shall

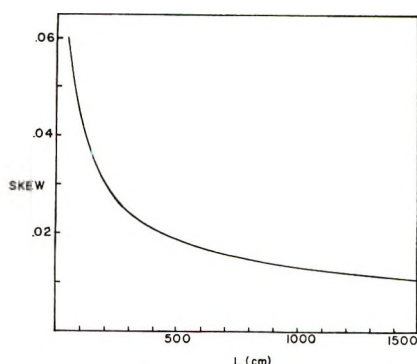


Figure 1. The skew as a function of the column length.

discuss in the examples a gas-liquid system only. We shall also assume that $k_t = \infty$. Whenever this assumption might be invalid we shall so indicate in the discussion. We shall also neglect the effect of the pressure drop on the diffusion coefficients. In calculating the skew and excess, the various parameters in the moments equations were given values approximating a real open tubular chromatographic systems.

Effect of Column Length. The following values were assigned to the different parameters

$$U = 10 \text{ cm/sec}$$

$$k = 10$$

$$D = 0.1 \text{ cm}^2/\text{sec}$$

$$D_s = 1 \times 10^{-5} \text{ cm}^2/\text{sec}$$

$$d_t = 1 \times 10^{-4} \text{ cm}$$

The behavior of the skew as a function of the column length is shown in Figure 1. As the column length increases, the peak becomes more symmetrical. This is in agreement with the long-time theories of chromatography.¹ In actual practice, at short column length (*i.e.*, small plate number) the contribution of a finite k_t might be very important and the actual plot of the skew *vs.* the column length can differ from that of Figure 1. Nonetheless, Figure 1 has an important practical implication. Increasing the column length increases the resolution between two peaks not only because of a larger plate number, but also because of increased peak symmetry. In fact Figure 1 indicates that the skew is proportional to $(1/L)^{1/2}$.

For the system described here (including the $k_t = \infty$ assumption), the excess remains practically a constant, having a value of about 6.32, as the column length increases. This is, perhaps, not surprising, since the excess is related to a normalized width of the peak which, like the plate height, is independent of the length.

Effect of Carrier Velocity. The following values were assigned to the different parameters

$$L = 1500 \text{ cm}$$

$$D = 0.1 \text{ cm}^2/\text{sec}$$

$$D_s = 1 \times 10^{-5} \text{ cm}^2/\text{sec}$$

$$d_t = 1 \times 10^{-4} \text{ cm}$$

$$k = 10$$

The behavior of the skew and excess is shown in Figure 2. Up to 50 cm/sec, the skew decreases while the excess increases. The skew does not decrease continuously but rather, at velocities of about 95 cm/sec, begins to increase (not shown in Figure 2). Both the skew and excess dependence on the velocity is similar

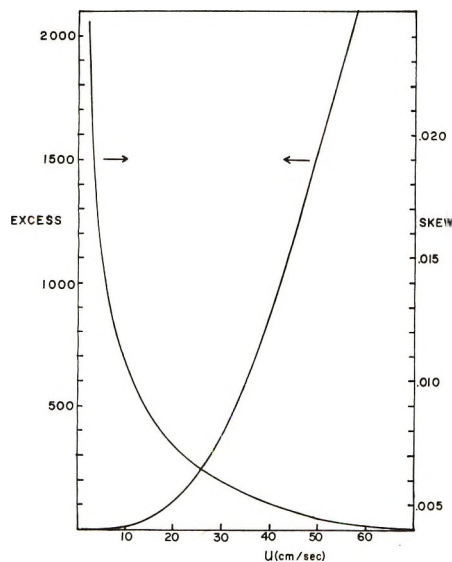


Figure 2. The skew and excess as a function of the mobile phase velocity.

to that of the plate height. The same conclusion was reached by Grubner¹⁷ in his investigation of $(m_3/m_1^3)L^2$ and $(m_4/m_1^4)L^3$. It is interesting to note that for this system the maximum efficiency (minimum in the plate height) occurs at about 60 cm/sec. The minimum in the skew is at 70–80 cm/sec. The excess minimum is, on the other hand, at very low velocities. At the optimum velocity (in the van Deemter sense), the excess is over 2000. Large positive excess indicates that the peak is taller and slimmer than a gaussian with the same second moment. For this system, then, a velocity of 60–80 cm/sec is most beneficial. It should be pointed out that as the velocity increases, the contribution of a finite rate of mass transfer across the stationary–mobile phases interface (finite k_f) becomes more important and the actual shape of the skew and excess plots might be different from these in Figure 2.

Effect of the Amount of Stationary Phase. This presents a slightly more complicated case, since the value of the capacity ratio k depends on the amount of stationary phase, or d_f . We can assume, however, that k is proportional to d_f and as the amount of stationary phase doubles so does k . Arbitrarily, we took k to be equal to unity at $d_f = 1 \times 10^{-5}$ cm. The rest of the parameters were given the following values

$$U = 10 \text{ cm/sec}$$

$$L = 1500 \text{ cm}$$

$$D = 0.1 \text{ cm}^2/\text{sec}$$

$$D_s = 1 \times 10^{-5} \text{ cm}^2/\text{sec}$$

The behavior of the excess and skew is shown in Figure 3. The skew decreases almost linearly from 0.0109 to 0.0103 as d_f increases from 1×10^{-5} cm to 5×10^{-3} cm. It seems that as the amount of stationary phase

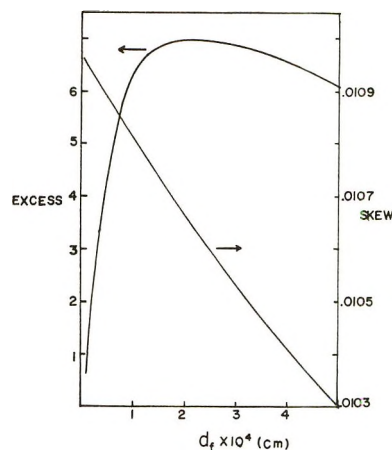


Figure 3. The skew and excess as a function of the stationary phase film thickness.

increases both the skew and the excess, the latter after reaching a maximum, decrease, again in agreement with the long-time limit of chromatography. The error in neglecting k_f is the largest at the low d_f values, since the retention time is shortest at that region. Moreover, it should be realized that as the film thickness decreases the plug flow approximation becomes progressively worse.

The strong dependence of the excess on the film thickness should be noted. Since even the highest value of the skew is rather small, Figure 2 indicates the practical value of a small d_f system.

Effect of the Temperature. Both diffusion coefficients as well as the capacity ratio are functions of the temperature, T . In order to study the dependence of the skew and excess on T , the following approximation can be made. The diffusion of the solute in the liquid phase can be written as¹

$$D_s = D_0 \exp[-W/RT] \quad (35)$$

D_0 is a constant, T is the absolute temperature, R is the gas constant, and W is an activation energy. A typical value of W is 8 kcal/mol. We assumed that at 350°K D_s is 1×10^{-5} cm²/sec. The dependence of the diffusion coefficient in the mobile phase, D , on T was taken as¹

$$D \propto T^{1.75} \quad (36)$$

At 350°K we assumed D to be 0.1 cm²/sec. The dependence on temperature of the capacity ratio k is as follows

$$k = A \exp[-\Delta G^\circ/RT] \quad (37)$$

A is a constant and ΔG° is the free energy change of the solute in going from the mobile to the stationary phase. A typical ΔG° value is -8 kcal/mol. At 350°K we took k to be 10. The rest of the parameters were given the following values

$$L = 1500 \text{ cm}$$

$$U = 10 \text{ cm/sec}$$

$$d_t = 1 \times 11^{-4} \text{ cm}$$

Figure 4 shows the behavior of the skew and excess. While the excess has a maximum value in this system, the skew continuously increases. At lower temperatures the retention time increases, the long-time limit is being approached, and the skew and excess decrease. The error introduced by omitting k_t is most pronounced at high temperatures, when the retention time is very short.

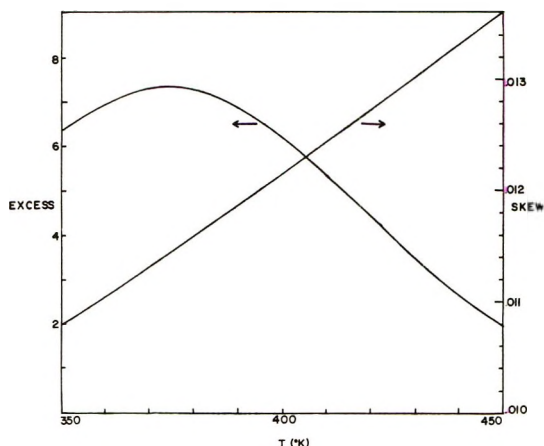


Figure 4. The skew and excess as a function of the column temperature.

Figure 4 strengthens the contention that operating at low temperatures is beneficial. Plots like this can help the researcher to maximize his system. For example, in this assumed system, if time is important, operating at around 400° might be the compromise between increasing skew and decreasing excess. If time is not a problem, the temperature of 350°K is better yet.

The Effect of the Partition Coefficient (or the Capacity Ratio). Finally, we can investigate the effect of the nature of solute on the peak shape. The following values were given to the various parameters

$$U = 10 \text{ cm/sec}$$

$$L = 1500 \text{ cm}$$

$$d_t = 1 \times 10^{-4} \text{ cm}$$

$$D = 0.1 \text{ cm}^2/\text{sec}$$

$$D_s = 1 \times 10^{-5} \text{ cm}^2/\text{sec}$$

It should be noted that as the partition coefficient changes, D and D_s probably vary in magnitude. However, the dependence of k on the partition coefficient is greater than that of the diffusion coefficient.

Figure 5 shows the behavior of the excess. The skew changes very slightly and was not included in Figure

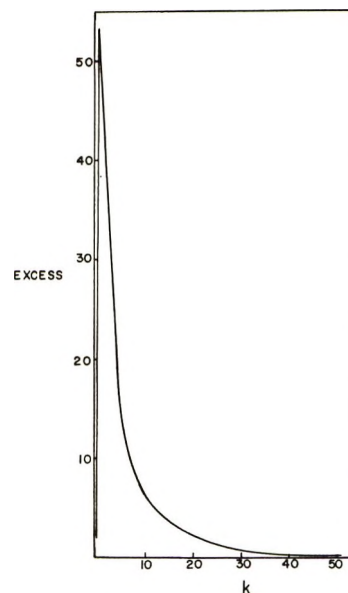


Figure 5. The excess as a function of the capacity ratio.

5. Concerning the skew, it can be shown that from a value of 0.0109 at $k = 0$ it drops to 0.0106 at $k = 1$ and gradually rises back to the original value of 0.0109 at $k = 30-50$. The excess, on the other hand, increases rapidly as the capacity factor changes from 0 to 1, and then it decreases with further increase in k . The maximum at $k = 1$ is a typical behavior of a normalized peak width in chromatography, and it has been observed with plate heights.³⁰ The omission of the k_t terms will have its greatest effect at low k values (short retention times). In addition, at low k values the assumption of a plug shape flow is most serious, especially in capillary columns, where the resistance to mass transfer in the actual parabolic flow profile can affect the peak shape.

Figure 5 indicates that the excess can be utilized in peak identification, at least within a homologous family, since each k has a unique excess value associated with it.

Conclusion

It is thus seen that the peak shape and its moments are dependent on many parameters, each of which is affected by the experimental conditions. Since most frequently the actual peak shape is not known exactly, the moments, or more specifically the skew and excess, can be utilized in studying the importance of the laboratory set-up. This knowledge, in return, can be employed by the researcher to maximize the chromatographic system. More importantly, perhaps, is the better understanding of chromatographic processes. The ultimate test of any chromatographic theory lies in its ability to predict correctly the peak shape and its dependence on the various parameters involved.

(30) S. dal Nogare and J. Chin, *Anal. Chem.*, **34**, 890 (1962).

This dependence must be studied and verified experimentally. The moment approach might be the easiest method by which this investigation can be made. Currently, the importance of the various operating conditions is being studied in our laboratory.

It is interesting to note that the moments of a chromatographic peak can be used to measure various kinetic and thermodynamic quantities. For example, Smith and coworkers used some simplified moment expressions to obtain chemisorption rates and equilibrium constants of hydrogen on nickel,³¹ cobalt,³² and copper-zinc oxide.³³ This further demonstrates

the importance of understanding the origin of the peak shape and the affects of the experimental conditions on it.

Acknowledgments. The author wishes to thank Robert Kurland for many helpful discussions. The work was partially supported by the Research Foundation of the State University of New York.

(31) G. Padberg and J. M. Smith, *J. Catal.*, **12**, 172 (1968)

(32) J. C. Adrian and J. M. Smith, *ibid.*, **18**, 57 (1970).

(33) M. Suzuki and J. M. Smith, *ibid.*, **21**, 335 (1971).

The Crystal Structures of Hydrated and Dehydrated

Thallium-Exchanged Zeolite A

by Paul E. Riley, Karl Seff,*

Chemistry Department, University of Hawaii, Honolulu, Hawaii 96822

and David P. Shoemaker¹

Department of Chemistry, Massachusetts Institute of Technology, Cambridge, Massachusetts 02139

(Received February 28, 1972)

Publication costs assisted by the Army Research Office (Durham)

The crystal structures of hydrated ($a = 12.32 \text{ \AA}$) and vacuum-dehydrated ($a = 12.17 \text{ \AA}$) thallium-exchanged zeolite A have been determined by single crystal X-ray techniques. Tl(I) ions are distributed among three equipoints in each structure: two such sites are on the threefold axis on either side of the six-oxygen ring and the third is near the center of the eight-oxygen ring. Small changes in cation positions and in the zeolite framework are observed upon dehydration. The shortest Tl(I)-O approaches are 2.75 (2), 2.81 (2), and 2.86 (3) \AA in the hydrated crystal and 2.64 (1), 2.60 (3), and 2.82 (3) \AA , respectively, for the dehydrated form. Changes in framework angles of $+14$, -17 , and -6° at the three nonequivalent oxygen atoms, corresponding to rotations of aluminosilicate tetrahedra, are observed upon dehydration.

Introduction

The positions of thallium ions in Tl(I)-exchanged zeolite A are of interest because they are likely to be similar, except for the effect of ionic radius, to those in the sodium form of zeolite A. In the hydrated sodium form, it is difficult to distinguish crystallographically between water oxygen atoms and sodium ions because of their similar X-ray scattering factors.² Meier³ had determined, by a comparison of powder photographs, that the Tl(I) positions did not change appreciably upon dehydration. Before that, Reed and Breck⁴ had reported approximate coordinates for the principal Tl(I) position in a dehydrated sample. The crystal structure of dehydrated Tl(I)-exchanged

zeolite A had been determined⁵ less accurately by powder methods.

Experimental Section

Crystals of zeolite 4A were prepared by Charnell's⁶

(1) The work done at MIT, leading to a set of atomic coordinates for the hydrated zeolite derived by least-squares refinement of powder photographic data, was supported by a grant from the Army Research Office (Durham). The computational work associated therewith was done in part at the MIT Computation Center.

(2) V. Gramlich and W. M. Meier, *Z. Kristallogr.*, **133**, 134 (1971).

(3) W. M. Meier, private communication (1964).

(4) T. B. Reed and D. W. Breck, *J. Amer. Chem. Soc.*, **78**, 5972 (1956).

(5) D. P. Shoemaker and K. Seff, unpublished (1964).

(6) J. F. Charnell, *J. Cryst. Growth*, **8**, 291 (1971).

method, modified to include a second crystallization using seed crystals from the first preparation. This sample was found by chemical analysis to have an approximate framework formula of $\text{Al}_{11}\text{Si}_{13}\text{O}_{48}^{11-}$ per unit cell. Single crystals (0.5 g) from 30 to 70 μ on an edge were allowed to exchange at 80° with 40 ml of nearly saturated TlNO_3 solution. The solution was agitated periodically. After 30 days, the crystals were filtered and washed, and chemical analysis indicated that the exchange was complete. The resulting crystals were colorless and mostly clear, although some cloudy striations were observed. These were substantially avoided in the selection of the two relatively large single crystals used in this work.

One crystal, a cube 55 μ on an edge, was dehydrated at 350° and 10^{-5} Torr for 36 hr. The capillary tube containing this crystal was then sealed off under vacuum and mounted on a goniometer head. Diffraction intensities were collected at 20° for $0 < 2\theta < 70^\circ$. The second crystal, 55 μ on an edge, was mounted on a glass fiber and was not isolated from the atmosphere. Subsequent diffraction intensities were collected at 23° at a relative humidity of 30% for $0 < 2\theta < 60^\circ$. Another data set, valid but slightly less suitable for experimental reasons, and not presented herein, was collected from the same hydrated crystal at the same relative humidity but at 20° for $0 < 2\theta < 70^\circ$.

A Syntex four-circle computer-controlled diffractometer with graphite-monochromatized $\text{Mo K}\alpha$ radiation ($\text{K}\alpha_1$, λ 0.70926 Å; $\text{K}\alpha_2$, λ 0.71354 Å) and a pulse-height analyzer was used throughout for preliminary experiments and for the collection of diffraction intensities. The cubic cell constants ($a = 12.32$ (1) Å at 20° and $a = 12.33$ (1) Å at 23° for hydrated Tl-exchanged zeolite A; $a = 12.17$ (1) Å for the dehydrated sample) were determined in each case by a least-squares treatment of 11 intense reflections with 2θ values up to 29°. The approximate space group $Pm\bar{3}m$ (no systematic absences) was used instead of $Fm\bar{3}c$ because the stoichiometry of our sample ensures a disorder which cannot be better described by another space group, and because Gramlich and Meier² have shown that deviations from the former space group are small even when appropriate.

The θ - 2θ scan technique was employed at a constant scan rate of 1.0°/min (in 2θ). The scan range varied from 2.0° at $2\theta = 3^\circ$ to 2.5° at $2\theta = 70^\circ$. All unique reciprocal lattice points (620 and 863 for the hydrated and dehydrated crystals, respectively) below the respective maximum 2θ values (60 and 70°) were examined. (High upper limits were chosen for 2θ to maximize the size of the data set even though few reflections with large 2θ values showed significant intensity.) A time equal to one-half of the scan time for each reflection was spent counting background at each end of the scan range. Two check reflections which were measured periodically during the collection of

each data set showed no significant trend in intensity. To examine the diffraction intensities for the possible effects of Renninger reflection, intensities were collected for the dehydrated material by a ψ -scan procedure in which each reflection was observed twice, at two positions differing by a rotation of 17° about its reciprocal lattice vector. No significant discrepancies were observed, and these two data sets were merged.

Standard deviations were assigned according to the formula

$$\sigma(I) = [CT + 0.25(t_c/t_b)^2(B_1 + B_2) + (pI)^2]^{1/2}$$

where CT is the total integrated count obtained in a scan time of t_c , B_1 and B_2 are the background counts each obtained in time t_b , and $I = CT - 0.5(t_c/t_b)(B_1 + B_2)$. A value of 0.04 was assigned to the empirical parameter p to account for instrument instability, but only for the dehydrated structure; for the hydrated case reported, this correction was omitted. The net counts were then corrected for Lorentz and polarization effects, and a small spherical absorption correction corresponding to $\mu R = 0.5$ was applied with little effect to the dehydrated Tl-A data set. All unique reflections (171 and 209 for the hydrated and dehydrated crystals, respectively) for which the net intensity exceeded three times its standard deviation were used throughout, except for the 001 reflection for which background counts indicated beam-stop interference in each data set.

Structure Determination

Initial full-matrix least-squares refinement of each structure was begun using parameters determined and refined⁵ with powder X-ray diffraction data on a sample of dehydrated $\text{Tl}_{12}\text{Al}_{12}\text{Si}_{12}\text{O}_{48}$. One Tl(I) position near 0, 0, 0.152, which had been found before to have a low occupancy parameter, was found to be unoccupied in our samples. Fourier syntheses failed to reveal new atomic positions which could be successfully refined by least-squares in either structure; that is, even in the hydrated case, no water molecules could be located. Alternate cycles of occupancy and thermal parameter refinement indicated 11.7 Tl(I)'s per unit cell. For reasons discussed in the next section, this value was decreased by a small amount to 11.0. The final values of the observed and calculated structure factors are available elsewhere⁷ and the structural and thermal parameters are presented in Table I. Bond lengths and angles are presented in Table II. The final values of the R_1 index, $(\sum |F_o| - |F_c|) / \sum F_o$, are 0.112 and 0.109 for the dehydrated and hydrated

(7) Listings of the observed and calculated structure factors for both structures will appear immediately following this article in the microfilm edition of this volume of the journal. Single copies may be obtained from the Business Operations Office, Books and Journals Division, American Chemical Society, 1155 Sixteenth St., N.W., Washington, D. C. 20036, by referring to code number JPC-72-2593. Remit check or money order for \$3.00 for photocopy or \$2.00 for microfiche.

Table I: Positional, Thermal and Occupancy Parameters^a

Atom	Position	<i>x</i>	<i>y</i>	<i>z</i>	<i>B</i> , Å ²	Occupancy factor
I. Dehydrated						
(Si, Al)	24(<i>k</i>)	0	0.183 (1)	0.368 (1)	0.3 (2)	1
O(1)	12(<i>h</i>)	0	0.204 (4)	¹ / ₂	1.5 (10)	1
O(2)	12(<i>i</i>)	0	0.306 (3)	0.306 (3)	1.2 (10)	1
O(3)	24(<i>m</i>)	0.114 (2)	0.114 (2)	0.330 (3)	0.9 (7)	1
Tl(1)	8(<i>g</i>)	0.2591 (2)	0.2591 (2)	0.2591 (2)	2.4 (1)	⁷ / ₈
Tl(2)	8(<i>g</i>)	0.100 (2)	0.100 (2)	0.100 (2)	1.8 (6)	¹ / ₈
Tl(3)	12(<i>i</i>)	0	0.457 (1)	0.457 (1)	5.9 (6)	¹ / ₄
II. Hydrated						
(Si, Al)	24(<i>k</i>)	0	0.184 (1)	0.370 (1)	0.0 (2)	1
O(1)	12(<i>h</i>)	0	0.221 (3)	¹ / ₂	0.7 (8)	1
O(2)	12(<i>i</i>)	0	0.293 (2)	0.293 (2)	0.5 (8)	1
O(3)	24(<i>m</i>)	0.113 (2)	0.113 (2)	0.340 (2)	0.8 (6)	1
Tl(1)	8(<i>g</i>)	0.2604 (2)	0.2604 (2)	0.2604 (2)	3.0 (1)	⁷ / ₈
Tl(2)	8(<i>g</i>)	0.108 (4)	0.108 (4)	0.108 (4)	8.7 (19)	¹ / ₈
Tl(3)	12(<i>i</i>)	0	0.454 (1)	0.454 (1)	8.7 (8)	¹ / ₄

^a Standard deviations are in the units of the least significant digit given for the corresponding parameter; see Figure 1 also.

Table II: Interatomic Distances and Angles^a

	Dehydrated	Hydrated
(Si, Al)-O(1)	1.63 (2) ^b	1.67 (1)
(Si, Al)-O(2)	1.67 (4)	1.64 (2)
(Si, Al)-O(3)	1.68 (2)	1.69 (2)
Tl(1)-O(3)	2.64 (2)	2.75 (2)
Tl(1)-O(2)	3.25 (1)	3.26 (4)
Tl(2)-O(3)	2.82 (3)	2.86 (3)
Tl(2)-O(2)	3.74 (3)	3.48 (3)
Tl(3)-O(2)	2.60 (3)	2.81 (2)
Tl(3)-O(1)	3.11 (5)	2.92 (4)
O(1)-(Si, Al)-O(2)	108 (1) ^c	110 (1)
O(1)-(Si, Al)-O(3)	110 (2)	110 (1)
O(2)-(Si, Al)-O(3)	109 (1)	107 (1)
O(3)-(Si, Al)-O(3)	111 (2)	111 (1)
(Si, Al)-O(1)-(Si, Al)	162 (2)	148 (1)
(Si, Al)-O(2)-(Si, Al)	144 (2)	161 (2)
(Si, Al)-O(3)-(Si, Al)	138 (2)	144 (2)

^a Standard deviations are in the units of the least significant digit given for the corresponding parameter. ^b Distances in angstroms. ^c Angles in degrees.

materials, respectively. The corresponding weighted R_2 indices, $(\sum w(F_o - |F_c|)^2 / \sum w F_o^2)^{1/2}$, are 0.125 and 0.080. The goodness-of-fit values, $(\sum w(F_o - |F_c|)^2 / (m - s))^{1/2}$, are 3.2 and 2.0.

The full-matrix least-squares program used⁸ minimizes $\sum w(\Delta|F|)^2$; the weights were the reciprocal squares of σ , the standard deviation of each observation. Atomic scattering factors for Tl⁺,⁹ Si²⁺,¹⁰ Al^{1.5+},¹⁰ and O⁻⁹ were used. The values for Tl(I) were decreased by 3.2 to 3.6 electrons to account for the real component of anomalous dispersion.¹¹ In the last cycle of least-squares refinement, all shifts were less than 1% of their corresponding esd's.

The second data set collected for the hydrated crystal was processed in the same manner, in detail, as the data for the dehydrated material. The 167 observed reflections were refined to error indices of $R_1 = 0.106$, $R_2 = 0.123$, and the "goodness of fit" = 3.1. No significant differences exist between this refined structure and the one reported in Table I. The greatest difference in a fractional coordinate is an increase of 0.003 in the Tl(3) *y* parameter.

Discussion

Tl(I) ions occupy three kinds of sites in the dehydrated structure (see Figures 1 and 2).¹² Two, Tl(1) and Tl(2), are on the three-fold axes on opposite sides of the six-oxygen window. Alternate cycles of least-squares refinement of isotropic thermal parameters and occupancy parameters for these two positions indicate that each six-oxygen window has 1.012 Tl(I) ions associated with it. (The two occupancy parameters were 0.866 and 0.146.) It is reasonable to assume that this number should be no greater than 1.000 so that Tl(1)-Tl(2) approaches of 3.36 Å might be avoided. Accordingly the refined occupancy parameters for Tl(1) and Tl(2) were decreased proportionately and held invariant in further cycles of least-squares refinement. The occupancy parameter for Tl(3) was not allowed to vary upwards from one per eight-oxygen

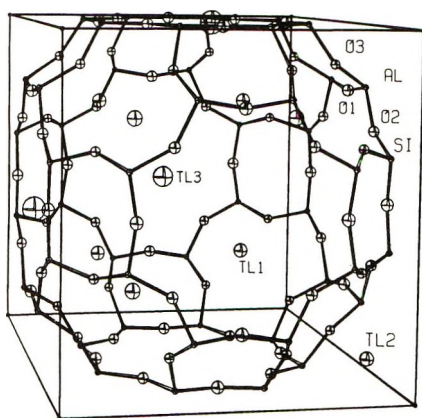
(8) P. K. Gantzel, R. A. Sparks, and K. N. Trueblood, UCLALS4, American Crystallographic Association Program Library (old) No. 317, modified.

(9) "International Tables for X-Ray Crystallography," Vol. III, Kynoch Press, Birmingham, 1962, p 212.

(10) Reference 9, p 202.

(11) Reference 9, p 215.

(12) C. K. Johnson, ORTEP, Report ORNL-3794, Oak Ridge National Laboratory, Oak Ridge, Tenn., 1965.



DEHYDRATED TL-EXCHANGED ZEOLITE A

Figure 1. The Tl(I)-exchanged zeolite A unit cell.¹² The Tl(I) ions are statistically placed within each of the three kinds of sites. Positions of partial occupancy are represented so as to maximize the approach distances between Tl(I)'s. Ellipsoids of 50% probability are shown.

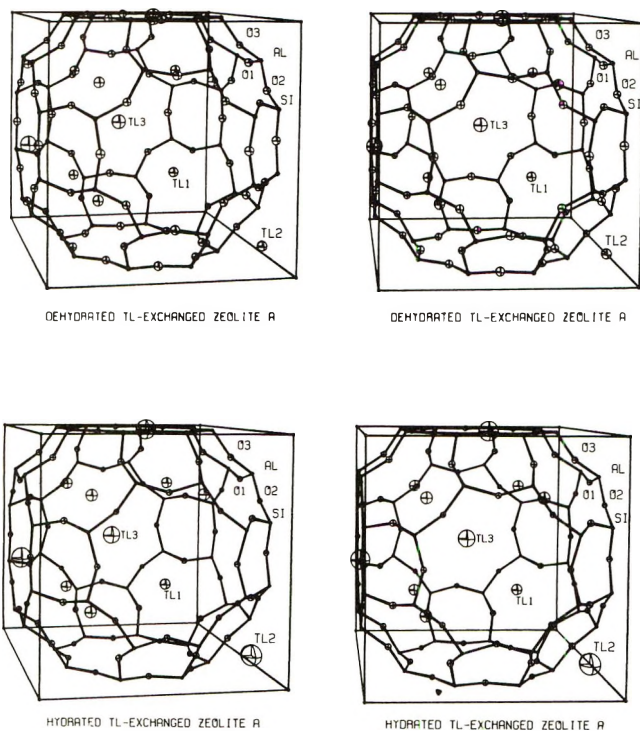


Figure 2. Stereoviews¹² of Tl(I)-exchanged zeolite A. Ellipsoids of 50% probability are shown: top, dehydrated; bottom, hydrated.

ring, as it tended to do to a small extent. Despite the expected high correlations between occupancy and thermal parameters in least squares, the refinements agree adequately with the chemical analyses. These occupancy parameters for Tl(1) and Tl(2) were assumed to apply to the hydrated material as well.

In the dehydrated structure, the principal Tl(I) position, Tl(1), is close (2.64 Å) to three O(3) framework oxygen atoms. In the sodalite unit, Tl(2) is further (2.82 Å) from these same three O(3) atoms.

In zeolite A structures with smaller cations, positions on this threefold axis but closer to or in the plane of the O(3) atoms are occupied. Clearly it is the large ionic radius of Tl(I) which requires that positions well out of the six-oxygen window be occupied (see Table III). The sum of the ionic radii¹³ of Tl(I) and O²⁻ is 1.40 + 1.40 = 2.80 Å, somewhat more than the shortest contacts observed. Tl(3) is 2.60 Å from O(2) and 3.11 Å from two O(1) atoms. If it were located at the center of the eight-oxygen ring, the closest approach, to O(2), would be 3.34 Å, appreciably more than the sum of the ionic radii; hence, the off-center position found is reasonable.

Table III: Deviations of Atoms from 111 Planes at O(3) (in Å)^a

	Dehydrated	Hydrated
Tl(2)	-1.82	-1.71
O(3)	0	0
O(2)	0.37	0.14
Tl(1)	1.54	1.53

^a A negative deviation indicates that the atom lies on the same side of the plane as the origin.

In the hydrated structure, several differences are observed. The shortest Tl(I) approach distances to framework oxygen atoms are longer (see Table II); their average is approximately the sum of the corresponding ionic radii. While the tetrahedral arrangement around each average Si or Al position is nicely maintained, small rotations of these tetrahedra have occurred, resulting in appreciable changes of the framework angles at the oxygen atoms, especially at O(1) and O(2) which form the eight-oxygen window. Table IV¹⁴ shows that, in the four univalent-cationic forms of zeolite A for which accurate single crystal diffraction

Table IV: Aluminosilicate Framework Angles^c (in degrees)

	4A hy- drated ^a	4A ammoni- ated ^b	Tl-ex- changed A hy- drated	Tl-ex- changed A dehy- drated
O(1)-(Si, Al)-O(2)	108	108	110	108
O(1)-(Si, Al)-O(3)	111	113	110	110
O(2)-(Si, Al)-O(3)	108	106	107	109
O(3)-(Si, Al)-O(3)	111	111	111	111
(Si, Al)-O(1)-(Si, Al)	146	146	148	162
(Si, Al)-O(2)-(Si, Al)	160	160	161	144
(Si, Al)-O(3)-(Si, Al)	144	142	144	138

^a Reference 2. ^b Reference 14. ^c The average standard deviation is less than 2°.

(13) L. Pauling, "The Nature of the Chemical Bond," 3rd ed, Cornell University Press, Ithaca, N. Y., 1960, p 518.

studies have been completed (as evidenced by the nearly tetrahedral (Si,Al)O₄ groups), the angles at the oxygens are very nearly the same for the three "full" structures, whether hydrated or ammoniated. The corresponding angles for the "empty" structure are appreciably different. The small decrease in the cell constant upon dehydration is approximately twice as great as that which can be calculated from the (Si,Al)-O-(Si,Al) angular changes alone, principally the one at O(2).

These structures show that Tl(I) makes qualitatively similar approaches to framework oxygen atoms irrespective of hydration. It is expected that sodium

ions would be similarly located, except for the effects of ionic radius, near the centers of all six-oxygen and eight-oxygen rings in the hydrated form of zeolite 4A, confirming the assignments of Gramlich and Meier² for the atoms, Na(1), IV, and IV'.

Acknowledgments. This work was supported by the U. S. Army Research Office-Durham. We are also indebted to the NSF for their assistance (Grant No. GP-18213) in the purchase of the diffractometer and to the University of Hawaii Computation Center.

(14) R. Y. Yanagida and K. Seff, *J. Phys. Chem.*, **76**, 2597 (1972)

The Crystal Structure of an Ammonia Sorption Complex of Zeolite 4A

by Russell Y. Yanagida and Karl Seff*

Chemistry Department, University of Hawaii, Honolulu, Hawaii 96822 (Received February 28, 1972)

Publication costs assisted by the Army Research Office (Durham)

The crystal structure of an ammonia sorption complex of zeolite A has been determined by single-crystal X-ray techniques. Fully vacuum-dehydrated zeolite A of approximate composition Na₁₁Al₁₁Si₁₃O₄₈ per unit cell was allowed to sorb 32.0 molecules of dry NH₃ at a pressure of 604 Torr. The approximate cubic space group *Pm3m* was used with *a* = 12.29 (1) Å. Twelve NH₃ molecules are found at two kinds of sites in the sodalite unit; eight of these are coordinated to threefold axis cations and the remaining four hydrogen-bond to these eight and to framework oxygen atoms. Of the 20 NH₃'s in the large cavity, eight are coordinated to the threefold axis sodium ions. The resulting 12 hydrogen-bond to these eight and to other framework oxygen atoms and may loosely coordinate the cations which are near the centers of the large eight-oxygen windows.

Introduction

Numerous investigations have been conducted into the thermodynamics and kinetics of the sorption of ammonia onto zeolites such as zeolite X¹ and sepiolite² or other materials such as γ -alumina.³ Many of these have limited their guest molecule concentrations to small values so that the assumption that there is only one kind of sorption site may apply. Various workers^{1,4-8} have shown that sites near the cations are the most favored positions at low coverages. However, there are three such sites in zeolite A (one on either side of Na(1) and one near Na(2)) each of which may have several specific symmetries (on or off of symmetry elements), so that even at low coverages several non-equivalent sites may participate in sorption. Accordingly, the interpretation of measurements of the heats and the kinetics of sorption and of the extent of sorption onto zeolites modified by presorption of ammonia⁹⁻¹² must take these multiple sites into account. Sorption by sodalite,¹ although slow, indicates that

NH₃ can enter the sodalite cavity. The work of Rees and Berry,¹³ however, has been interpreted assuming that no sites within the sodalite unit are accessible.

- (1) R. M. Barrer and R. M. Gibbons, *Trans. Faraday Soc.*, **59**, 2569 (1963).
- (2) A. J. Dandy, *J. Chem. Soc. A*, 2383 (1971).
- (3) J. B. Peri, *J. Phys. Chem.*, **69**, 231 (1965).
- (4) C. L. Angell and P. C. Schaffer, *J. Phys. Chem.*, **70**, 1413 (1966).
- (5) L. Bertsch and H. W. Habgood, *J. Phys. Chem.*, **67**, 1321 (1963).
- (6) E. Rabinowitch and W. C. Wood, *Trans. Faraday Soc.*, **32**, 947 (1936).
- (7) P. Cannon and C. P. Rutkowski, *J. Phys. Chem.*, **63**, 1292 (1959).
- (8) D. N. Stamires, *J. Chem. Phys.*, **36**, 3174 (1962).
- (9) P. H. Emmett and T. W. DeWitt, *J. Amer. Chem. Soc.*, **65**, 1253 (1943).
- (10) R. M. Barrer and L. V. C. Rees, *Trans. Faraday Soc.*, **50**, 852 (1954).
- (11) R. M. Barrer and L. V. C. Rees, *ibid.*, **50**, 989 (1954).
- (12) A. B. Lamb and J. C. Woodhouse, *J. Amer. Chem. Soc.*, **58**, 2637 (1936).
- (13) L. V. C. Rees and T. Berry, "Molecular Sieves," Society of Chemical Industry, London, 1968, p 149.

Table II: Positional, Thermal, and Occupancy Parameters^a

Atom	Position	<i>x</i>	<i>y</i>	<i>z</i>	<i>B</i> , Å ² , or <i>b</i> ₁₁ and <i>b</i> ₂₂	Occupancy factor
(Si, Al)	24(<i>k</i>)	0	0.182 (1)	0.372 (1)	1.0 (1)	1
O(1)	12(<i>h</i>)	0	0.222 (2)	¹ / ₂	1.7 (3)	1
O(2)	12(<i>i</i>)	0	0.294 (1)	0.294 (1)	1.9 (4)	1
O(3)	24(<i>m</i>)	0.113 (1)	0.113 (1)	0.338 (1)	2.8 (3)	1
Na(1)	8(<i>g</i>)	0.217 (2)	0.217 (2)	0.217 (2)	0.014 (2); 0.022 (4)	1
Na(2)	24(<i>m</i>)	0.056 (13)	0.445 (8)	0.445 (8)	12 (4)	¹ / ₈
N(1)	8(<i>g</i>)	0.102 (8)	0.102 (8)	0.102 (8)	26 (6)	1 (0.18)
N(2)	6(<i>e</i>)	0	0	0.147 (10)	9 (3)	² / ₃ (0.13)
N(3)	8(<i>g</i>)	0.320 (7)	0.320 (7)	0.320 (7)	21 (5)	1 (0.15)
N(4)	24(<i>l</i>)	0.233 (9)	0.294 (10)	¹ / ₂	18 (4)	¹ / ₂ (0.08)

^a Standard deviations, except for those in the last column, are in the units of the least significant digit given for the corresponding parameter. See Figures 2 and 3 for the identities of the atoms. For Na(1), the anisotropic temperature factor = $\exp[-b_{11}(h^2 + k^2 + l^2) - b_{12}(hk + hl + kl)]$.

Structure Determination

Initial full-matrix least-squares refinement using framework and threefold axis cation positions found by Smith¹⁶ for dehydrated zeolite 4A converged quickly to an R_1 index, $R_1 = (\sum |F_o - |F_c||) / \sum F_o$, of 0.28. Successive Fourier syntheses and least-squares refinements served to reveal the positions of the remaining three sodium ions and the 32 nitrogen atoms and to yield a final R_1 index of 0.082. The corresponding generalized weighted R_2 index, $R_2 = (\sum w(F_o - |F_c|)^2 / \sum w F_o^2)^{1/2}$, is 0.064. Calculated and observed structure factors are presented in Table I, and the final structural parameters are presented in Table II. The goodness-of-fit, $(\sum w(F_o - |F_c|)^2 / (m - s))^{1/2}$, is 1.25; m is the number of observations (148), and s (27) is the number of variables in least-squares.

All four nitrogen positions were examined extensively by Fourier and least-squares methods to determine whether the selection of a position off of an n -fold axis ($n = 2, 3$, or 4) was crystallographically justified. For N(1), N(2), and N(3), although successful refinement was achieved, the R indices were negligibly affected and the additional parameters were unjustified. N(4) refined at Wyckoff position 12(*j*) to $x = 0.262$, but R_1 was greater by 0.003; accordingly 24(*l*) was selected. The standard deviation of the electron density on Fourier functions was $0.1 \text{ e}^-/\text{\AA}^3$.

The N(2) position on a four-fold axis was considered further because of the unreasonably short N(1)–N(2) approach distance (1.8 Å), and because the symmetry of NH₃ requires that it be disordered at such a site. With this position removed, R_1 increased by 0.008. Even though no changes in the signs of the calculated structure factors occurred, a difference Fourier along the line 0,0, z still showed a peak, with a height of $0.9 \text{ e}^-/\text{\AA}^3$, which had been early obscured by a much larger peak attributable to termination-of-series error. It is expected that the 1.8 Å approach does not occur

and that the N(1) and N(2) ammonia molecules are somewhat disordered, lying near to the mean positions observed.

The full-matrix least-squares program used¹⁷ minimizes $\sum w(\Delta|F|)^2$; the weights were the reciprocal squares of σ , the standard deviation for each observation. Atomic scattering factors¹⁸ for Si^{1.5+}, Al^{1.5+}, Na⁺, O⁻, and N (valence) were used. In the last cycle of least-squares refinement, all shifts were less than 1% of their corresponding esd's. Stereoviews¹⁹ of the structure are shown in Figures 2 and 3.

Discussion

Eight NH₃'s at N(1) are found in the sodalite unit on the threefold axes, 2.5 Å from Na(1). Four more NH₃'s at N(2) hydrogen-bond to these at an apparent distance of 1.8 Å at a position within the sodalite unit on the fourfold axis. N(2) can also hydrogen bond to two framework O(3)'s at a distance of 3.1 Å. Apparently the four N(2) atoms lie in a plane at x, y , or $z = 1/2$ in each sodalite unit and, for steric reasons which would make the true N(1)–N(2) approach longer, the composite symmetry of the N(1) equipoint is reduced from cubic to tetragonal or lower, although to a small extent. This effect would explain why the N(2) site holds only four NH₃'s instead of six, as well as the unusually high N(1) thermal parameter.

Just as eight NH₃'s coordinate the eight Na(1)'s in the sodalite unit, eight NH₃'s at N(3) coordinate (2.2 Å) the Na(1)'s in the larger cavity. N(3) lies on the threefold axis and is 2.5 Å from N(4) and

(16) J. V. Smith and L. G. Dowell, *ibid.*, 126, 135 (1968).

(17) P. K. Gantzel, R. A. Sparks, and K. N. Trueblood, UCLALS4, American Crystallographic Association Program Library (old) No. 317, modified.

(18) "International Tables for X-Ray Crystallography," Vol. III, Kynoch Press, Birmingham, 1962, p 202.

(19) C. K. Johnson, ORTEP, Report ORNL-3794, Oak Ridge National Laboratory, Oak Ridge, Tenn. (1965).

Table III: Interatomic Distances and Angles^a

(Si, Al)-O(1)	1.65 (1) ^b	N(1)-Na(1)	2.5 (2)
(Si, Al)-O(2)	1.67 (1)	N(1)-O(3)	3.0 (1)
(Si, Al)-O(3)	1.68 (1)	N(1)-O(2)	3.6 (1)
Na(1)-O(3)	2.35 (2)	N(1)-N(1)	2.4 (2)
Na(1)-O(2)	2.98 (1)	N(1)-N(2)	1.8 (1)
Na(2)-O(2)	2.70 (14)	N(2)-N(2)	2.6 (2)
Na(2)-O(1)	2.90 (14)	N(2)-O(3)	3.1 (1)
		N(3)-Na(1)	2.2 (2)
O(1)-(Si, Al)-O(2)	107.1 (6) ^c	N(3)-O(3)	3.6 (1)
O(1)-(Si, Al)-O(3)	112.5 (6)	N(3)-N(4)	2.5 (1)
O(2)-(Si, Al)-O(3)	106.6 (7)	N(4)-Na(2)	2.9 (2)
O(3)-(Si, Al)-O(3)	111.2 (9)	N(4)-O(1)	3.0 (1)
(Si, Al)-O(1)-(Si, Al)	145.2 (6)	N(4)-O(1)	3.7 (1)
(Si, Al)-O(2)-(Si, Al)	159.0 (9)	N(4)-O(3)	3.3 (1)
(Si, Al)-O(3)-(Si, Al)	141.9 (10)		
		Na(1)-N(1)-N(2)	126 (9)
N(1)-O(3)-(Si, Al)	103 (1)	Na(1)-N(1)-O(3)	50 (1)
N(1)-O(2)-(Si, Al)	80 (2)	Na(2)-N(4)-O(3)	88 (3)
N(2)-O(3)-(Si, Al)	92 (1)	Na(2)-N(4)-N(3)	69 (4)
N(3)-O(3)-(Si, Al)	104 (1)	Na(1)-N(3)-N(4)	101 (4)
N(4)-O(3)-(Si, Al)	102 (1)	O(3)-N(4)-N(3)	75 (4)
N(4)-O(1)-(Si, Al)	95 (2)	O(3)-N(4)-O(3)	73 (1)
		N(4)-N(3)-N(4)	117 (7)
		O(3)-N(2)-O(3)	80 (3)
		N(1)-N(2)-O(3)	105 (1)
		N(2)-N(1)-O(3)	133 (3)
		O(3)-N(1)-O(3)	84 (4)
		O(1)-N(4)-O(1)	71 (1)
		N(3)-N(4)-O(1)	118 (3)

^a Standard deviations are in the units of the least significant digit given for the corresponding parameter. ^b Interatomic distances are in ångstroms. ^c Angles are in degrees.

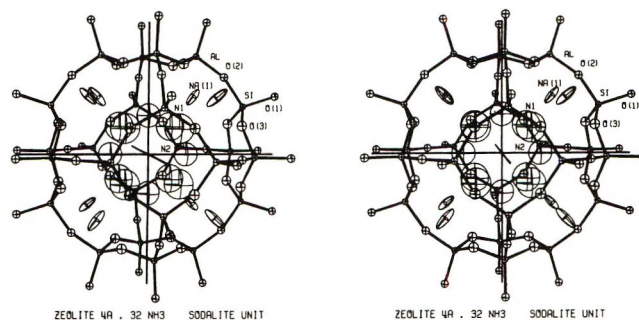
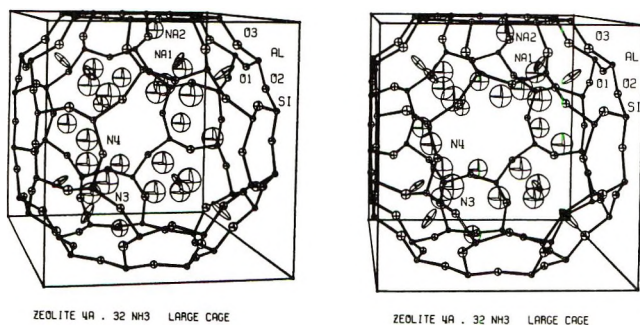


Figure 2. A stereodrawing of the large cavity in zeolite A containing 20 NH_3 's. The unit cell is shown.

Figure 3. A stereodrawing of the sodalite unit in zeolite A containing 12 NH_3 's. The unit cell origin and axes are shown.

3.6 Å from three O(3)'s. Perhaps N(3), like N(1), lies irresolvably off of this axis and is able to make two shorter hydrogen bonds to O(3). Na(2), which is in the vicinity of the center of the eight-oxygen window, is 2.9 Å from N(4) and each of the three Na(2) ions per unit cell could be coordinated by up to four N(4) ligands within the limits of uncertainty and disorder. The thermal parameters are large for the atoms of this possible group, probably due to the disorder caused by the many opportunities for hydrogen bonding available to N(4) (N(4) to N(3) (2.5 Å), N(4) to O(1) (3.0 Å), and N(4) to O(3) (3.3 Å)). Altogether, N(4) hydrogen-

bonded interactions appear to be more significant than those involving the disordered Na(2) ions.

of NH_3^{20} and $\text{NH}_3 \cdot \text{H}_2\text{O}^{21}$) are justified for two reasons. First, the oxygen atoms bear an approximate -0.23 formal charge, and most ammonia hydrogens, because the nitrogen is in the first coordination sphere of a cation, can be expected to be more acidic. Second, some of the ammonia to ammonia contacts can be viewed as intramolecular nonbonded approach distances within the aluminosilicate complex.

The separations between atoms lying on or near to the threefold axis are given in Table IV. Three O(3) atoms of the six-oxygen ring are chosen as the reference plane. Na(1) is displaced into the large cavity by 0.6 \AA from this plane. The N(1)–O(3) distance (3.0 \AA) indicates that three (or perhaps only two if N(1) is actually somewhat disordered with respect to the threefold axis as has been suggested above) hydrogen bonds can form simultaneously between the hydrogen atoms of the N(1) ammonia molecule and the O(3) atoms of the six-ring, lending stability to the out-of-plane Na(1) position. The ligand structure is very similar to that found for hydrated zeolites 4A^{15,22} and 5A.²³ However, the long N(4)–N(4) distances (4.2 \AA) ensures that six edges of the pentagonal dodecahedron observed for hydrated structures are nonbonding here. This was expected because NH_3 has insufficient lone pairs (too many hydrogen atoms) to complete such a figure with

Table IV: Deviations of Atoms from the 111 Plane at O(3) (in \AA)^a

N(1)	–1.9
O(3)	0
O(2)	0.18
Na(1)	0.59
N(3)	2.8

^a A negative deviation indicates that the atom lies on the same side of the plane as the origin.

hydrogen bonds. This structure appears to support the long ($>10^{-2}$ sec) dielectric relaxation times²⁴ observed for ammonia in zeolite A.

Acknowledgment. This work was supported by the U. S. Army Research Office–Durham. We are also indebted to the NSF for their assistance (Grant No. GP-18213) in the purchase of the diffractometer.

(20) I. Olovsson and D. H. Templeton, *Acta Crystallogr.*, **12**, 832 (1959).

(21) I. Olovsson and D. H. Templeton, *ibid.*, **12**, 827 (1959).

(22) K. Seff and D. P. Shoemaker, unpublished (1964).

(23) K. Seff, Ph.D. Thesis, Massachusetts Institute of Technology, (1964), p 93.

(24) B. Morris, "Molecular Sieves," Society of Chemical Industry, London, 1968, p 34.

The Crystal Structure of a Sulfur Sorption Complex of Zeolite 4A

by Karl Seff

Chemistry Department, University of Hawaii, Honolulu, Hawaii 96822 (Received March 31, 1972)

Publication costs assisted by the Army Research Office (Durham)

The crystal structure of a sulfur sorption complex of zeolite A has been determined by single-crystal X-ray techniques. Fully vacuum-dehydrated zeolite A of approximate composition $\text{Na}_{11}\text{Al}_{11}\text{Si}_{13}\text{O}_{48}$ per unit cell was exposed to dry sulfur for 240 hr at 270° . The approximate cubic space group $Pm\bar{3}m$ was used with $a = 12.289 (2) \text{ \AA}$. Two S_8 rings, each in a crown configuration, are found in the large cavity of each unit cell. The planes of the two molecules in a single cavity are parallel but are not in van der Waals contact. Four alternating sulfur atoms in each ring are each 2.8 \AA from a threefold-axis sodium ion, and the other four are each 3.2 \AA from a framework oxygen atom. Threefold disorder exists in the sorbate structure; the normal to the planes of the pair of rings in each cavity can be $[100]$, $[010]$, or $[001]$.

Introduction

Nearly rectangular reversible sorption isotherms for sulfur onto Ca(II)-exchanged zeolite A and the sodium form of zeolite X have been determined.¹ These indicate that a single structure may describe each sorption complex over a wide range of conditions. The heats of sorption¹ (-25 and -31 kcal/mol , respectively) also

indicate that these complexes are relatively stable. Such systems afford a unique opportunity for investigating the configurations of physical sorption complexes crystallographically. Na(I)–zeolite A was selected as the host material and long exposure times were

(1) R. M. Barrer and J. L. Whiteman, *J. Chem. Soc. A*, **13** (1967).

used in anticipation of slower sorption rates for these crystals, which are larger than those used previously¹ and whose pores can be considered somewhat blocked by sodium ions.

Experimental Section

More than 100 g of single crystals of zeolite A was prepared using Charnell's² method, modified to include a second crystallization using seed crystals from the first preparation. Crystals formed nicely as cubes from 30 to 70 μ on an edge. Elemental analysis indicated that the framework formula for these preparations is best represented as $Al_{11}Si_{13}O_{48}^{11-}$ and that the number of sodium ions per unit cell is therefore approximately 11.

A sample of zeolite A, approximately 100 mg, was dehydrated at 350° and 10^{-6} Torr for 24 hr. Similarly, about 10 g of finely divided sublimed sulfur powder was dried at 105° and 10^{-6} Torr for 36 hr. The two samples were mixed, under vacuum, and maintained at 300° for 100 hr, then at 270° for 240 hr, and finally at 115° for 90 hr as the sulfur either distilled away or formed separate crystals mixed with those of the zeolite in a loose brown powder. The product did not change in color during this last 90-hr process. Microscopic examination of the zeolite crystals revealed that they were clear, bright yellow, and entirely uninjured. The crystals have not become clouded even upon prolonged exposure to the local (humid) atmosphere, indicating that they are hydrophobic. The density, measured by flotation in aqueous ZnI_2 solution, is 1.99 (2) $g\ cm^{-3}$ and agrees adequately with the calculated value of 1.97 $g\ cm^{-3}$ for 16 sulfur atoms per unit cell. A single crystal, a cube 65 μ on an edge, was selected for X-ray investigation.

A Syntex four-circle computer-controlled diffractometer with graphite-monochromatized Mo $K\alpha$ radiation ($K\alpha_1$, λ 0.70926 Å; $K\alpha_2$, λ 0.71354 Å) and a pulse-height analyzer was used throughout for preliminary experiments and for the collection of diffraction intensities. The cubic cell constant (12.289 (2) Å at 20°) was determined by a least-squares refinement of 15 intense reflections with 2θ values up to 23.6°. The approximate space group $Pm\bar{3}m$ (no systematic absences) was used instead of $Fm\bar{3}c$ because the stoichiometry of our sample ensures a disorder which cannot be better described by the latter space group, because Gramlich and Meier³ have shown that deviations from the former space group are small, and because a brief check of Gramlich and Meier's most intense "b" reflections indicated that they were absent here. The θ - 2θ scan technique was employed at a constant scan rate of 0.5°/min (in 2θ). The scan range varied from 2.0° at $2\theta = 3^\circ$ to 2.5° at $2\theta = 70^\circ$. All 888 unique reciprocal lattice points for which $2\theta < 70^\circ$ were examined. A time equal to half of the scan time for each reflection was spent counting background at each end of the scan

range. Three check reflections which were measured periodically during data collection showed no significant trend in intensity.

Standard deviations were assigned according to the formula

$$\sigma(I) = [CT + 0.25(t_c/t_b)^2(B_1 + B_2) + (pI)^2]^{1/2}$$

where CT is the total integrated count obtained in a scan time of t_c , B_1 and B_2 are the background counts each obtained in time t_b , and $I = CT - 0.5(t_c/t_b)(B_1 + B_2)$. A value of 0.02 was assigned to the empirical parameter p to account for instrument instability. The net counts were then corrected for Lorentz and polarization effects. An absorption correction ($\mu R = 0.03$) was unnecessary. The 184 reflections for which the net count exceeded three times its standard deviation were used throughout.

Structure Determination

Initial full-matrix least-squares refinement using framework and threefold axis cation positions found for the 32 ammonia complex⁴ of zeolite 4A converged

Table I: Observed and Calculated Structure Factors^a

0, k = 0	10 372	404	1, k = 6	6 371	334	4, k = 8	
1 459	524	11 772	756	6 248	-273	8 1527	-1534
3 1074	1290	16 525	473	7 248	-253	9 475	-462
4 247	373	8 383	400	8 383	400	13 438	-440
5 1056	1051	12 315	-353	12 315	-353	14 418	-467
6 1888	1896	19 403	-352	19 403	-352	11 307	-284
8 1071	983	6 713	641				
9 650	659	8 364	344	1, k = 8		5, k = 5	
10 1146	1167	10 417	444	9 279	260	8 591	721
11 1124	1206	11 720	714	12 310	369	5 197	-159
16 669	889	16 376	376			6 328	344
17 376	424			2, k = 2		7 581	521
				3 1171	-1042	10 248	199
				4 552	543	11 603	653
				5 682	674	16 436	362
0, k = 1				6 358	-322		
1 444	-774			7 229	-131	3, k = 5	
2 426	-351			8 420	-322	6 415	388
4 1100	-1026	11 745	748	9 531	526	8 377	-377
6 314	289	16 429	372	11 296	-290	9 386	-347
7 662	-731			12 282	215	6 328	344
9 252	-286			15 352	256	7 581	521
11 251	188	1 907	-1307			10 248	199
12 303	-284	3 1236	1207			11 603	653
15 305	-258	4 420	-391	2, k = 3		16 436	362
		5 378	-296	3 1278	-1174		
		7 507	-459	6 355	-309	3, k = 7	
0, k = 2		8 339	323	7 207	150	6 622	639
2 608	-679	10 547	-527	8 870	-854	8 234	-94
3 530	-374			11 256	-290	9 383	358
4 628	-608			12 282	-213	10 338	368
7 277	-293						
8 436	-484			1, k = 2		5, k = 9	
9 466	-484	2 731	591	2, k = 4		9 284	-291
		3 867	846	3 1278	165		
		5 332	251	5 297	-262	3, k = 8	
		7 426	396	7 426	396	6 468	-550
0, k = 3		7 270	235	7 426	396	11 556	553
3 418	-368	8 352	334	8 245	206		
5 380	-311	9 359	347	9 367	395	4, k = 4	
6 231	192					6 261	177
7 284	260					7 332	-352
8 344	-348	5 408	-321	5 220	175	8 208	-244
9 399	-468	7 740	741	6 208	-244	11 308	249
10 300	297	8 271	271	8 712	683	12 282	-172
11 314	313	9 245	302	9 642	702		
		10 375	366	7 404	-377	6, k = 6	
				7 283	-248	11 466	-420
						11 433	380
0, k = 4							
4 1061	1032			1, k = 4		4, k = 5	
5 504	413	5 496	-549	2, k = 4		5 397	-407
6 230	-199	6 670	-686	9 296	373	6 271	-220
7 452	-490	8 447	441			7 656	-664
9 637	-586	10 239	-156	2, k = 8		12 282	-263
12 336	-369	11 289	-378	8 728	-692		
15 344	-299	12 275	-283	12 285	214	4, k = 6	
						7 373	-361
						9 642	702
						17 348	-145
0, k = 5							
5 1722	1658	7 418	-415	1, k = 5		11, k = 11	
6 839	811	8 408	360	12 337	333	11 440	415
7 392	-412	9 303	-325				
9 452	-470			3, k = 3		7 397	372
				3 646	-616	8 243	321
				4 312	377	11 274	-264

^a The running index is l ; values of h and k for each group immediately precede that group. The central column is $10F_0$; the right-hand column is $10F_6$.

- (2) J. F. Charnell, *J. Crystal Growth*, **8**, 291 (1971).
- (3) V. Gramlich and W. M. Meier, *Z. Kristallogr.*, **133**, 134 (1971).
- (4) R. Y. Yanagida and K. Seff, *J. Phys. Chem.*, **76**, 2597 (1972).

Table II: Positional, Thermal, and Occupancy Parameters^a

Atom	Position	<i>x</i>	<i>y</i>	<i>z</i>	<i>B</i> , Å ² , or <i>b</i> ₁₁ and <i>b</i> ₁₂	Occupancy factor
(Si, Al)	24(<i>k</i>)	0	0.1824 (4)	0.3706 (3)	1.20 (6)	1
O(1)	12(<i>h</i>)	0	0.219 (2)	1/2	2.6 (4)	1
O(2)	12(<i>i</i>)	0	0.295 (1)	0.295 (1)	2.0 (3)	1
O(3)	24(<i>m</i>)	0.112 (1)	0.112 (1)	0.339 (1)	2.8 (3)	1
Na(1)	8(<i>g</i>)	0.209 (2)	0.209 (2)	0.209 (2)	0.014 (2); 0.021 (4)	1
Na(2)	12(<i>i</i>)	0	0.440 (12)	0.440 (12)	19 (1)	1/4
S(1)	24(<i>m</i>)	0.293 (13)	0.358 (8)	0.358 (8)	30 (7)	1/3
S(2)	24(<i>l</i>)	0.246 (7)	0.307 (7)	1/2	20 (3)	1/3

^a Standard deviations are in the units of the least significant digit given for the corresponding parameter. See Figures 1 and 2 for the identities of the atoms. For Na(1), the anisotropic temperature factor = $\exp[-b_{11}(h^2 + k^2 + l^2) - b_{12}(hk + hl + kl)]$.

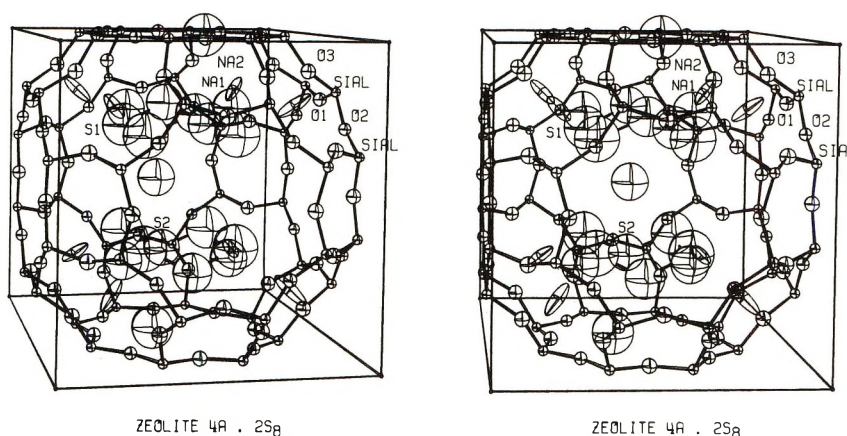


Figure 1. A stereodrawing of the large cavity in zeolite A containing two S₈ rings. The unit cell is shown. Ellipsoids of 50% probability are used.

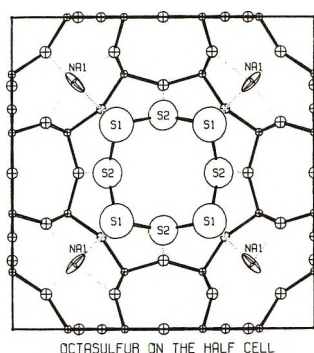


Figure 2. A view of a complexed S₈ ring in one-half of a unit cell. Ellipsoids of 30% probability are used.

quickly to an R_1 index ($R_1 = (\sum |F_o - |F_c||) / \sum F_o$) of 0.150. Correct sulfur positions were guessed and refined by full-matrix least-squares methods to $R_1 = 0.115$. A subsequent Fourier synthesis prepared without sulfur atoms included in the calculation of phases corroborated this result. The principal sodium ion position was allowed to refine anisotropically in the final cycles of least squares, resulting in a final R_1 index of 0.093. The corresponding generalized weighted

R_2 index ($R_2 = (\sum w(F_o - |F_c|)^2 / \sum wF_o^2)^{1/2}$) is 0.094. Calculated and observed structure factors are presented in Table I and the final structural parameters are presented in Table II. The goodness of fit ($(\sum w(F_o - |F_c|)^2 / (m - s))^{1/2}$) is 1.29; m is the number of observations (184) and s (22) is the number of variables in least squares.

Anisotropic refinement of the two sulfur atoms allowed R_1 to fall to 0.089 and R_2 to 0.091, but very elongated ellipsoids with large standard deviations appeared. The largest anisotropic thermal parameter by a factor of 3.5 for S(1) ($b_{11} = 0.15$) corresponds to motion normal to the plane of the S₈ ring, and the largest by a factor of 2.5 for S(2) ($b_{22} = 0.075$) describes a motion in the plane of the ring and tangent to it. The results of these anisotropic refinements for positions of fractional occupancy may not correspond to real thermal motions, because of the disorder present, and are not included in subsequent tables and figures.

Alternate cycles of occupancy and thermal parameter refinement for the sulfur atoms converged at 1.6 (3) S₈ rings per unit cell and R_1 and R_2 decreased to 0.087 and 0.092, respectively. Owing to expected high least-squares correlations, these results are also not

Table III: Interatomic Distances and Angles^a

(Si, Al)-O(1)	1.653 (7)	S(1)-S(2)	1.94 (8)
(Si, Al)-O(2)	1.663 (6)	S(1)-Na(1)	2.80 (15)
(Si, Al)-O(3)	1.675 (5)	S(2)-O(1)	3.21 (9)
Na(1)-O(3)	2.32 (1)		
Na(1)-O(2)	2.97 (2)	S(1)-S(2)-S(1)	128 (9)
Na(2)-O(2)	2.5 (2)	S(2)-S(1)-S(2)	119 (8)
Na(2)-O(1)	2.8 (1)		
		S(2)-S(1)-Na(1)	105 (3)
O(1)-(Si, Al)-O(2)	108.2 (7)	S(1)-Na(1)-O(3)	94 (2)
O(1)-(Si, Al)-O(3)	114.4 (6)	S(1)-Na(1)-O(3)'	115 (3)
O(2)-(Si, Al)-O(3)	107.4 (8)	O(1)-S(2)-S(1)	113 (4)
O(3)-(Si, Al)-O(3)	110.8 (9)	S(2)-O(1)-(Si, Al)	95 (2)
(Si, Al)-O(1)-(Si, Al)	148.4 (6)		
(Si, Al)-O(2)-(Si, Al)	158.0 (12)		
(Si, Al)-O(3)-(Si, Al)	143.0 (9)		

^a Standard deviations are in the units of the least significant digit given for the corresponding parameter. Distances in ångströms, angles in degrees.

taken to be sufficient cause for modifying the structural model. The standard deviation of the electron density on Fourier functions was approximately $0.2 \text{ e}/\text{Å}^3$, and the largest peak on the final differences synthesis was $0.8 \text{ e}/\text{Å}^3$ in height and appeared at an unlikely position. The full-matrix least-squares program used⁵ minimizes $\sum w(\Delta|F|)^2$; the weights were the reciprocal squares of σ , the standard deviation for each observation. Atomic scattering factors⁶ for $\text{Si}^{1.5+}$, $\text{Al}^{1.5+}$, Na^+ , O^- , and S^0 were used. In the last cycle of least-squares refinement, all shifts were less than 2% of their corresponding esd's. A stereoview⁷ of the structure is shown in Figure 1.

Discussion

Two equivalent S_8 rings in the crown configuration lie parallel to each other in the large cavity of the zeolite A structure. The molecular symmetry of the octasulfur ring is $4mm$ (C_{4v}), substantially greater than $2(C_2)$ as is found^{8,9} in orthorhombic sulfur, but less than the ideal symmetry found¹⁰ in the vapor phase, $\bar{8}2m$ (D_{4d}). Threefold disorder exists: the molecular planes of the two octasulfur molecules coexisting in the same large cavity are both normal to $[001]$, $[010]$, or $[100]$. After one set of disordered positions is selected for one ring, however, packing considerations allow only the parallel position for the second molecule. The closest approach between the two rings is 4.96 Å , much more than the sum (4.0 Å) of the van der Waals radii for sulfur.

Two nonequivalent sulfur atoms, S(1) and S(2), alternate to form the S_8 ring. Each atom in the sulfur ring makes only one important approach to a nonsulfur atom (see Figure 2 and Table III). The S(1)-Na(1) distance, $2.80 (15) \text{ Å}$, is the same as the sum of the corresponding van der Waals and ionic radii,¹¹ $1.85 + 0.95 \text{ Å}$. In complexes¹² between alkali metal ions and cyclic polyethers (crown ethers), the Na^+ to O distances average 2.70 Å , 0.35 Å more than the sum of the

corresponding van der Waals and ionic radii ($1.40 + 0.95 \text{ Å}$). Accordingly, a significant ion-induced dipole interaction is indicated. The S(2)-O(1) distance, $3.21 (9) \text{ Å}$, is close to the sum of the corresponding van der Waals radii, 3.25 Å . In the SO_2 complex¹³ of zeolite 5A, the sulfur atom makes only a single significant approach of 2.95 Å to O(1), the same framework oxygen atom as in the present structure. It is reasonable to expect that a symmetric electric octupole is induced in the plane of the sulfur ring, and that a dipole is induced normal to that plane, by the host lattice.

The heats of sorption indicate that the enthalpy of sorption for octasulfur is approximately -200 to $-250 \text{ kcal mol}^{-1}$. S_8 rings, then, effectively seal the 8-oxygen windows at environmental temperatures.

The large thermal motions of the octasulfur ring obscure the observations of significant structural differences with respect to previous findings. The S(1)-S(2) bond length, $1.94 (8) \text{ Å}$, is insignificantly shorter than that found in rhombic sulfur, 2.048 Å . The S-S-S angles, averaging $123 (6)^\circ$, are again insignificantly greater than that found in rhombic sulfur, 107.9° . The dihedral angle has decreased from 98° to 72° , and

(5) P. K. Gantzel, R. A. Sparks, and K. N. Trueblood, UCLALS4, American Crystallographic Association Program Library (old), No. 317, modified.

(6) "International Tables for X-Ray Crystallography," Vol. III, Kynoch Press, Birmingham, England, 1962, p 202.

(7) C. K. Johnson, "ORTEP," Report ORNL-3794, Oak Ridge National Laboratory, Oak Ridge, Tenn., 1965.

(8) (a) S. C. Abrahams, *Acta Crystallogr.*, **8**, 661 (1955); (b) *ibid.*, **14**, 311 (1961); (c) A. S. Cooper, W. L. Bond, and S. C. Abrahams, *ibid.*, **14**, 1008 (1961); (d) S. C. Abrahams, *ibid.*, **18**, 566 (1965).

(9) (a) A. Caron and J. Donohue, *ibid.*, **14**, 548 (1961); (b) A. Caron and J. Donohue, *ibid.*, **18**, 562 (1965).

(10) C. S. Lu and J. Donohue, *J. Amer. Chem. Soc.*, **66**, 818 (1944).

(11) L. Pauling, "The Nature of the Chemical Bond," 3rd ed, Cornell University Press, Ithaca, N. Y., 1960.

(12) M. A. Bush and M. R. Truter, *J. Chem. Soc. B*, 1440 (1971).

(13) K. Seff, Ph.D. Thesis, Massachusetts Institute of Technology, 1964, p 175.

the distance between the plane of the four S(1) atoms of a single ring and that of the four S(2)'s decreased from 0.99 to 0.6 Å. These changes, although marginally significant, are qualitatively consistent with the expected effects of the assumed induced electric octupole.

The aluminosilicate framework differs insignificantly from those of the 32-ammonia complex⁴ of zeolite 4A or of the hydrated sodium³ or thallium(I)¹⁴ forms of zeolite A. This can be considered the relaxed configuration, the geometry adopted by zeolite A at its synthesis. The thermal parameters of the aluminosilicate structure are insignificantly larger, even for O(1), the oxygen atom involved in the close S(2) contact, indicating that the tetragonal distortions expected by the sorption of sulfur are small. The sodium ions at Na(1) are found out of the plane of their nearest oxygen neighbors (Table IV), but less so by 0.15 Å than was found in the ammonia complex. The anisotropic thermal parameters for Na(1), demonstrating motion along the threefold axes, are identical in these two structures.

The average S(1)–Na(1)–O(3) angle is $(94 + 94 + 115)/3 = 101 (2)^\circ$, close to tetrahedral, and the O(1)–S(2)–S(1) angle, $113 (4)^\circ$, is tetrahedral.

Table IV: Deviations^a (Å) of Atoms from the 111 Plane at O(3)

O(3)	0	Na(1)	0.45
O(2)	0.18	S(1)	3.0

^a A negative deviation indicates that the atom lies on the same side of the plane as the origin.

Acknowledgment. This work was supported by the U. S. Army Research Office–Durham. We are also indebted to the NSF for assistance (Grant No. GP-18213) in the purchase of the diffractometer, and to the University of Hawaii Computation Center.

(14) P. E. Riley, K. Seff, and D. P. Shoemaker, *J. Phys. Chem.*, **76**, 2593 (1972).

Transitions in Mesophase Forming Systems. IV. Transformation

Behavior and Pretransition Effects in *p*-Azoxyanisole¹

by Fraser P. Price* and Joachim H. Wendorff

Polymer Science and Engineering, University of Massachusetts, Amherst, Massachusetts 01002
(Received December 13, 1971)

Publication costs assisted by the National Institutes of Health

The equilibrium density–temperature behavior of *p*-azoxyanisole has been studied over the temperature range 25–145°. Equilibrium transition temperatures of 117.0 and 134.2° were found for the solid–nematic and the nematic–isotropic phases, respectively. Linear reversible density temperature behavior was observed in all phases except on the low temperature side of each transition. Here marked downward curvature, attributable to increasingly significant disordering, was observed. Thermal expansion coefficients of 4.1×10^{-4} , 9.4×10^{-4} , and 8.4×10^{-4} were calculated, respectively, for the crystalline, the nematic, and the isotropic phases, while latent volumes of transitions of 6.9 and 0.34% were measured for the solid–nematic and the nematic–isotropic transition. Transformation rates for the isotropic–nematic transformation were at all supercoolings too rapid to measure. The nematic–solid transformation required supercoolings of greater than 20° at which temperature the transformation rates were immeasurably fast.

We are engaged in a systematic study of the equilibrium density–temperature behavior and the interphase transformation kinetics of the cholesteryl esters. Thus far we have studied cholesteryl myristate,^{2a} acetate,^{2b} and nonanoate.³ These substances form stable mesophases whose order is intermediate between that of crystals and isotropic liquids. The cholesteryl esters exhibit smectic and cholesteric mesophases but never

a nematic phase. It is desirable to establish whether mesophase forming substances which do form nematic phases behave like the cholesteryl esters. Accordingly

(1) This work was supported by Grant No. HE13188 from the National Institutes of Health.

(2) (a) F. P. Price and J. H. Wendorff, *J. Phys. Chem.*, **75**, 2839 (1971); (b) F. P. Price and J. H. Wendorff, *ibid.*, **75**, 2849 (1971).

(3) F. P. Price and J. H. Wendorff, *ibid.*, **76**, 276 (1972).

we have made and report here studies of *p*-azoxyanisole. This substance is considered one of the "classic" mesophase formers, and numerous investigations have been made of it.⁴⁻⁶ It exhibits only one mesophase, a nematic one with an existence range of 117 to 134°. In such nematic phases, the order is supposed to be random except for a parallel arrangement of the molecules. X-Ray diffraction studies of solid *p*-azoxyanisole do indeed show that the molecules are parallel but that there is a tendency for the ether group of one molecule to lie close to the azoxy group of its nearest neighbor.^{7,8} This produces a staggered "imbricated" structure.

Experimental Section

Materials. *p*-Azoxyanisole was obtained from the Aldrich Chemical Co. It was recrystallized three times from water-ethanol mixture and dried *in vacuo* at a series of temperatures up into the isotropic melt. Reagent grade (ACS) mercury was obtained from the Sargent-Welch Co.

Methods. Measurements of equilibrium density and transformation rates employed sensitive sealed-off dilatometers. In the work reported here three dilatometers were used, two with bulbs in the form of flat disks for studies of the solid phase, the nematic phase, and the solid-nematic transformation and one with the bulb in the form of a long cylinder for the study of the nematic and the isotropic phases. The transformation from the nematic to the solid state is so rapid that voids are formed in the sample and the final mercury level is not reproducible. However, it was found that after annealing at temperatures above 100° for at least 12 hr, a reproducible mercury level was attained regardless of the crystallization temperature. Samples thus annealed were used to determine the density-temperature relationships of the solid and the nematic phases. Two equilibrium density-temperature runs were performed over the temperature range 25-120° in each of the two dilatometers. The spread of the densities at all temperatures was less than 0.2%.

The dilatometer with the long cylindrical bulb was used to study the equilibrium density-temperature behavior of the nematic and the isotropic phases and the transformation between them. Because of the fluidity of these phases and the facility of the transformation between them, no difficulty was experienced here in the attainment of reproducible data. The construction of these dilatometers, the procedures followed and the corrections applied are described elsewhere.^{2a} In the present work the removal of air bubbles and solvent from the dilatometer encased sample was particularly difficult. This was finally accomplished by repeatedly evacuating, melting, and refreezing the sample in the dilatometer until no further bubbles were evolved. In the work reported below there was

no evidence of bubble formation in the dilatometer. This indicates that the degassing was successful and that no gaseous degradation products were formed during the heating of these samples. The density of the nematic phase was determined at 120.0° using a pycnometer.

In this study, it was found, in contradistinction to the cholesteryl esters that the transformation behavior did not depend on an extended annealing period in the isotropic state. However, even though the measurements showed no irreversible property changes with annealing, to be absolutely certain of erasing all memory effects, the *p*-azoxyanisole samples were all annealed at 145° for 30 min prior to the transformation experiments.

Part of the present work involved use of the differential scanning calorimeter DSC-1, Perkin-Elmer Corp. The precision and calibration of this instrument has been described elsewhere.⁹ Heating and cooling rates between 0.625 and 5°/min were used.

Results and Discussion

Equilibrium Measurements. These experiments are carried out by heating or cooling the sample in a step-wise fashion in the temperature range between room temperature and 145°. The sample was held at each temperature until no further change in mercury level was noted in a 1-hr period. In the region of the solid-nematic transition the waiting time was as long as 10 hr. The results of the equilibrium studies are shown in Table I and in Figures 1 and 2.

Table I: Summary of Equilibrium Volume-Temperature Relations for *p*-Azoxyanisole

Temp. °C	State	Transition volume change, %	α , °C ⁻¹
$T < 80$	Solid	...	4.1×10^{-4}
$110 < T < 117.0$...	6.9	...
$117.0 < T < 130.2$	Nematic	...	9.4×10^{-4}
$130.2 < T < 134.2$...	0.34	...
$134.2 < T$	Isotropic	...	8.4×10^{-4}

The transition temperatures of 117.0 and 134.2° for the solid-nematic and the nematic-isotropic transitions are in reasonably good agreement with those

(4) G. W. Gray, "Molecular Structure and the Properties of Liquid Crystals," Academic Press, New York, N. Y., 1962.

(5) W. Maier and A. Saupe, *Z. Naturforsch. A*, **15**, 287 (1960).

(6) E. McLaughlin, M. A. Shakespeare, and A. R. Ubbelohde, *Trans. Faraday Soc.*, **60**, 25 (1964).

(7) J. D. Bernal and D. Crowfoot, *ibid.*, **29**, 1032 (1933).

(8) W. Krigbaum, Y. Chatane, and P. G. Barber, *Acta Crystallogr., Sect. B*, **26**, 97 (1970).

(9) G. J. Davis, R. S. Porter, and E. M. Barrall, II, *Mol. Cryst.*, **10**, 1 (1970).

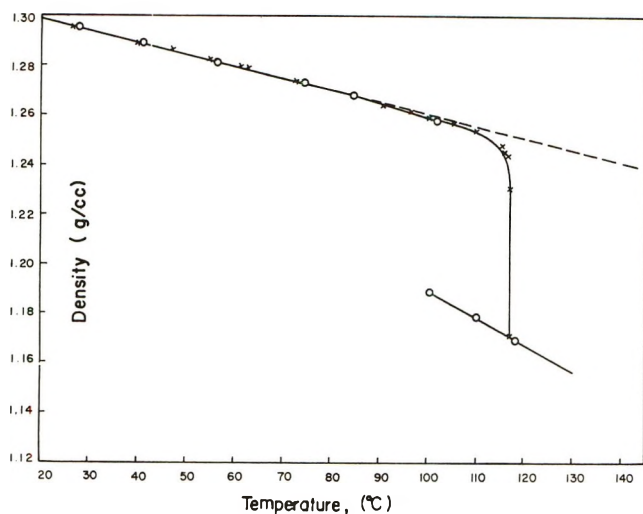


Figure 1. Equilibrium density-temperature behavior of solid *p*-azoxyanisole: X, heating; O, cooling.

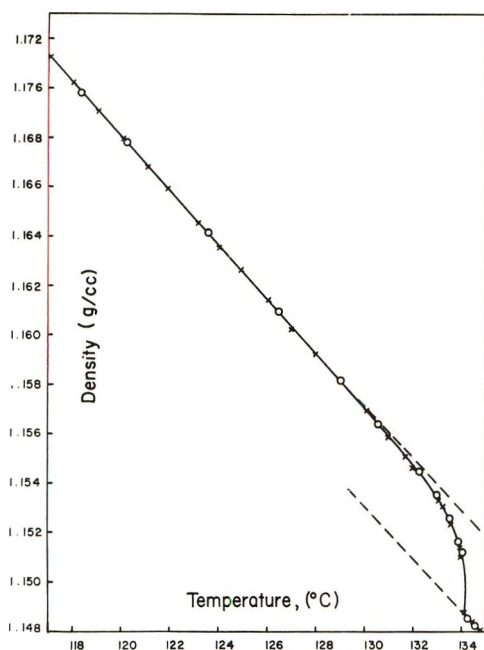


Figure 2. Equilibrium density-temperature behavior of nematic *p*-azoxyanisole: X, heating; O, cooling.

found by other investigators.⁴⁻⁶ Using the DSC these same temperatures were observed as sharp peaks on heating. On cooling, however, the position of the low temperature peak depended on cooling rate, the higher the cooling rate the lower the temperature. At a cooling rate of 0.625°/min the peak was observed around 80°. It is clear that crystallization kinetics have intervened here.

Figure 1 displays the results of a typical equilibrium density-temperature run. Here and as indicated in the above table, below 80° the density of the solid is an essentially linear function of the temperature. Between 80 and 110° the density decreases at an ever increasing rate, with the overwhelming majority (90%) of the transformation taking place within 0.3° of the

final transition temperature of 117.0°. The data in the premelting region between 80 and 117° do not fit the van't Hoff equation, and it seems probable that the density variation is due to a disordering of the solid as was found in the cases of the cholesteryl esters.^{2,10} If, however, it is assumed that the 0.3° melting range for 90% of the material is the result of impurities then using a value of $\Delta H = 7440$ cal/mol¹¹ a maximum impurity content of 0.6 mol % is calculated.

It is noteworthy that the present results of the density-temperature behavior and the volume change of the solid \rightarrow nematic transition do not agree with those of previous investigations.⁶ There is satisfactory agreement on the density of the nematic phase 1.170 and 1.167 g/cm³ in the present and previous work, respectively, but the volume changes on crystallization are in marked disagreement, being 6.9 and 11.03%, respectively. Although it is possible that in the present work, voids were left in the crystalline sample, this seems not highly probable. The reproducibility of the results (0.2% in density) both within single dilatometers and between dilatometers mitigates against this conclusion. Further, the expansion coefficient of the nematic phase is essentially the same in Figures 1 and 2 (9.49×10^{-4} in the former and 9.35×10^{-4} in the latter). This indicates that there is no error in the scaling factor used to correct changes in mercury height in the capillary into density changes in the disk-type dilatometers. Thus it appears that the discrepancy in the volume change on crystallization is not resolvable.

Figure 2 shows that in the nematic phase the density is a linear function of the temperature between 117 and 130.2°. The expansion coefficient is larger than that of the solid and somewhat larger than that of the isotropic phase. This behavior is similar to that shown by the cholesteric phases of some cholesteryl esters we have studied.² This observation is consistent with the concept that with falling temperature the order of the molecular arrays increases exceptionally rapidly in both nematic and cholesteric phases. This excess ordering is superimposed on the normal decrease of free volume with decreasing temperature and accounts for the observation of other investigators of high specific heat of nematic phases^{12,13} and strong temperature dependence of surface tension.¹⁴

Between 130.2° and the final nematic-isotropic transition temperature of 134.2° there is marked curvature in the density-temperature relationship shown in Figure 2. In this region the data do not fit the

(10) J. H. Wendorff and F. P. Price, unpublished results.

(11) E. M. Barrall, II, R. S. Porter, and J. F. Johnson, *J. Phys. Chem.*, **68**, 2801 (1964).

(12) E. M. Barrall, II, R. S. Porter, and J. F. Johnson, *ibid.*, **71**, 895 (1967).

(13) H. Arnold, *Z. Phys. Chem. (Leipzig)*, **226**, 146 (1964).

(14) W. A. Schwartz and H. W. Moseley, *J. Phys. Colloid. Sci.*, **51**, 826 (1947).

van't Hoff equation but do fit a plot of \ln (fraction isotropic) vs. $1/T$ ($^{\circ}\text{K}^{-1}$). The slope of this line is 5.46×10^4 ($^{\circ}\text{K}$), and the deviance of the eight points from the line is 0.05. Both the high expansion coefficient and the pretransition region are consistent with a theory proposed by Saupe.¹⁵ This theory expresses the order, and hence the volume, in terms of a parameter which depends on the dispersion that the angles the axes of the molecules make about their average direction. It seems improbable that our observations can be explained either in terms of Frenkel's¹⁶ heterophase fluctuation theory or on the basis of impurities.

The density of the isotropic phase from 134.2 to 145 $^{\circ}$ showed complete linear reversibility. We estimate an error in the volume expansion coefficient of less than $\pm 1\%$.

It is noteworthy that within the error of these measurements neither the solid-nematic nor the nematic-isotropic transitions show any pretransition effects on the high temperature side. This is in contrast to previous reports based on measurements of specific heat,¹² density,¹⁷⁻¹⁹ ultrasonic absorption,¹⁸ and nmr relaxation times.¹⁹ The present behavior is however in agreement with our previous studies on the cholesteryl esters² and the studies of others on viscosity and specific heats.^{17,20} As we have discussed previously^{2a} the data of these types supporting high temperature pretransition effects are not compelling, and it seems more probable that disordering of the type discussed before is taking place in *p*-azoxyanisole below both the solid-nematic and the nematic-isotropic transitions. It is worth noting that the absence of detectable pretransition effects in this type of observation is not necessarily in contradiction with observations of such effects using light scattering and magnetic birefringence techniques.²¹

Transformation Kinetics. The transformation from the isotropic to the nematic phase is extremely rapid. At temperatures of 133.4 and 132.1 $^{\circ}$ (0.8 and 2.1 $^{\circ}$, supercooling) the transformation is complete in less than 2 and 1 min, respectively.

Microscopical observation⁴ of this transformation shows that the nematic phase appears as tiny growing spheres. These spheres coalesce upon impingement. The use of the Avrami equation²² to describe this transformation is inappropriate because noncoalescence is assumed in its derivation.

When viewed with the polarizing microscope between crossed polars, each of the nematic droplets exhibits a black cross whose arms are parallel to the direction of the polars. Thus the optic axes are either radial or tangential.

The transformation from the nematic into the solid state is characterized by significant supercooling (greater than 20 $^{\circ}$), by an abrupt start of transformation, and by an extremely rapid rate of transformation thereafter. There is an induction period which is very sensitive to supercooling. We observed induction periods

of 22 min and less than 1 min at temperatures of 95 and 90 $^{\circ}$, respectively. In the temperature range of 90-95 $^{\circ}$ the induction period seems to depend on about the twentieth power of the supercooling. During the induction period the volume of the system does not change at all. This is followed by a very rapid crystallization. About two-thirds of the transformation takes place in less than 10 sec. Because of the extreme rate of transformation the mercury level in the capillary is no measure of the extent of transformation. Also, voids which are inaccessible to the mercury are produced in the sample. These voids complicated the determination of the equilibrium volume-temperature behavior. In the range of 100 to 117 $^{\circ}$ they were eliminated by annealing for at least 12 hr. This annealing resulted in reproducible volume-temperature behavior regardless of the temperature of crystallization of the samples.

Because the rate of transformation is so large once the induction time has passed, the transformation behavior is clearly dominated by nucleation rather than growth processes. We do not know, however, whether the induction periods are due to slow attainment of an embryo distribution characteristic of the transformation temperatures or to heterogeneities acting as nucleating sites which are only weakly wetted by the crystalline *p*-azoxyanisole. In any event interpretation of the data in terms of the Avrami equation is here clearly inappropriate.

Conclusions

The equilibrium density-temperature behavior of *p*-azoxyanisole, like that of the cholesteryl esters, indicates a pretransition region on the low temperature side of each transition but none on the high temperature side.

The isotropic-nematic transformation is extremely facile, being five to ten times more rapid than the isotropic-cholesteric transformation in cholesteryl nonanoate and myristate.

The nematic-solid transformation exhibits a very temperature-sensitive induction period and the whole transformation is clearly dominated by nucleation rather than growth rates.

Acknowledgments. The authors wish to express their gratitude to Professors R. S. Stein and R. S. Porter for encouragement and much helpful discussion during the course of this study.

(15) A. Saupe, *Angew. Chem.*, **80**, 99 (1968).

(16) J. Frenkel, "Kinetic Theory of Liquids," Dover Publications, New York, N. Y., 1955.

(17) R. S. Porter and J. F. Johnson, *J. Appl. Phys.*, **34**, 51 (1953).

(18) W. A. Hoyer and A. W. Nolle, *J. Chem. Phys.*, **24**, 803 (1956).

(19) W. R. Runyan and A. W. Nolle, *ibid.*, **27**, 1081 (1957).

(20) H. Martin and F. H. Muller, *Kolloid. Zh.*, **187**, 107 (1963).

(21) T. Stinson and D. Litster, *Phys. Rev. Lett.*, **25**, 503 (1970).

(22) M. Avrami, *J. Chem. Phys.*, **7**, 1103 (1938); **8**, 212 (1940).

Formation of Vapor Nuclei in High Temperature Melts¹

by Herman S. Levine

Sandia Laboratories, Albuquerque, New Mexico 87115 (Received March 8, 1972)

Publication costs assisted by Sandia Laboratories

A theory for the kinetics of bubble nucleation in binary Zr-O and ternary Fe-C-O melts is developed based on the known surface-active behavior of oxygen and a reasonable model for the vaporization of a single species for each system (ZrO(g) and CO(g), respectively). The formation of vapor nuclei in these systems has been unexplained because of the high surface tension and relatively low vapor pressures known to exist at critical conditions. It is shown that the thermodynamic behavior of both systems is similar and that the electrochemical potential is required to characterize the surface region of the melt because of the charge on the chemisorbed oxygen. Three conditions are required for a vapor embryo to coexist in an unstable equilibrium with the superheated melt, namely, chemical, chemisorptive, and mechanical equilibrium. The latter is in the form of a Laplace equation modified by the electrostatic energy density of the surface region. Because of this change, the reversible work to form the critical embryo is found to differ from the usual $\sigma \cdot 4\pi r^2/3$. These results are incorporated into the classical equations for the nucleation frequency and compared with available results for the two systems. It is found that a small excess oxygen ion concentration in the surface region is sufficient to counteract the very large surface tension barrier to a change of phase.

Introduction

Curious and puzzling explosions have been observed, during combustion in oxygen-nitrogen mixtures, of droplets of zirconium, titanium, tantalum, samarium, plutonium, uranium, beryllium, iron-carbon alloys, and other metals. Although this explosion phenomenology has been studied for many years in industrial and scientific processes,²⁻¹² its basic mechanism was never satisfactorily developed. In the past, models involving thermal shock, contractile skin, and boiling (according to a summary by Nelson⁴), N-atom recombination,¹¹ and various nucleation processes^{6,7,9,10} have been proposed and were found to be inadequate.¹³ This explosion phenomenon, however, was recently found¹³ to be consistent with a two-stage bubble nucleation-vapor expansion mechanism for the ternary Zr-O-N system if chemisorption effects were included in the nucleation process. This type of process, involving the formation of an electric double layer at the new interface, has not yet been included in the classical theory of nucleation. Indeed, earlier theories of bubble nucleation¹⁴⁻¹⁷ were formulated and applied mainly to simpler one-component systems where electrostatic effects were essentially absent.

In the case of zirconium, it was found that the explosions change to a gentle sac-forming process at a reduced nitrogen partial pressure and then disappear at even lower pressures.^{2,4,11,12} A similar behavior can be inferred for other materials. Using a reasonable extrapolation of Nelson's⁴ data, a related change in explosion behavior is found to occur in the absence of nitrogen in the gas phase as the droplet size of zirconium decreases from 525 μm .⁴ These results suggest that all the essential elements of the explosion process occur in the simpler binary Zr-O system.

By use of the known surface active behavior of oxygen^{8,18,19} and a reasonable model for the vaporization of ZrO(g) and CO(g) from the binary Zr-O and ternary Fe-C-O melts, respectively, the kinetics of bubble formation in these two models systems was developed and is reported here. A major problem encountered here, and by others,^{6,7,9,10} concerned the formation of vapor nuclei in a system with relatively low vapor pressure and high surface tension. It will be shown

- (1) This work was supported by the U. S. Atomic Energy Commission.
- (2) L. S. Nelson in "Eleventh Symposium (International) on Combustion," 1966, Combustion Institute, Pittsburgh, Pa., 1967, p 409.
- (3) L. S. Nelson, *Pyrodynamics*, **3**, 121 (1965).
- (4) L. S. Nelson, Research Report SC-RR-65-569, Sandia Laboratories, Albuquerque, N. M., Jan 1966.
- (5) (a) J. L. Prentice, *Combust. Flame*, **9**, 208 (1965); (b) J. L. Prentice and L. S. Nelson, *J. Electrochem. Soc.*, **115**, 809 (1968).
- (6) D. G. C. Robertson and A. E. Jenkins in "Heterogeneous Kinetics at Elevated Temperatures," G. R. Belton and W. L. Worrell, Ed., Plenum Publishing Co., New York, N. Y., 1970, p 393.
- (7) L. A. Baker, N. A. Warner, and A. E. Jenkins, *Trans. Met. Soc. AIME (Amer. Inst. Mining, Met., Petrol. Eng.)*, **239**, 857 (1967).
- (8) J. H. Swisher and E. T. Turkdogan, *ibid.*, **239**, 602 (1967).
- (9) P. A. Distin, G. D. Hallett, and F. D. Richardson, *J. Iron Steel Inst.*, **206**, 821 (1968).
- (10) L. A. Baker and R. G. Ward, *ibid.*, **205**, 714 (1967).
- (11) R. T. Meyer and L. S. Nelson, *High Temp. Sci.*, **2**, 35 (1970).
- (12) R. T. Meyer and W. G. Breiland, *ibid.*, **2**, 286 (1970).
- (13) H. S. Levine, *ibid.*, **3**, 237 (1971).
- (14) L. D. Landau and E. M. Lifshitz, "Statistical Physics," 2nd ed, Addison-Wesley, Reading, Mass., 1969.
- (15) J. P. Hirth and G. M. Pound, "Condensation and Evaporation," Macmillan, New York, N. Y., 1963.
- (16) J. P. Hirth, G. M. Pound, and G. R. St. Pierre, *Met. Trans.*, **1**, 939 (1970).
- (17) Yu. Kagan, *Russ. J. Phys. Chem.*, **34**, 42 (1960).
- (18) F. A. Halden and W. D. Kingery, *J. Phys. Chem.*, **59**, 557 (1955).
- (19) P. Kozakevitch and G. Urbain, *Rev. Met.*, **58**, 931 (1961).

that inclusion of the electrostatic energy density, stored in the chemisorbed layer, in a thermodynamic description of both systems effectively reconciles this problem and results in reasonable agreement between theory and experiment. The role played by nitrogen in the ternary Zr–O–N system is also discussed.

In the following, a vaporization model for the Zr–O and Fe–C–O systems is developed based on a rate-limiting surface reaction, for the desorption of a single vapor species, with the entire process limited by the extent of oxygen chemisorption. It is then shown that the thermodynamic behavior of the two systems is congruent and that the electrochemical potential is required to describe the surface region of the melt. The conditions required for a vapor embryo to coexist with the superheated melt and the free energy change to form a noncritical vapor embryo are established. These results are then incorporated into the nucleation process and compared with available results for the two systems.

Vaporization Reactions

According to Swisher and Turkdogan⁸ and King, Karasev, and Dastur,²⁰ the adsorption and desorption of CO(g) from liquid iron–carbon–oxygen alloys appears to occur *via* a slow surface reaction influenced by the presence of chemisorbed oxygen. The slow step, for the desorption reaction, is the combination of oxygen and carbon from the melt to form an activated complex at a surface site



(where the boldface type indicates a component of the melt) which then desorbs by one or more rapid steps into the vapor phase with the overall desorption reaction represented by



Because of this rapid desorption, the concentration of the activated complex is small. The same mechanism also applies in reverse for the adsorption process with dissociation of the activated complex being the rate-limiting reaction. Since oxygen is surface active, it influences the vaporization reaction only by limiting the available number of surface sites for the activated complex. Chemisorption equilibrium, represented by



must therefore be included in the rate equations for adsorption and desorption.

Swisher and Turkdogan⁸ summarized and analyzed the results of Halden and Kingery¹⁸ and Kozakevitch and Urbain¹⁹ on the surface tension of iron in the presence of added elements. By applying the Gibbs' adsorption equation to the surface tension data of the binary oxygen alloy, a Langmuir-type oxygen adsorption isotherm for liquid iron at 1823 K was derived.

Since carbon is not surface active in iron,¹⁸ these results are also believed valid for the ternary Fe–C–O system in the 1773 to 1873 K temperature range.

There have been no adsorption or desorption studies performed on the Zr–O system nor have there been any surface tension or chemisorption experiments. It is argued, however, that a similar vaporization mechanism is reasonable for the Zr–O system in the absence of experimental results, for it has been found⁸ that a slow surface reaction may be a general feature of gas–metal reactions at high temperatures when a strongly adsorbed solute is present. In fact, this general model has been successfully applied to decarburization experiments, the solution of nitrogen and sulfur in solid iron, and nitrogen in liquid iron.⁸ Thus the rate-limiting reaction for the Zr–O system is postulated to be



followed by a desorption through several rapid steps represented by



with the number of sites again limited by chemisorption equilibrium as in eq 3. Note that heat effects are not considered so that the model is isothermal. In addition, diffusional processes in the gas and condensed phases are considered fast relative to the rate of the surface reaction so that concentration gradients do not exist near the interface. Finally, the excess surface concentration of oxygen ions is determined entirely by the oxygen concentration in the melt in accord with eq 3.

Thermodynamic System

Consider a spherical vapor embryo in the Fe–C–O system containing V_2 molecules of CO. The radius of the embryo, r , is that of a Gibbs dividing surface located in the interface so that the adsorption of iron is zero. This location may not coincide with the surface of tension. The volume of the entire system is constant and the temperature, T , is constant and uniform throughout. The pressure and volume of the melt and embryo are p_1, V_1 , and p_2, V_2 , respectively. Let N_{10}, N_{11}, N_{12} be the atom inventory of **C**, **O**, and **Fe**, respectively, in the melt. Let Γ_3 be the relative adsorption of oxygen with respect to iron.^{21,22} Then $N_3 = \Gamma_3 4\pi r^2$ is the number of $\mathbf{O}^{2-}(\text{ads})$ at the interface.

The Zr–O system can be described in the same manner with N_{10}, N_{11}, N_2 , and N_3 the inventory of **Zr**, **O**, **ZrO(g)**, and $\mathbf{O}^{2-}(\text{ads})$, respectively. In this case, however, Γ_3 is the relative adsorption of oxygen with

(20) T. B. King, R. A. Karasev, and P. Dastur, "Heterogeneous Kinetics at Elevated Temperatures," G. R. Belton and W. L. Worrell, Ed., Plenum Publishing Co., New York, N. Y., 1970, p 409.

(21) R. Defay, I. Prigogine, A. Bellemans, and D. H. Everett, "Surface Tension and Adsorption," Wiley, New York, N. Y., 1966.

(22) H. Reiss, "Methods of Thermodynamics," Blaisdell, New York, N. Y., 1965.

respect to zirconium. Note that the subscripts 1, 2, and 3 refer, respectively, to the melt, the vapor, and the surface regions, and that a second subscript is used to identify a component in the melt.

Since the total number of atoms of each species and the volume of the entire system is constant, then

$$\begin{aligned} V_1 + V_2 &= 1 \\ N_{10} + N_2 &= n_1 \\ N_{11} + N_2 + N_3 &= n_2 \end{aligned} \quad (6)$$

for both systems where n_1 and n_2 are constants. In the case of the Fe-C-O system, N_{12} is also constant.

For an isothermal, constant volume system, the probability of a fluctuation producing a critical vapor embryo somewhere in the melt is proportional to^{14,23} $\exp[-\Delta F^*/kT]$ where ΔF^* is the increase in Helmholtz free energy as the change is made from the homogeneous melt to the melt plus critical vapor embryo. The total Helmholtz free energy of the melt plus vapor embryo is given by

$$F_f = F_1 + F_2 + F_3 \quad (7)$$

Since the system is isothermal

$$F_1 = -p_1V_1 + N_{10}\mu_{10} + N_{11}\mu_{11} + N_{12}\mu_{12} \quad (8)$$

$$F_2 = -p_2V_2 + N_2\mu_2 \quad (9)$$

$$F_3 = \sigma A + N_3\bar{\mu}_3 \quad (10)$$

where μ is the chemical potential. The electrochemical potential, $\bar{\mu}_3$, is required for the surface region²⁴ because of the charge associated with the chemisorbed oxygen.

Before any vapor embryo forms, the free energy of the melt is given by

$$F_i = -p_1(V_1 + V_2) + \mu_{10}(N_{10} + N_2) + \mu_{11}(N_{11} + N_2 + N_3) + \mu_{12}N_{12} \quad (11)$$

Thus the free energy change to form a vapor embryo that does not differ greatly in size from the critical embryo is given approximately by

$$\Delta F = -(p_2 - p_1)V_2 + \sigma A + N_2(\mu_2 - \mu_{10} - \mu_{11}) + N_3(\bar{\mu}_3 - \mu_{11}) \quad (12)$$

where it is assumed that σ is practically the same as that for an embryo in equilibrium with the melt and p_2 is the same as the equilibrium vapor pressure corresponding to the size r . The extremum condition $\delta(\Delta F) = 0$ results in

$$\mu_2^* = \mu_{10} + \mu_{11} \quad (13)$$

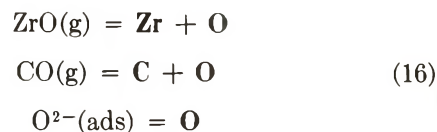
$$\bar{\mu}_3^* = \mu_{11} \quad (14)$$

$$(p_2^* - p_1) = 2\sigma/r^* +$$

$$\left\{ (1/A) \partial [N_3(\bar{\mu}_3 - \mu_{11})] / \partial r \right\}_{r=r^*} \quad (15)$$

which are three conditions that must be met simultaneously for the embryo and melt to coexist in an

unstable equilibrium. The first two equations are requirements for chemical and chemisorption equilibrium, *i.e.*



and the last equation is a modified Laplace equation for mechanical equilibrium.

It is interesting to note that Gibbs-Duhem equation for the surface region at constant temperature is $A d\sigma + N_3 d\bar{\mu}_3 = 0$. But since equilibrium between the surface and the melt requires that $d\bar{\mu}_3 = d\mu_{11}$, then $(d\sigma/d \ln a_{11}) = -kT\Gamma_3$ where a_{11} is the activity of oxygen in the melt. This last result is recognized as the standard Gibbs adsorption equation and is consistent with the analysis of surface tension results by Swisher and Turkdogan.⁸

It has been shown²⁴⁻²⁷ that $\bar{\mu}_3 = \mu_3 + ze\chi$ where ze is the charge on the chemisorbed ion and χ is the surface or contact potential. If the dipoles formed by the adsorbed oxygen ions are radially oriented, uniformly distributed and have their positive ends directed into the melt region, then (ignoring the small contribution from the activated complex)

$$\chi = -4\pi\Gamma_3zel \quad (17)$$

where l is the dipole length. Let

$$\sigma_0 = -ze\Gamma_3\chi = 4\pi\Gamma_3^2ze^2l \quad (18)$$

Then σ_0 is the electrostatic energy density of the surface region. Note that σ_0 is not a function of curvature and that $\bar{\mu}_3N_3 = \mu_3N_3 - \sigma_0A$. Then eq 15 simplifies to

$$(p_2^* - p_1) = 2(\sigma - \sigma_0)/r^* \quad (15a)$$

By use of eq 13 and 14 it is found that

$$\Delta F = -(p_2 - p_1)V_2 + \sigma A + N_2(\mu_2 - \mu_2^*) + N_3(\bar{\mu}_3 - \bar{\mu}_3^*) \quad (19)$$

so that at the extremal point

$$\Delta F^* = -(p_2^* - p_1)V_2^* + \sigma A^* \quad (20)$$

which simplifies further by use of eq 15a to

$$\Delta F^* = (\sigma + 2\sigma_0)A^*/3 = (16\pi/3)\Sigma^3/(p_2^* - p_1)^2 \quad (21)$$

where $\Sigma^3 = (\sigma - \sigma_0)^2(\sigma + 2\sigma_0)$. This equation differs from the usual expression¹⁶ for ΔF^* .

(23) F. F. Abraham, *J. Atmos. Sci.*, **25**, 47 (1968).

(24) R. Parsons in "Modern Aspects of Electrochemistry," J. O'M. Bockris and B. E. Conway, Ed., Butterworths, London, 1954, p 103.

(25) F. C. Tompkins in "The Solid-Gas Interface," Vol. 2, E. A. Flood, Ed., Marcel Dekker, New York, N. Y., 1967, p 765.

(26) M. Boudart, *J. Amer. Chem. Soc.*, **74**, 3556 (1952).

(27) I. Higuchi, T. Ree, and H. Eyring, *ibid.*, **77**, 4969 (1955); **79**, 1330 (1957).

It can be shown, by use of a Gibbs–Duhem relation, that

$$kT \ln (p_2/p_{2,\infty}) = (v_{10} + v_{11})[(p_2 - p_{2,\infty}) - 2(\sigma - \sigma_0)/r] \quad (22)$$

which is a modified Kelvin equation for the equilibrium vapor pressure as a function of curvature where the $(p_2 - p_{2,\infty})$ term on the right is relatively small and usually ignored. In eq 22, $p_{2,\infty}$ is the vapor pressure at zero curvature and v_{10} and v_{11} are partial molecular volumes in the liquid. It is then found that

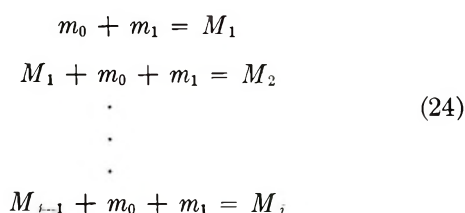
$$(\partial^2 \Delta F / \partial r^2)_{r=r^*} = -8\pi(\sigma - \sigma_0)[1 + O(v^2)] \quad (23)$$

which is a result that will be used later, where use has been made of eq 22 and the facts that $(\mu_2 - \mu_2^*) = kT \ln (p_2/p_2^*)$ and $v \ll 1$. The parameter $v \equiv [(v_{10} + v_{11})/v_2^*]$ where v_2^* is the molecular volume of the vapor in the critical embryo.

According to the vaporization model, the relative adsorption of oxygen is a function *only* of the oxygen content of the melt. If it were, instead, also a function of the pressure of the vapor species, due to a different vaporization mechanism, then the adsorption would change with curvature due to a change in the equilibrium vapor pressure with curvature. The analysis would then require σ_0 to vary with embryo size. The fact that other vapor species (such as Zr(g) and ZrO₂(g) in the Zr–O system, and Fe(g) and CO₂(g) in the Fe–C–O system) also exist suggests that some of these problems might occur. It seems likely, however, that any effects caused by the presence of other species would be small because they are present at a much lower concentration than the ones considered.

Kinetics of Nucleation

The classical theory of nucleation describes a phase change process in terms of a sequence of homogeneous bimolecular reactions between embryos and a monomer, and many good reviews^{15,28–32} have been written on the subject. In the present case, however, a minor modification is required because of the rate-limiting vaporization reactions of eq 1 and 4. If M_i represents an embryo containing i molecules (for convenience, $i \equiv N_2$) and m_0 and m_1 the two components in the melt (C and O for the Fe–C–O system and Zr and O for the Zr–O system), then the sequential reactions leading to M_i become



Thus, at subcritical conditions, the system will contain a distribution of vapor embryos up to a maximum

$i < i^*$. For a critical set of conditions, i will equal or exceed i^* . The classical theory then leads directly to the following expression for the steady-state rate of nuclei formation

$$J = \left[\int_1^\infty \frac{di}{\beta A(i)n(i)} \right]^{-1} \quad (25)$$

where use was made of detailed balancing and $A(i)$ is the surface area of an i embryo, $n(i)$ is the metastable equilibrium number density of vapor embryos of size i , and β is the rate of molecular gain by an i embryo per unit area of surface. A change of variable from i to r is made and, since $[1/n(r)]$ has a sharp maximum at $r = r^*$ and $\beta A(r)$ varies slowly, the latter is removed from the integral as $\beta^* A^*$. Also, $[1/n(r)]$ can be expressed by

$$[1/n(r)] \simeq \exp \left[\frac{\Delta F^*}{kT} + \frac{1}{2kT} \left(\frac{\partial^2 \Delta F}{\partial r^2} \right)_{r=r^*} (r - r^*)^2 \right] \quad (26)$$

in which ΔF is expanded in a Taylor series about $r = r^*$. Then eq 25 becomes

$$J = Z\beta^* A^* N \exp[-\Delta F^*/kT] \quad (27)$$

where Z , the nonequilibrium factor,²⁹ is

$$Z = [(-1/2\pi kT)(\partial^2 \Delta F / \partial r^2)_{r=r^*}] / (\partial N_2 / \partial r)_{r=r^*} \quad (28)$$

and

$$N \simeq n_1 + n_2 + N_{12} \quad (29)$$

is the number density of atoms in the system. Since

$$(\partial N_2 / \partial r)_{r=r^*} \simeq A^* p_2^* / kT \quad (30)$$

then eq 27 simplifies to

$$J = J_0 \exp(-\Delta F^*/kT) \quad (31)$$

where

$$J_0 = 2N\beta^* kT [(\sigma - \sigma_0)/kT]^{1/2} / p_2^* \quad (32)$$

From eq 1–3, the desorption frequency is found to be⁸

$$\beta^* = K\Gamma_0(1 - \theta)a_{10}a_{11} \quad (33)$$

where Γ_0 is the asymptotic adsorption limit of oxygen at high concentrations of O, $\theta \equiv \Gamma_3/\Gamma_0$, a_{10} and a_{11} are activities of the two components in the melt, and K is a desorption rate constant. However, this type of data is not available for the Zr–O system. As a rough estimate, the following will be used for β^* which probably overestimates the desorption frequency

(28) J. E. McDonald, *Amer. J. Phys.*, **30**, 870 (1962); **31**, 31 (1963).

(29) J. Feder, K. C. Russell, J. Lothe, and G. M. Pound, *Advan. Phys.*, **15**, 111 (1966).

(30) H. Reiss, *Ind. Eng. Chem.*, **44**, 1284 (1952).

(31) H. Reiss, *J. Stat. Phys.*, **2**, 83 (1970).

(32) R. L. Gerlach, *J. Chem. Phys.*, **51**, 2186 (1969).

$$\beta^* \approx (1 - \theta)p_2^*/(2\pi m_2 kT)^{1/2} \quad (33a)$$

where m_2 is the molecular weight of the vapor. Such a crude estimate is evidently acceptable, since β^* appears only in the pre-exponential term and it has been shown¹³ that orders of magnitude changes in J_0 do not greatly influence the nucleation frequency. Thus

$$J_0 \approx N(1 - \theta)[2(\sigma - \sigma_0)/\pi m_2]^{1/2} \quad (32a)$$

Discussion

The known behavior and essential facts relating to the two systems are as follows.

(1) Droplets of zirconium, initially 525 μm in diameter, explode violently in gas mixtures containing more than 4% nitrogen at a total pressure of 625 Torr before the reaction is complete. If the partial pressure of nitrogen is reduced while the total pressure is maintained constant, the explosion gradually changes to a gentle sac-forming process, again before complete reaction, at a definite threshold nitrogen (TN) pressure. Below this TN pressure, the explosion disappears and the reaction proceeds to a ZrO_2 end point. Figure 1, taken from a report by Nelson,⁴ illustrates how the TN varies with the initial droplet size. As shown, a reasonable extrapolation of the threshold curve intercepts the abscissa at a finite droplet size of about 300 μm . Such an extrapolation would imply that the *explosion/sac formation/complete reaction behavior should occur with or without nitrogen in the gas phase as the droplet size decreases from 525 μm* . Thus, nitrogen may not be a *necessary* feature of the sac-forming process and the simpler binary Zr-O system is considered in detail in this report.

(2) The threshold temperature in the binary Zr-O system is estimated to be about 4000 K. This estimate is based on a *ca.* 4300 K peak burning temperature for a 525- μm zirconium droplet burning in oxygen at 625 Torr³³ (the effect of size on the peak temperature is unknown) and the fact that sac formation occurs as the droplet cools after the peak temperature is observed.¹¹ At 4000 K, the vapor pressure of $\text{ZrO}(\text{g})$ above the melt is estimated to be about 1200 Torr, which is at least an order of magnitude greater than that of $\text{Zr}(\text{g})$ or $\text{ZrO}_2(\text{g})$ according to Meyer and Nelson.¹¹ The surface tension of the melt is expected to be at least 350 dyn/cm according to estimates made¹³ for $\text{ZrO}_2(\text{l})$ at 4000 K.

(3) There have been no systematic studies of threshold conditions in the Fe-C-O system. However, "carbon boil" and explosions have been observed^{6,7,9,10} at roughly 1800 K, with the vapor pressures of $\text{CO}(\text{g})$ estimated to be as high as 60 atm and the surface tension in excess of 1100 dyn/cm. In addition, the surface tension of oxygen-iron alloys decreases from about 1720 to about 1200 dyn/cm as the oxygen content of the melt increases to about 0.05% by weight.⁸

While these experimental parameters are uncertain, they do establish a set of critical parameters subject to

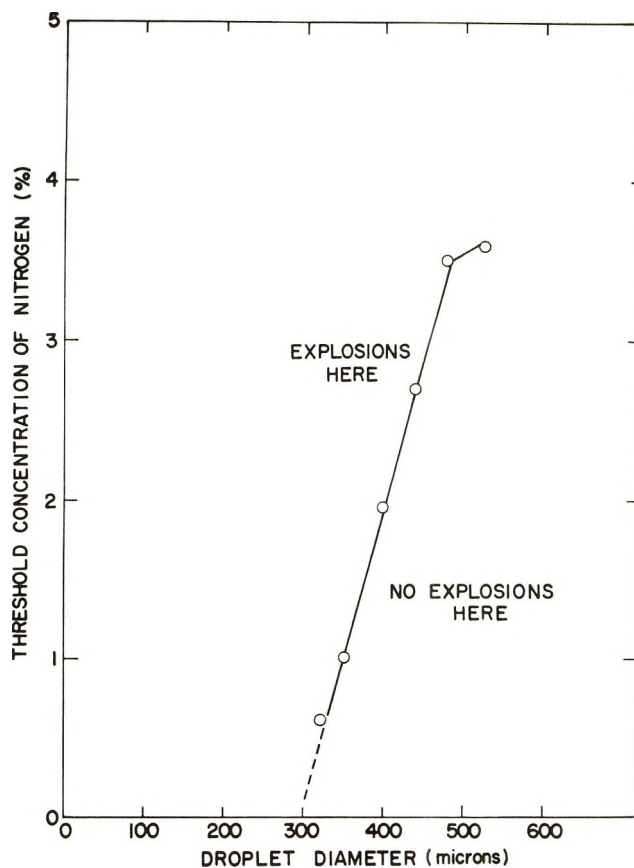


Figure 1. Concentration of nitrogen in oxygen gas at a total pressure of 625 Torr that causes explosive phenomena to occur during combustion of zirconium droplets. Extrapolation is assumed. Taken from Nelson, SC-RR-65-569, Sandia Laboratories, Albuquerque, N. M., Jan 1966.

future refinement. Moreover, they illustrate the fact that both systems have a high surface tension and *relatively* low vapor pressure.

Using the volume and time intervals described in a previous report,¹³ it is found that a critical vapor embryo will form in the Zr-O system at 4000 K and at an ambient pressure of 625 Torr if $\sigma \approx \sigma_0$. Thus, if $l = 1.40 \text{ \AA}$ (radius of O^{2-} ion¹⁸), $z = 2$, and $\Gamma_0 = 10^{15} \text{ cm}^{-2}$, then since $\sigma_0 \approx 350 \text{ dyn/cm}$, the fraction of surface sites occupied by oxygen ions is found to be $\theta = 0.046$. This means that a very small excess oxygen ion concentration at the interface is sufficient to counteract the very large surface tension barrier to a change of phase. Moreover, it is found that the critical embryo contains 215 molecules (N_2^*) and that the critical radius (r^*) is 260 \AA . The content and size of this vapor nucleus is large enough for macroscopic thermodynamics to be valid in describing the system.

A similar analysis for the Fe-C-O system at 1800 K with $(p_2^* - p_1)$ assumed to be 50 atm results in the formation of a single critical vapor embryo if $\Sigma \approx 12.5 \text{ dyn/cm}$. If $(p_2^* - p_1)$ is less, then the corresponding

(33) L. S. Nelson, H. S. Levine, D. E. Rosner, and S. C. Kurzius, *High Temp. Sci.*, 2, 343 (1970).

value Σ is also smaller. Thus $\sigma_0 \approx \sigma$ and $0.082 \leq \theta \leq 0.098$ for $1200 \leq \sigma \leq 1720$. This range in the value of θ , however, is more consistent with $\sigma \approx 1700$ and an oxygen activity in the melt of about 0.0014 (weight per cent oxygen). The results are again quite insensitive to the magnitude of the excess critical pressure and temperature (within reasonable limits).

There have been interesting discussions²⁻⁴ of the role played by nitrogen in causing explosions and sac formation in the ternary Zr-O-N system. The present study provides additional insight on this matter. Nitrogen is also known to be surface active in iron,¹⁸ and as mentioned earlier, its adsorption in iron appears to occur *via* a slow surface reaction. If a similar surface active behavior and vaporization mechanism occurs in the zirconium system, which is a possibility, then the formation of N⁻(ads) would occur along with the O²⁻(ads). The existence of chemisorbed nitrogen would reduce the number of O²⁻(ads) required to overcome the surface tension barrier to phase change, for the electrostatic work to form the dipole layer would be summed over all ions at the surface. Thus, in terms of the present approach to the sac-forming process, the

presence of nitrogen in the melt would alter the behavior of the system by acting as a source for additional chemisorbed ions.

Summary and Conclusions

(1) Prior studies of the explosion and sac-forming processes in the zirconium and iron systems failed to reconcile the very high surface tension with the relatively low vapor pressures in a description of the phase change process. (2) A self-consistent description of the thermodynamic behavior of the binary Zr-O and ternary Fe-C-O systems must include the electrostatic energy density, σ_0 , in the chemisorbed layer. (3) The nucleation frequency in the binary and ternary systems is modified by the electrostatic energy density when chemisorption occurs. (4) Small excess oxygen ion concentrations at the interface are sufficient to counteract the very large surface tension barrier to change of phase in systems with relatively low vapor pressure. (5) Nitrogen in the ternary Zr-O-N system may act only as a source for additional chemisorbed ions in the sac-forming process.

Two Familiar Gas Reactions at Suprahigh Pressure

by Melvyn L. Dutton, Don L. Bunker,* and Harold H. Harris

Department of Chemistry, University of California, Irvine, California 92664 (Received March 31, 1972)

Publication costs assisted by the National Science Foundation

We studied the pyrolysis of NO₂Cl and of N₂O₅, with up to 300 atm of added N₂, in an apparatus permitting optical measurement of NO₂ concentration. NO₂Cl appears to be a well-behaved RRKM molecule over the whole range of accessible pressures. There is some evidence for a rise in the N₂O₅ disappearance rate at very high pressure. The possible implications of this are discussed.

Introduction

"Suprahigh" is a description coined by Rabinovitch, *et al.*,¹ to describe the range of pressures from somewhat above 1 atm to that corresponding to about 10⁻¹³ sec between collisions. These pressures are obtainable from commercial gas cylinders. For simple gases, this is also the range in which collisions are mostly binary. There are several reasons for wanting to study simple gas reactions with suprahigh inert diluent pressures.

It has been proposed on theoretical grounds that a high rate of binary collisions might diagnose departures of unimolecular reactions from conventional

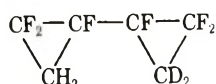
RRKM kinetics. Baetzold and Wilson² pointed to the possibility of a transient appearing in the distribution of natural lifetimes of energized molecules, caused by nonrandomness in the way collisions produce short-lived states. The most prominent effect of this would probably be a deficiency of very short-lived molecules, leading to a decline of the unimolecular rate constant at high enough pressures. A phenomenon having the

(1) I. Oref, D. Schuetzle, and B. S. Rabinovitch, *J. Chem. Phys.*, **54**, 575 (1971).

(2) R. C. Baetzold and D. J. Wilson, *J. Phys. Chem.*, **68**, 3141 (1964); *J. Chem. Phys.*, **43**, 4299 (1965). "RRKM" is Rice, Ramsperger, Kassel, Marcus.

opposite sense was suggested by one of the present authors as a result of early trajectory studies.³ The main assumption of RRKM theory, that of rapid intramolecular vibrational relaxation, was found to fail for certain model triatomic molecules. For these, transition from relaxation-controlled to true RRKM behavior occurs at a collision rate high enough to require nearly all reactive states to be formed on the favorable side of the intramolecular energy bottleneck. Acceleration of decomposition at suprahhigh pressures would be expected.

Several experiments have been done, and as a result some of the unimolecular kineticist's favorite molecules have come under suspicion of non-RRKM behavior. Rate decline at high pressure⁴ and temperature⁵ for cyclopropane, and at high pressure for ethylcyclobutane,⁶ has been tentatively reported. Methyl isocyanide seems to be a badly behaved molecule in preliminary trajectory studies,⁷ and there is a suggestion that a free-radical mechanism contributes to its high-pressure isomerization.⁸ (Some of these results have been challenged.⁹) On the other hand, the *sec*-butyl radical shows no anomalous behavior¹ up to 203 atm of added H₂. Our measurements are on NO₂Cl, which has had a prior, unpublished high-pressure study¹⁰ not directed at the effects under discussion here. We wanted a simpler molecule because it was thought at one time that this would favor the second type of deviation mentioned above.³ It turned out that NO₂Cl is free of non-RRKM behavior up to 310 atm of added N₂ and is now perhaps the best characterized molecule that conforms to the standard theory. (Meanwhile, this type of non-RRKM behavior has been rather conclusively shown at lower pressures by Rynbrandt and Rabinovitch¹¹ for



and convincing photochemical demonstrations of non-random energy partitioning in the decomposition of ground-state molecules have begun to appear.¹²)

The relationship between gaseous first-order unimolecular behavior and that in inert solvents is also of interest, although we have not attacked the question in this paper. For example, NO₂Cl decomposition in a halocarbon solvent is appreciably slower¹³ than we find. What is the relationship between rates measured under these two sets of conditions? Variation of the ideality of the pressurizing gas might help show this.

A problem to which little attention has been given is that of the possible high-pressure dependence of bimolecular reaction rates. Sufficiently frequent collisions should produce relaxed intermediates for which the description used in transition state theory is an actuality, rather than an approximation requiring separability or adiabaticity of nonreactive motions.

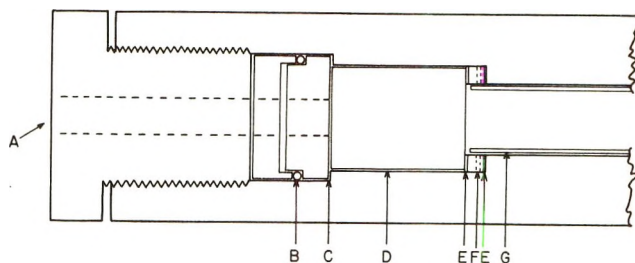


Figure 1. Reaction cell (overall length 14 in., diameter 3 in.). All unlabeled parts are made of Type 316 stainless steel: A, light path; B, silicone O-ring; C, 0.002-in. Teflon spacer; D, 2-in. fused silica window; E, 0.015-in. Teflon rings; F, pressure distribution channel; G, Pyrex liner.

Reaction rates might be expected to change when the time between collisions approaches the lifetime of the activated complex. One possible way of exploring this, for one of the bimolecular steps in the N₂O₅ decomposition, is described in this paper. The results are faintly positive.

Experimental Section

We use a simple apparatus.¹⁴ Its only novel feature is a reaction cell that permits optical transmission at the pressure of our experiments.

One end of the cell is shown in Figure 1. The materials are Type 316 stainless steel, polished cylindrical fused-silica windows, and a Pyrex liner. The closure is made by compressing a Teflon annulus against the outside face of the window, so that the unloaded surface of the silica cylinder is minimized. This arrangement fails reproducibly by slow leakage at about 320 atm. We did not have any violent accidents.

The cell holds 65 ml and is connected through a side fitting and double Aminco 30,000-psi valves to a conventional vacuum line and to a pressure gauge. Two

(3) D. L. Bunker, *J. Chem. Phys.*, **40**, 1946 (1964).

(4) H. Yokokawa, L. Dell'Osso, and E. W. Graham, to be published; private communication.

(5) J. N. Bradley and M. A. Friend, *Trans. Faraday Soc.*, **67**, 72 (1971).

(6) J. Aspden, N. A. Khawaja, J. Reardon, and D. J. Wilson, *J. Amer. Chem. Soc.*, **91**, 7580 (1969).

(7) H. H. Harris and D. L. Bunker, *Chem. Phys. Lett.*, **11**, 433 (1971).

(8) C. K. Yip and H. O. Pritchard, *Can. J. Chem.*, **48**, 2942 (1970).

(9) In particular, these are ref 5 and 8 (B. S. Rabinovitch, private communication). The results in ref 6 were interpreted in terms of the volume of activation, which is an empirical construct rather than an alternative physical interpretation to the ones used here. The exact relationship of the trajectory studies to the CH₃NC experiments requires a careful discussion which will appear in a future publication (D. L. Bunker and W. L. Hase).

(10) G. J. Casaletto, Thesis, Stanford University, 1956; University Microfilms, Ann Arbor, Mich.

(11) J. D. Rynbrandt and B. S. Rabinovitch, *J. Phys. Chem.*, **75**, 2164 (1971).

(12) F. H. Dorer and S. N. Johnson, *ibid.*, **75**, 3651 (1971).

(13) D. Beggs, C. Block, and D. J. Wilson, *ibid.*, **68**, 1494 (1964).

(14) For additional details see M. L. Dutton, Thesis, University of California, Irvine, 1972; University Microfilms, Ann Arbor, Mich.

windings of Nichrome over asbestos are used to heat the cell. One is controlled to $\pm 1^\circ$ or better from a thermocouple inserted $\frac{3}{8}$ in. into the cell wall. The other is for final rapid destruction of the sample, as described below.

A double-beam spectrophotometer is folded around the cell in such a way as to keep photomultipliers (931-A), filters (Corning 3398 + 5113), and the lamp (W filament) out of the way of possible flying fragments of silica. The lamp is operated by a regulated voltage source. Concentration of NO_2Cl vs. time is recorded by means of an electrometer and strip-chart recorder. Illumination of the sample during the experiment produced no detectable photochemistry.

Gases at the high densities employed here have to be mixed as if they were liquids. We ordinarily use a premixing cylinder that can be detached from the apparatus and shaken (some Teflon beads were put inside). If the volume of the premixing cylinder greatly exceeds that of the cell, the cell can be filled directly with little pressure loss. Subsequently attaining constant temperature requires an appreciable portion of a half-life, so that initial rates are not accessible with this method. Analysis of the data requires knowledge of the initial NO_2Cl concentration, however; this is found at the end of the useful kinetic measurement by rapid pyrolysis of the remaining NO_2Cl to NO_2 .

Nitryl chloride and nitrogen pentoxide were prepared by literature methods,¹⁵ purified by repeated distillation, and checked for purity by ir spectrometry.¹⁶ Matheson dry N_2 of 99.99% purity, from 6000 psi cylinders, was used directly. Rather than trying to remove residual O_2 , we established its unimportance experimentally by adding some more. Auxiliary runs with variable initial reactant concentrations were also made to verify the order of the reaction under our conditions.

Results for NO_2Cl

The experimental results at three temperatures are displayed in Figure 2. The high-pressure values of k are 2.00 , 3.48 , and $7.05 \times 10^{-4} \text{ sec}^{-1}$ at 105 , 115 , and 123° , respectively. The most important feature of these observations is that no appreciable deviation from the high-pressure k limit was found for mean collision intervals as small as $2.8 \times 10^{-13} \text{ sec}$ (calculated using the second virial coefficient of N_2). This is shorter than most of the intramolecular relaxation times found for badly behaved model molecules in the trajectory studies.³ Therefore there is a strong presumption that NO_2Cl is a well behaved RRKM molecule under all conditions. In view of the results cited earlier, it would seem that at least at the moment, NO_2Cl is the molecule of whose compliance with the theory we are most nearly sure.

Our temperature range is not broad enough for an independent determination of the activation energy.

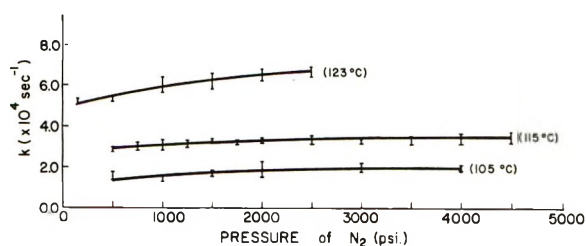


Figure 2. Observed rate constant for NO_2Cl decomposition, vs. pressure of added N_2 .

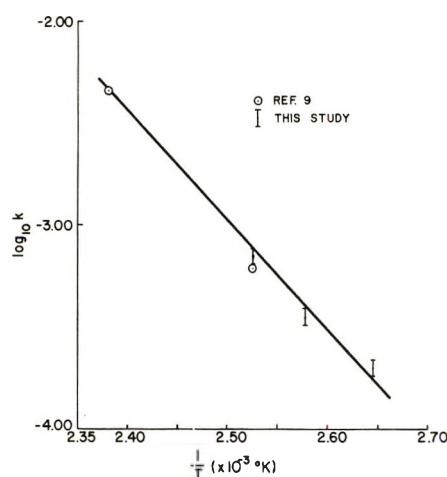


Figure 3. Activation energy determination for NO_2Cl .

In combination with the data of Casaletto,¹⁰ our results lead to $E_{\text{act}} \cong 25 \text{ kcal/mol}$ (see Figure 3), with enough uncertainty not to contradict earlier estimates.^{13,17}

Although our study did not produce many data on the falloff of k with pressure, we are able to make a comparison which clarifies some of the findings in the earlier high-pressure study.¹⁰ In that work, two groups of measurements were made, one at moderate and the other at relatively high pressure. Mismatch of these was attributed to a grease-catalyzed contribution to the reaction rate at moderate pressures. Our system does not have this hazard, and we agree better with the moderate-pressure measurements; our high-pressure data are systematically higher than those of ref 10. In Figure 4 we have displayed (at 123°) our results, both groups of those of ref 10, and data from a low-pressure study (Cordes and Johnston^{17b}). Our view is that the moderate pressure data of ref 10 are the more reliable of the two sets.

(15) NO_2Cl : H. Schechter, F. Conrad, A. L. Daulton, and R. B. Kaplan, *J. Amer. Chem. Soc.*, **74**, 3052 (1951). N_2O_5 : N. S. Gruen-hut, M. Goldfrank, M. L. Cushing, and G. V. Caesar, *Inorg. Syn.*, **3**, 78 (1950).

(16) Spectra: NO_2Cl , R. Ryason and M. K. Wilson, *J. Chem. Phys.*, **22**, 2000 (1954); N_2O_5 , I. Hisatsune, J. Devlin, and Y. Wada, *Spectrochim. Acta*, **18**, 1641 (1962).

(17) (a) H. Hiraoka and R. Hardwick, *J. Chem. Phys.*, **36**, 2164 (1962); (b) H. F. Cordes and H. S. Johnston, *J. Amer. Chem. Soc.*, **76**, 4264 (1954); (c) H.-J. Schumacher and G. Sprenger, *Z. Anorg. Allg. Chem.*, **182**, 139 (1929).

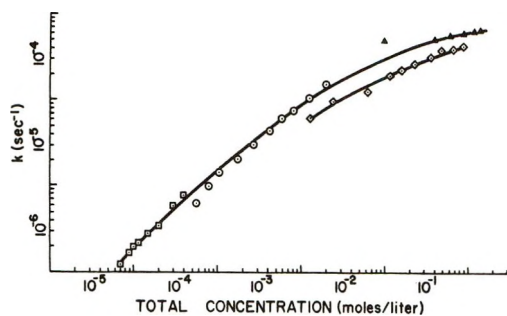
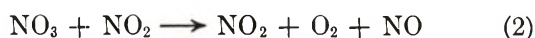


Figure 4. Rate constants for NO_2Cl decomposition, vs. pressure; results of Casetto¹⁰ (\circ , moderate pressure); \diamond , high pressure), Cordes and Johnston^{17b} (\square), and this work (\triangle).

Results for N_2O_5

The textbook mechanism is



with (1) maintained rapidly and (2) rate determining. At high pressure the overall rate constant is twice that for (2) multiplied by the equilibrium constant for (1). We are thus testing (2) for possible high-pressure effects due to the collisional relaxation of an intermediate aggregate (N_2O_5)*.

This would be an important effect if definitely established, and our results are only marginally positive, so they must be stated with some care. All the data were taken at 35° . Figure 5 shows the results on an expanded ordinate so that the visual level of uncertainty can be assessed. The least-squares slope and its standard deviation—using 67 observations individually, not the centers of the error bars—is $1.11 \times 10^{-4} \pm 0.21 \times 10^{-4}$ in the units of the figure. The individual observations are shown with a zero base line in Figure 6. For comparison, the 115° data in Figure 2 have a slope of $1.28 \times 10^{-4} \pm 0.21 \times 10^{-4}$ with 62 observations; the 28 points with $p > 2000$ psi have a slope of $0.83 \times 10^{-4} \pm 0.45 \times 10^{-4}$. This suggests that we see an effect in Figure 5 with about the same reliability that we can discern a high-pressure limit and a portion of the falloff region with NO_2Cl . Note that exactly the same kind of concentration measurement was made in each case and that any minor heterogeneous effects should be least important at high pressure.

The confidence level of this finding is roughly 90%—not very high, but high enough to suggest that further experiments would be desirable. If the effect is real, it represents a partial thermalization of one or more of the nonreactive degrees of freedom of (N_2O_5)* and a

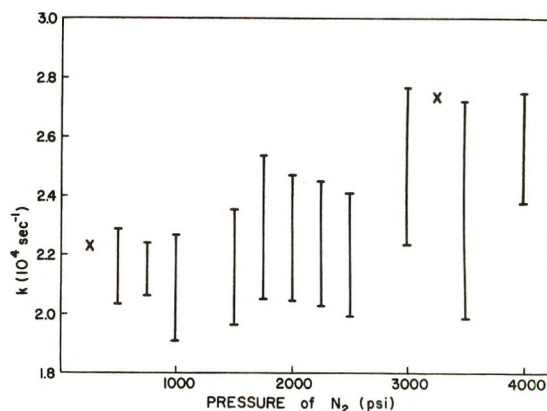


Figure 5. Rate constant for N_2O_5 disappearance, vs. pressure of added N_2 . The \times 's are single observations and the standard error bars have about six observations per bar.

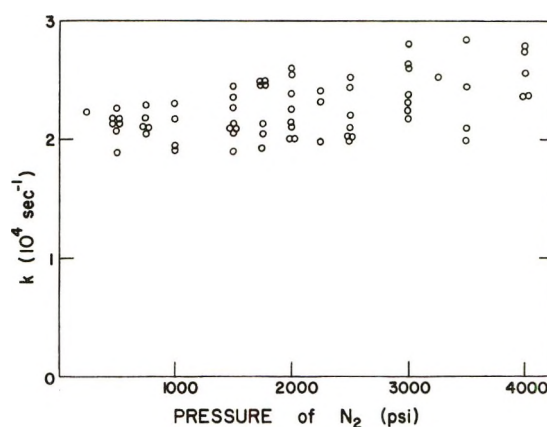


Figure 6. The individual data points corresponding to Figure 5. All measurements were made at multiples of 250 psi; some of the points have been slightly displaced for better visibility.

resulting change in the splitting between the two reactive channels—(2) and the reverse of (1). The potential surface must be rather complicated, and there is no way to decide whether an increase or decrease of rate at high pressure would be the more probable.

Comments

Although the method does not have high precision, it is simple and inexpensive and can yield information worth having at this stage of our understanding. We chose reactions in this study mainly for their feasibility as a test of the apparatus and for the ease with which they lent themselves to spectrophotometry. More reactions of both types need to be studied in this pressure range.

Acknowledgment. We thank the National Science Foundation for supporting this work.

The Photochemistry of the Monoxalatoiron(III) Ion

by G. D. Cooper and B. A. DeGraff*

Department of Chemistry, University of Virginia, Charlottesville, Virginia 22903 (Received November 1, 1971)

The photochemistry of the monoxalatoiron(III) ion in aqueous perchloric acid with and without excess Fe^{3+} was studied by kinetic spectroscopy. Deaerated solutions of $\text{Fe}(\text{C}_2\text{O}_4)^+$ flash irradiated in the charge-transfer spectral region display absorbance changes distinctly characterized by the time scale on which they occur. The initial decay, complete within 50 μsec , is controlled by the rate of photolysis and is due to the primary photoredox and reactions of the resulting $\cdot\text{C}_2\text{O}_4^-$ free radical with $\text{Fe}(\text{C}_2\text{O}_4)^+$, Fe^{3+} , or itself. Subsequent absorbance changes are the result of the decomposition of the product of the $\cdot\text{C}_2\text{O}_4^- + \text{Fe}(\text{C}_2\text{O}_4)^+$ reaction and, for experiments using excess Fe^{3+} , the anation of $\text{Fe}(\text{III})$ by HC_2O_4^- . In contrast to the bis- and trisoxalatoferate(III) ions, photoaquation is not a significant primary process. Quantitative kinetic values are reported for the various reactions.

Introduction

A study of the photochemistry of the tris- and bisoxalatoferate(III) ions in aqueous media using kinetic spectroscopy has appeared recently.¹ While this study did delimit and outline the general features of the mechanism, the complexity of the system did not allow a quantitative kinetic treatment of the data. Thus, a number of significant details regarding the proposed individual steps were left unresolved. The purpose of the present study was to obtain quantitative kinetic data on these steps through the study of a less complex system.

The monoxalatoiron(III) system has been studied extensively, and the stability constant² as well as the rate constants for anation² and electron exchange³ with Fe^{II} are known. Since fewer species and their related equilibria were involved, we hoped to obtain quantitative kinetic values for the reaction of $\cdot\text{C}_2\text{O}_4^-$ with the ferrioxalate ion, to examine the apparent Fe^{III} dependence of the ferrous oxalate decay, and to study the Fe^{III} anation reaction in greater detail.

Experimental Section

The basic flash photolysis apparatus has been described previously.⁴ Three different analysis lamps were used: an Osram 100-W Hg lamp for the 0–200- μsec range, a Hanovia 150-W Xe lamp for the 0.2–5-msec range, and a Philips 50-W tungsten-iodine lamp for $t > 5$ msec. When the observation period exceeded 10 msec, the ac-coupled cathode follower usually employed was removed, and the PMT output was dc-coupled to the scope through a bucking voltage supply. Initial and final transmittances were read from a 10-mV recorder.

Solutions for photolysis were prepared from stock solutions of standardized ferric perchlorate in 0.1 M HClO_4 , 1.0 M HClO_4 , 1×10^{-2} M oxalic acid, and reagent LiClO_4 . The solutions were prepared in the dark, purged with argon for at least 50 min, and transferred

under vacuum to a 5- or 13-cm fused quartz photolysis cell. Unless otherwise noted, the cell was filled with fresh solution for each flash. For the kinetic experiments the total percentage decomposition was limited to less than 15% by appropriately adjusting the flash energy. The observed activation energies were determined as previously described.¹

Results

The experimental results for the monoxalatoiron(III) ion with and without excess Fe^{III} are qualitatively similar to those observed for the bisoxalatoferate(III) ion.⁵ As shown in Figure 1, the absorbance–time profile shows three rather distinct regimes including a very fast initial decay complete within 50 μsec (trace 1), a slower decay complete within ~ 5 msec (trace 2), and for those experiments with excess Fe^{3+} , a slow rise in absorbance (trace 3), complete within about 1 to 4 sec. For the experimental conditions used in this study, the three regimes were sufficiently distinct as to allow separate treatment with only small corrections required.

Very Fast Decay. This decay was monitored at 313, 360, and 405 nm with the same results at each wavelength. At the latter two wavelengths $\text{Fe}(\text{III})$, Fe^{2+} , $\cdot\text{C}_2\text{O}_4^-$, and $\cdot\text{CO}_2^-$ do not absorb significantly. As shown in Figure 1, both the flash and decay are essentially complete within 40 μsec . The same relative flash profile was observed for both the 5- and 10- μF configurations with the flash peak occurring 10–12 μsec after the start and the intensity decay was exponential from 5 to 7 μsec past the flash peak. A comparison of the absorbance decay curve with the time integral

(1) G. D. Cooper and B. A. DeGraff, *J. Phys. Chem.*, **75**, 2897 (1971).

(2) E. G. Moorhead and N. Sutin, *Inorg. Chem.*, **5**, 1866 (1966).

(3) R. A. Horne, *J. Amer. Chem. Soc.*, **64**, 1512 (1960).

(4) B. A. DeGraff and K. J. Lang, *J. Phys. Chem.*, **74**, 4181 (1970).

(5) C. G. Hatchard and C. A. Parker, *Proc. Roy. Soc., Ser. A*, **235**, 518 (1956).

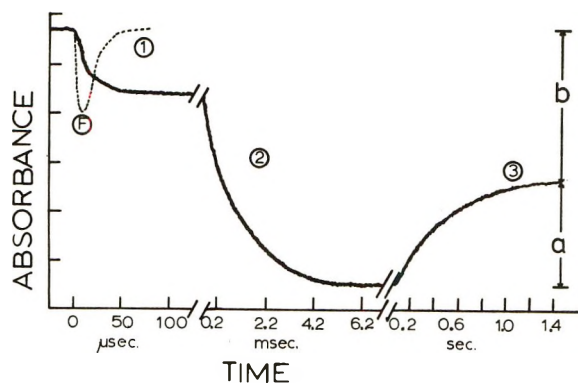


Figure 1. Oscilloscope trace of sample absorbance monitored at 360 nm for solutions $1 \times 10^{-3} M \text{Fe}^{3+}$, $1 \times 10^{-4} M$ oxalate, and $0.11 M \text{HClO}_4$. Flash profile also shown as F.

of the flash profile for both 5- and 10- μF capacitor configurations clearly showed that the very fast decay followed the integrated flash profile. Absorbance decay data taken starting at $7 \mu\text{sec}$ after the flash peak fit first-order kinetics over three half-lives by which time the trace deflection was comparable to the trace width. The "rate constants" were obtained from $\log [\text{Abs}(t) - \text{Abs}(50 \mu\text{sec})]$ vs. time plots.

Several experimental parameters were varied in the hope of sufficiently perturbing the secondary or thermal chemistry involved in the decay that it would become rate limiting. Thus, a sample of $1 \times 10^{-4} M \text{Fe}(\text{C}_2\text{O}_4)^+$ in $0.109 M \text{HClO}_4$ flashed three successive times with about 15% decomposition/flash yielded "rate constants" of $8.5 \pm 0.5 \times 10^4$, $8.9 \pm 0.5 \times 10^4$, and $8.2 \pm 0.5 \times 10^4 \text{sec}^{-1}$ for the first, second, and third flashes, respectively. A sample of $1 \times 10^{-4} M \text{Fe}(\text{C}_2\text{O}_4)^+$ in $0.11 M \text{HClO}_4$ flashed such that 30% of the $\text{Fe}(\text{C}_2\text{O}_4)^+$ was decomposed by the flash ($\sim 55\%$ total decomposition) gave a "rate constant" of $k = 8.3 \pm 0.5 \times 10^4 \text{sec}^{-1}$. Increasing the RC time of the detector circuit by doubling the pmt load resistor was without effect. Experiments performed at four temperatures over the range 14.5 to 46° gave "rate constants" for the absorbance decay that were the same within experimental error. Also, oxygen was without visible effect on the decay. Thus, in all cases, the rate of photolysis was controlling the absorbance decay in trace 1.

Fast Decay. This decay, trace 2 of Figure 1, was the dominant absorbance change from about $50 \mu\text{sec}$ to 5msec after the flash. A spectrum of the transient involved is shown along with the spectra of Fe^{III} and $\text{Fe}(\text{C}_2\text{O}_4)^+$ in Figure 2. The molar extinction values for the transient were computed from the difference in sample absorbance at 0.3 and 5msec after the flash for a solution containing $5.0 \times 10^{-4} M \text{Fe}^{3+}$, $5.0 \times 10^{-4} M$ oxalate, and $0.11 M \text{HClO}_4$ using concentration relationships derived from the mechanism as discussed in a later section. Though the values for the transient are no better than $\pm 20\%$, the spectrum of the intermediate

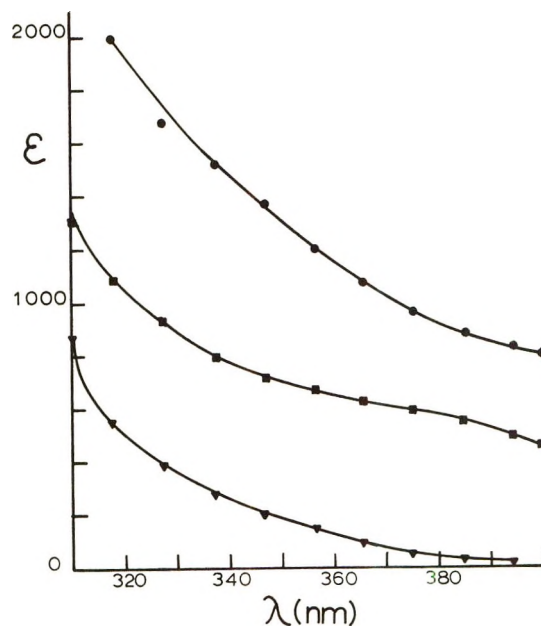


Figure 2. Molar extinction values for the "fast decay" intermediate: $\text{Fe}(\text{C}_2\text{O}_4)$, \bullet ; $\text{Fe}(\text{C}_2\text{O}_4)^+$, \blacksquare ; and Fe^{III} in $0.11 M \text{HClO}_4$, \blacktriangledown . Under these conditions about 1.5% of the Fe^{III} is present as FeOH^{2+} . The observed molar (based on Fe^{III}) extinction values for this solution have been multiplied by ten.

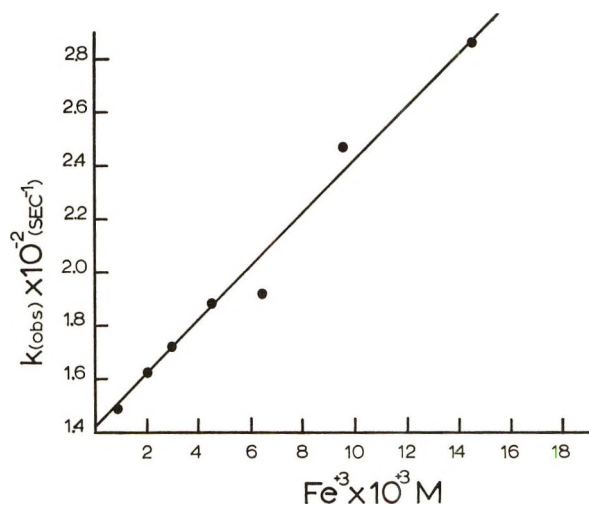


Figure 3. Plot of $k(\text{obsd})$ vs. excess added Fe^{3+} for "fast decay," total oxalate = $5 \times 10^{-4} M$, $[\text{H}^+] = 0.14 M$, and $I = 1.0 M$.

cannot be matched to that of $\text{Fe}(\text{C}_2\text{O}_4)^+$, Fe^{III} , $\cdot\text{C}_2\text{O}_4^-$ or $\cdot\text{CO}_2^-$. Further, the decay is not affected by O_2 saturation suggesting that a free radical is not involved. For these and other reasons presented in the Discussion, we attribute the spectrum to a Fe^{II} species.

The absorbance changes due to the decay of the Fe^{II} species were monitored at 430nm from about 0.4 to 4.5msec by which time the absorbance had reached a value which was nearly constant for several milliseconds. Taking this point as $A(\infty)$, plots of $\log [A(t) - A(\infty)]$ vs. time were linear over four half-

Table I: Rate Constants Derived from the Fast Absorbance Decay^a

[Fe ³⁺] (total), $M \times 10^4$	[Oxalate] (total), $M \times 10^4$	[H ⁺], M	% Fe ³⁺ as Fe(C ₂ O ₄) ⁺	$k(\text{obsd})$ $\times 10^{-2}$, sec^{-1}	$\frac{k(\text{obsd})}{[\text{Fe}(\text{C}_2\text{O}_4)^+]}$ $\times 10^{-4}$, $M^{-1} \text{sec}^{-1}$
$I = 1.0 M, T = 22^\circ$					
5.0	5.0	0.056	87.4	11.6	2.65
5.0	5.0	0.16	75.4	9.8	2.60
5.0	5.0	0.21	70.0	9.4	2.67
5.0	5.0	0.31	60.4	8.4	2.80
5.0	6.0	0.11	87.6	15.4	3.52
5.0	8.0	0.11	93.6	15.8	3.38
5.0	10.0	0.11	95.8	15.9	3.33
5.0	12.0	0.11	96.8	15.9	3.29
9.0	9.0	0.11	85.0	19.9	2.60
7.0	7.0	0.11	83.4	14.0	2.40
3.0	3.0	0.11	76.3	7.3	3.19
1.0	1.0	0.11	63.4	4.2	b
Av					2.95

^a Trace 2 of Figure 1. ^b See text.**Table II:** Rate Constants Derived from the Fast Absorbance Decay with Excess Fe³⁺

[Fe ³⁺] (total), $M \times 10^4$	[Oxalate] (total), ^a $M \times 10^4$	[H ⁺], M	$k(\text{obsd})$ $\times 10^{-4}$, sec^{-1}
$I = 1.0 M, T = 22^\circ$			
7.0	5.0	0.14	1.84
7.0 ^b	5.0	0.14	1.86
7.0	5.0	0.19	1.80
7.0	5.0	0.24	1.93
7.0	5.0	0.25	1.81
7.0	5.0	0.29	2.05
7.0	5.0	0.35	1.76
7.0	5.0	0.46	1.88
7.0	5.0	0.56	1.95
7.0 ^c	5.0	0.14	1.80
$I = 0.2 M, T = 22^\circ$			
4.0	5.0	0.15	1.54
6.0	5.0	0.17	1.51
8.0	5.0	0.19	1.72
4.0	7.0	0.15	1.68
5.0	9.0	0.16	2.06
6.0	11.0	0.17	2.41
7.0	13.0	0.18	2.76

^a Essentially all oxalate bound as Fe(C₂O₄)⁺. ^b Flash energy doubled. ^c $4.1 \times 10^4 M$ Fe²⁺ added.

lives of the reaction. Values for $k(\text{obsd})$ are given in Tables I and II and also in Figure 3.

As shown in Tables I and II, the decay of the Fe^{II} species is relatively insensitive to small pH changes, the presence of Fe²⁺ and flash intensity. For a given set of initial conditions, $k(\text{obsd})$ was smaller at $I = 0.2 M$ than for $I = 1.0 M$.

It was found that the decay of the Fe^{II} species was dependent on both Fe³⁺ and Fe(C₂O₄)⁺ and that the kinetic data could be described by

$$-\frac{d[\text{Fe}^{\text{II}} \text{ species}]}{dt} = \{k_4[\text{Fe}(\text{C}_2\text{O}_4)^+] + k_5[\text{Fe}^{3+}]\} [\text{Fe}^{\text{II}} \text{ species}]$$

which under our experimental conditions reduces to

$$-\frac{d[\text{Fe}^{\text{II}} \text{ species}]}{dt} = (k_4' + k_5') [\text{Fe}^{\text{II}} \text{ species}]$$

where $k_4' = k_4[\text{Fe}(\text{C}_2\text{O}_4)^+]$ and $k_5' = k_5[\text{Fe}^{3+}]$.

A plot of $k(\text{obsd})$ vs. $[\text{Fe}^{3+}]$ at a fixed $[\text{Fe}(\text{C}_2\text{O}_4)^+] = 5.0 \times 10^{-4} M$ is linear (Figure 3) with a slope which yields $k_5 = 1.0 \pm 0.1 \times 10^5 M^{-1} \text{sec}^{-1}$ and an intercept of $1420 \pm 80 \text{sec}^{-1}$. A plot of $k(\text{obsd}) - k_5'$ vs. $[\text{Fe}(\text{C}_2\text{O}_4)^+]$ is also linear (Figure 4) with a slope which yields $k_4 = 2.5 \pm 0.2 \times 10^6 M^{-1} \text{sec}^{-1}$. Although the intercept of Figure 4 is shown as essentially zero, the value of $k(\text{obsd})$ at the lowest Fe(C₂O₄)⁺ concentration used, last entry of Table I, is high by an amount outside experimental error. This suggests a third pathway for decay of the Fe^{II} species, possibly an acid-catalyzed path, with a much smaller rate constant (*i.e.*, $< 200 \text{sec}^{-1}$).

The temperature dependence of k_4 and k_5 was obtained from two series of experiments done with and without excess Fe³⁺. The data for the k_4 series, done without excess Fe³⁺, are shown in tabular form (Table III) because the observed rate constants must be corrected for incomplete complex formation. The initial Fe(C₂O₄)⁺ concentration used was obtained by measuring the initial sample absorbance at 430 nm and the temperature of the experiment. The data from Table III yield $k_4 = 10^{12.9 \pm 0.2} \exp(-8900 \pm 200/RT) M^{-1} \text{sec}^{-1}$.

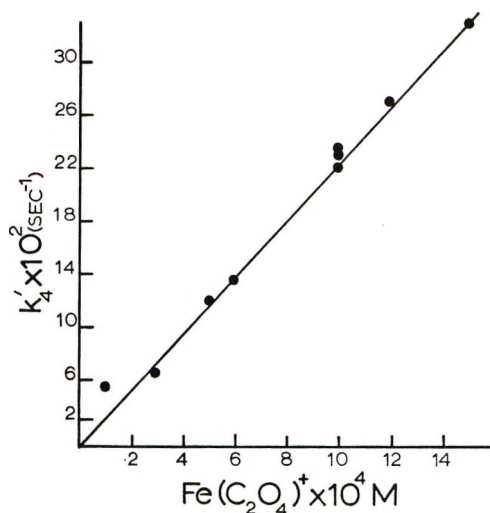


Figure 4. Plot of k_4 vs. $[\text{Fe}(\text{C}_2\text{O}_4)^+]$; $[\text{H}^+] = 0.15 M, I = 1.0 M$.

Table III: Temperature Dependence of k_4^a

Temp, °C	$k(\text{obsd})$ $= k_4',^b$ sec ⁻¹	Fe(C ₂ O ₄) ⁺ , M × 10 ⁴	$k_4 \times 10^{-6}$, M ⁻¹ sec ⁻¹
18.5	800	3.75	2.13
22.0	966	3.95	2.42
30.7	1660	4.20	3.95
39.8	2690	4.50	5.98
46.8	3910	5.00	7.95

^a Fe³⁺(total) = 5.0 × 10⁻⁴ M, oxalate(total) = 5.0 × 10⁻⁴ M, HClO₄ = 0.11 M. ^b The largest contribution from k_6' to $k(\text{obsd})$ was 1%.

The values for k_5 (Table IV) were obtained from $k(\text{obsd})$ values by subtracting the contribution from k_4' . The values so obtained are subject to some error due to the fact that $k_5' = k_5[\text{Fe}^{3+}]$ was less than 30% of $k(\text{obsd})$ for the series. The data from Table IV yield $k_5 = 10^{17.7 \pm 0.70} \exp(-17,000 \pm 950/RT) \text{ M}^{-1} \text{ sec}^{-1}$.

Table IV: Temperature Dependence of k_5^a

Temp, °C	$k(\text{obsd})$, sec ⁻¹	$k_4',^b$ sec ⁻¹	k_5' , sec ⁻¹	$k_5 \times 10^{-5}$, M ⁻¹ sec ⁻¹
18.3	1280	975	305	0.87
22.0	1620	1150	470	1.34
27.0	2200	1510	690	1.97
31.8	3020	1860	1160	3.32

^a Fe³⁺(total) = 4.0 × 10⁻³ M, oxalate = 5.0 × 10⁻⁴ M, HClO₄ = 0.15 M. ^b Essentially all the oxalate is present as Fe(C₂O₄)⁺.

Slow Absorbance Increase. This process was observed only for those experiments with excess Fe³⁺. The reaction was monitored at 430 nm and the increase in absorption, "a" of Figure 1, was equal to or less than 45% of the total drop, "a + b" of Figure 1. Taking the final absorption at $t = 5$ sec as $A(\infty)$, plots of $\ln [A(\infty) - A(t)]$ vs. t for $t \geq 0.1$ sec were linear over three half-lives. Values of $k(\text{obsd})$ for various conditions are shown in Table V. The reaction is first-order in Fe³⁺ and independent of Fe(C₂O₄)⁺ or Fe²⁺.

As previously reported,¹ experiments without excess Fe³⁺ but in which the predominant Fe^{III} species is Fe(C₂O₄)₂⁻ also show a slow absorbance increase. For a solution containing 5.0 × 10⁻⁴ M Fe³⁺, 2.0 × 10⁻² M oxalic acid, and 0.055 M HClO₄ the absorbance ratio "a/a + b" was 0.08 ± 0.02 and $k(\text{obsd}) = 0.45 \text{ sec}^{-1}$ for the slow absorbance increase.

Discussion

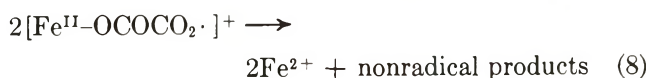
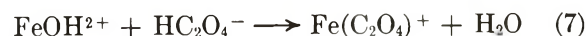
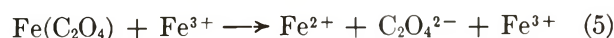
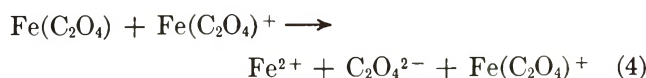
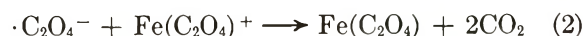
An acceptable mechanism for the photochemistry of this system must explain quantitatively the observed absorption changes. In addition, the rate constants

Table V: Rate Constants Derived from the Slow Absorbance Increase

[Fe ³⁺] (total), M × 10 ³	[Oxalate] (total), M × 10 ⁴	[H ⁺], M	$k(\text{obsd})$, sec ⁻¹
$I = 1.0 \text{ M}, T = 22^\circ$			
7.0	5.0	0.14	1.86
7.0 ^a	5.0	0.14	1.72
7.0 ^b	5.0	0.14	1.88
8.0	10.0	0.15	1.60
10.0	3.0	0.15	2.60
10.0	6.0	0.15	3.00
10.0	10.0	0.16	2.24
10.0	12.0	0.16	2.11
25.0	10.0	0.15	5.5
$I = 0.2 \text{ M}, T = 22^\circ$			
4.0	5.0	0.15	1.57
6.0	5.0	0.17	2.42
8.0	5.0	0.19	3.29

^a 4.1 × 10⁻⁴ M Fe²⁺ added. ^b 9.3 × 10⁻⁴ M Fe²⁺ added.

derived from the absorption changes must be reasonable and consistent with other available data. A mechanism which is consistent with all the available data is

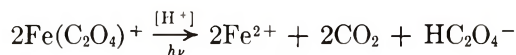


Reactions 3, 5, 6, and 7 occur only with excess Fe³⁺ present.

We now inquire as to how the proposed set of reactions is related to the observed sample absorbance changes. Referring to Figure 1, the maximum decrease in sample absorbance, shown as "a + b," occurs at about 5 msec and is a result of the reactions occurring in time regimes 1 and 2. During trace 1, 0 ≤ t ≤ 50 μsec, the primary photochemical reactions 1 and 1a and the radical reactions 2, 3, and 8 take place. This period is followed by trace 2, 50 μsec ≤ t ≤ 5 msec, during which the iron(II) intermediate decays to Fe²⁺ and oxalate, reactions 4 and 5. By 5 msec after the flash, the decay of the ferrous intermediate may reasonably be assumed complete as the

absorbance is essentially constant for at least 10 msec. In the absence of excess Fe^{3+} , no further absorbance changes are observed, indicating photoaquation is not an important primary process. If, however, the experiment is done with excess Fe^{3+} the absorbance increases slowly during trace 3, $10 \text{ msec} \leq t \leq 5 \text{ sec}$, as a result of reactions 6 and 7.

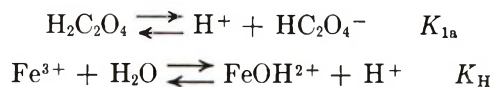
Slow Absorbance Increase (Reactions 6 and 7). In the absence of excess Fe^{3+} , the expected net reaction for the photolysis in the pH range used is⁵



However, in the presence of excess Fe^{3+} the released oxalate will react with the available Fe^{3+} to form $\text{Fe}(\text{C}_2\text{O}_4)^+$. The kinetics of the formation of $\text{Fe}(\text{C}_2\text{O}_4)^+$ have been examined previously by stopped-flow methods.² Under our conditions, the formation is adequately described by (6) and (7). Following the original treatment and neglecting the back reactions, we have

$$\frac{d[\text{Fe}(\text{C}_2\text{O}_4)^+]}{dt} = k_6[\text{Fe}^{3+}][\text{HC}_2\text{O}_4^-] + k_7[\text{FeOH}^{2+}][\text{HC}_2\text{O}_4^-]$$

The establishment of the equilibria



is considered to be rapid compared with reactions 6 and 7. Now $[\text{H}^+]$ and $[\text{Fe}^{3+}]$ are effectively constant during the experiment and using the relation

$$\begin{aligned} [\text{Fe}(\text{C}_2\text{O}_4)^+]_{\infty} - [\text{Fe}(\text{C}_2\text{O}_4)^+]_t &= \\ &[\text{HC}_2\text{O}_4^-] + [\text{H}_2\text{C}_2\text{O}_4] = \\ &\{1 + [\text{H}^+]/K_{1a}\}[\text{HC}_2\text{O}_4^-] = \beta[\text{HC}_2\text{O}_4^-] \end{aligned}$$

we have

$$\begin{aligned} \frac{d[\text{Fe}(\text{C}_2\text{O}_4)^+]}{dt} &= \frac{1}{\beta} \{k_6 + k_7 K_H / [\text{H}^+]\} \times \\ &[\text{Fe}^{3+}]([\text{Fe}(\text{C}_2\text{O}_4)^+]_{\infty} - [\text{Fe}(\text{C}_2\text{O}_4)^+]_t) = \\ &k(\text{obsd})([\text{Fe}(\text{C}_2\text{O}_4)^+]_{\infty} - [\text{Fe}(\text{C}_2\text{O}_4)^+]_t) \end{aligned}$$

Thus, a plot of $\beta k(\text{obsd})$ vs. $1/[\text{H}^+]$ at constant Fe^{3+} should be linear with the slope equal to $k_7 K_H [\text{Fe}^{3+}]$ and the intercept = $k_6 [\text{Fe}^{3+}]$. Figure 5 shows our data plotted in this fashion and from the slope we obtain $k_7 = 1.2 \pm 0.15 \times 10^4 \text{ M}^{-1} \text{ sec}^{-1}$ and $k_6 = 6.3 \pm 0.2 \times 10^2 \text{ M}^{-1} \text{ sec}^{-1}$ at 22° . These values are in satisfactory agreement with the stopped-flow study at 25° . Further, this agreement supports our assignment of reactions 6 and 7 as responsible for the slow absorbance increase during trace 3. Finally, the observed anation reaction implies that the preceding decay of the ferrous intermediate releases oxalate.

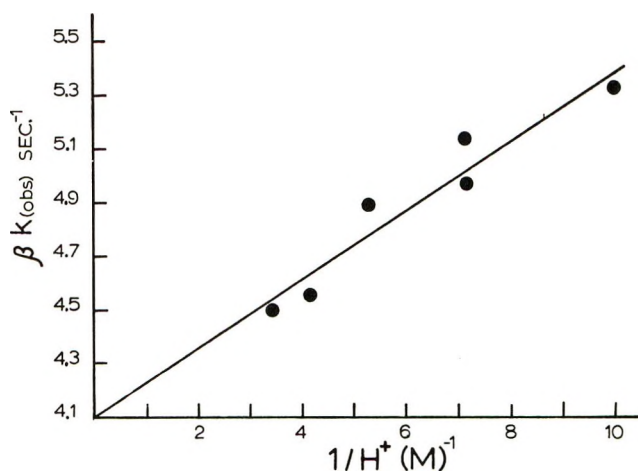
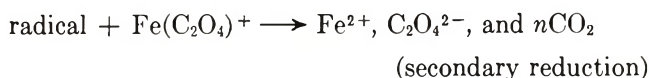
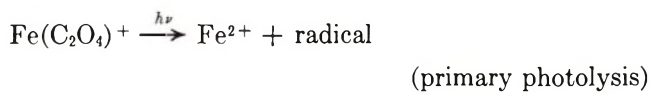


Figure 5. Plot of $\beta k(\text{obsd})$ vs. $[\text{H}^+]^{-1}$ for the anation of Fe^{3+} ; $[\text{Fe}^{3+}] = 7.0 \times 10^{-3} \text{ M}$, total oxalate = $5.0 \times 10^{-4} \text{ M}$, and $I = 1.0 \text{ M}$.

The primary purpose of the experiments with excess Fe^{3+} was to establish the ratio of primary photolysis of $\text{Fe}(\text{C}_2\text{O}_4)^+$ to secondary reduction resulting from radical attack. Our approach is based on the following net reactions



Thus, experiments with excess Fe^{3+} can be used to determine the extent of the secondary reduction since the amount of $\text{Fe}(\text{C}_2\text{O}_4)^+$ formed during trace 3 is a quantitative measure of the oxalate released as a result of radical reduction of $\text{Fe}(\text{C}_2\text{O}_4)^+$ even though both of the above net reactions may involve several steps. The formation of $\text{Fe}(\text{C}_2\text{O}_4)^+$ from the released oxalate is sufficiently slow relative to the reactions occurring in trace periods 1 and 2 of Figure 1 that the maximum decrease in sample absorbance, observed about 5 msec after the flash, is a true measure of the total decomposition of $\text{Fe}(\text{C}_2\text{O}_4)^+$ due to both primary photolysis and secondary reduction for experiments with and without excess Fe^{3+} . This change in absorbance is "a + b" of Figure 1. Further, since the total absorbance change during trace 3, shown as "a" of Figure 1, is a direct measure of the amount of secondary or radical reduction, the absorbance ratio "a/b" gives the ratio of $\text{Fe}(\text{C}_2\text{O}_4)^+$ decomposed by radical reduction to that decomposed in the primary photolysis.

To use the "a/b" ratio obtained from experiments with excess Fe^{3+} to interpret experiments without excess Fe^{3+} , we must inquire as to whether the ratio is dependent on the amount of excess Fe^{3+} . If the ratio were independent of the excess of Fe^{3+} , this would imply

either that the Fe^{3+} did not affect the primary photolysis or the secondary reactions or that it affected them equally. As expected, however, the "a/b" ratio did depend on the excess Fe^{3+} but not on the wavelength used to monitor the absorbance changes.⁶ A plot of "a/b" vs. excess Fe^{3+} was curved but a sufficient number of points were taken to allow a short extrapolation to zero excess Fe^{3+} which yields a ratio of 0.76 ± 0.04 for "a/b." Further, the ratio approached zero as $\text{Fe}^{3+}/\text{Fe}(\text{C}_2\text{O}_4)^+$ approached 100. These results clearly imply (1) that radical + Fe^{3+} reactions occur with excess Fe^{3+} present; and (2) that even in the absence of excess Fe^{3+} not all the radicals generated in the primary photolysis result in secondary reduction of $\text{Fe}(\text{C}_2\text{O}_4)^+$. However, the reasonable value obtained for "a/b" in the absence of excess Fe^{3+} suggests that our interpretation of the significance of this ratio is essentially correct.

Fast Absorbance Decay (Reactions 4 and 5). This decay, the only significant absorption change during trace 2, cannot be assigned to the free radical reactions 2, 3, and 8 for the following reasons. (1) Since a good fit to pseudo-first-order kinetics was always observed for this decay, reaction 8 cannot be responsible for it. (2) The fact that it is an absorbance decay indicates that the reactants absorb more strongly than the products in the 360–430-nm region. Since neither the reactants nor products of reaction 3 absorb significantly in this region, the decay cannot be due to this reaction. (3) For reaction 2 to account for the fast decay, $\epsilon_{\text{FeOx}^+} > \epsilon_{\text{FeOx}}$ is a requirement as neither $\cdot\text{C}_2\text{O}_4^-$ or $\cdot\text{CO}_2^-$ absorb significantly in the spectral region used for monitoring the fast decay. Since ϵ_{FeOx} is at least $0.5\epsilon_{\text{FeOx}^+}$,⁸ we should have observed the decay of $\text{Fe}(\text{C}_2\text{O}_4)$ if its decay rate were slower than reaction 2. No such decay was observed. If reaction 2 and the decay of $\text{Fe}(\text{C}_2\text{O}_4)$ have comparable rates, simple first-order kinetics would not be observed. Finally, if $\text{Fe}(\text{C}_2\text{O}_4)$ decays rapidly with respect to reaction 2, then the spectrum of the fast decay "intermediate" as we obtained it ($A(t = 300 \mu\text{sec}) - A(t = 5 \text{ msec})$) should be identical with $\text{Fe}(\text{C}_2\text{O}_4)^+$ as the decomposition products of $\text{Fe}(\text{C}_2\text{O}_4)$ do not absorb in this spectral region. (4) The kinetics of the fast decay are difficult to reconcile with those implied by reaction 2. Thus, while the absorbance decay rate is accelerated by $\text{Fe}(\text{C}_2\text{O}_4)^+$ as required by reaction 2, it is difficult to suggest a plausible explanation for the observed effect of Fe^{3+} in terms of reactions 2 and 3 in light of the known molar absorbances for $\text{Fe}(\text{C}_2\text{O}_4)^+$, $\cdot\text{C}_2\text{O}_4^-$, $\cdot\text{CO}_2^-$,⁹ Fe^{2+} , and Fe^{III} .¹⁰ Thus, on both kinetic and spectral grounds the species responsible for the fast decay must be formed during trace 1 and the absorbance changes during trace 2 assigned to its decay. The foregoing plus the additional fact that the "spectrum" of the intermediate is the same with and without excess Fe^{3+} point to the ferrous complex resulting from

reaction of $\cdot\text{C}_2\text{O}_4^-$ with $\text{Fe}(\text{C}_2\text{O}_4)^+$, reaction 2, as the intermediate whose decay is involved.

Several ferrous species are possible products from reaction 2 including binuclear ferrous oxalate complexes, mixed $\text{Fe}^{\text{II}}-\text{Fe}^{\text{III}}$ oxalates and the product shown, ferrous oxalate. The first of these possibilities was used to explain Mössbauer data obtained from the solid state pyrolysis of $\text{K}_3\text{Fe}(\text{C}_2\text{O}_4)_3 \cdot 3\text{H}_2\text{O}$.¹² The existence of a mixed $\text{Fe}^{\text{II}}-\text{Fe}^{\text{III}}$ oxalate has been invoked¹³ to explain the visible spectra of rather concentrated aqueous solutions of Fe^{II} , Fe^{III} , and oxalate (*i.e.*, 0.03 M Fe^{II} and Fe^{III} , 0.3 M oxalate). The formation of $\text{Fe}(\text{C}_2\text{O}_4)$ in reaction 2 has been suggested previously.^{1,14} It seems unlikely that any binuclear complex would form at all, let alone as rapidly as required, under our conditions of dilute solution and low pH. Further, we were able to fit qualitatively the spectrum of $\text{Fe}(\text{C}_2\text{O}_4)$ to the intermediate's "spectrum." Thus, we assign $\text{Fe}(\text{C}_2\text{O}_4)$ as the species whose decay is responsible for the absorbance changes during trace 2.

Since reaction 2 is complete by 50 μsec , all the $\text{Fe}(\text{C}_2\text{O}_4)$ has been formed by that time while its decomposition is complete by 5 msec. Further, the difference in sample absorbance at 50 μsec and 5 msec is a direct measure of the absorbance due to $\text{Fe}(\text{C}_2\text{O}_4)$.¹⁵ From our extrapolated value for "a/b" and the total sample absorbance change at 5 msec (*i.e.*, $A(t = 0) - A(t = 5 \text{ msec})$) we can calculate how much $\text{Fe}(\text{C}_2\text{O}_4)^+$ was reduced to $\text{Fe}(\text{C}_2\text{O}_4)$ by reaction 2, and this allows calculation of the extinction values for $\text{Fe}(\text{C}_2\text{O}_4)$ shown in Figure 2.

Several kinetic features of the decomposition of $\text{Fe}(\text{C}_2\text{O}_4)$ are somewhat surprising. That Fe^{III} species promote the decomposition is not unexpected, but both k_4 and k_5 are much greater than the rate constant for water exchange¹⁶ on Fe^{3+} . This is in contrast to the results obtained for the electron exchange³ between

(6) Primary photolysis of the excess Fe^{3+} was not a problem in these experiments as identical results were obtained with and without a "Plexiglass" filter ($\lambda \geq 340 \text{ nm}$).

(7) Throughout this paper, this radical is assigned as $\cdot\text{C}_2\text{O}_4^-$. However, the evidence for preferring $\cdot\text{C}_2\text{O}_4^-$ to $\cdot\text{CO}_2^-$ is strong though not compelling.^{9,11}

(8) G. D. Cooper and B. A. DeGraff, unpublished results.

(9) P. Neta, M. Simic, and E. Hayon, *J. Phys. Chem.*, **73**, 4207 (1969); N. Getoff, E. Schworer, V. M. Markovic, K. Sehested, and S. O. Nielson, *ibid.*, **75**, 749 (1971).

(10) Under our conditions about 1–2% of the excess Fe^{III} was present as FeOH^{2+} . For data on the spectrum of Fe^{III} as a function of pH, see R. C. Turner and K. E. Miles, *Can. J. Chem.*, **35**, 1002 (1957).

(11) A. C. Sarma, A. Fenerty, and S. T. Spees, *J. Phys. Chem.*, **74**, 4598 (1970).

(12) G. M. Bancroft, K. G. Dharmawardena, and A. G. Maddock, *Inorg. Chem.*, **9**, 223 (1970).

(13) B. Binder, *ibid.*, **10**, 2146 (1971).

(14) C. A. Parker, *Trans. Faraday Soc.*, **50**, 1213 (1954).

(15) This is rigorously true for solutions without excess Fe^{3+} and a very good approximation for $\text{Fe}^{3+}/\text{Fe}(\text{C}_2\text{O}_4)^+ \leq 5$ for $310 \leq \lambda \leq 450 \text{ nm}$.

(16) T. J. Swift and R. E. Connick, *J. Chem. Phys.*, **37**, 307 (1962).

Fe^{2+} and $\text{Fe}(\text{C}_2\text{O}_4)^+$. Further, while a simple electron-transfer mechanism might explain our results for the Fe^{3+} -assisted case, it clearly cannot explain the effect of $\text{Fe}(\text{C}_2\text{O}_4)^+$ as no net reaction would result. Any mechanism involving a reaction in which oxalate must penetrate the first coordination sphere of the Fe^{II} species is precluded.

The decomposition of $\text{Fe}(\text{C}_2\text{O}_4)$ is relatively pH insensitive under our experimental conditions, presumably because of the strong effect of the Fe^{II} species. The role of the proton in the acid-assisted aquation of other oxalate complexes¹⁷ is, in part, to prevent the detached end of the ligand from reattaching to the metal before water can occupy the vacant site. The $\text{Fe}(\text{C}_2\text{O}_4)^+$ and Fe^{3+} might function in such a fashion, subject to the condition that the opening end of the oxalate not be required to penetrate the first coordination sphere of the Fe^{II} species, a restriction which would seem to limit its effectiveness.

The observed activation energy for (4) is close to that found for water exchange¹⁶ on Fe^{2+} . The entropy term for (4), $\Delta S^\ddagger = 1.5$ eu, suggests that the effect of $\text{Fe}(\text{C}_2\text{O}_4)^+$ may be to reduce the electrostriction of the solvent for one or both of the separating ions. Despite the large uncertainty in the activation energy for (5), $\Delta S^\ddagger \geq 10.5$ eu. Both the sign and magnitude are rather unexpected and, if valid, suggest that an equilibrium constant may also be involved, possibly that for FeOH^{2+} . At present, however, we refrain from more detailed interpretation pending more complete data.

This work confirms the earlier observation¹ that the decay of the Fe^{II} species formed by reaction of the ferrioxalate ion with $\cdot\text{C}_2\text{O}_4^-$ is dependent on the Fe^{II} species present. The value of k_4 for the bisoxalato ion is very similar [$k_4(\text{bisoxalato}) = 1.1 \times 10^{13} \exp(-8600/RT) M^{-1} \text{sec}^{-1}$] to that observed for the mono-oxalato system. The similarity of the two rate constants suggests that the same reaction is involved and that for the bisoxalato case the first oxalate comes off rapidly and with small spectral consequence.

Very Fast Absorbance Decay (Reactions 1, 1a, 2, 3, and 8. Previous observations¹ on the absorbance changes occurring in the first few hundred microseconds after the start of the flash for the tris- and bisoxalato-ferrate(III) ions were consistent with an initial photoredox of the complex followed by rapid expulsion of the ligand radical, $\cdot\text{C}_2\text{O}_4^-$ or $\cdot\text{CO}_2^-$, into the bulk solution. The ligand radical was then rapidly removed either by reaction with the complex or bimolecular self-destruction. Our present data support a similar picture for the mono-oxalato-ferrate(III) ion and allow calculation of lower limits for k_{1a} , k_2 and k_3 .

The insensitivity of the very fast decay to percentage decomposition, temperature, and monitoring wavelength as well as the close correlation between the fractional absorbance decay and the integrated flash pro-

file indicate that the very fast decay is controlled by the rate of photolysis for all our experimental conditions. This precludes any attempt to decide on kinetic grounds whether the ligand radical is or is not bound to the $\text{Fe}(\text{II})$ when reduction of the second molecule of $\text{Fe}(\text{C}_2\text{O}_4)^+$ occurs. However, from a knowledge of the photolysis rate we can set lower limits on the values the rate constants must have for either mechanism.

The correspondence between the absorbance decay and the flash profile was maintained for at least 35 μsec by which time both signals were too small to evaluate with accuracy. For the present case, our calculations are based on the time interval 25–35 μsec after the start of the flash. The flash profile, as monitored in our apparatus, is a measure of the incident intensity, $I_0(t)$. The rate of photolysis is related to the flash profile in a simple fashion only if the sample absorbance remains constant. By limiting the percentage decomposition (total) to less than 10% this condition can be approximated.

Using the above approach we calculate that for the 25–35- μsec interval the average rate of photolysis for five experiments was $0.15 \pm 0.03 M \text{sec}^{-1}$. From this we calculate that $k_{1a} \geq 8 \times 10^4 \text{sec}^{-1}$ and that $k_2 \geq 8 \times 10^8 M^{-1} \text{sec}^{-1}$. The limiting value of k_2 suggested here would be the same for either $[\text{Fe}^{\text{II}}-\text{OCOCO}_2\cdot]^+$ or $\cdot\text{C}_2\text{O}_4^-$ as the reducing radical. The limit for k_2 calculated here, while consistent with the limit previously suggested for the bis- and trisoxalato-ferrate(III) ions,¹ suggests that the earlier value could be raised. While the lower limit for k_{1a} is well below the water exchange rate¹⁶ for Fe^{2+} , the Fe^{2+} water exchange rate may well not be an upper limit to k_{1a} since the newly formed $[\text{Fe}^{\text{II}}-\text{OCOCO}_2\cdot]^+$ may be formed with excess vibrational energy and hence loose the ligand radical very rapidly.

According to our mechanism, the change in the absorbance ratio "a/b" with excess Fe^{3+} is a direct measure of the competition between reaction 2 and reactions 3 + 8. As noted earlier, a plot of this ratio as a function of excess Fe^{3+} did not go to 1 in the limit $\text{Fe}^{3+}/\text{Fe}(\text{C}_2\text{O}_4)^+ \rightarrow 0$, and hence we must conclude that reaction 8 is nonzero under these conditions.¹⁸ However, it is not possible from our data to determine whether it is the ligand radical, $\cdot\text{C}_2\text{O}_4^-$, or the ferrous-radical complex, $[\text{Fe}^{\text{II}}-\text{OCOCO}_2\cdot]^+$, which is the reactant in reaction 8. Based on the $\text{Fe}^{3+}/\text{Fe}(\text{C}_2\text{O}_4)^+$ ratio at which "a/b" $\rightarrow 0$, we calculate that $k_3 \geq 8 \times 10^7 M^{-1} \text{sec}^{-1}$. From the lower limiting values for k_2 and k_3 it appears that the reduction of Fe^{3+} and $\text{Fe}(\text{C}_2\text{O}_4)^+$ by $\cdot\text{C}_2\text{O}_4^-$ or $[\text{Fe}^{\text{II}}-\text{OCOCO}_2\cdot]^+$ is an outer-sphere process. The electron transfer is enhanced

(17) K. V. Krishnamurty and G. M. Harris, *Chem. Rev.*, **61**, 231 (1961).

(18) The failure of this ratio to extrapolate to 1.0 cannot be attributed to instrumental artifacts such as baseline drift due to photolysis by the monitoring lamp.

by the bound oxalate, possibly as a result of transfer through the ligand.

Summary

From this and the previous study, it appears that the first mechanism suggested by Parker¹⁴ on the basis of his steady illumination studies is substantially correct. The possibility that the ligand radical remains bound to the metal center after photoredox and that the $[\text{Fe}^{\text{II}}-\text{OCOCO}_2\cdot]^+$ is the reducing species is in line with some recent low-temperature epr work with manganese oxalate.^{19,20} Interestingly, photoaquation is not an important primary process for the monooxalato ion. This is in marked contrast to the behavior of the tris- and bisoxalato ions. Though the estimation of $\phi(\text{aquation})$ for $\text{Fe}(\text{C}_2\text{O}_4)^{2-}$ from our present data is very sensitive to the ϵ values used for $\text{Fe}(\text{C}_2\text{O}_4)^{2-}$, we estimate from the observed "a/b" ratio $0.08 \leq \phi(\text{aquation}) \leq 0.12$. We are, of course, unable to detect photoaquation when the ligand is water. Since the quantum yield of Fe^{2+} is quite similar for the mono-, bis-, and trisoxalato ions and yet the importance of photoaquation increases with increased oxalate sub-

stitution, it is probable that photoinduced water exchange is an important process for the monooxalato ion.

The observation that photoaquation occurs along with photoredox raises some interesting questions about the primary process. Since the $d \rightarrow d$ transitions are spin forbidden, it is not expected that these excited states would couple strongly with the CT state (s) which is connected to the ground state by a spin-allowed transition. Thus population of the ligand field states *via* the CT state is not a likely mechanism to explain the photoaquation. A number of possible explanations remain, but until a quantitative measure of the photoaquation quantum yield is available and the wavelength dependence known, discussion of these possibilities would be idle speculation.

Acknowledgments. We wish to thank The Petroleum Research Fund, The Research Corporation, and the Department of Chemistry for support of this work.

(19) G. A. Shagisultanova, L. N. Neokladnova, and A. L. Posnyak, *Dokl. Akad. Nauk SSSR*, **162**, 1333 (1965).

(20) A. L. Posnyak, G. A. Shagisultanova, and L. N. Neokladnova, *Teor. Frksp. Khim.*, **4**, 567 (1968).

Effects of Neutron Radiation on the Catalytic Activities of Lithium-Doped Copper, Nickel, and Copper-Nickel

by Toyosaburo Takeuchi,* Daisaku Miyatani, Yutaka Takada, and Kinji Okamoto

Faculty of Literature and Science, Toyama University, Toyama, Japan (Received February 21, 1972)

The effects of lattice imperfections produced by the nuclear reaction of ${}^6\text{Li}(n,\alpha){}^3\text{H}$ upon the catalytic activities in the hydrogenation reaction of ethylene on powdered copper, nickel, and copper-nickel which had previously been doped with lithium and irradiated with thermal neutrons were investigated. In addition, the amount of tritium taken from the catalyst was measured by placing it in contact with normal hydrogen and raising the temperature of the catalyst. The irradiation of neutrons increased the activities of nickel and copper-nickel by 3-4 times, but it did not affect the activity of copper. The dependence of the amount of tritium upon the composition of the catalyst was very similar to that of the catalytic activity, suggesting that the diffusion of tritium from the interior is the rate-determining step.

Introduction

The catalytic activities of metals have been interpreted in terms either of an electronic factor or a geometric factor of the metal. Recently, lattice imperfections have been taken up as an important factor in the elucidation of the catalytic activity. Most studies of the effects of lattice imperfections on the catalytic reaction have been concentrated on methods

of heat treatment or of cold working, such as the stretching of metals.¹⁻⁴ Here, lattice imperfections are pro-

(1) I. Uhara, S. Yanagimoto, K. Tani, G. Adachi, and S. Teratani, *J. Phys. Chem.*, **66**, 2691 (1962).

(2) I. Uhara, T. Hikino, Y. Numata, and Y. Kageyama, *ibid.*, **66**, 1371 (1962).

(3) E. M. A. Willhoft, *Chem. Commun.*, 146 (1968).

(4) E. Miyazaki, H. Kawasaki, Y. Fukuyama, and K. Nakata, Japan Chemical Society Meeting, April 1970.

duced by the collisions of neutrons or charged particles with metal atoms^{5,6} or by the fission products of the nuclear reactions.

Several reports concerned with the effects of neutron radiation upon the catalytic activity of oxides doped with lithium oxide or boron oxide have been published.⁷⁻⁹ The results of these studies have been discussed from the standpoint of a semiconductor. However, there are, unfortunately, no reports on the effect of nuclear fission products upon the catalytic activity of reduced metal. The difficulty in performing such studies lies in recovery of freshly produced lattice imperfections due to the elevation of temperature during the nuclear reaction.

This paper deals with the effects of radiation damage on the catalytic activities of lithium-doped copper, nickel, and copper-nickel, all of which had been irradiated with neutrons at liquid nitrogen temperature. The average energy of the thermal neutrons used was 0.025 eV. However, an enormous energy is produced by nuclear fission in the reaction: ${}^6\text{Li} + n = {}^3\text{H} + {}^4\text{He}$. The recoil energy of ${}^3\text{H}$ and that of ${}^4\text{He}$ are 2.7 and 2.1 MeV, respectively, and the threshold energies of copper and nickel are *ca.* 24 eV. Many fresh lattice imperfections are produced by these fission products, and a considerable number of these lattice imperfections are preserved if the temperature of the metal is kept low during irradiation.

Experimental Section

(1) *Preparation of Catalysts.* Lithium-doped copper, nickel, and copper-nickel alloy catalysts were prepared from mixed solutions of the nitrates of these metals. The atomic ratios of copper and nickel in the alloy catalysts were 3:7, 1:1, and 7:3. The nitrates of copper and nickel were provided by the Wako Chemical Co. The lithium nitrate was provided by the Kanto Chemical Co. These nitrates were all of an extra pure grade and were used without further purification. The lithium nitrate used was normal. It contained 7.4% ${}^6\text{Li}$ which is associated with a nuclear reaction. A large amount of lithium, therefore, remains without change in the metal after the neutron irradiation. For this reason, the effects of lithium on the catalytic reaction were studied by changing the content of lithium in the nickel.

The mixed solution of the nitrates was gradually dried in a sand bath, with the temperature increased until the crystallized mixture appeared. Then the mixture was decomposed to oxide at 1000° in an electric furnace; 0.1 g of the oxide was placed in a quartz ampoule with a volume of 1 cm³. The oxide was reduced with hydrogen at 350° for 4 days. Meanwhile, fresh hydrogen was introduced. After evacuation under a pressure of 10⁻⁶ Torr, the ampoule was sealed. The irradiation with neutrons was performed in the atomic pile, JRR-2, of the Japan Atomic Energy Re-

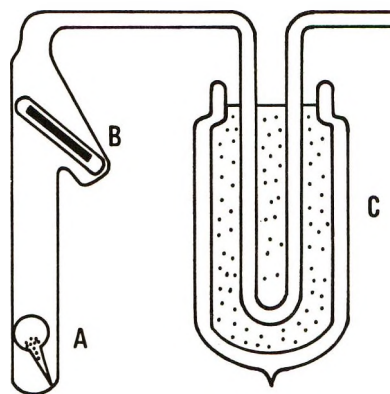


Figure 1. Reaction vessel.

search Institute. A liquid-nitrogen-temperature loop was installed in a horizontal experimental hole of the atomic pile. Helium gas, which had been cooled by being passed through a helical tube in liquid nitrogen and a heat exchanger, flowed through and so cooled the sample in the aluminum capsule placed in the loop. The radiation dose of each sample was in the range between 10¹⁸ and 10¹⁹ nvt. The catalytic activity tests for these samples were carried out after 2 months, while the samples were kept in a liquid nitrogen bath. However, every sample was exposed at room temperature for the time that the sample was placed in the reaction vessel. The radioactivity produced by the irradiation had decayed to the safety standard before the test.

(2) *Catalytic Activity Tests.* The catalytic activity was tested by the hydrogenation reaction of ethylene. The reaction was carried out in a cylindrical vessel, shown in Figure 1. The vessel was 15 mm in diameter and 200 mm in length. In this figure, A is the catalyst and B is the iron rod covered with glass. The ampoule was crushed in the reaction vessel which had been evacuated to 10⁻⁶ Torr. The rate of the reaction was obtained from the pressure decrease measured by an oil manometer. Contamination of the catalyst by oil vapor or by grease from the stopcocks was avoided by the use of the U-type trap, C, which was connected before the reaction vessel and cooled by a Dry Ice bath.

The ethylene furnished by the Takachiho Chemical Co. was distilled under vacuum before use. Commercial hydrogen was used. It was purified by diffusion through a palladium thimble. These gases, with a stoichiometric mixture (1:1) and at a pressure of *ca.* 20 Torr, were then introduced into the reaction vessel. The BET areas of the catalysts were measured by ob-

(5) A. Seeger, *Proc. U. N. Int. Conf. Peaceful Uses At. Energy*, 2nd, No. 998 (1958).

(6) N. Riel and R. Sizmann, *Z. Angew. Phys.*, 11, 202 (1959).

(7) Y. Saito, Y. Yoneda, and S. Mizushima, *Nature (London)*, 183, 388 (1959).

(8) T. Braun and I. Maxim, *ibid.*, 192, 548 (1961).

(9) I. Maxim, T. Braun, and G. Glantz, *Kinet. Katal.*, 5, 90 (1964).

serving the adsorption of ethylene at -183° or of krypton at -195° .

(3) *Assay of Tritium.* The measurement of tritium which had switched from a catalyst to hydrogen or ethane after normal hydrogen or a mixture of ethylene and hydrogen had come in contact with the catalyst was carried out by means of a gas proportional counter (Aloka G. C. 1005), the volume of which was 50 cm^3 . The cathode of the counter was tungsten wire, 0.05 mm in diameter, while the anode was a cylindrical pipe of Coval, the alloy of Ni, Co, Mn, and Fe. The details of the counting were essentially the same as have been described elsewhere.¹⁰ Prior to the measurement, 20 Torr of normal hydrogen, ethylene, or a mixture of ethylene and hydrogen (1:1) were introduced into the reaction vessel and placed in contact with the catalyst at 140° for 2 hr. At the end of the contact, a small part of the gas, *ca.* 10^{-1} Torr, was introduced into the proportional counter and the assay of tritium was carried out by adding methane as the filling gas. The same experiments were repeated by introducing fresh gas into the reaction vessel after the vessel had been evacuated under a pressure of 10^{-4} Torr at 140° . A virgin catalyst was used for each run of the test.

In order to study the dependence of the amount of tritium evolved from the catalyst upon the temperature, the reaction vessel was heated, step by step, from room temperature to 350° in an atmosphere of normal hydrogen. The assay of tritium was carried out after 14 hr; meanwhile, the exchange of tritium with hydrogen was observed to attain equilibrium.

Results

The order of the hydrogenation reaction of ethylene on each catalyst was found to be first for hydrogen and zero for ethylene. Figure 2 shows the doping effects of lithium on the specific activities and the BET areas of the catalysts. This figure shows that the addition of lithium markedly decreased the specific activity and the BET area. However, the addition of more than 2% lithium did not cause any further decrease in either the activity or the BET area.

Figure 3 shows the Arrhenius plots of the hydrogenation reaction on 4.3% lithium-doped nickel and those on pure nickel. The aim of the study of pure nickel was to ascertain the effects of the nuclear fission of ^6Li and the recovery of radiation damage upon the catalytic activity. In this study, the irradiation was carried out under two different conditions—one by cooling with liquid nitrogen and the other one by cooling without liquid nitrogen. The temperature of the sample in the latter case was assumed to be higher than 400° during the irradiation. Figure 4 shows the results on the lithium-doped copper-nickel and nonlithium-doped copper-nickel. The concentration of lithium in the alloy was 4.3%. It is evident in Figure 3 that the irradiation under the cooling condition with liquid ni-

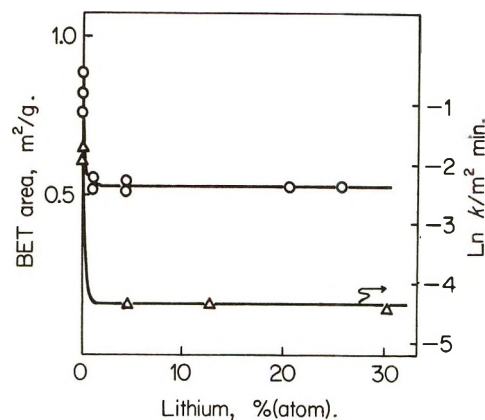


Figure 2. The doping effects of lithium on the specific activity and the BET area: Δ , activity; \circ , BET area.

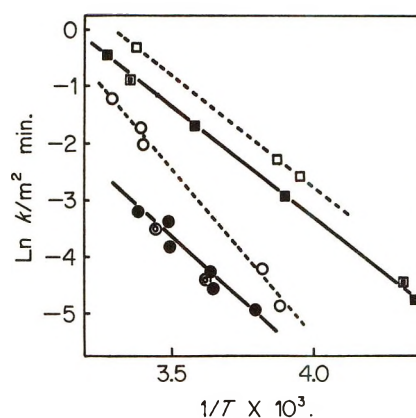


Figure 3. Arrhenius plots of the hydrogenation reaction on nickel catalysts: \circ , Ni-Li irradiated; \bullet , Ni-Li unirradiated; \odot , Ni-Li irradiated without cooling; \square , Ni irradiated; \blacksquare , Ni unirradiated; \boxplus , Ni irradiated without cooling.

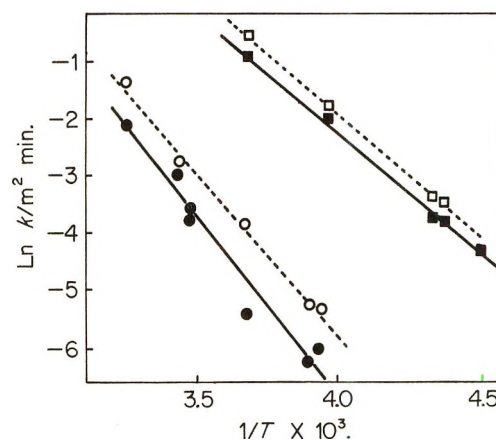


Figure 4. Arrhenius plots of the hydrogenation reaction on copper-nickel (1:1) catalysts: \circ , Cu-Ni-Li irradiated; \bullet , Cu-Ni-Li unirradiated; \square , Cu-Ni irradiated; \blacksquare , Cu-Ni unirradiated.

trogen increased the catalytic activity. However, the activity did not increase when the irradiation was carried out without cooling.

(10) T. Takeuchi, M. Sakaguchi, and M. Tatsushima, *Radioisotopes*, 10, 106 (1961).

Of particular interest is the fact that no radiation effect was found in the activity of the lithium-doped copper. The temperatures of the hydrogenation reaction on this catalyst were 19 and 26.5°. No decrease in the pressure due to the reaction was found, even after 18 hr.

The comparison of the radiation effects on the catalytic activity is made by the use of the expression of A_{irr}/A_0 , where A_{irr} and A_0 are the activity of the irradiated catalyst and that of the unirradiated catalyst, respectively. These results are shown, together with the activation energy of the reaction, in Table I. This table indicates that the increase in the activity upon irradiation is promoted by the doping of lithium.

Table I: Activation Energies and Ratios of the Activity of Irradiated Catalyst to That of Unirradiated Catalyst

Catalyst	Activation energy, kcal/mol	Ratio of activity, K_{irr}/K_{unirr}
Ni irr.	8.0	2
Ni unirr.	7.8	
Ni-Li irr.	11.2	3-4
Ni-Li unirr.	9.2	
Cu-Ni irr.	8.3	1.5
Cu-Ni unirr.	8.3	
Cu-Ni-Li irr.	12.3	3
Cu-Ni-Li unirr.	12.0	
Cu unirr.	...	
Cu-Li irr.	...	
Cu-Li unirr.	...	

Table II shows the amounts of tritium obtained by the contact of normal hydrogen or by the mixture of ethylene and hydrogen with the catalyst. These results indicate that the amount of tritium obtained by the second or third contact is about $1/10$ that of the first contact; the amount of tritium obtained by the contact of hydrogen was approximately the same as that obtained by the contact of the mixture of ethylene and hydrogen. Both amounts are 50 times greater than that obtained by the contact with ethylene alone. In the case of the mixture of ethylene and hydrogen, these gases were completely changed to ethane in the contact time.

Figure 5 shows the dependence of the temperature of the treatment of lithium-doped catalysts upon the amount of tritium taken out by the contact with normal hydrogen. The dotted line in the figure indicates the amount of tritium obtained theoretically by means of the equation

$$(^3\text{H}) = W/M\lambda \cdot N\phi\delta_{act}(1 - e^{-\lambda t})e^{-\lambda T}$$

where W is the amount (g) of ^6Li , M is the atomic mass of ^6Li , N is the Avogadro number, ϕ is the irradiation dose ($\text{cm}^{-2} \text{sec}^{-1}$), δ_{act} is a cross section of the neutron (barns), λ is the disintegration constant, t is the irra-

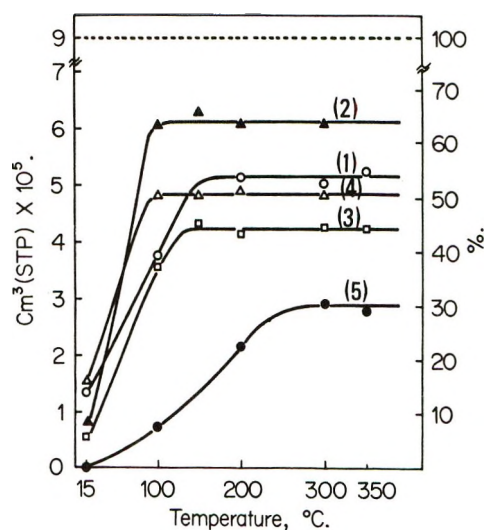


Figure 5. The dependence of the temperature of the treatment of catalyst upon the amount of tritium taken out: (1) Ni-Li; (2) Cu-Ni(3:7)-Li; (3) Cu-Ni(1:1)-Li; (4) Cu-Ni(7:3)-Li; (5) Cu-Li.

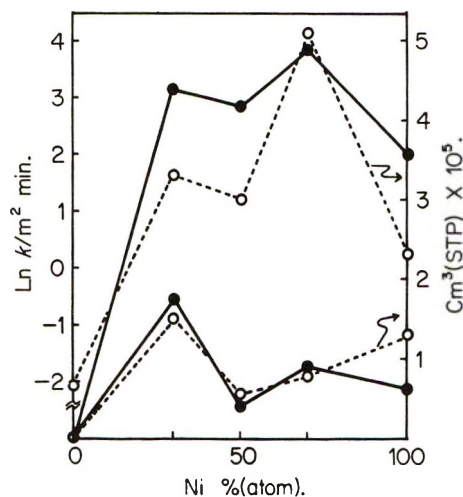


Figure 6. The correlation between the amount of tritium taken out and the catalytic activity for the hydrogenation reaction: ○, amount of tritium; ●, catalytic activity; upper two lines at 100°; lower two lines at 15°.

diation time, and T is the cooling time. Figure 5 indicates that more than 50% of the total tritium was taken out from nickel and copper-nickel at 150°, but that only 30% was taken out from copper at 300°.

Figure 6 shows the correlation between the amount of tritium taken out from each catalyst (4.3% Li) and the composition of the catalyst. In this figure, the catalytic activities of the hydrogenation reaction on each catalyst at 15 and 100° are shown for the sake of comparison. The two correlations are very similar.

Discussion

The lithium nitrate used for the preparation of the catalysts contained 7.4% ^6Li , which is preferentially related to the nuclear reaction, as has been mentioned

Table II: The Amount of Tritium Obtained by the Contact of Hydrogen, Ethylene, or the Mixture of Ethylene and Hydrogen

Series	Gas admitted	Order of contact	Amount of gas, cc(STP)	Temp, °C	Contact time, hr	Amount of ³ H, cpm
1	H ₂	1	2.76	140	2	1.26 × 10 ⁷
		2	2.80	140	2	2.16 × 10 ⁶
		3	2.80	140	2	1.23 × 10 ⁶
		4	13.30	140	2	7.77 × 10 ⁵
2	C ₂ H ₄	1	2.50	145	2	1.02 × 10 ⁶
		2	2.44	142	2	2.96 × 10 ⁴
		3	2.44	138	2	2.90 × 10 ⁴
3	C ₂ H ₄ + H ₂	1	2.60	140	2	7.70 × 10 ⁵
		2	2.30	145	2	7.10 × 10 ⁵
		3	2.42	140	2	1.90 × 10 ⁶
		4	2.46	140	2	2.39 × 10 ⁵

above. The cross section of ⁶Li is 945 barns. Therefore, only 1/10³ of the total ⁶Li reacts with neutrons (10¹⁹ nvt) in this study. A large portion of the lithium doped in the catalysts remains without change after the irradiation. According to metallurgical concepts, lithium does not alloy with nickel and copper, and the lithium oxide produced by the calcination of a lithium-doped catalyst is difficult to reduce by means of hydrogen. On the other hand, the X-ray diffraction pattern did not show any difference between the lithium-doped catalysts and those with no lithium. This finding would be explained in terms of scattering power, which is very small for lithium. The decrease in the catalytic activity upon the doping of lithium would be the result of the lithium oxide on the surface. That is, the effective area of the surface must be diminished.

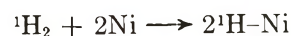
The increase in the catalytic activity upon irradiation suggests the occurrence of structural change in the metal—that is, the formation of fresh lattice imperfections. The increase in the irradiated catalysts which were not doped with lithium is probably due to the increase in the lattice imperfections produced by fast neutrons included in the flux. It may also be concluded that the greater increase in the catalytic activity of lithium-doped nickel and lithium-doped copper-nickel is attributable to the additional increase in lattice imperfections produced by the fission products.

The results on the irradiated copper imply that the electronic properties of perfect metal affect the catalytic reaction, independently of the lattice imperfections. Pure copper has been regarded as intrinsically inactive as a catalyst for hydrogenation reactions;¹¹⁻¹³ the inactive nature of copper has been interpreted by means of an electronic theory.¹⁴ If the lattice imperfections can always act as effective sites for the catalytic reaction, the copper should become active as a result of the irradiation. The unexpected results in this study suggest that the increase in catalytic activity as a result of the increase in the amount of lattice

imperfections arises only in the metal which is consistent with the electronic properties.

There have been many reports¹⁵⁻¹⁸ concerned with retardation of the catalytic hydrogenation of nickel by preadsorbed hydrogen; it has been explained in terms of the occupation of the d band of metal by electrons of hydrogen atoms. In addition, there is evidence of the isotope effect on the catalytic hydrogenation reaction.¹⁹ A far smaller rate in the reaction on the lithium-doped catalysts can be expected by taking these facts into consideration because of the existence of preadsorbed or dissolved tritium. In this study, however, only 3/10² of the total tritium was consumed by the hydrogenation reaction, and the tritium which was shifted to ethane by the reaction constituted 1/10⁶ of the total number of ethane molecules. These results show that the influence of tritium upon the rate of hydrogenation reaction can be disregarded.

The similarity between the amount evolved from each catalyst and the rate of the hydrogenation reaction suggests that the tritium switches from catalyst to hydrogen by means of the exchange reaction



The rate of the exchange reaction, as well as that of the

(11) J. H. Long, J. C. W. Frazer, and E. Otto, *J. Amer. Chem. Soc.*, **56**, 1101 (1934).

(12) P. H. Emmett and N. Skau, *ibid.*, **65**, 1029 (1943).

(13) G. C. Bond, "Catalysis by Metals," Academic Press, New York, N. Y., 1962, p 320.

(14) D. A. Dowden and P. W. Reynolds, *J. Chem. Soc.*, **242**, 265 (1950); *Discuss. Faraday Soc.*, **8**, 184 (1950).

(15) J. H. Singleton, *J. Phys. Chem.*, **60**, 1606 (1956).

(16) W. K. Hall and P. H. Emmett, *ibid.*, **63**, 1102 (1959).

(17) P. B. Shallercross and W. W. Russell, *J. Amer. Chem. Soc.*, **81**, 4139 (1959).

(18) W. Palczewska, A. Frackiewicz, and Z. Karpinski, *Proc. Int. Congr. Catal.*, **4th**, No. 52 (1968).

(19) S. S. Roginski, "Theoretische Grundlagen der Isotopenchemie," Veb. Deutscher Verlag der Wissenschaften, Berlin, 1962, p 361.

hydrogenation reaction, must be related to the amount of tritium chemisorbed.

The very small activities of the copper catalyst in both reactions probably result from the difficulty of the diffusion of tritium from the interior of copper to its surface. The tritium produced in copper by the irradiation might be trapped forming the molecular state in lattice defects.

It has been reported that many types of lattice imperfections are produced in metals as the results of the neutron irradiation and that the stability of the lattice imperfections varies with their types.²⁰⁻²² It is difficult, however, to propose from the results of our study what type of lattice imperfections remained and asso-

ciated with the catalytic reaction. Further studies are necessary for this purpose.

Acknowledgments. We are grateful to Dr. Kunio Ozawa for his helpful suggestions and Mr. Tadao Morita for his technical assistance in this study. We also wish to thank the Japan Atomic Energy Research Institute for allowing us to use their instruments.

(20) S. Billington and J. H. Crawford, Jr., "Radiation Damage in Solids," Princeton University Press, Princeton, N. J., 1961, p 100.

(21) D. K. Holms, "The Interaction of Radiation with Solids," R. Strumane, Ed., North-Holland Publishing Co., Amsterdam, 1964, p 147.

(22) L. T. Chadderton and I. M. Torrens, "Fission Damage in Crystals," Methuen and Co. Ltd., London, 1968, p 35.

Photochemical Reactions of Borazine with Ammonia and Methyl Bromide¹

by Melvin A. Neiss and Richard F. Porter*

Department of Chemistry, Cornell University, Ithaca, New York 14850 (Received April 4, 1972)

Publication costs assisted by the Army Research Office—Durham and the Advanced Research Projects Agency

Quantum yield studies of the borazine–ammonia and borazine–methyl bromide photochemical reactions at 1849 Å have revealed aspects of the two systems which may be general features of borazine photochemistry at this wavelength. The quantum yields for formation of *B*-monoaminoborazine and H₂ increase with an increasing ammonia to borazine ratio and reach limiting values at approximately an equimolar mixture. The limiting value for Φ_{H_2} is 1.1 ± 0.1 . In the borazine–CH₃Br system, the quantum yield for methane production increases with the ratio of methyl bromide to borazine to a maximum of about 0.75 ± 0.1 at a 30-fold excess of methyl bromide, and at higher ratios decreases slowly. Studies of these reactions with added inert gas indicate that at high borazine/reactant ratios the reacting intermediate is a vibrationally excited borazine molecule. In experiments with high reactant/borazine ratios corresponding to predominant reactant absorption, radical production results in abstraction or replacement of hydrogen atoms on the borazine ring. The extent of the photodecomposition of borazine is also a considered factor.

Introduction

A photochemical procedure for the preparation of *B*-monosubstituted borazine derivatives has been described previously.² The method involves photolysis of gas-phase borazine–reactant mixtures with 1849-Å radiation. However, quantitative information about the photochemical reactions of borazine is lacking for all but the borazine photodecomposition³ and the photochemical exchange reaction of borazine and deuterium.⁴ *B*-Monoaminoborazine^{2,5} and *B*-monobromoborazine⁶ are among the compounds that have been prepared by this method and characterized by spectroscopic analysis. The present quantum yield study concentrates on the reactions leading to these products and has been undertaken in order to extend our understanding of the photochemistry of borazine in systems where a chemical reactant is also present.

Experimental Section

The apparatus for large-scale preparations² and for the quantum yield determinations³ have been described previously. In most experiments an Hg-free system was used to eliminate the possibility of Hg-sensitized reactions. Borazine was prepared by the reduction of *B*-trichloroborazine with NaBH₄.⁷ *B*-Trideuterio-

(1) Work supported by the Army Research Office, Durham, N. C., and the Advanced Research Projects Agency through the Materials Science Center, Cornell University.

(2) G. H. Lee, II, and R. F. Porter, *Inorg. Chem.*, **6**, 648 (1967).

(3) M. A. Neiss and R. F. Porter, *J. Amer. Chem. Soc.*, **94**, 1438 (1972).

(4) M. P. Nadler and R. F. Porter, *Inorg. Chem.*, **8**, 599 (1969).

(5) R. F. Porter and E. S. Yeung, *ibid.*, **7**, 1306 (1968).

(6) M. Oertel and R. F. Porter, *ibid.*, **9**, 904 (1970).

(7) L. F. Hohnstedt and D. T. Haworth, *J. Amer. Chem. Soc.*, **82**, 89 (1960).

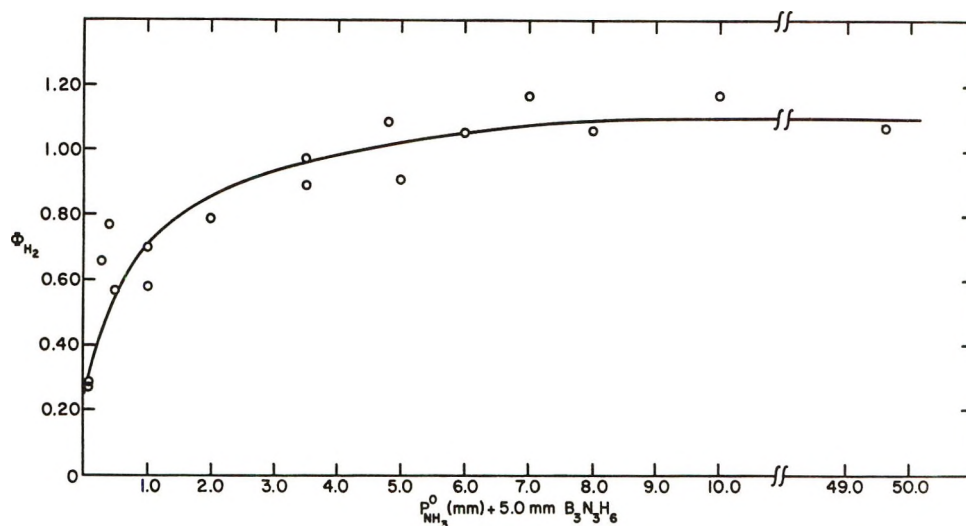


Figure 1. Plot of the hydrogen production quantum yield vs. $P_{\text{NH}_3}^0$ (mm) at a constant 5.0 mm of $\text{B}_3\text{N}_3\text{H}_6$.

borazine was prepared by the photochemical exchange reaction between borazine and deuterium⁴ and perdeuterioborazine was prepared from the reaction of ND_3 and B_2D_6 .⁸ Reagent grade ammonia and methyl bromide were obtained from Matheson and further purified by fractional distillation.

Photolyses were performed in which the ratio of reactant to borazine ranged from 0.20:1 to 200:1. In further mechanistic studies excess inert gas (Xe, CO_2 , and cyclohexane) and a radical scavenger (I_2) were added to the reactants. Following irradiations, the vessel contents were opened to a series of traps. Gases noncondensable at -196° were transferred by means of a Toepler pump to a calibrated volume containing a McLeod gauge. A CEC 21-103A mass spectrometer was used for product identification and quantitative analysis. D_2 (Matheson) and CD_4 (International Chemical and Nuclear Corp.) served as calibrating gases for H_2 determinations in borazine-ammonia reactions and CH_4 determinations in borazine-methyl bromide reactions, using a procedure described earlier.³ Actinometry of the 1849-Å line intensity was accomplished using the photodecompositions of N_2O ($\Phi_{\text{N}_2} = 1.44$)⁹ and C_2H_4 ($\Phi_{\text{H}_2} = 0.62$)¹⁰ and 2537-Å intensity was measured using an HI standard ($\Phi_{\text{H}_2} = 1.0$).¹¹ The photochemical production of a borazine polymer³ necessitated thorough cleaning of reaction vessels following most irradiations.

Results

B-Monoaminoborazine and *B*-monobromoborazine are extremely sensitive to moisture. These compounds also exhibit a tendency to adhere strongly to vessel walls and stopcock grease. These properties prevented complete stoichiometric studies of the two reactions and necessitated the choice of H_2 and CH_4 for principal investigation.

Borazine-Ammonia Reaction. Preparative-scale photolysis experiments with borazine-ammonia mixtures have shown that *B*-monoaminoborazine is an isolable product when the initial borazine/ammonia ratio was varied between 5:1 to 1:1 and the total pressure was 10 mm. The best conditions for obtaining the product correspond approximately to an equal molar mixture of the starting reagents. In addition to H_2 and aminoborazine, the only other product observed in these photolyses was a very small amount of borazanaphthalene ($\text{B}_5\text{N}_5\text{H}_8$), in the experiments at a high borazine to ammonia ratio. Nitrogen was not observed, even at the lowest ratio of borazine to ammonia.

A preliminary investigation was performed using the quantum yield apparatus to determine the quantum yields of H_2 and N_2 production in a pure ammonia system under conditions of varied ammonia pressure. The results would be compared with those obtained under the same conditions in the presence of borazine. The values $\Phi_{\text{H}_2+\text{N}_2} = 0.4-0.6$ were obtained over the pressure range 0.4–201 mm of ammonia. The quantum yields for ammonia decomposition ($= 0.5\Phi_{\text{H}_2+\text{N}_2}$) were generally within about 20% of those reported in the literature.¹² Subsequent quantum yield experiments with ammonia pressures up to 50 mm in the presence of 5 mm of borazine yielded the H_2 quantum yields presented in Table I. There was no detectable N_2 production. These data are plotted in Figure 1 as a func-

(8) A. Stock and E. Pohland, *Ber. Deutsch. Chem. Ges.*, **59**, 2215 (1926).

(9) N. R. Greiner, *J. Chem. Phys.*, **47**, 4373 (1967).

(10) P. Borrell, P. Cashmore, and A. E. Platt, *J. Chem. Soc. A*, 3063 (1968).

(11) R. M. Martin and J. E. Willard, *J. Chem. Phys.*, **40**, 2999 (1964).

(12) W. Groth and H. J. Rommel, *Z. Phys. Chem. (Frankfurt am Main)*, **45**, 96 (1965).

tion of ammonia pressure. Blank runs were made both with the lamp off and with a Vycor filter eliminating the 1849-Å line. H₂ production was not observed in either case. A qualitative experiment was run to determine if the reaction could be mercury photosensitized at 2537 Å. It is known that the photodecomposition of ammonia is sensitized at this wavelength by Hg(³P₁).¹³ A quantum yield cell was exposed to Hg vapor for several hours and borazine and ammonia at partial pressures of 5 mm were then added. Photolysis was for 1 hr with the Vycor filter in place. Following irradiation, mass spectral analysis revealed H₂, but N₂ other than the normal background could not be detected. In one experiment an approximately tenfold excess of cyclohexane was added to a mixture of 5.1 mm of borazine and 1.1 mm of ammonia (Table I). Φ_{H_2} was reduced by less than 10% when compared with the run made with the same reactant ratio in the absence of cyclohexane.

Table I: Quantum Yield Data for the Photochemical Reaction of B₃N₃H₆ and NH₃

$P_{\text{B}_3\text{N}_3\text{H}_6}^0$, mm	$P_{\text{NH}_3}^0$, mm	Time, sec	$I_a \times 10^{10}$, einsteins/ sec	Φ_{H_2}
5.0	0.1	1800	1.82	0.27
5.0	0.1	3600	1.82	0.28
5.0	0.3	3600	1.29	0.66
5.0	0.4	3600	1.16	0.77
5.0	0.5	3600	1.51	0.57
4.6	1.0	3600	1.37	0.70
5.0	2.0	3600	1.19	0.79
5.0	3.5	1800	1.87	0.97
5.0	3.5	2700	1.56	0.89
5.0	4.8	3600	1.60	1.09
5.0	6.0	3600	1.23	1.05
5.0	7.0	3600	1.63	1.17
5.0	8.0	3600	1.25	1.06
5.0	1.0	1800	8.9	0.58
5.1 ^a	1.1	1600	11.0	0.53
4.9	5.0	1800	9.0	0.91
5.0	10.0	1860	8.7	1.17
5.0	49.6	1800	8.5	1.07

^a Photolysis in the presence of 49 mm of cyclohexane.

Borazine-Methyl Bromide Reaction. The first set of experiments in the borazine-methyl bromide system using the 2-l. reactor was a determination of the relative yields of methane, ethane, and hydrogen produced under conditions in which borazine absorbed a major fraction of the 1849-Å radiation. After photolysis the vessel contents were pumped through traps at -80 and -127° using the Toepler pump and the noncondensed gases were collected for mass spectral analysis. The relatively warm traps were used to ensure that all the ethane was collected in the calibrated volume. A small amount of methyl bromide also passed through

the traps, but it gave no significant contribution to any of the peaks of interest: m/e 2, 16, and 30. Finally, the relative mass spectral peak heights were calibrated to pressure ratios by analysis of known mixtures on the mass spectrometer. The results are given in Table II. A summary of similar experiments performed with deuterated borazines is given in Table III. The predominant product species in the photolyses of B₃N₃D₆ and CH₃Br are CH₃D and D₂. There appears to be a degree of hydrogen atom scrambling or, more probably, an isotope effect in which preference is shown for the small hydrogen atom impurity (~5%) in the B₃N₃D₆. The runs in which D₃B₃N₃H₃ was photolyzed with methyl bromide produced a surprisingly high CH₄ to CH₃D ratio. This point will be further discussed in the next section. The predominant hydrogenic species observed was HD. Other products detected mass spectrometrically at excess borazine pressure were *B*-monobromoborazine and borazanaphthalene. When isotopically substituted borazines were used, the parent masses of these two products were seen to increase accordingly. Runs made with large excesses of methyl bromide also produced H₂, CH₄, and C₂H₆, as well as *B*-mono- and *B*-dibromoborazine. In addition, small amounts of borazanaphthalene and CH₂Br₂ were observed.

Table II: Hydrogen, Methane, and Ethane Ratios from the Photochemical Reaction of Borazine and Methyl Bromide

$P_{\text{B}_3\text{N}_3\text{H}_6}^0$, mm	$P_{\text{CH}_3\text{Br}}^0$, mm	% B ₃ N ₃ H ₆ absorption	Time, sec	$P_{\text{H}_2}:P_{\text{CH}_4}:P_{\text{C}_2\text{H}_6}$
5.1	2.0	97	1800	81:100:9.8
8.2	15.5	88	3600	29:100:4.3

Unlike borazine and ammonia, methyl bromide exhibits absorption of the 2537-Å mercury radiation, with an extinction coefficient of about 1.4 l./(mol cm).¹⁴ Its extinction coefficient at 1849 Å was determined to be 73 l./(mol cm). In the photolysis of CH₃Br at 1849 Å, Φ_{CH_4} has been reported as 0.020,¹⁵ and at 2537 Å it is 0.0038.¹⁵ Several photolyses with an unfiltered mercury lamp were performed in an effort to approximate the literature value for Φ_{CH_4} at 1849 Å. The light absorbed by the CH₃Br at 2537 Å in these experiments was always less than that absorbed at 1849 Å. Therefore, because of the difference in Φ_{CH_4} at the two wavelengths, the use of the unfiltered lamp introduced a maximum of 20% error in the determination. Values for $\Phi_{\text{CH}_4}(\text{CH}_3\text{Br})$ obtained in this way

(13) M. Z. Hoffman, M. Goldwasser, and P. L. Damour, *J. Chem. Phys.*, **47**, 2195 (1967).

(14) N. Davidson, *J. Amer. Chem. Soc.*, **73**, 467 (1951).

(15) P. C. Kobrinisky and R. M. Martin, *J. Chem. Phys.*, **48**, 5728 (1968).

Table III: Methane and Hydrogen Isotope Ratios from the Photochemical Reactions of Deuterated Borazines and Methyl Bromide

$P^0_{B_3N_3H_6}$, mm	$P^0_{D_2B_3N_3H_5}$, mm	P_{CH_3Br} , mm	$P^0_{C_6H_{12}}$, mm	Time, sec	$P_{CH_4}:P_{CH_3D}$	$P_{B_2}:P_{BD}:P_{D_2}$
3.1		1.0		300	17:100	5:27:100
2.7 ^a		0.67		1860	25:100	8:16:100
2.9 ^a		0.72	31	2700	100:32	56:100:11
	10.5	3.0		1800	100:63	78:100:18
	9.6	3.0		3600	100:91	69:100:43
	14.7	4.3		2700	100:71	82:100:40
	10.5	2.1		900	100:56	7:100:14

^a Reaction performed in quantum yield cell.

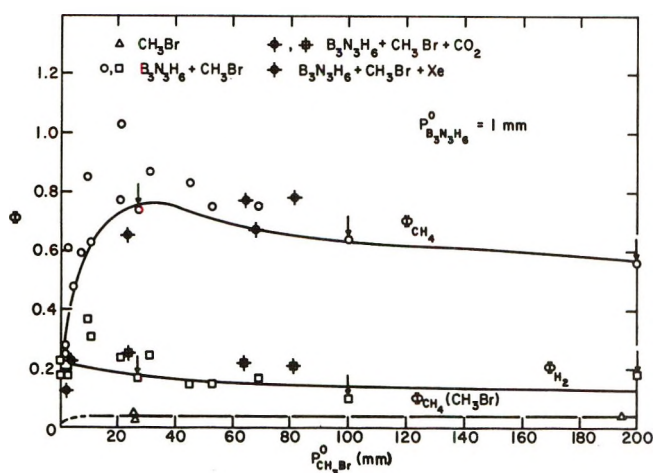


Figure 2. Plots showing the approximate 1849-Å quantum yields of CH_4 and H_2 production vs. $P^0_{CH_3Br}$ (mm). For the top two curves $P^0_{B_3N_3H_6} = 1$ mm. In designated runs added gases were CO_2 and Xe. Points with vertical arrows represent true 1849-Å quantum yields, corrected for the CH_3Br absorption at 2537 Å.

are seen in Figure 2. They are in the range 0.03–0.05. The apparent discrepancy with the reported value at 1849 Å is attributed to errors inherent in working with the small methane pressures obtained in these runs.

Quantum yield data obtained for the methyl bromide reaction with borazine are included in Table IV and presented in Figures 2 and 3. Methane and hydrogen production were monitored in these experiments, while most of the ethane was trapped at -196° . The yield of H_2 was calculated assuming that $P_T - (P_{CH_4} + P_{CD_4}) = P_{H_2}$ in the calibrated volume. P_T is the total pressure measured. For most of the runs presented in Table IV and Figures 2 and 3, an unfiltered Hg lamp was again used with the assumption that the methane and hydrogen contribution from CH_3Br absorption at 2537 Å was small. Vertical arrows in Figure 2 are seen at points representing true 1849-Å quantum yield values. The product yields at these points have been corrected for methyl bromide absorption at 2537 Å and subsequent reaction with the borazine. Three paired runs at the designated reactant pressure

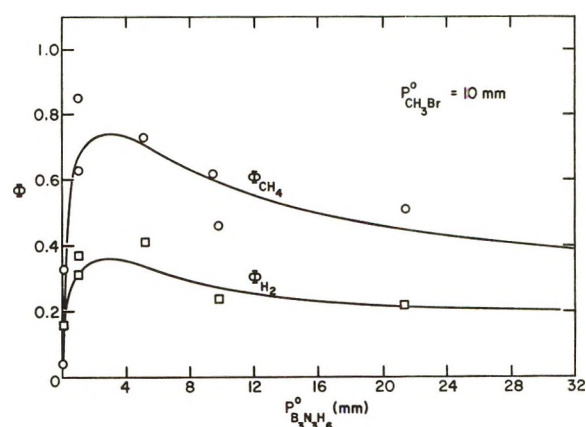


Figure 3. Plots showing the CH_4 and H_2 quantum yields vs. $P^0_{B_3N_3H_6}$ at a constant 10 mm of CH_3Br .

ratios were performed with and without a Vycor filter in the light path. Because the filter absorbed a small fraction of the light at 2537 Å (while completely eliminating the 1849-Å line), photolysis times of the filtered runs were lengthened so that the total numbers of 2537-Å photons absorbed by the CH_3Br with and without the filter were equal. The methane and hydrogen pressures measured in the filtered runs were subtracted from the pressures obtained without the filter, and the quantum yields at 1849 Å were calculated using the absorbed intensities at this wavelength (Table IV). Φ_{CH_4} (2537 Å) and Φ_{H_2} (2537 Å) are given in the respective columns for the second mixture in each of the paired runs. In the table only true quantum yields are given in parentheses. The approximate values for Φ_{CH_4} (1849 Å) and Φ_{H_2} (1849 Å) given in Table IV obtained using the full light of the Hg lamp are probably too large by less than 25% for CH_3Br pressures below about 80 mm (see Figure 2).

One can clearly see in Figure 2 the greatly increased values for Φ_{CH_4} obtained when borazine was present with the methyl bromide, even when it absorbed only a small fraction of the light. Large excesses of the inert gases Xe and CO_2 had no effect on Φ_{CH_4} (or Φ_{H_2}) at high methyl bromide pressures, but appeared to decrease Φ_{CH_4} slightly at lower CH_3Br pressures. A ten-

Table IV: Quantum Yield Data for the Photochemical Reaction of Borazine and Methyl Bromide

$P^0_{B_3N_3H_6}$, mm	$P^0_{CH_3Br}$, mm	P^0_{other}	Time, sec	$I_a \times 10^{10}$, einsteins/sec	$\Phi_{CH_4}^a$	$\Phi_{H_2}^a$
3.0			3600	9.85		0.23
2.69 ^b	0.67		1860	8.60	0.24	
2.90 ^b	0.72	31(C ₆ H ₁₂)	2700	8.32	0.058	
0.94	21.0		2400	6.10	0.77	0.24
1.1	23.5	458(CO ₂)	1950	6.10	0.65	0.25
0.92	27		2000	13.8	0.86 (0.74)	0.22 (0.17)
1.0 ^c	30		2760	2.5	(0.48)	(0.20)
1.0	31	$\sim 10^{-3}$ (Hg)	3600	5.15	0.87	0.25
1.0	64	307(CO ₂)	1860	6.40	0.77	0.22
1.0	68	511(Xe)	2000	5.75	0.67	
0.94	69		1400	7.25	0.75	0.17
1.0	100		1950	14.4	0.87 (0.64)	0.21 (0.10)
1.0 ^c	99		2030	8.2	(0.39)	(0.18)
1.0	200		1650	15.9	1.04 (0.56)	0.25 (0.18)
0.94 ^c	196		2120	13.5	(0.44)	(0.07)
1.0	191	0.23(I ₂)	1100	9.72	0.14	0.28
	195		2400	18.0	0.047	

^a Only values in parentheses are true quantum yields. Other values are approximations to 1849-Å quantum yields obtained using the unfiltered lamp. ^b B₃N₃D₆ was used in these runs. The quantum yields given are for CH₃D production (and CH₄ production due to some partially protiated borazine species). ^c Run with Vycor filter. I_a and quantum yields refer to 2537 Å.

fold excess of cyclohexane added to a 2.90 mm of B₃N₃D₆-0.72 mm of CH₃Br mixture lowered the methane quantum yield to 25% of the value obtained in the absence of the inert gas (Table IV). A decrease in D₂ production relative to HD and H₂ was also observed. This has been seen in Table III. A run was also made in which Hg was present in the cell during photolysis (Table IV). Neither the methane nor hydrogen quantum yield was affected. In one experiment a small amount of I₂ was added to act as a methyl radical scavenger. It was first determined that borazine and I₂ did not react thermally or photochemically. The effect was to decrease the methane quantum yield (uncorrected for 2537-Å radiation) by a factor of 7.5 (Table IV). In the 1.0 mm of borazine-191 mm of methyl bromide-0.23 mm of I₂ mixture the I₂ absorbed only about 7% of the light at 1849 Å and a negligible fraction at 2537 Å.

Discussion

The data presented on the borazine-ammonia photochemical reaction indicate that the quantum yields of *B*-monoaminoborazine and hydrogen production at 1849 Å exhibit similar qualitative behavior. In the region of predominant borazine absorption both rise due to the reaction



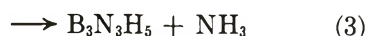
The species B₃N₃H₆' has been discussed in a previous paper³ and is considered to be a vibrationally excited borazine molecule which, if not quenched, can eliminate

H₂ and result in a borazyne species. The borazyne in turn can react with a borazine molecule to form borazanaphthalene. It is seen, therefore, that reaction 1 is in competition with intramolecular H₂ elimination ($\Phi_{H_2} = 0.2$).³ The observed decrease in borazanaphthalene production with increasing ammonia pressure is consistent with these arguments. The extinction coefficients of borazine and ammonia at 1849 Å have been determined to be 980³ and 1240 l./(mol cm), respectively. The latter value agrees well with 1210 l./(mol cm) measured by McDonald and coworkers.¹⁶ Neither molecule exhibits absorption at 2537 Å. The condition of 50% absorption by each reactant species at 1849 Å is met at 5 mm of borazine and 4 mm of ammonia. The total quantum yield of H₂ production at this point is 1.0 (Figure 1). Assuming that at this pressure ratio $\Phi_{H_2} \approx 1$ for the light actually absorbed by the ammonia (as at 50 mm of ammonia), we see that Φ_{H_2} as a result of borazine absorption at this point is also about unity. Thus, between ammonia pressures of 0 and 4 mm the quantum yield of H₂ production resulting from light absorption by borazine rises from 0.2 to about 1 as a consequence of reaction 1. It has been noted that excess cyclohexane addition under the condition of predominant borazine absorption in the borazine-ammonia reaction does not significantly reduce the H₂ quantum yield. Cyclohexane has proved to be a good inert gas for the purpose of vibrationally

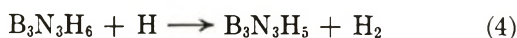
(16) C. C. McDonald, A. Kahn, and H. E. Gunning, *J. Chem. Phys.*, **22**, 908 (1954).

deactivating the $B_3N_3H_6'$ reacting species.³ Therefore, our data point to a relatively low vibrational energy threshold required for reaction 1. The rapid approach to $\Phi_{H_2} = 1$ is consistent with a low energy requirement.

It was important to learn that a sizable quantity of *B*-monoaminoborazine was produced in addition to H_2 at a reactant pressure ratio at which borazine absorbed only about 7% of the light (10 mm of borazine:100 mm of ammonia). This was an indication that NH_2 radicals produced in the first step of the ammonia photodecomposition are capable of displacing hydrogen atoms at boron positions on borazine molecules. The reaction of an amino radical with borazine can be of two possible types



The substitution reaction 2 is probably the principal means of *B*-monoaminoborazine production at predominant ammonia absorption. The abstraction reaction 3 is proposed in analogy to the reaction of borazine with CH_3 radicals discussed below. H_2 formation can result principally from the abstraction reaction



The interpretation of radical attack on the borazine is substantiated by the results of the Hg_2 -photosensitized decomposition of ammonia at 2537 Å. The lack of N_2 production at this wavelength and at 1849 Å is a good indication that the NH_3 scheme of photodecomposition proceeding through radical intermediates is interrupted by the borazine. The fate of the $B_3N_3H_5$ radical in reactions 3 and 4 is not clearly understood. One might suggest a reaction with borazine to produce diborazinyl ($B_6N_6H_{10}$), but no evidence for the production of this species has been found in the present work. Borazanaphthalene and/or a polymer may instead be formed.

Experiments using the borazine-methyl bromide system (Table II and Figure 2) indicate that the production of H_2 decreases relative to CH_4 with increased percentages of CH_3Br in the reaction mixture. These results are consistent with the interpretation that the borazine-methyl bromide reaction, eq 5, is in competition with the borazine photodecomposition (discussed above). Excess cyclohexane under conditions of pre-



dominant borazine absorption has been shown to substantially reduce the methane quantum yield. This is an indication that reaction 5 has a higher vibrational energy state requirement than does the analogous reaction with ammonia, eq 1. The excitation in $B_3N_3H_6'$ may lead to a highly vibrationally excited CH_4 species, which may dissociate rapidly unless quenched by collisions. Observed ethane would be formed by com-

bination of two resultant methyl radicals. The decreases in ethane (Table II) and hydrogen (Figures 2 and 3) noted with increased reactant pressure may be due to collisional deactivation of vibrationally excited methane. The small maximum of Φ_{H_2} seen in Figure 3 may have a contribution from H_2 produced by further reactions of H atoms arising from the CH_4 dissociation. The excess cyclohexane has also been seen to effect a significant change in the product isotope distribution from the reaction of $B_3N_3D_6$ (containing $B_3N_3D_5H$ impurity) and CH_3Br (Table III). In a previous paper³ it was noted that cyclohexane served to reduce significantly the D_2 to H_2 product ratio from the photolysis of equimolar mixtures of $B_3N_3D_6$ and $B_3N_3H_6$. In the present situation the amount of D_2 elimination was reduced significantly relative to the "impurities" HD and H_2 . In addition, despite a substantial reduction of the overall methane quantum yield, a greatly enhanced CH_4 to CH_3D ratio may have resulted from the CH_3Br reaction with the less easily quenched partially protiated borazine species.

Isotope studies with $D_3B_3N_3H_3$ and CH_3Br (Table III) also indicate that in the region of predominant borazine absorption methane is formed with about equal hydrogen atom contributions from the boron and nitrogen sites. A possible mechanism offered as explanation must account for the fact that in this process only *B*-monobromoborazine is produced. Let us assume a symmetrical approach of the methyl bromide to the borazine molecule between vibrationally excited B-H and N-H bonds, with its molecular axis perpendicular to the plane of the borazine ring. If the necessary activation energy is present in the excitation there might be about equal probability of B-H or N-H bond cleavage in methane formation. If the B-H bond is broken, the bromine atom would substitute on the ring at that position. If, however, the N-H bond is broken, the boron position might still be bromine substituted if there is also a hydrogen atom transfer. The driving force might be the nucleophilic character of the bromine atom and the electrophilic nature of the boron atom.

When methyl bromide absorption predominates, there is a multitude of possible reactions, but only one which might produce the relatively large yield of methane that has been observed. This would be the abstraction reaction



presumably at a boron site. A "hot" methyl radical is generated in the photodissociation of the methyl bromide.¹⁵ However, before reaction with the borazine it will have been cooled by collisions with the methyl bromide. Additional inert gas does not affect the quantum yield, indicating the participation of an already thermalized radical. I_2 was noted to quickly scavenge these methyl radicals, resulting in decreased

reaction with the borazine. Reaction 6 has a $\Delta H_f \approx -20$ kcal/mol, based on a B-H bond strength of about 85 kcal/mol.¹⁷ The analogous reaction with benzene has an activation energy of 9.2 kcal/mol,¹⁸ but one would expect a lower E_a for reaction 6. Methyl bromide absorption at 2537 Å also results in methyl radical production¹⁵ and in the subsequent hydrogen atom abstraction from the borazine yielding methane. *B*-Monomethylborazine, a result of CH₃ substitution, has not been observed as a product of the photochemical reaction of borazine and methyl bromide. On the other hand, the observed *B*-mono- and *B*-dibromoborazine at excess CH₃Br would result from bromine

atom reaction and substitution on the borazine ring. This difference in behavior between the CH₃ and Br radicals may be due to the more electronegative nature of the latter.

Acknowledgment. We are grateful for support by the Army Research Office—Durham and the Advanced Research Projects Agency through the Materials Science Center, Cornell University.

(17) M. P. Nadler, Ph.D. Thesis, Cornell University, 1969.

(18) A. F. Trotman-Dickenson and E. W. R. Steacie, *J. Chem. Phys.*, **19**, 329 (1951).

COMMUNICATIONS TO THE EDITOR

On the Existence of a Spin-Forbidden Predissociation in the Mass Spectrum of Isocyanic Acid

Sir: In a recent paper,¹ Bogan and Hand suggested that the experimental data on the production of the ion HCO⁺ in the mass spectrum of isocyanic acid, HNCO, is adequately explained by a mechanism (1) which involves the formation of nitrogen atoms in the excited ²D state. This is contrasted with our suggestion² that the



fragmentation proceeds through a spin-forbidden predissociation (2), (2a) leading to ground state products.



Since the publication of our mechanism, Okabe³ has reported a value for the heat of formation of isocyanic acid which enables us to demonstrate directly that at threshold for the production of HCO⁺ there is not enough energy available for the nitrogen atoms to be formed in an excited state.

Using the appearance potential for HCO⁺ given by Bogan and Hand¹ and the heat of formation of HNCO of Okabe,³ we have for the heat of formation of the transition state leading to HCO⁺

$$\Delta H_f = \Delta H_f(\text{HNCO}) + \text{A.P.}(\text{HCO}^+) = 14.76 \text{ eV} = 340 \text{ kcal/mol}^{-1}$$

For the formation of the products HCO⁺(¹Σ) + N(²D), using the data $\Delta H_f(\text{HCO}^+) = 196 \text{ kcal/mol}^{-1}$ ⁴

and $\Delta H_f(\text{N}) = 113 \text{ kcal/mol}^{-1}$ ⁵

$$\Delta H_f(\text{doublet products}) = 376 \text{ kcal/mol}^{-1}$$

These products are, therefore, energetically inaccessible at threshold. The only products which can be formed are, as we suggested,² HCO⁺(¹Σ) + N(⁴S) + 0.5 eV with

$$\Delta H_f(\text{quartet products}) = 321 \text{ kcal/mol}^{-1}$$

Okabe's value for $\Delta H_f(\text{HNCO})$ is based on measurements of the threshold energy of incident photons for the production of fluorescing NH *c*¹Π. The photolysis products may be produced with some kinetic energy at threshold, so the calculated heat of formation is numerically an upper limit. The error, however, is unlikely to be more than a few kilocalories and its inclusion would not affect the validity of our conclusions.

In the thermochemical calculations outlined above we have used the value of A.P.(HCO⁺) given by Bogan and Hand. The difference between their value (15.76 eV) and that found by us (15.1–15.3 eV) may be attributed to the use of different standards to establish the energy scales. Bogan and Hand measure their appearance potentials relative to the ionization potential of argon and obtain a value for I.P.(HNCO) which is 0.55 eV higher than the photoelectron spectroscopic value. In our measurements we used the photoelectron spec-

(1) D. J. Bogan and C. W. Hand, *J. Phys. Chem.*, **75**, 1532 (1971).

(2) (a) C. G. Rowland, J. H. D. Eland, and C. J. Danby, *Chem. Commun.*, 1535 (1968); (b) C. G. Rowland, J. H. D. Eland, and C. J. Danby, *Int. J. Mass Spectrom. Ion Phys.*, **2**, 457 (1969).

(3) H. Okabe, *J. Chem. Phys.*, **53**, 3507 (1970).

(4) C. S. Mathews and P. Warneck, *ibid.*, **51**, 854 (1969).

(5) J. Himpan, *Z. Naturforsch.*, **11a**, 761 (1956).

troscopic ionization potential as a standard and thus avoided any errors due to contact potential differences. Any reduction in the value of A.P.(HCO⁺) used in the thermochemical calculation would reduce the heat of formation of the transition state leading to HCO⁺ and would reinforce our conclusion that the doublet process is inaccessible at threshold.

It may be anticipated that some doublet nitrogen atoms will be formed as the electron energy is raised above the thermodynamic threshold for the production of N²D. Such behavior has, for example, been observed in the photoionization mass spectrum of N₂O.⁶ It is difficult to estimate the relative importance of the doublet and quartet processes in the 70-eV spectrum of HNCO, but two pieces of experimental evidence indicate that most of the HCO⁺ ions in the high energy spectrum are produced by the same process as at threshold.

First, if most of the HCO⁺ ions in the high energy spectrum were produced together with doublet nitrogen atoms, the HCO⁺ ionization efficiency curve would show pronounced curvature in the region in which the doublet processes became energetically accessible. Bogan and Hand find no irregularities in their ionization efficiency curve and conclude that all the HCO⁺ ions have a single origin. Similarly, our own unpublished curves show no evidence of the onset of a higher probability process 2–3 eV above threshold.

The second piece of evidence comes from our work^{2b} on the kinetic energy distributions of the fragment ions. We found that the kinetic energy distribution in the center of mass coordinates for the production of HCO⁺ + N remained sharply peaked near 0.5 eV between threshold and 70 eV. If two different dissociation processes were involved, the kinetic energy distribution might be expected to show some variation with electron energy.

The structure of the ground state of HNCO⁺ is an interesting problem which merits separate attention. There is no evidence for the excitation of bending modes in the first band of the photoelectron spectrum of HNCO⁷ and the HNC angle must be of similar magnitude in the ground state of the ion and the neutral molecule (128°). Bogan and Hand have, however, carried out INDO calculations which indicate, contrary to the experimental evidence, that the ground state of the ion is more stable in the linear form. It is possible that the INDO calculations converge on the first excited state of the ion, formed by removal of an electron from an in-plane orbital which, to a first approximation, is a nitrogen atom lone pair. Bogan and Hand also find that the most stable form of doublet HNCO⁺ is cyclic and base their arguments in favor of the formation of doublet nitrogen atoms on the supposed existence of a stable, cyclic intermediate. Semiempirical methods such as INDO are, however, unreliable for determining the relative energies of cyclic and open-chain

ions. Sustmann, *et al.*,⁸ have found, for example, that because of some of the assumptions made in the calculations, such methods systematically favor the isomer displaying the greater connectivity. The stability of the cyclic structure for HNCO⁺ could only be considered as firmly established if it were supported by *ab initio* calculations.

(6) V. H. Dibeler, J. A. Walker, and S. K. Liston, *J. Res. Nat. Bur. Stand., Sect. A*, **71**, 371 (1967).

(7) J. H. D. Eland, *Phil. Trans. Roy. Soc. London, Ser. A*, **268**, 87 (1970).

(8) R. Sustmann, J. E. Williams, M. J. S. Dewar, L. C. Allen, and P. von R. Schleyer, *J. Amer. Chem. Soc.*, **91**, 5350 (1969).

THE PHYSICAL CHEMISTRY LABORATORY
UNIVERSITY OF OXFORD
OXFORD, ENGLAND

C. G. ROWLAND
J. H. D. ELAND
C. J. DANBY*

RECEIVED NOVEMBER 4, 1971

Electron Spin Resonance Evidence for the Photosensitized Dissociation of Hydrogen Molecules on Vanadium Oxide

Sir: Since Cario and Franck¹ demonstrated the photosensitization process in which electronic excitation energy is transferred from an excited Hg(³P₁) atom to a ground-state Tl atom, a large volume of research work has been devoted to the investigation of the so-called primary processes in photosensitized reactions.² Recently, in the course of our studies on the photodecomposition processes of simple molecules adsorbed on solid surfaces, we have found a new type of photosensitizer, namely, vanadium oxide and other transition metal oxides, and have presented evidence of the photosensitizing activities of these metal oxides for the formation of alkyl radicals from the corresponding alkyl hydrocarbons by irradiation with light of wavelength longer than 350 nm ($\lambda > 350$ nm) at 77°K.^{3,4} These results prompted us to search the photosensitizing activities of these metal oxides for the photodissociation of hydrogen molecules with light of longer wavelength at 77°K. For this purpose, the form of metal oxides dispersed on the surface of porous Vycor glass (abbreviated PVG(metal oxide)) is superior to others since the PVG transmits light of $\lambda > 220$ nm efficiently and, moreover, a bare surface part of the PVG(metal oxide) may provide trapping sites for the photodissociated hydrogen atoms which enable us to observe them by the esr method. In this report, we will pre-

(1) G. Cario and J. Franck, *Z. Phys.*, **11**, 161 (1922).

(2) J. G. Calvert and J. N. Pitts, Jr., "Photochemistry," Wiley, New York, N. Y., 1966.

(3) Y. Fujita, K. Hatano, M. Yanagita, T. Katsu, M. Sato, and T. Kwan, *Bull. Chem. Soc. Jap.*, **44**, 2884 (1971).

(4) T. Katsu, M. Yanagita, and Y. Fujita, *J. Phys. Chem.*, **75**, 4064 (1971).

Table I: Isotope Effect on the β -Proton Hyperfine Splitting of Ethyl Radicals

Radical	Method	Temp. °C	a_{α^H} or a_{α^D}		a_{β^H} or a_{β^D}		Ref
	<i>In situ</i> electron irradiation						
CH ₃ CH ₂	C ₂ H ₆	-180	22.38		26.87		
CHD ₂ CD ₂	C ₂ H ₆ + C ₂ D ₆	-175	(22.6) ^c	3.46	(25.2) ^c	3.88	a
					29.77		
CD ₃ CD ₂	C ₂ D ₆	-172	(22.6)	3.47	(26.6)	4.08	
	Photolysis on PVG(V ₂ O ₅)						
CH ₃ CH ₂	C ₂ H ₄ + H ₂	-195.8	21.5		26.7		
CH ₂ DCH ₂	C ₂ H ₄ + D ₂	-195.8	Unresolved ^d		(22.1)	3.4	b
					28.5		
CHD ₂ CD ₂	C ₂ D ₄ + H ₂	-195.8	(23.4)	3.6	(23.4)	3.6	
					30.4		
CD ₃ CD ₂	C ₂ D ₄ + D ₂	-195.8	(24.7)	3.8	(24.7)	3.8	

^a R. W. Fessenden and R. H. Schuler, *J. Chem. Phys.*, **39**, 2147 (1963). ^b This work. ^c The values in parentheses (a_{α^H} or a_{β^H}) were calculated from the values of a_{α^D} or a_{β^D} using the theoretical ratio of $a^H/a^D = \gamma^H/\gamma^D = 6.51$. ^d The $m_I = \pm 1$ lines for the two α protons are not resolved due to anisotropy line broadening.

sent esr evidence of the photodissociation of hydrogen molecules on the PVG(V₂O₅) surfaces with light of $\lambda > 350$ nm and the H atom scavenging experiment with preadsorbed ethylene molecules to demonstrate the photosensitized decomposition of hydrogen molecules on the surface of the PVG(V₂O₅) at 77°K.

Experimental methods are as follows. PVG rods (Corning code No. 7930, 4 mm in diameter, 1 cm in length, surface area 38 m²/sample) were immersed in aqueous solutions of various concentrations of ammonium metavanadate (NH₄VO₃) containing nitric acid to make up samples whose surface coverages of vanadium pentoxide range from 10⁻⁵ to 10⁻³. The surface coverage was estimated by assuming that the amount of the solution which entered into the pore volume of the PVG (25% by volume) was effective. A sample thus treated, after drying at 110°, was ignited at about 550° in air to convert the salt into an oxide, then oxidized again with oxygen and evacuated for 2 hr at 550° in a quartz sample tube attached to a conventional high-vacuum system. After a tenth of the monolayer amount of hydrogen molecules was introduced into the sample tube at room temperature, irradiation was carried out at 77°K directly in a dewar vessel inserted in the cavity of an esr apparatus. The light from an ultra-high-pressure mercury lamp (USH-500D, Ushio Electric Ltd.) transmitted through a Pyrex or a UV-35 glass filter (Toshiba Electric Co., Ltd., effective wavelength is longer than 320 or 350 nm, respectively) was used. ESR spectra were recorded at 77°K with a JEOL P-10 spectrometer (X-band, 100-KHz field modulation).

The esr signal of hydrogen atoms grew with irradiation time with light of $\lambda > 350$ nm in the H₂-PVG(V₂O₅) system at 77°K. Thus trapped hydrogen atoms exhibited a well-known characteristic doublet signal.

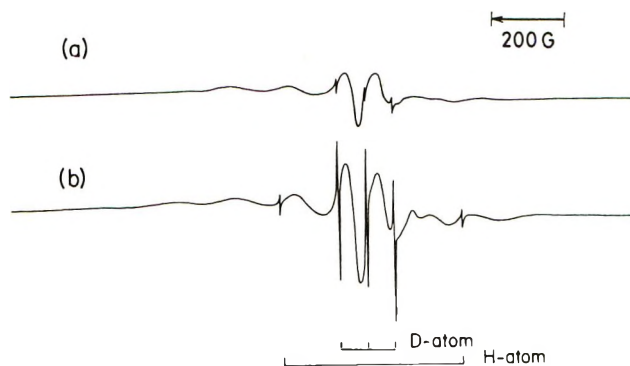


Figure 1. ESR signals of the system of D₂-PVG(V₂O₅) at 77°K after the irradiation with (a) light of $\lambda > 320$ nm for 20 min and (b) full light of a low-pressure mercury lamp for 5 min.

On the other hand, the system of a well-degassed PVG without hydrogen molecules also exhibited a relatively large H atom signal when irradiated with a low-pressure mercury lamp. The latter hydrogen atoms are considered to be the ones trapped on the surface of PVG which were produced by the photolysis of silanol groups under energetic irradiation. This was confirmed by the result that a relatively large H atom signal was observed even in the D₂-PVG(V₂O₅) system under irradiation with a low-pressure mercury lamp at 77°K (Figure 1b). To reject such a possibility that the silanol groups are photolyzed with light of low energy through an energy transfer process from V₂O₅ sites where photons are absorbed to remote silanol groups, the D₂-PVG(V₂O₅) system was studied under irradiation with light of $\lambda > 320$ nm. Accordingly, the D atom signal shown in Figure 1a was observed in place of the H atom signal. Under the photosensitization condition, the distinct esr signal of V⁴⁺ was observed along with that of hydrogen (or deuterium)

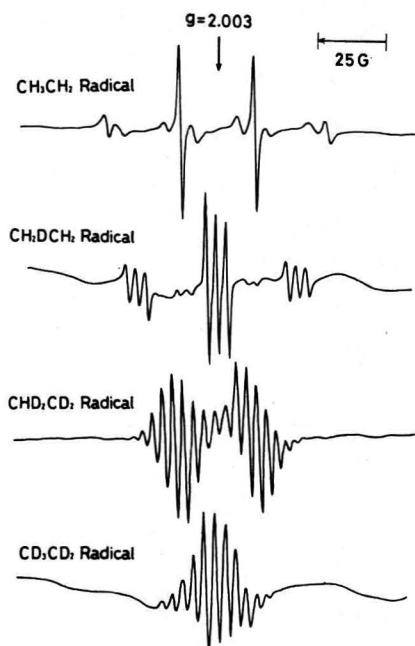


Figure 2. ESR signals of variously deuterated ethyl radicals trapped on the surface of PVG(V_2O_5) at 77°K.

atoms, increasing its intensity with irradiation time. This result implies that a large number of hydrogen atoms react with V_2O_5 to reduce V^{5+} into V^{4+} and a limited number of them are able to migrate to the trapping sites on the PVG surface decreasing rapidly in their numbers on the way by the recombination process. Consequently, it appears that only a small number of hydrogen atoms were trapped on the surface of PVG; in other words, the surface traps on the PVG were not so efficient for the hydrogen atom trapping. Therefore, we tried a "spin-trapping" method to stabilize the hydrogen atoms more efficiently using ethylene molecules as a scavenger and changing them into ethyl radicals which are well known to be trapped effectively on the surface of the PVG at 77°K.⁴ It was confirmed beforehand that ethylene molecules adsorbed alone on the PVG(V_2O_5) were not photosensitized with light of $\lambda > 320$ nm. In the coexistence of hydrogen and ethylene molecules on the surface, the photoproducted hydrogen atoms were stabilized as ethyl radicals as shown in Figure 2. By the combination of H_2 or D_2 molecules with C_2H_4 or C_2D_4 molecules, respectively, we could trap various ethyl radicals, namely, CH_3CH_2 , CH_2DCH_2 , CHD_2CD_2 , and CD_3CD_2 radicals shown in Figure 2. It is very interesting that the isotope effect in the β -proton hyperfine splitting was observed as in the case of ethyl radicals in liquid phases.⁵ With an increase of D atom substitution into the methyl group, the β -proton hyperfine splitting constant, a_β^H , was increased considerably notwithstanding a small change in a_β^D , as may easily be seen in Table I. This isotope effect may be interpreted by the postulate that an anisotropic averaging occurs

over the internal rotation with preferential orientation of the p orbital coplanar with the C-H bond. A similar β -proton isotope effect has also been observed in methylamino radicals photoproducted from variously deuterated methylamines adsorbed on the PVG surface.⁶

The above results clearly show that hydrogen molecules are photodissociated on the surface of vanadium oxide with light of $\lambda > 350$ nm, and this is the first time that the photosensitizing activity of the metal oxide, such as V_2O_5 , for the dissociation of hydrogen molecules has been confirmed.

Acknowledgment. The authors wish to express their thanks to Professor J. Turkevich of Princeton University for his gift of the porous Vycor glass rods used in this study.

(5) R. W. Fessenden and R. H. Schuler, *J. Chem. Phys.*, **39**, 2147 (1963).

(6) K. Hatano and Y. Fujita, to be submitted for publication; presented at the 24th Annual Meeting of the Chemical Society of Japan, Osaka, 1971, Paper No. 14411.

FACULTY OF PHARMACEUTICAL SCIENCES
THE UNIVERSITY OF TOKYO
HONGO, BUNKYO-KU, TOKYO, JAPAN

TAKASHI KATSU
MITSUO SATO
YUZABURO FUJITA*

RECEIVED APRIL 17, 1972

Hot-Atom Reactions of Iodine in the Liquid Phase Induced by X-Ray Resonance Absorption¹

Sir: The generation of energetic ions as a consequence of X-irradiation of gaseous molecules has been observed by Carlson and White.^{2,3} They established that activation occurs as the consequence of mutual coulombic repulsion of the constituent atoms following the ejection of Auger electrons in a vacancy cascade, the latter being initiated by resonance absorption of X-ray quanta in an inner electronic shell of a heavy atom in the affected molecule. When gaseous methyl iodide was irradiated, iodine, carbon, and hydrogen ions with energies of up to 25, 73, and 31 eV, respectively, were generated. However, Carlson and White were not concerned with the subsequent chemical fate of the energetic species, nor have these investigations been extended to studies in the condensed phases.

We are now reporting evidence for hot-atom reactions of iodine following low-energy X-irradiation of liquid iodobenzene. Samples of iodobenzene were

(1) This investigation was supported in part by Grant No. AT(11-1) 1728 from the U. S. Atomic Energy Commission.

(2) T. A. Carlson and R. M. White in "Chemical Effects of Nuclear Transformations," Vol. 1, International Atomic Energy Agency, Vienna, 1965, pp 23-33.

(3) (a) T. A. Carlson and R. M. White, *J. Chem. Phys.*, **44**, 4510 (1966); (b) *ibid.*, **48**, 5191 (1968).

purified by preparative gas chromatography and irradiated using a GE CA-7 X-ray tube with a 20-in. thick beryllium window, at the tube currents and voltages indicated. The samples were analyzed by gas-liquid chromatography.

The product spectrum generated upon X-irradiation of a degassed sample of liquid iodobenzene consisted of the following compounds, listed here in the order of emergence from an SE-30 gas chromatographic column: benzene, iodine, iodobenzene, the *o*-, *m*-, and *p*-diiodobenzenes, biphenyl, and the *o*-, *m*-, and *p*-iodobiphenyls. Upon irradiation in the presence of air, phenol was found as an additional product. No other peaks were observed. No change in the product spectrum was found when a 4.7 mol % solution of iodine in iodobenzene was irradiated instead of pure iodobenzene. No products whatever were found, within the limits of our detection method, upon irradiation of a 2.1 mol % solution of iodine in benzene at 40 keV with a dose of 1.4 Mrads.

The yields of the isomers of diiodobenzene are given in Table I for a dose of 1.18 Mrads at 45 keV, while Table II shows the yield of benzene at increasing values of maximum photon energy and total dose.

Table I: Yields of Diiodobenzenes from Sealed Capillary Irradiations of Iodobenzene with X-Rays of $E_{\max} = 45$ keV^a

Yield, mol $\times 10^3$ / mol of iodobenzene	Diiodobenzene		
	Ortho	Meta	Para
	1.53	1.31	0.58

^a Tube current 12 mA, radiation dose 1.18 Mrads (irradiation time 10 hr).

Table II: Yield of Benzene from X-Irradiation of Iodobenzene as a Function of Maximum Photon Energy^a

Tube voltage, keV	Tube current, mA	Radiation dose, Mrads	Mol of benzene $\times 10^4$ /mol of iodobenzene \times Mrad
25	22	0.51	3.88
30	19	0.82	3.31
33.5	17	1.01	4.93
35	16	1.13	3.62
40	14	1.45	4.23
45	12	1.75	3.79

^a Irradiation time 15 hr.

Kazanjian and Libby⁴ argue that they have demonstrated, in the *n*-propyl bromide system, the equivalence of nuclear recoil activation and Auger activation, the latter initiated by isomeric transition rather than by X-ray resonance absorption. They found identical results for (*n*, γ) and isomeric transition processes in condensed media, although the recoil energies involved

in both processes are not the same. They pointed out that the charge developed by the Auger process following internal conversion caused the molecule to explode and gives a neutral recoiling atom, neutralization after bond rupture being rapid in the solid and liquid. This assumption of rapid neutralization will be used implicitly by us, though one cannot rule out the possibility that a fraction of the observed products might have been formed in ion-molecule reactions, as observed in the ¹²⁸I-CH₄ system by Rack and Gordus,⁵ and considered a possibility in the ¹²⁸I-pentene systems by Ayres, *et al.*⁶

Two primary reactions of hot iodine atoms can be visualized: (a) reaction with a neighboring iodobenzene molecule, leading to one of the isomeric diiodobenzenes through substitution of a hydrogen atom, and (b) reentry into the parent molecule. The product of the latter reaction is, of course, indistinguishable from the parent compound. Once the energy of the iodine atoms has by collisions been moderated to a few eV, recombination or abstraction of iodine from iodobenzene to form molecular iodine becomes a more probable process.

We considered carrying out scavenger experiments to decide whether at least a fraction of the diiodobenzene found by us has been formed in hot reactions. However, our system is already exhaustively scavenged by the iodine produced during irradiation, as shown by the fact that we observed no change in the product spectrum when we irradiated a solution of iodine in iodobenzene instead of pure iodobenzene. The fact that no products whatever, and specifically no iodobenzene, were observed within the limits of our detection method when we irradiated a solution of iodine in benzene, indicates a low level of background radiation damage in our system at the doses used by us. We believe that the best argument for a hot mechanism of diiodobenzene formation is based on the fact the isomeric diiodobenzenes are observed in the approximate statistically expected ratio of 2:2:1 for the ortho, meta, and para isomers (Table I). A similar distribution of the isomers has been observed by Berei and Stöcklin in the recoil iodination of chlorobenzene, using the ¹²⁷I(*n*,2*n*)¹²⁸I and ¹²⁷I(*n*, γ)¹²⁸I nuclear reactions.⁷ This is indicative of indiscriminate attack of energetic iodine atoms on iodobenzene molecules. Unfortunately, comparison of our results with those obtained in a published study of the γ -radiolysis of iodobenzene is not possible because in the latter work no separation of the isomers was attempted.⁸ In a more recent investigation using recoil activation in

(4) A. R. Kazanjian and W. F. Libby, *J. Chem. Phys.*, **42**, 2778 (1965).

(5) E. P. Rack and A. A. Gordus, *ibid.*, **34**, 1855 (1961).

(6) R. L. Ayres, O. C. Gadeken, and E. P. Rack, *J. Phys. Chem.*, **75**, 2880 (1971).

(7) K. Berei and G. Stöcklin, *Radiochim. Acta*, **15**, 39 (1971).

(8) S. U. Choi and J. E. Willard, *J. Phys. Chem.*, **66**, 1041 (1962).

iodobenzene, a radiochemical yield of 0.5 to 1.5% in the range of the paper chromatographic R_f values of the diiodobenzenes was ignored.⁹

To demonstrate that X-ray resonance absorption is indeed involved in the chemical events described, we have measured the yield of benzene, which we postulate to be a primary reaction product of the hot phenyl moiety remaining after Coulomb ejection of iodine from iodobenzene, as a function of maximum photon energy by varying the X-ray tube voltage. It is evident from Table II that there is a discontinuous increase in benzene yield beyond the iodine K absorption edge (33.16 keV). At 33.5 keV, the yield is higher than at 35 keV, despite a higher dose at the latter tube voltage. This is similar to the situation in the solid iodothyronines, where we have demonstrated a distinct resonance peak of the iodine yield.¹⁰

One might ask why iodobenzene, unlike methyl and ethyl iodide and tetramethyl lead in the gas phase,^{3b} does not disintegrate as the ultimate result of Auger electron emission. We have observed a similar resistance toward fragmentation with the crystalline thyroid hormones,⁹ and one might argue that perhaps in a condensed phase, intermolecular electron redistribution or deexcitation occurs fast enough to prevent disintegration. However, both iodobenzene and the iodothyronines resemble each other in that iodine is in each case attached to an aromatic ring, and the suggestion is reasonable that the observed tendency toward ejection of an iodine atom rather than fragmentation of the ring is caused by the buffering effect of the π -electron cloud of the conjugated system. To test this hypothesis, we have X-irradiated liquid iodocyclohexane, the non-resonance-stabilized analog of iodobenzene, and indeed observed fragmentation of the ring as evidenced by the appearance of ethyl iodide among the reaction products.

(9) D. H. Wheeler and E. Lecumberry, *Radiochim. Acta*, **14**, 119 (1970).

(10) E. M. Diefallah, L. Stelter, and B. Diehn, *Radiat. Res.*, **44**, 273 (1970).

DEPARTMENT OF CHEMISTRY
THE UNIVERSITY OF TOLEDO
TOLEDO, OHIO 43606

BODO DIEHN*
V. GEORGE THOMAS

RECEIVED MAY 17, 1972

Time-Dependent Scavenging of Trapped Electrons in 2-Methyltetrahydrofuran Glass at 77°K¹

Publication costs assisted by the U. S. Atomic Energy Commission

Sir: Exposure of a hydrocarbon glass at 77°K to ionizing radiation produces trapped electrons. The yield of such electrons is reduced by solutes which are electron scavengers. The fraction of electrons captured

by a given concentration of an electron scavenger at 1 μ sec after pulse radiolysis² is less than the fraction at minutes after γ irradiation,^{3,4} indicating that electrons which are physically trapped at the shorter time can transfer to scavenger molecules during the longer time.

We report here observations designed to observe directly this transfer in the interval from 1 msec to 1 min for electrons produced by flash photolysis of naphthalenide anions in 2-methyltetrahydrofuran (MTHF) glass containing $3 \times 10^{-2} M$ naphthalene at 87°K. The anions were generated by prior γ irradiation of the glass at 87°K. The sample, in a 10 cm long cylindrical cell, was immersed in liquid argon in a polyurethane foam box, with a conventional flash lamp suspended above it. The analyzing beam passed through evacuated end compartments on the cell.⁵ Liquid argon (87°K) was used as the coolant, rather than liquid nitrogen (77°K), in order to avoid cracking of the MTHF glass.

Figure 1 shows data from oscilloscope traces and a recorder trace ($t > 1$ sec) for absorbance of 1050-nm light (the e_t^- spectrum in MTHF peaks at ca. 1200 nm) measured by a silicon photodiode (Texas Instruments TIL57). Each trace is from a different flash, and the intensities of the flashes were not reproducible to better than ca. $\pm 10\%$. The traces for the various time scales do not match smoothly, but the shape of the decay curve on a given time scale was not significantly changed when reexamined after several flashes to observe other time scales. Beyond 100 sec, the electrons continue to decay, but good measurements were

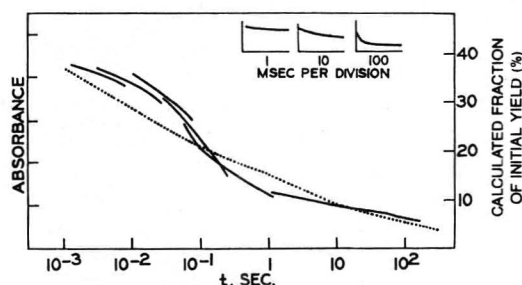


Figure 1. Decay of trapped electrons at 87°K in MTHF containing $3 \times 10^{-2} M$ naphthalene. Solid lines show oscilloscope traces (< 1 sec) and recorder trace (> 1 sec) of 1050-nm absorbance after 0.3 msec flash ionization of naphthalenide ions. Dotted line shows calculated decay (see text). "Initial yield" is defined as the yield in the absence of scavenger. Inserts show decay curves for times of 10 msec, 100 msec, and 1 sec.

(1) This work has been supported in part by U. S. Atomic Energy Commission Contract AT(11-1)-1715 and by the W. F. Vilas Trust of the University of Wisconsin.

(2) J. T. Richards and J. K. Thomas, *J. Chem. Phys.*, **53**, 218 (1970).

(3) J. B. Gallivan and W. H. Hamill, *ibid.*, **44**, 1279 (1966).

(4) J. R. Miller, *ibid.*, **56**, 5173 (1972).

(5) For a detailed description of the experimental procedures, see J. R. Miller, Ph.D. Thesis, University of Wisconsin, 1971.

not possible because of the inadequate long-term stability of the photodiode.

MTHF is a rigid glass at 87°K in which no trapped electron decay is observed from 1 min to 1 hr following γ irradiation unless electron scavengers are present.⁴ The decay observed here following flash photolysis of MTHF containing an electron scavenger and similar decays observed on the minutes time scale following γ irradiation⁴ are apparently due to reaction of trapped electrons with the scavenger *via* quantum mechanical tunneling over distances up to 35 Å. The unusual kinetics, in which similar absolute amounts of decay occur per order of magnitude change in time for several orders of magnitude, are expected for the tunneling process.⁴ By contrast substantially all of the decay for a process following first- or second-order kinetics would occur within two orders of magnitude change in time, as observed for trapped electrons in MTHF warmed to higher temperatures.⁶

A crude model for estimating the distance a trapped electron in MTHF can tunnel to react with an electron scavenger suggests this tunneling distance increases by 2.0 Å for each order of magnitude change in time, reaching about 40 Å at 5 min.⁴ Naphthalene used as an electron scavenger in γ -irradiation experiments^{5,7} gives results consistent with a capture radius of 33–35 Å. The dotted line in Figure 1 is calculated for a concentration of $3 \times 10^{-2} M$ scavenger assuming that

a trapped electron is captured if there is a scavenger molecule within a distance r , which increases by 2 Å per order of magnitude change in time, reaching 34 Å at 5 min.

In Figure 1 the experimental curve is normalized to the calculated curves at 1 msec. Since the method of producing trapped electrons by flash photolysis of a scavenger anion requires the presence of scavenger molecules, the initial yield of trapped electrons is not observable. The basic forms of the experimental and calculated decay curves in Figure 1 are similar, but the experimental curve shows some S-shaped character, which may be an experimental artifact or may be due to relaxation of the traps^{2,8,9} in a way to change the binding energies of the trapped electrons and distort the decay curve.

(6) F. S. Dainton and G. A. Salmon, *Proc. Roy Soc. Ser. A.*, **285**, 319 (1965).

(7) (a) J. P. Guarino, M. R. Ronayne, and W. H. Hamill, *Radiat. Res.*, **17**, 379 (1962); (b) M. R. Ronayne, J. P. Guarino, and W. H. Hamill, *J. Amer. Chem. Soc.*, **84**, 4230 (1962).

(8) L. Kevan, *J. Chem. Phys.*, **56**, 838 (1972).

(9) H. Hase, M. Noda, and T. Higashimura, *ibid.*, **54**, 2975 (1971).

DEPARTMENT OF CHEMISTRY
THE UNIVERSITY OF WISCONSIN
MADISON, WISCONSIN 53706

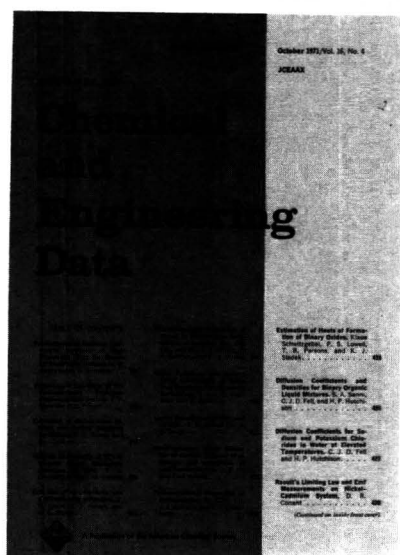
J. R. MILLER
JOHN E. WILLARD*

RECEIVED JUNE 14, 1972

There when you need them...

are the annual 700 pages of data published quarterly in the **Journal of Chemical & Engineering Data**

This American Chemical Society journal is especially valuable
in light of today's new instrumentation.



You'll find *four* clearly defined areas in JC & ED. They are:

- Experimental data relating to pure compounds or mixtures covering a range of states.
 - Manuscripts based on published experimental information, which make tangible contributions through the reorganization or systematic presentation of such data . . . or which set forth a well documented method of prediction of properties as a function of state.
 - Experimental data which aid in the identification or utilization of new organic or inorganic compounds.
 - Papers relating primarily to newly developed or novel synthesis of organic compounds and their properties.
- Sending for a subscription to the JOURNAL OF CHEMICAL & ENGINEERING DATA is so much easier than searching for data deposited in archives. Just fill in and return the form below. We'll do the rest.*

American Chemical Society / 1155 Sixteenth Street, N.W., Washington, D.C. 20036

Please enter my subscription to **The Journal of Chemical & Engineering Data** at the rates checked below.

ACS Members: U.S. \$15.00 Canada, PUAS \$18.00 Other Nations \$18.50
Nonmembers: U.S. \$45.00 Canada, PUAS \$48.00 Other Nations \$48.50

Bill me Bill employer Payment enclosed (Payable to American Chemical Society)

Name _____ Title _____

Employer _____

Address: Home Business _____

City _____ State/Country _____ Zip _____

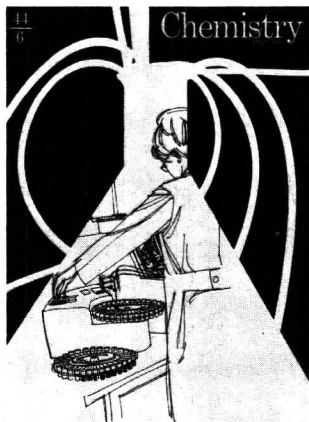
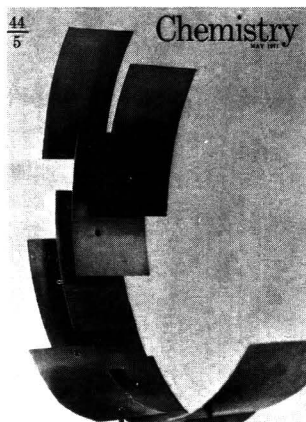
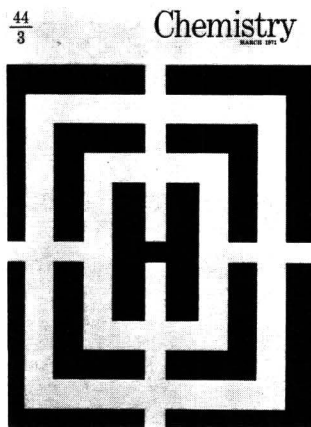
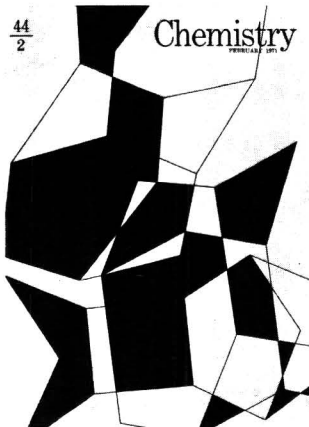
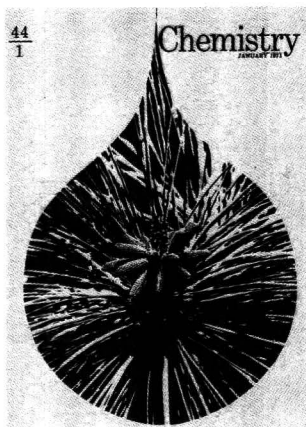
Nature of employer's business? Manufacturing or processing Academic Government
 Other _____

(Please indicate)

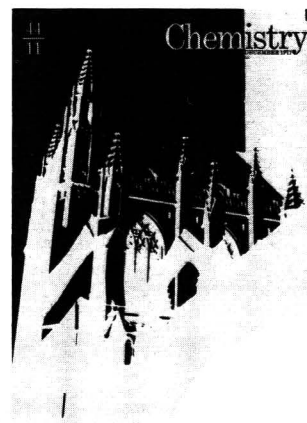
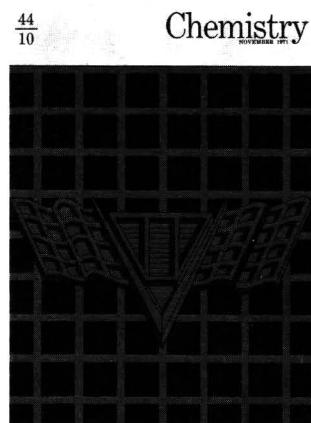
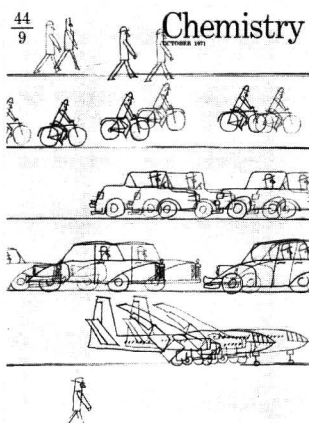
Note: Subscriptions at ACS Member Rates are for personal use only.

I am an ACS member I am not an ACS member

Payment must be made in U.S. currency, by international money order, UNESCO coupons, U.S. bank draft; or order through your book dealer.



*it's colorful
it's lively
it's appealing*



it's chemistry

Outstanding scientists broaden the student chemist's experience by sharing their knowledge with him. The latest research developments, biography, history and applied and theoretical chemistry are given new life in its relevant feature articles. Fill in the form below and mail today. You'll be glad you did!

American Chemical Society, 1155 16th Street, N.W., Washington, D.C. 20036

Please enter my one-year subscription for 11 issues of CHEMISTRY.

- U.S. \$6.00 **Canada & PUAS \$9.50
 **All Other Nations \$10.50 Bill me
 Payment enclosed (*Payable to the American Chemical Society*).

Notice: CHEMISTRY has a special group rate for ten or more subscriptions entered on a single order. If you wish to take advantage of this offer, please include all of the information requested above for each subscriber.

- U.S. \$4.50 each **Canada & PUAS \$8.00 each
 **All Other Nations \$9.00 each

Name _____

Address _____

City _____ State/Country _____ Zip _____

*NOTE: Subscriptions at ACS member rates are for personal use only.
 **Remit in U.S. funds, by international money order, UNESCO coupon, or draft on a U.S. bank; or order through your book dealer.